Characterization of physics-based mechanisms during ultrasonic fatigue loading based on analysis of higher harmonic generation

Shawn Kiser

HESAM UNIVERSITÉ

Arts et Métiers Sciences et Technologies

EÇOLE DOCTORALE SCIENCES ET METIERS DE L'INGENIEUR

Laboratoire Procédés et Ingénierie en Mécanique et Matériaux (**PIMM**)

Campus de **Paris, France**

THESE

Présentée par : **M. Shawn Lee KISER**

Soutenue le: 26 janvier 2025

Pour obtenir le titre de : **Docteur d'HESAM Université**

Préparée à : **Ecole Nationale Supérieure d'Arts et Métiers**

Spécialité : ingénierie mécanique

Characterization of physics-based mechanisms during ultrasonic fatigue loading based on analysis of higher harmonic generation

Thèse dirigée par :

M. Nicolas RANC

et **co**-encadrée par **:**

M. Marc RÉBILLAT
M. Mikhail GUSKOV

Jury

M. Renald BRENNER	Directeur de Recherche, Sorbonne Université	Président du jury
M. Rémy BOYER	Professeur, Université de Lille	Rapporteur
M. Jean-Yves BUFFIÈRE	Professeur, INSA Lyon	Rapporteur
M. Mikhail GUSKOV	Maître de Conférences, ENSAM	Encadrant
M. Marc RÉBILLAT	Maître de Conférences, ENSAM	Encadrant
M. Nicolas RANC	Professeur, ENSAM	Directeur de thèse

THÈSE

Abstract

Research into the very high cycle fatigue (VHCF) regime is made possible through the usage of ultrasonic fatigue tests, which can achieve billions of cycles in just a few days. However classical measurement and analysis are insensitive to microplasticity and/or damage (microcracks and microvoids), which eventually lead to fatigue failure. Consequently, these fatigue mechanisms are difficult to detect at early stages. However, the material nonlinearities may be sensitive to high-frequency loading and exhibit nonlinear behavior such as higher harmonic generation at multiples of the applied frequency. Thus, the standing wave vibration of the fatigue specimen is explored in the context of nonlinear harmonic generation.

The modeling of different nonlinear material phenomena is explored at their different length scales. Mesoscopic models of diffuse microplastic inclusions and microcracks are at a length scale of the same order as the vibration wavelength, and is attributed to be a potential source of harmonic generation. The multi-harmonic input given by the ultrasonic fatigue testing machine significantly influences the sensitivity and behavior of harmonic generation of the material nonlinearities. To address this, a multiscale fatigue specimen model which accompanies this boundary condition is employed. The experimental setup is modified to include an additional laser vibrometer to account for this effect. Accurate signal processing algorithms for the extraction of experimental harmonic parameters are benchmarked, and a new algorithm is developed for speed and accuracy. A non-convex penalty is introduced for data-driven sparse nonlinear system identification, surpassing existing state-of-the-art algorithms. Finally, the ultrasonic fatigue test vibration signals from copper and steel fatigue specimens in the VHCF regime are used to assess the multiscale model's ability to model the observed harmonic generation.

Keywords : Very high cycle fatigue, Higher harmonic generation, Micromechanics, Homogenization, Signal processing, Nonlinear dynamics, Optimization.

Résumé

La recherche sur le régime de fatigue à très haut cycle (VHCF) est rendue possible par l'utilisation d'essais de fatigue ultrasonore qui permettent d'atteindre en quelques jours des milliard de cycles. Les mesures et analyses classiques sont cependant limitées car peu sensibles à la microplasticité ou aux dommages (microfissures et microvides) qui conduisent finalement à la rupture par fatigue lors de ces essais. Ces mécanismes de fatigue sont donc en pratique difficiles à détecter expérimentalement à un stade précoce. Cependant, les dommages décrits précédemment peuvent présenter un comportement dynamique non linéaire qui peut être exploiter pour surveiller l'apparition d'endommagement par fatigue. Ainsi, les vibrations non-linéaires d'ondes stationnaires dans un l'échantillon de fatigue endommagé sont étudiées dans le contexte de la détection d'endommagement lors d'essais de fatigue ultrasonore.

La modélisation de différents phénomènes non linéaires est étudiée à différentes échelles spatiales. Les modèles mésoscopiques d'inclusions microplastiques diffuses et de microfissures se situent à une échelle de longueur du même ordre que la longueur d'onde de la vibration, et sont considérés comme une source potentielle de génération d'harmoniques. L'entrée multi-harmonique fournie par la machine d'essai de fatigue ultrasonique influence de manière significative la sensibilité et le comportement de la génération d'harmoniques des non-linéarités du spécimen. Pour y remédier, un modèle de spécimen de fatigue multi-échelle qui accompagne cette condition limite est utilisé. Le dispositif expérimental est modifié pour inclure un vibromètre laser supplémentaire afin de tenir compte de cet effet. Des algorithmes de traitement du signal permettant l'extraction des paramètres harmoniques expérimentaux sont comparés, et un nouvel algorithme est développé et sélectionné pour sa rapidité et sa précision. Une pénalité non convexe est introduite pour l'identification de systèmes non linéaires guidée par les données, surpassant les algorithmes de pointe existants. Enfin, les signaux de vibration des essais de fatigue par ultrasons des éprouvettes de fatigue en cuivre et en acier dans le régime VHCF sont utilisés pour évaluer la capacité du modèle multi-échelle à modéliser la génération d'harmoniques observée.

Mote-clé : Fatigue à très grand nombre de cycles, Génération d'harmoniques d'ordre élevé, Micromécanique, Homogénéisation, Traitement du signal, Dynamique non linéaire, Optimisation.

Table of Contents

List of Tables

List of Figures

Introduction

Context

The study of metallic fatigue dates back to the 19th century when engineers first noticed that metal structures subjected to repeated loading could fail at stress levels significantly lower than their tensile strength. Early research into metallic fatigue focused on understanding the mechanisms underlying this phenomenon. It was observed that fatigue failure typically involved the initiation and propagation of cracks within the material, often at stress concentrations in geometric or large defects. This led to fatigue design using experimental data from the fatigue life (S-N) curve, which represents the relationship between the stress amplitude and the number of cycles to failure. This approach continues to be a cornerstone of fatigue research in predicting the fatigue behavior of materials.

Previously, the shape of the S-N curve beyond 10^7 cycles has remained an uncertainty, where solicited stresses below an observed asymptote, i.e. the fatigue limit, assumed metals would endure an infinite number of load cycles without failing. However, the past two decades of literature as well as engineering failures in the past century have lead to the consensus that fatigue failure is regime dependent phenomena. The exploration of the fatigue behaviors greater than 10^7 cycles, the very high cycle fatigue (VHCF) regime, also known as gigacyclic fatigue, has thus been an academic and industrial focus for widely used metallic materials. This has led to the development and adoption of ultrasonic fatigue testing methods. Operating at $\approx$ 20 kHz, these machines significantly accelerate testing compared to hydraulic-based machines which operate at $\approx$ 10s Hz. Piezoelectric fatigue machines are highly reliable and capable of producing 10^{10} cycles in less than a week.

Many industries, from automotive to aerospace, deal with components that are subjected to fatigue cycles at VHCF regimes. These components must withstand these cycles without failure during their service life to ensure safety and reliability. In this context, fatigue research represents a small but crucial piece of in mechanical engineering. Ultrasonic fatigue testing, performed at high frequencies, has become de facto for practical and timely analysis in the literature. However, analysis *in-situ* characterization during these tests is challenging, leading to most research focusing on post-fatigue failure characterization. Classically, the time-history of a fatigue test is discarded, and instead the fatigue characterization is summarized at the moment of fatigue failure, i.e. a point on the S-N curve.

Problems and difficulties in the literature

Fatigue characterization is a broad term which refers to measuring or predicting the fatigue life of materials and falls mainly into two categories: post-fatigue failure and *in-situ* measurements. Post-fatigue measurements has largely been both experimentally and theoretically driven with the most popular methods characterizations being S-N curves or other observational-based methods such as microscopy/fractography, X-ray tomography, and electron backscatter diffraction (EBSD). *In-situ* measurements refer to data that can be acquired during fatigue tests, and can potentially be processed in real-time. These measurements vary depending on the frequency of the fatigue tests. For example, stress-strain evolution can be effectively monitored during low-frequency tests, but such measurements are not feasible in high-frequency scenarios. Conversely, vibration measurements are pertinent in high-frequency tests, but cannot be utilized effectively at low frequencies. Other techniques like acoustic monitoring and thermography offer other avenues exist and have been implemented in the literature.

One critical aspect of VHCF research involves the challenge of detecting and estimating the size of internal cracks, which are particularly common in certain material in the VHCF regime. The choice of experimental equipment used in VHCF tests can complicate their observation and measurement. This is compounded by the fact that the solicitation occurs at low stress amplitudes, resulting in slower crack growth rates not described well in conventional fracture mechanics. Thus, classical measurements and analysis are insensitive in the VHCF regime to microplasticity and/or damage phenomena (microcracks or microvoids), if any, occurring during fatigue loading. For example, the measured macroscopic stress-strain cycle is mistakenly assumed to be a straight line in an estimated stress-strain plot. If microplasticity precedes the emergence of microcracks, then a stress-strain hysteresis curve with a minuscule aperture should manifest prior to the damage onset. Yet, it remains uncertain whether such a phenomenon can be accurately measured. These combination of factors presents significant challenges in accurately identifying and characterizing internal crack initiation and propagation in VHCF environments. Therefore, a more reliable approach is needed for characterizing VHCF fatigue behavior during accelerated ultrasonic fatigue tests.

A promising direction lies in high-frequency *in-situ* measurements during fatigue tests, which often overlaps with methods found in non-destructive evaluation and acoustics. These frequency-based characterizations would not discard the time history of the tests, which would enable detailed monitoring and analysis of damage kinetics or internal crack growth rates during ultrasonic fatigue

tests. In the ultrasonic and acoustic literature, these frequency-based techniques have been shown to be sensitive to the wave interactions with material nonlinearities, resulting in nonlinear harmonic generation. The harmonics refer to sinusoids, where the fundamental harmonic refers to the sinusoid at the working frequency and higher harmonics refer to integer multiples of this fundamental.

The analysis of the fatigue specimen's tip harmonics in ultrasonic fatigue tests was first introduced by Kumar et al. [Kum+09]. In their work, the relative second harmonic versus first harmonic ratio (β_{rel}) was studied with respect to the number of cycles. This can be seen in Fig. 1 **(a)**, where the presence of the fundamental (20 kHz) and higher harmonics, and evolve during an ultrasonic fatigue test shown in in Fig. 1 **(b)**. Kumar et al. attempt to correlate the value of β_{rel} with the observed post-fatigue fractography. However, the source of the second (and higher) harmonic generation is not studied with respect to any underlying fatigue mechanisms such as microplasticity and/or damage.

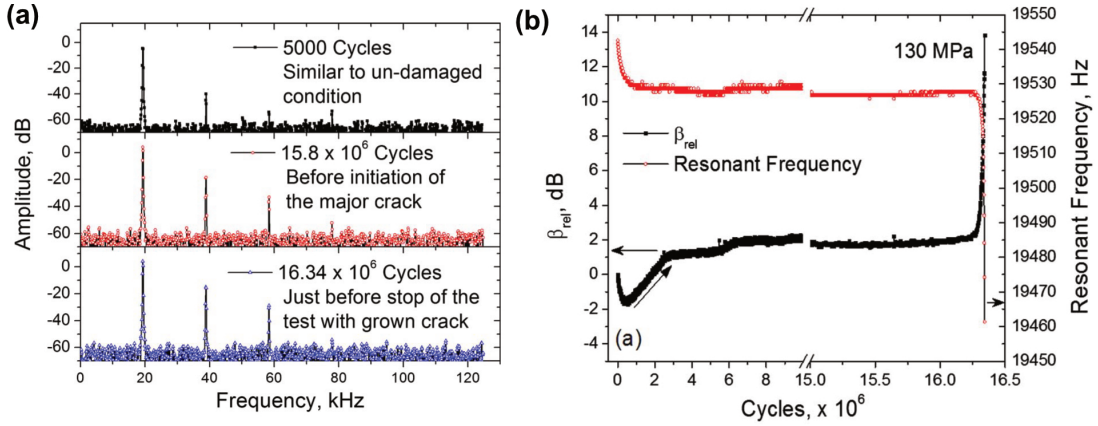

Figure 1: In **(a)**, the appearance of harmonics in the frequency spectra of vibration signals collected at various cycles during an ultrasonic fatigue test of 6061-T6511 Al alloy at 130 MPa. In **(b)**, the changes in β_{rel} and resonant frequency throughout the same ultrasonic fatigue test, taken from [Kum+09].

Objective of the dissertation

The primary objective of this dissertation is to develop a new *in-situ* methodology for estimating and interpreting the nonlinearities present during an ultrasonic fatigue test. Particularly, the detection of the onset of microplasticity, microcracks, in addition to macroscopic crack initiation and propagation. This detection is crucial as these fatigue mechanisms are suspected as the source of material nonlinearities which generate higher harmonics at multiples of the applied frequency. Such an *in-situ* characterization approach is particularly appealing, especially to determine if material behavior

throughout the fatigue test exhibits slow and fast nonlinearities depending on the material state. An attractive methodology would satisfy the following:

- A nonlinear dynamical model which integrates the nonlinearities of microcrack closure, microplastic behavior, and macroscopic crack development. This model should efficiently simulate the entire specimen's behavior under ultrasonic fatigue testing, characterized by tension-compression loads at high frequencies. Of such interest would be accurately representing the diffuse effects of mesoscale microplastic zones and microcrack closure. The goal is to facilitate the use of high-frequency vibration data *in-situ*, enabling the parameterization of a dynamic model that reflects the fatigue behaviors across the entire lifespan of the test.
- Suggest alternatives to the currently adopted signal processing algorithms used to analyze ultrasonic fatigue vibration signals. Specifically, those that are more accurate while maintaining a computational efficiency for real-time usage.

Using measured vibration data is one such data source that satisfies the requirements above and has shown promise in the literature: non-contact laser Doppler vibrometers allow for various experimental configurations, as well as usage along with other measurement methods (strain gauges, x-ray diffraction, thermography). To formulate a proper problem description to utilize the vibration data, it is necessary to derive and justify a dynamic model and the boundary conditions associated with the ultrasonic fatigue setup. This necessitates defining and optimizing the experimental setup to acquire the most reliable and precise data. Key considerations include the number and placement of measurement points, as well as the selection of an appropriate sampling frequency, all of which are critical for effectively using vibration data in a dynamic model. Successful implementation could lead towards an understanding of ultrasonic-based fatigue life mechanisms and predictions for materials.

Scientific approach

This dissertation adopts a methodical scientific approach, primarily focusing on the development and implementation of an experimental setup and corresponding nonlinear modeling techniques to investigate fatigue mechanisms. The methodology comprises three key components:

1. Development of an experimental device to measure velocity at various points on the specimen.

The measurement locations are strategically chosen to account for the nonlinear effects introduced by the testing machine.

2. Formulation of classical nonlinear models of fatigue mechanisms, integrated within a dynamic macroscopic model to accurately simulate the generation of harmonics under ultrasonic fatigue testing conditions.

3. Establishment of a signal processing methodology to precisely estimate the amplitude of the generated harmonics, essential for analyzing the fatigue test vibration data.

The experimental approach involves using a laser vibrometer to measure vibrations at the base and free tip of the fatigue specimen, allowing for the measurement of the harmonics. A multiscale nonlinear dynamical model is employed whose microcracks and microplastic inclusions are modeled using Mori-Tanaka mean-field homogenization [MT73] and Eshelby's inclusions [Esh57]. This modeling approach is represented in Fig. 2 , where the nonlinear behavior of microcracks and microplastic inclusions defined at the centroid.

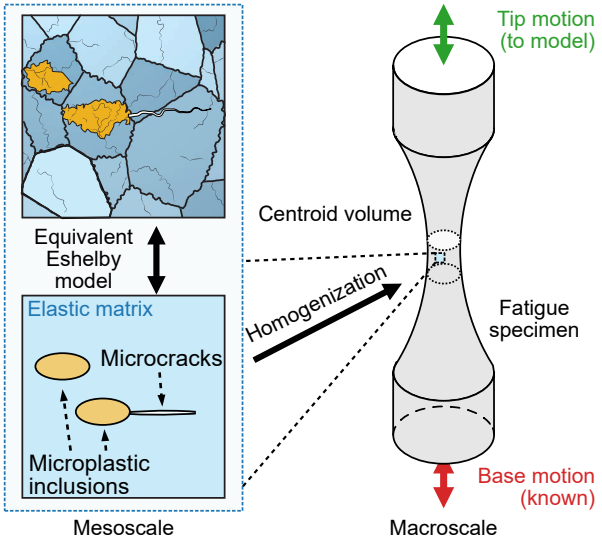

Figure 2: The proposed modeling approach taken in this dissertation.

Structure of the dissertation

The structure of this dissertation is designed to detail the proposed methodology and its theoretical justifications. Following this introduction, which sets the context and outlines the objectives, the thesis is divided into several chapters:

Chapter 1 provides a detailed literature review on the fatigue of metals, and the differences between fatigue behavior in the LCF to HCF and VHCF regimes and beyond. The juxtaposition between these two regimes are made in their experimental approach (hydraulic versus ultrasonic), the microstructural mechanisms, and finally the discrepancies found in the literature. The nonlinear harmonic generation due to fatigue micromechanical phenomena and the high-frequency vibration of ultrasonic fatigue is considered. The analysis of second harmonic generation due to nonlinear elasticity by Kumar et al. [Kum+09] is introduced, which has been adopted by the ultrasonic fatigue community. A departure from this parameter is suggested in the form of a micromechanical models. This lays the foundation for the contributions made by the dissertation in ultrasonic fatigue specimen modeling and the signal processing of vibration signals.

Chapter 2 is dedicated to the comprehensive modeling of an ultrasonic fatigue specimen and test machine to understand the harmonic generation seen in the vibration of the fatigue specimen. First, the harmonic generation due to length-scale material behaviors at different length scales are considered: starting from the atomic scale effects of nonlinear elasticity due to the crystal lattice; then the micro- to mesoscale effects that manifest from microcrack closures (damage) and microplastic mechanisms; finally the macroscale during the formation of a macroscopic crack. Next, a macroscopic model detailing the dynamic loading and structural aspects of an ultrasonic fatigue specimen, enabling the material nonlinearities effect on the specimen's dynamical behavior. Finally, an electrodynamical model of the ultrasonic fatigue test machine is calibrated, but experimental data uncovers small nonlinearities, evidenced by higher harmonics, challenging the notion of a single harmonic input wave in ultrasonic fatigue tests.

Chapter 3 is a dedicated chapter to inverse problems with a linearizable model described in vector-matrix form. This vector-matrix form arises in estimating sinusoidal parameters (harmonics) for signal processing. First, a benchmark of state-of-the-art algorithms are compared for usage in ultrasonic fatigue vibration signals. A classical, computationally expensive subspace algorithm is found to be the best suited, despite its high computational complexity. The next section introduces a novel estimation technique, which reduces its complexity from cubic to quasi-linear, enabling its real-time use for ultrasonic fatigue vibration signals. Finally, the last section introduces the problem of nonlinear system identification using a data-driven method, specifically the Sparse Identification of Nonlinear Dynamical systems [BPK16]. The goal here is to identify the

dynamic nonlinearities of a system, given the inputs and outputs a system. Here, an alternative optimization algorithm is proposed, by introduction of a non-convex penalty. It's shown that this non-convex penalty has a higher chance of identifying the true nonlinear system when the measurements are finite and noisy compared to those in literature.

Chapter 4 derives the model parameters that describe the harmonic generation of experimental tip vibration data for polycrystalline copper and C70 steel specimens. The model parameters correspond to the nonlinear mesoscopic response due to microcracks and microplastic inclusions and the contribution of the multi-harmonics at the base vibration. An analysis on the sensitivity of the model, as well as interpretation of the evolution of micromechanical parameters along the fatigue test are provided. It's suggested that the microcrack volume fraction is a consistent indicator of microcrack to macrocrack onset for polycrystalline copper, and that microplasticity tends to grow linearly. C70 steel, on the other hand, shows inconsistent results, possibly due to a lacking of harmonic amplitude increases in experimental data.

Chapter 1

Bibliography and preliminaries

Contents

The influence of material and fatigue regime on fatigue behavior is a well-established concept in the field of metallic fatigue. In this chapter, the mechanisms of plasticity in the low to high cycle fatigue fatigue are summarized, which has been established for metals that experience failures $< 10^7$ *cycles. The recent advances into very high cycle fatigue,* $> 10^7$ *cycles, has manifested literature of complex material mechanisms that challenge the applicability of classical fatigue theory. Three main challenges exist in this fatigue regime:* 1°*, the observation and characterization of the micromechanical phenomena leading to fatigue failure;* 2°*, the incorporation of micromechanical phenomena, e.g. dislocation dynamics or microplasticity models, into a fatigue specimen model;* 3°*, the discrepancy between ultrasonic fatigue test and conventional fatigue test data. This dissertation aims to exploit nonlinear vibration generated by localized phenomena during ultrasonic fatigue tests to address* 1° *the observation of microcracks and microplasticity using* 2° *a dynamic fatigue specimen model.*

1.1 Context

Fatigue research traces back to the mid-1800s with Wöhler's foundational approach for metals, considering key applications like railcar axles and steam engines. With engines operating around 50 cycles per minute, Wöhler defined the S-N curve, which allowed one to determine the number of cycles of a component before fracture. In short, Wöhler concluded that for a reliable mechanical part design, cyclic stress σ_a on a material is more crucial than peak stress from a monotonous applied load. Classical fatigue design for mechanical components has been based on this S-N curve for a conventional fatigue limit at a large number of cycles (10^7). If there is no failure until 10^7, conventional engineering standards consider that the structure will never break, i.e. an infinite fatigue limit [BP05].

In the most basic sense, fatigue damage in mechanical parts arises from repeated material deformation, resulting in microstructural changes. These changes often lead to crack formation. A fatigue crack, initially stemming from microscopic mechanisms, grows slowly and stably, as noted by Sir James Alfred Ewing in 1903 [BP05]. While these cracks may not pose an immediate threat, they can become critical once they reach a certain length, leading to rapid propagation and eventual component or structural failure. Despite the research into classical fatigue, fatigue failures have been shown to exist beyond this infinite fatigue limit. The current fatigue life of industrial and consumer transportation reaches the well beyond (10^9) cycles, while aircraft turbines approach 10^{10} cycles due to high rotation speeds. As recently as 2021, engine failures due to turbine blade fatigue failure have been featured in the news. Despite fail-safe measures designed into the Boeing aircraft, fatigue failure can still result

(a) (b)

Figure 1.1: In **(a)**, the inspection of a non-crashed Boeing 777-200 engine which suffered from turbine blade fatigue failure on United Airlines Flight 328, on Feb. 20, 2021. In **(b)**, a crashed Boeing 737-7H4 which suffered from turbine blade fatigue failure and killed a passenger on Southwest Airlines Flight 1380, on Apr. 17, 2018.

in lethal harm to passengers, see some recent aeronautic fatigue-related accidents shown in Fig. 1.1. Real-world loading conditions can differ from those assumed during fatigue design, potentially causing fatigue cracks. If there are existing non-propagating cracks, early detection is attractive and crucial in the structure's fatigue life. Regular maintenance can identify and monitor these cracks throughout the structure's lifespan. Hence, understanding a material's fatigue properties is essential, emphasizing the need to accurately determine the fatigue characteristics of metallic materials.

1.2 Bibliography of conventional and VHCF fatigue

1.2.1 Characterization of LCF to HCF regimes

For mechanical components made up of metallic crystalline materials, a precise definition of the concept of fatigue loading is needed. When mechanical components are in service, they experience variable loadings. To enable reproducible research for fatigue behaviors, fatigue is studied on the basis of cyclic tests carried out on servo-hydraulic machines or ultrasonic fatigue test machines, whose differences are later introduced. Based on the description by Wöhler [Wöh58], an imposed cyclic load is characterized by the amplitude of the stress $\sigma_a := \frac{\sigma_{max}-\sigma_{min}}{2}$, a mean stress $\sigma_m := \frac{\sigma_{max}+\sigma_{min}}{2}$ and the stress ratio $R := \frac{\sigma_{min}}{\sigma_{max}}$, where σ_{min} is the minimum stress and σ_{max} the maximum stress of a test. The speed of the cyclic load is defined by a working frequency of the loading f, see Fig. 1.2 **(a)**. Unless otherwise specified, the literature referenced within concerns tension-compression, alternating and symmetrical, of constant amplitude loading, that is i.e. $\sigma_m = 0$ and $R = -1$.

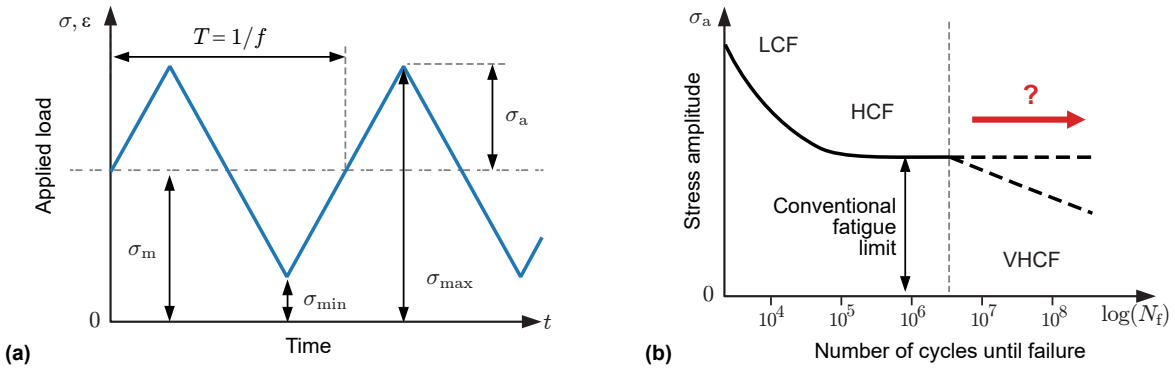

Figure 1.2: In **(a)**, the variables used to describe a constant strain rate loading, adapted from [Mug02]. In **(b)**, a classical schema of a S-N curve with different fatigue regimes.

Wöhler proposed a stress to life (S-N) curve to characterize material fatigue behavior, correlating

the logarithmic number of cycles to failure with stress amplitude [Wöh58]. The commonly used term, fatigue life, refers to the number of cycles N_f before failure. To obtain the S-N curve across different number of cycles, a staircase like testing campaign can be performed by varying the stress amplitudes per test [BP05]. On a classical S-N curve of Fig. 1.2 **(b)**, it can be seen that as the stress amplitude diminishes, the number of cycles until failure increases. These zones are categorized into three fatigue domains depending on stress amplitude:

- The low cycle fatigue (LCF) regime, where the number of cycles is less than 10^4. In this regime, the amplitude of stress is large enough such that the strain has a plastic component per cycle. Fatigue tests are typically conducted with constant stress amplitudes on hydraulic fatigue test machines.
- The high cycle fatigue (HCF) regime, where the number of cycles is from 10^4 to 10^7. In this range, the applied stress remains below the elastic limit, and at the start of the test, plastic deformations are localized in stress concentration zones (surface defects, microstructural heterogeneities). On average, plastic deformation amplitudes on a macroscopic scale remain small for each cycle. Fatigue tests are typically conducted with constant strain amplitudes.
- The very high cycle fatigue (VHCF) regime, where the number of cycles above 10^7 show an apparent fatigue limit as a horizontal asymptote on the S-N curve. In order to study this regime in a reasonable amount of time, an ultrasonic fatigue machine is utilized and to be detailed later.

The conventional fatigue limit, also referred to the endurance limit or fatigue strength, describes the amplitude of cyclic stress a material can withstand without fatigue failure after N_f cycles. Many fatigue standards suggest a horizontal asymptote between 10^6 and 10^7 cycles, and beyond 10^7 is considered to have infinite fatigue life. A characteristic of the regime change between LCF to HCF and VHCF can be observed from the failure mode of mechanical components, shown in Fig. 1.3. For the turbine blade fatigue failure in the Southwest Airlines Flight 1380 of Fig. 1.1, the failure was due to a sub-surface crack initiation, an example shown in Fig. 1.4. For United Airlines Flight 328, the cause was reported as an internal crack initiation which occurred in two previously incidents on PW4000-112 series engines with hollow-core fan blades. For LCF failures, cracks are typically initiated at the surface due to stress concentrations. These kinds of complex loadings have components of cyclic stress-induced plastic strain, which initiates cracks and continual tensile stress driving their growth.

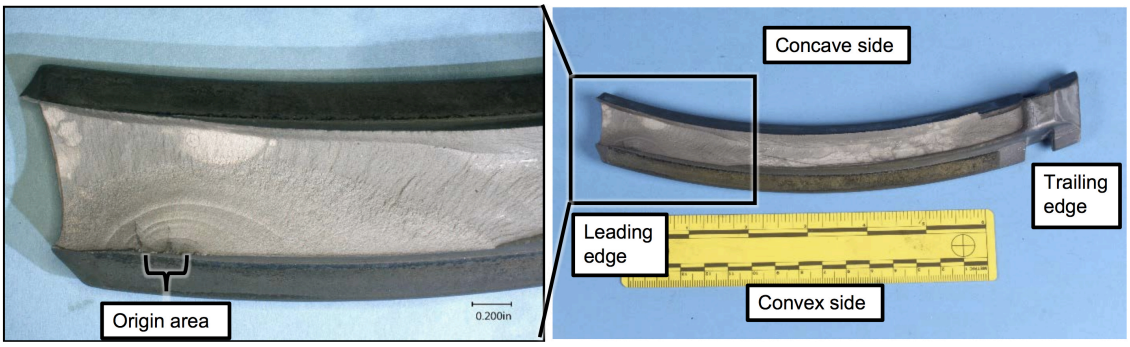

Figure 1.3: Surface fracture of the turbine blade fatigue failure of Southwest Airlines Flight 1380 with fatigue indications, taken from [Boa18].

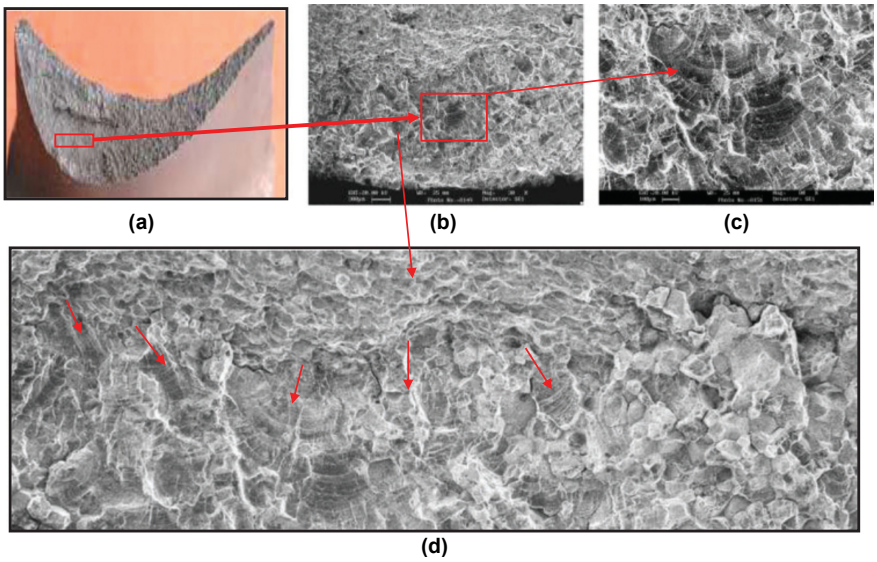

Figure 1.4: Sub-surface fracture due to fatigue failure of a turbine blade, showcasing **(a)** the fracture surface, **(b)** the fatigue crack origin, **(c)** a detailed view of fatigue striation and inside-to-outside crack propagation, and **(d)** the initiation of multiple cracks within the blade material, taken from [SSP16].

Stages of fatigue failure The consensus in fatigue research is that fatigue failure is not an instantaneous occurrence, but rather a progressive sequence of events. For ductile metals, four stages leading fatigue failure are schematized in Fig. 1.5: sequential stages of cyclic hardening or softening, fatigue damage evolution due to irreversible micromechanical phenomena, and crack initiation and growth leading to failure. For non-ductile metals, stages I and II are often not observed since pre-existing defects generally serve the role as stress concentrators at a smaller length-scale. These stages have been observed in numerous materials in the literature [LK73; Mug84]. Observations on the mechanism of stage I which lead to failure fatigue are thus of upmost importance.

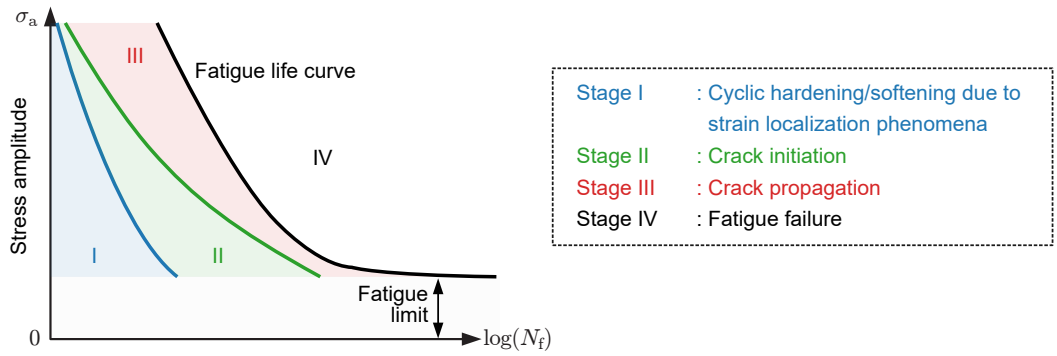

Figure 1.5: Schematic illustration of an S-N curve overlaid with the four stages of fatigue in ductile metals until failure. In the general case of non-ductile metals, stages I and II are typically absent since their failure are defect driven and act as pre-existing cracks, adapted from [Mug15].

1.2.2 Influence of microscale plastic deformation mechanisms

Depending on the material's initial state of the material, a phenomenon of cyclic softening or hardening can be observed. After a many cycles, the area of the hysteresis loop in a stress-strain diagram stabilizes, see Fig. 1.5. Point (1) corresponds to the LCF regime, where macroscopic plasticity behavior such as plastic shakedown are measurable during fatigue tests. As N_f increases, the aperture of the hysteresis loop decreases and therefore the plastic strain. At point (2), microscale plastic deformation mechanisms, is present. Before the VHCF regime at point (3), cyclic strain localization in Persistent Slip Bands (PSBs) lead to the onset of fatigue damage. Between points (2) and (3), the amount of plastic strain is minuscule but still measurable, around 10^{-5} - 10^{-4} in [LK73]. Point (4) corresponds to the case of an unbroken specimen, where seemingly macroscopic elastic behavior is observed beneath the fatigue limit. Mughrabi [Mug84] describes this as point as the irreversibility

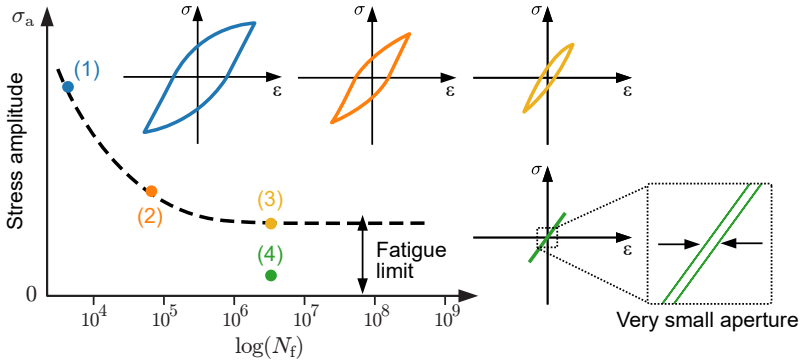

Figure 1.6: A schematized S-N curve with a fatigue limit drawn, where different indication of hysteresis loops are notated at different stress levels, adapted from [Mug84].

threshold of the cyclic slip, but this can be misinterpreted as if there is no form of dissipation under this threshold. Instead, it's posited that a macroscopic stress-strain measurement is unable to resolve the small aperture of the hysteresis, which is detailed further Section 1.2.3. In order to give this micromechanical argument, cyclic slip is described in the context of dislocations. This definition allows a study of the difference in HCF and VHCF regimes; the emergence of dislocation structures, e.g PSBs, will be given next.

Irreversibility of cyclic slip As defined by Mughrabi, the initiation of fatigue damage in ductile crystalline materials (stage I in Fig. 1.5) is deeply connected to cyclic slip irreversibility within the material's bulk, resulting in unreversed slip steps at the material surface [Mug13]. Slip irreversibility, $0 < p < 1$, is defined quantitatively as the ratio of microstructural irrecoverable plastic shear strain to the total plastic shear strain [Mug09; Mug13]. Here, the term irreversibility does not refer to a thermodynamical definition, but refers to permanent microstructural changes. A variety of microscopic mechanisms are responsible for cyclic slip irreversibility, including the cross slip of screw dislocations, mutual annihilation of dislocations, and slip asymmetry in body-centered cubic (BCC) metals, see [Mug09; Mug13] for an overview of these processes. The cyclic slip irreversibility is proportional to the loading amplitude, with lower loading amplitudes leading to higher fatigue life and vice versa [Mug09; Mug13]. Despite the challenges in estimating p for practical application, studying the irrecoverable nature of dislocation movements gives crucial insights into the microstructural mechanisms that trigger damage in the HCF and above [Mug09; Mug15]. The prevalence of these irreversibilities increases under certain stress conditions for various materials, linking them directly to the onset of the formation of dislocation structures, localization of the plastic strain in shear bands, and the formation of PSBs [BE79; Nab97; CKM11; MDK11; JR18].

Previously, it was suggested that at point (4) in Fig. 1.6 that there is irreversibility, contrary to the original figure by Mughrabi [Mug84], i.e. dislocation motion has an associated friction and is dissipated into heat. To understand this, consider a Frank-Read source: if the imposed shear stress on the slip plane is above the critical shear stress required to operate a Frank-Read source, a hysteresis loop should exist. When the shear stress is large enough to induce a dislocation ring, the phenomena becomes mechanically irrecoverable[1]. When these type of phenomena occurs within the bulk of the

[1]The term recoverable means that after one cycle the microstructure, or the dislocation configuration, is the same after one stress cycle. When the dislocation configuration is unable to return, it will be denoted as irrecoverability.

material, a hysteresis loop with a very small aperture must exist, with its aperture dependent on the density of such dislocation phenomena. Dislocations at low enough strain levels can be mechanically recoverable but irreversible and non-damaging, as proposed by Ranc in [Ran14].

Dislocation structures – persistent slip bands The parameterization of a plastic strain and its amplitude $\Delta\varepsilon_{\mathrm{pl}}$ describes the mechanisms at the grain scale of a material. These mechanisms are at the level of dislocations and the structures that emerge from their motion. To summarize: dislocations arise on slip planes, with the Frank-Read source serving as a perpetual generator of dislocation loops. These loops can accumulate into an avalanche on a single slip plane, with each loop countering the applied stress near the source. Once a sufficient number of loops emerge, the accumulation of dislocation loops promote multiple cross slip and generate an irreversibility of the cyclic slip. For polycrystalline metals, subsequent avalanches are delayed since loops encounter resistance at grain boundaries, necessitating a significant external stress increase for another avalanche.

PSBs are an example of well studied slip irreversibility in the HCF regime for pure materials. For commercial materials which are alloyed, the phenomena is more elusive. To isolate the number of factors in studying this phenomena, typically single crystal metals are studied, with single crystal copper being showcased here. Copper is well studied in terms of a given plastic strain amplitude $\Delta\varepsilon_{\mathrm{pl}}$. The stabilized plots of shear stress as a function of the plastic strain amplitude can be plotted to give a cyclic stress-strain curve. A compiled cyclic stress strain curve from [Li+11] is presented in Fig. 1.7, which transmission electron microscopy (TEM) observations of dislocation structures are also shown. Three specific domains are emphasized for copper according to resolved plastic strains (notated γ_{pl}):

- Region A of Fig. 1.7 is characterized by resolved plastic deformations of $\gamma_{\mathrm{pl,AB}} \lessapprox 6.0 \cdot 10^{-5}$. As plastic deformation amplitude escalates, screw dislocations initially tend to cancel each other out, while wedge dislocations form dipole aggregates of opposite signs. With continued cycling, these wedge dislocations aggregate further, leading to the formation of cylindrical, more stable, vein-type dislocation structures with diameters around $\approx \mu$m. These structures, based on the observation plane, manifest as either veins or patches. Surrounding these high dislocation density veins are channels with low dislocation densities, which allows easy motion of primarily screw dislocations. Fig. 1.8 **(a)** provides a schematic representation of dislocation organization within these veins, where dislocations structure minimizes the internal energy of the crystal.

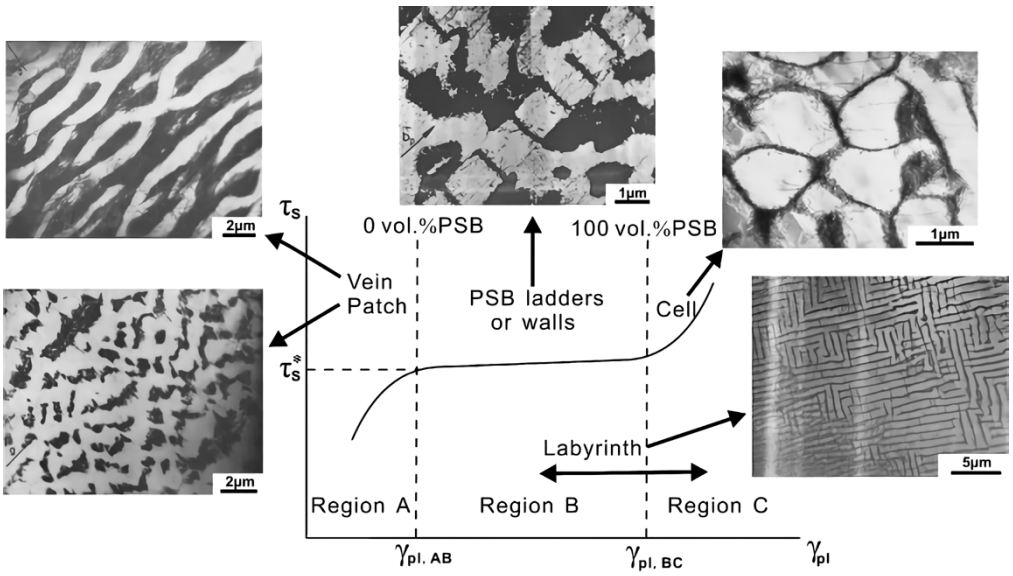

Figure 1.7: The cyclic stress-strain curve for a copper single crystal features three qualitative microstructures, with the threshold corresponding to the formation of PSBs, taken from [Li+11].

- Region B of Fig. 1.7 is characterized by resolved plastic deformations of $6.0 \cdot 10^{-5} \lessapprox \gamma_{\mathrm{pl,AB}} \lessapprox 7.5 \cdot 10^{-3}$. Notable is the horizontal asymptote where the stress amplitude is independent of the plastic deformation amplitude. With TEM, this region has the emergent dislocation ladder structure of PSBs, which expand upon loading and retract during unloading. Such formations are inherently more stable than the previously described veins configurations. In pure copper contexts, PSBs span $\approx \mu$m widths, while the thickness of the walls and inter-wall distances within a PSB vary between $1/10$ μm to 1 μm . Interesting patterns emerge due to the interaction between PSB zones and matrix regions (consisting of veins and channels structures) described as ladders and walls. The concentrated plastic deformation predominantly resides within the PSBs, which enables larger-scale deformation [DKS19].

- Region C of Fig. 1.7 is characterized by resolved plastic deformations of $\gamma_{\mathrm{pl,AB}} \gtrapprox 7.5 \cdot 10^{-3}$. Here, an augmentation in plastic strain amplitude is coincidental with a rise in stress amplitude. This domain is marked by the emergence of cell and labyrinth dislocation structures.

Once formed, PSBs can contribute to the emergence of intrusions and extrusions, see Fig. 1.8 **(b)**, which subsequently result in fatigue cracks. For polycrystalline copper, PSBs contribute to complex behaviors such as slip-band cracking in PSBs but also cause intergranular cracks, see Fig. 1.9 **(a)**.

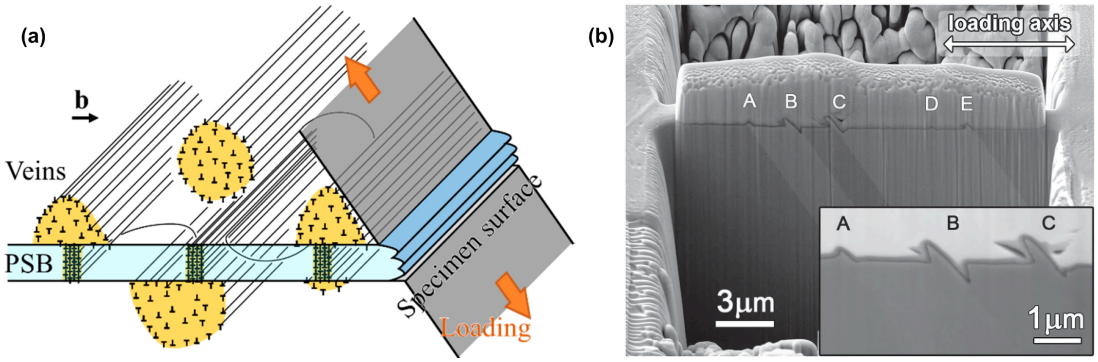

Figure 1.8: In **(a)**, an illustration of a PSB, vein structure, specimen surface, and the PSB's surface manifestation as intrusions, taken from [Dod+20]. In **(b)**, a side profile of a sliced polycrystalline copper specimen subject to 5000 cycles of $\gamma_{\text{pl}} = 7.5 \cdot 10^{-4}$, showing intrusions and extrusions, taken from [Pol+17].

For other materials, a brief review is given: Generally, face-centered cubic (FCC) metals manifest these dislocations as veins, shown in Fig. 1.8 **(a)**, that have identical Burgers vectors. The collapse of these veins along the primary slip direction leads to the formation of PSBs, as previously mentioned for pure copper. For alloyed metals, PSBs in such age-hardened alloys are much thinner (≈ 0.1 μm) [Mug84]. In BCC metals like α-iron, strain localizes in bands similar to PSBs, though these adopt a cell structure rather than the ladder structure [MAH79], see Region C in Fig. 1.7.

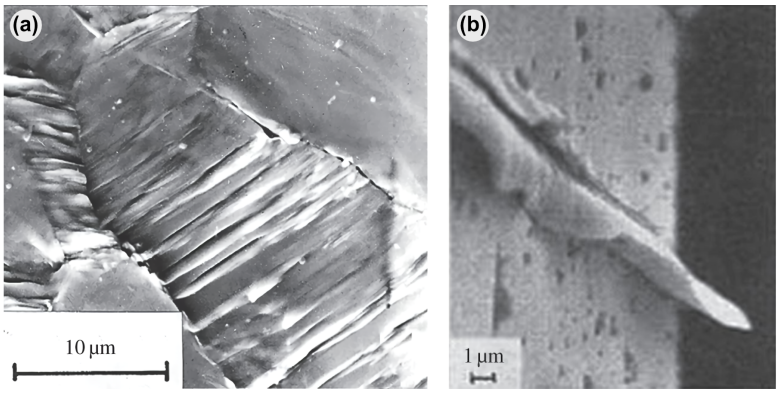

Figure 1.9: In **(a)**, intergranular mesocracks induced by PSBs colliding with the boundary of the grain of single crystal copper, close to the HCF limit, taken from [Mug+83]. In **(b)**, an extrusion on the surface of a copper single crystals in the HCF regime, taken from [Mug09].

Difference of fatigue mechanisms between HCF and VHCF regimes Since PSBs tend to form within a specified range of resolved plastic shear strain amplitude, the volume fraction of the PSBs linearly ranges from 0% to 100%. Changing the loading amplitude affects the PSB density and structure, with increased loading correlating to higher PSB density, as illustrated in Fig. 1.8. Consequently, the

loading amplitude is proportional to this PSB threshold and the aperture of the hysteresis loop at Fig. 1.6 point (3), corresponding with PSB formation over time. This raises the question: *what is the distinction between fatigue mechanisms at Region A and below Region A for copper of Fig. 1.7?* Or for all metallic materials, *what is the distinction between fatigue mechanisms at points (3) and (4) of Fig. 1.6?* These micro- to mesoscale observations of fatigue mechanisms for the LCF to HCF regimes have motivated the need to understand the fundamental mechanisms of fatigue in the VHCF regime.

1.2.3 Characterization of VHCF regimes

The need of accelerated fatigue test to reach the VHCF regime was proposed at the 1998 "EUROMECH 382 - Fatigue life in the gigacycle regime" conference in Paris. Experimental fatigue test results at ultrasonic frequencies were presented notably by Bathias [Bat99] and Stanzl-Tschegg [Sta99]. The most frequently employed device for these tests is the 20 kHz piezoelectric machine, shown in Fig. 1.10 **(a)**, derived from the work of by Manson in the 1950s [MB51]. These ultrasonic fatigue test machines accelerate fatigue tests, e.g. about 6 days for 10^{10} cycles, as shown in Fig. 1.10 **(b)**. These ultrasonic fatigue test machine differs with hydraulic-based fatigue test machines in a number of factors. The most critical is the method of applying the required stress amplitude to the fatigue specimen: these details will be relegated to Section 1.3.

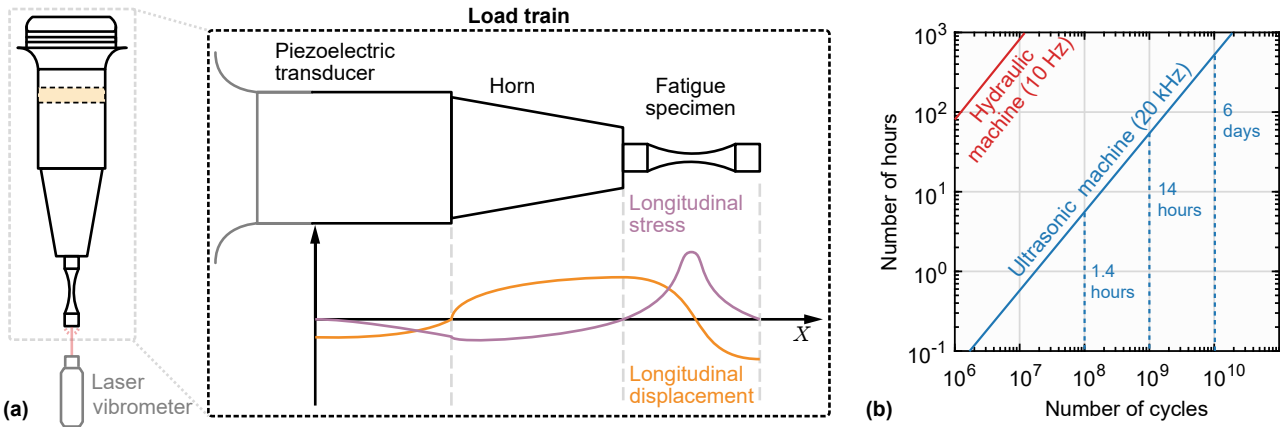

Figure 1.10: In **(a)**, a common ultrasonic fatigue test machine for $R = -1$. In **(b)**, a schema showing the duration to reach a number of cycles for conventional hydraulic and ultrasonic fatigue test machines.

Following the adoption of ultrasonic fatigue test machines, experimental data revealed that the underlying fatigue mechanisms were even more material specific. For example, materials with microstructural heterogeneities like inclusions as fatigue transitions from HCF to VHCF, failure origins

shift from the surface to interior fish-eye fractures at non-metallic inclusions. For ductile single-phase materials, research results becomes sparse due to the fact that the VHCF regime coincides with low stress amplitudes below the PSB threshold, and obvious PSB structures vanish. To aid in this distinction, Mughrabi [Mug02] introduces a classification of metallic materials according to their microstructure and mechanisms for crack initiation in the VHCF regime.

Type I materials These materials are typically ductile single-phase metals and alloys which do not contain precipitates nor inclusions, e.g. FCC metals. However, low carbon steels, some stainless steels, and spheroid graphite cast iron have similar behavior. Observations of the rupture face after VHCF reveal that the nucleation site for the source of failure occurs at the surface for Type I materials [Mug02].

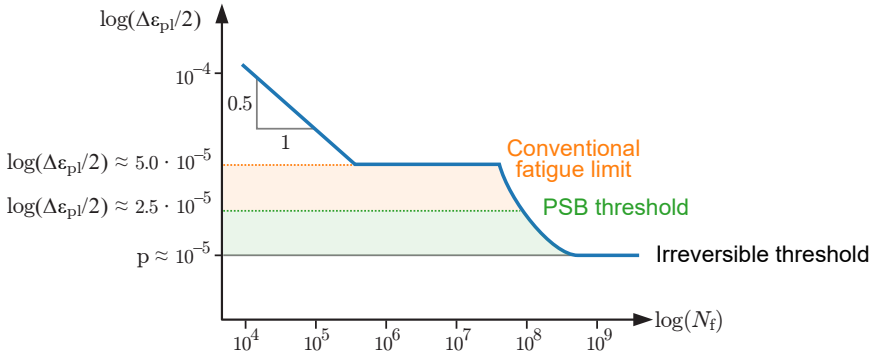

Figure 1.11: Evolution of strain amplitude as a function of the number of cycles in the case of Type I materials, such as pure polycrystalline copper, adapted from [Ran14]. The diagram illustrates the phenomena that PSB generation can occur below reduced a threshold stress and initiate microcracks, but the microcracks are non-propagating.

The research done on Type I materials has mainly focused on pure copper. Even beneath the traditional HCF PSB threshold, some level of surface roughening due to the irreversibility of the cyclic slip might slowly manifest after some number of high number of cycles, such as 10^9. This could lead to stress concentrations in the surface roughness, potentially instigating a form of persistent slip that might ultimately lead to shear fatigue crack initiation [Mug06]. This is schematized in Fig. 1.11 for fatigue crack initiations, where the traditional PSB threshold is shown in green.

Some model predictions have been confirmed through experimental work on ultrasonically fatigued copper polycrystals. Specifically, the gradual development of slip bands with an increasingly rough surface profile was observed at loading amplitudes well below the traditional HCF PSB threshold

[Mug06; Wei+10]. The cyclic slip irreversibility p can vary significantly, from around $p \approx 10^{-5}$ in the VHCF regime of copper with over 10^{10} cycles [Wei+10], to about $p \approx 10^{-1}$ within PSBs in the HCF regime of FCC metals [Mug09; Mug13]. In a study on a copper polycrystal subjected to 10^{10} cycles of fatigue [Wei+10], PSB-like cyclic slip localization are observed along with stage I crack initiation at the surface, shown in Fig. 1.12. It remains unclear whether these stage I cracks would remain non-propagating or eventually lead to failure. SEM on metallography cross-sections revealed localized slip in lamellae approximately 45° to the stress axis in Fig. 1.12 **(b)**. Meanwhile, imagery of cross-sections perpendicular to PSMs exhibited a roughness profile in Fig. 1.12 **(a)** resulting in a minuscule cyclic slip irreversibility $p \approx 3.6 \cdot 10^{-5}$ [Wei+10]. It's hypothesized that this irreversibility can eventually accumulate a substantial irreversible shear strain due to the vast number of cycles, resulting in fatigue damage similar to that observed after fewer cycles at higher loading amplitudes at the traditional HCF PSB threshold. This substantiates the concept of an effective reduction in the cyclic strain localization threshold in the VHCF regime.

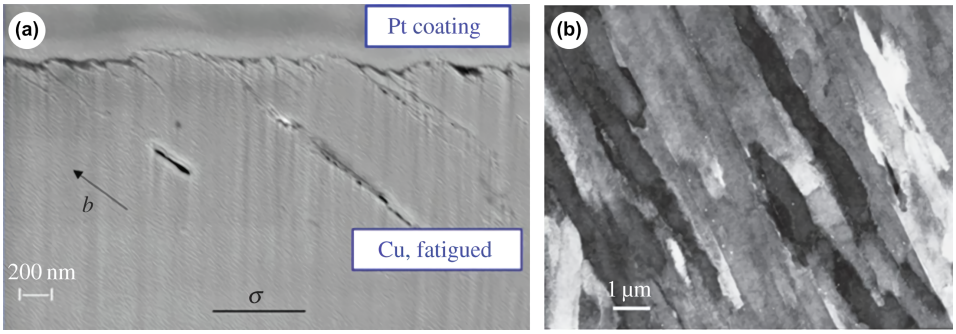

Figure 1.12: Ultrasonically fatigued polycrystalline copper subjected to 10^{10} cycles at room temperature, with stress applied horizontally to the image, slightly below the PSB threshold. In **(a)**, a surface roughness is shown, with subsurface shear cracks. In **(b)**, SEM imagery reveal lamellae of cyclic slip localization, taken from [Wei+10].

Type II materials These materials are metals and alloys with a more complex microstructure. They contain heterogeneities in the form of inclusions, pores, coarse second phase particles, which act as local stress concentrators for initiating internal fatigue crack sites. High strength steels are typical of this category [BP05; Wag+09], as are multiphase alloys, like Ti6Al4V. VHCF cracks start mainly in the volume of the test piece at the level of a defect or microstructural heterogeneity. It appears that the higher the ultimate tensile strength for type II materials, the steeper the S-N curve is in the VHCF regime.

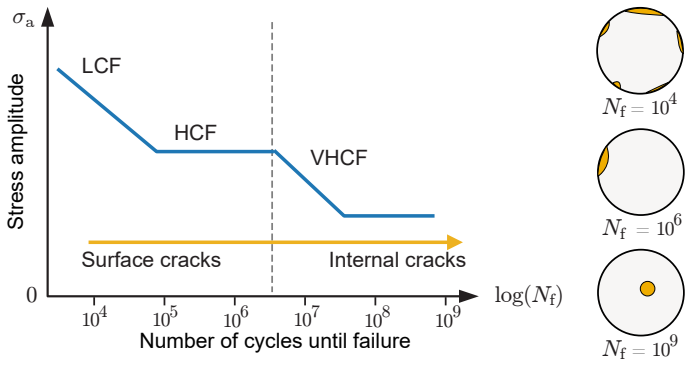

Figure 1.13: A schema of an S-N curve valid for type II materials, adapted from [Mug02] (left) and common fatigue crack initiation sites at the cross-section of a fatigue specimen (right).

Based on various researchers' findings [NK99], a multistage fatigue life diagram can be seen in Fig. 1.13, in which [Mug02] referenced a staggered S-N curve separating VHCF and LCF/HCF regimes. Along with the conventional HCF fatigue limit, a second, significantly lower fatigue limit appears in the VHCF regime. As the transition goes from HCF to VHCF, the mode of fatigue crack initiation shifts from surface to subsurface fish-eye cracking, originating from internal non-metallic inclusions. In [NP00], SEM imagery of a typical fish-eye failure is shown in Fig. 1.14. This subsurface fish-eye fracture can be understood as follows: at very low amplitudes, almost no fatigue damage forms on the surface. Conversely, in materials containing considerable defects like brittle inclusions or pores, cracks can initiate either on the surface or internally. In the absence of surface inclusions, internally initiated cracks can slowly grow outward until failure. Cracking may occur in the inclusion, at the interface, or due to the impingement of cyclic slip bands, as observed in [TM82].

Crack propagation A conceptual understanding of crack propagation for polycrystalline materials can be found in Fig. 1.15. The difficulty of a definition of crack propagation is not only limited due to the micro length-scale observations, but also the definition of the crack length at which initiation begins [SS10a]. One proposition is the inclusion of all stages of the cracking process into the initiation process until the crack is sufficiently large to have its propagation describable by classical linear elastic fracture mechanics (LEFM) [Mug06]. Another defines the transition as the shift from a system of microcracks, controlled by cyclic plastic strain, to crack propagation governed by LEFM [ASM96]. For a good overview of both type I and type II fatigue crack propagation and the role of specific microstructures of different materials, see [Cha10].

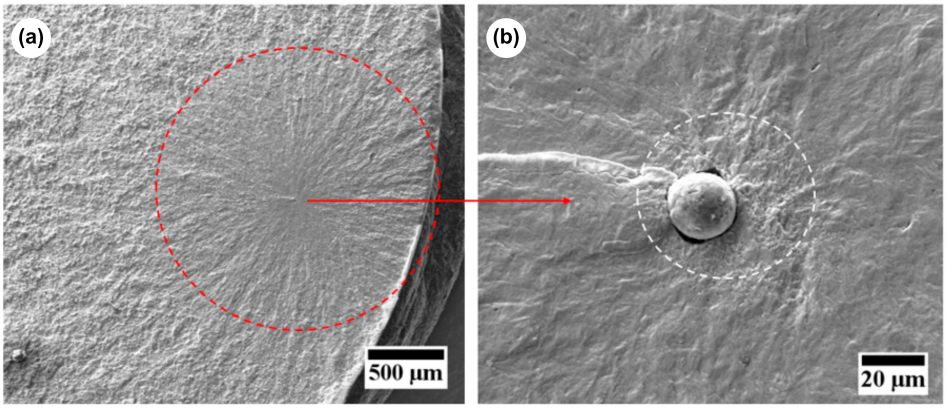

Figure 1.14: In **(a)**, the examination of the fracture surface of high-strength steel fatigue specimen displaying a fish-eye (circled in red). In **(b)**, the initiation of a crack at a non-metallic inclusion surrounded by a fine granular area (FGA) (highlighted by a white circle), taken from [KG22].

Even though these definitions may seem arbitrary, for some fatigue prediction models, it is critical to know when initiation ends and propagation begins, as well as what size and/or geometry constitutes a crack. For linear fracture mechanics, there is a distinction between stages II and III in Fig. 1.15 **(a)**: the crack-growth rates of short cracks are higher than those of long cracks Fig. 1.15 **(b)**. Short cracks grow and pass through grains (stage II), where stress and strain fields at the crack front are different from those calculated using the fracture mechanics approach in an isotropic continuum [CL87]. These cracks grow at stress intensities below the threshold value for long cracks. In the long crack regime, the growth in the threshold region is classically described using the Paris-Erdogan law [PE63].

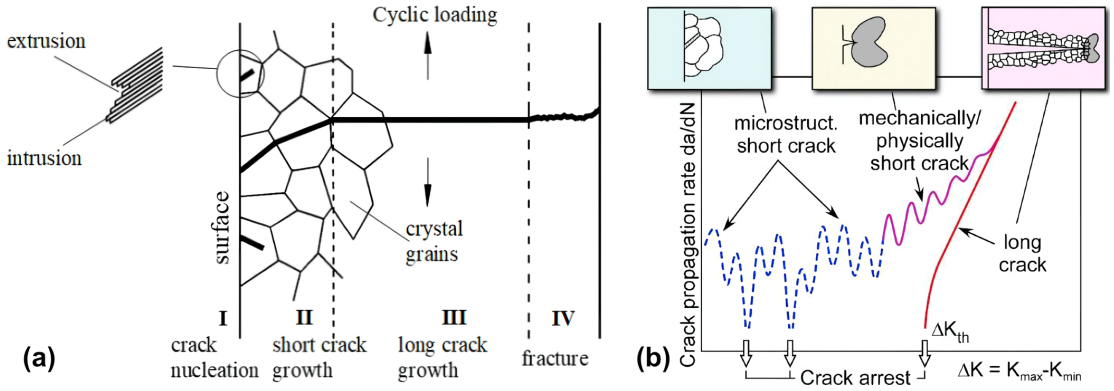

Figure 1.15: In **(a)**, the common stages of crack initiation to fatigue failure in polycrystalline metals, in this case with surface extrusions and intrusions, taken from [GA20]. In **(b)**, a schematic plot of the crack-growth rates of short and long cracks in LEFM, where ΔK the stress concentration factor, and ΔK_{th} the threshold that blunts crack growth, taken from [MZW22].

Lastly, the influence of environment before and after manufacturing materials plays a strong role in crack initiation and growth in fracture mechanic literature, where gaseous oxygen and hydrogen are most commonly focused on. In [Zha+18], oxygen presence in sintered samples influenced the oxide content in the microstructure. These oxide particles, identified as fatigue initiation zones, induce stress concentration and crack nucleation, consequently reducing fatigue life. In [Shi+21], a model addressing hydrogen-induced intergranular fatigue crack growth in steels and α-iron-based alloys is presented. The model posits that cyclic loading leads to hydrogen adsorption and dissociation at the crack tip, with accumulating dislocations transporting hydrogen to grain boundaries. This, combined with microvoid formation, intensifies intergranular failure compared to a hydrogen-free environment.

Ambiguities in identifying crack initiation The identification of when crack initiation and growth stages occur during ultrasonic fatigue tests is difficult to pinpoint (stages II and III in Fig. 1.5), especially at lower loading amplitudes. Especially at the VHCF regime, there are conflicting results on the significance of fatigue crack initiation and propagation periods in fatigue life. In early works for low-carbon steel in [Kle65], crack initiation was studied by comparing the S-N curve with the French curve[2] in Fig. 1.16. The French curve, representing the phase of crack propagation in the fatigue life, helps to highlight the shift in crack initiation as load decreases. The sizes of the initially formed microcracks varied, ranging from a few micrometers at stress levels beneath the French curve to approximately hundreds of micrometers above the French curve. Thus the works of [Kle65] indicate that crack initiation can constitute a major fraction of fatigue life in the HCF regime, noted by others with similar observations [KK00; Sur98].

However, in certain literature in LEFM claim that fatigue crack initiation is relatively insignificant, as materials inherently possess defects from which cracks will propagate right from the start, see [Mil84b]. Given that all materials inherently exhibit defects, one can argue that crack propagation begins from the outset. This has been observed for many commercial Type II materials with observed defects [Mug99; Wan+99; BP07; Mar+07] in the VHCF regimes. However, some outlier Type II materials which exist which reflect the complexities in fatigue. In recent research comparing low and high-frequency loading on DP600 steel by [Tor+17], it was observed for ultrasonic loadings, a significant number of microvoids nucleated and coalesced along slip bands. This process led to the

[2]The French curve represents a curve obtained at constant crack length, which makes it different from the Kitagawa-Takahashi diagram which was introduced in 1976 [BP05].

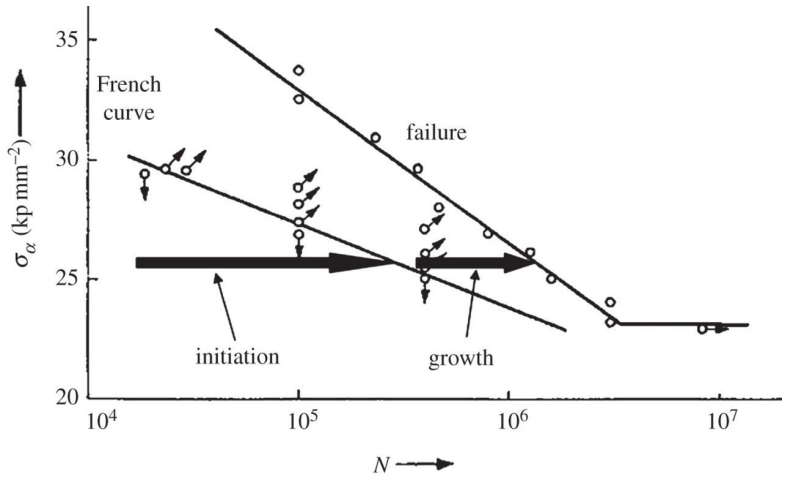

Figure 1.16: S-N and French curves for low-carbon steel, illustrating the increase in fatigue crack initiation range as the loading level decreases (1 kp·mm^{-2} = 9.81 MPa), taken from [KG22].

initiation of microcracks. These observations highlight the distinct mechanisms of crack initiation under different loading frequencies, challenging the conventional categorization by Mughrabi.

For Type I materials, the notion that crack propagation commences immediately from the start is also not substantiated, especially below the PSB threshold. In [Wei+10], stage I microcracks were only observed in polycrystalline copper after $1.59 \cdot 10^{10}$ cycles at 1.5 MPa below the PSB threshold, shown in Fig. 1.17. As elaborated by Stanzl-Tschegg et al. [SS10b], based on fracture mechanics measurements of threshold stress intensities for crack growth, stage I cracks would be considered non-propagating.

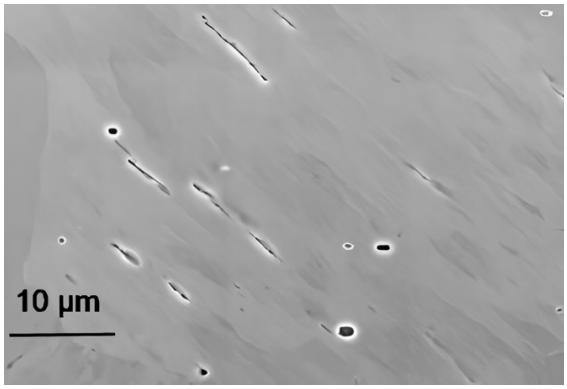

Figure 1.17: Intergranular microcracks (stage I) in copper after $1.59 \cdot 10^{10}$ cycles, taken from [Wei+10].

1.3 Ultrasonic fatigue experimental setup

1.3.1 Ultrasonic fatigue machine & fatigue specimen design

Understanding fatigue mechanisms in the VHCF regime necessitated the development of fatigue machines operating at higher frequencies. For ultrasonic fatigue test machines, the fatigue specimen is loaded at its first longitudinal vibration mode. For fully reversible uniaxial tests ($R = -1$), the fatigue specimen is fixed at an acoustic horn which amplifies the wave, and the opposite end is free to vibrate. The configuration used in this dissertation is shown in Fig. 1.18 **(a)**; the horizontal configuration is designed for use with X-ray diffraction instruments, see [Jac22]. In Fig. 1.18 **(b)**, the applied load to the fatigue specimen corresponds to a sinusoidal wave. This differs from the applied load for LCF to HCF regimes shown in Fig. 1.2: at larger stress amplitudes, a constant strain rates allow for the identification of the cyclic behavior (e.g. hysteresis) to develop differential material laws [LCS02]. The applied load in the ultrasonic tests instead prioritizes the number of cycles of failure, and the very slow stress evolution is a negligible effect [BP05].

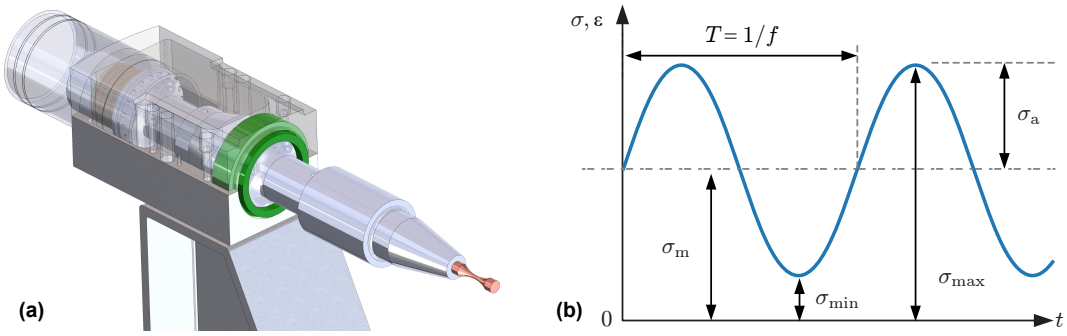

Figure 1.18: In **(a)**, an experimental setup of an ultrasonic fatigue test machine with a copper specimen with hourglass geometry. In **(b)**, the variables used to describe an applied sinusoidal load.

To obtain this applied load, the ultrasonic fatigue specimen must have its first longitudinal vibration mode at the working frequency of the ultrasonic fatigue test machine, ≈ 20 kHz. To design this, Bathias [BP05] suggests to first estimate the resonant frequency of the fatigue specimen with a linear one-dimensional wave propagation differential equation for a rod. A candidate specimen length is tuned, with known mass density and a dynamic modulus of elasticity, such that the desired resonance frequency is at the working frequency of the ultrasonic fatigue machine. Linear finite element harmonic analysis, under fixed-free boundary conditions with a known displacement, facilitates refinement of the

ultrasonic fatigue specimen's geometry based on desired resonance frequency and longitudinal stress [Jac+21]. Two geometries used in the dissertation are shown in Fig. 1.19, whose design ensures a Gaussian-like stress distribution along the longitudinal axis (see Fig. 1.10 **(a)**), with the peak stress at the centroid.

Figure 1.19: In **(a)** and **(b)**, a hourglass and a rectangular ultrasonic fatigue specimen, respectively.

The ultrasonic frequencies can be reached via a piezoelectric transducer that can transform a signal from the power generator into mechanical vibration. These are readily available by adapting industrial transducers for ultrasonic fatigue tests, e.g. from Branson [Bra] and Telsonic [AG]. Examples in the literature which discuss these ultrasonic fatigue machine and the design of a fatigue specimen can be found in [Bat06; May06; ILI20; Jac+21]. A more detailed working principle of the ultrasonic fatigue test machine is detailed in Chapter 2. Here, an electrodynamical model demonstrates the working frequency of the ultrasonic machine is controlled at the minimum voltage to current transfer function of the system. Additionally, the model predicts the acoustic horn's motion in response to applied voltage, facilitating an estimation of peak longitudinal stress for an attached fatigue specimen.

Ensuring the quality of VHCF tests necessitates the control of the applied stress load, e.g. when investigating fatigue behavior below the PSB threshold in Type I materials. Precise control of the vibration amplitude is pivotal to prevent a stress overshoot at the pulse onset, which would jeopardize test accuracy. To mitigate this, industrial generators employ a control circuit that gradually ascends to a desired voltage, further elaborated in Chapter 2. Additionally, ultrasonic fatigue test machines in the literature begin to deviate in applied loadings. The relationship between high-frequency loading and dissipation into heat at the centroid of the ultrasonic fatigue specimen can be problematic for certain material. Thus, two solutions are presented in the literature:

- A continuous, un-paused loading at ultrasonic frequencies is sustained, and continuous cooling counteracts self-heating phenomena, facilitated with VORTEC cold air guns, e.g. see in [Gor+23].
- To further mitigate the self-heating phenomena for ultrasonic fatigue tests, and intermittent

loading with paused time separations of $\approx 2 - 10$ seconds. This is done through another closed-loop control circuit that controls the time between two loading blocks [May06]. This also includes continuous cooling of the fatigue specimen.

Similarly to conventional fatigue tests, variations of the ultrasonic fatigue test machine enable research into fatigue behavior closer to real-life conditions. For instance, sustained high temperatures create conditions that are more conducive to diffusion mechanisms within the material, as discussed in [Ava+22]. Additionally, the load ratio R significantly influences crack-tip plasticity, which in turn affects the fatigue crack growth rates in Stages I and III more than in Stage II, as depicted in Fig. 1.15. The former is facilitated by the usage of an induction coil around the ultrasonic fatigue specimen. The latter requires the ultrasonic specimen to be fixed-fixed so that a mean stress can be applied, usually by an additional hydraulic machine. Common ultrasonic fatigue tests machines in the literature and industry with their capabilities are listed in Table 1.1.

Ultrasonic fatigue tests for VHCF research have only been actively pursued for the past two decades. Although the American Society for Metals [KM07] and the Japan Welding Engineering Society [Fur+22] recommends a standardization, a consensus has yet to be established within the ultrasonic fatigue community. This maybe due to the fact that certain metals exhibit different fatigue behaviors between low- and high-frequency loading effect, see [Tah+23] for a state of the art. Hence, literature on the use of frequencies over 40 kHz are infrequent[3]. Even with efforts to mitigate this through air cooling and pulse-pause loading, a change in the fatigue life still manifests in the S-N curves of some metals [Tah+23].

1.3.2 Measurements used in ultrasonic fatigue tests

As mentioned previously, the estimation of the longitudinal stress at the centroid of the fatigue specimen requires a known displacement combined with a harmonic analysis. Thus there is a need to calibrate the imposed displacement by ultrasonic fatigue test machine, which promotes the elongation of the fatigue specimen. As far as the author knows, there are three primary instruments whose strain or vibration measurements enable the estimate of the imposed stress amplitudes:

- The usage of an (intrusive) strain gauge located at the centroid of the fatigue specimen. Calibra-

[3]Notable exceptions Girard's work in 1959 at 92 kHz, and Kikukawa's work in 1965 at 199 kHz [Bat99].

Notable ultrasonic fatigue test machines	**Induction heating**	**Continuous/ pulse-pause**	**Load ratio**	**Ref.**
University of Natural Resources and Life Sciences, Vienna (BOKU)	Yes [Sch+20]	Cont., P-P	T-T, T-C, C-C [Kar+17]	[May06]
Institut des technologies et matériaux avancés (CNAM/ITMA)	No	Cont.	T-C	[Bat06]
Technical University of Lisbon, Lisboa (IST)	No	Cont., P-P	T-C	[Lag+12]
Laboratoire Pprime, Poitiers	Yes	Cont.	T-T, T-C	[Ppr]
Slovak University of Technology, Bratislava (STU)	No	Cont.	T-C	[Pus93]
University of Kaiserslautern, Kaiserslautern (WKK)	No	Cont.	T-C	[Hei+13]
University of Michigan, Ann Arbor (UMICH)	Yes	Cont.	T-C	[Shy+04]
Shimadzu (Japan) USF-2000	No	Cont.	T-T, T-C	[Wei+22]
3R (France) MEG20	No	Cont.	T-T, T-C	[3R]
ItalSigma (Italy) MU-26, MU-90	No	Cont.	T-C	[IMC21]
Mbrosia (South Korea) 103	Yes	Cont.	T-C	[Mbr]

Table 1.1: A small overview of notable ultrasonic fatigue uniaxial test machines in the literature. The acronyms are defined here: P-P, pulse-pause; T-T, tension-compression to tension-tension ($-1 < R \leq 1$); T-C, fully reversed tension-compression ($R = -1$); C-C, compression-compression.

tion specimen are utilized with different loading amplitudes. By assuming linear elasticity in the direction x, the stress amplitude is found with the isotropic linear Young's modulus: $\sigma_{xx} = E\varepsilon_{xx}$.

- The usage of a non-contact laser vibrometer or laser displacement sensors to measure the free-end vibration of the fatigue specimen. Given the velocity measurement $\dot{u}_x$, the displacement is estimated by integration:

$$u_x(t) = \int_{t_0}^{t_1} \dot{u}_x(t)dt \tag{1.1}$$

  This estimated displacement is then used as a boundary condition in a finite element harmonic analysis considering the linear elastic behavior of the material. From the finite element analysis, the longitudinal stress distribution along the specimen's length is available, and the peak stress at the centroid is the applied stress amplitude.

- The usage of a eddy current displacement sensor to measure the free-end of the fatigue specimen. The method of calculating the stress amplitude is identical to the laser vibrometer. However, the eddy current displacement sensors do not work for all metals, and suffer from a smaller frequency bandwidth compared to laser vibrometers (100 kHz versus 1 MHz).

However, other various experimental measurements are possible, shown in Table 1.2. The rows remaining in Table 1.2 are discussed briefly in the following:

- Thermal measurements of the temperature variation on the surface of the specimen. This increase of temperature is an accumulation of heat generating effects: e.g. dissipation due to internal friction due dislocation movement [Mac76], microplasticity, and the plastic zone at crack tip especially during crack propagation [Ran04]. Experimental measurements of the surface of the specimen recorded by high speed infrared cameras for non-contact [RWP08], or with the use of thermocouples [Pap+02]. As shown by the work done by Ranc [RWP08] in Fig. 1.20, high-speed infrared cameras allows for sufficient time resolution to monitor crack propagation.

- Acoustic emission refers to the propagation of transient elastic waves within a material, stemming from the swift energy discharge from acoustic sources like the nucleation of microcracks [MVK15]. It's claimed by Máthis et al. [Mát+12] that even Frank-Read sources and twin nucleation generate acoustic waves. These elastic waves propagate through the fatigue specimen in the form of sound waves [Shi+10]. For non-ultrasonic fatigue tests, the measurement and analysis of acoustic emissions typically use thresholded acoustic events [Han+11], cumulative spectral energy [Shr+21], or Shannon information entropy [Cha+18]. In ultrasonic fatigue tests, a setup is shown in Fig. 1.21, where thresholded acoustic events [Sel+21] have been demonstrated successfully for an in-contact piezoelectric microphone. This nondestructive technique has been

Measurement	**Instruments**	**Uses in ultrasonic fatigue**	**Reference**
Strain	Strain gauges	Estimate stresses at specimen centroid	[Wil80]
Velocity, displacement	Laser vibrometer Eddy current sensor	Estimate frequency drift Detection of crack Estimate stresses at specimen centroid	[Hac+21] [Kum+09] [Jac+21]
Thermal	Infrared camera	Estimation of dissipation into heat	[Bla+15]
Acoustic	Acoustic microphone	Detection of crack	[Shi+10]
Ferromagnetic	Eddy current sensor	Observe phase change-based damage	[BWM22]
X-ray	Computed tomography	Mesoscopic stresses and strains Observe phase change Detection of crack	[Jac+21] [Fit+20] [Mes+20]

Table 1.2: Examples of experimental measurements used for characterization for ultrasonic fatigue tests along with an example found in literature.

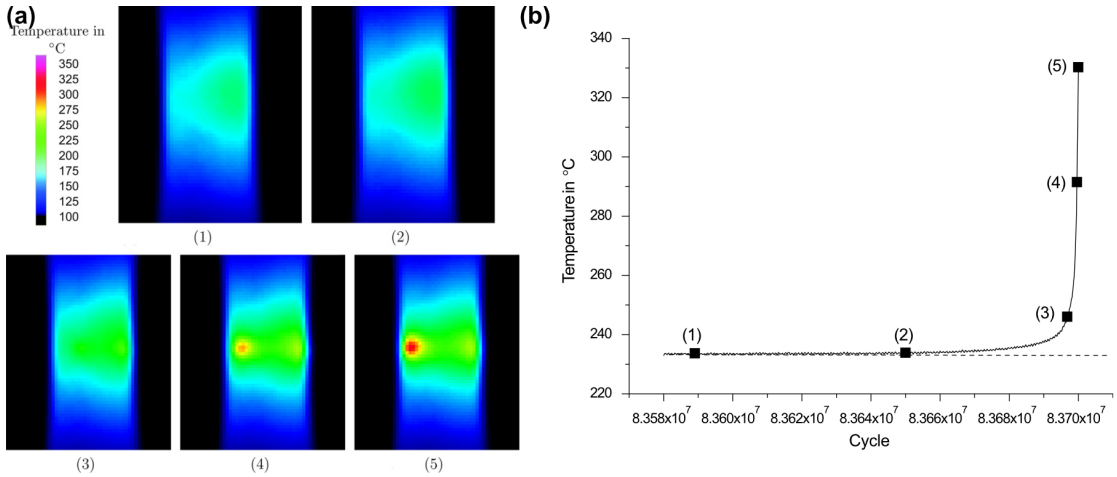

Figure 1.20: In **(a)**, the temperature distribution across the specimen's surface just before the occurrence of fracture. In **(b)**, the progression of averaged temperature on the specimen's surface immediately prior to fracture, with the failure occurring at $N_\mathrm{f} = 8.37 \times 10^7$ cycles, taken from [RWP08].

in practice since the 1980s [FB95] with the advantage of being insensitive to geometries, but has disadvantages due to non-contact microphones being sensitive to external noises not of the fatigue specimen, e.g. the air cooling of a fatigue specimen. This leads to difficulty correlating acoustic events with actual material damage.

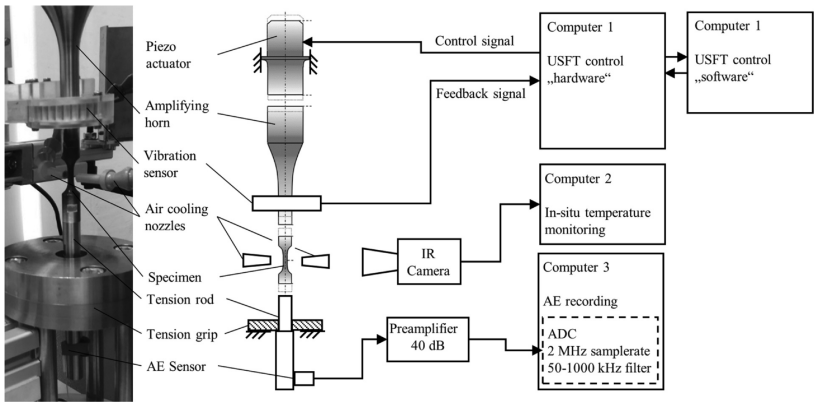

Figure 1.21: The adapted ultrasonic fatigue test machine from BOKU for an in-situ acoustic emission monitoring. The acoustic microphone is fixed at the bottom of the tension rod, taken from [Sel+21].

- The ferromagnetic measurement, i.e. the eddy current sensor, has previously been mentioned in order to estimate displacements. However, Barton et al. [BWM22] have also extended its use to monitoring microstructural changes in nickel-based alloys subjected to high-temperature and cyclic mechanical loading. The eddy current sensor is sensitive to changes in the subsurface

microstructure, specifically chromium depletion, which was continuously tracked and correlated with magnetic material properties.

- X-ray measurements utilize computed tomography in order to obtain imagery of the materials bulk. This is done through accelerating X-rays, usually by synchrotron radiation, through the fatigue specimen and into a detector. The X-rays that are absorbed by the fatigue specimen produces contrast between microstructure and defects within the material. The benefit in this method has been shown to be useful in various literature. For example in [Mes+20] the generation of voxel data with resolutions less than $1\,\mu\text{m}^3$ allows to see hairline internal cracks. This resolution has also been useful to study phase change-based fatigue damage in [Fit+20]. To the author's knowledge, X-ray tomography cannot be performed *in-situ*, and requires stoppage of the test.

1.4 Exploiting the high-frequency loading in ultrasonic fatigue tests

Given the various possible *in-situ* measurements, there is interest in exploring if the high-frequency loading in ultrasonic fatigue tests can provide more information on the material state. Kumar et al. [Kum+09] introduced the idea of analyzing the vibrating free-end of the fatigue specimen. In this context, the traveling high-frequency elastic wave through the fatigue specimen has a nonlinear distortion which is measurable in the vibration signal. A core characteristic of linear systems is their incapacity to transfer energy between different frequencies [Pea99]. Consequently, nonlinear distortion refers to the energy transfer from the fundamental harmonic to the higher harmonics. The definition of harmonics is presented in Fig. 1.22: Given a vibration signal measured in their experimental setup, a short time window of the signal is analyzed in the frequency domain through the Fourier transform. The fundamental harmonic refers to the sinusoidal amplitude and frequency of the longitudinal vibration, and higher harmonics refer to integer multiples of this sinusoid.

Kumar et al. [Kum+09] introduces a nonlinear damage index that is extracted *in-situ* during the ultrasonic fatigue test. Specifically, the harmonics' amplitude ratio of the second harmonic with the squared fundamental harmonic is defined for the measured signal:

$$\alpha(t) \coloneqq 20 \log_{10} \left(\frac{A_2(t)}{A_1^2(t)} \right); \quad \text{and} \quad \alpha_{\text{rel}}(t) \coloneqq \alpha(t) - \alpha(0), \ \forall t > 0 \tag{1.2}$$

where α is the ratio, and α_{rel} is the time relative index. The notation in the works of Kumar et

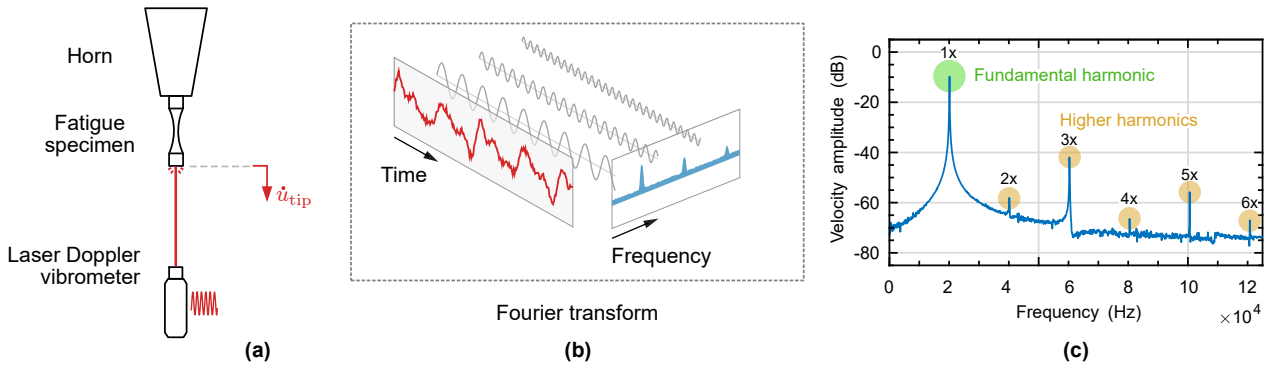

Figure 1.22: In **(a)**, vibration signals are measured and in **(b)** are visualized in the frequency domain by Fourier transform of the vibration signal. In **(c)**, an an ultrasonic fatigue test frequency spectra showing a fundamental harmonic at approximately 20 kHz and its higher harmonics.

al. [Kum+09] uses β and β_{rel}, whereas here it is α and α_{rel}, respectively. The notation is differentiated due to the fact that β is the acoustic nonlinear parameter and has a different value from α, but $\alpha \propto \beta$.

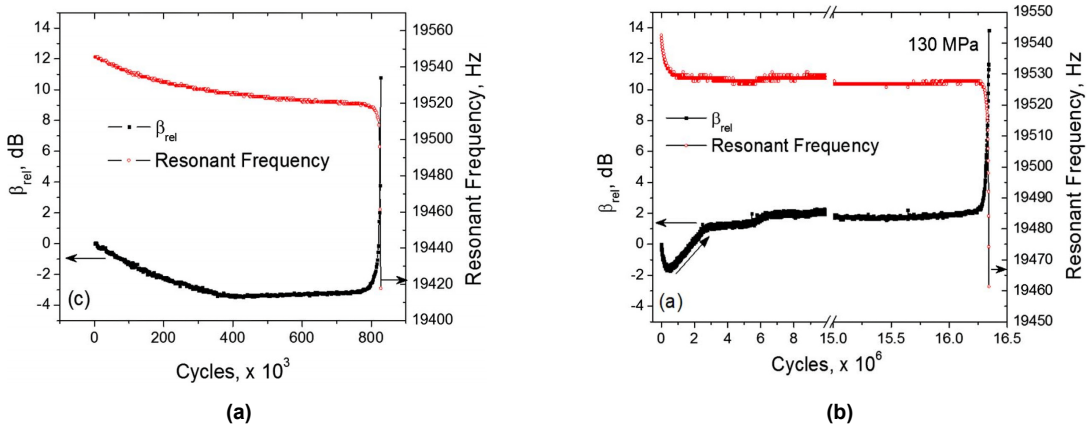

Figure 1.23: In **(a)**, the amplitude spectra of feedback signals collected at various cycles during an ultrasonic fatigue test of 6061-T6511 Al alloy at 130 MPa. In **(b)**, the changes in β_{rel} and resonant frequency throughout the same ultrasonic fatigue test, taken from [Kum+09].

Kumar et al. [Kum+09] study the evolution of their nonlinear damage index, a testing campaign was performed for an aluminum alloy for different loading amplitudes, which is shown in Fig. 1.23. With the initiation and progression of the major crack, the measured α_{rel} and the system's resonant frequency increased and decreased rapidly, respectively, shown in Fig. 1.23 **(a)** at a stress amplitude of 160 MPa and in **(b)** at 130 MPa. A general trend of decrease in α_{rel} during the early stages of cycling and its rapid increase towards the end of the test is observed. However, the early life decreases were posited by Kumar et al. to cyclic softening or the increase in temperature of the samples but

not researched further. Additionally, Kumar et al. investigated the correlation with the crack growth from fractograph with the per-cycle increase of α_{rel} and decrease of resonant frequency. This was done by correlating the values of $d\alpha_{\text{rel}}/dN$ and $-df/dN$ with da/dN where a is the crack size and N the number of cycles, during the crack growth portion of the ultrasonic fatigue test, see Fig. 1.24. When comparing their slopes with the dimensions of the initial cracks used for calculating Paris law, a good agreement was found for $d\alpha_{\text{rel}}/dN$.

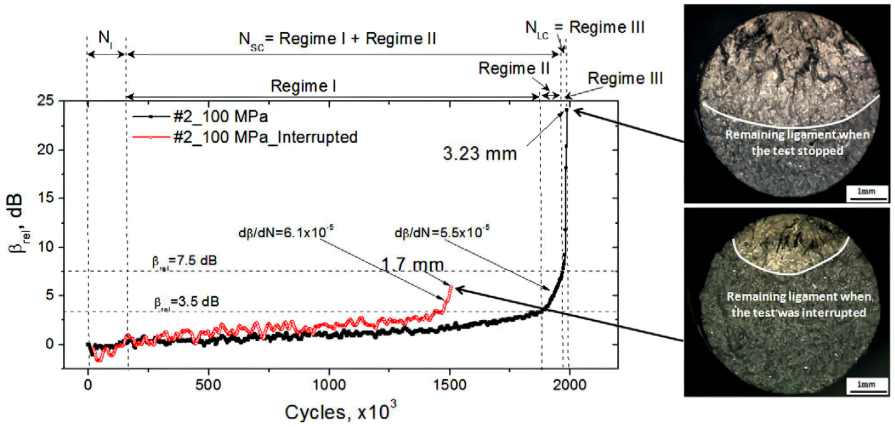

Figure 1.24: The evolution of β_{rel} and the slopes $d\beta_{\text{rel}}/dN$ correlated with the crack size measured from aluminum alloy fatigue specimens, taken from [Kum+10].

The works of Kumar et al. [Kum+09] have demonstrated that under high-frequency loading, a nonlinear phenomena of second harmonic generation is present in the vibration signal of the ultrasonic fatigue test. Due to its accessibility and *in-situ* application, the approach has been widely adopted by those in the ultrasonic fatigue community [Kum+10; Kum+11; MFS13; Fit+14; Li+15; Li+16; Ban+18; Mes+20], but has only been qualitatively used to infer macrocrack initiation and propagation. Additionally, there are fundamental oversights in the usage of β in ultrasonic fatigue tests and will be demonstrated in Chapter 2.

1.5 Summary

This chapter presents a comprehensive review of fatigue behavior of metallic materials from the LCF to VHCF, within the context of irreversible cyclic slip by Mughrabi [Mug84]. It's well accepted that the unique micromechanical changes in a metallic material during fatigue loadings are a progressive sequence of events. However, for HCF and VHCF regimes, fatigue mechanisms become

increasingly material specific and when damage initiates becomes uncertain. This underlines the critical importance of *in-situ* measurements whose analysis is intricately linked to the specific fatigue mechanisms prevalent in HCF and VHCF regimes during ultrasonic fatigue tests.

The analysis of the nonlinear harmonic generation in the vibration fatigue specimen during ultrasonic fatigue tests, inspired by Kumar et al. [Kum+09], is adopted in this dissertation. In order to study the nonlinear harmonic generation, vibrations measurements via laser vibrometers are a good candidate for *in-situ* monitoring, as they are non-intrusive (compared to strain gauges) and are easily accessible. The dissertation aims to contributes to the broader understanding of ultrasonic fatigue in metallic materials through some key questions: *At what stage in the fatigue life cycle does microcrack initiation occur?* And *what are the sources of the higher harmonics observed in the tip vibration of ultrasonic fatigue specimens?* These inquiries are crucial towards understanding the complex fatigue behavior of materials in the HCF and VHCF regimes. Ideally, analysis of these signals can provide insights into specific microstructural changes occurring within the material.

Chapter 2

Analytical models for forward problems in ultrasonic fatigue

Contents

The second chapter of this dissertation is dedicated to presenting the forward problem that models the nonlinear harmonic generation of an ultrasonic fatigue specimen. Specfically, microscopic and mesoscopic models are presented whose nonlinear harmonic generation manifests under dynamic loading. The dynamics of the fatigue specimen is then modeled where material nonlinearities are defined at its centroid. A clear delineation between the ultrasonic fatigue test machine and the fatigue specimen becomes essential when one considers the assumptions of boundary conditions on the fatigue specimen model. Experimentally, it can be observed that there are higher harmonics in the vibration measured at the horn. With this in mind, a model of the fatigue specimen is proposed that is invariant to experimental setup and control and can provide a basis to model material nonlinearities.

2.1 Introduction

Chapter 2 is dedicated to the comprehensive modeling of an ultrasonic fatigue specimen and test machine to understand the harmonic generation seen in the vibration of the fatigue specimen. The emphasis is to distinguish the sources of the harmonic generation, and understand the material nonlinearities that manifest from damage and microplastic mechanisms in the fatigue specimen. The structure of this chapter follows a hierarchical order that reflects the various length scales present within the fatigue specimen. This organization facilitates a systematic examination of the specimen's responses under ultrasonic fatigue loading. The first section details nonlinear fatigue-based models below the macroscopic scale and their higher harmonic generation:

- First, nonlinear elasticity (or the acoustic nonlinearity) is considered since it is frequently described by the acoustic community and recently adopted by the ultrasonic fatigue community. The derivation of the nonlinear acoustic parameter for longitudinal wave motion is detailed, where the interatomic potential of a crystal lattice is considered. The issues with this characterization is detailed and numerical simulations substantiate the fact that nonlinear elasticity cannot describe various fatigue mechanisms. This substantiates a different modeling approach above the atomic scale.

- Second, its proposed a mesoscopic description of the material nonlinearity due to fatigue mechanisms in a representative volume. Specifically, two sources of higher harmonic generation are proposed: microcracks and microplasticity. This is facilitated by using a mean-field homogenization scheme of multiple phases of Eshelby's inclusions [Esh57]. Additionally, the inclusions are defined to have nonlinear behavior: the microcracks are modeled as penny-shaped cracks with a specific closure criterion and microplastic inclusions modeled as spheres exhibiting plastic behavior. Compared to classical homogenization by finite element analysis, this approach accelerates the computation of the dynamical response greatly.

- Third, a uniaxial model of a mode I macrocrack is considered. This is defined when the crack length supersedes the size of the representative volume element. Here the change in the ratio between the crack surface and total surface area characterizes a stiffness degeneration.

These nonlinearities represent the different possible material states and their length scales within an

ultrasonic fatigue specimen. The nonlinear harmonic generation for these models are detailed when their fatigue-based parameters vary, e.g. the accumulation of fatigue damage corresponds to an increase of the volume fraction of microcracks with closure. The emphasis here demonstrates a dependency of the fatigue loading (a pure harmonic input verus a multi-harmonic input) and the material state on the generation of higher harmonics during ultrasonic fatigue tests.

The second section considers a macroscopic model of the structure of an ultrasonic fatigue specimen and the dynamic loading it undergoes. This enables description of the effects of mass and geometry, as well as any localized behavior which occurs at the centroid of a fatigue specimen. When material nonlinearities are defined at the centroid, the dynamical behavior of the fatigue specimen differs. For instance, stiffness degeneration due to microcracks can lower the resonance frequency and their closure manifests higher harmonics. The experimental setup of an ultrasonic fatigue tests has dynamic properties which can be exploited, namely that the ultrasonic fatigue specimen is solicited at its first longitudinal mode (≈ 20 kHz), and thus forms a standing wave. A reduced order model in this narrow frequency range by the vibration normal modes can be used instead of a finite element model, namely the classic approach of modal truncation [GR15].

The third section describes an electrodynamical model of the ultrasonic fatigue test machine without an attached fatigue specimen, described through transfer functions and validated with experimental data. However, a frequency analysis of the experimental applied voltage, current to the piezoelectric transducer, and the experimental velocity data of the acoustic horn reveals small system nonlinearities which manifest as higher harmonics. This challenges the conventional assumption in the ultrasonic fatigue literature that the acoustic horn provides a pure harmonic input wave to the fatigue specimen.

2.2 Nonlinear material models and higher harmonic generation

2.2.1 Nonlinear acoustics of atomic lattices

Symbol	Description
a, r	Undeformed and deformed interatomic distance
$\mathcal{A}, \mathcal{B}$	Interatomic attractive and repulsive forces
$\mathbb{C}$	Stiffness tensor
E, ν	Young's modulus, Poisson's ratio
f, ω	Frequency and angular frequency
L	Length of a slender bar
U	Internal energy
$u(X_1, t)$	Longitudinal motion at position $\boldsymbol{X}$ and time t
β, γ	Acoustic nonlinearity parameter of the second and third harmonic
κ, λ	Wavenumber, wavelength
ϕ, Φ	Interatomic potential, continuum potential
ρ	Mass density
$\boldsymbol{\sigma}, \boldsymbol{\varepsilon}$	Stress and strain tensors
$\langle \square \rangle_V$	Volume averaged quantity

Table 2.1: For the nonlinear acoustic lattice model in Sec. 2.2.1 only, this notation is adopted.

Early research into ultrasonic harmonic generation suggested that the crystal lattice as a cause for this second harmonic generation for vibrating metals. This was modeled as nonlinear elasticity in a atomic lattice, established by acoustic studies in the 1960s [BT63; BF65]. Most these studies focused on single crystals or samples with very low dislocation densities, with the prevailing body of research employing bulk waves for ultrasonic harmonic generation, see [Mat+15] for a state of the art. Here, it's derived an atomic description of a nonlinear theory of elasticity [Mur51]. Subsequently, an analysis of the acoustic nonlinear parameter is given, focusing on the generation of higher harmonics using the loading parameters derived from ultrasonic fatigue tests. This subsection distinguishes the results from nonlinear acoustic community, with the work later presented in this dissertation.

Nonlinear elasticity due to the crystal lattice

Consider a single crystal FCC lattice, which will serve as a nonlinear medium for wave motion, shown in Fig. 2.1 **(a)**. The interatomic potential energy ϕ for two atoms with an undeformed atomic

separation distance a can be broadly defined as:

$$\phi(a) \coloneqq \mathcal{A}(a) + \mathcal{B}(a) \tag{2.1}$$

where $\mathcal{A}$ is a repulsive force and $\mathcal{B}$ is an attractive force. Here an appropriate potential for metallic bonding should consider the density of the electron cloud, e.g. the Finnis-Sinclair potential [FS84]. The derivative of its potential energy $F(a) \coloneqq d\phi(a)/da$ gives the associated interatomic force, which is zero at the potential energy well. The interatomic potential and force for two atoms with respect to their interatomic distance is schematized in Fig. 2.1 **(b)**. Here it can be seen that the interatomic elasticity (in the Hookean sense) is not perfectly linear.

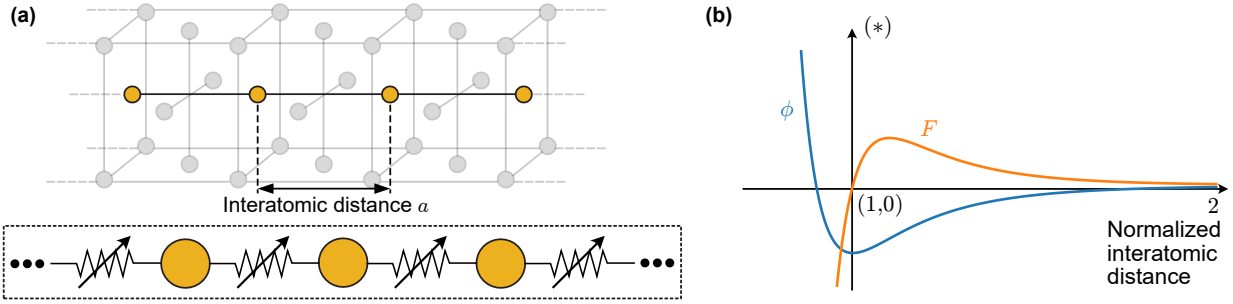

Figure 2.1: In **(a)**, a FCC crystal lattice whose plane wave motion is of interest. A string of atoms are modeled with a nonlinear stiffness. In **(b)**, a schematic of interatomic potential energy and force of two atoms.

This observation was originally described as the *anharmonicity of the crystal lattice* in the 1950s. To model this interatomic nonlinear elasticity under isentropic assumptions, the interatomic potential energy is approximated by Taylor series expansion at the deformed atomic separation distance r:

$$\phi(r) \approx \phi(a) + \frac{(r-a)^2}{2!}\left(\frac{d^2\phi}{dr^2}\right)_{r=a} + \frac{(r-a)^3}{3!}\left(\frac{d^3\phi}{dr^3}\right)_{r=a} + \dots \tag{2.2}$$

The potential energy density of the lattice ρU is taken as a sum over $N-1$ touching atomic pairs in the unit cell:

$$\rho U = \frac{1}{V}\sum_{i=1}^{N-1}\phi_i(r) \tag{2.3}$$

where V is the volume of the unit cell with a mass density ρ. To transition from the atomic scale to a macroscopic perspective, one applies the continuum limit as $r, a \to 0$. Let the compatibility equations for finite deformations be $\varepsilon_{ij} \coloneqq \frac{1}{2}(u_{ij}+u_{ji}+u_{ki}u_{kj})$, where $u_{ij} = \partial u_i/\partial X_j$ is the displacement gradient and X is the material point. The continuum potential energy attributable to strains, $\Phi(\boldsymbol{X}, \varepsilon_{ij})$, is

written as a Taylor series approximation of nonlinear elasticity:

$$\Phi(\boldsymbol{X}, \varepsilon_{ij}) = \Phi_0 + \mathbb{C}^{(1)}_{ij}\varepsilon_{ij} + \frac{1}{2!}\mathbb{C}^{(2)}_{ijkl}\varepsilon_{ij}\varepsilon_{jk} + \frac{1}{3!}\mathbb{C}^{(3)}_{ijklmn}\varepsilon_{ij}\varepsilon_{jk}\varepsilon_{mn} + \dots \tag{2.4}$$

where the superscript $^{(\square)}$ refers to the order of differentiation and the stiffness tensors $\mathbb{C}$ are:

$$\mathbb{C}^{(1)}_{ij} = \frac{\partial^{(1)}\Phi}{\partial\varepsilon_{ij}}; \qquad \mathbb{C}^{(2)}_{ijkl} = \frac{\partial^{(2)}\Phi}{\partial\varepsilon_{ij}\partial\varepsilon_{kl}}; \qquad \mathbb{C}^{(3)}_{ijklmn} = \frac{\partial^{(3)}\Phi}{\partial\varepsilon_{ij}\partial\varepsilon_{kl}\partial\varepsilon_{mn}}; \quad \dots \tag{2.5}$$

with $\mathbb{C}, \boldsymbol{\sigma}, \boldsymbol{\varepsilon}$ written in Voigt notation [Voi66]. Therefore, the nonlinear constitutive relationship is:

$$\sigma_{ij} = \frac{\partial\Phi}{\partial\varepsilon_{ij}} = \mathbb{C}^{(1)}_{ij} + \mathbb{C}^{(2)}_{ijkl}\varepsilon_{ij} + \frac{1}{2}\mathbb{C}^{(3)}_{ijklmn}\varepsilon_{ij}\varepsilon_{jk} + \dots \tag{2.6}$$

where $\mathbb{C}^{(1)} \equiv \boldsymbol{\sigma}_0$ is a static initial stress in the solid.

For displacements along a single direction X_1 without the presence of a static stress and simplified using nonlinear parameters, one can write the constitutive relationship to the third term:

$$\begin{aligned}\sigma_{11} &= \mathbb{C}^{(2)}_{1111}\varepsilon_{11} + \frac{1}{2}\mathbb{C}^{(3)}_{111111}\varepsilon^2_{11} + \frac{1}{6}\mathbb{C}^{(4)}_{11111111}{\varepsilon_{11}}^3 + \dots \\ &= \mathbb{C}^{(2)}_{1111}\varepsilon_{11} + \frac{1}{2}\beta\mathbb{C}^{(2)}_{1111}\varepsilon^2_{11} + \frac{1}{6}\gamma\mathbb{C}^{(2)}_{1111}{\varepsilon_{11}}^3 + \dots\end{aligned} \tag{2.7}$$

The quantities β and γ are nonlinear parameters which relate the longitudinal higher order stiffness coefficients to the conventional stiffness coefficient. Since the goal is to describe the relationship in terms of $\mathbb{C}^{(2)}_{1111}$, the superscript is dropped from notation. In fact, β has analytical derivations [Can94] where the Brugger elastic constants [Bru64] defined for a direction of the crystal lattice is projected along the coordinate of motion [TT77]. For non-single crystal materials, analytical derivations of β are nonexistent in the literature and instead rely on the measurement of β through the inverse problem of longitudinal wave motion.

Nonlinear acoustic parameter for a longitudinal propagating wave

In nonlinear acoustic literature, nonlinear elasticity is quantified by the effect of β on the one-dimensional motion of a longitudinal (plane) wave. Through this derivation, an estimate of β can be measured in practice. For longitudinal motion $u(X_1, t)$ along the X_1 direction and neglecting external body forces, the one-dimensional equation of motion is:

$$\rho\frac{\partial^2 u}{\partial t^2} = \frac{\partial\sigma_{11}}{\partial x} \tag{2.8}$$

where $x \equiv X_1$ is written for ease of reading. By defining the wave speed $c^2 \coloneqq \mathbb{C}_{1111}/\rho$, combining Eqs. (2.7) and (2.8), and truncating the term γ, the resulting nonlinear wave equation is:

$$\frac{\partial^2 u}{\partial t^2} = c^2 \frac{\partial^2 u}{\partial x^2}\left[1 + \beta \frac{\partial u}{\partial x}\right] \tag{2.9}$$

The classic assumption taken by the acoustic community [Mat+15] is that Eq. (2.9) is subject to a single harmonic wave at its boundary condition $u(0,t) = A_1 \cos(\omega_1 t)$, where $\omega \coloneqq 2\pi f$.

By using a perturbation approximation, the solution of Eq. (2.9) is $u = u^{(0)} + u^{(1)}$, where $u^{(0)}$ is the contribution to the linear solution, $u^{(1)}$ the perturbation due to the nonlinearity, and $|u^{(0)}| \gg |u^{(1)}|$. The contribution $u^{(0)}$ is the solution to the linear wave equation:

$$\frac{\partial^2 u^{(0)}}{\partial t^2} - c^2 \frac{\partial^2 u^{(0)}}{\partial x^2} = 0; \qquad u^{(0)}(0,t) = A_1 \cos(\omega_1 t) \tag{2.10}$$

The solution to Eq. (2.10) subject to the above boundary condition is:

$$u^{(0)}(x,t)_{x>0} = A_1 \cos(\kappa x - \omega_1 t) \tag{2.11}$$

where $\kappa \coloneqq \omega/c$ is the wave number. The first-order perturbation for $u^{(1)}$ is obtained by substituting Eq. (2.11) into the nonlinear portion of Eq. (2.9) which gives:

$$\begin{aligned} \frac{\partial^2 u^{(1)}}{\partial t^2} - c^2 \frac{\partial^2 u^{(1)}}{\partial x^2} &= c^2 \beta \frac{\partial u^{(0)}}{\partial x} \frac{\partial^2 u^{(0)}}{\partial x^2}; \\ &= c^2 \frac{\beta A_1^2 \kappa^3}{2} \sin(2\kappa x - 2\omega_1 t); \end{aligned} \qquad u^{(1)}(0,t) = 0 \tag{2.12}$$

It can be seen that the nonlinear term in Eq. (2.12) is a second harmonic. One general solution of Eq. (2.12) has the form:

$$u^{(1)}(x,t)_{x>0} = F(x)\cos(2\kappa x - 2\omega_1 t) + G(x)\sin(2\kappa x - 2\omega_1 t) \tag{2.13}$$

Here the coefficients are assumed to be functions of x. Due to the fact that the boundary condition dictates that the second harmonic disappears at $x = 0$, the coefficients $F(x)$ and $G(x)$ must vanish as well. When substituting Eq. (2.13) into Eq. (2.12):

$$\left(4\kappa \frac{dG}{dx} + \frac{d^2F}{dx^2}\right)\cos(2\kappa x - 2\omega_1 t) + \left(-4\kappa \frac{dF}{dx} + \frac{d^2G}{dx^2}\right)\sin(2\kappa x - 2\omega_1 t) = -\frac{\beta A_1^2 \kappa^3}{2}\sin(2\kappa x - 2\omega_1 t) \tag{2.14}$$

and equating coefficients of the harmonic terms, one obtains:

$$4\kappa \frac{dG}{dx} + \frac{d^2F}{dx^2} = 0; \quad \text{and} \quad -4\kappa \frac{dF}{dx} + \frac{d^2G}{dx^2} = -\frac{\beta A_1^2 \kappa^3}{2} \tag{2.15}$$

A consistent solution to these coefficients can be found if $dG/dx = d^2F/dx^2 = 0$: this implies that $G(x) =$ constant, $d^2G/dx^2 = 0$, and that $dF/dx =$ constant. This simplifies Eq. (2.15) to:

$$\frac{dF}{dx} = \frac{\beta A_1^2 \kappa^2}{8}; \quad \text{and} \quad \int \frac{dF}{dx} = F(x) = \frac{\beta A_1^2 \kappa^2 x}{8} + F_c \tag{2.16}$$

where F_c is a constant of integration. However, since the second harmonic must disappear at $x = 0$, both $G(x) = 0$ and $F_c = 0$.

The resulting perturbation solution $u = u^{(0)} + u^{(1)}$ is the same amplitudes found in existing nonlinear acoustic literature [TT77; Can84]:

$$u(x,t)_{x>0} = A_1 \cos(\kappa x - \omega_1 t) + \frac{\beta A_1^2 \kappa^2 x}{8} \cos(2\kappa x - 2\omega_1 t) \tag{2.17}$$

If the perturbation solution can be solved for an additional iteration with the third term γ in Eq. (2.9), as done by [TT77]. This gives the resulting solution:

$$u(x,t)_{x>0} = A_1 \cos(\kappa x - \omega_1 t) + \frac{\beta A_1^2 \kappa^2 x}{8} \cos(2\kappa x - 2\omega_1 t) + \frac{\gamma A_1^3 \kappa^4 x^2}{32} \cos(3\kappa x - 3\omega_1 t) \tag{2.18}$$

The coefficients β and γ can be solved for, with $A_2 \coloneqq \beta A_1^2 \kappa^2 x/8$ and $A_3 \coloneqq \gamma A_1^2 \kappa^4 x^2/32$:

$$\beta = \frac{8}{\kappa^2 x} \frac{A_2}{A_1^2}; \qquad \gamma = \frac{32}{\kappa^4 x^2} \frac{A_3}{A_1^3}; \tag{2.19}$$

When written in this form, β is commonly referred to the acoustic nonlinearity parameter causing second harmonic generation (SHG) and γ causes third harmonic generation (THG) [Mat+15].

The relationships of Eq. (2.19) allow for experimental measurements of β. These exist for basic elements like single crystal or polycrystalline copper [Li+19], but come from a sample and neglect the microstructure of the material. The experimental measurements of of β rely on thickness propagation with an ultrasonic transducer and receiver [Mat+15] with the solution of Eq. (2.18). Some experimental values of β for metallic materials are given in Table 2.2. Due to the smallness of THG of γ has garnered limited attention within the acoustic community, resulting in a sparse literature.

Material	**Measured β**	**Wave frequency**	**Respective reference(s)**
Polycrystalline copper	1.6 - 3.6, 2.1 - 3.5	5 MHz, 2.3 MHz	[Li+19; Par+21]
Al 6061-T6	5.1, 5.0 - 5.8	10 MHz, 10 MHz	[Li+85; KSJ17]
Al 2024-T4	7.7	10 MHz	[Li+85]
Single crystal copper [100]	5.2	30 MHz	[YCB81]
Single crystal copper [110]	11.2	30 MHz	[YCB81]
Single crystal copper [111]	7.9	30 MHz	[YCB81]

Table 2.2: Measured absolute parameters of β at room temperature found in the literature.

Nonlinear acoustic parameter for a longitudinal standing wave

Instead of using the solution of a longitudinal propagating wave, a longitudinal standing wave is sought for since this kind of wave motion is formed for a fatigue specimen during ultrasonic fatigue tests. This corresponds to an additional reflective wave at the free end of the fatigue specimen. In a similar fashion to before, the 1D simplified model now requires the displacement to be maximum at both ends of the rod, via a harmonic solution:

$$\left.\frac{\partial u}{\partial x}\right|_{x=0} = 0; \quad \text{and} \quad \left.\frac{\partial u}{\partial x}\right|_{x=L} = 0; \qquad u(x,t) = \text{real}\left(U(x)e^{\mathrm{j}\omega_1 t}\right)$$

A perturbation approximation of the nonlinear wave equation Eq. (2.9) has a solution of $u = u^{(0)} + u^{(1)}$, where $u^{(0)}$ is the contribution to the linear solution, $u^{(1)}$ the perturbation due to the nonlinearity, and $|u^{(0)}| \gg |u^{(1)}|$. The contribution $u^{(0)}$ is the solution to the linear wave equation:

$$\frac{\partial^2 u^{(0)}}{\partial t^2} - c^2 \frac{\partial^2 u^{(0)}}{\partial x^2} = 0; \qquad u^{(0)}(x,t) = U(x)e^{\mathrm{j}\omega_1 t} \tag{2.20}$$

The general harmonic solutions to Eq. (2.20) of the linear wave equation yields:

$$U = Ae^{\mathrm{j}\kappa x} + Be^{-\mathrm{j}\kappa x}; \quad \text{and} \quad \frac{\partial U}{\partial x} = \mathrm{j}A\kappa e^{\mathrm{j}\kappa x} - \mathrm{j}B\kappa e^{-\mathrm{j}\kappa x} \tag{2.21}$$

for unknown coefficients A and B. The boundary conditions $\frac{\partial U}{\partial x}\big|_{x=0} \frac{\partial U}{\partial x}\big|_{x=L} = 0$ gives the values of the undetermined coefficients:

$$j\kappa(A+B) = 0 \implies A = B \quad \text{and} \quad \sin(\kappa L) = 0 \implies \kappa L = n\pi; \quad n \in \mathbb{N} \tag{2.22}$$

for the nth mode. For the first longitudinal mode $n = 1$, and substituting Eqs. (2.21) and (2.22) into Eq. (2.20) obtains the solution to $u^{(0)}$ for a maximum amplitude A:

$$u^{(0)}(x,t) = A\cos(\kappa x)\cos(\omega_1 t) \tag{2.23}$$

The first-order perturbation for $u^{(1)}$ is obtained by substituting Eq. (2.23) into the nonlinear portion of Eq. (2.9) which gives:

$$\begin{aligned} \frac{\partial^2 u^{(1)}}{\partial t^2} - c^2 \frac{\partial^2 u^{(1)}}{\partial x^2} &= c^2\beta \frac{\partial u^{(0)}}{\partial x}\frac{\partial^2 u^{(0)}}{\partial x^2}; \\ &= -c^2\beta A^2\kappa^3 \sin(\kappa x)\cos(\kappa x)\cos^2(\omega_1 t) \\ &= -\frac{1}{4}c^2\beta A^2\kappa^3 \sin(2\kappa x) - \frac{1}{4}c^2\beta A^2\kappa^3 \sin(2\kappa x)\cos(2\omega_1 t) \end{aligned} \tag{2.24}$$

which is simplified using the trigonometric identity $\cos^2(\theta) = \frac{1+\cos(2\theta)}{2}$ and the double-angle identity $\sin(2\theta) = 2\sin(\theta)\cos(\theta)$.

It can be seen that the nonlinear term in Eq. (2.24) is a second harmonic with an additional static term (to be neglected as a non-oscillatory deformation which does not contribute to the standing wave). One general solution of Eq. (2.24) has the form:

$$u^{(1)}(x,t) = Q(x)\cos(2\omega_1 t) + R(x)\cos(2\omega_1 t) \tag{2.25}$$

Here the coefficients are assumed to be functions of x. When substituting Eq. (2.25) into Eq. (2.24):

$$\begin{aligned}\left(-4\omega_1^2 Q - c^2\frac{d^2Q}{dx^2}\right)\cos(2\omega_1 t) + \left(-4\omega_1^2 R - c^2\frac{d^2R}{dx^2}\right)\sin(2\omega_1 t) = \\ -\frac{c^2\beta A^2\kappa^3\sin(2\kappa x)}{4}\cos(2\omega_1 t) - \frac{c^2\beta A^2\kappa^3\sin(2\kappa x)}{4}\end{aligned} \tag{2.26}$$

and equating coefficients of the harmonic terms, one obtains:

$$-4\omega_1^2 Q - c^2\frac{d^2Q}{dx^2} = -\frac{c^2\beta A^2\kappa^3\sin(2\kappa x)}{4}; \quad \text{and} \quad -4\omega_1^2 R - c^2\frac{d^2R}{dx^2} = 0 \tag{2.27}$$

The stress-free boundary conditions impose:

$$\frac{dQ}{dx}|_{(x=0)} = 0; \quad \frac{dQ}{dx}|_{(x=L)} = 0; \quad \frac{dR}{dx}|_{(x=0)} = 0; \quad \frac{dR}{dx}|_{(x=L)} = 0$$

A consistent solution to these coefficients can be found if $R(x) = 0$ and $Q(x) = S\sin(2\kappa x)$. The particular solution of $Q(x)$ is to be determined by substitution $Q(x) = S\sin(2\kappa x)$ into Eq. (2.27) to yield the ODE:

$$(4\omega_1^2 S + 4c^2\kappa^2 S)\sin(2\kappa x) = \frac{c^2\beta A^2\kappa^3}{4}\sin(2\kappa x)$$

The particular solution is found as:

$$S = \frac{c^2\beta A^2\kappa^3}{16(\omega_1^2 + c^2\kappa^2)} \implies Q(x) = \frac{c^2\beta A^2\kappa^3}{16(\omega_1^2 + c^2\kappa^2)}\sin(2\kappa x) = \frac{\beta A^2\kappa}{32}\sin(2\kappa x) \tag{2.28}$$

The resulting perturbation solution $u = u^{(0)} + u^{(1)}$ for a standing wave, at the first longitudinal mode, gives a different result compared to the wave propagation of Eq. (2.17):

$$\begin{aligned}u(x,t) &= A\cos(\kappa x)\cos(\omega_1 t) &&+ \frac{\beta A^2\kappa}{32}\sin(2\kappa x)\cos(2\omega_1 t) \\ &= A_1\cos(\omega_1 t) &&+ A_2\cos(2\omega_1 t)\end{aligned} \tag{2.29}$$

where $A_1 = A\cos(\kappa x)$ is the first harmonic amplitude, and β:

$$\beta_{\text{standing}} = \frac{32\cos^2(\kappa x)}{\kappa \sin(2\kappa x)} \frac{A_2}{A_1^2} \tag{2.30}$$

Note that $\beta_{\text{standing}} \propto A_2/A_1^2$ for a propagating wave in Eq. (2.19), and that the coefficient is slightly larger for a standing wave.

Numerical example

Here, a numerical simulation of the propagating wave solution at the first longitudinal mode are used to study the effect of β. In order to elicit the first longitudinal wave at frequencies used in ultrasonic fatigue tests ($f \approx 20$ kHz), the resonant frequency occurs when the length of the bar is half the wavelength of the wave. The relationship for a non dispersive wave mechanism between wavelength λ, frequency f, speed of sound c, and resonant length L is given by the following:

$$c = f\lambda; \quad \lambda = 2L; \quad L = \frac{c}{2f} \tag{2.31}$$

Next, it is assumed that the stresses in the radial direction are zero (1D stress assumption). The relationship between the speed of sound and the material constants E, ν are used:

$$c = \sqrt{\frac{E}{\rho}} \tag{2.32}$$

The boundary condition $u(0,t) = A_1\cos(\omega_1 t)$ is applied for the propagating wave solution.

For numerical simulation, values of polycrystalline copper are used: with $E = 130$ GPa and $\nu = 0.34$, the resulting speed of sound is $c = 3817$ m/s and the resonant length of the slender bar must be $L = 9.54 \cdot 10^{-2}$ m. The boundary condition's amplitude is $A_1 = 1$ μm, which corresponds to the same magnitude used for polycrystalline copper ultrasonic fatigue experiments in the VHCF regime (see Chapter 4). For $\beta = 2.6$ (refer to Table 2.2), Fig. 2.2 **(b)** illustrates the standing wave over two stabilized periods.

In Fig. 2.3 **(a)**, the velocity spectra of the bar's tip $x = L$ is shown for the same solution, which shows the fundamental harmonic and second harmonic when $\beta = 2.6$. Here, it shows that the ratio between the second harmonic amplitude and fundamental harmonic differs by tens of magnitude compared to experimental results for an undamaged specimen in Chapter 4. This discrepancy cannot be explained by the variation of experimentally measured β shown in Table 2.2. Numerically this is shown with the

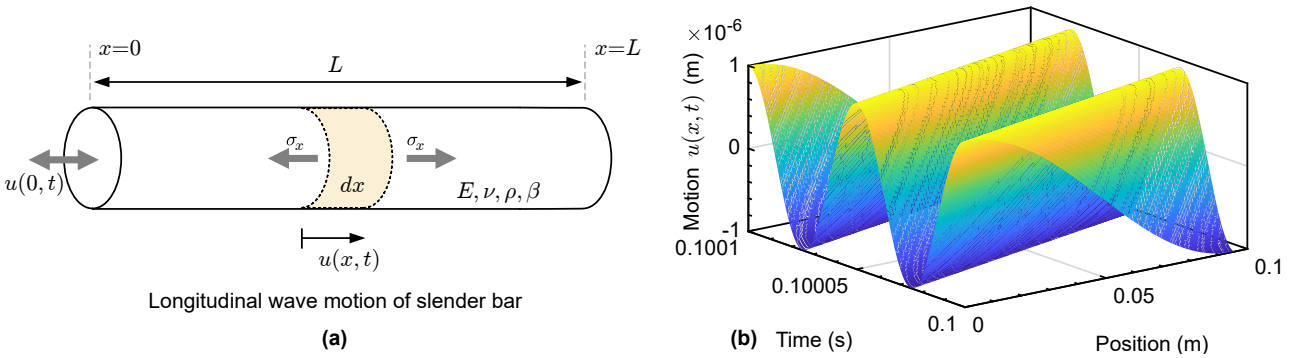

Figure 2.2: In **(a)**, the problem of longitudinal standing wave motion in a slender bar is shown. In **(b)**, the standing wave solution for the bar of two periods.

second harmonic and fundamental harmonics' amplitude ratios which are plotted for $1.6 \leq \beta \leq 3.6$ in Fig. 2.3 **(b)**. Here, it can be seen the variation of the harmonic amplitude ratios only range from $\approx 4 \cdot 10^{-5}$ to $9 \cdot 10^{-5}$. This indicates that the material nonlinearity of β coupled with Eq. (2.9) cannot solely describe the harmonic amplitude ratios seen in the fatigue specimen's tip vibration for the ultrasonic fatigue tests in Chapter 4. Additionally, the nonlinearity induces a frequency shift independent of the value of β (see the term of $\kappa x - \omega_1 t$ in Eq. (2.17)). Finally, the ratio of energy distribution between the fundamental stress harmonic and second harmonics is constant. Therefore, to visualize the energy transfer from the fundamental stress harmonic to the higher harmonics due to the nonlinearity, this ratio is adopted henceforth.

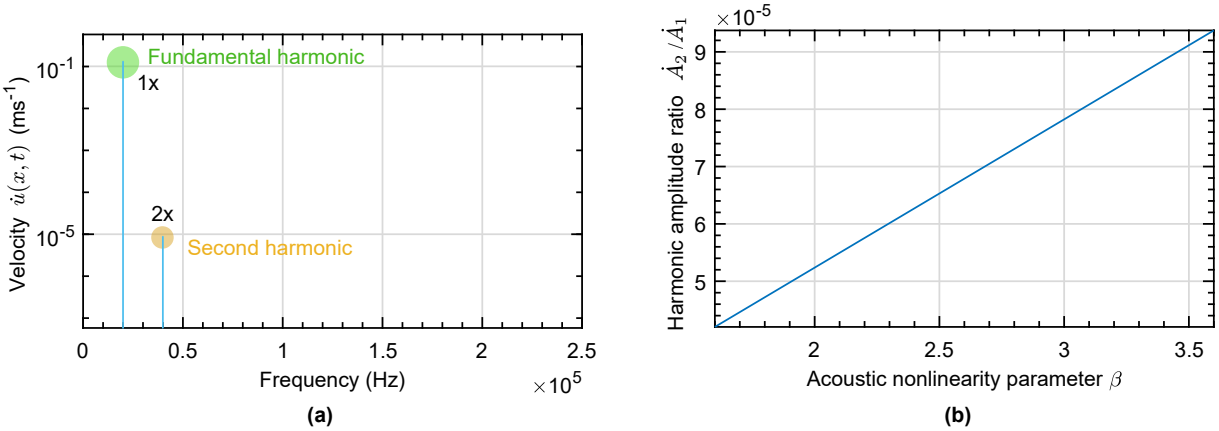

Figure 2.3: In **(a)**, the velocity frequency spectra for the bar's tip motion at $x = L$ with the fundamental and second harmonic. In **(b)**, the ratio of the second to fundamental harmonic for varying β values for polycrystalline copper.

Issues and departure from the acoustic nonlinearity model for ultrasonic fatigue

Here it's remarked on β's usefulness in ultrasonic fatigue research becomes limited. Firstly, the wave equation of Eq. (2.18) corresponds the longitudinal propagation solution to a pure harmonic input wave. For an ultrasonic fatigue test, this corresponds to the vibration at the junction of the acoustic horn and the base of the ultrasonic fatigue specimen. However, the fatigue specimen is solicited at a standing wave. Therefore, the nonlinear wave equation was solved for a steady-state solution, i.e forming a standing wave. The amplitude ratios reveals that the ratios for β values for polycrystalline copper differ with the experimentally measured harmonic amplitude ratios in ultrasonic fatigue experiments by factors of ten.

Additionally, it's been mentioned by the author [Kis+21] and others [Heb+23] that the input wave in ultrasonic fatigue tests is in fact multi-harmonic. The multi-harmonic input is due to the nonlinearities coming from the load train, i.e. the piezoelectric converter and the power and signal generator circuit, which is detailed later in Section 2.4. This consequently implies that the harmonics present in the tip vibration of an undamaged fatigue specimen are not representative of only nonlinear acoustic parameter β but also the input vibration.

Lastly, the acoustic nonlinearity parameter is a distributed material property. This does not reflect the fact that the active fatigue mechanisms are localized at the centroid volume of the ultrasonic fatigue specimen. Experimentally, the accumulation of material nonlinearities as heterogeneities at this centroid volume has been observed in fractograph and X-ray diffraction imagery (see Chapter 1).

For these reasons, a departure from the acoustic nonlinearity parameter is warranted. Instead, the acknowledgement of the the nonlinear influence of microscale defects such as microcracks and voids, dislocation structures, and other forms of microplasticity is warranted. Nonlinear contributions from microcracks, attributed to contact nonlinearity [Bro+14], have been thoroughly explored by both the acoustic and dynamics communities [Kle+17; Bro+14]. It is well documented that macroscopic crack closure, also known as a breathing crack, generates strong even-integer higher harmonics [Ruo+96; CDY01]. Macroscopic hysteresis-type behaviors, whether defined for materials [GJ99] or friction in structures [GN01], generate strong odd-integer higher harmonics. Consequently, should microscale defects exhibit a parallel mechanism to their macroscopic analogs, a similar pattern in their nonlinear harmonic generation can be anticipated. Thus, the following subsection proposes models of the mate-

rial nonlinearities that capture the nonlinear higher harmonic generation due to the accumulation of material nonlinearities as heterogeneities.

2.2.2 Microplasticity and microcrack homogenization models

Symbol	Description
a, b, c	Principle axes of ellipsoid
$\mathbb{A}, \mathbb{B}$	Strain and stress concentration tensors
$\mathbb{C}, \mathbb{S}$	Stiffness and compliance tensor
$\mathbb{E}, \mathbb{P}$	Eshelby's and Hill's tensor
E, ν	Young's modulus, Poisson's ratio
h	The hth harmonic
$\mathbb{I}^2, \mathbb{I}^4$	Second and fourth-order identity tensor
$\boldsymbol{n}$	Outward normal unit vector
$\boldsymbol{N}$	Normal to yield (stress) surface
$\mathbb{T}$	Microcrack limit tensor
S, V	Surface, volume
$\alpha = c/a$	Ellipsoidal aspect ratio
$\boldsymbol{\varepsilon}, \overline{\boldsymbol{\varepsilon}}$	Microscopic, macroscopic strain tensors
$\Delta\square$	Incremental value
κ, μ	Bulk and shear modulus
ρ	Mass density
$\boldsymbol{\sigma}, \overline{\boldsymbol{\sigma}}$	General or microscopic, macroscopic stress tensors
ω, f	Angular frequency and frequency
ξ	Volume fraction
$\overline{\square}, \langle\square\rangle_V$	Macroscopic or volume averaged quantity

Table 2.3: For the microplasticity and microcrack homogenization models in Sec. 2.2.2 only, this notation is adopted.

To enable a description of material-based heterogeneities within the centroid of an ultrasonic fatigue specimen, the nonlinear mesoscopic effect must be modeled. The objectives of this subsection are multiple: First, mean-field homogenization theories are introduced since they offer a computationally attractive alternative to directly modeling microscopic heterogeneities by finite element analysis. The homogenization occurs for a representative volume element (RVE) which represents a section of the microstructure that statistically mirrors the behavior at the macroscopic scale. Second, two sources of higher harmonic generation due to fatigue mechanisms are modeled: diffuse microplastic and microcrack inclusions, see Fig. 2.4. Due to their nonlinear nature, linearization schemes are implemented for homogenization. Additionally, mesoscale models – which discuss material behavior at a length scale

at the same order as the wavelength of the ultrasonic wave– are more appropriate; fatigue researchers may be more interested how these relevant fatigue mechanisms accumulate during ultrasonic fatigue tests. Lastly, a rudimentary crack model is introduced in the cases when the crack length violates the length-scale assumptions made by homogenization theories. This corresponds to the effect of a large crack near fatigue failure during ultrasonic fatigue tests.

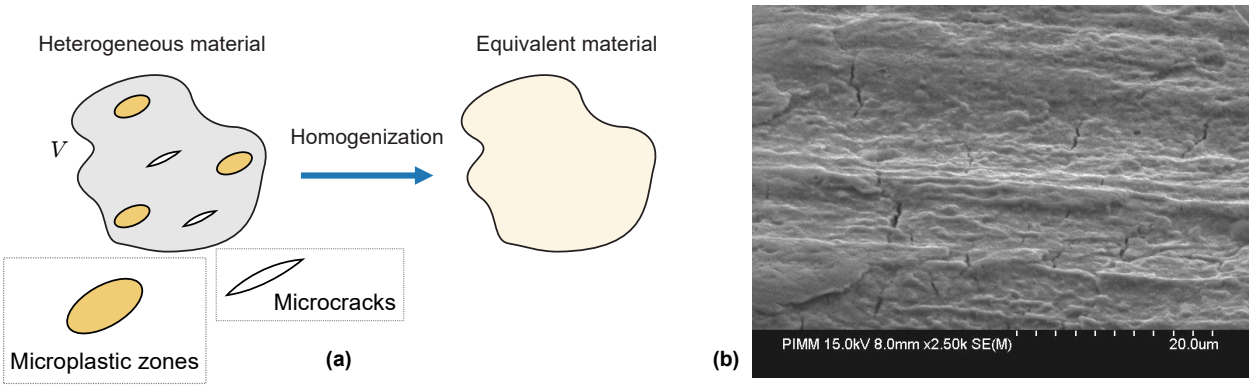

Figure 2.4: In **(a)**, a heterogeneous material at lower length scales is modeled as having microplastic and microcrack inclusions. Through homogenization, an equivalent material is found. In **(b)**, SEM imagery shows evidence of microscopic cracks in C70 steel in the VHCF regime, taken from [Yah13].

Mean-field homogenization of linear phases

Homogenization enables a length scale transition between both macroscopic quantities and lower scales for a fictitious RVE, see Fig. 2.5. Classically, this is done using a volume averaging operator:

$$\langle g(\boldsymbol{x})\rangle_V \coloneqq \frac{1}{V}\int_V g(\boldsymbol{x})\mathrm{d}V \coloneqq \overline{g} \tag{2.33}$$

where g is any kinematically admissible field over the domain and $\overline{g}$ represents the macroscopic value, and $\langle g(\boldsymbol{x})\rangle_V$ is the averaged value of g over the coordinates in the volume $\forall \boldsymbol{x} \in V$. This definition enables that the volume averaged field can be decomposed into sub-domains:

$$\langle g(\boldsymbol{x})\rangle_V = \frac{1}{V}\sum_i \int_{V_i} g(\boldsymbol{x})\mathrm{d}V_i, \quad V = \bigcup_i V_i$$

or in terms of the ith volume fraction ξ_i:

$$\langle g(\boldsymbol{x})\rangle_V = \sum_i \xi_i \langle g(\boldsymbol{x})\rangle_{V_i}, \quad \xi_i = \frac{V_i}{V} \tag{2.34}$$

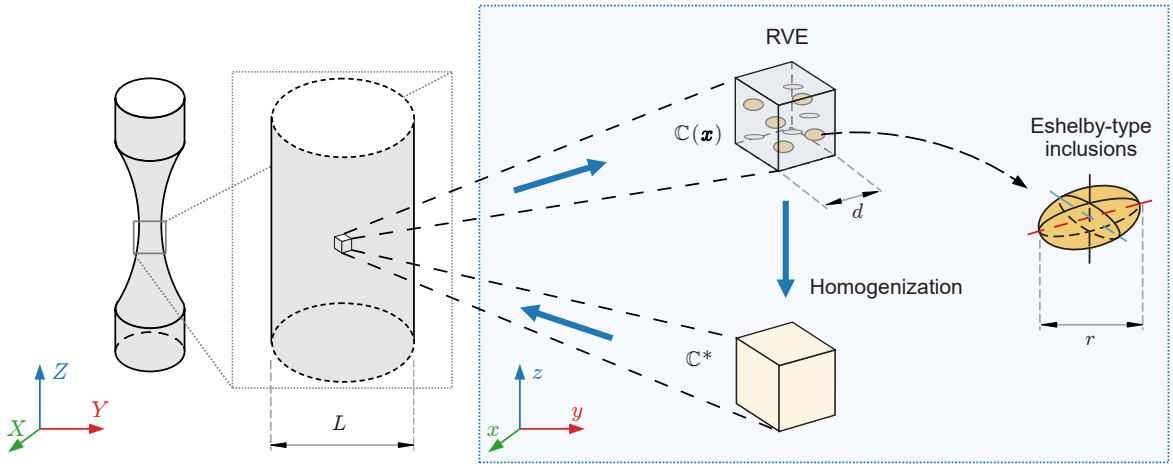

Figure 2.5: An ultrasonic fatigue specimen with a centroid of heterogeneities. Eshelby-based homogenization is valid for characteristic length scales $r \ll d \ll L$ between matrix and inclusion phases.

The consistency of internal work must be equivalent for both macroscopic and volume average quantities of stresses and strains:

$$\overline{\boldsymbol{\sigma}} : \overline{\varepsilon} = \langle \boldsymbol{\sigma} \rangle_V : \langle \varepsilon \rangle_V = \langle \boldsymbol{\sigma} : \varepsilon \rangle_V \tag{2.35}$$

Eq. (2.35) is the Hill-Mandel condition [Hil65], which is a necessary condition for equilibrium and compatibility inside the RVE, in addition to the boundary conditions applied to the surface of the RVE. Therefore, the per-phases' volume averages for stress and strain are:

$$\overline{\boldsymbol{\sigma}} = \sum_i \xi_i \langle \boldsymbol{\sigma} \rangle_{V_i}, \quad \overline{\boldsymbol{\varepsilon}} = \sum_i \xi_i \langle \boldsymbol{\varepsilon} \rangle_{V_i} \tag{2.36}$$

From hereon the ith per-phase volume averaged stresses and strains are written $\boldsymbol{\sigma}_i \equiv \langle \boldsymbol{\sigma} \rangle_{V_i}$ and $\boldsymbol{\varepsilon}_i \equiv \langle \boldsymbol{\varepsilon} \rangle_{V_i}$. Here it can be defined the two main relationships in mean-field homogenization theory:

- The *homogenization equation* relates the average stress and average strain of the RVE:

$$\overline{\boldsymbol{\sigma}} = \mathbb{C}^* : \overline{\boldsymbol{\varepsilon}} \tag{2.37}$$

  where $\mathbb{C}^*$ is the homogenized stiffness. This consequently implies that the ith per-phase average stiffness $\mathbb{C}_i$ gives the relationship:

$$\boldsymbol{\sigma}_i = \mathbb{C}_i : \varepsilon_i \tag{2.38}$$

- The *localization equation* relates the per-phase average strain and stress with the average stress and average strain of the RVE:

$$\boldsymbol{\varepsilon}_i = \mathbb{A}_i : \overline{\varepsilon}; \qquad \boldsymbol{\sigma}_i = \mathbb{B}_i : \overline{\boldsymbol{\sigma}} \tag{2.39}$$

where $\mathbb{A}_i$ and $\mathbb{B}_i$ are the fourth-order strain and stress concentration tensors for the ith phase. Due to the linearity of the phases, the strain and stress concentration tensors can be shown to fulfill the relations:

$$\sum_i \xi_i \, \mathbb{A}_i = \mathbb{I}^4; \qquad \sum_i \xi_i \, \mathbb{B}_i = \mathbb{I}^4 \tag{2.40}$$

where $\mathbb{I}^4$ is the symmetric fourth-order identity tensor.

The values of these concentration tensors lies in the choice of the simplifying assumptions in various mean-field homogenization schemes. Therefore, the main goal here is to determine the ith per-phase strain concentration tensor $\mathbb{A}_i$. This enables the homogenized stiffness of the RVE:

$$\begin{aligned} \mathbb{C}^* &= \sum_i \xi_i \mathbb{C}_i : \mathbb{A}_i \\ &= \mathbb{C}_\mathrm{m} + \sum_i \xi_i (\mathbb{C}_i - \mathbb{C}_\mathrm{m}) : \mathbb{A}_i \end{aligned} \tag{2.41}$$

where $\mathbb{C}_\mathrm{m}$ is the isotropic elastic matrix.

Voigt and Reuss homogenization The most basic example of homogenization scheme only accounts for the phases' volume fractions ξ_i and neglects their geometry in the material. The Voigt (isostrain) and Reuss (isostress) homogenization estimates correspond to $\mathbb{A}_i^{\mathrm{Voigt}} \coloneqq \mathbb{I}^4$ and $\mathbb{B}_i^{\mathrm{Reuss}} \coloneqq \mathbb{I}^4$ respectively. Using Eq. (2.41), the homogenized Voigt stiffness tensor can be easily found by the relationship:

$$\mathbb{C}^{\mathrm{Voigt}} = \sum_i \xi_i \mathbb{C}_i \tag{2.42}$$

Similarly for the homogenized Reuss stiffness tensor:

$$\mathbb{C}^{\mathrm{Reuss}} = \sum_i (\xi_i \mathbb{S}_i)^{-1} \tag{2.43}$$

where $\mathbb{S} = \mathbb{C}^{-1}$ is the compliance tensor. These approximations of effective elastic properties by the average stiffness or the average compliance are often referred to as *rules of mixtures* in the literature. Despite neglecting the geometry of the inclusion phases, the Voigt and Reuss stiffness estimates can be shown to have the property [NH99]:

$$\mathbb{C}^{\mathrm{Voigt}} \geq \mathbb{C}^* \geq \mathbb{C}^{\mathrm{Reuss}} \tag{2.44}$$

Equation 2.44 sets fundamental bounds for all valid mean-field homogenization stiffness estimates, allowing the validation of any homogenization scheme's estimate to fall between the Voigt and Reuss

limits. Next, a widely recognized approach that improves these homogenization stiffness estimates incorporates the geometrical considerations of the inclusions.

Eshelby's inclusion and dilute homogenization To take into account geometries, Eshelby [Esh57] addressed the strain concentration estimate for ellipsoidal inclusion within an infinite isotropic matrix. It was shown that the strain inside an ellipsoidal inclusion is uniform and can be calculated based on the properties of both the inclusion and an infinite matrix, as well as the applied external strain. A closed-form expression of Eshelby's tensor $\mathbb{E}$ can be obtained for and the case of an isotropic matrix and aligned spheroidal inclusions (an ellipsoid with two identical principle axes). In this case, $\mathbb{E}$ is a function of the ellipsoids axes $a = b, c$, usually denoted by its aspect ratio $\alpha \coloneqq c/a$ and the matrix's Poisson's ratio ν_{m}. These values are given in Appendix A.1. When the inclusions are not aligned (e.g. randomly oriented) or are embedded in an anisotropic matrix, Eshelby's tensor must be numerically evaluated using a method such as [GL90].

Due to the assumption of inclusions within an infinite matrix, this corresponds to the case when the volume fraction of inclusions are sufficiently small so that they do not interact with one another. The strain concentration tensor for a single inclusion i within the infinite elastic matrix can be written as [Ben87]:

$$\mathbb{A}_i^{\mathrm{dilute}} \coloneqq \left(\mathbb{I}^4 + \mathbb{E}_i : \mathbb{S}_{\mathrm{m}} : (\mathbb{C}_i - \mathbb{C}_{\mathrm{m}})\right)^{-1} \tag{2.45}$$

Due to the superposition principle, the individual contributions of each inclusion can be summed. This allows one to obtain the dilute homogenized stiffness tensor estimate by substitution Eq. (2.45) into Eq. (2.41) to give [BBG01]:

$$\mathbb{C}^{\mathrm{dilute}} = \mathbb{C}_{\mathrm{m}} + \sum_i \Big(\xi_i \, (\mathbb{C}_i - \mathbb{C}_{\mathrm{m}}) : \left(\mathbb{I}^4 + \mathbb{E}_i : \mathbb{S}_{\mathrm{m}} : (\mathbb{C}_i - \mathbb{C}_{\mathrm{m}})\right)^{-1}\Big) \tag{2.46}$$

According to [Esh57], the volume fraction of the inclusions $\sum_i \xi_i$ must be small enough to warrant the assumption of negligible interactions between the inclusions. However, this assumption is not entirely robust, where it has been demonstrated in literature that inclusion interactions become non-negligible even at low volume fractions [NH99]. The forthcoming subsubsection will elucidate an approximation of the inclusions' interactions as well as the limitations of the dilute model.

Mori-Tanaka homogenization The Mori-Tanaka model [MT73] improves upon the dilute model by considering the interaction between inclusions and matrix. Classically, the Mori-Tanaka model pro-

vides a better estimate for larger volume fraction of the inclusions (up to $\sum_i \xi_i \approx 0.2$ [NH99]). The dilute model can be shown to provide worst estimates as $\sum_i \xi_i$ increases [NH99]. Additionally, it has been demonstrated that the dilute estimate suffers from more limitations than previous assumed. This is particularly pronounced in cases involving significant contrasts in material properties between inclusions and matrix [Chr90] (e.g. opened cracks and voids whose stiffness is $\mathbf{0}$).

The Mori-Tanaka model approximates the inclusions-matrix interaction by employing an average stress field in the matrix material and assumes that each inclusion is embedded in this average field. Thus, the stress or strain fields acting on each inhomogeneity is accounted for while retaining the original approach for dilute distributions. Here the Mori-Tanaka strain concentration tensor is given with the same notations previously. Due to this intermediate step of approximating this interaction, the ith phase's strain tensor is given by Benveniste [Ben87]:

$$\mathbb{A}_i^{\mathrm{MT}} \coloneqq \mathbb{A}_i^{\mathrm{dilute}} : \Big(\sum_j \xi_j \mathbb{A}_j^{\mathrm{dilute}}\Big)^{-1} \tag{2.47}$$

Following similar steps as before, the Mori-Tanaka homogenized stiffness tensor estimate can be simplified by substitution of Eq. (2.47) into Eqs. (2.40) and (2.41):

$$\begin{aligned}\mathbb{C}^{\mathrm{MT}} &= \mathbb{C}_{\mathrm{m}} + \sum_i \Bigg(\xi_i \left(\mathbb{C}_i - \mathbb{C}_{\mathrm{m}}\right) : \big(\mathbb{I}^4 + \mathbb{E}_i : \mathbb{S}_{\mathrm{m}} : (\mathbb{C}_i - \mathbb{C}_{\mathrm{m}})\big)^{-1} : \Big(\sum_j \xi_j \big(\mathbb{I}^4 + \mathbb{E}_j : \mathbb{S}_{\mathrm{m}} : (\mathbb{C}_j - \mathbb{C}_{\mathrm{m}})\big)^{-1}\Big)^{-1}\Bigg) \\ &= \xi_{\mathrm{m}}\mathbb{C}_{\mathrm{m}} : \big(\xi_{\mathrm{m}}\mathbb{I}^4 + \sum_i \xi_i (\mathbb{I}^4 - \mathbb{E}_i)^{-1}\big)^{-1}\end{aligned} \tag{2.48}$$

where the second line of Eq. (2.48) is obtained by using Hill's tensor $\mathbb{P}_i$ [Hil65], which is defined as: $\mathbb{E}_i = \mathbb{P}_i : \mathbb{C}_{\mathrm{m}}$.

At this point, it's recalled that the goal of the Mori-Tanaka homogenization scheme is to estimate the strain concentration tensor $\mathbb{A}_i^{\mathrm{MT}}$ for each ith phase. This relies on knowledge of Eshelby's tensor $\mathbb{E}$, which is a function of the inclusion's geometry and the Poisson's ratio when the matrix phase is isotropic elastic. Therefore, these parameters must be derived for diffuse microplastic and microcrack inclusions. Additionally, these inclusion phases do not exhibit linear behaviors, e.g. microcrack closure during compression. Therefore, a linearization scheme must be considered in order to be utilized in Eq. (2.48). Henceforth, the notation of $^{\mathrm{MT}}$ is dropped, where it should be assumed that all concentration and homogenization tensors follow the Mori-Tanaka model. The notation for a linear elastic matrix phase, an aligned microplastic phase, and an aligned microcrack phase are denoted $\square_{\mathrm{m}}$, $\square_{\mathrm{pl}}$,

and $\square_{\mathrm{cr}}$ respectively.

Nonlinear Mori-Tanaka microplastic model

To consider an aligned microplastic inclusion phase, the geometry is first introduced. Let a set of spheres be characterized by the aspect ratio $\alpha = 1$, whose microplastic volume fraction is expressed as ξ_{pl}. In this context, the microplastic inclusions are modeled to follow a perfect plastic law governed by J_2 plasticity. This choice is motivated by its relative simplicity in simulating a fundamental plastic response (hysteresis) while avoiding overcomplicating the model with crystal plasticity-based formulations. Lastly, the Mori-Tanaka strain concentration tensor of Eq. (2.47) is inherently a function of the inclusion's nonlinear stiffness, and thus requires linearization.

Rate-independent plasticity First it's recalled the rate-independent plastic constitutive relationship, and afterwards perfect plasticity is considered. A total strain $\boldsymbol{\varepsilon}$ is assumed to be the sum of two parts: an elastic strain $\boldsymbol{\varepsilon}^{(\mathrm{el})}$ and a plastic strain $\boldsymbol{\varepsilon}^{(\mathrm{pl})}$. The stress tensor $\boldsymbol{\sigma}$ and the elastic strain $\boldsymbol{\varepsilon}^{(\mathrm{el})}$ are related:

$$\boldsymbol{\varepsilon} = \boldsymbol{\varepsilon}^{(\mathrm{el})} + \boldsymbol{\varepsilon}^{(\mathrm{pl})} \quad \text{and} \quad \boldsymbol{\sigma} = \mathbb{C} : \boldsymbol{\varepsilon}^{(\mathrm{el})} \tag{2.49}$$

A yield function $\mathcal{F}(\boldsymbol{\sigma})$ defines a yield surface ($\mathcal{F}(\boldsymbol{\sigma}) = 0$) and an elasticity domain ($\mathcal{F}(\boldsymbol{\sigma}) \leq 0$) for each phase:

$$\mathcal{F}(\boldsymbol{\sigma}) = \sigma_{\mathrm{eq}}(\boldsymbol{\sigma}) - \sigma^{\mathrm{Y}} + R(\psi) \tag{2.50}$$

where σ^{Y} is the yield stress of the material, $\sigma_{\mathrm{eq}} \coloneqq \left(\frac{3}{2}\boldsymbol{\sigma}_{\mathrm{D}} : \boldsymbol{\sigma}_{\mathrm{D}}\right)^{1/2}$ is the equivalent stress, $\boldsymbol{\sigma}_{\mathrm{D}} = \boldsymbol{\sigma} - \frac{1}{3}\operatorname{tr}(\boldsymbol{\sigma})\mathbb{I}^2$ is the deviatoric stress, and R is a hardening stress law. The evolution of the plastic strain tensor $\boldsymbol{\varepsilon}^{(\mathrm{pl})}$ is given by the plastic flow rule:

$$\dot{\boldsymbol{\varepsilon}}^{(\mathrm{pl})} = \dot{\lambda}\frac{\partial \mathcal{F}}{\partial \boldsymbol{\sigma}} = \dot{\lambda}\frac{3}{2}\frac{\boldsymbol{\sigma}_{\mathrm{D}}}{\sigma_{\mathrm{eq}}} \coloneqq \dot{\lambda}\boldsymbol{N} \tag{2.51}$$

where the scalar $\dot{\lambda} \geq 0$ is the plastic multiplier, and $\boldsymbol{N}$ is the normal vector to the yield surface in stress space. λ's sign is positive if $\mathcal{F} = 0$ and $\dot{\mathcal{F}} = 0$ (plastic), or negative if $\mathcal{F} < 0$ (elasticity) or $\mathcal{F} = 0$ and $\dot{\mathcal{F}} < 0$ (elastic unloading). The flow rule is termed associative since the plastic strains occur in a direction normal to the yield surface. The condition $\dot{\mathcal{F}} = 0$ is called the consistency condition, it provides a constraints: if there is plastic yielding during a time step, the solution should always remain

on the yield surface during all that time. Finally, the internal variable of accumulated plasticity ψ tracks the plastic history, and is related to the plastic strain rate by:

$$\dot{\psi} = \left(\frac{2}{3}\dot{\boldsymbol{\varepsilon}} : \dot{\boldsymbol{\varepsilon}}\right)^{1/2} = \dot{\lambda} \tag{2.52}$$

To link the strain rate to the stress rate via a tangent stiffness, one can write:

$$\dot{\boldsymbol{\sigma}} = \mathbb{C} : (\dot{\boldsymbol{\varepsilon}} - \dot{\boldsymbol{\varepsilon}}^{(\mathrm{pl})}) \tag{2.53}$$

If the regime is elastic, then $\dot{\boldsymbol{\varepsilon}}^{\mathrm{pl}} = 0$, and $\dot{\boldsymbol{\sigma}} = \mathbb{C} : \dot{\boldsymbol{\varepsilon}}$. Otherwise for plasticity:

$$\dot{\boldsymbol{\sigma}} = \mathbb{C} : \left(\dot{\boldsymbol{\varepsilon}} - \dot{\psi}\frac{\partial \mathcal{F}}{\partial \boldsymbol{\sigma}}\right) \tag{2.54}$$

The time derivative of the yield function $\dot{\mathcal{F}}$ expanded is:

$$\dot{\mathcal{F}} = \frac{\partial \mathcal{F}}{\partial \boldsymbol{\sigma}}\dot{\boldsymbol{\sigma}} - \frac{dR}{dp}\dot{\psi} = \frac{\partial \mathcal{F}}{\partial \boldsymbol{\sigma}} : \mathbb{C} : \dot{\boldsymbol{\varepsilon}} - p\dot{\psi} \tag{2.55}$$

where:

$$p \coloneqq \frac{\partial \mathcal{F}}{\partial \boldsymbol{\sigma}} : \mathbb{C} : \frac{\partial \mathcal{F}}{\partial \boldsymbol{\sigma}} + \frac{dR}{d\psi} \tag{2.56}$$

When $\mathcal{F} = 0$ (plasticity) and $\dot{\mathcal{F}} = 0$, there are two cases: When $\dot{\mathcal{F}} < 0$, $\dot{\psi} = 0$ and Eq. (2.55) gives:

$$\frac{\partial \mathcal{F}}{\partial \boldsymbol{\sigma}} : \mathbb{C} : \dot{\boldsymbol{\varepsilon}} < 0 \tag{2.57}$$

When $\dot{\mathcal{F}} = 0$ then Eq. (2.55) gives:

$$\dot{\psi} = \frac{1}{p}\frac{\partial \mathcal{F}}{\partial \boldsymbol{\sigma}} : \mathbb{C} : \dot{\boldsymbol{\varepsilon}} > 0 \tag{2.58}$$

Combining Eqs. (2.54) and (2.58), a relationship between strain rate and stress rate is given:

$$\dot{\boldsymbol{\sigma}} = \mathbb{C}_{\mathrm{ep}} : \dot{\boldsymbol{\varepsilon}} \quad \text{with} \quad \mathbb{C}_{\mathrm{ep}} \coloneqq \mathbb{C} - \frac{1}{p}\left(\mathbb{C} : \frac{\partial \mathcal{F}}{\partial \boldsymbol{\sigma}}\right) \otimes \left(\frac{\partial \mathcal{F}}{\partial \boldsymbol{\sigma}} : \mathbb{C}\right) \tag{2.59}$$

where $\mathbb{C}_{\mathrm{ep}}$ is the elasto-plastic stiffness. It has the same symmetries (major and minor) as $\mathbb{C}$ but is not constant; it depends on the deviatoric stress $\boldsymbol{\sigma}_{\mathrm{D}}$. If $\mathbb{C}$ is isotropic, simplifications can be made since $\mathbb{C} : \frac{\partial \mathcal{F}}{\partial \boldsymbol{\sigma}} = 2\mu\frac{\partial \mathcal{F}}{\partial \boldsymbol{\sigma}}$ and $\frac{\partial \mathcal{F}}{\partial \boldsymbol{\sigma}} : \frac{\partial \mathcal{F}}{\partial \boldsymbol{\sigma}} = \frac{3}{2}$ where μ is the shear modulus. This gives the expressions:

$$\mathbb{C}_{\mathrm{ep}} = \mathbb{C} - \frac{(2\mu)^2}{p}\boldsymbol{N} \otimes \boldsymbol{N}; \qquad p = 3\mu + \frac{dR}{d\psi}; \tag{2.60}$$

In the case of perfect plasticity, then $R(\psi) = 0$, and it follows from Eq. (2.55) that $\dot{\mathcal{F}} = \partial\mathcal{F}/\partial\boldsymbol{\sigma}$ and $p = \partial\mathcal{F}/\partial\boldsymbol{\sigma} : \mathbb{C} : \partial\mathcal{F}/\partial\boldsymbol{\sigma}$. This simplifies Eq. (2.59), where in plasticity for uniaxial tension (e.g. about X_1) is $\partial\sigma_{11}/\partial\varepsilon_{11} = 0$. The other components are not null since it is a multi-axial tangent modulus that depends on the deviatoric stress.

Linearization of the elasto-plastic stiffness tensor To determine the stress strain relationship, the rate-form is linearized. By denoting a discretization in time $\Delta\square \coloneqq \square(t+1) - \square(t)$, the rate form of Eq. (2.59) can be rewritten:

$$\Delta\boldsymbol{\sigma} = \mathbb{C}_{\text{alg}} : \Delta\boldsymbol{\varepsilon} \tag{2.61}$$

where $\Delta\boldsymbol{\sigma}$ and $\Delta\boldsymbol{\varepsilon}$ are the average stress and average strain increments over a time interval, respectively, and $\mathbb{C}^{\text{alg}}$ is the algorithmic tangent stiffness. While Eq. (2.61) looks similar to Eq. (2.59), the difference lies in a few mathematical derivations. Otherwise, the algorithmic tangent stiffness acts similar to the elasto-plastic tangent stiffness: if the increment is entirely elastic, then $\mathbb{C}_{\text{alg}} = \mathbb{C}_{\text{m}}$. Doghri [Dog00] derives a simple and explicit relationship which shows the relationship between the algorithmic and elasto-plastic tangent stiffness:

$$\mathbb{C}_{\text{alg}} = \mathbb{C}_{\text{ep}} - (2\mu)^2 \cdot \Delta\psi \frac{\sigma_{\text{eq}}}{\hat{\sigma}_{\text{eq}}} \frac{\partial \boldsymbol{N}}{\partial \boldsymbol{\sigma}} \tag{2.62}$$

where $\hat{\sigma}_{\text{eq}}$ is the trial (elastic predictor) of σ_{eq}. The partial derivative of the normal vector $\boldsymbol{N}$ with respect to $\boldsymbol{\sigma}$ is given as:

$$\frac{\partial \boldsymbol{N}}{\partial \boldsymbol{\sigma}} = \frac{1}{\sigma_{\text{eq}}} \left(\frac{3}{2} \mathbb{I}^{\text{D}} - \boldsymbol{N} \otimes \boldsymbol{N} \right) \tag{2.63}$$

where $\mathbb{I}^{\text{D}} \coloneqq \mathbb{I}^4 - (1/3)(\mathbb{I}^2 \otimes \mathbb{I}^2)$ is the deviatoric part of the fourth-order identity tensor and $\mathbb{I}^2$ is the second-order identity tensor.

Mori-Tanaka microplastic homogenized stiffness In order to be able to use the formulation of the Mori-Tanaka strain concentration tensor Eq. (2.47), the average inclusion's stress-strain relationship is linearized. This is done by substituting the stress dependence of the tangent stiffness tensors with a dependence on microplastic inclusions' averaged deviatoric stress $\langle \overline{\boldsymbol{\sigma}}_{\text{D,pl}} \rangle$. This leads to an linearized material behavior with a tangent stiffness tensor:

$$\Delta\overline{\boldsymbol{\sigma}}_{\text{pl}} = \mathbb{C}_{\text{alg}} \left(\langle \overline{\boldsymbol{\sigma}}_{\text{D,pl}} \rangle \right) : \Delta\overline{\boldsymbol{\varepsilon}}_{\text{pl}} \tag{2.64}$$

where $\Delta\overline{\boldsymbol{\sigma}}_{\text{pl}}$ and $\Delta\overline{\boldsymbol{\varepsilon}}_{\text{pl}}$ are the average stress and average strain increments of each phase over a time interval, respectively. Eq. (2.64) can be written for the microplastic phase and form a set of linearized constitutive equations over a time step. For each time step (t), given a macroscopic strain increment, a trial value of the average strain increment in the inclusions is computed. A fixed-point iterative scheme converges to average strain values in the phases from which the effective stiffness and the macroscopic response can be computed.

The final homogenized tangent stiffness is found by substituting the derived tangent stiffness $\mathbb{C}_{\text{alg}} \equiv \mathbb{C}_{\text{pl}}$ into the Mori-Tanaka model of Eq. (2.48):

$$\mathbb{C}_{\text{pl}}^{\text{MT}} = \mathbb{C}_{\text{m}} + \xi_{\text{pl}} \left(\mathbb{C}_{\text{pl}} - \mathbb{C}_{\text{m}}\right) : \left(\mathbb{I}^4 + \mathbb{E}_{\text{pl}} : \mathbb{S}_{\text{m}} : \left(\mathbb{C}_{\text{pl}} - \mathbb{C}_{\text{m}}\right)\right)^{-1} : \left(\xi_{\text{pl}}\left(\mathbb{I}^4 + \mathbb{E}_{\text{pl}} : \mathbb{S}_{\text{m}} : \left(\mathbb{C}_{\text{pl}} - \mathbb{C}_{\text{m}}\right)\right)^{-1}\right)^{-1} \tag{2.65}$$

where $\mathbb{E}_{\text{pl}}$ is Eshelby's tensor for spherical inclusions.

Isotropization of Eshelby elasto-plastic inclusions It has been shown in the literature that Eshelby-based approaches tend to overestimate the macroscopic strain hardening in the plastic regime, i.e. the homogenized macroscopic behavior is too stiff compared to the finite element analog. Correct predictions are obtained only when Eshelby's tensor is computed with an isotropic tangent stiffness $\mathbb{C}_{\text{iso}}$ (instead of the algorithmic tangent stiffness $\mathbb{C}_{\text{alg}}$), see [DO03] and [DF05]. Here the method defined by [BBG01] is used. Recall a fourth-order isotropic tensor can always be written under the form:

$$\mathbb{C}_{\text{iso}} \coloneqq (\mathbb{I}^{\text{S}} :: \mathbb{C}_{\text{ani}})\mathbb{I}^{\text{S}} + \frac{1}{5}(\mathbb{I}^{\text{D}} :: \mathbb{C}_{\text{ani}})\mathbb{I}^{\text{D}} \tag{2.66}$$

where $\mathbb{I}^S \coloneqq (1/3)(\mathbb{I}^2 \otimes \mathbb{I}^2)$ is the spherical operator, and :: is the tensor product over four indices. The extraction of $\mathbb{C}_{\text{iso}}$ from $\mathbb{C}_{\text{ani}}$ is written for isotropic linear elasticity:

$$\mathbb{C}_{\text{iso}} = 3\kappa_{\text{iso}}\mathbb{I}^{\text{S}} + 2\mu_{\text{iso}}\mathbb{I}^{\text{D}} \tag{2.67}$$

where κ_{iso} and μ_{iso} are isotropized bulk and shear moduli, respectively. The Eshelby's tensor $\mathbb{E}$ is only a function of the ellipsoid aspect ratio α and the matrix's isotropized Poisson's ratio:

$$\nu_{\text{iso}} = \frac{3\kappa_{\text{iso}} - 2\mu_{\text{iso}}}{2(3\kappa_{\text{iso}} + \mu_{\text{iso}})} \tag{2.68}$$

As shown by [BBG01], the projection of the (anisotropic) elasto-plastic tangent stiffness onto the isotropic subspace has the following values for J_2 plasticity:

$$\kappa_{\text{iso}} = \kappa \quad \text{and} \quad \mu_{\text{iso}} = \mu - \frac{3}{5}\mu^2\left(\frac{1}{p} + 4\frac{\Delta\psi}{\hat{\sigma}_{\text{eq}}}\right) \tag{2.69}$$

Henceforth, the isotropized stiffness is only used to compute the Eshelby's tensor of the elasto-plastic inclusions, while the previous definition of the algorithmic tangent stiffness is used for all other computations.

Behavior of microplastic inclusions – single harmonic wave Throughout the remainder of this dissertation, the inclusions have a perfectly plastic law (no hardening law $R = 0$). This is employed since the microplasticity behavior in a real fatigued material is not well quantified. Due to the J_2 plasticity definition of microplastic inclusions, the microplastic inclusions have their own yield stress and is thus a parameter of the model. For example, the macroscopic yield strength of 1070 steel is approximately $\sigma^{\mathrm{Y}} = 495$ MPa. However, at the VHCF regime, the longitudinal strain amplitudes are too small to elicit macroscopic plastic behavior. Therefore, to represent microplastic behavior, the microplastic inclusions must have a microplastic yield stress $\sigma^{\mathrm{Y}}_{\mathrm{pl}} \ll \sigma^{\mathrm{Y}}$ less than the macroscopic material, but otherwise their stiffnesses $\mathbb{C}_{\mathrm{m}} = \mathbb{C}_{\mathrm{pl}}$ should be equal. This microplastic yield stress is posited to be connected with dislocation density for crystal plasticity, see Chapter 1.

First, the behavior of microplastic inclusions are studied with respect to to their separate model parameters: the microplastic yield stress $\sigma^{\mathrm{Y}}_{\mathrm{pl}}$ and afterwards their volume fraction ξ_{pl}. One assumption typically used in ultrasonic fatigue tests is the assumption of a pure single harmonic loading. This corresponds to a single harmonic uniaxial strain $\varepsilon_{33}(t) = \varepsilon_{\mathrm{a}} \cos(\omega_0 t)$, where the frequency is $f_0 = 20$ kHz and $\omega_0 \coloneqq 2\pi f_0$.

To demonstrate the model parameter of $\sigma^{\mathrm{Y}}_{\mathrm{pl}}$, the behavior of the longitudinal stress and strain for the macroscopic behavior **(a)**, the matrix **(b)**, and the inclusion phase **(c)** are plotted in Fig. 2.6. The RVE of microplastic inclusions are subject this single harmonic loading while $\sigma^{\mathrm{Y}}_{\mathrm{pl}}/\sigma^{\mathrm{Y}}$ is varied. Specifically, a longitudinal strain amplitude of $\varepsilon_a = 5 \cdot 10^{-4}$ at a reversible load of $R = -1$ is imposed. When $\sigma^{\mathrm{Y}}_{\mathrm{pl}}/\sigma^{\mathrm{Y}} = 1$, the homogenized RVE's response, matrix phase, and inclusion phase in Fig. 2.6 all have elastic behavior. As the ratio of $\sigma^{\mathrm{Y}}_{\mathrm{pl}}/\sigma^{\mathrm{Y}}$ decreases, the inclusions begin to plastify. A too small microplastic yield stress for the microplastic inclusions would manifest plasticity at too low of a strain amplitude, making the apparent behavior elastic with the plastic tangent, see Fig. 2.6 **(a)** in the case $\sigma^{\mathrm{Y}}_{\mathrm{pl}}/\sigma^{\mathrm{Y}} = 0.01$. Therefore, the microplastic yield stress is defined to have a clear elastic-plastic response for the homogenized RVE at $\sigma^{\mathrm{Y}}_{\mathrm{pl}}/\sigma^{\mathrm{Y}} = 0.1$, i.e. 10% of the macroscopic yield stress.

The second free parameter that can vary is the microplastic inclusion volume fraction ξ_{pl}. In Fig. 2.7, the homogenized RVE's response **(a)**, matrix phase **(b)**, and inclusion phase **(c)** are shown similarly to before, except that $\sigma^{\mathrm{Y}}_{\mathrm{pl}}/\sigma^{\mathrm{Y}} = 0.1$ is imposed and ξ_{pl} is varied. When the volume fraction increases, it can be seen that as $\xi_{\mathrm{pl}} \to 1$, the homogenized RVE's behavior resembles more that of the microplastic inclusions. It should be noted that this volume fraction is expected to be very small in

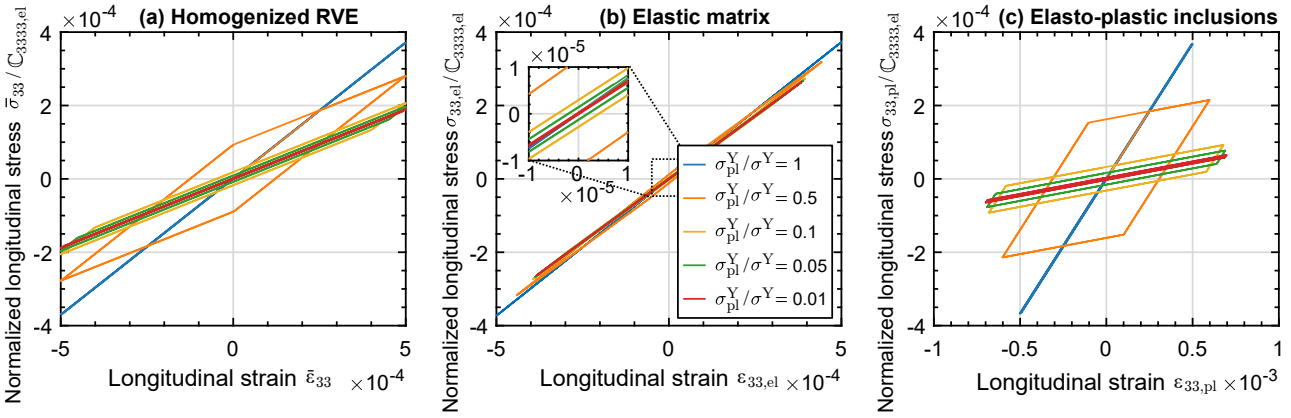

Figure 2.6: In **(a)**, **(b)**, and **(c)**, the stress-strain hysteresis seen by the RVE, matrix phase, and inclusion phase respectively, with $R = -1$ and $\xi_{\mathrm{pl}} = 10^{-1}$ is shown for varying the microplastic yield stress ratio with the elastic material's macroscopic yield stress $\sigma^{\mathrm{Y}}_{\mathrm{pl}}/\sigma^{\mathrm{Y}}$.

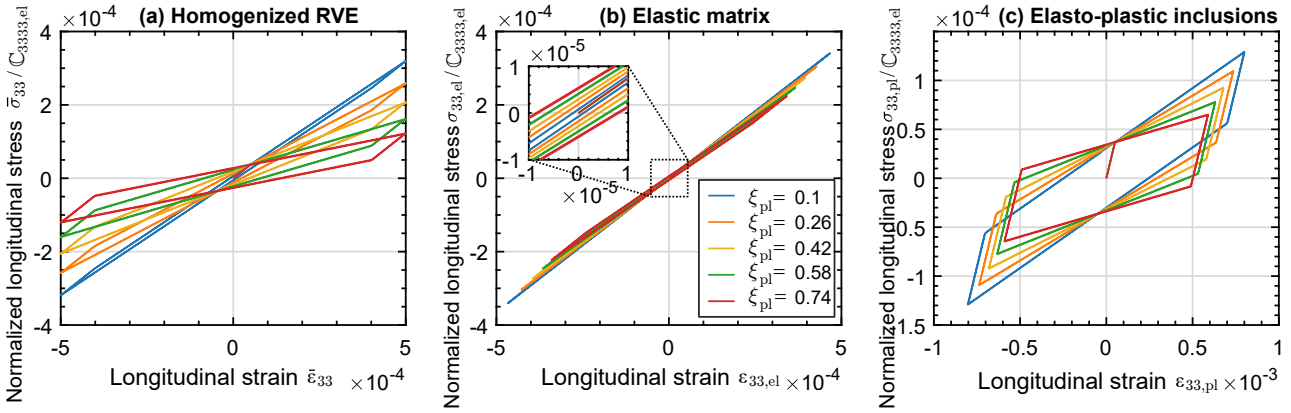

Figure 2.7: In **(a)**, **(b)**, and **(c)**, the stress-strain hysteresis seen by the RVE, matrix phase, and inclusion phase respectively, with $R = -1$ and $\sigma^{\mathrm{Y}}_{\mathrm{pl}}/\sigma^{\mathrm{Y}} = 10^{-1}$ is shown for varying microplastic inclusion volume fraction parameter ξ_{cr}.

practice. A limit at $\xi_{\mathrm{pl}} \approx 0.74$ is shown in Fig. 2.7 just to emphasize the behavior of the model, and represents the max sphere packing. Past this limit, the problem is physically ill defined, except for $\xi_{\mathrm{pl}} = 1$, where the entire RVE is the microplastic inclusion phase.

Next, the higher harmonic generation is to be studied in Fig. 2.8 for the loading case of a reversible pure sine longitudinal strain load of $R = -1$ with amplitude $\varepsilon_a = 5 \cdot 10^{-4}$ at $f_0 = 20$ kHz. In **(a)**, the frequency spectra is shown corresponding to a 10% microplastic volume fraction. It can be seen that the third harmonic is stronger than the second harmonic, and overall the odd harmonics stronger than the even harmonics. In **(b)**, the microplastic volume fraction is varied for so that the higher

harmonic ratios can be studied as the volume fraction grows. Here, the third harmonic ratio is the most prominent, followed by the second harmonic ratio, both of which monotonically increase. Interestingly, the presence of a even harmonics is typically not found in the literature rudimentary models of hysteresis [GJ99; GN01]. This is due to the fact that most models of hysteresis are a one-dimensional model which neglect complexities such as the geometries and their triaxial stress effects.

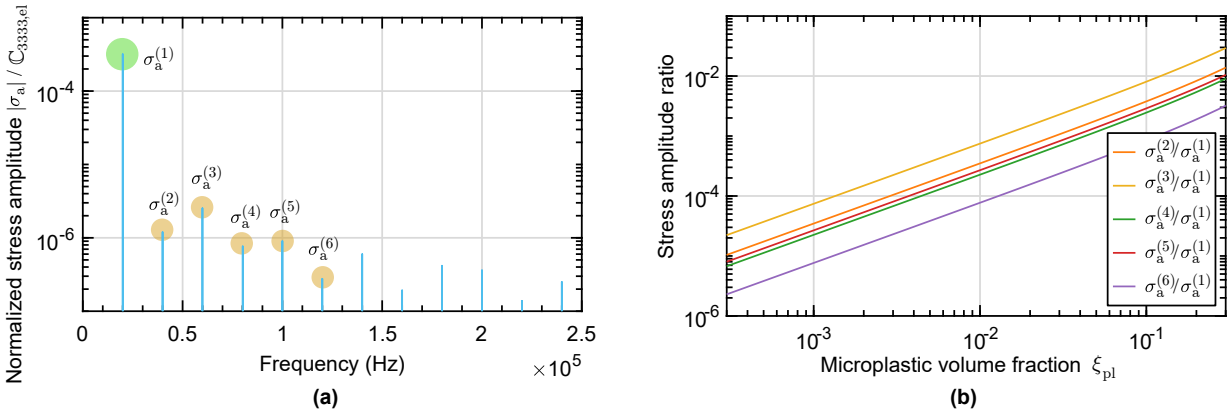

Figure 2.8: In **(a)**, the normalized frequency spectra of an uniaxial stress wave in the RVE for a single harmonic strain $\varepsilon_{33}(t)$ at $f_0 = 20$ kHz with load ratio $R = -1$ and $\xi_{cr} = 10^{-1}$. In **(b)**, the ratio of higher harmonics to fundamental harmonic follow the same trajectory.

Behavior of microplastic inclusions – multi-harmonic wave To study the effect of a multi-harmonic strain wave on microplasticity, an imposed multi-harmonic strain wave is defined as:

$$\varepsilon_{33}(t) = \varepsilon_a^{(1)} \cos(1 \cdot \omega_0 t) + \varepsilon_a^{(2)} \cos(2 \cdot \omega_0 t) + \varepsilon_a^{(3)} \cos(3 \cdot \omega_0 t) \tag{2.70}$$

with the values $\varepsilon_a^{(1)} = 5 \cdot 10^{-4}$, $\varepsilon_a^{(2)} = 2.5 \cdot 10^{-7}$, and $\varepsilon_a^{(3)} = 2.9 \cdot 10^{-6}$. Observing Fig. 2.9, the influence of microcracks on the second and third harmonic ratios are most evident. From $10^{-3} < \xi_{pl} < 10^{-1}$, the gap between the second and third harmonics' ratios widely differ compared with the results for single multi-harmonic strain wave (shown as dotted lines). The strongest higher harmonic, the third harmonic can be shown to be insensitive to the microplastic volume fraction until $\xi_{pl} \approx 2 \cdot 10^{-2}$. At this point the third harmonic begins to increase monotonically, and converge with the single-harmonic results as the microplastic inclusions increase in volume fraction.

The plot of the second harmonic ratio (represented by the orange line) indicates a region of ambiguity in determining the volume fraction. Specifically, for certain values of the second harmonic ratio

between $4 \cdot 10^{-4}$ to $3 \cdot 10^{-2}$, there are two possible corresponding volume fractions. This crossover results in an ambiguous interpretation if one were to only study the second harmonic ratio. This suggests that interpreting acoustic nonlinearity measurements, as discussed in Section 2.2, in the presence of multi-harmonic inputs may lead to inaccuracies in the analysis. indicates a region of ambiguity in determining the volume fraction.

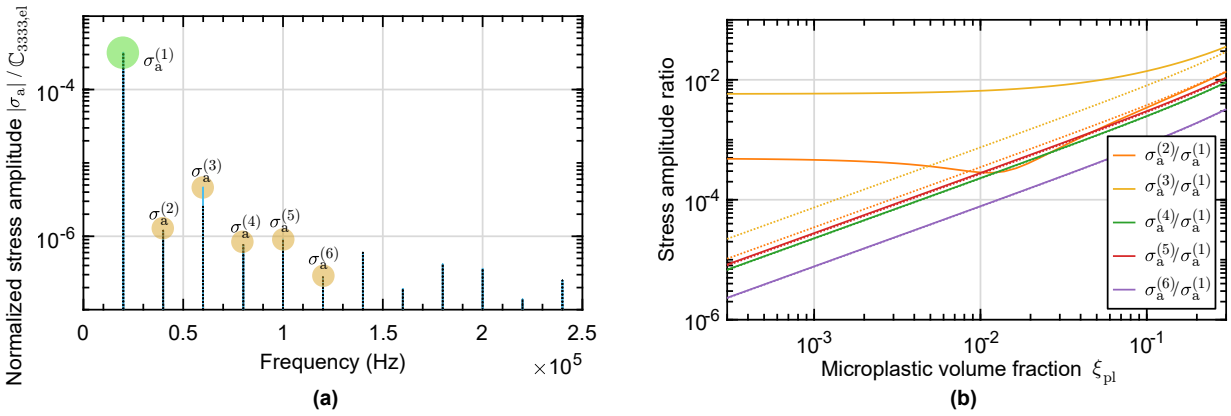

Figure 2.9: In **(a)**, the normalized frequency spectra of an uniaxial stress wave in the RVE for a multi-harmonic strain Eq. (2.70) at $f_0 = 20$ kHz with load ratio $R = -1$ and $\xi_{cr} = 10^{-1}$. In **(b)**, the ratio of higher harmonics to fundamental harmonic no longer follow the same trajectory. The dotted lines represent previously extract harmonic ratios from Fig. 2.8 for a single harmonic strain wave.

Nonlinear Mori-Tanaka microcrack model

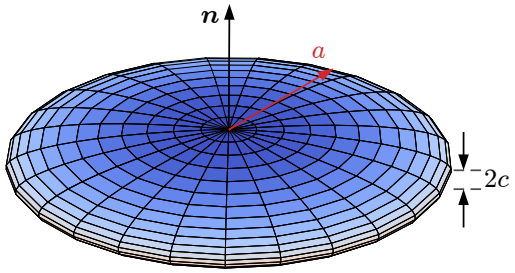

Figure 2.10: A schematic representation of an opened ellipsoidal microcrack.

To consider an aligned microcrack phase, the geometry is first introduced. Let a set of ellipsoid-shaped cracks be characterized by a small aspect ratio α and unit normal vector $\boldsymbol{n}$; for mode-I cracks, this corresponds to the unit vector parallel to the $a - b$ plane, see Fig. 2.10. The volume fraction of the microcracks refers to the geometry of an opened microcrack, which is expressed as ξ_{cr}. Here, it's adopted the methods from of Deudé et al. and Bluthe et al. [Deu+02; BBL20] for Eshelby-based

microcracks, which experience a perfect interface with no friction. The strain rate of an elliptical elastic heterogeneity with aspect ratio $\alpha \coloneqq c/a$ embedded in an infinite elastic matrix is given as:

$$\dot{\boldsymbol{\varepsilon}}_{\mathrm{cr}} = \left(\mathbb{I}^4 + \mathbb{E}_{\mathrm{cr}} : \mathbb{S}_{\mathrm{m}} : (\mathbb{C}_{\mathrm{cr}} - \mathbb{C}_{\mathrm{m}})\right)^{-1} : \dot{\bar{\boldsymbol{\varepsilon}}} \tag{2.71}$$

For an open crack $\mathbb{C}_{\mathrm{cr}} = \mathbf{0}$, the definition of Eshelby's tensor Eq. (A.1) with Eq. (2.71) becomes:

$$\dot{\boldsymbol{\varepsilon}}_{\mathrm{cr}} = (\mathbb{I}^4 - \mathbb{E}_{\mathrm{cr}})^{-1} : \dot{\bar{\boldsymbol{\varepsilon}}} \tag{2.72}$$

Here, one can define the strain rate concentration $\mathbb{A}_{\mathrm{cr}} \coloneqq (\mathbb{I} - \mathbb{E}_{\mathrm{cr}})^{-1}$ for a single microcrack. The individual components of its strain concentration tensor $\mathbb{A}_{\mathrm{cr}}$ can be found using a Taylor series expansion on Hill's tensor [DK16]. Assuming the microcrack normal unit vector is $\boldsymbol{n} = \boldsymbol{e}_3$, the out-of-plane components are:

$$\mathbb{A}_{\mathrm{cr},1111} = 1 - \frac{\nu_{\mathrm{m}}}{2}; \qquad \mathbb{A}_{\mathrm{cr},1122} = -\frac{\nu_{\mathrm{m}}}{2}; \qquad \mathbb{A}_{\mathrm{cr},1133} = \frac{\nu_{\mathrm{m}} - 1}{2}; \qquad \mathbb{A}_{\mathrm{cr},1212} = \frac{1}{2} \tag{2.73}$$

where ν_{m} is the isotropic Poisson's ratio of $\mathbb{C}_{\mathrm{m}}$. The magnitude of the components in the crack plane can be shown on the same order of the far-field strain rate. For the normal strain rate components:

$$\mathbb{A}_{\mathrm{cr},3311} = \frac{1}{\alpha}\frac{4\nu_{\mathrm{m}}\,(1-\nu_{\mathrm{m}})}{\pi\,(1-2\nu_{\mathrm{m}})}; \qquad \mathbb{A}_{\mathrm{cr},3333} = \frac{1}{\alpha}\frac{4\,(1-\nu_{\mathrm{m}})^2}{\pi\,(1-2\nu_{\mathrm{m}})}; \qquad \mathbb{A}_{\mathrm{cr},2323} = \frac{1}{\alpha}\frac{2\,(1-\nu_{\mathrm{m}})}{\pi\,(2-\nu_{\mathrm{m}})} \tag{2.74}$$
$$\mathbb{A}_{\mathrm{cr},1313} = \mathbb{A}_{\mathrm{cr},2323}; \qquad \mathbb{A}_{\mathrm{cr},3322} = \mathbb{A}_{\mathrm{cr},3311}$$

Note, the normal components are an order of magnitude larger than the far-field strain rate. This highlights the nonlinear strain concentration effect due to the spheroidal crack geometry. This justifies the choice of using a strain-rate formulation.

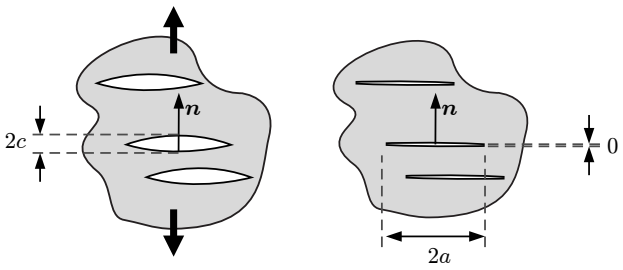

Figure 2.11: Representation of multiple aligned microcracks with opened aperture $2c$ and an non-strained aperture 0. When $\boldsymbol{n}$ aligns with the loading direction, the microcracks are mode I.

To consider a crack closure criterion, the strain concentration effect in the normal direction (Eq. (2.73) versus Eq. (2.74)) has the largest variation. The normal strain rate is thus equivalent

to the rate of change of the crack's aspect ratio:

$$\dot{\boldsymbol{\varepsilon}}_{\mathrm{cr}}^{(\boldsymbol{n})} = (\boldsymbol{n} \otimes \boldsymbol{n}) : \left(\alpha \cdot (\mathbb{I}^4 - \mathbb{E}_{\mathrm{cr}})^{-1} : \dot{\bar{\boldsymbol{\varepsilon}}}\right) \tag{2.75}$$

Since the opened crack is assumed flat $\alpha \ll 1$, the product $\alpha \cdot (\mathbb{I}^4 - \mathbb{E}_{\mathrm{cr}})^{-1}$ can be replaced by the opened crack strain concentration tensor $\mathbb{T}_{\mathrm{cr}}$ as the aspect ratio approaches the limit $\alpha \to 0$:

$$\alpha \cdot (\mathbb{I}^4 - \mathbb{E}_{\mathrm{cr}}(\alpha))^{-1} \approx \mathbb{T}_{\mathrm{cr}} \coloneqq \lim_{\alpha \to 0} \alpha \cdot (\mathbb{I}^4 - \mathbb{E}_{\mathrm{cr}}(\alpha))^{-1} \tag{2.76}$$

Since $\mathbb{T}_{\mathrm{cr}}$ is independent of the opened crack state, the integration of the rate of change of the crack aspect ratio of Eq. (2.75) gives:

$$\boldsymbol{\varepsilon}_{\mathrm{cr}}^{(\boldsymbol{n})} = (\boldsymbol{n} \otimes \boldsymbol{n}) : (\mathbb{T}_{\mathrm{cr}} : \bar{\boldsymbol{\varepsilon}}) \tag{2.77}$$

where c represents current aperture of the microcrack, and the aperture of the crack in a non-strained state is 0. From the crack strain concentration tensor, $\mathbb{T}_{\mathrm{cr}}$ is derived similarly with the normal components:

$$\begin{gathered} \mathbb{T}_{\mathrm{cr},3311} = \frac{4\nu_{\mathrm{m}}\left(1-\nu_{\mathrm{m}}\right)}{\pi\left(1-2\nu_{\mathrm{m}}\right)}; \qquad \mathbb{T}_{\mathrm{cr},3333} = \frac{4\left(1-\nu_{\mathrm{m}}\right)^2}{\pi\left(1-2\nu_{\mathrm{m}}\right)}; \qquad \mathbb{T}_{\mathrm{cr},2323} = \frac{2\left(1-\nu_{\mathrm{m}}\right)}{\pi\left(2-\nu_{\mathrm{m}}\right)} \\ \mathbb{T}_{\mathrm{cr},1313} = \mathbb{T}_{\mathrm{cr},2323}; \qquad \mathbb{T}_{\mathrm{cr},3322} = \mathbb{T}_{\mathrm{cr},3311} \end{gathered} \tag{2.78}$$

with the rest equal to zero in an isotropic medium. From this point, one can see that at crack closure $\boldsymbol{\varepsilon}_{\mathrm{cr}}^{(\boldsymbol{n})} < 0$.

When the crack is closed and has frictionless contact, this corresponds to the crack aperture being zero. In this context, the crack solely transmits normal compressive forces, while the shear stress within the crack plane is zero. By assuming that the shear modulus is zero $\mathbb{C}_{\mathrm{m}} \to \mathbb{K}_{\mathrm{m}}$, one can rewrite Eq. (2.72):

$$\dot{\boldsymbol{\varepsilon}}_{\mathrm{cr}}^{(\boldsymbol{n})} = (\mathbb{I}^4 - \mathbb{E}_{\mathrm{cr}} : \mathbb{K}_{\mathrm{m}})^{-1} : \dot{\bar{\boldsymbol{\varepsilon}}}; \quad \text{at} \quad \boldsymbol{\varepsilon}_{\mathrm{cr}}^{(\boldsymbol{n})} < 0 \tag{2.79}$$

Following the previous steps for the opened crack, the closed crack strain concentration tensor $\tilde{\mathbb{T}}_{\mathrm{cr}}$ is defined as the aspect ratio which approaches the limit $\alpha \to 0$:

$$\alpha\mathbb{K}_{\mathrm{m}} : (\mathbb{I}^4 - \mathbb{E}_{\mathrm{cr}}(\alpha) : \mathbb{K}_{\mathrm{m}})^{-1} \approx \tilde{\mathbb{T}}_{\mathrm{cr}} \coloneqq \lim_{\alpha \to 0} \alpha \cdot (\mathbb{I}^4 - \mathbb{E}_{\mathrm{cr}}(\alpha))^{-1} \tag{2.80}$$

This indicates that when the microcracks are closed, the closed crack strain concentration tensor $\tilde{\mathbb{T}}_{\mathrm{cr}} \neq \mathbf{0}$, but there is a very small contribution in the shear strain when cracks are aligned in $\boldsymbol{n} = \boldsymbol{e}_3$:

$$\tilde{\mathbb{T}}_{\mathrm{cr},2323} = \frac{2\left(1-\nu_{\mathrm{m}}\right)}{\pi\left(2-\nu_{\mathrm{m}}\right)}; \qquad \tilde{\mathbb{T}}_{\mathrm{cr},1313} = \tilde{\mathbb{T}}_{\mathrm{cr},2323} \tag{2.81}$$

Given the microcrack strain concentration tensors, the crack closure criterion with a homogenized stiffness of the material is defined using the framework of Mori-Tanaka.

Mori-Tanaka microcrack homogenized stiffness with closure criterion By substituting the open $\mathbb{T}_{\mathrm{cr}}$ (or closed $\tilde{\mathbb{T}}_{\mathrm{cr}}$) crack strain concentration tensors into the Mori-Tanaka homogenized stiffness of Eq. (2.48), one obtains:

$$\mathbb{C}_{\mathrm{cr}}^{\mathrm{MT}} = \xi_{\mathrm{m}}\mathbb{C}_{\mathrm{m}} : \left(\xi_{\mathrm{m}}\mathbb{I}^4 + \xi_{\mathrm{cr}}\mathbb{T}_{\mathrm{cr}}\right)^{-1} \tag{2.82}$$

To account for the closure of the microcracks, the closure criterion results in a homogenized tangent stiffness which is piecewise linear. The final homogenized tangent stiffness is:

$$\mathbb{C}_{\mathrm{cr}}^{\mathrm{MT}} = \begin{cases} \xi_{\mathrm{m}}\mathbb{C}_{\mathrm{m}} : \left(\xi_{\mathrm{m}}\mathbb{I}^4 + \xi_{\mathrm{cr}}\mathbb{T}_{\mathrm{cr}}\right)^{-1} & \text{if } \boldsymbol{\varepsilon}_{\mathrm{cr}}^{(\boldsymbol{n})} \geq 0 \\ \xi_{\mathrm{m}}\mathbb{C}_{\mathrm{m}} : \left(\xi_{\mathrm{m}}\mathbb{I}^4 + \xi_{\mathrm{cr}}\tilde{\mathbb{T}}_{\mathrm{cr}}\right)^{-1} & \text{if } \boldsymbol{\varepsilon}_{\mathrm{cr}}^{(\boldsymbol{n})} < 0 \end{cases} \tag{2.83}$$

Behavior of microcrack inclusions with closure criterion – single harmonic wave For microcrack model, a single harmonic uniaxial strain, $\varepsilon_{33}(t) = \varepsilon_{\mathrm{a}}\cos(\omega_0 t)$, is performed for Eq. (2.83). Specifically, a aspect ratio of the microcracks is defined as $\alpha = 0.01$. First, a behavior of instantaneous stiffness change of the RVE is seen for the longitudinal stress, which is normalized by the elastic matrix stiffness in Fig. 2.12. Therefore, the model of diffuse microcracks can mirror rudimentary crack models frequently used in nonlinear acoustic and dynamic literature [Bro+14].

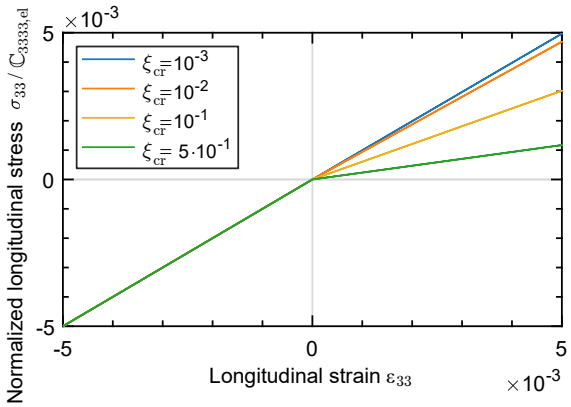

Figure 2.12: The manifestation of bilinear stiffness for distributed aligned microcracks in a RVE with cylic loading.

When the microcrack volume fraction is varied with an imposed reversible longitudinal strain wave of $R = -1$ at $f_0 = 20$ kHz, the frequency spectra of Fig. 2.13 reveals a small generation of odd harmonics. Interestingly, the presence of odd harmonics is typically not found in the nonlinear acoustic and dynamic literature [Bro+14]: this difference is due to the fact that an anisotropic stress state is generated due to the disc shape of the microcracks. The monotonic increase of the microcrack

volume fraction increases the stiffness degeneration as it nears $\xi_{\text{cr}} \to 1$, and the higher harmonic ratios increase.

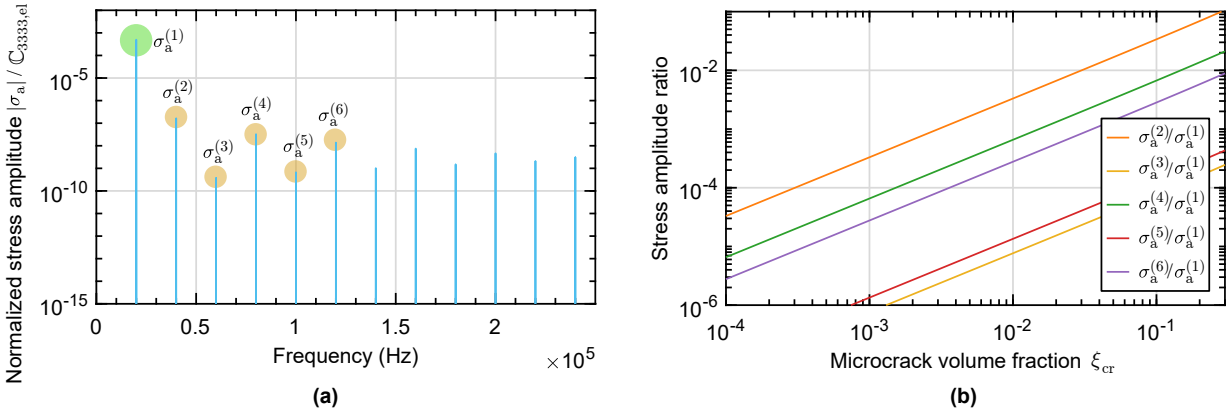

Figure 2.13: In **(a)**, the normalized frequency spectra of an uniaxial stress wave in the RVE for a single harmonic strain $\varepsilon_{33}(t)$ at $f_0 = 20$ kHz with load ratio $R = -1$ and $\xi_{\text{cr}} = 10^{-1}$. In **(b)**, the ratio of higher harmonics to fundamental harmonic follow the same trajectory as the microcrack volume fraction varies, which are amplitude and frequency independent.

Behavior of microcrack inclusions with closure criterion – multi-harmonic wave In the case of a multi-harmonic wave, e.g. created by a piezoelectric transducer and horn that is driven by the Branson signal and power generator of Fig. 2.38, the assumption of superposition no longer holds. In terms of harmonic magnitudes, the contribution of a second, third, and highers harmonic maybe be amplified or attenuated depending on the nonlinear model. For ratios of harmonics, it can no longer be assumed to be uniformly increasing in unison, as shown in Fig. 2.13 **(b)**.

To investigate the influence of a multi-harmonic strain wave on diffuse microcracks, the same procedure for multi-harmonic waves on microcracks is preformed: i.e. the horn vibration's fundamental, second, and third harmonics from Fig. 2.38 are utilized to ascertain their respective ratios. The multi-harmonic strain wave employed is that of Eq. (2.70) where the values for $\varepsilon_{\text{a}}^{(1)}$, $\varepsilon_{\text{a}}^{(2)}$, and $\varepsilon_{\text{a}}^{(3)}$ remain as $5 \cdot 10^{-4}$, $2.5 \cdot 10^{-7}$, and $2.9 \cdot 10^{-6}$, respectively. Evident from Fig. 2.14 is the distinct shift of behavior in the third harmonic, transitioning to a marginally descending trend in the log-log scale rather than a consistently ascending harmonic. Additionally, the second harmonic demonstrates sharp drop offs at $\xi_{\text{cr}} \approx 1.5 \cdot 10{-}3$ which can be attributed to the sinc modulation of the crack closure and its geometry. Due to the numerical nature of homogenization, this cannot be easily explained, but instead has an analytical explanation later derived in Section 2.2.3. These observations indicates that an input

multi-harmonic wave can complicate the nonlinear characteristics of the second and third harmonic.

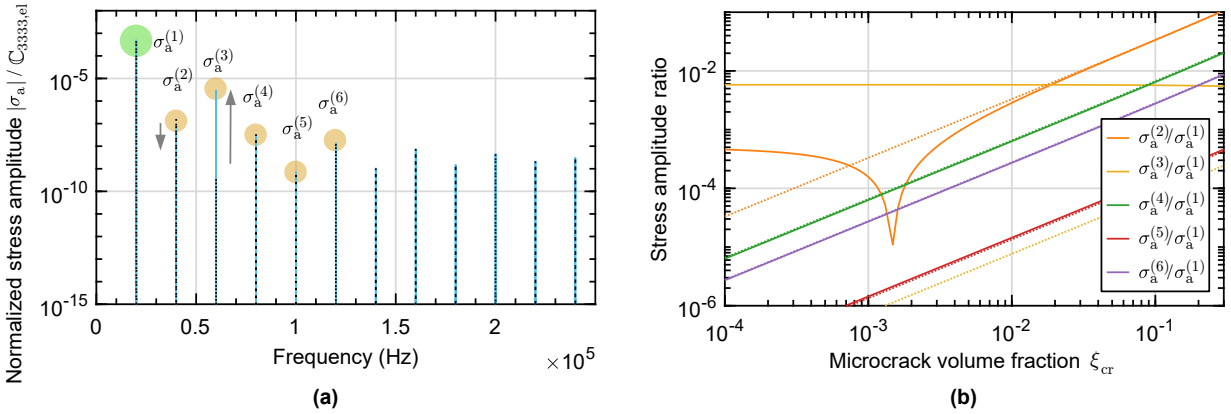

Figure 2.14: In **(a)**, the normalized frequency spectra of an uniaxial stress wave in the RVE for the multi-harmonic sinusoidal strain Eq. (2.70) at $f_0 = 20$ kHz with load ratio $R = -1$ and $\xi_{cr} = 10^{-1}$. In **(b)**, the ratio of higher harmonics to fundamental harmonic no longer follow the same trajectory as the microcrack volume fraction varies, which are amplitude and frequency independent. The dotted lines represent previously extracted harmonic ratios from Fig. 2.13 for a single harmonic strain wave.

Mori-Tanaka homogenization of multiple phases

When there are multiple phases, Eq. (2.47) can be written for each phase and their summation inside Eq. (2.48) gives the Mori-Tanaka stiffness; i.e the homogenization of all heterogeneities may be conducted during one step. However, heterogeneities can also be divided into groups which can be homogenized in multiple steps; the effective properties calculated in the previous step are used as a new effective matrix phase. In the case of our three-phase material, the presence of microcracks transforms the problem into a three-phase system with effective properties that are now anisotropic. This immediately limits the applicability of the one-step Mori-Tanaka homogenization model [BDC91].

The work by Abaimov et al. [Aba+19] deals with the question of how the results of one-step homogenization procedures differs when adapted into a multi-step procedure. In short, it was found that homogenizing the most distinct inhomogeneities first in a multistep scheme yielded more accurate predictions of the stiffness compared to one-step schemes, especially when more prevalent inhomogeneities are accounted for in initial steps. Additionally, it was found that for inclusions low volume fractions, the difference in results were negligible. Therefore, Eq. (2.48) is split into a two-step homogenization scheme, where the most compliant phase is homogenized first (the microcracks) with the elastic matrix. Then, the microplastic inclusions are homogenized with the previous equivalent material, as

shown in Fig. 2.15. This two-step approach not only enhances accuracy but also simplifies solving the nonlinear tangent problem by addressing two phases separately rather than concurrently. This homogenized stiffness is given as follows:

$$\mathbb{C}^*_{\mathrm{cr}} = \begin{cases} (1-\hat{\xi}_{\mathrm{cr}})\mathbb{C}_{\mathrm{m}} : \left((1-\hat{\xi}_{\mathrm{cr}})\mathbb{I}^4 + \hat{\xi}_{\mathrm{cr}}\mathbb{T}_{\mathrm{cr}}\right)^{-1} & \text{if } \boldsymbol{\varepsilon}^{(\boldsymbol{n})}_{\mathrm{cr}} \geq 0 \\ (1-\hat{\xi}_{\mathrm{cr}})\mathbb{C}_{\mathrm{m}} : \left((1-\hat{\xi}_{\mathrm{cr}})\mathbb{I}^4 + \hat{\xi}_{\mathrm{cr}}\tilde{\mathbb{T}}_{\mathrm{cr}}\right)^{-1} & \text{if } \boldsymbol{\varepsilon}^{(\boldsymbol{n})}_{\mathrm{cr}} < 0 \end{cases} \quad \text{with} \quad \hat{\xi}_{\mathrm{cr}} \coloneqq \frac{\xi_{\mathrm{cr}}}{1-\xi_{\mathrm{pl}}} \qquad \text{(Step 1)}$$

$$\mathbb{C}^* = \mathbb{C}^*_{\mathrm{cr}} + \xi_{\mathrm{pl}}\,(\mathbb{C}_{\mathrm{pl}} - \mathbb{C}^*_{\mathrm{cr}}) : \left(\mathbb{I}^4 + \mathbb{E}_{\mathrm{pl}} : \mathbb{S}^*_{\mathrm{cr}} : (\mathbb{C}_{\mathrm{pl}} - \mathbb{C}^*_{\mathrm{cr}})\right)^{-1} : \left(\xi_{\mathrm{pl}}\left(\mathbb{I}^4 + \mathbb{E}_{\mathrm{pl}} : \mathbb{S}^*_{\mathrm{cr}} : (\mathbb{C}_{\mathrm{pl}} - \mathbb{C}^*_{\mathrm{cr}})\right)^{-1}\right)^{-1} \qquad \text{(Step 2)} \tag{2.84}$$

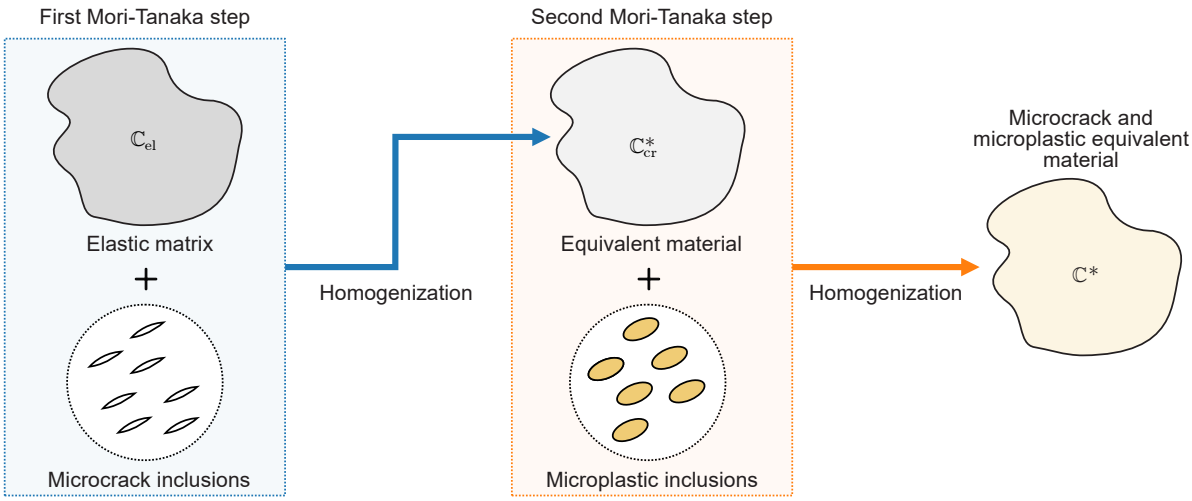

Figure 2.15: Schematic of the two-step Mori-Tanaka homogenization procedure.

Behavior of microplastic and microcrack inclusions with closure – single harmonic wave Microcracks and elasto-plastic inclusions yield notable higher harmonics, primarily the second and third, respectively. Under a multi-harmonic input strain wave with dominant third and second harmonics, the responses of microplastic and microcrack volume fractions diverge significantly from those subjected to a single harmonic wave. While mode I-aligned microcracks exert minimal influence on the third harmonic ratio, as illustrated in Fig. 2.14, the ratio for microplastic inclusions remains obscured until a critical volume fraction is reached. Beyond this threshold, the ratio starts to ascend, eventually aligning with the ratios observed for a pure single harmonic wave input. This implies that a single-

harmonic input wave is crucial for detecting tiny amounts of diffuse microplasticity and microcracks in the ultrasonic fatigue specimen.

When both nonlinear inclusions are integrated in the two-step Mori-Tanaka homogenization scheme of Eq. (2.84), the behavior becomes increasingly complex. An example of the interacting behavior for a single harmonic strain wave can be given for strong nonlinearity, where the values of $\xi_{\mathrm{cr}} = 0.1$, $\xi_{\mathrm{pl}} = 0.25$, and $\sigma_{\mathrm{pl}}^{\mathrm{Y}}/\sigma^{\mathrm{Y}} = 0.1$ are given for an RVE. These values represent an exaggerated scenario with strong microplasticity due to microcrack fronts, with both phenomena easily visible in Fig. 2.16. Despite the larger volume fraction of microplastic inclusions, it can be seen that the microcracks are a stronger nonlinearity contributing to the a larger second harmonic amplitude, versus the third harmonic amplitude. Consequently, the nature of the input wave (single harmonic versus multi-harmonic) becomes a critical factor in accurately quantifying higher harmonic generation. This combination specifically facilitates the study of the second and third harmonics, which represent the most prominent harmonics in the vibration spectrum.

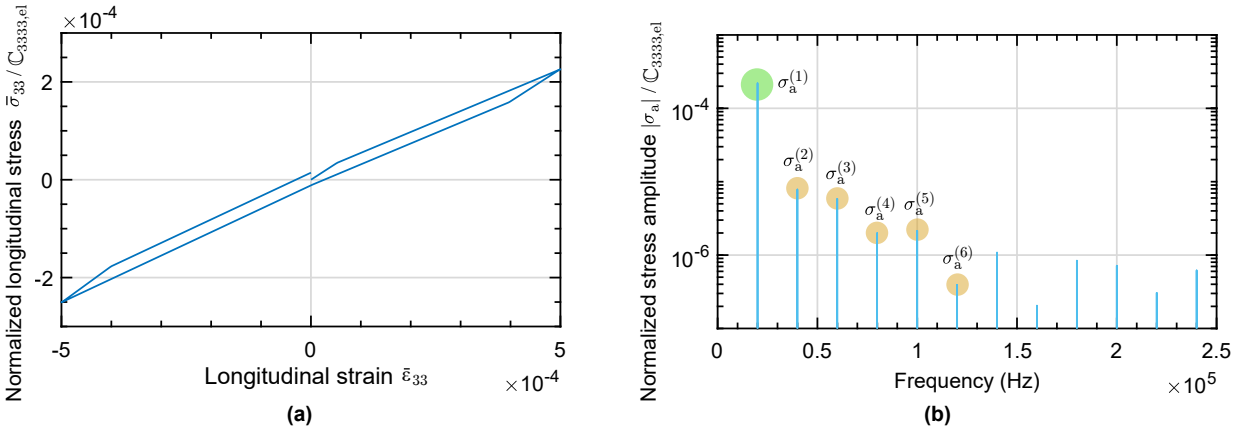

Figure 2.16: In **(b)**, the first stress-strain hysteresis cycle seen by the RVE with $R = -1$, $\xi_{\mathrm{cr}} = 0.1$, $\xi_{\mathrm{pl}} = 0.25$, and $\sigma_{\mathrm{pl}}^{\mathrm{Y}}/\sigma^{\mathrm{Y}} = 0.1$. In **(b)**, the normalized frequency spectra of an uniaxial stress wave in the RVE for a single harmonic strain $\varepsilon_{33}(t)$ at $f_0 = 20$ kHz.

2.2.3 Nonlinear macrocrack model

Symbol	Description
$\mathbb{C}, \mathbb{S}$	Stiffness and compliance tensor
E, ν	Young's modulus, Poisson's ratio
F, K, l	Force, stiffness, length
$\mathcal{F}(\square), \mathcal{F}(\square)^{-1}$	Fourier and inverse Fourier transform operators
$\mathcal{H}(\square)$	Heaviside function
h	The hth harmonic
S, V	Surface, volume
$\boldsymbol{\varepsilon}$	Strain tensors
$\mathcal{E}$	Energy of system
Γ	Surface of the crack face
Λ	Stiffness degeneration factor
$\boldsymbol{\sigma}$	Stress tensors
ω, f	Angular frequency and frequency

Table 2.4: For the macrocrack models in Sec. 2.2.3 only, this notation is adopted.

This section deals with macroscopic crack models which arise in ultrasonic fatigue tests. Specifically, mode I cracks which occurs internally or about the surface results in a strong crack contact effect during reversible loadings, see Fig. 2.17. Classical approaches which a finite element model explicitly represents crack faces as discontinuities in the mesh. Currently adopted by the literature Phase Field methods [BLR11], is detailed briefly but still requires a finite element model. Thus, an uniaxial simplification is introduced to the dynamic problem and then analyzed.

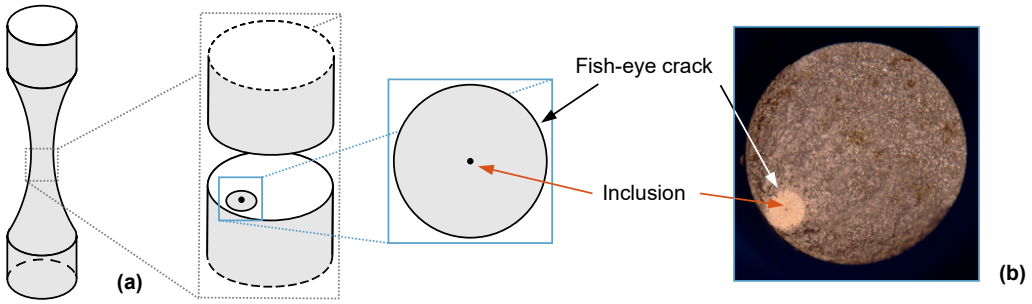

Figure 2.17: In **(a)**, a schematic of a post-fatigue failure fish-eye crack and inclusion subject to VHCF. In **(b)**, optical microscopy of fatigue specimen failure surface, taken from [RWP08]

Classical phase-field elastic crack model

As mentioned in Chapter 1, cracks are a geometrically dominated phenomena and their crack propagation are categorized by their length. For larger cracks, their dynamics are dictated by the contact during crack closure, where contact induces a rectification of stresses in compression. Here, the phase-field approach to model a fracture is introduced, which regularizes the localized discontinuity [MHW10]. For an elastic cracked body, shown in Fig. 2.18, defined in the volume V with sharp crack

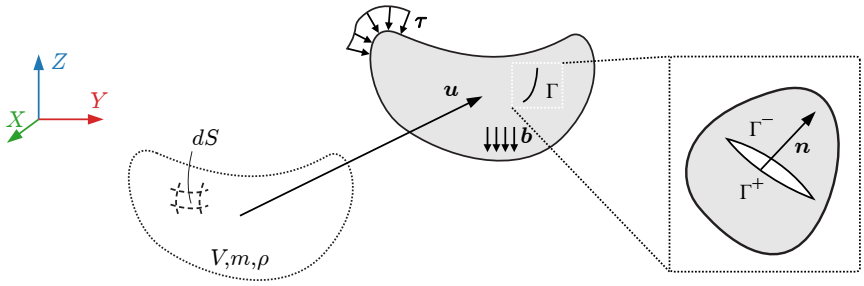

Figure 2.18: An arbitrary solid volume V in motion $\boldsymbol{u}$ with surface boundary S, with traction $\boldsymbol{\tau}$ and body $\boldsymbol{b}$ forces shown. The crack is defined by $\Gamma = \Gamma^+ \cup \Gamma^-$, where the zoom of the crack has faces Γ^+ and Γ^-, and outer unit vector $\boldsymbol{n}$

surface Γ, the total energy of the system $\mathcal{E}_{\text{crack}}$ is:

$$\mathcal{E}_{\text{crack}} = \int_V \Psi(\boldsymbol{\varepsilon}, \Gamma) dV + g_c \int_\Gamma d\Gamma \approx \int_\Omega \Psi(\boldsymbol{\varepsilon}, d) d\Omega + g_c \int_\Omega \gamma(d, \nabla d) d\Omega \tag{2.85}$$

where Ψ is the total strain energy, g_c represents the critical energy release rate as defined by Griffith [BLR11] and a regularized diffuse field $d(\boldsymbol{X})$ replaces the sharp surface defined by the crack [MHW10]. While not considered in this disseration, a crack is modeled to propagate in a specific material point when $g_c > g$. The damage variable and the elastic strain energy Ψ are related through a degradation function $g(d)$:

$$\Psi(\boldsymbol{\varepsilon}, d) = g(d)\Psi^+ + \Psi^- \tag{2.86}$$

where $g(d) = (1-d)^2$ is a typical degradation function for brittle fracture such that $g(0) = 1$ and $g(1) = 0$ [Sar+18]. Here, the elastic strain energy Ψ is divided into positive (tension) $\Psi^+(\varepsilon^+)$ and negative (compression) components $\Psi^+(\boldsymbol{\varepsilon}^-)$ using the principal strains $\boldsymbol{\varepsilon}$ and the trace of the strain tensor:

$$\Psi^\pm(\boldsymbol{\varepsilon}) = \frac{\lambda}{2}\left(\frac{1}{2}\langle\boldsymbol{\varepsilon}\rangle^\pm\right)^2 + \mu \operatorname{tr}\left(\left(\boldsymbol{\varepsilon}^\pm\right)^2\right) \tag{2.87}$$

where λ and μ are elastic Lamé constants, and $\langle \boldsymbol{\varepsilon} \rangle^{\pm} := (\mathrm{tr}(\boldsymbol{\varepsilon}) \pm |\,\mathrm{tr}(\boldsymbol{\varepsilon})|)$. The positive and negative parts are employed to differentiate between compression and extension. Eq. (2.86) indicates that in tension, both the tensile stiffness and elastic stress decrease with the damage variable. The solution to this problem comes from solving the internal energy from the principle of virtual work, with $\frac{\partial \Psi(\boldsymbol{\varepsilon},d)}{\partial \boldsymbol{\varepsilon}} = \boldsymbol{\sigma}$:

$$\int_V \boldsymbol{\sigma} : \delta\boldsymbol{\varepsilon}\, dV - \int_{\partial\Omega_F} \boldsymbol{\tau} \cdot \delta\boldsymbol{u}\, d\Gamma = 0; \text{ where } \boldsymbol{\sigma} = (1-d)^2 \left(\lambda \langle \boldsymbol{\varepsilon} \rangle^{+} \mathbf{1} + 2\mu\boldsymbol{\varepsilon}^{+}\right) + \lambda \langle \boldsymbol{\varepsilon} \rangle^{-} \mathbf{1} + 2\mu\boldsymbol{\varepsilon}^{-} \tag{2.88}$$

Rudimentary uniaxial crack model

From Eq. (2.88), the 3D crack problem is shown to be a geometrically dominated mechanical problem which must rely on a finite element solution. To capture the first order dynamical effects of a mode I crack as an instantaneous change of stiffness, one can simplify Eq. (2.88) using uniaxial assumptions. However, other complexities are not considered, e.g. the friction contact forces when the crack is not perfectly perpendicular to the loading direction, crack growth modeling, and the plastic crack tip.

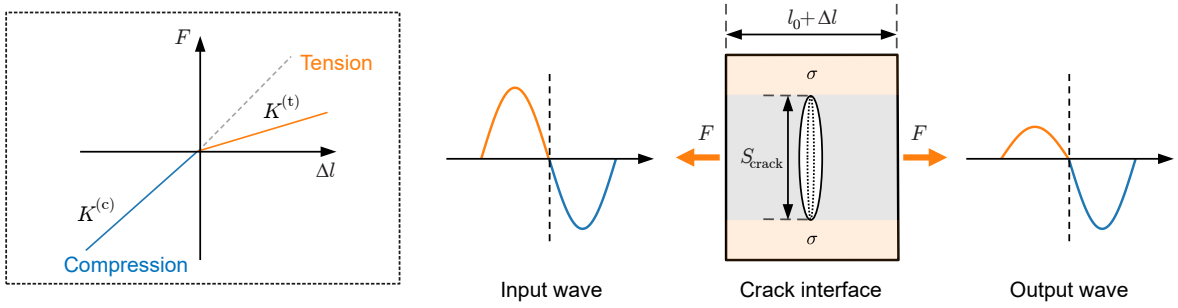

Figure 2.19: The bilinear stiffness of a rudimentary mode I crack for compressive and tension regimes for uniaxial forces. In a dynamical system, the force is rectified during crack-opening, leading to a reduced stiffness.

Consider the figure shown in Fig. 2.19, in which a body has length l_0 is subject to force F, which is embedded with a mode I crack with the surface S_{crack}. When the force is compressive, $F := K^{(c)}\Delta l$ for a stiffness $K^{(c)}$ and the elongation Δl. When the force is tensile, the crack opens and reduces the stiffness since only part of the bulk remains engaged $S_{\text{eff}} := S_0 - S_{\text{crack}}$: this gives $F := K^{(t)}\Delta l = K^{(c)} S_{\text{eff}}/S_0$. The bilinear stiffness can be represented as:

$$F = \left(K^{(c)} + \mathcal{H}(\Delta l)\left[K^{(c)} - K^{(t)}\right]\right)\Delta l \tag{2.89}$$

where $\mathcal{H}(\square)$ is the Heaviside function. To enable a constitutive uniaxial description in the longitudinal

direction $\boldsymbol{e}_3$, an average approximation is made $\langle\sigma_{33}\rangle \coloneqq F/S$ and $\langle\varepsilon_{33}\rangle \coloneqq \Delta l/l_0$. This gives:

$$\sigma_{33} = \left(\mathbb{C}_{33}^{(\mathrm{c})} + \mathcal{H}(\varepsilon_{33})\left[\mathbb{C}_{33}^{(\mathrm{c})} - \mathbb{C}_{33}^{(\mathrm{t})}\right]\right)\varepsilon_{33} \tag{2.90}$$

where $\mathbb{C}_{33}^{(\mathrm{c})}$, $\mathbb{C}_{33}^{(\mathrm{t})}$ are the uniaxial stiffnesses in compression and tension respectively, the stiffness tensor is written in Voigt notation such that $\mathbb{C}_{3333} \equiv \mathbb{C}_{33}$. By defining a stiffness degradation factor $\Lambda \coloneqq 1 - S_{\mathrm{eff}}/S_0 \in [0,1]$, the expression simplifies to:

$$\sigma_{33} = \mathbb{C}_{33}^{(\mathrm{c})}\left[1 - \mathcal{H}(\varepsilon_{33})\Lambda\right]\varepsilon_{33} \tag{2.91}$$

Eq. (2.91) aims to capture the dynamic effects at ultrasonic frequencies for large crack closure [Bro+14].

Behavior of macrocrack with closure – single harmonic wave The assumption of a pure single harmonic loading in ultrasonic fatigue tests is to be analyzed. This corresponds to a single harmonic uniaxial strain $\varepsilon_{33}(t) = \varepsilon_{\mathrm{a}}\cos(\omega_0 t)$, where the frequency is $f_0 = 20$ kHz and $\omega_0 \coloneqq 2\pi f_0$. An analytical solution of the hth harmonic of Eq. (2.91) can be derived from a convolution of $(\varepsilon_{33} \circledast \mathcal{H}(\varepsilon_{33}))(t)$ in the frequency domain. The convolution's definition is:

$$(\varepsilon_{33} \circledast \mathcal{H}(\varepsilon_{33}))(t) = \int_{-\infty}^{+\infty} \varepsilon_{33}(\tau)\mathcal{H}\left(\varepsilon_{33}(t-\tau)\right)d\tau$$

The Fourier transform of $\varepsilon_{33}(t) = \varepsilon_{\mathrm{a}}\cos(\omega_0 t)$ and $\mathcal{H}(\varepsilon_{33}(t))$ is:

$$\mathcal{F}\left(\varepsilon_{33}(t)\right) = \frac{\varepsilon_{\mathrm{a}}}{2}\left[\delta\left(\omega-\omega_0\right) + \delta\left(\omega+\omega_0\right)\right]; \quad \mathcal{F}\left(\mathcal{H}(\varepsilon_{33}(t))\right) \approx \sum_{i=-\infty}^{\infty} \mathrm{sinc}(i\omega_0)\delta(\omega - i\omega_0) \tag{2.92}$$

where δ is the Dirac delta function and the approximation of $\mathcal{F}\left(\mathcal{H}(\varepsilon_{33}(t))\right)$ is derived in [SKB02]. Their convolution in the frequency domain is simply a multiplication:

$$\mathcal{F}\left((\varepsilon_{33} \circledast \mathcal{H}(\varepsilon_{33}))(t)\right) \approx \frac{\varepsilon_{\mathrm{a}}}{2}\sum_{i=-\infty}^{\infty} \mathrm{sinc}(i\omega_0)[\delta(\omega - \omega_0 - i\omega_0) + \delta(\omega + \omega_0 - i\omega_0)]$$

By defining $\sigma_{33}(t) = \sum_h \sigma_{\mathrm{a}}^{(h)}\cos(h\cdot\omega_0 t)$, and $T = 2\pi/\omega_0$, the convolution sum of the spectra is:

$$\sigma_{\mathrm{a}}^{(h)}(h\cdot\omega_0) = \frac{\mathbb{C}_{33}^{(\mathrm{t})}\Lambda\varepsilon_{\mathrm{a}}}{2\mathbb{C}_{33}^{(\mathrm{c})}}\sum_{i=-\infty}^{+\infty}\mathrm{sinc}\left(\frac{i}{2}\right)\delta(h\pm 1 - i)$$

Due to the frequency shifting property of the Fourier transform [SM05], one obtains:

$$\sigma_{\mathrm{a}}^{(h)} = \frac{\Lambda\mathbb{C}_{33}^{(\mathrm{t})}\varepsilon_{\mathrm{a}}}{2\mathbb{C}_{33}^{(\mathrm{c})}}\left(\mathrm{sinc}\left(\frac{h+1}{2}\right) + \mathrm{sinc}\left(\frac{h-1}{2}\right)\right) \tag{2.93}$$

In Fig. 2.20, the first twelve harmonics are plotted using Eq. (2.93), and are normalized by the stiffness coefficient $\mathbb{C}_{33}^{(c)}$. It can be seen in Fig. 2.20 **(a)** for a given stiffness degradation Λ generates even higher harmonics, where the even harmonics are more prominent than the odd harmonics. In Fig. 2.20 **(b)** as the stiffness degradation increases, so does the stress higher harmonics ratios, which follow similar trajectories dependent on the strain amplitudes. For typical strain amplitudes seen in ultrasonic VHCF ($\varepsilon_a \approx 10^{-4}$ - 10^{-3}), it's demonstrated that the even higher harmonics increase monotonically.

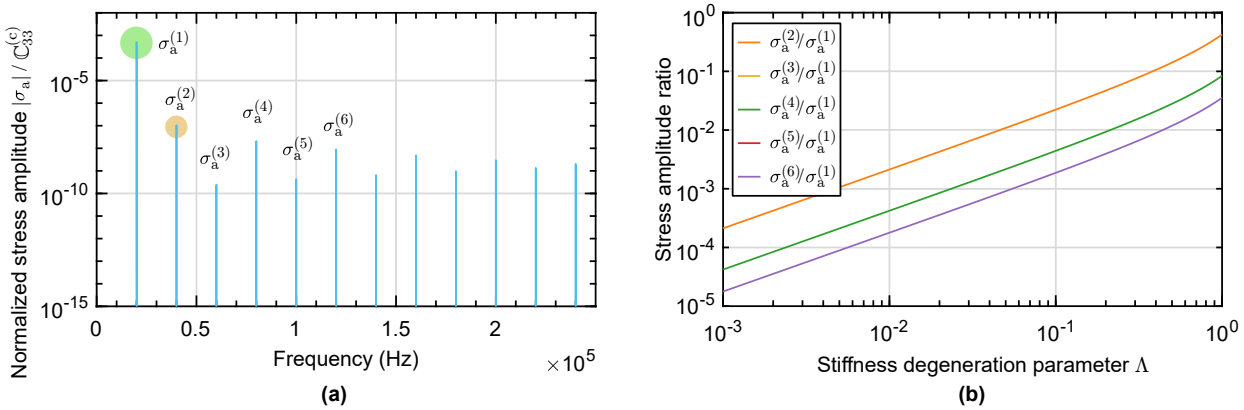

Figure 2.20: In **(a)**, the normalized frequency spectra of an uniaxial stress wave for a single harmonic strain $\varepsilon_{33}(t)$ at $f_0 = 20$ kHz with $\Lambda = 10^{-3}$. In **(b)**, the stress ratios of higher harmonics divided by the fundamental harmonic for varying damage parameter are amplitude and frequency independent, with only even higher harmonics prominent.

Behavior of macrocrack with closure – single harmonic wave with change in load ratio Due to the analytical form of Eq. (2.93), the load ratio R can be studied when it is not perfectly reversible. This can be represented as adding a small static uniaxial tension or compression such that $\varepsilon_{33}(t) = \varepsilon_a \cos(\omega_0 t) - \varepsilon_m$. Eq. (2.93) can be changed to an offset to the Heaviside function, e.g. $\mathcal{H}(\varepsilon_{33}(t) - \varepsilon_m)$. The resulting derivation, following the previous steps with the convolution sum, gives the expression:

$$\sigma_a^{(h)}(h \cdot \omega_0) = \frac{\Lambda \mathbb{C}_{33}^{(t)} \cos^{-1}(\varepsilon_m/\varepsilon_a)\varepsilon_a}{\pi \mathbb{C}_{33}^{(c)}} \sum_{i=-\infty}^{+\infty} \operatorname{sinc}\left(\frac{i \cos^{-1}(\varepsilon_m/\varepsilon_a)}{\pi}\right) \delta(h \pm 1 - i)$$

which simplifies to:

$$\sigma_a^{(h)} = \frac{\Lambda \mathbb{C}_{33}^{(t)} \varrho \varepsilon_a}{\pi \mathbb{C}_{33}^{(c)}} \left(\operatorname{sinc}\left(\frac{(h+1)\varrho}{\pi}\right) - 2\cos(\varrho)\operatorname{sinc}\left(\frac{h\varrho}{\pi}\right) + \operatorname{sinc}\left(\frac{(h-1)\varrho}{\pi}\right)\right) \tag{2.94}$$

where $\varrho = \cos^{-1}(\varepsilon_m/\varepsilon_a)$.

In Fig. 2.21, the frequency spectra of the first twelve harmonics' normalized stress amplitudes are shown using Eq. (2.94). In Fig. 2.21 **(a)**, the load ratio is set to $R = -0.8$, which is not perfectly reversible. The harmonics reveal stronger generation of odd harmonics with respect to the even harmonics. In this case, the sinc modulated harmonics with large enough Λ can give dramatic increase to the higher harmonic ratios; in this case the odd harmonics ratios. In the broader context, as $\Lambda \to 1$, subharmonic generation becomes a possibility in structural dynamical systems, which is indicative of period doubling/tripling bifurcation, etc. [Sey10].

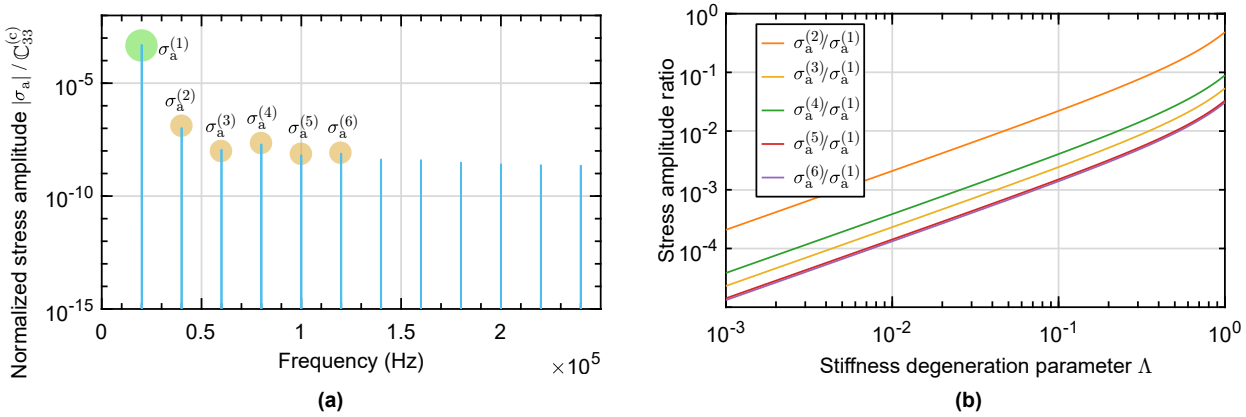

Figure 2.21: In **(a)**, the normalized frequency spectra of an uniaxial stress wave for a single harmonic strain $\varepsilon_{33}(t)$ at $f_0 = 20$ kHz with load ratio $R = -0.8$ and $\Lambda = 10^{-3}$. In **(b)**, the ratio of higher harmonics to fundamental harmonic follow the same trajectory as the damage parameter varies, which are amplitude and frequency independent.

Finally, the load ratio can be studied easily due to the analytical form of Eq. (2.94). The load ratio used for metals in ultrasonic fatigue tests usually range from $-1 \leq R < 0$. Thus, for a fixed stiffness degeneration Λ, the modulation of the higher harmonics can be shown to be highly nonlinear due to the modulation of the sinc function. In Fig. 2.22, the ratio of higher harmonics to fundamental harmonic are extracted for a fixed $\Lambda = 10^{-2}$ for **(a)** and $\Lambda = 10^{-3}$ **(b)**. As the load ratio is modulated, the sinc modulation affects the second harmonic amplitude ratio predictably, where it is maximal when $R = -1$ and decreases monotonically as $R \to 0$. For the other higher harmonics ratios, each have sharp drop offs which are proportional to the pulse width (period) $\tau \coloneqq T/\pi\varrho$, e.g. the fourth harmonic amplitude ratio occurs at $R \approx -0.6$. When the load ratio approaches $R \to 0$, this physically indicates an opening of the crack aperture such that contact cannot occur during compression.

This analysis might be important if it is suspected that ultrasonic fatigue test machine would not

be able to maintain a perfect the load ratio R in the experimental setting. Many factors could be postulated which would incur a temporary deviation for fully-reversible $R = -1$ for ultrasonic fatigue tests including: the self-heating at high frequency can introduce thermal strains, which can shift the mean strain and affect the load ratio; and maintenance of the load ratio is dependent on the feedback controller's ability to maintain resonance (elongation). However, for the remaining of the dissertation it's assumed that the perfect reversibility is maintained and ε_{m} can be neglected.

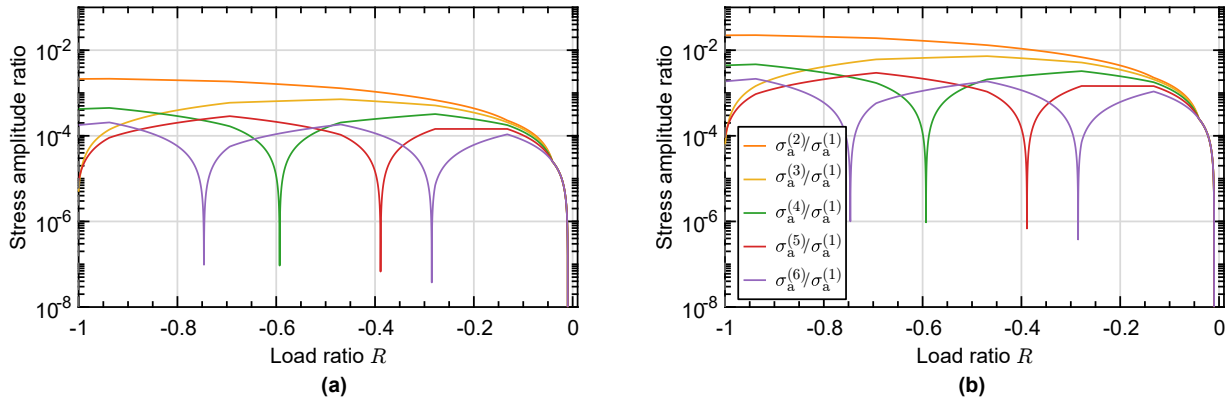

Figure 2.22: The ratio of higher harmonics and the fundamental harmonic yields reveal that odd harmonic generation is dependent on the static strain and the modulation, i.e. the load ratio R. The harmonic ratios show an upwards translation from **(a)**, $\Lambda = 10^{-2}$ to **(b)** $\Lambda = 10^{-1}$.

2.3 Modal model of ultrasonic fatigue specimen

Symbol	Description
$\boldsymbol{b}$	Body forces vector
C	Equivalent modal damping coefficient
$\mathbb{C}$	Stiffness tensor
$\mathbb{D}, \mathbb{D}^{\mathrm{T}}$	Gradient and divergence matrix operators
F	Equivalent modal force
K	Equivalent modal stiffness coefficient
M	Equivalent modal mass coefficient
$\boldsymbol{n}$	Outward normal surface unit vector
$q_0(t), q_1(t)$	Rigid body and first longitudinal normal modes amplitudes
$\boldsymbol{u}, \dot{\boldsymbol{u}}, \ddot{\boldsymbol{u}}$	Displacement, velocity, acceleration vector
S, V, Γ	Surface, volume, crack surface of a region of solid body
$\mathbb{V}$	Viscous tensor
$\mathcal{W}$	Potential energy
$\boldsymbol{X}, \boldsymbol{x}$	Macroscopic and microscopic position vector
$\boldsymbol{\varepsilon}, \overline{\boldsymbol{\varepsilon}}$	General or microscopic, macroscopic strain tensors
$\boldsymbol{\phi}_0(\boldsymbol{X}), \boldsymbol{\phi}_1(\boldsymbol{X})$	Static and first longitudinal normal modes shapes
ρ	Mass density
$\boldsymbol{\sigma}, \overline{\boldsymbol{\sigma}}$	General or microscopic, macroscopic stress tensors
$\boldsymbol{\tau}$	Traction forces vector
ω_1	Resonant (angular) frequency of the first longitudinal normal mode
ζ_1	Damping ratio of the first longitudinal normal mode
$\delta\square, \delta(\cdot)$	Virtual (variational) quantity, Dirac delta function
$\square_{\mathrm{nl}}$	Nonlinear quantity
$\mathrm{grad}, \mathrm{div}$	Gradient and divergence operators

Table 2.5: For the ultrasonic fatigue specimen model in Sec. 2.3 only, this notation is adopted.

Here, the aim is to provide a physically consistent model of the fatigue specimen. Specifically one that takes into account the specimen's shape on the dynamics, and allows for continuum theories, while benefitting as a reduced order model. To begin, the principle of virtual work is given:

$$\underbrace{-\int_V \boldsymbol{\sigma} : \delta\boldsymbol{\varepsilon}\, dV}_{\delta\mathcal{W}_{\mathrm{int}}} + \underbrace{\int_V \boldsymbol{b}\cdot\delta\boldsymbol{u}\, dV + \int_S \boldsymbol{\tau}\cdot\delta\boldsymbol{u}\, dS}_{\delta\mathcal{W}_{\mathrm{ext}}} = \underbrace{\int_V \rho\ddot{\boldsymbol{u}}\cdot\delta\boldsymbol{u}\, dV}_{\delta\mathcal{W}_{\mathrm{acc}}} \tag{2.95}$$

where $\delta\mathcal{W}_{\mathrm{int}}$, $\delta\mathcal{W}_{\mathrm{ext}}$, and $\delta\mathcal{W}_{\mathrm{acc}}$ denote the virtual work due to internal forces, external forces, and inertial forces respectively. The ultrasonic fatigue specimen's has a volume V, surface S, traction force $\boldsymbol{\tau}$, body force $\boldsymbol{b}$, Cauchy stress $\boldsymbol{\sigma}$, strain $\boldsymbol{\varepsilon}$, and motion $\boldsymbol{u}$, as shown in Fig. 2.23. Note it is valid for

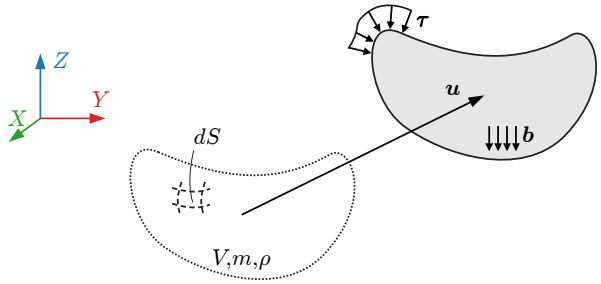

Figure 2.23: An arbitrary volume V in motion $\boldsymbol{u}$ with surface boundary S with traction $\boldsymbol{\tau}$ and body $\boldsymbol{b}$ forces shown.

any deformable body because no constitutive law is used, and thus is extendable to any non-elastic deformations. A derivation of the principle of virtual work is given in Appendix A.2. Furthermore, the subsequent derivation operates under the presumptions:

- The mechanical system under consideration consists of a deformable body, the fatigue specimen. Its outer surface is divided into a free surface and the fixture interface, the latter connecting to the horn and where displacement is imposed.
- The displacement field of the fatigue specimen is composed of a modal deformed shape (the first free-free longitudinal eigenmode), modulated by the motion imposed at the fixture end (the connection of the fatigue specimen and acoustic horn).
- External work is solely attributed to interaction at the specimen-horn interface, with gravity effects being negligible.
- The material behavior of the specimen is globally linear viscoelastic, but incorporates diffuse microplastic and microcrack contributions localized in a centroid volume about the fatigue specimen. The acoustic nonlinearity parameter is assumed negligible since the most relevant material behavior occurs at the mesoscale due to the order of strain (wavelength) during ultrasonic fatigue tests near and beyond the VHCF regime.

The reduced order model is proposed to utilize the vibration normal modes of the ultrasonic fatigue specimen, namely modal truncation [GR15]. The precomputed modal basis by offline finite element modal analysis (as illustrated in Fig. 2.24), captures the fatigue specimen's geometry in terms of its resonance characteristics and mode shapes specific to the narrowband frequency range under

consideration. This model entails the previously derived principle of virtual work by using a Galerkin projection of the modal basis to approximate the displacement field of the ultrasonic fatigue specimen, making it a powerful tool for dynamic analyses while bridging the gap to constitutive mechanics.

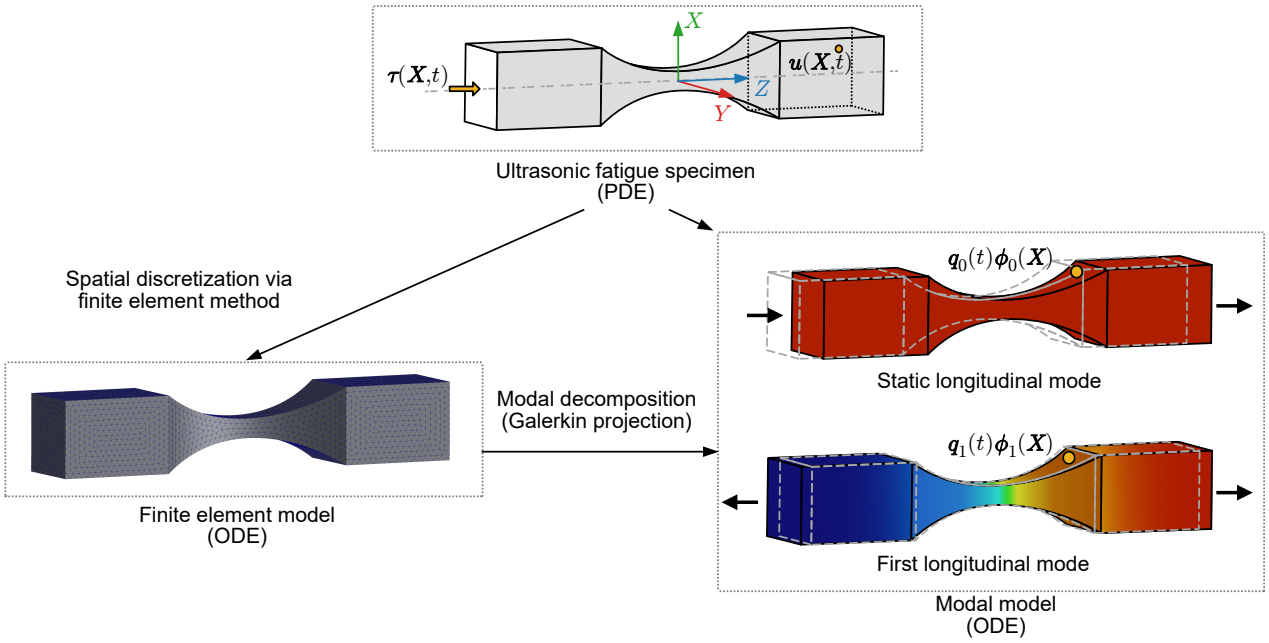

Figure 2.24: An intrusive model order reduction of an ultrasonic fatigue specimen whose equilibrium is dictated by a partial differential equation. Through spatial discretization via finite elements, a modal analysis reveals a subsequent modal shape functions. The modal model is simply a modal truncation of the static and first longitudinal normal modes.

Mandel notation is adopted, a normalized form of Voigt notation, to facilitate matrix operations and algorithmic implementation. This notation maintains consistency between tensor norms in both the original and reduced spaces, unlike the traditional Voigt notation [Man65]. Moreover, the tensor operations carry over to vector operations, e.g. $\boldsymbol{\sigma} : \boldsymbol{\sigma} \equiv \boldsymbol{\sigma}^{\mathrm{T}}\boldsymbol{\sigma} = \sigma_{11}^2 + \sigma_{22}^2 + \sigma_{33}^2 + 2\sigma_{23}^2 + 2\sigma_{13}^2 + 2\sigma_{12}^2$. In Mandel notation, the stress tensor can be related to the strain through the stiffness matrix $\mathbb{C}$:

$$\underbrace{\begin{bmatrix} \sigma_{11} \\ \sigma_{22} \\ \sigma_{33} \\ \sqrt{2}\sigma_{23} \\ \sqrt{2}\sigma_{13} \\ \sqrt{2}\sigma_{12} \end{bmatrix}}_{\boldsymbol{\sigma}} = \underbrace{\begin{bmatrix} \mathbb{C}_{1111} & \mathbb{C}_{1122} & \mathbb{C}_{1133} & \sqrt{2}\mathbb{C}_{1123} & \sqrt{2}\mathbb{C}_{1113} & \sqrt{2}\mathbb{C}_{1112} \\ \mathbb{C}_{2211} & \mathbb{C}_{2222} & \mathbb{C}_{2233} & \sqrt{2}\mathbb{C}_{2223} & \sqrt{2}\mathbb{C}_{2213} & \sqrt{2}\mathbb{C}_{2212} \\ \mathbb{C}_{3311} & \mathbb{C}_{3322} & \mathbb{C}_{33} & \sqrt{2}\mathbb{C}_{3323} & \sqrt{2}\mathbb{C}_{3313} & \sqrt{2}\mathbb{C}_{3312} \\ \sqrt{2}\mathbb{C}_{2311} & \sqrt{2}\mathbb{C}_{2322} & \sqrt{2}\mathbb{C}_{2333} & 2\mathbb{C}_{2323} & 2\mathbb{C}_{2313} & 2\mathbb{C}_{2312} \\ \sqrt{2}\mathbb{C}_{1311} & \sqrt{2}\mathbb{C}_{1322} & \sqrt{2}\mathbb{C}_{1333} & 2\mathbb{C}_{1323} & 2\mathbb{C}_{1313} & 2\mathbb{C}_{1312} \\ \sqrt{2}\mathbb{C}_{1211} & \sqrt{2}\mathbb{C}_{1222} & \sqrt{2}\mathbb{C}_{1233} & 2\mathbb{C}_{1223} & 2\mathbb{C}_{1213} & 2\mathbb{C}_{1212} \end{bmatrix}}_{\mathbb{C}} \underbrace{\begin{bmatrix} \varepsilon_{11} \\ \varepsilon_{22} \\ \varepsilon_{33} \\ \sqrt{2}\varepsilon_{23} \\ \sqrt{2}\varepsilon_{13} \\ \sqrt{2}\varepsilon_{12} \end{bmatrix}}_{\boldsymbol{\varepsilon}}$$

The compatibility equation for infinitesimal deformations is:

$$\underbrace{\begin{bmatrix} \varepsilon_{11} \\ \varepsilon_{22} \\ \varepsilon_{33} \\ \sqrt{2}\varepsilon_{23} \\ \sqrt{2}\varepsilon_{13} \\ \sqrt{2}\varepsilon_{12} \end{bmatrix}}_{\boldsymbol{\varepsilon}} = \underbrace{\begin{bmatrix} \frac{\partial}{\partial x} & 0 & 0 \\ 0 & \frac{\partial}{\partial y} & 0 \\ 0 & 0 & \frac{\partial}{\partial z} \\ 0 & \frac{\sqrt{2}}{2}\frac{\partial}{\partial z} & \frac{\sqrt{2}}{2}\frac{\partial}{\partial y} \\ \frac{\sqrt{2}}{2}\frac{\partial}{\partial z} & 0 & \frac{\sqrt{2}}{2}\frac{\partial}{\partial x} \\ \frac{\sqrt{2}}{2}\frac{\partial}{\partial y} & \frac{\sqrt{2}}{2}\frac{\partial}{\partial x} & 0 \end{bmatrix}}_{\mathbb{D}} \underbrace{\begin{bmatrix} u_1 \\ u_2 \\ u_3 \end{bmatrix}}_{\boldsymbol{u}}$$

where $\mathbb{D}$ is simply the matrix analog to the gradient operator in symbolic notation. The divergence operator can be shown to be the transposed gradient matrix operator $\mathbb{D}^{\mathrm{T}}$. Next, it's assume that through a proper modal analysis with free-free boundary conditions such that the mass-normalized static longitudinal $\boldsymbol{\phi}_0(\boldsymbol{X})$ and first longitudinal modes $\boldsymbol{\phi}_1(\boldsymbol{X})$ are obtained. From inspection of Fig. 2.25, the longitudinal mode shapes are symmetric about the centroid of the specimen. The approximation of the displacement field is given by the Galerkin projection:

$$\begin{aligned} \boldsymbol{u}(\boldsymbol{X}, t) &\approx q_0(t)\,\boldsymbol{\phi}_0(\boldsymbol{X}) + q_1(t)\,\boldsymbol{\phi}_1(\boldsymbol{X}) \\ &\approx \left[\ \boldsymbol{\phi}_0(\boldsymbol{X}) \ \middle|\ \boldsymbol{\phi}_1(\boldsymbol{X})\ \right] \begin{bmatrix} q_0(t) \\ q_1(t) \end{bmatrix} \end{aligned} \tag{2.96}$$

where $q_0(t)$ and $q_1(t)$ are time-varying modal amplitudes which describe the motion for their corresponding spatial mode shapes. Substituting Eq. (2.96) into Eq. (2.95), the matrix formulation of the

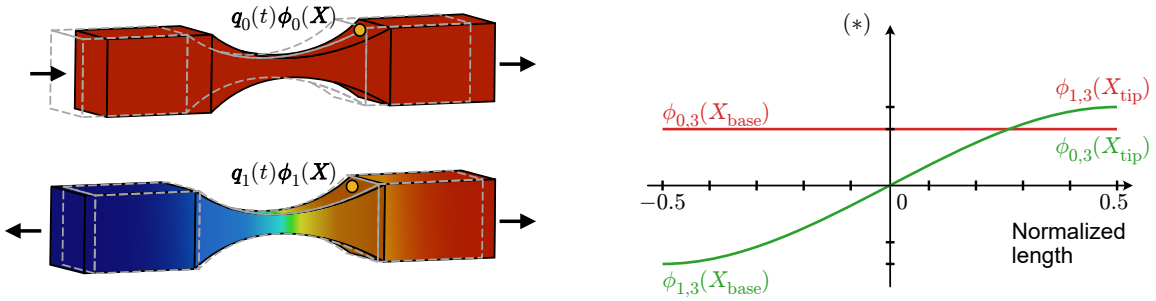

Figure 2.25: On the left, the Galerkin projected static and longitudinal normal modes for a 1070 steel specimen with rectangular geometry. On the right, the shape functions of the static (in red) and longitudinal (in green) mass-normalized modes through the longitudinal axis.

principle of virtual work is:

$$\underbrace{-\int_V (\delta\boldsymbol{\varepsilon})^{\mathrm{T}}\boldsymbol{\sigma}\,dV}_{\delta\mathcal{W}_{\mathrm{int}}} + \underbrace{\int_V (\delta\boldsymbol{u})^{\mathrm{T}}\boldsymbol{b}\,dV + \int_S (\delta\boldsymbol{u})^{\mathrm{T}}\boldsymbol{\tau}\,dS}_{\delta\mathcal{W}_{\mathrm{ext}}} = \underbrace{\int_V \rho(\delta\boldsymbol{u})^{\mathrm{T}}\ddot{\boldsymbol{u}}\,dV}_{\delta\mathcal{W}_{\mathrm{acc}}} \tag{2.97}$$

The virtual work of inertial forces $\delta\mathcal{W}_{\mathrm{acc}}$ is derived with some manipulation:

$$\begin{aligned}
\delta\mathcal{W}_{\mathrm{acc}} &= \int_V \rho\,(\delta\boldsymbol{u})^{\mathrm{T}}\,\ddot{\boldsymbol{u}}dV \\
&= \int_V \rho\left([\boldsymbol{\phi}_0 \mid \boldsymbol{\phi}_1]\begin{bmatrix}\delta q_0\\ \delta q_1\end{bmatrix}\right)^{\mathrm{T}}\left([\boldsymbol{\phi}_0 \mid \boldsymbol{\phi}_1]\begin{bmatrix}\ddot{q}_0\\ \ddot{q}_1\end{bmatrix}\right)dV \\
&= \begin{bmatrix}\delta q_0\\ \delta q_1\end{bmatrix}^{\mathrm{T}}\int_V \rho\,([\boldsymbol{\phi}_0 \mid \boldsymbol{\phi}_1])^{\mathrm{T}}([\boldsymbol{\phi}_0 \mid \boldsymbol{\phi}_1])\,dV\begin{bmatrix}\ddot{q}_0\\ \ddot{q}_1\end{bmatrix} && \triangleright \text{since } \frac{dq}{d\boldsymbol{X}} = 0 \\
&= \begin{bmatrix}\delta q_0\\ \delta q_1\end{bmatrix}^{\mathrm{T}}\int_V \rho\left[\begin{array}{c|c}\boldsymbol{\phi}_0^{\mathrm{T}}\boldsymbol{\phi}_0 & \boldsymbol{\phi}_0^{\mathrm{T}}\boldsymbol{\phi}_1\\ \hline \boldsymbol{\phi}_1^{\mathrm{T}}\boldsymbol{\phi}_0 & \boldsymbol{\phi}_1^{\mathrm{T}}\boldsymbol{\phi}_1\end{array}\right]dV\begin{bmatrix}\ddot{q}_0\\ \ddot{q}_1\end{bmatrix} \\
&= \begin{bmatrix}\delta q_0\\ \delta q_1\end{bmatrix}^{\mathrm{T}}\left[\begin{array}{c|c}\int_V \rho\boldsymbol{\phi}_0^{\mathrm{T}}\boldsymbol{\phi}_0 dV & 0\\ \hline 0 & \int_V \rho\boldsymbol{\phi}_1^{\mathrm{T}}\boldsymbol{\phi}_1 dV\end{array}\right]\begin{bmatrix}\ddot{q}_0\\ \ddot{q}_1\end{bmatrix} && \triangleright \text{since } \int_V \boldsymbol{\phi}_1^{\mathrm{T}}\boldsymbol{\phi}_0 = \int_V \boldsymbol{\phi}_0^{\mathrm{T}}\boldsymbol{\phi}_1 = 0 \\
&= \begin{bmatrix}\delta q_0\\ \delta q_1\end{bmatrix}^{\mathrm{T}}\boldsymbol{M}\begin{bmatrix}\ddot{q}_0\\ \ddot{q}_1\end{bmatrix}
\end{aligned} \tag{2.98}$$

where the modal mass matrix $\boldsymbol{M}$ and modal mass coefficients M_0 and M_1 can be defined:

$$\boldsymbol{M} = \begin{bmatrix}M_0 & 0\\ 0 & M_1\end{bmatrix};\quad M_0 \coloneqq \int_V \rho\|\boldsymbol{\phi}_0\|_2^2\,dV;\quad M_1 \coloneqq \int_V \rho\|\boldsymbol{\phi}_1\|_2^2\,dV \tag{2.99}$$

The virtual work of external forces $\delta\mathcal{W}_{\mathrm{ext}}$ is:

$$\begin{aligned}
\delta\mathcal{W}_{\mathrm{ext}} &= \int_V (\delta\boldsymbol{u})^{\mathrm{T}}\,\boldsymbol{b}dV + \int_S (\delta\boldsymbol{u})^{\mathrm{T}}\,\boldsymbol{\tau}dS \\
&= \int_S (\delta q_0\boldsymbol{\phi}_0 + \delta q_1\boldsymbol{\phi}_1)^{\mathrm{T}}\,\boldsymbol{\tau}dS \quad (\text{since } \boldsymbol{b} = \boldsymbol{0}) \\
&= \begin{bmatrix}\delta q_0\\ \delta q_1\end{bmatrix}^{\mathrm{T}}\int_S \begin{bmatrix}\boldsymbol{\phi}_0^{\mathrm{T}}\boldsymbol{\tau}\\ \boldsymbol{\phi}_1^{\mathrm{T}}\boldsymbol{\tau}\end{bmatrix}dS \\
&= \begin{bmatrix}\delta q_0\\ \delta q_1\end{bmatrix}^{\mathrm{T}}\begin{bmatrix}\int_S \boldsymbol{\phi}_0^{\mathrm{T}}\boldsymbol{\tau}dS\\ \int_S \boldsymbol{\phi}_1^{\mathrm{T}}\boldsymbol{\tau}dS\end{bmatrix} \\
&= \begin{bmatrix}\delta q_0\\ \delta q_1\end{bmatrix}^{\mathrm{T}}\boldsymbol{F}_{\mathrm{ext}}
\end{aligned} \tag{2.100}$$

where the modal external forces $\boldsymbol{F}_{\mathrm{ext}}$ coefficients can be defined:

$$\boldsymbol{F}_{\mathrm{ext}} = \begin{bmatrix}F_{\mathrm{ext},0}\\ F_{\mathrm{ext},1}\end{bmatrix};\quad F_{\mathrm{ext},0} \coloneqq \int_S \boldsymbol{\phi}_0^{\mathrm{T}}\boldsymbol{\tau}\,dS = F_{\mathrm{base}}\phi_{0,3};\quad F_{\mathrm{ext},1} \coloneqq \int_S \boldsymbol{\phi}_1^{\mathrm{T}}\boldsymbol{\tau}\,dS = F_{\mathrm{base}}\phi_{1,3} \tag{2.101}$$

and $\phi_{\cdot,3}$ corresponds to the longitudinal value, i.e. $\boldsymbol{\phi}_1(\boldsymbol{X}) = [\phi_{1,1}(\boldsymbol{X})\ \phi_{1,2}(\boldsymbol{X})\ \phi_{1,3}(\boldsymbol{X})]^{\mathrm{T}}$.

The virtual work of internal forces $\delta\mathcal{W}_{\mathrm{int}}$ is expanded to be a decomposition of linear and nonlinear stresses. It's assumed that there is an underlying linear Kelvin-Voigt material which represents the dynamic elasticity and viscosity by tensors $\mathbb{C}$ and $\mathbb{V}$ respectively. To characterize a nonlinear stress due to material heterogeneities, the homogenized equivalent material $\mathbb{C}^*$ is contained in a nonlinear volume within the linear bulk of the material, $V_{\mathrm{nl}} \subset V$. The homogenized stress components constitute a nonlinear force $\boldsymbol{F}_{\mathrm{nl}}$, as demonstrated:

$$\begin{aligned}
-\delta\mathcal{W}_{\mathrm{int}} &= \int_V (\delta\boldsymbol{\varepsilon})^{\mathrm{T}}\boldsymbol{\sigma}\, dV \\
&= \underbrace{\int_V (\delta\boldsymbol{\varepsilon})^{\mathrm{T}} (\mathbb{C}\boldsymbol{\varepsilon} + \mathbb{V}\dot{\boldsymbol{\varepsilon}})\, dV}_{\text{Linear Kevin-Voigt material}} + \underbrace{\int_{V_{\mathrm{nl}}} (\delta\boldsymbol{\varepsilon})^{\mathrm{T}} (\mathbb{C}^* - \mathbb{C})\, \boldsymbol{\varepsilon}\, dV_{\mathrm{nl}}}_{\text{Nonlinear stress contribution}} \\
&= \int_V (\mathbb{D}\delta\boldsymbol{u})^{\mathrm{T}}\mathbb{C}\mathbb{D}\boldsymbol{u}\, dV + \int_V (\mathbb{D}\delta\boldsymbol{u})^{\mathrm{T}}\mathbb{V}\mathbb{D}\dot{\boldsymbol{u}}\, dV + \int_{V_{\mathrm{nl}}} (\mathbb{D}\delta\boldsymbol{u})^{\mathrm{T}} (\mathbb{C}^* - \mathbb{C})\, \mathbb{D}\boldsymbol{u}\, dV_{\mathrm{nl}} \\
&= \vdots \text{ (expanded derivation in Appendix A.3)} \\
&= \begin{bmatrix}\delta q_0 \\ \delta q_1\end{bmatrix}^{\mathrm{T}} \left(\boldsymbol{K} \begin{bmatrix} q_0 \\ q_1 \end{bmatrix} + \boldsymbol{C} \begin{bmatrix} \dot{q}_0 \\ \dot{q}_1 \end{bmatrix} + \boldsymbol{F}_{\mathrm{nl}} \right)
\end{aligned} \tag{2.102}$$

The stiffness matrix $\boldsymbol{K}$ can be characterized by the Rayleigh quotient [GR15] since $\boldsymbol{\phi}_1$ is mass normalized:

$$\boldsymbol{K} = \begin{bmatrix} 0 & 0 \\ 0 & K_1 \end{bmatrix}; \quad K_1 \coloneqq \int_V (\mathbb{D}\boldsymbol{\phi}_1)^{\mathrm{T}}\mathbb{C}\mathbb{D}\boldsymbol{\phi}_1 dV = \omega_1^2 \tag{2.103}$$

The damping matrix $\boldsymbol{C}$ is assumed to be of small viscous damping, where the definition of a modal damping ratio $\zeta_1 = C_1/2\sqrt{M_1 K_1}$ gives:

$$\boldsymbol{C} = \begin{bmatrix} 0 & 0 \\ 0 & C_1 \end{bmatrix}; \quad C_1 \coloneqq \int_V (\mathbb{D}\boldsymbol{\phi}_1)^{\mathrm{T}}\mathbb{V}\mathbb{D}\boldsymbol{\phi}_1 dV = 2\zeta_1\omega_1 \tag{2.104}$$

The nonlinear force vector $\boldsymbol{F}_{\mathrm{nl}}$ is the difference between the homogenized nonlinear stress heterogeneity and the elastic bulk inside the nonlinear volume:

$$\begin{aligned}
\boldsymbol{F}_{\mathrm{nl}} = \begin{bmatrix} 0 \\ F_{\mathrm{nl},1} \end{bmatrix}; \quad F_{\mathrm{nl},1} \coloneqq \int_{t_0}^{t_1} K_{\mathrm{nl},1}\, \dot{q}_1 dt; \quad K_{\mathrm{nl},1} &\coloneqq \int_{V_{\mathrm{nl}}} (\mathbb{D}\boldsymbol{\phi}_1)^{\mathrm{T}}\mathbb{C}^*\mathbb{D}\boldsymbol{\phi}_1\, dV_{\mathrm{nl}} - \int_{V_{\mathrm{nl}}} (\mathbb{D}\boldsymbol{\phi}_1)^{\mathrm{T}}\mathbb{C}\mathbb{D}\boldsymbol{\phi}_1 dV_{\mathrm{nl}} \\
&\coloneqq K^*_{\mathrm{nl}}\big|_{V_{\mathrm{nl}}} - K_{\mathrm{lin}}\big|_{V_{\mathrm{nl}}}
\end{aligned} \tag{2.105}$$

The nonlinear description is consistent in the sense that if $\mathbb{C}^*$ is set to be a linear material $\mathbb{C}$, then the nonlinear force on the first longitudinal normal mode is $F_{\mathrm{nl},1} = 0$, and the modal equations of motion due to a purely elastic material are recovered.

2.3.1 Internal energy of the modal model

The principle of virtual work yields an equation of motion for the modes:

$$\begin{bmatrix} M_0 & 0 \\ 0 & M_1 \end{bmatrix} \begin{bmatrix} \ddot{q}_0 \\ \ddot{q}_1 \end{bmatrix} + \begin{bmatrix} 0 & 0 \\ 0 & C_1 \end{bmatrix} \begin{bmatrix} \dot{q}_0 \\ \dot{q}_1 \end{bmatrix} + \begin{bmatrix} 0 & 0 \\ 0 & K_1 \end{bmatrix} \begin{bmatrix} q_0 \\ q_1 \end{bmatrix} + \begin{bmatrix} 0 \\ F_{\mathrm{nl},1} \end{bmatrix} = \begin{bmatrix} F_{\mathrm{ext},0} \\ F_{\mathrm{ext},1} \end{bmatrix}$$

This characteristic equation represents the weights of the modal coordinates on the strain energies and external forces mapped by the Galerkin projection. First, the rigid body longitudinal normal mode coordinate $q_0(t)$ has an equation:

$$M_0 \ddot{q}_0 = F_{\mathrm{ext},0} = F_{\mathrm{base}} \phi_{0,3} \tag{2.106}$$

The rigid body longitudinal normal mode induces no elongation and thus has no influence on the strain energies. Conversely, the longitudinal normal mode coordinate $q_1(t)$ has an equation of motion:

$$M_1 \ddot{q}_1 + C_1 \dot{q}_1 + K_1 q_1 + F_{\mathrm{nl},1} = F_{\mathrm{ext},1} = F_{\mathrm{base}} \phi_{1,3} \tag{2.107}$$

which takes the form of a classical oscillator with external forcing and nonlinearity. To capture the effects on elongation in terms measurable states, i.e. the base acceleration, one can use the fact of the modal coupling.

An equivalence between the force driven oscillator and the acceleration driven oscillator at the base of the specimen $\ddot{\boldsymbol{u}}(\boldsymbol{X}_{\mathrm{base}})$ is sought. First by definition (Eq. (2.101) cf. Fig. 2.25):

$$F_{\mathrm{base}} = \frac{F_{\mathrm{ext},0}(\boldsymbol{X}_{\mathrm{base}})}{\phi_{0,3}(\boldsymbol{X}_{\mathrm{base}})} = \frac{F_{\mathrm{ext},1}(\boldsymbol{X}_{\mathrm{base}})}{\phi_{1,3}(\boldsymbol{X}_{\mathrm{base}})} \Rightarrow F_{\mathrm{ext},1}(\boldsymbol{X}_{\mathrm{base}}) = \frac{M_0 \, \ddot{q}_0 \, \phi_{1,3}(\boldsymbol{X}_{\mathrm{base}})}{\phi_{0,3}(\boldsymbol{X}_{\mathrm{base}})} \tag{2.108}$$

When the external force vector $\boldsymbol{F}_{\mathrm{ext}}(\boldsymbol{X}_{\mathrm{base}})$ is applied, the Galerkin projection about the base is:

$$\begin{aligned} \ddot{\boldsymbol{u}}(\boldsymbol{X}_{\mathrm{base}}) = \begin{bmatrix} 0 \\ 0 \\ \ddot{u}(\boldsymbol{X}_{\mathrm{base}}) \end{bmatrix} &\Rightarrow \ddot{u}(\boldsymbol{X}_{\mathrm{base}}) = \ddot{q}_0 \, \phi_{0,3}(\boldsymbol{X}_{\mathrm{base}}) + \ddot{q}_1 \, \phi_{1,3}(\boldsymbol{X}_{\mathrm{base}}) \\ &\Rightarrow \ddot{q}_0 = \frac{1}{\phi_{0,3}(\boldsymbol{X}_{\mathrm{base}})} \left(\ddot{u}(\boldsymbol{X}_{\mathrm{base}}) - \ddot{q}_1 \, \phi_{1,3}(\boldsymbol{X}_{\mathrm{base}}) \right) \end{aligned} \tag{2.109}$$

where u is the axial component of $\boldsymbol{u}$. Substituting Eqs. (2.108) and (2.109) into the first modal equation of motion Eq. (2.107) gives:

$$M_1 \ddot{q}_1 + C_1 \dot{q}_1 + K_1 q_1 + F_{\mathrm{nl},1} = \frac{M_0 \, \phi_{1,3}(\boldsymbol{X}_{\mathrm{base}})}{\left(\phi_{0,3}(\boldsymbol{X}_{\mathrm{base}})\right)^2} \ddot{u}(\boldsymbol{X}_{\mathrm{base}}) - \frac{M_0 \left(\phi_{1,3}(\boldsymbol{X}_{\mathrm{base}})\right)^2}{\left(\phi_{0,3}(\boldsymbol{X}_{\mathrm{base}})\right)^2} \ddot{q}_1$$

and isolating the base motion yields:

$$\frac{\left(\phi_{0,3}(\boldsymbol{X}_{\mathrm{base}})\right)^2}{M_0 \, \phi_{1,3}(\boldsymbol{X}_{\mathrm{base}})} \left[(M_1 + \frac{M_0 \left(\phi_{1,3}(\boldsymbol{X}_{\mathrm{base}})\right)^2}{\left(\phi_{0,3}(\boldsymbol{X}_{\mathrm{base}})\right)^2}) \ddot{q}_1 + C_1 \dot{q}_1 + K_1 q_1 + F_{\mathrm{nl},1} \right] = \ddot{u}(\boldsymbol{X}_{\mathrm{base}}) \tag{2.110}$$

Therefore, the equivalent modal equation of motion described with base acceleration[1] is:

$$\ddot{q}_1 + \underbrace{2\overline{\zeta}_1\overline{\omega}_1\dot{q}_1 + \overline{\omega}_1^2 q_1 + \overline{F}_{\mathrm{nl},1}}_{\overline{F}_{\mathrm{int},1}} = \overline{G}\ddot{u}(\boldsymbol{X}_{\mathrm{base}}) \tag{2.111}$$

where the coefficients are defined:

$$\begin{aligned} \mu &\coloneqq \frac{\phi_{1,3}(\boldsymbol{X}_{\mathrm{base}})}{\phi_{0,3}(\boldsymbol{X}_{\mathrm{base}})} \quad \overline{\omega}_1^2 \coloneqq \frac{K_1}{M_1 + M_0\mu^2} \quad \overline{\zeta}_1 \coloneqq \frac{C_1}{2\sqrt{K_1(M_1 + M_0\mu^2)}} \\ \overline{F}_{\mathrm{nl},1} &\coloneqq \frac{F_{\mathrm{nl},1}}{M_1 + M_0\mu^2} \quad \overline{G} \coloneqq \frac{M_0\,\mu}{(M_1 + M_0\mu^2)\phi_{0,3}(\boldsymbol{X}_{\mathrm{base}})} \end{aligned} \tag{2.112}$$

and $\overline{F}_{\mathrm{int},1}$ regroups the internal forces.

Finally, to enable a problem description with measurable states, the longitudinal normal mode has an explicit relationship dependent on the difference of the base and tip motion of the fatigue specimen. First let the notation $u(\boldsymbol{X}_{\mathrm{base}}, t) \coloneqq u_{\mathrm{base}}$ represent the base motion and $u(\boldsymbol{X}_{\mathrm{tip}}, t) \coloneqq u_{\mathrm{tip}}$ the tip motion, which is substituted in the Galerkin approximation of Eq. (2.96):

$$\begin{aligned} \ddot{u}_{\mathrm{base}} &= \ddot{q}_0\phi_{0,\mathrm{base}} + \ddot{q}_1\phi_{1,\mathrm{base}} = \ddot{q}_0\phi_{0,\mathrm{base}} - \ddot{q}_1\phi_{1,\mathrm{tip}} \\ \ddot{u}_{\mathrm{tip}} &= \ddot{q}_0\phi_{0,\mathrm{tip}} \;+\; \ddot{q}_1\phi_{1,\mathrm{tip}} \;= \ddot{q}_0\phi_{0,\mathrm{base}} + \ddot{q}_1\phi_{1,\mathrm{tip}} \end{aligned} \tag{2.113}$$

Note that, by the symmetry of the mode shape $\boldsymbol{\phi}_1$, one obtains $\phi_{1,\mathrm{tip}} = -\phi_{1,\mathrm{base}}$. An explicit form is obtained with the substitution of Eqs. (2.109) and (2.113):

$$\ddot{u}_{\mathrm{tip}} = 2\phi_{1,\mathrm{tip}}(\overline{G}\ddot{u}_{\mathrm{base}} - \overline{F}_{\mathrm{int},1}) + \ddot{u}_{\mathrm{base}} \tag{2.114}$$

with $\overline{F}_{\mathrm{int},1}$ in Eq. (2.112) or with the internal forces isolated:

$$\left(\frac{1}{2\phi_{1,\mathrm{tip}}} + \overline{G}\right)\ddot{u}_{\mathrm{base}} - \frac{1}{2\phi_{1,\mathrm{tip}}}\ddot{u}_{\mathrm{tip}} = \overline{F}_{\mathrm{int},1} \tag{2.115}$$

Eq. (2.115) shows that the relative motion is proportional to the internal forces due to elongation of the ultrasonic fatigue specimen. The experimental implications of this fact are substantiated in Chapter 4.

2.3.2 Nonlinear force of the centroid volume

In order to model the structural effects (e.g. a change in structural stiffness corresponding to a shift in eigenfrequency), material nonlinearities due to fatigue mechanisms must be embedded into

[1] Using experimental modal values obtained from a finite element analysis, one can confirm this derivation is correct when $\overline{\omega}_1 = \omega_1\sqrt{2}$, c.f. [Inm14]

a local volume about the centroid of the fatigue specimen model, i.e. the centroid volume. The expression for $K_{\mathrm{nl},1}$ of Eq. (2.105) represents the modal stiffness contribution of the centroid volume; the linear elastic volume is replaced with with a volume with the same geometry whose nonlinear constitutive behavior $\mathbb{C}^*$ is defined by Eq. (2.84). The internal modal force due to this nonlinear behavior is $F_{\mathrm{nl},1} \coloneqq \int_{t_0}^{t_1} K_{\mathrm{nl},1}\, \dot{q}_1 dt$. In a manner analogous to the tangent stiffness tensor utilized in the incremental formulation of the microplastic inclusions' plasticity law, the nonlinear internal modal force is expressed incrementally:

$$\Delta F_{\mathrm{nl},1} \coloneqq K_{\mathrm{nl},1} \cdot \Delta q_1 = \Bigg(\underbrace{\int_{V_{\mathrm{nl}}} (\mathbb{D}\boldsymbol{\phi}_1)^{\mathrm{T}} \mathbb{C}^* \mathbb{D}\boldsymbol{\phi}_1 \, dV_{\mathrm{nl}}}_{\text{Nonlinear stiffness contribution}} - \underbrace{\int_{V_{\mathrm{nl}}} (\mathbb{D}\boldsymbol{\phi}_1)^{\mathrm{T}} \mathbb{C} \mathbb{D}\boldsymbol{\phi}_1 \, dV_{\mathrm{nl}}}_{\text{Linear stiffness contribution}} \Bigg) \cdot \Delta q_1 \tag{2.116}$$

where the incremental macroscopic strain is defined by the quantity $\Delta\bar{\boldsymbol{\varepsilon}} \coloneqq \mathbb{D}\boldsymbol{\phi}_1 \Delta q_1$.

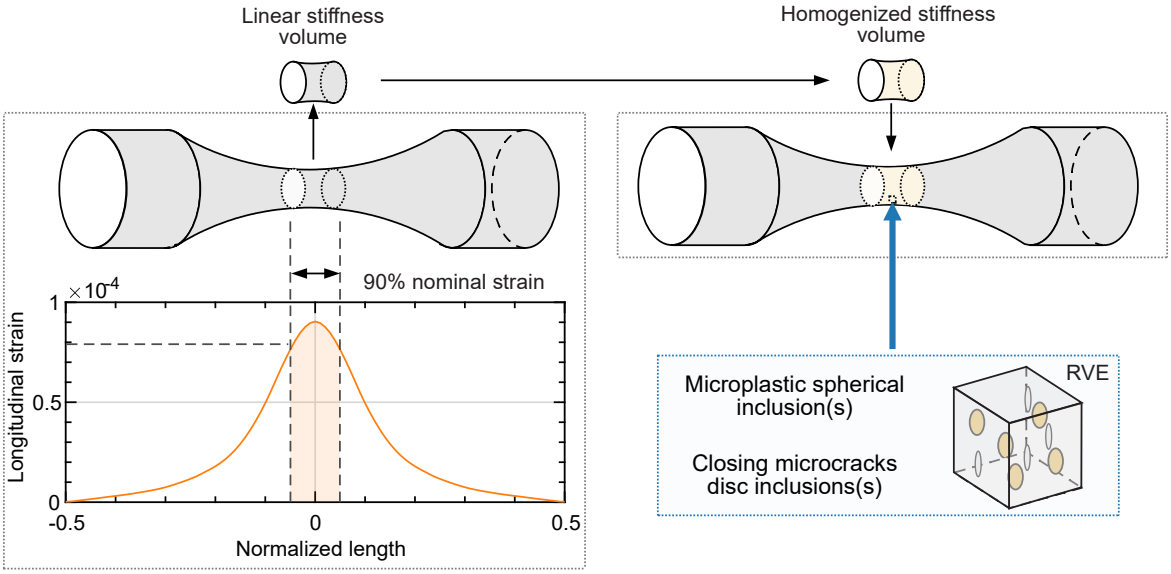

Figure 2.26: On the left, the maximum 90% nominal longitudinal strain of a copper specimen is used to define the boundaries of the nonlinear volume about the centroid. The volume then is defined to have a nonlinear constitutive relationship due to homogenization of microcracks and/or microplasticity, and subtracts the contribution of the elastic stiffness.

For the volume integral, there is a quasi-free parameter which must be chosen, namely the starting and ending lengths which integrates the centroid's cross-sectional profile. Here it is fixed that the centroid volume is defined for the 10th decile of the maximum longitudinal stress/strain seen by the ultrasonic fatigue specimen. This volume, notated V_{nl}, is accountable for the internal forces acting upon the centroid volume. For the specimen whose centroid shape is of a profile of hyperbolic cosine,

as shown in Fig. 2.26, the approximation of the volume integral is expressed as:

$$\int_{V_{\mathrm{nl}}} (\square)\, dV_{\mathrm{nl}} \approx 2 \int_{z_{\mathrm{nl},1}}^{z_{\mathrm{nl},2}} S(z) \cdot \square \, dz \tag{2.117}$$

where the quantity in $\square$ is a constant and S is the area of the cross-section as presented by Bathias [BP05] in Fig. 2.27:

$$S(z) \coloneqq \frac{\pi d_1^2}{4} \cosh^2(\lambda z); \quad \lambda \coloneqq \frac{1}{L_2} \operatorname{arccosh}\left(\frac{d_2}{d_1}\right) \tag{2.118}$$

Given the closed form expressions, the line integral can be numerically estimated by trapezoidal rule or other numerical quadratures. In the cases where an analytical closed form solution does not exist, the central geometry can be estimated by an elementary shape: e.g. a cylinder for a cylindrical specimen, or a rectangular prism for a rectangular shaped specimen. The effect of such a small deviation from the true geometry will still capture the first order-effects, that is because Eq. (2.117) can also be approximated as a Riemann sum.

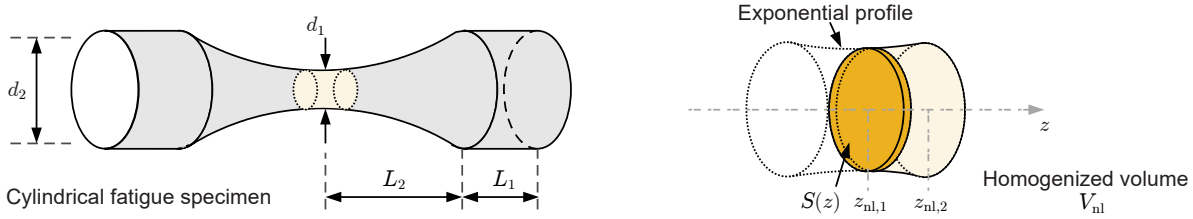

Figure 2.27: An exponential/cylindrical ultrasonic fatigue specimen with defined geometry from [BP05]. For the centroid volume bounded by $z_{\mathrm{nl},1}$ to $z_{\mathrm{nl},2}$, a line integral can be evaluated numerically.

2.4 Ultrasonic fatigue machine and piezoelectric solicitation

Symbol	Description
A_s	Surface area of piezoelectric disc
$\boldsymbol{c^E}$	Stiffness tensor under constant electric field
C_p	Capacitance coefficient
$\boldsymbol{\mathcal{D}}$	Dielectric displacement tensor
D, d	Damping coefficients
$\boldsymbol{E}$	Electric field tensor
$\boldsymbol{e}$	Piezoelectric tensor
$\boldsymbol{\eta^S}$	Permittivity tensor under constant strain
F	Force
H, J	Electromechanical conversion coefficient and its inverse
h_s	Piezoelectric disc thickness
i	Current
K, k	Stiffness coefficients
l_s	Piezoelectric stack thickness
M, m	Mass coefficients
Q	Electric charge coefficient
R_p	Resistor coefficient
$\boldsymbol{S}$	Strain tensor
$\boldsymbol{T}$	Stress tensor
V	Voltage
$x, \dot{x}, \ddot{x}$	Displacement, velocity, acceleration
α	Linear acoustic amplification coefficient
$\omega_\mathrm{a}, \omega_\mathrm{r}$	Anti-resonant/resonant frequency
$\square_\mathrm{h}, \square_\mathrm{p}$	Equivalent booster + horn / transducer quantity

Table 2.6: For the electrodynamical model in Sec. 2.4 only, this notation is adopted.

The objective of this section is to develop a detailed understanding through the modeling of the ultrasonic fatigue machine. Compared to conventional fatigue machines, the piezoelectric transducer of the ultrasonic fatigue machine has a working frequency that consists of the entire testing system, which can be different from the eigenfreqencies of the fatigue specimen. In other words, the fatigue specimen is forced to vibration due to its base motion at the acoustic horn. This is accomplished by imposing a voltage at the piezoelectric transducer, and is converted into mechanical vibration by the piezoelectric effect. A global view of this ultrasonic fatigue machine and its measurable quantities is shown as simple block diagram in Fig. 2.28. This enables an electromechanical model by transfer functions, which can aide in understanding the ultrasonic fatigue test machine's global properties.

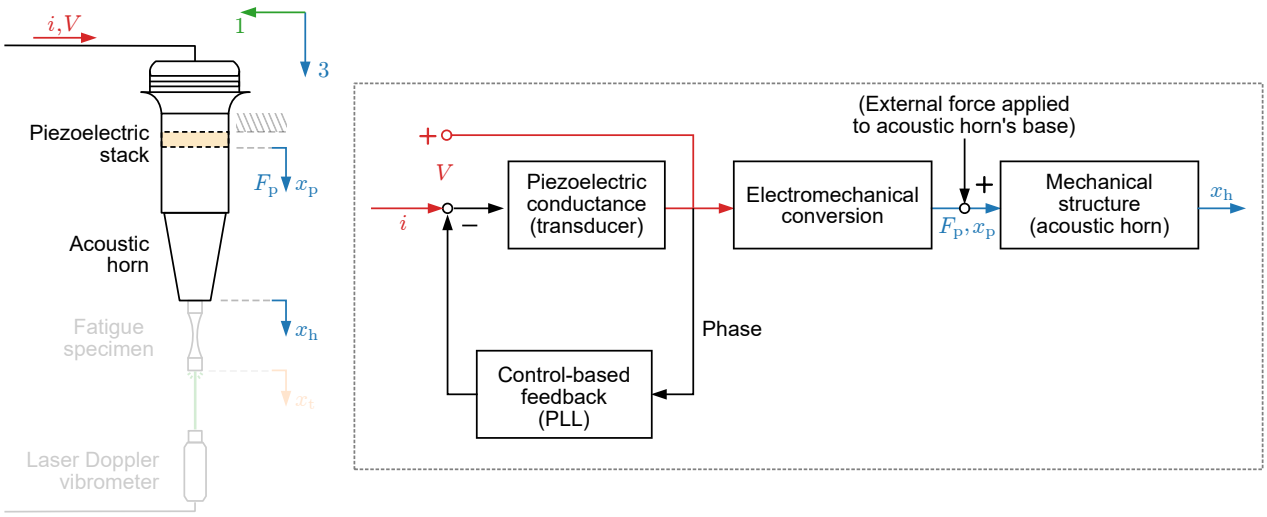

Figure 2.28: An ultrasonic fatigue test machine. The quantities of focus are shown in color and imposed onto a block-diagram: namely the input voltage (post amplification) V and current i to the piezoelectric stack, the mechanical force F_p and motion x_p of the piezoelectric stack, and the motion or solicitation provided by the acoustic horn x_h.

Briefly, the piezoelectric effect and piezoelectric transducers are introduced. Piezoelectric materials, convert electrical signals into mechanical motion via the piezoelectric effect. In these materials, microscopic ferroelectric domains are initially randomly oriented, resulting in no net polarization and no piezoelectric effect. However, when exposed to a strong electric field, these domains align with the field, creating a net polarization, see Fig. 2.29 **(a)**. This alignment causes the crystalline structure to elongate in response to the electric field, which is the fundamental mechanism behind the piezoelectric effect. To exploit this effect for ultrasonics, the piezoelectric material is assembled into a Langevin-type piezoelectric transducer [Bat06], shown in Fig. 2.29 **(b)**. The piezoelectric transducer utilized in this dissertation is the Branson model CR-20, which operates in a thickness-mode of the piezo-ceramic disc (typically denoted with the direction 3 or subscript $_{33}$). These transducers consist of one or more piezoceramics, mechanically compressed between a two masses. This prestress serves a dual purpose: it prevents the piezoceramics from experiencing tensile stresses during ultrasonic vibration and ensures clapping contact at the piezoceramic interfaces.

A popular approach to modeling an ultrasonic transducer and load train is by an equivalent circuit [She+97]. When using an equivalent electrical circuit as a model, the complexities of mechanical quantities and electromechanical interactions become reduced to a 0D model. However, there have been instances in the literature [Hay84] where a negative capacitance coefficient is used for a model thickness-

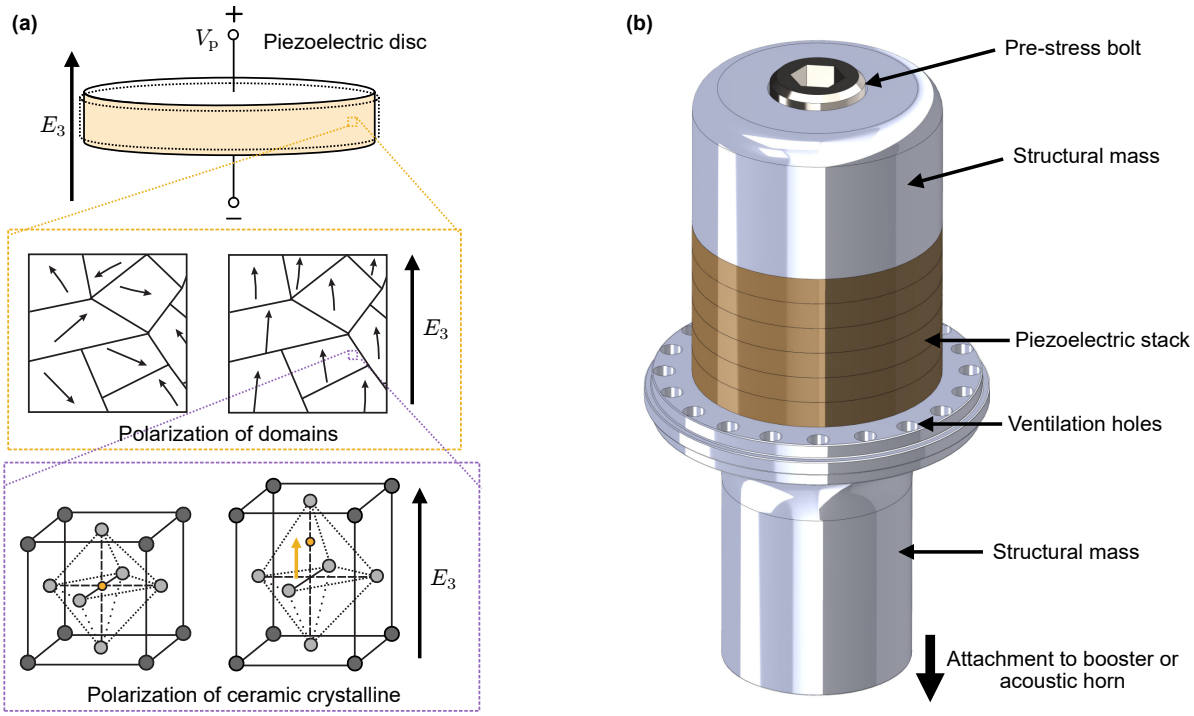

Figure 2.29: In **(a)**, the multiscale effects of piezoelectricity for in Lead Zirconate Titanate (PZT) ceramics. In **(b)**, a diagramed Langevin-type piezoelectric transducer.

mode transducers, which is impossible with physical circuit elements. A more physically consistent model in the recent 2019 work of Zhang et al. [Zha+19] uses a chain of oscillators with a lumped circuit. This approach obtains physically consistent values and can be validated with experimental data. Furthermore, the coupled equations can be analyzed using traditional control theory and facilitates the analysis of system characteristics like resonance and sensitivity.

2.4.1 Ideal electrodynamical model

The material constitutive equations which describes the piezoelectric effect in the linear (reversible) case, for small mechanical deformations and electric fields is given in Voigt notation:

$$\begin{aligned} \boldsymbol{T} &= \boldsymbol{c}^{\boldsymbol{E}}\boldsymbol{S} - (\boldsymbol{e})^{\mathrm{T}}\boldsymbol{E} \\ \boldsymbol{\mathcal{D}} &= \boldsymbol{e}\boldsymbol{S} + \boldsymbol{\eta}^{\boldsymbol{S}}\boldsymbol{E} \end{aligned} \tag{2.119}$$

Here, the mechanical stress tensor $\boldsymbol{T}$, the dielectric displacement $\boldsymbol{\mathcal{D}}$ are related to the mechanical strain $\boldsymbol{S}$ and the electric field $\boldsymbol{E}$, whose tensor notations is given in Appendix A.4, $\boldsymbol{e}$ is the piezoelectric tensor, $\boldsymbol{C}^{\boldsymbol{E}}$ is the stiffness tensor under constant electric field, and $\boldsymbol{\eta}^{\boldsymbol{S}}$ denotes permittivity tensor under constant strain. The superscripts $^{\boldsymbol{S},\boldsymbol{E}}$ for the parameters denote the physical field quantity

which is held constant while one determines the parameter, according to IEEE standards [EE78]. For motion in the thickness mode (longitudinal direction), this can be simplified to:

$$\begin{bmatrix} T_3 \\ \mathcal{D}_3 \end{bmatrix} = \begin{bmatrix} c_{33}^E & -e_{33} \\ e_{33} & \eta_{33}^S \end{bmatrix} \begin{bmatrix} S_3 \\ E_3 \end{bmatrix} \tag{2.120}$$

For a Langevin transducer, piezo-ceramic discs are stacked in parallel with a pre-load to amplify the vibration, with a three-disc system shown in Fig. 2.30. Assuming uniform electric fields during longitudinal vibration with opposing fields in each disc, the constitutive equations can be simplified to a 0D analog [FGS08] with the relations:

$$T_3 = \frac{F_\mathrm{p}}{A_\mathrm{s}}; \quad \mathcal{D}_3 = \frac{Q_3}{A_\mathrm{s}}; \quad S_3 = \frac{x_\mathrm{p}}{l_\mathrm{s}}; \quad E_3 = \frac{V_\mathrm{p}}{h} \tag{2.121}$$

where F_p is the piezoelectric stack's internal axial force, Q_3 is the electric charge due to the deformation

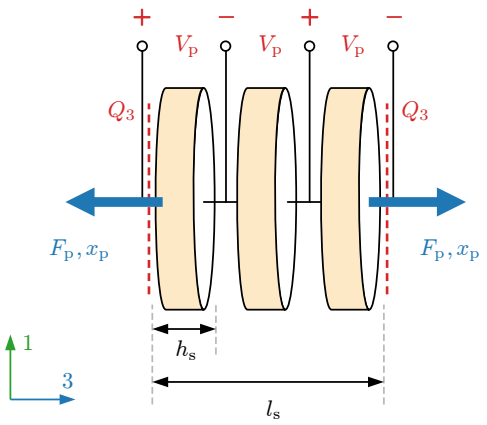

Figure 2.30: A 0D model of an expanded Langevin transducer with a three disc piezoelectric stack.

x_p, and V_p is the applied voltage. The A_s is the cross-sectional area of the piezoelectric disc and its thickness h, the total thickness of the piezo-ceramic discs is ($l_\mathrm{s} = n \cdot h$) with n being the number of discs.

The constitutive equations from Eq. (2.120) can be reformulated by substitution of Eq. (2.121) as:

$$\begin{bmatrix} F_\mathrm{p} \\ Q_3 \end{bmatrix} = \begin{bmatrix} k_\mathrm{p} & -H \\ H & c_\mathrm{p} \end{bmatrix} \begin{bmatrix} x_\mathrm{p} \\ V_\mathrm{p} \end{bmatrix} \tag{2.122}$$

From Eq. (2.122), the piezoelectric stack's internal axial force F_p and electric charge Q_3 arise from deformation x_p and applied voltage V_p. Deformation can be produced by a force on the piezoelectric disc, even without electrical input. Eq. (2.122) gives the stiffness coefficient $k_\mathrm{p} = c_{33}^E A/l$ for characteristic $A, l > 0$, and the relationship between voltage and charge in piezoelectricity which can be

depicted as a capacitor $C_\mathrm{p} = \eta_{33}^S nA/h$. Additionally, the electromechanical conversion coefficient H represents the voltage-force and deformation-charge relationship $H = e_{33}A_\mathrm{s}/l_\mathrm{s}$.

A steady-state electrodynamical model of the ultrasonic fatigue machine draws inspiration from the schematization of Fig. 2.31 of [Zha+19]. The mechanical properties of a piezoelectric stack can be represented by a 0D oscillator model, which consists of an equivalent mass m_p, spring k_p, and damper d_p and for the booster and horn by another mass m_h, spring k_h, and damper d_h. The piezoelectric transducer is constructed where x_h and x_p are defined as the vibration amplitudes of the horn and piezoelectric stack, respectively. An equivalent circuit can be utilized to represent the impedance curves of dielectric and electrical losses of the piezoelectric transducer [She+97] via a capacitor C_p, resistor R_p, and transformer which provides force $F_\mathrm{p} \coloneqq HV_\mathrm{p}$, found from Eq. (2.122).

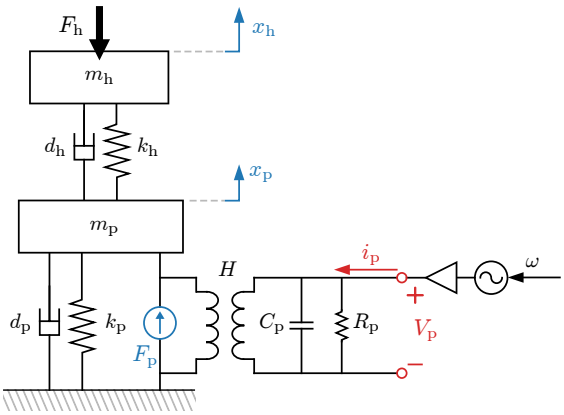

Figure 2.31: A 0D electrodynamical model of the ultrasonic fatigue machine with external force applied to the horn F_h.

The force balance of Fig. 2.31 is given as:

$$\begin{aligned} m_\mathrm{h}\ddot{x}_\mathrm{h} &= -d_\mathrm{h}\left(\dot{x}_\mathrm{h} - \dot{x}_\mathrm{p}\right) - k_\mathrm{h}\left(x_\mathrm{h} - x_\mathrm{p}\right) - F_\mathrm{h} \\ m_\mathrm{p}\ddot{x}_\mathrm{p} &= d_\mathrm{h}\left(\dot{x}_\mathrm{h} - \dot{x}_\mathrm{p}\right) + k_\mathrm{h}\left(x_\mathrm{h} - x_\mathrm{p}\right) - d_\mathrm{p}\dot{x}_\mathrm{p} - k_\mathrm{p}x_\mathrm{p} + F_\mathrm{p} \end{aligned} \tag{2.123}$$

and the electrical circuit is given as:

$$i_\mathrm{p} = C_\mathrm{p}\frac{dV_\mathrm{p}}{dt} + \frac{V_\mathrm{p}}{R_\mathrm{p}} \tag{2.124}$$

These set of equations are utilized by the 2019 publication of Zhang et al. [Zha+19], but the authors instead use them to create an equivalent circuit model. The coupling of the electronic and mechanical systems are done through the (electrical) transformer's coefficient H. However, the experimental piezoelectric transducer used in this thesis is sealed so the motion of the piezoelectric stack x_p is not measurable.

To mitigate this, it is commonly acknowledged that the booster and acoustic horn provide amplification [BP05] for longitudinal motion when properly designed[2]. This can be characterized as a linear amplification in the longitudinal motion such that $x_\mathrm{h} = \alpha x_\mathrm{p}$. In accordance to [BP05], substituting $x_\mathrm{h} = \alpha x_\mathrm{p}$ into Eq. (2.123) and combining equations gives:

$$M\ddot{x}_\mathrm{h} + D\dot{x}_\mathrm{h} + Kx_\mathrm{h} = F_\mathrm{p} - F_\mathrm{h} \tag{2.125}$$

whose schematic is shown in Fig. 2.32 (left) and the equivalent characteristic mass-spring-damper coefficients are:

$$M = m_\mathrm{h} + \frac{m_\mathrm{p}}{\alpha}; \quad D = \frac{d_\mathrm{p}}{\alpha}; \quad K = \frac{k_\mathrm{p}}{\alpha} \tag{2.126}$$

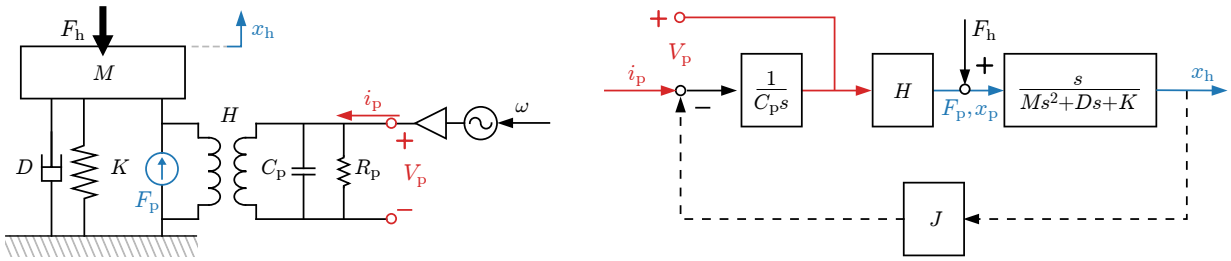

Figure 2.32: A simplified electrodynamical model of the ultrasonic fatigue machine with external force applied to the horn F_h and when $R_\mathrm{p} \gg 1$. The dotted line indicates a fictitious block relationship.

Fig. 2.32 depicts the input-output behavior of the ultrasonic fatigue test machine, with vibration velocity $\dot{x}_\mathrm{h}$ as the system output and both the voltage V_p and external force F_h as inputs. Current i_p serves as a fictitious output variable for assessing equivalent electrical conductance which transforms into force F_p through the electromechanical conversion coefficient H.

Utilizing the block diagram in Fig. 2.32 (right) via Mason's rule, various input-output behaviors can be determined, including electrical and mechanical impedance (or admittance). In the case of an unloaded horn (no tension or compression forces), like in ultrasonic fatigue test with load ratios $R = -1$, the closed loop transfer function by Fourier transform $s = \mathrm{j}\omega$ from V_p to i_p is:

$$\left.\frac{i_\mathrm{p}(s)}{V_\mathrm{p}(s)}\right|_{F_\mathrm{h}=0} = \frac{C_\mathrm{p}s\left(Ms^2 + DS + K + \frac{H^2}{\alpha C_\mathrm{p}}\right)}{Ms^2 + DS + K} \tag{2.127}$$

[2]If the resulting longitudinal ultrasonic wave meets the resonance condition between the mechanical components, i.e. transducer, booster, and horn, for an acoustic wavelength $\lambda/2 = L$ and characteristic length L.

and from i_p to $\dot{x}_\mathrm{h}$ is:

$$\left.\frac{\dot{x}_\mathrm{h}(s)}{i_\mathrm{p}(s)}\right|_{F_\mathrm{h}=0} = \frac{H}{C_\mathrm{p}\left(Ms^2 + DS + K + \frac{H^2}{\alpha C_\mathrm{p}}\right)} \tag{2.128}$$

From inspection of Eq. (2.127), the resonant and anti-resonant frequencies can be found from the poles and the zeros respectively, such that $\omega_\mathrm{r} = \sqrt{\frac{K}{M} + \frac{H^2}{\alpha C_\mathrm{p} M}}$ and $\omega_\mathrm{a} = \sqrt{\frac{K}{M}}$. Here, it can be seen that the anti-resonant frequency of the ultrasonic fatigue test machine is independent of the electrical system.

2.4.2 Experimental parameterization of an ideal system

To demonstrate the forward problem of the 0D electrodynamics model, the system parameters of Eq. (2.127) and Eq. (2.128) are identified via an experimental setup used in the thesis: The ultrasonic transducer (Branson model CR-20) is driven by a signal generator (Keysight 33500B) in series with a voltage amplifier (FLC electronics P100). The load train consists of a titanium booster (Branson 800-series, 1:1 amplification) followed by a titanium horn (1:2.65 amplification). The voltmeter (Pico Technology TA044) and ammeter (Tektronix A622) provide voltage and current measurements respectively. The velocity measurement of the free-end of the horn is measured using a laser vibrometer (Polytec VibroFlex Xtra). The schematic of the experiment is shown in Fig. 2.33, where the input and output data acquisition (Genesis Highspeed & Perception) are simultaneously recorded.

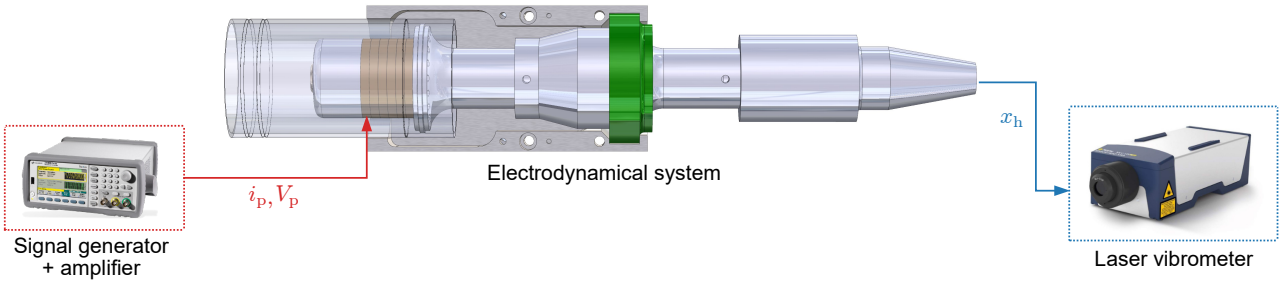

Figure 2.33: A simplified schematic of the experimental setup used for the parameterization of the electrodynamical model of the piezoelectric transducer coupled with the booster and horn.

First, the parameterization of Eq. (2.127) is sought through:

$$\left.\frac{i_\mathrm{p}(s)}{V_\mathrm{p}(s)}\right|_{F_\mathrm{h}=0} = \frac{C_\mathrm{p} s\left(s^2 + a_1 s + a_2\right)}{s^2 + a_3 s + a_4} \tag{2.129}$$

where the coefficients of Eq. (2.129) are related with Eq. (2.127) by:

$$a_1 = a_3 = \frac{D}{M}; \quad a_2 = \frac{K}{M} + \frac{H^2}{\alpha C_\mathrm{p} M}; \quad a_4 = \frac{K}{M} \tag{2.130}$$

With four unknown coefficients, the Fourier transform $s = \mathrm{j}\omega$ is used whose complex form yields the real component:

$$\mathrm{real}\left(\left.\frac{i_\mathrm{p}(\mathrm{j}\omega)}{V_\mathrm{p}(\mathrm{j}\omega)}\right|_{F_\mathrm{h}=0}\right) = \frac{C_\mathrm{p}\left[\omega^2\left(a_1^2+\omega^2\right)+a_2\left(a_2-2\omega^2\right)\right]}{a_1\left(a_4-2\omega^2-a_2\right)} \tag{2.131}$$

and the imaginary component:

$$\mathrm{imag}\left(\left.\frac{i_\mathrm{p}(\mathrm{j}\omega)}{V_\mathrm{p}(\mathrm{j}\omega)}\right|_{F_\mathrm{h}=0}\right) = \frac{C_\mathrm{p}\omega\left[\omega^2\left(a_1^2+\omega^2\right)+a_2\left(a_2-2\omega^2\right)\right]}{a_1^2\omega^2+\left(a_4-\omega^2\right)\left(a_2-\omega^2\right)} \tag{2.132}$$

To obtain a unique solution of Eq. (2.129), the steady-state responses at experimental resonant and anti-resonant frequencies are used with Eq. (2.131) and Eq. (2.132) to find the coefficients $\{C_\mathrm{p}, a_1, a_2, a_4\}$. The sampling frequency is 10^6 Hz. To obtain an experimental frequency response function of $i_\mathrm{p}/V_\mathrm{p}$, a sine sweep was conducted in the range of 19.80 to 20.50 kHz, employing a linear frequency increment of 3 Hz/s. The magnitude and phase plot of $i_\mathrm{p}/V_\mathrm{p}$ are shown in Figs. 2.34 and 2.35. Next the experimental anti-resonant frequency $\omega_\mathrm{a} = 1.271 \cdot 10^5$ rad/s and resonant frequency $\omega_\mathrm{r} = 1.262 \cdot 10^5$ rad/s are identified from the maximum and minimum magnitudes. At these two points, additional two steady-state signals are measured to obtain the coefficients in Table 2.7. At these two points, four equations are obtained via Eqs. (2.131) and (2.132), which yield the estimates of $\{C_\mathrm{p}, a_1, a_2, a_4\}$.

Using these coefficients with the experimental frequency response of the mechanical impedance, the coefficient H/M can be identified from Eq. (2.128):

$$\left.\frac{M}{H}\frac{\dot{x}_\mathrm{h}(s)}{i_\mathrm{p}(s)}\right|_{F_\mathrm{h}=0} = \frac{1}{C_\mathrm{p}\left(s^2+a_1 s+a_2\right)} \tag{2.133}$$

Experimentally, this is found through minimizing the residual between the experimental and previously found model parameters such that $M/H = 1.108 \cdot 10^{-5}$. Finally, the remaining non-mass normalized coefficients can be found from Eq. (2.130), since $a_2 = K + HJ/C_\mathrm{p}$, and by rearranging a_2:

$$J = C_\mathrm{p}\frac{M}{H}\left(a_2 - a_4\right) \tag{2.134}$$

where the resulting dynamical and electromechanical conversion that are coefficients found are shown in Table 2.8. The modeled electrical impedance of Eq. (2.129) is visualized on the magnitude and phase plots in Fig. 2.34. The current to velocity magnitude plot and the voltage to velocity plot (found by multiplying Eqs. (2.129) and (2.133) together) is shown in Fig. 2.35. Note that the maximum (at the anti-resonance) of the current to velocity magnitude plot indicates that the current draw is most

efficient at this frequency. This coincides with the fact that most industrial piezoelectric transducers are driven at its anti-resonant frequency for material and dynamical stability [Zha+19; Jac+21].

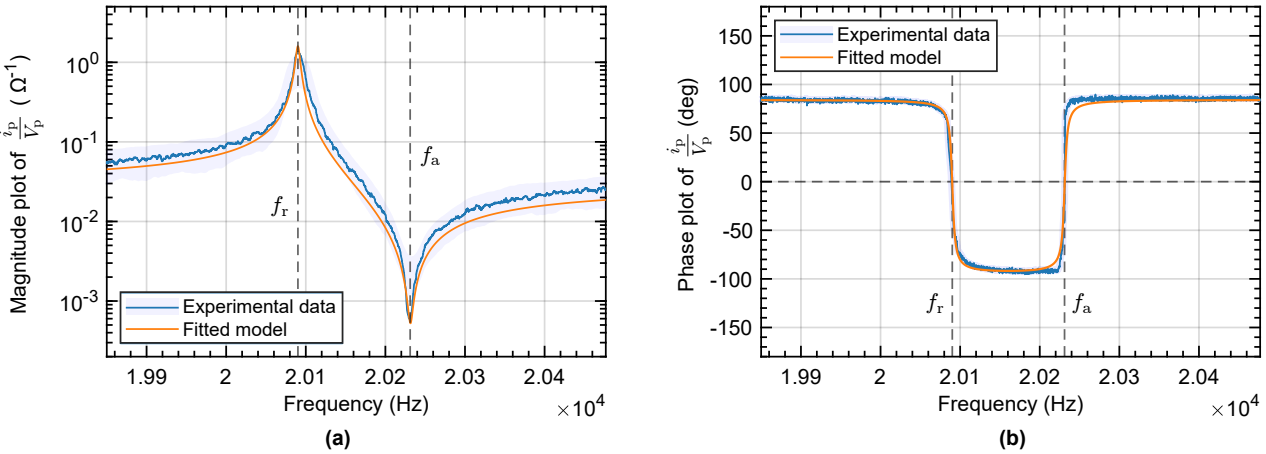

Figure 2.34: The magnitude plot **(a)** and phase plot **(b)** of i_p/V_p (Eq. (2.129)) and the experimental data. The experimental data has been smoothed by a median filter of window size 10 and the shaded entries correspond to the noisy signal's envelope.

Parameter	**Value**	**Units**
C_p	$2.275 \cdot 10^{-7}$	F/m
$a_1 = D/M$	32.000	$N/m^2/s$
$a_2 = K/M + H^2/(\alpha C_p M)$	$16.159 \cdot 10^9$	N/m^2
$a_4 = K/M$	$15.934 \cdot 10^9$	N/m^2

Table 2.7: Identified coefficients from the experimental sine sweep for electrical impedance.

In practice, the ultrasonic fatigue test machine operates by closely monitoring and adjusting to its anti-resonance frequency f_a, ensuring continuous and optimal performance. Critical to this process is the tracking of the machine's zero-phase at this point (Fig. 2.34 **(b)**). The machine identifies this anti-resonance frequency by a sine sweep at a low voltage input; the frequency where the phase equals zero degrees is pinpointed as the anti-resonance point. A phase-locked loop (PLL) circuit then keeps the machine's working frequency at this point, see Fig. 2.36. When a fatigue specimen is attached to the acoustic horn and undergoes a stiffness change ΔK (e.g. due to crack propagation), it's clear to see that the system's anti-resonance $\omega_a = \sqrt{K/M}$ will change as well. The role of the PLL adjusts the working frequency to this anti-resonant point which ensures the fatigue specimen is working at its first longitudinal eigenmode.

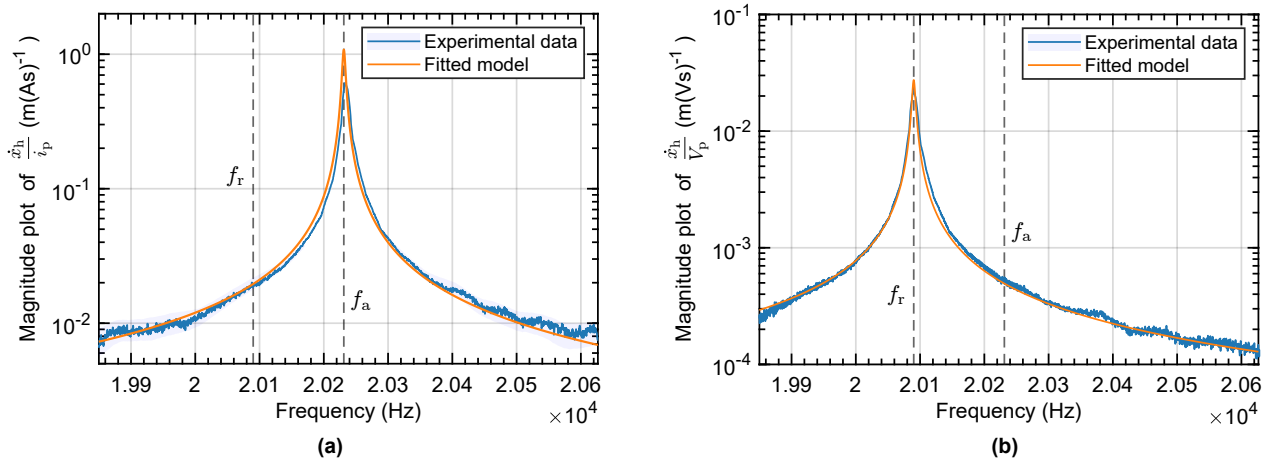

Figure 2.35: The magnitude plot of $\dot{x}_h/i_p$ **(a)**(Eq. (2.133)), $\dot{x}_h/V_p$ **(a)**, and experimental data. The experimental data has been smoothed by a median filter of window size 10 and the shaded entries correspond to the noisy signal's envelope. The fitted model coefficients identified in Table 2.7 are shown by scaling model's curve by M/H.

Parameter	**Value**	**Units**
M/H	$1.108 \cdot 10^{-5}$	$\mathrm{A \cdot s^2 m}$
J	38.305	$\mathrm{A \cdot s/m}$

Table 2.8: Identified coefficients from the experimental sine sweep for Fig. 2.35.

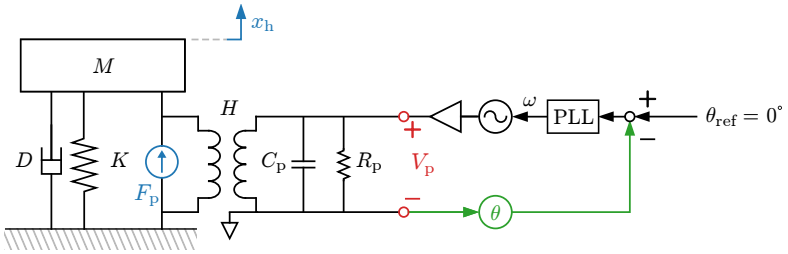

Figure 2.36: A simplified electrodynamical model of the piezoelectric transducer coupled with the booster and horn with resonance frequency tracking via a phase locked loop (PLL). Given a reference phase θ_{ref}, the PLL corrects the phase and provides a working frequency ω.

2.4.3 Source of nonlinearities in horn's vibration

The frequency response functions of the previous introduced linear models can capture the dominating system behavior, and thus can directly estimate of the stress amplitude load given to the fatigue specimen given the measured input voltage or current, see the procedure of Jacquemin et al. [Jac+21]. However, it's been observed experimentally by the author [Kis+21] and others [Heb+23] that the input

wave is in fact multi-harmonic. In these studies, laser vibrometer measurements made on the acoustic horn revealed a velocity spectra with higher harmonics. Here it's briefly mentioned the origins of these nonlinearities at the acoustic horn, with three suspected sources:

- *Nonlinearity in the signal and power generation*: The proprietary PLL-controlled signal and power generator from Branson (Branson DC480b), may introduce nonlinearity due to complex circuitry to deal with the high power capacitive load of the piezoelectric device [Zha+23]. This could result in a nonlinear excitation of the piezoelectric transducer, affecting the waveforms generated. It's also known that a PLL circuit is nonlinear itself and can effect the waveform, usually due to the internal voltage controlled oscillator [LKS09].

- *Material nonlinearity of piezoelectric materials*: The inherent material properties of the piezoelectric ceramic used can contribute to nonlinearity. Given that piezoelectric materials often exhibit nonlinear stress-strain relationships. It's well documented that PZT has a hysteric material behavior due to a ferroelectric polarization effect, see [GDS11]. In the presence of large applied electric fields, a saturation nonlinearity can also take place, [GAE97]. Lastly, piezoelectric materials are also sensitive to thermal effects, necessitating air cooling [Miy+19].

- *Mechanical interface and fixture nonlinearities*: Nonlinearities can also arise from mechanical interfaces and fixtures within the system. These include factors like friction, and other contact-related contact nonlinearity [Bro+14] at the interfaces and joints, have been thoroughly explored by both the acoustic and dynamics communities [Kle+17; Bro+14].

To demonstrate experimental measurements of nonlinearities (with no fatigue specimen), results will be presented for two different power systems: a signal generator (Keysight 33500B) in series with a voltage amplifier (FLC electronics P100), as well as a proprietary PLL-controlled signal and power generator from Branson (Branson DC480b). First it's demonstrated that there is an intrinsic nonlinearity either in both the piezoelectric material and regardless of power source. An experimental steady-state signal frequency spectra is presented in Fig. 2.37 by using the FFT with a Hann window of signal size 2^{10}. Here it can be seen the magnitude of the harmonics, as well as the noise floor of the vibrometer. Despite the linear signal generator and amplifier being used without any other control feedback circuitry, higher and interharmonics are present, yet at small magnitudes. In the Branson

setup, a larger third harmonic is present as well as an additional interharmonic near the fundamental harmonic.

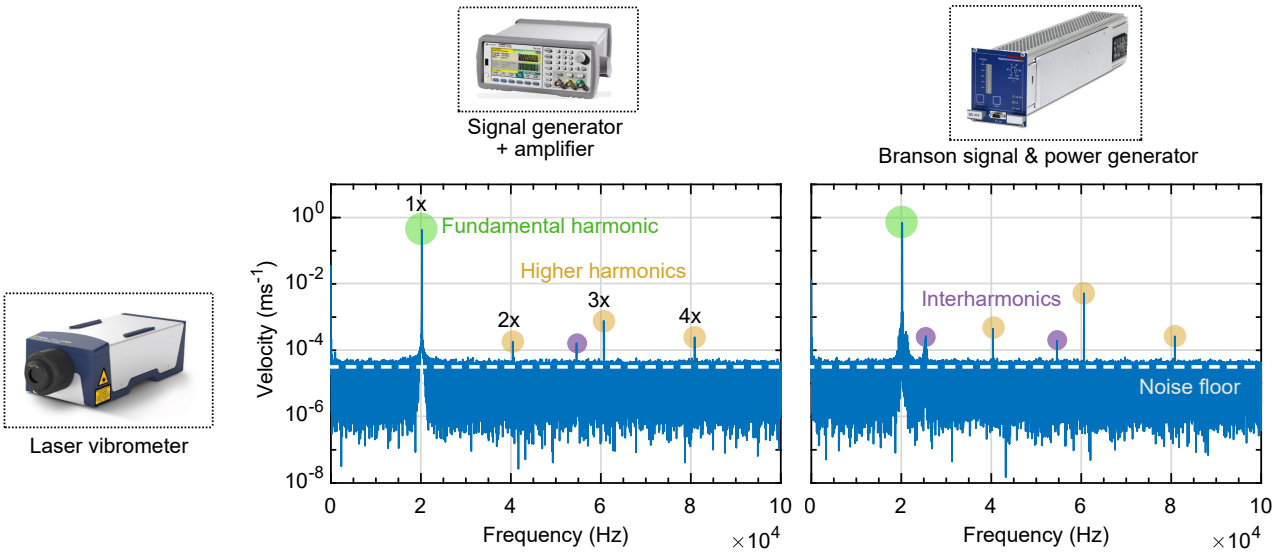

Figure 2.37: The steady-state velocity response of the horn of the piezoelectric transducer system with the left and right columns representing the frequency spectra of the system driven by the linear signal generator and power supply and the Branson PLL-controlled signal and power generator, respectively. The noise floor of the laser vibrometer is clearly seen at $\approx 5 \cdot 10^{-5}$ m/s.

Next the thermal effect is investigated, a low amplitude is imposed on the electrodynamical system without air cooling, which allows for heat to accumulate in the piezoelectric stack. Here, an experimental time-frequency power spectral density is presented in Fig. 2.37. It features the linear setup used in Fig. 2.32 and the setup with a PLL-controlled signal Fig. 2.36. For the linear signal generator and amplifier, the previously found anti-resonant frequency is utilized, whereas the Branson PLL-controlled signal and power generator automatically detects and tracks the anti-resonant frequency during solicitation. No piezoelectric transducer cooling provided to allow any transient thermal effects during loading for approximately 15 minutes at a low displacement amplitude. Velocity, current, and voltage signals were simultaneously recorded at a sampling frequency of 200 kHz, and their power spectral densities were computed using MATLAB's `specgram` using a Hann window of signal size 2^{10} with a 25% overlap. It can be seen in the linear setup of Fig. 2.38, the higher harmonics are present in the velocity signal, with little to no effect in the presence of thermal effects. For the Branson setup, the presence of higher harmonics are stronger, with a rapidly degrading voltage and current signals due to the effect of thermal transients. These results demonstrate that the thermal effects exists when

the piezoelectric transducer is not properly cooled with compressed air, but the underlying higher harmonics at $\{40, 60, 80, \ldots\}$ kHz can be expected to persist during ultrasonic fatigue tests.

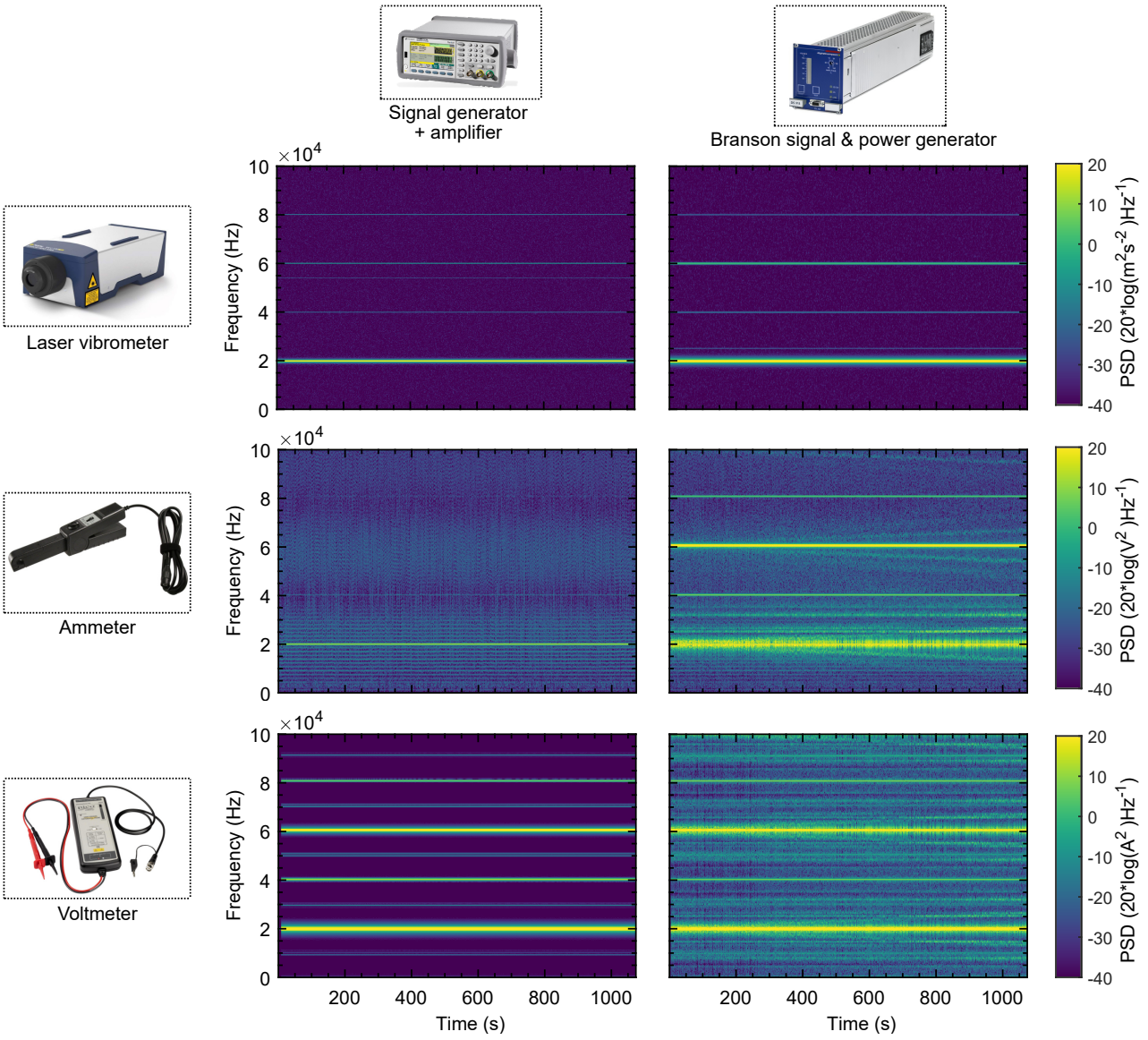

Figure 2.38: A comparison of thermal heating effects on the piezoelectric transducer system with the power spectral density, with the left and right columns representing the system driven by the linear signal generator and power supply and the Branson PLL-controlled signal and power generator, respectively. It can be seen that the Branson system at ≈ 400 s begins to display additional harmonic components especially in the voltage and current measurements.

2.5 Summary

The organization of the Chapter 2 reflects the various length scale phenomena and their influence. First various material nonlinearities are hierarchically detailed with respect to their harmonic generation. At the atomic length scale, the acoustic nonlinearity β due to the crystal lattice is derived. A preliminary analysis for a standing wave about a slender suggests that nonlinearity due to values of β in the literature for polycrystalline copper are smaller by a factor of ten for undamaged polycrystalline copper fatigue specimens from Chapter 4. Additionally, the nonlinearity is a material property and thus cannot reflect the nonlinearity of fatigue mechanisms that manifest during ultrasonic fatigue tests. This encourages a departure and alternative material models.

Next, a mean-field homogenization model of diffuse microplastic inclusions and microcracks with closure are considered. Mesoscale models – which discuss material behavior at a length scale of the same order as the wavelength of the ultrasonic wave– are more appropriate. Due to the nonlinearities of both the microplastic inclusions and microcracks with closure, their derivation and linearization is detailed. It's shown that the microcrack model has a predominately even harmonic generation whereas the microplastic inclusions have a predominately odd harmonic generation. The combination of both these phases can generate a complex higher harmonic generation which will be revisited for experimental results in Chapter 4. Finally, a uniaxial macroscopic crack model is considered, and its higher harmonic generation is also analyzed. Qualitatively, it's harmonic generation is very close to the microcrack model and it is expected there is overlap in their behavior. It is shown for all nonlinearities modeled, that the effect of the input oscillation being single or multi-harmonic, greatly affects the ability to discern the model's nonlinear parameters.

Next the structure of the ultrasonic fatigue specimen is modeled. a macroscopic model of the fatigue specimen is detailed. The standing wave formed during the fatigue test allows for a modal basis to be utilized: a modal truncation of a static longitudinal mode and first longitudinal mode. The Galerkin projection of the modal basis onto the weak form of dynamic equilibrium gives a 2 degree of freedom equation of motion; for base excitation it can be further reduced to a 1 degree of freedom oscillator. This explicit form demonstrates that the boundary condition at the base of the fatigue specimen, i.e. its input vibration must be considered. The micromechanical constitutive behavior from the previous subsection can be embedded into the centroid volume through numerical

quadrature. The size of this centroid volume is a quasi-free parameter, and is defined in our work for the 10th decile of longitudinal stress seen by the fatigue specimen.

Finally the ultrasonic fatigue test machine is considered. First a 0D transfer function model of the electrodynamics is validated with experimental data. However, the frequency spectra reveals the presence of small harmonics in the experimental voltage, current, and vibration signals. The sources of these weak nonlinearities are suspected to stem from the ultrasonic fatigue test machines contact interfaces, the piezoelectric material nonlinearity, and the signal and power generation. When the ultrasonic fatigue specimen is attached to the horn, the imposed base motion will be multi-harmonic: this is schematized as a block diagram in Fig. 2.39 **(b)** which is compared to an ideal system in **(a)**.

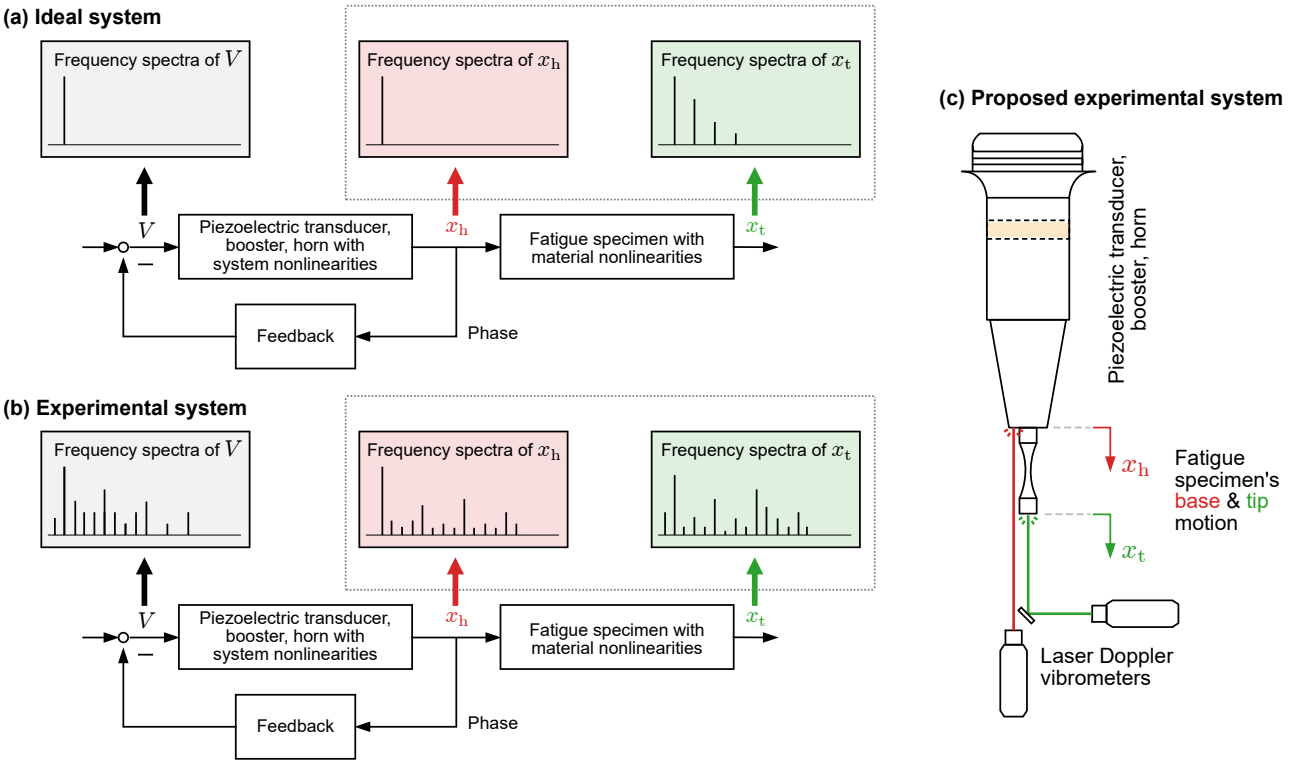

Figure 2.39: An ideal (**(a)**) and experimental (**(b)**) ultrasonic fatigue test machine with accompanying block diagrams of their frequency spectra, where V is the imposed voltage, x_h is the motion of the horn, and x_t is the motion of the fatigue specimen's tip. In **(c)**, the proposal of additional measurement of the experimental system for ultrasonic fatigue tests.

Through these previous sections, a comprehensive view of the ultrasonic fatigue specimen can be understood. Due to the fact that the ultrasonic fatigue test machine provides a multi-harmonic input to the fatigue specimen, this implies that the harmonics present in the tip vibration of the fatigue

specimen are not representative of only material-based nonlinearities but also of the input vibration. This is clearly seen in Fig. 2.9 and Fig. 2.14, where the multi-harmonic input masks the higher harmonics generation for low values of microcrack and microplastic volume fractions. Therefore, the classical experimental setup of an ultrasonic fatigue test with a single laser vibrometer is changed to include an additional laser vibrometer measurement at the base, which is shown in Fig. 2.39 **(c)**. This modification is implemented for experimental results in Chapter 4.

Chapter 3

Signal processing for harmonic estimation and nonlinear system identification

Contents

Content here has been published or submitted to the following journals:

[Kis+23c] S. L. Kiser, M. Rébillat, M. Guskov, and N. Ranc, "Real-time sinusoidal parameter estimation for damage growth monitoring during ultrasonic very high cycle fatigue tests," *Mechanical Systems and Signal Processing*, vol. 182, p. 109544, Jan. 2023.

[Kis+23b] S. L. Kiser, P. Margerit, M. Rébillat, M. Guskov, and N. Ranc, "Fast Kernel-based Signal Subspace Estimates for Line Spectral Estimation," *Submitted to IEEE Transactions on Signal Processing*, doi:10.36227/techrxiv.22294222, June 2023.

[Kis+23a] S. L. Kiser, M. Guskov, M. Rébillat, and N. Ranc, "Exact identification of nonlinear dynamical systems by Trimmed Lasso," *Preprint*, doi:10.48550/arXiv.2308.01891 [cs, eess, math], Aug. 2023.

3.1 Introduction

In this chapter, the focus is directed towards the analysis of ultrasonic fatigue vibration signals. These signals, which are quasi-stationary and harmonics, may hold information about fatigue mechanisms and other systemic nonlinearities inherent in signal. The goal here is to accurately estimate harmonics and to and interpret this information to gain insights into the fatigue behavior of material.

Addressing this challenge requires solving inverse problems of linearizable models. Many engineering problems, including the analysis of vibration signals, can be expressed in a vector-matrix formulation. Consider, for instance, the representation of a periodic signal $x \in \mathbb{C}$ with P complex sinusoids for signal processing:

$$x(t) = \sum_{i=1}^{P} \beta_i e^{\mathrm{j}2\pi\omega_i(t)} \quad \Longleftrightarrow \quad \boldsymbol{x} = \boldsymbol{A}_N\boldsymbol{\beta} = \sum_{i=1}^{P} \beta_i \boldsymbol{a}_i$$

Here, $\beta_i \in \mathbb{C}$ represents the complex amplitude, and $\{\omega_i \in [0,1); \omega_i \neq \omega_j : \forall i\}$ the normalized frequency. Typically, engineers apply the Discrete Fourier transform (DFT) to the signal, and extract the frequency peaks to fit this model. However, by incorporating more knowledge about the particular problem, a better performing estimation can be obtained in the presence of noise, short window lengths, and/or nonstationarity.

The underlying model of the problem has the structure:

$$\underbrace{\boldsymbol{z}}_{\text{Known \& measurable}} = \underbrace{\boldsymbol{\Theta}\boldsymbol{\xi}}_{\text{Unknown/semi-known}} = \sum_{i=1}^{P} \xi_i \boldsymbol{\theta}_i$$

This general form allows for a wide array of problems in engineering to be expressed and tackled effectively. Another form which has applications is in the identification of nonlinear dynamics. Specifically the sparse identification of nonlinear dynamics (SINDy) [BPK16]. For example, dynamics can be described by ordinary differential equations (ODEs) in the form:

$$\frac{d\boldsymbol{z}}{dt} = f(\boldsymbol{z}(t)) \quad \Longleftrightarrow \quad \boldsymbol{z} = \boldsymbol{\Theta}\boldsymbol{\xi} = \sum_{i=1}^{P} \xi_i \theta_i(z(t))$$

or even partial differential equations (PDEs):

$$\frac{\partial \boldsymbol{z}}{\partial t} = f(\boldsymbol{z}(x,t)) \quad \Longleftrightarrow \quad \boldsymbol{z} = \boldsymbol{\Theta}\boldsymbol{\xi} = \sum_{i=1}^{P} \xi_i \boldsymbol{\theta}_i(\boldsymbol{z})$$

where $\boldsymbol{z}(t) \in \mathbb{R}^{n\times 1}$ is an n-dimensional state vector at time t, and $f(\cdot) : \mathbb{R}^{n\times 1} \to \mathbb{R}^{n\times 1}$ is an n-dimensional state mapping function. The goal is to estimate the form of $f(\cdot)$ which can be assembled into a matrix $\boldsymbol{\Theta}$ from vector columns of measurable states $\boldsymbol{z}_i$. However, the assembly of $\boldsymbol{\Theta}$ is semi-known, meaning that a physically informed dictionary can be large and redundant, and that an algorithm must converge to the solution that is only composed of a few elements that represent the true equation. Multitudes of sparsity promoting algorithms exist that come from mathematical, statistical, and machine learning domains. However, this problem is quite difficult since the matrix-vector equations do not have a unique solution when $\boldsymbol{\theta}$ is a wide matrix.

This chapter remains very general so that the methods can be used in any domain, we remind the reader that both these problems are directly related to ultrasonic fatigue:

- Frequency and amplitude estimation gives information about the harmonics of the signal, which is a classical method of vibration analysis for nonlinear harmonic generation.
- Forward models of the fatigue specimen have been presented in Chapter 2, but the nonlinearities within the system are not well known. Nonlinear system identification may help in identifying macroscopic material nonlinearities during different stages during the ultrasonic fatigue tests.

3.2 Signal processing ultrasonic vibration signals for harmonic extraction

One technique for assessing damage and microstructural characteristics in materials during ultrasonic fatigue tests relies on measuring multiple sinusoidal parameters, specifically amplitudes and/or frequencies [Kum+09; Kum+10; Kum+11; MFS13; Fit+14; Li+16; Ban+18; Mes+20; Fit+21]. These techniques would benefit from *in-situ* and accurate sinusoidal parameter estimation since it could correspond to a real-time assessment of microstructural evolution leading to macroscopic damage.

UFT signals can be observed to have harmonics at integer multiples of the working frequency, corresponding to the fatigue specimen's longitudinal eigenfrequency, see Fig. 3.1. However, throughout the UFT, nonlinear phenomena can introduce interharmonics which exceeds the scope of algorithms that only estimate fundamental frequency [Hes83]. Additionally, UFTs that require a large amount of cycles have signals that are nonstationary, but can be adequately modeled as being locally stationary signal within a finite segment of length N of the data, or window. We refer to the windowed signal as quasi-stationary, which we define as a trend-stationary sequence by the Kwiatkowski-Phillips-Schmidt-

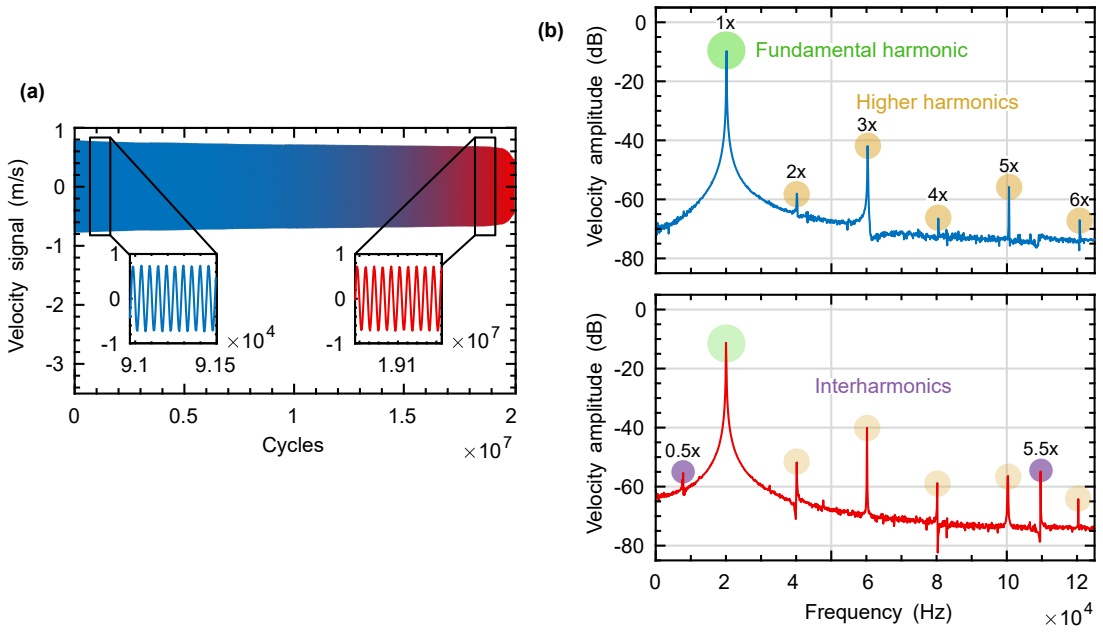

Figure 3.1: (Left) Velocity signal from a typical ultrasonic fatigue test with segmented signal windows near the beginning and end of the fatigue test. Frequency spectra corresponding to an undamaged (right,top) and damaged (bottom) fatigue specimen are obtained through a DFT. Harmonics correspond to integer multiples of the fundamental harmonic while interharmonics correspond to non-integer multiples of the fundamental harmonic.

Shin test [ES10]. One main concern is the method of estimating such sinusoidal parameters for a quasi-stationary signal: a choice must be made between choosing algorithms whose basis are either in spectral analysis or time-frequency analysis.

To date, a sliding window approach has only been coupled with the discrete Fourier transform (DFT) in UFT damage monitoring. When applied per window, the DFT yields a respective frequency spectrum, and a peak picking algorithm extracts sinusoidal parameters, i.e. the frequencies and amplitudes. This is one of the most rudimentary forms of a line spectral estimator (LSE): where sinusoidal parameters correspond to Dirac deltas (lines) in the frequency spectra. However, a finite period (time length) of the data corresponds to the sinc function convolving with the DFT resulting in a loss of frequency resolution, see Fig. 3.2. This directly poses problems for an UFT signal of a damaged fatigue specimen, where introduced interharmonics can influence the estimation of harmonics. Additional factors can skew the DFT's spectra affecting the accuracy of the peak picking: nonstationary sinusoidal components smearing the spectral envelope, non-periodicity of the data manifesting as spectral leakage, aliasing due to violation of the Nyquist-Shannon sampling theorem, and noise introducing

uncertainty into the measured signal. Due to the difficulties seen by the DFT, alternative spectral estimators should be considered, such as nonparametric and parametric spectral estimators.

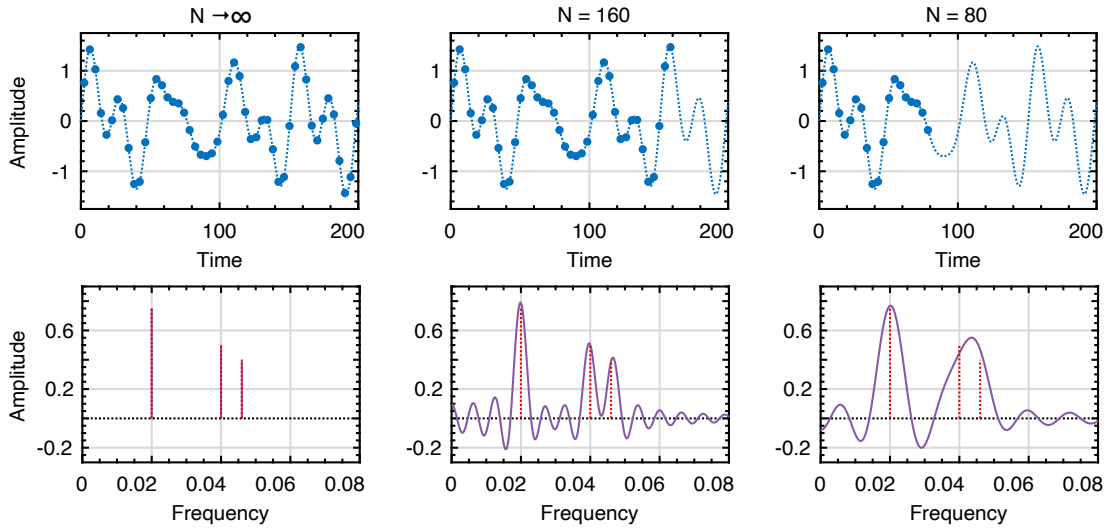

Figure 3.2: Demonstration of the frequency resolution of a signal with a fixed sampling frequency, with respect to the Rayleigh limit $1/N$ seen by the DFT, adapted from [IMF21]. A multi-sinusoidal signal (dashed blue line) and its Nyquist-Shannon samples (blue circles) are depicted on the top row. The bottom row shows the DFT's frequency resolution (purple line) and the true line spectra (dashed red line). For a finite N, the DFT's frequency resolution is equal to the convolution between the DFT of the signal and the sinc function.

Nonparametric algorithms estimate the entire frequency spectra which include include the DFT-based methods [SM05; SSC11] and filter-bank methods [Cap69; SHJ99]. Filter-bank methods' frequency resolution depends on the spectra length and can achieve super-resolution [CF14], or resolve closely-spaced frequencies beyond the DFT in Fig. 3.2. Recently, nonparametric algorithms have been coupled with a peak picking algorithm to become LSEs, but require a method to estimate the number of sinusoids [SQ20] or utilize an amplitude/power threshold [Sel17]. On the other hand, parametric algorithms only estimate parameters for a known number of sinusoids and some are also capable of super-resolution. These parametric estimators are formulated as sinusoidal frequency estimation problems since the estimation of amplitudes and phases become least squares solvable when the frequencies are known [SHJ00]. Many of the parametric LSE established in the 1980s and beyond are inspired by Prony's method [dPro95] of converting a non-linear approximation by solving a set of linear equations and a root-finding problem. One of the most popular parametric LSEs are the subspace methods, which include MUSIC [Sch86] and ESPRIT [RK89]. Subspace methods decompose the finite

data into signal and noise subspaces via an eigenvalue decomposition (EVD) and/or singular-value decomposition (SVD). Exploiting the low-rank structure of the signal's covariance matrix allows for these methods to achieve super-resolution. A sliding window approach [Bas85] is commonly used with a spectral estimator to circumvent the problem of quasi-stationarity, where the signal is uniformly discretized in time. The sinusoidal parameters in each window are obtained by applying a spectral estimator, and the window is shifted in time and the process is repeated.

Other dominant parametric LSEs are derived from the maximum likelihood principle of estimators [BM86], where the estimated sinusoidal parameters are the most likely to explain the finite data. Two classes exist: deterministic maximum likelihood [Han71] and stochastic maximum likelihood [Par60] which have criterion derived in the case the sinusoidal parameters are unknown deterministic and stochastic, respectively. Deterministic maximum likelihood has been most often referred to as the non-linear least squares method in literature [SM05] since it estimates parameters by minimizing ℓ_2 norm of the difference between the finite data and signal model. Some deterministic maximum likelihood methods separate the full multidimensional minimization into iterative searches in lower-dimensional parameter subspaces: these include Expectation-Maximization [FW88] and RELAX [JS96]. Stochastic maximum likelihood methods, until most recently, are generally only found in direction of arrival literature, e.g. [OVK92].

New LSEs have been introduced due to innovations in data science domains, specifically those relating to compressed sensing, sparse regularization, and deep learning. LSEs that use compressed sensing for sparse regularization [Don06] are sometimes referenced as semi-parametric since they sometimes rely on model order or on other signal parameters a priori, such as its noise covariance. One issue arises when specializing the compressed sensing problem onto LSE, since it normally assumes a discrete basis for signal recovery, whereas a sparse signal is continuous in frequency space. Thus grid-based approaches divide the frequency spectra into finite discrete grid points and build bases from these grid points. Popular solutions to this approach can be through convex optimization algorithms like basis pursuit [CD98] or LASSO [WNF09]. However, the true frequency parameters are not guaranteed to lie within the frequency grid, a problem commonly referred to as basis or grid mismatch [CSK10]. Attempts to remediate grid mismatch include iterative grid refinement [MRM16], using a dense grid and iteratively optimize sparse solutions [DB13], generalizing the ℓ_1 norm as continuous in frequency space via an Atomic Norm minimization problem [BTR13; YX15], or Bayesian approaches

which iteratively refine the grid [Han+14; HFR18]. Artificial neural networks for LSE have been used for LSEs in the early 1990s [HB97], whereas recent deep neural network approaches have provided state-of-the-art performance through adopting convolutional neural network (CNN) [IBF19; IMF21].

The section is motivated by the tradeoffs between finite window lengths and accuracy when dealing with quasi-stationarity and the Rayleigh limit. Despite the loss of information which affects estimation performance, a small time window is sought for many reasons:

- Smaller window lengths along the entire fatigue vibration signal will be more locally stationary compared to larger windows.
- Parameter estimation algorithms are quicker for smaller data lengths, meaning that a computationally complex algorithm can still be used in real-time.
- A smaller window length about the entire fatigue vibration signal will yield more discrete parameters, which is attractive for data-driven models. While using window overlap [Bas85] can also increase the number of discrete parameter estimates, this would carry over for all spectral estimators. Within the context of ultrasonic fatigue experiments, more discrete parameters would allow for conditional-based rules for stopping a fatigue test before crack failure, and for deterministic models, a prediction of damage evolution.

Thus the merits of potential algorithms have to weigh between window length and parameter accuracy, noise robustness, and computational performance.

Our contribution lies in the study of sinusoidal parameter estimation accuracy on quasi-stationary signals, with a focus on signals found in VHCF vibration. Specifically, we establish two compounding influences that are at play when using a windowed approach to the real-time estimation of sinusoidal parameters: (1) estimators face a frequency and time uncertainty dictated by the Rayleigh limit, and (2) the usage of estimators who assume a stationary signal model being used on a quasi-stationary signal. Minimizing the window length negatively influences the frequency resolution, as mentioned in (1), but increases time resolution and has positive contributions stated in the bullets previously. Additionally, the statistical performance and accuracy of estimators are numerous in literature but generally utilize synthetic signals that are purely stationary, whose results cannot be said for quasi-stationary signals, mentioned in (2). Therefore, we choose to investigate five LSEs, specifically Unitary

ESPRIT [HN95], RELAX [JS96], CFH [SQ20], NOMP [MRM16], and DeepFreq [IMF21] with respect to the problems aforementioned. These five algorithms were chosen since their theoretical basis are a diverse (subspace-based, maximum likelihood-based, DFT peak interpolation-based, greedy algorithm for grid refinement-based, and deep neural network-based, respectively) representation of the many LSE that exist in the literature, and most are considered to be state-of-the-art LSE for the purely stationary case. We choose not to use fast versions of these algorithms (for example ESPRIT with partial SVDs [PT15]) since they trade computational complexity for accuracy; here it's assumed the original algorithms provide their best asymptotic performance. It should be noted that except for the former two algorithms listed, the original authors provide open access to their algorithms. The remaining part of the section is organized as follows. Section 3.2.1 outlines the theory of each implemented LSE algorithm. The benchmark methodology is described in Section 3.2.2. Results and discussions are presented in Section 3.2.3.

Algorithms	**Main principle**	**Advantages**	**Disadvantages**	**Tunable parameters**
Unitary ESPRIT* [HN95]	Rotational invariance of signal's subspaces	Forward-backwards averaging of signal's covariance	Computation complexity dictated by SVD	Sub-vector length
RELAX [JS96]	Frequency domain (zero-padding) interpolation, iterative refinement	Conceptually easy to implement	Asymptotic gains in performance tuning large zero-padding	Zero-padding length
CFH [SQ20]	Frequency domain (peak) interpolation, iterative refinement	One of the fastest parametric estimators	Algorithm is not tunable	-
NOMP [MRM16]	Greedy algorithm, iterative refinement	Newton refinements alleviates restriction to DFT basis	Unknown performance in the case of basis mismatch	Number of refinements, zero-padding length†
DeepFreq [IMF21]	Deep convolution neural network	Fully-automatic frequency estimates‡	Expensive offline training	Training data, CNN architecture

Table 3.1: Summary of LSE algorithms implemented.
*: The amplitude can be estimated after the estimation of frequencies, using the LS estimate Eq. (3.20).
†: In this section, the zero-padding is removed to further differentiate NOMP from RELAX.
‡: DeepFreq, as published, features a frequency representation module, which is used in this section, but also a component counting module which estimates the model order, making the algorithm fully-automatic compared to other LSEs.

3.2.1 Implemented spectral estimation algorithms

In this section, the mathematical formulation of the implemented LSE algorithms is described. A practical summary of the algorithms used in this work exists in Table 3.1. The estimation of frequencies and amplitudes for P complex sinusoids of $x[n]$ can be written as the signal model:

$$\check{x}[n] = \sum_{i=1}^{P} \beta_i e^{\mathrm{j}2\pi\omega_i n} + \varepsilon[n] = x[n] + \varepsilon[n] \tag{3.1}$$

where $n \in \mathbb{Z}$ is a discrete index and $\varepsilon[n]$ represents additive white Gaussian noise (AWGN) with variance η. The sinusoidal parameter β_i is the complex amplitude such that its modulus $|\beta_i|$ is the amplitude, and $\{\omega_i \in [0,1); \omega_i \neq \omega_j : \forall i \neq j\}$ is the normalized frequency (units of cycles per sample) whose set is distinct. In matrix-vector notation, Eq. (3.1) is:

$$\check{\boldsymbol{x}} = \boldsymbol{A}_N \boldsymbol{\beta} + \boldsymbol{\varepsilon} \tag{3.2}$$

the complex amplitudes for P complex sinusoids $\boldsymbol{\beta}(n) \in \mathbb{C}^P$, and the matrix $\boldsymbol{A}_N \in \mathbb{C}^{N \times P}$ is a Vandermonde matrix of P complex sinusoids:

$$\begin{aligned} \boldsymbol{A}_N &= \begin{bmatrix} 1 & \cdots & 1 \\ e^{\mathrm{j}(2\pi)\omega_1} & \cdots & e^{\mathrm{j}(2\pi)\omega_P} \\ e^{\mathrm{j}(2)(2\pi)\omega_1} & \cdots & e^{\mathrm{j}(2)(2\pi)\omega_P} \\ \vdots & \ddots & \vdots \\ e^{\mathrm{j}(N-1)(2\pi)\omega_1} & \cdots & e^{\mathrm{j}(N-1)(2\pi)\omega_P} \end{bmatrix} \\ &= \begin{bmatrix} \boldsymbol{a}(\omega_1) & \cdots & \boldsymbol{a}(\omega_P) \end{bmatrix} \end{aligned} \tag{3.3}$$

Lastly, it should be reminded real-valued signals can be represented using the complex notation in Eq. (3.1) through two methods: the use of the (downsampled) analytic signal [RFB94], provided that there is no spectral content in the real-valued signal near zero and Nyquist frequencies; or simply realizing real-valued sinusoidal signals can be represented as complex-valued and applying the algorithms. The latter case is preferred in this work because of its simplicity and to prevent issues seen in computing the analytic signal.

Unitary ESPRIT The Unitary ESPRIT algorithm is used since it is one of the most economical and accurate among all ESPRIT implementations [HN95]. First, Eq. (3.1) is converted into the necessary matrix notation with overlapping segments such that:

$$\check{\boldsymbol{X}} \coloneqq \begin{bmatrix} \check{x}[1] & \check{x}[2] & \cdots & \check{x}[L] \\ \check{x}[2] & \check{x}[3] & \cdots & \check{x}[L+1] \\ \vdots & \vdots & \ddots & \vdots \\ \check{x}[M] & \check{x}[M+1] & \cdots & \check{x}[N-1] \end{bmatrix} \tag{3.4}$$

where $\boldsymbol{X}(n) \in \mathbb{C}^{M \times L}$ is a Hankel matrix, M is a chosen sub-vector size such that $P \leq M < N+1-P$, and $L = N - M$ is the remaining length. Unitary ESPRIT, as opposed to the standard ESPRIT algorithm, inherently includes forward-backward smoothing [RK89]. A forward-backward observation matrix $\boldsymbol{X}'$ is estimated and converted to real-values by the unitary transformation of $\boldsymbol{X}$:

$$\boldsymbol{X}' = \begin{bmatrix} \operatorname{real}\left\{\mathbf{Q}_M^{\mathrm{H}} \boldsymbol{X}\right\} & \operatorname{imag}\left\{\mathbf{Q}_M^{\mathrm{H}} \boldsymbol{X}\right\} \end{bmatrix} \in \mathbb{R}^{M \times 2L} \tag{3.5}$$

where $\square'$ indicates a unitary transformed component, $\square_M$ indicates the square matrix dimension of size $M \times M$, and $\square^{\mathrm{H}}$ indicates the Hermitian (complex conjugate) transpose. This processing steps has been shown to improve parametric and nonparametric estimators that rely on covariance estimates [JS99]. The even- and odd-dimensioned unitary matrices are given, for an arbitrary D:

$$\begin{aligned} \mathbf{Q}_{2D} &= \frac{1}{\sqrt{2}} \begin{bmatrix} \mathbf{I}_D & \mathrm{j}\mathbf{I}_D \\ \mathbf{\Pi}_D & -\mathrm{j}\mathbf{\Pi}_D \end{bmatrix} \\ \mathbf{Q}_{2D+1} &= \frac{1}{\sqrt{2}} \begin{bmatrix} \mathbf{I}_D & 0 & \mathrm{j}\mathbf{I}_D \\ 0 & \sqrt{2} & 0 \\ \mathbf{\Pi}_D & 0 & -\mathrm{j}\mathbf{\Pi}_D \end{bmatrix} \end{aligned} \tag{3.6}$$

where $\mathbf{I}_D$ and $\mathbf{\Pi}_D$ are the identity matrix and the antidiagonal identity matrix (ones along the antidiagonal) of size $D \times D$, respectively. To obtain the signal subspace $\boldsymbol{U}'_{\mathrm{s}}$, a SVD is performed on $\boldsymbol{X}'$ to yield:

$$\boldsymbol{X}' = \begin{bmatrix} \boldsymbol{U}'_{\mathrm{s}} & \boldsymbol{U}'_{\perp} \end{bmatrix} \begin{bmatrix} \boldsymbol{\Sigma}'_{\mathrm{s}} & 0 \\ 0 & \boldsymbol{\Sigma}'_{\perp} \end{bmatrix} \begin{bmatrix} \boldsymbol{V}'^{\mathrm{H}}_{\mathrm{s}} \\ \boldsymbol{V}'^{\mathrm{H}}_{\perp} \end{bmatrix} = \boldsymbol{U}'\boldsymbol{\Sigma}'\boldsymbol{V}'^{\mathrm{H}} \tag{3.7}$$

where $\boldsymbol{\Sigma}'$ corresponds to a diagonal matrix which contains the singular values on the main diagonal in descending order, and $\boldsymbol{V}'$ is an identity matrix orthogonal to $\boldsymbol{U}'$. The signal subspace is extracted via a priori knowledge of the left P column singular vectors:

$$\boldsymbol{U}'_{\mathrm{s}} = \begin{bmatrix} \boldsymbol{u}'(1) & \cdots & \boldsymbol{u}'(P) \end{bmatrix} \tag{3.8}$$

To exploit the signal subspace, selection matrices are introduced corresponding to a time shift of one sample value:

$$\begin{aligned} \boldsymbol{J}_1 &= \begin{bmatrix} \mathbf{I}_{N-1} \mid \mathbf{0}_N \end{bmatrix} \\ \boldsymbol{J}_2 &= \begin{bmatrix} \mathbf{0}_N \mid \mathbf{I}_{N-1} \end{bmatrix} \end{aligned} \tag{3.9}$$

where $\mathbf{0}_N$ is the zero vector of size $N \times 1$. Since the signal model of Eq. (3.1) has distinct frequencies, the rotational invariance of Eq. (3.9) allows one to form:

$$\boldsymbol{J}_1\boldsymbol{A}_N\boldsymbol{\Phi} = \boldsymbol{J}_2\boldsymbol{A}_N \tag{3.10}$$

where $\boldsymbol{\Phi} = \mathrm{diag}\left(e^{\mathrm{j}2\pi\omega_1}, \ldots, e^{\mathrm{j}2\pi\omega_P}\right)$ is the diagonal matrix of signal poles. The steering matrix $\boldsymbol{A}_N$ spans the P-dimensional signal subspace $\boldsymbol{U}_{\mathrm{s}}$, such that a transformation matrix $\boldsymbol{T}$ has the property:

$$\boldsymbol{A}_N = \boldsymbol{U}_{\mathrm{s}}\boldsymbol{T} \tag{3.11}$$

Eq. (3.10) can thus be expressed as a function of the eigenvectors of the signal subspace:

$$\boldsymbol{J}_1\boldsymbol{U}_{\mathrm{s}}\boldsymbol{T}\boldsymbol{\Phi} = \boldsymbol{J}_2\boldsymbol{U}_{\mathrm{s}}\boldsymbol{T} \tag{3.12}$$

which is equivalent to:

$$\boldsymbol{J}_1\boldsymbol{U}_\mathrm{s}\boldsymbol{\Psi} = \boldsymbol{J}_2\boldsymbol{U}_\mathrm{s} \quad \text{where} \quad \boldsymbol{\Psi} = \boldsymbol{T}\boldsymbol{\Phi}\boldsymbol{T}^{-1} \tag{3.13}$$

Eq. (3.13) is also equivalent to its real-valued counterpart through unitary transformation:

$$\boldsymbol{J}_1'\boldsymbol{U}_\mathrm{s}'\boldsymbol{\Psi}' = \boldsymbol{J}_2'\boldsymbol{U}_\mathrm{s}' \quad \text{where} \quad \boldsymbol{\Psi}' = \boldsymbol{T}'\boldsymbol{\Phi}'\boldsymbol{T}'^{-1} \tag{3.14}$$

with the respective unitary transformed selection matrices:

$$\begin{aligned} \boldsymbol{J}_1' &= \mathrm{real}\left\{\mathbf{Q}_{M-1}^\mathrm{H}\boldsymbol{J}_2\mathbf{Q}_M\right\} \\ \boldsymbol{J}_2' &= \mathrm{imag}\left\{\mathbf{Q}_{M-1}^\mathrm{H}\boldsymbol{J}_2\mathbf{Q}_M\right\} \end{aligned} \tag{3.15}$$

This representation results in an overdetermined system of equations for calculating the eigenvalues of which correspond to the diagonal elements of the matrix $\boldsymbol{\Phi}$, i.e., the signal poles with the frequency parameters ω_i. The LS approach is taken over the total LS approach [HN95] to reduce computational complexity with negligible accuracy loss for uniformly sampled signals:

$$\boldsymbol{\Psi}' \approx \left(\boldsymbol{J}_1'\boldsymbol{U}_\mathrm{s}'\right)^{-1}\boldsymbol{J}_2'\boldsymbol{U}_\mathrm{s}' \tag{3.16}$$

The right hand of Eq. (3.14) is the EVD of $\boldsymbol{\Psi}'$ since $\boldsymbol{\Phi}'$ is diagonal, such that:

$$\widehat{\omega}_i = \angle\lambda_i(\boldsymbol{\Psi}') \;\; \text{for} \;\; i = 1, \ldots, P \tag{3.17}$$

where $\widehat{\square}$ indicates a consistent estimate, $\lambda_i(\boldsymbol{\Psi}')$ is the eigenvalue of the ith entry of $\boldsymbol{\Psi}'$. When the signal is consistent with the model of Eq. (3.1), then the signal poles will lie close to the unit circle. The amplitude estimate vector $\widehat{\boldsymbol{\beta}}$ is then LS solvable using the frequency estimate vector $\widehat{\boldsymbol{\omega}}$ through Eq. (3.20).

RELAX The RELAX algorithm attempts to estimate the maximum likelihood estimate by decoupling the nonlinear least squares problem into iterative one-dimensional minimizations. This idea will be introduced by a description of the nonlinear least squares problem for frequency estimation:

$$\{\widehat{\boldsymbol{\beta}}, \widehat{\boldsymbol{\omega}}\} = \underset{\{\boldsymbol{\beta},\boldsymbol{\omega}\}}{\arg\min}\, \mathcal{C}_1(\boldsymbol{\beta}, \boldsymbol{\omega})$$

with:

$$\mathcal{C}_1(\boldsymbol{\beta}, \boldsymbol{\omega}) = \|\boldsymbol{x} - \boldsymbol{A}_N\boldsymbol{\beta}\|_2^2 \tag{3.18}$$

where $\|\square\|_2$ is the ℓ_2 norm. Eq. (3.18) minimized with respect to $\boldsymbol{\omega}$ yields the estimate:

$$\widehat{\boldsymbol{\omega}} = \arg\max_{\boldsymbol{\omega}} \left[\boldsymbol{x}^{\mathrm{H}} \boldsymbol{A}_N \left(\boldsymbol{A}_N^{\mathrm{H}} \boldsymbol{A}_N \right)^{-1} \boldsymbol{A}_N^{\mathrm{H}} \boldsymbol{x} \right] \tag{3.19}$$

and with respect to $\boldsymbol{\beta}$, the least squares error can be minimized through the pseudoinverse:

$$\widehat{\boldsymbol{\beta}} = \left(\boldsymbol{A}_N{}^{H} \boldsymbol{A}_N \right)^{-1} \boldsymbol{A}_N^{\mathrm{H}} \boldsymbol{x} \Big|_{\boldsymbol{\omega}=\widehat{\boldsymbol{\omega}}} \tag{3.20}$$

Eq. (3.19) is a multimodal function and its maximization corresponds to searching for its sharp global maxima. The RELAX algorithm is based on the relaxation of Eq. (3.18) to minimize the squared error between the observation and the parameterized signal model. A minimization of Eq. (3.18) with respect to both $\boldsymbol{\omega}$ and $\boldsymbol{\beta}$ through a cyclic minimization approach is detailed [JS96]. The subsequent minimization can be solved to yield the estimate of $\{\widehat{\beta}_j, \widehat{\omega}_j\}$:

$$\{\widehat{\beta}_j, \widehat{\omega}_j\} = \arg\min_{\{\beta_j, \omega_j\}} \mathcal{C}_2(\beta_j, \omega_j)$$

with:

$$\mathcal{C}_2(\beta_j, \omega_j) = \|\widehat{\boldsymbol{x}}_j - \beta_j \boldsymbol{a}(\omega_j)\|_2^2 \tag{3.21}$$

where $\widehat{\boldsymbol{x}}_j$ is defined in Eq. (3.24). Eq. (3.21) minimized similarly to before with respect to ω_j will yield:

$$\begin{aligned} \widehat{\omega}_j &= \arg\min_{\omega_j} \left\| \left[\mathbf{I} - \frac{\boldsymbol{a}(\omega_j)\boldsymbol{a}^{\mathrm{H}}(\omega_j)}{N} \right] \widehat{\boldsymbol{x}}_j \right\|_2^2 \\ &= \arg\max_{\omega_j} \left| \frac{\boldsymbol{a}^{\mathrm{H}}(\omega_j)\widehat{\boldsymbol{x}}_j}{N} \right|^2 \end{aligned} \tag{3.22}$$

and with respect to β_j:

$$\widehat{\beta}_j = \left. \frac{\boldsymbol{a}^{\mathrm{H}}(\omega_j)\widehat{\boldsymbol{x}}_j}{N} \right|_{\omega_j=\widehat{\omega}_j} \tag{3.23}$$

Note Eq. (3.22) is the definition of the periodogram $\left|\boldsymbol{a}^{\mathrm{H}}(\omega_j)\boldsymbol{x}\right|^2/N$ whose estimate $\widehat{\beta}_j$ corresponds to the maximum peak. This corresponds to a maximum likelihood estimate [RB74] when the signal only contains a single sinusoid. Eqs. (3.22) and (3.23) are interpolated through using a zero-padding [JS96], appending zeros to the signal:

$$x[n] = \begin{cases} x[n], & n \leq N \\ 0, & N < n \leq Z_{\mathrm{p}} \end{cases}$$

where Z_{p} is the new signal length such that $\boldsymbol{x}(n) \in \mathbb{C}^{Z_{\mathrm{p}}}$.

The RELAX algorithm starts from the strongest signal component to determine $\{\widehat{\beta}_1, \widehat{\omega}_1\}$ using Eqs. (3.22) and (3.23). Then the successive separation of the signal is performed:

$$\widehat{\boldsymbol{x}}_j = \boldsymbol{x} - \sum_{i=1}^{j} \widehat{\beta}_i \boldsymbol{a}(\widehat{\omega}_i) \quad \text{for} \quad j = 1, \ldots, P \tag{3.24}$$

where Eq. (3.24) is used to obtain $\{\widehat{\beta}_j, \widehat{\omega}_j\}$ from Eqs. (3.22) and (3.23), and $\{\widehat{\beta}_i, \widehat{\omega}_i\}_{i=1}^{j-1}$ are re-estimated in a sub-iteration:

$$\widehat{\boldsymbol{x}}_k = \boldsymbol{x} - \sum_{i=1}^{k} \widehat{\beta}_i \boldsymbol{a}(\widehat{\omega}_i) \quad \text{for} \quad k = 1, \ldots, j-1 \tag{3.25}$$

until $\mathcal{C}_2 < \epsilon$, where ϵ is a tolerance. This cyclic iterative procedure helps remove bias made from initial estimates done before successive separation of the signal.

CFH The coarse-to-fine HAQSE (CFH) algorithm also exploits the idea of the maximum likelihood estimator. Many estimators exist which attempt to refine a frequency estimate via interpolation of the DFT grid via zero-padding [SSC11], parabolic fitting [Can11], and iteratively [AM05]. However, most have not been extended to the multiple sinusoidal case and thus require a posteriori knowledge of frequencies to interpolate via peak picking. CFH utilizes the HAQSE interpolator [Ser19] which shifts the DFT coefficients by $\pm q$ with:

$$|q| \leq N^{-1/3} \tag{3.26}$$

where it was shown that it obtains better accuracy compared to parabolic interpolators. CFH begins by finding the dominant signal component:

$$\tilde{\omega}_j = \arg\max_{\omega_j} \left| \frac{\boldsymbol{a}^{\mathrm{H}}(\omega_j)\widehat{\boldsymbol{x}}_j}{N} \right|^2 \tag{3.27}$$

where $\tilde{\square}$ is a coarse estimate. [AM05] is used to iterate to the fractional residual components:

$$\delta_1 = \frac{N}{2\pi} \sin^{-1}\left(\sin\left(\frac{\pi}{N}\right) \operatorname{real}\left\{ \frac{S_{0.5} + S_{-0.5}}{S_{0.5} - S_{-0.5}} \right\} \right) \tag{3.28}$$

and refined residual component:

$$\delta_2 = \frac{1}{c(q)} \operatorname{real}\left\{ \frac{S_{+q} - S_{-q}}{S_{+q} + S_{-q}} \right\} + \delta_1 \tag{3.29}$$

where S are the interpolation functions:

$$\begin{aligned} S_{\pm 0.5} &= \boldsymbol{a}^{\mathrm{H}}(\tilde{\omega}_j \pm 0.5)\widehat{\boldsymbol{x}}_j \\ S_{\pm q} &= \boldsymbol{a}^{\mathrm{H}}(\tilde{\omega}_j + \delta_1 \pm q)\widehat{\boldsymbol{x}}_j \end{aligned} \tag{3.30}$$

and c is the bias correction:

$$c(q) = \frac{1 - \pi q \cot(\pi q)}{q \cos^2(\pi q)} \tag{3.31}$$

The coarse frequency estimate is composed of an integer and a residual component, which can be expressed as:

$$\widehat{\omega}_j = \frac{\tilde{\omega}_j + \delta_2}{F_s} N \tag{3.32}$$

where F_s is the sampling frequency, and the respective complex amplitude:

$$\widehat{\beta}_j = \left. \frac{\boldsymbol{a}^{\mathrm{H}}(\omega_j)\, \widehat{\boldsymbol{x}}_j}{N} \right|_{\omega_j = \widehat{\omega}_j} \tag{3.33}$$

It then uses a similar procedure of RELAX, obtaining $\{\widehat{\beta}_j, \widehat{\omega}_j\}$ from Eqs. (3.32) and (3.33), and successfully separates the signal:

$$\widehat{\boldsymbol{x}}_j = \boldsymbol{x} - \sum_{i=1}^{j} \widehat{\beta}_i \boldsymbol{a}(\widehat{\omega}_i) \quad \text{for} \quad j = 1, \ldots, P \tag{3.34}$$

where Eq. (3.34) is used to obtain $\{\widehat{\beta}_j, \widehat{\omega}_j\}$ by repeating Eqs. (3.27) to (3.33) until the P components are coarsely interpolated. The coarsely estimated signal components are all subtracted from the signal:

$$\widehat{\boldsymbol{x}}_k = \boldsymbol{x} - \sum_{i=1}^{P} \widehat{\beta}_i \boldsymbol{a}(\widehat{\omega}_i) \quad \text{for} \quad \text{for} \quad k = 1, \ldots, P \tag{3.35}$$

where Eq. (3.35) is used to obtain $\{\widehat{\beta}_j, \widehat{\omega}_j\}$ by repeating Eqs. (3.27) to (3.33) until the P components are finely interpolated. The fine step corrects for selection bias due to estimation from strongest to weakest signal component in the coarse step of the algorithm.

NOMP Newtonized orthogonal matching pursuit (NOMP) algorithm is built upon orthogonal matching pursuit, which is based on the greedy algorithm that iterates a sparse selection of the best fitting basis of matrix $\boldsymbol{A}_N$. An LS optimization is then performed in the subspace spanned by all previously selected bases. The grid mismatch is mitigated through the Newton-Raphson method, which iteratively refines the DFT grid. We describe this algorithm with complete measurements (sensing matrix is an identity matrix) first by rewriting nonlinear least squares problem Eq. (3.18) as a maximization:

$$\{\tilde{\beta}_j, \tilde{\omega}_j\} = \underset{\{\beta_j, \omega_j\}}{\arg\max}\, \mathcal{C}_3(\beta_j, \omega_j)$$

with:

$$\mathcal{C}_3(\beta_j, \omega_j) = 2\,\mathrm{real}\left\{\boldsymbol{x}^{\mathrm{H}} \beta_j \boldsymbol{a}(\omega_j)\right\} - |\beta_j|^2 \|\boldsymbol{a}(\omega_j)\|_2^2 \tag{3.36}$$

Eq. (3.36) maximized with respect to ω_j will yield:

$$\tilde{\omega}_j = \arg\max_{\omega_j} \frac{\zeta(\omega_j)}{N} \tag{3.37}$$

where ζ is the power of the spectra:

$$\zeta(\omega_j) = \left|\boldsymbol{a}^{\mathrm{H}}(\omega_j)\widehat{\boldsymbol{x}}_j\right|^2 \tag{3.38}$$

and Eq. (3.36) maximized with respect to β_j:

$$\tilde{\beta}_j = \left.\frac{\boldsymbol{a}^{\mathrm{H}}(\omega_j)\widehat{\boldsymbol{x}}_j}{N}\right|_{\omega_j=\tilde{\omega}_j} \tag{3.39}$$

The DFT grid of Eqs. (3.37) and (3.39) can be densely defined through zero-padding as indicated by [MRM16]. To improve a coarse estimate of $\{\tilde{\beta}_j, \tilde{\omega}_j\}$, the Newton-Raphson method is used for refine the frequency estimate:

$$\widehat{\omega}_j = \tilde{\omega}_j - \frac{\dot{\mathcal{C}}_3(\beta_j, \omega_j)}{\ddot{\mathcal{C}}_3(\beta_j, \omega_j)} \tag{3.40}$$

where the derivatives are defined:

$$\dot{\mathcal{C}}_3(\beta_j, \omega_j) = \mathrm{real}\left\{\left(\widehat{\boldsymbol{x}}_j - \tilde{\beta}_j\boldsymbol{a}(\tilde{\omega}_j)\right)^{\mathrm{H}} \tilde{\beta}_j \frac{d\boldsymbol{a}(\tilde{\omega}_j)}{d\tilde{\omega}_j}\right\} \tag{3.41}$$

and:

$$\ddot{\mathcal{C}}_3(\beta_j, \omega_j) = \mathrm{real}\left\{\left(\widehat{\boldsymbol{x}}_j - \tilde{\beta}_j\boldsymbol{a}(\tilde{\omega}_j)\right)^{\mathrm{H}} \tilde{\beta}_j \frac{d^2\boldsymbol{a}(\tilde{\omega}_j)}{d\tilde{\omega}_j^2}\right\} - |\tilde{\beta}_j|^2 \left\|\frac{d\boldsymbol{a}(\tilde{\omega}_j)}{d\tilde{\omega}_j}\right\|_2^2 \tag{3.42}$$

The NOMP algorithm first estimates $\{\tilde{\beta}_j, \tilde{\omega}_j\}$ using Eqs. (3.37) and (3.39) and successively separates the signal:

$$\widehat{\boldsymbol{x}}_j = \boldsymbol{x} - \sum_{i=1,}^{j} \widehat{\beta}_i \boldsymbol{a}(\widehat{\omega}_i) \quad \text{for} \quad j = 1, 2, \ldots \tag{3.43}$$

until $\zeta(\tilde{\omega}_j) < \tau$, where Eq. (3.43) is used to obtain $\{\widehat{\beta}_j, \widehat{\omega}_j\}$ from Eqs. (3.39) and (3.40) and τ represents a sparsity promoting ℓ_0 norm regularization, which implicitly determines the model order P:

$$\tau = \eta^2 \log(N) - \eta^2 \log\log\left(\frac{1}{1-\varrho}\right) \tag{3.44}$$

where η is the noise variance and ϱ is the probability of a false alarm. For the jth estimate, an initial refinement is performed through the Newton step of Eq. (3.40). The refinement is conditionally accepted only if it serves to maximize $\mathcal{C}_3$, i.e. locally concave $\ddot{\mathcal{C}}_3(\beta_j, \mu_j) < 0$, and if the refinement

globally reduces the residual energy such that $\zeta(\widehat{\omega}_j) > \zeta(\tilde{\omega}_j)$. After each singular refinement, the sub-iteration of cyclic refinement is performed R_c times to reestimate $\{\widehat{\beta}_j, \widehat{\omega}_j\}$:

$$\widehat{\boldsymbol{x}}_k = \boldsymbol{x} - \sum_{i=1}^{k} \widehat{\beta}_i \boldsymbol{a}(\widehat{\omega}_i) \quad \text{for} \quad k = 1, \ldots, j-1 \tag{3.45}$$

At the end of the jth estimate, the least square procedure of Eq. (3.39) is performed to refine complex amplitudes $\{\widehat{\beta}_i\}_i^j$. Performing this step just prior to detecting a new sinusoid increases the rate of convergence of NOMP by mirroring arguments used to establish matching pursuit convergence [Bar+08].

DeepFreq A fully connected neural network trained on the signal model of Eq. (3.1) is unlikely to converge to the maximum likelihood solution of the cost function Eq. (3.18). In general, the nonlinear least squares problem of Eq. (3.18) has many local minima, and training generally iterates to some local minimum (or a point near a local minimum). This is opposed to converging to the sought global minimum, which can depend on the initialization conditions and loss function optimization. DeepFreq differs from this direct problem in that it is schematized into different deep neural networks. A pseudospectrum is generated in a data-driven manner, training the frequency representation neural network to produce superimposed Gaussian kernels directly from the measurements. The representation is fed into a second frequency counting neural network that estimates the number of sinusoids. Frequency estimation is then carried out through selection of the P most prominent peaks of the frequency representation, see Fig. 3.3.

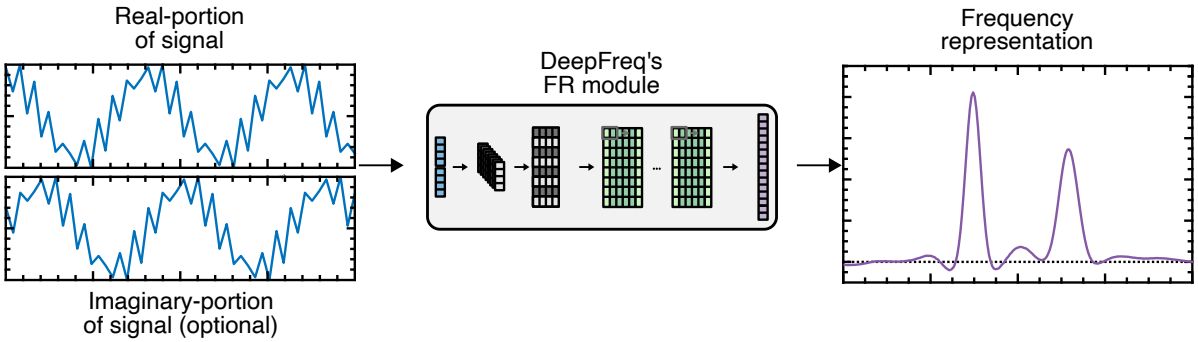

Figure 3.3: Algorithm flowchart of DeepFreq's frequency representation module. The assumed complex input of the DeepFreq is split into its real and imaginary parts before input. For real-valued signals, the imaginary-valued portion is supplied with zeros of equal length. The frequency representation generates a pseudospectrum (purple line) subject to a peak-picking algorithm.

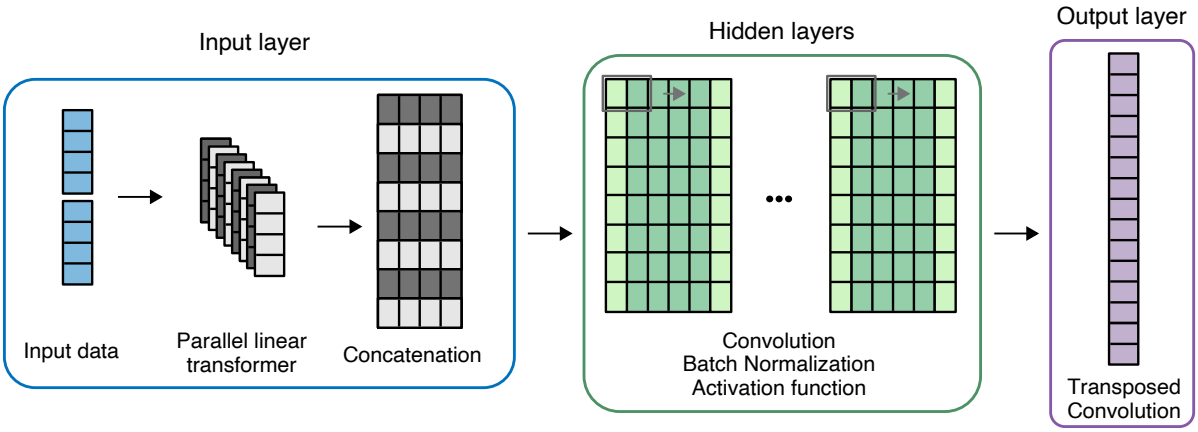

Figure 3.4: Architecture of the DeepFreq frequency representation module.

While this yields a fast, fully-automatic method for frequency and model estimation, we are interested only in the frequency representation module. The pseudospectrum FR is defined as the convolution of the P frequencies of the signal with Gaussian kernels $K : \mathbb{R} \to \mathbb{R}$:

$$\mathrm{FR}(n) \triangleq \sum_{i=1}^{P} K\left(n - \omega_i\right) \tag{3.46}$$

This frequency representation is continuously differentiable and features smooth peaks at the true frequencies for the signal model of Eq. (3.1). Despite not including amplitude and/or phase information into the CNN, this pseudospectrum serves as the regression that the CNN weights are tasked to learn from a noisy and finite signal. This is achieved by the loss function that penalizes the ℓ_2 norm between the output of the CNN and the true pseudo-spectra for a large number of training data.

Fig. 3.4 shows the proposed architecture for the frequency representation neural network. First, the

Layer		Features	Filter	Stride	Padding	Output
Input		-	-	-	-	$1 \times 2N$
Linear*		-	-	-	-	1×8000
$20 \times$	Conv*	64	3	-	1, Circ	$1 \times 64 \times 125$
	BatchNorm	64	-	-	-	$1 \times 64 \times 125$
	ReLU	-	-	-	-	$1 \times 64 \times 125$
ConvTrans*		64	17+Stride	$2^{\log_2(N)-3}$	9	$1 \times \frac{125}{8}N$

Table 3.2: Layer summary of frequency representation module with respect to input size N, where layers notated by * have no bias. The set of convolution, batch normalization, and ReLU layers are repeated for a depth of 20.

input layer maps the complex signal to a real-valued feature space. Then, the features are processed in the hidden layers which contain a series of convolutional layers with localized filters of length three and batch normalization, interleaved with rectified linear activation unit (ReLUs). The dimension of the input is preserved using circular padding. No pooling layers are used since frequency sensitivity is prioritized over invariance. Finally, the output utilizes a decoder which produces the estimate FR applying a transposed convolution. The original network described in [IMF21] is slightly modified to accept signals $N > 50$. This and all technical details are detailed in Table 3.2.

3.2.2 Experimental benchmark methodology

The performance of the implemented LSEs was analyzed using five benchmarks, each using relevant performance metrics defined below. All chosen algorithms were subjected to the same signal model shown in Eq. (3.1). Additionally, estimation of the number of sinusoidal components P is given a priori. This is because LSEs are parametric and the algorithms typically used for estimation of the number of sinusoidal components within a signal is a separate problem, see [SM05] for a brief introduction on model order estimation. The normalized frequencies are wrapped on the bounds $[0, 1)$. The AWGN variance η is defined such that a desired signal-to-noise ratio (SNR) can be obtained, $\text{SNR} \triangleq \|\boldsymbol{A}_N(\boldsymbol{\omega})\boldsymbol{\beta}\|_2^2/\eta$. A Raspberry Pi 4b, which is an affordable option for control of ultrasonic fatigue tests, is utilized for all benchmarks using Python 3.8.8 via the Anaconda distribution. We readily make available our algorithms and synthetic data [21]. This subsection aims to define a benchmark for LSEs which are lacking in the literature. Specifically, the test aims to demonstrate the degeneration of LSEs when exposed to quasi-stationarity within each window: this corresponds to the effects of the Rayleigh limit (if the signal was stationary) compounded with signal noise. Another test looks at the asymptotic computational costs and the algorithm runtimes for a Raspberry Pi 4b.

Test signals For usage in the first two tests, a synthetic real-valued signal is generated from an experimental UFT signal. The discrete UFT velocity signal has a sampling frequency $F_s = 10^6$ Hz which was performed on a pure copper fatigue specimen in a setup similar to Fig. 1.11. The time-evolving amplitude and frequencies are extracted from the signal per window via the DFT for the first three harmonics. Then cubic polynomial fits are evaluated on a quasi-stationary basis for each ith window along the entire experimental signal seen in Fig. 3.5. These averaged sinusoidal parameters

can be quantified as:

$$a^{(i)} = \frac{1}{T}\int_{t_0}^{t_1} \bar{a}(t)\,dt; \quad \text{and} \quad \omega^{(i)} = \frac{1}{TF_s}\int_{t_0}^{t_1} \bar{f}(t)\,dt$$

where T is the time length, $a^{(i)}$ and $\omega^{(i)}$ are the ith window-averaged amplitude and normalized frequencies, respectively. The frequencies are normalized to cycles per sample corresponding to the wrapped bounds $[0, 1)$. This achieves a similar signal model defined in Eq. (3.1) with a model order of $P = 6$ complex sinusoids, but has a symmetrical frequency component about $\omega = 0.5$. The real-valued synthetic signal is created with a sampling frequency $F_s = 250$ kHz which is compared with the experimentally obtained signal in Fig. 3.5. The time evolving sinusoidal parameters cubic polynomial fits can be found in Appendix B.1. For all tests except the first, the synthetic signal excludes the last 10 seconds of the data, where the formation of a large crack manifests large nonstationary components unsuitable for the LSEs.

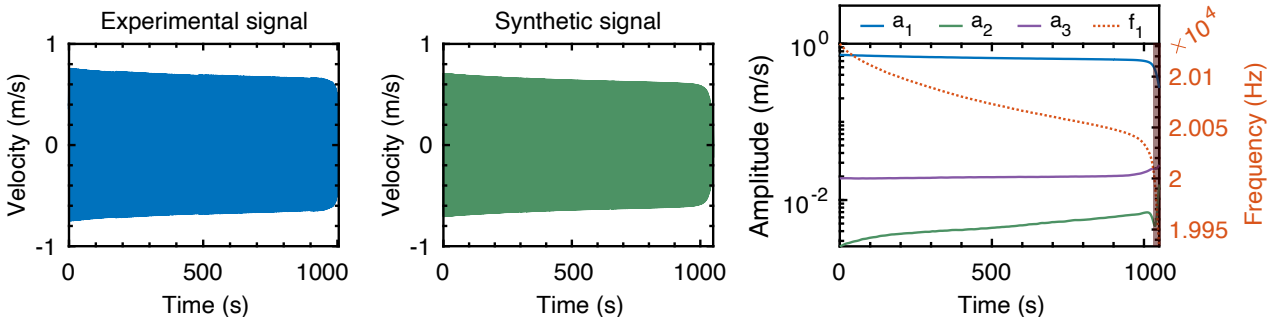

Figure 3.5: Copper specimen ultrasonic fatigue test excited at 20 kHz with vibration signal sampled at 200 kHz (left). A synthetic signal (center) is created from the first 3 harmonics' amplitudes and frequencies fits (right). The frequency f_1 is only shown, where it should be understood that higher harmonic frequencies occur at integer multiples, e.g. $f_2 = 2f_1$. Near the end of the ultrasonic fatigue test, the signal becomes increasingly nonstationary, where the last 20 seconds (shaded) are excluded from evaluation.

Configuration of algorithms We compare the five algorithms Unitary ESPRIT [HN95], RELAX [JS96], CFH [SQ20], NOMP [MRM16], and DeepFreq [IMF21] with configurations:

- Unitary ESPRIT requires an estimate of the measurement matrix and the model order. The former is estimated from the signal vector with size $M = N/2$ since this sub-vector length was shown to be optimal by [Gol11]. After obtaining the frequency estimates $\widehat{\boldsymbol{\omega}}$, the complex amplitude estimates $\widehat{\boldsymbol{\beta}}$ are LS solvable using Eq. (3.20).

- RELAX utilizes a zero-padded DFT and iterates over the model order. We select the zero-padding length such that its grid size is interpolated over $Z_{\mathrm{p}} = 4N$. This was chosen since it corresponded to a computational speed similar to other iterative LSEs, see Fig. 3.11.

- CFH requires only a model order and a minimum separation parameter which is already set by default to the Rayleigh limit and is considered optimal by [SQ20].

- NOMP requires a cyclic refinement parameter R_c and the sparsity promoting parameter τ which implicitly determines the model order. We set $R_c = 3$ since it was shown by [MRM16] that beyond number of cycles of Newton refinement has diminishing returns in estimation accuracy. We modify the NOMP algorithm to terminate on model order P, bypassing the regularization Eq. (3.44) to put it on par with other LSEs, especially when trying to test model order robustness. We also remove the zero-padding from its DFT operation to further distinguish it from RELAX.

- DeepFreq is inherently input data length-dependent so that separate frequency representation neural networks are trained per input length. We specifically use Table 3.2 and a standard deviation of the Gaussian kernel to $0.3/N$. It was found that for all input sizes, DeepFreq was able to generalize for all SNR when its frequency representation neural network was trained on AWGN with SNR $= 1$ dB. The training data consists of the generating signals with the following sets on uniformly distributed bounds: $\{P \in [1, 10]\}$, $\{\boldsymbol{\omega} \in [0, 1) : |\omega_i - \omega_j| > 2/N, \forall j \neq i\}$, and $\{|\boldsymbol{\beta}| \in [0.001, 1]\}$. For other training data parameters, we used the defaults described in the original paper [IMF21]. The amplitude estimates are obtained from its frequency representation through peak-picking via amplitude prominence with a minimum separation of $2/N$, when appropriate.

We also include the DFT, utilizing the Fast Fourier Transform algorithm, as a baseline which determines the P sinusoidal parameters through peak-picking via amplitude prominence. with a minimum separation of $2/N$, when appropriate.

Performance metrics Two performance metrics are featured: the matched frequency distance (MFD) and matched amplitude distance (MAD). All metrics are averaged over each window (discretized) of the entire synthetic signal for the first test, and the number of Monte Carlo trials for the latter test.

To determine the accuracy of the recovered sinusoidal parameters, the MFD is defined as:

$$\begin{aligned}\text{MFD} \triangleq \sum_{\widehat{\omega}_i \in \widehat{\boldsymbol{\omega}}} \left(\min_{\bar{\omega}_j \in \bar{\boldsymbol{\omega}}} |\widehat{\omega}_i - \bar{\omega}_j| \right) + \\ \sum_{\bar{\omega}_j \in \bar{\boldsymbol{\omega}}} \left(\min_{\widehat{\omega}_i \in \widehat{\boldsymbol{\omega}}} |\bar{\omega}_j - \widehat{\omega}_i| \right)\end{aligned} \tag{3.47}$$

The MFD aims to match each estimated frequency with its closest window-averaged frequency, and vice versa, and record a chamfered error. The MAD follows a similar logic, seen in Eq. (3.48).

$$\begin{aligned}\text{MAD} &\triangleq \widehat{\sum} + \bar{\sum} \\ \text{with } \widehat{\sum} &= \sum_{\hat{\omega}_i \in \hat{\boldsymbol{\omega}}} \frac{|\hat{a}_i(\hat{\omega}_i) - \bar{a}_j(\bar{\omega}_j)|}{\bar{a}_j(\bar{\omega}_j)}, \quad \bar{\omega}_j = \underset{\bar{\omega}_j \in \bar{\boldsymbol{\omega}}, \widehat{\omega}_i \in \widehat{\boldsymbol{\omega}}}{\arg\min} |\widehat{\omega}_i - \bar{\omega}_j| \\ \bar{\sum} &= \sum_{\bar{\omega}_j \in \bar{\boldsymbol{\omega}}} \frac{|\hat{a}_i(\hat{\omega}_i) - \bar{a}_j(\bar{\omega}_j)|}{\bar{a}_j(\bar{\omega}_j)}, \quad \widehat{\omega}_i = \underset{\bar{\omega}_j \in \bar{\boldsymbol{\omega}}, \widehat{\omega}_i \in \widehat{\boldsymbol{\omega}}}{\arg\min} |\widehat{\omega}_i - \bar{\omega}_j|\end{aligned} \tag{3.48}$$

Note that, MAD is normalized by the window-averaged amplitude to remove the scaling bias from amplitudes with larger magnitudes. Lastly, it's to be understood that all metrics are subject to the constraint $\{\omega_k \backslash \boldsymbol{\omega} : \forall \omega_{k+1} \in \boldsymbol{\omega}\}$, i.e. no components are repeated for evaluation.

3.2.3 Results and discussion

Parameter estimation for synthetic and experimental signals The differences between an estimator's ability to extract the first three harmonics of a synthetic and experimental signal are demonstrated in this test. The vibration signal is distinguished by a large amplitude variability between the first harmonic and higher harmonics, seen in Fig. 3.5. Harmonics are extracted through all estimators using the following methodology: the maximum prominent amplitude is assumed to be the fundamental harmonic, and the following peak at integer multiples of the fundamental harmonic are searched for within $\pm 2/N$ and extracted. These details are visualized in Fig. 3.6 for windows of both the synthetic and experimental signals. The SNR for the experimental signal is estimated to be 50 dB through a periodogram-based method [SSC11]; the synthetic signal has AWGN applied per window such that its SNR matches the experimental signal. A signal length of $N = 2^8$ is empirically chosen to trade off computational time for the LSEs and still allow for peak resolution in the DFT frequency spectra. For the LSEs, the model order $P = 6$ and $P = 12$ are imposed for the synthetic and experimental signals respectively.

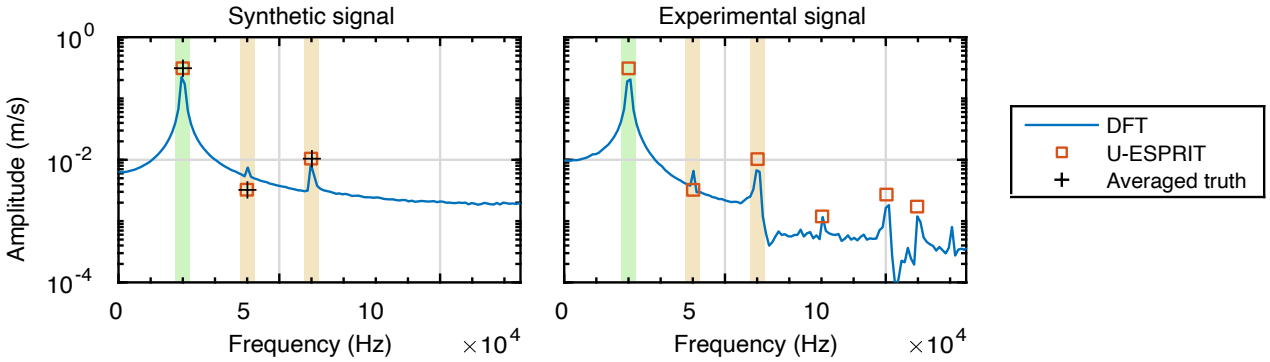

Figure 3.6: Demonstration of the DFT spectra and Unitary ESPRIT line spectra for the synthetic signal (left) and experimental signal (right). To extract sinusoidal parameters of the first three harmonics: first, a maximum amplitude of the fundamental is searched for, represented by the green shaded area; second, integer multiples (two and three times) of the green shaded area are created and represented by the yellow shaded area; lastly the peak is searched within the yellow shaded area, within a $\pm 2/N$ tolerance.

In Fig. 3.7, the estimation of harmonics is plotted against the synthetic signal. For Unitary ESPRIT and NOMP, the estimation of the amplitudes match most closely to the averaged truth; their frequency estimates are slightly outperformed by DeepFreq. However, DeepFreq demonstrates that it fails to estimate accurate amplitudes, even for a strong fundamental harmonic. Due to the small signal length, it can be seen that the DFT struggles to accurately capture even the fundamental harmonic's amplitude. It should be reminded that even though zero-padding the DFT would improve the amplitude results (to a certain extent), its frequency estimation ability would remain the same in resolution. CFH outperforms RELAX for fundamental harmonic amplitude estimation, despite its fundamental harmonic frequency estimation being offset more than RELAX. However, both CFH and RELAX struggle to steadily estimate the second harmonic's amplitude due to a difference of magnitudes with respect to the fundamental and third harmonic. In general, Unitary ESPRIT and NOMP show the most stability in parameter estimation for the synthetic signal. DeepFreq is unique in that it completely fails to provide accurate amplitude estimates for any part of the synthetic signal, however, it is able to only track the fundamental frequency with success. While not shown, it is unable to extract the frequencies of the higher harmonics.

In contrast with the synthetic signal, the estimation of harmonics is performed for the experimental signal. A glance of Fig. 3.8 reveals a qualitative difference in the behavior of all estimators. For the fundamental harmonic's amplitude, Unitary ESPRIT, NOMP, and CFH all closely estimate

with one another. For the fundamental harmonic's frequency, CFH follows more closely to RELAX, while Unitary ESPRIT and NOMP overlap one another. All LSEs struggle with stability more than compared with the synthetic signal, e.g. Unitary ESPRIT and NOMP demonstrate a large oscillation at the beginning of the experimental signal before stabilizing for the second harmonic's amplitude. This might be because of the presence of more harmonics within the real experimental signal, which presents more difficult estimation problem for the LSEs. Similar to the synthetic test, DeepFreq has a subpar performance for extraction of amplitudes, but can capture the fundamental harmonic only. If the LSEs' behavior on the synthetic signal test is to be indicative of its behavior on the experimental signal, one may conclude that the general results of the LSEs can be carried over. For example, the wide spread and oscillatory nature of amplitude estimation should be understood to be an uncertainty of the estimator instead of a detectable very small vibratory oscillation. Lastly, it can be noted that during the nonstationary evolution of sinusoidal parameters near fatigue failure, i.e., the end of the synthetic signal, the LSEs provide frequency estimates which diverge from truth, but still maintain accurate amplitude estimates.

Tolerance to noise, sensitivity to signal length In this test, we opt study the quasi-stationary synthetic signal of three well-separated sinusoids, with large amplitude variability between the first harmonic and higher harmonics, seen in Fig. 3.5. Grid-based simulations with respect to (windowed) signal lengths and AWGN levels are applied per window along the entire signal. For purely stationary signals, it's well known that an increase of signal length and/or a decrease in noise variance increases the performance of LSEs. A specific quality of the synthetic signal is the unknown interaction between frequency resolution and non-stationarity with respect to signal length.

In Fig. 3.9, the mean MFD, with outliers outside of five standard deviations removed, is plotted as a heatmap for specific LSEs with respect to signal length and AWGN. Most notably, Unitary ESPRIT has the largest area of *best* frequency estimation performance (in dark blue) compared to other estimators. Additionally, similarities between estimators that explicitly rely on the DFT are also seen, despite their attempts to refine frequency estimation: the DFT has an area of *best* frequency estimation which roughly intersects the CFH, RELAX, and NOMP's areas of *best* frequency estimation. As mentioned previously, CFH, RELAX, and NOMP all utilize DFT operations in their algorithm, but their refinements can be characterized as peak parabolic interpolation, zero-padding interpolation, and

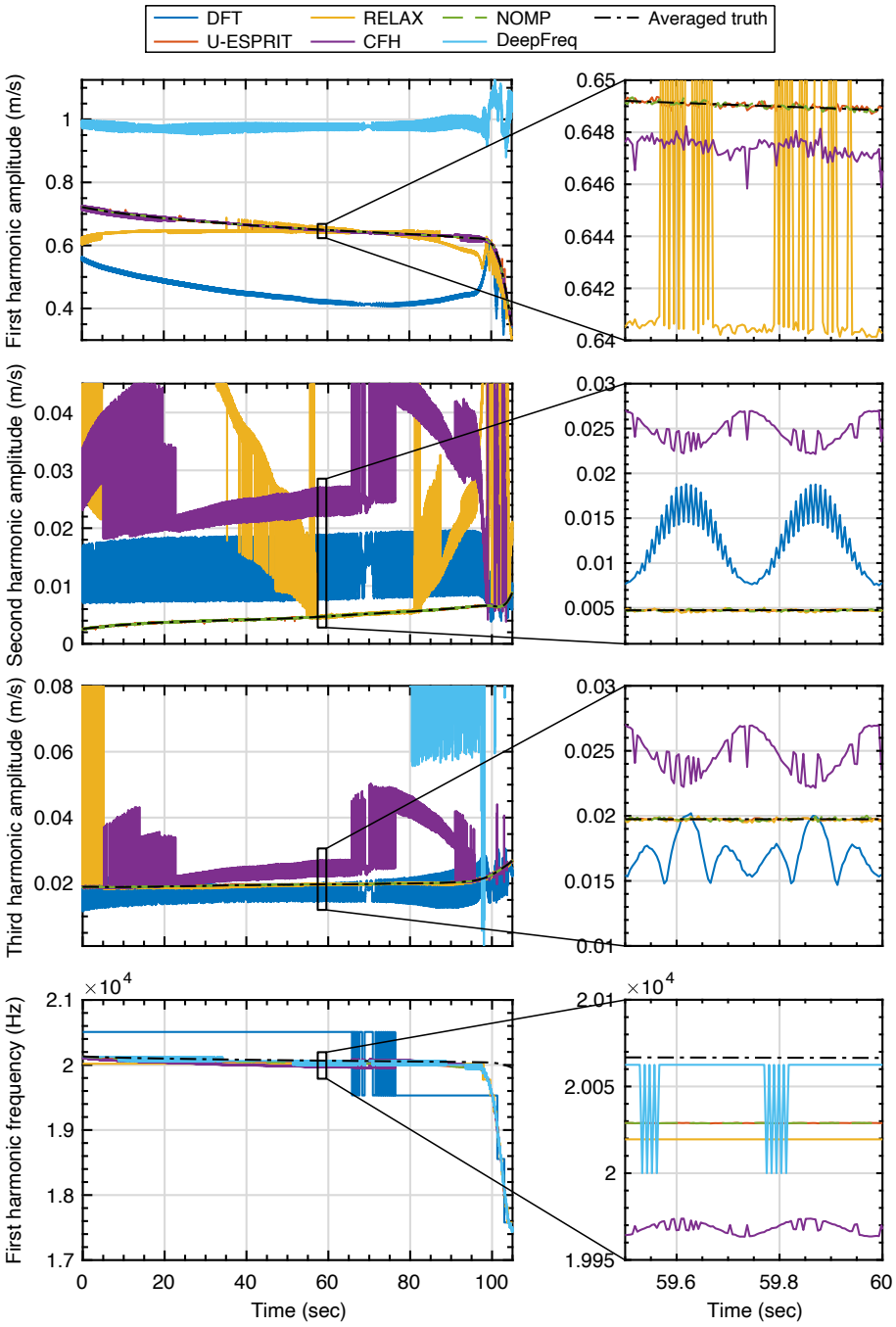

Figure 3.7: Sinusoidal parameter estimation of the three harmonics' amplitudes and fundamental harmonic's frequency for synthetic signal. The legend shown above applies to all plots.

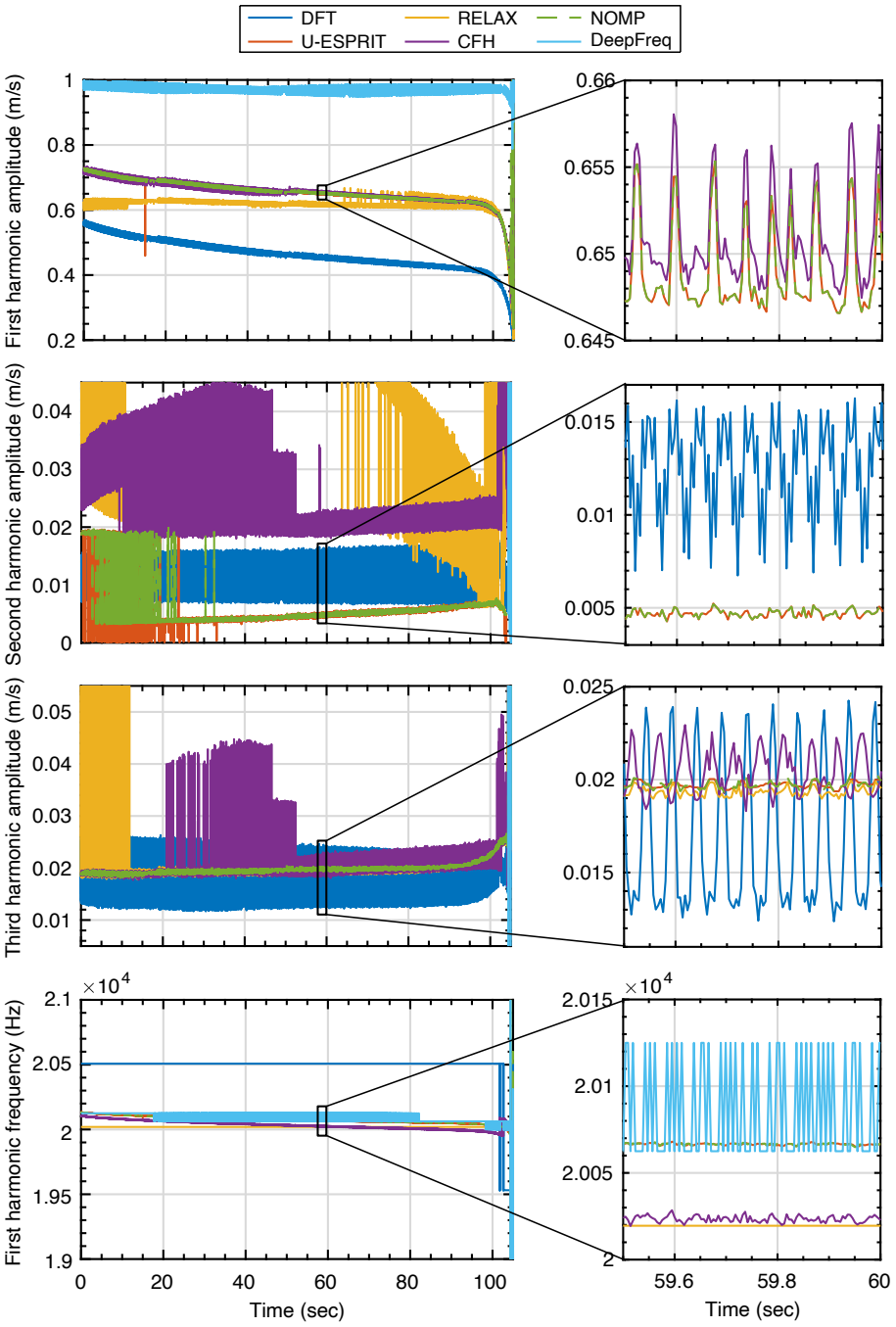

Figure 3.8: Sinusoidal parameter estimation of the three harmonics' amplitudes and fundamental harmonic's frequency for experimental signal. The legend shown above applies to all plots.

Newton-Raphson refinements of the DFT grid, respectively. This is likely due to the limitations of the DFT operation with respect to the quasi-stationarity in the sinusoidal parameters, whose expression can be seen in the polynomial fits in B.1. The other LSEs' expanded area in Fig. 3.9 compared to the DFT represents their ability to mitigate the quasi-stationarity and AWGN in each signal segment.

Lastly, it should be mentioned that DeepFreq has errors larger than any of the other LSEs presented; the frequency representation produced by DeepFreq is unable to compensate for any quasi-stationarity in the signal and creates a problem for a peak picking algorithm. This is a realistic reminder that this particular data-driven approach cannot be deployed so easily even if the data is quasi-stationary. Similarly, the average MAD is shown in Fig. 3.10, with outliers outside of five standard deviations removed, LSEs show a similar pattern with the MFD. As seen in the previous test, the LSEs have a better amplitude estimation ability compared to their frequency estimation, indicating amplitude estimation is less stringent. The exception is the large difference of amplitude estimation performance for the DFT: the corresponding ranges at which the DFT provides excellent frequency estimations (dark blue) provide poor amplitude estimates with a MAD of approximately one magnitude higher than other LSEs. For all LSEs for this particular synthetic signal, in the low SNR region (below 20 dB) provides unsatisfactory results for even the best-performing LSEs.

Computational effort and offline training The computational time plays a large factor when considering LSE algorithms for real-time usage. In Fig. 3.11, averaged computation times are shown with respect to signal lengths. It can be seen that the DFT always achieves the best runtime, this is due to the usage of the Fast Fourier Transform algorithm, which has the relatively lowest asymptotic complexity in Table 3.3. RELAX, CFH, and NOMP can be seen to have similar runtimes as the signal length varies. ESPRIT begins to diverge at $N = 10$, having the greatest runtime analogous to its large asymptotic complexity. It and the other LSE's asymptotic complexities in Big-$\mathcal{O}$ notation can be found in Table 3.3. Unique to DeepFreq, offline training requires a considerable amount of computational effort and training data that is a good representation of experimental data. The GPU training times can be seen at the bottom of Fig. 3.11 on a specialized computer for offline training

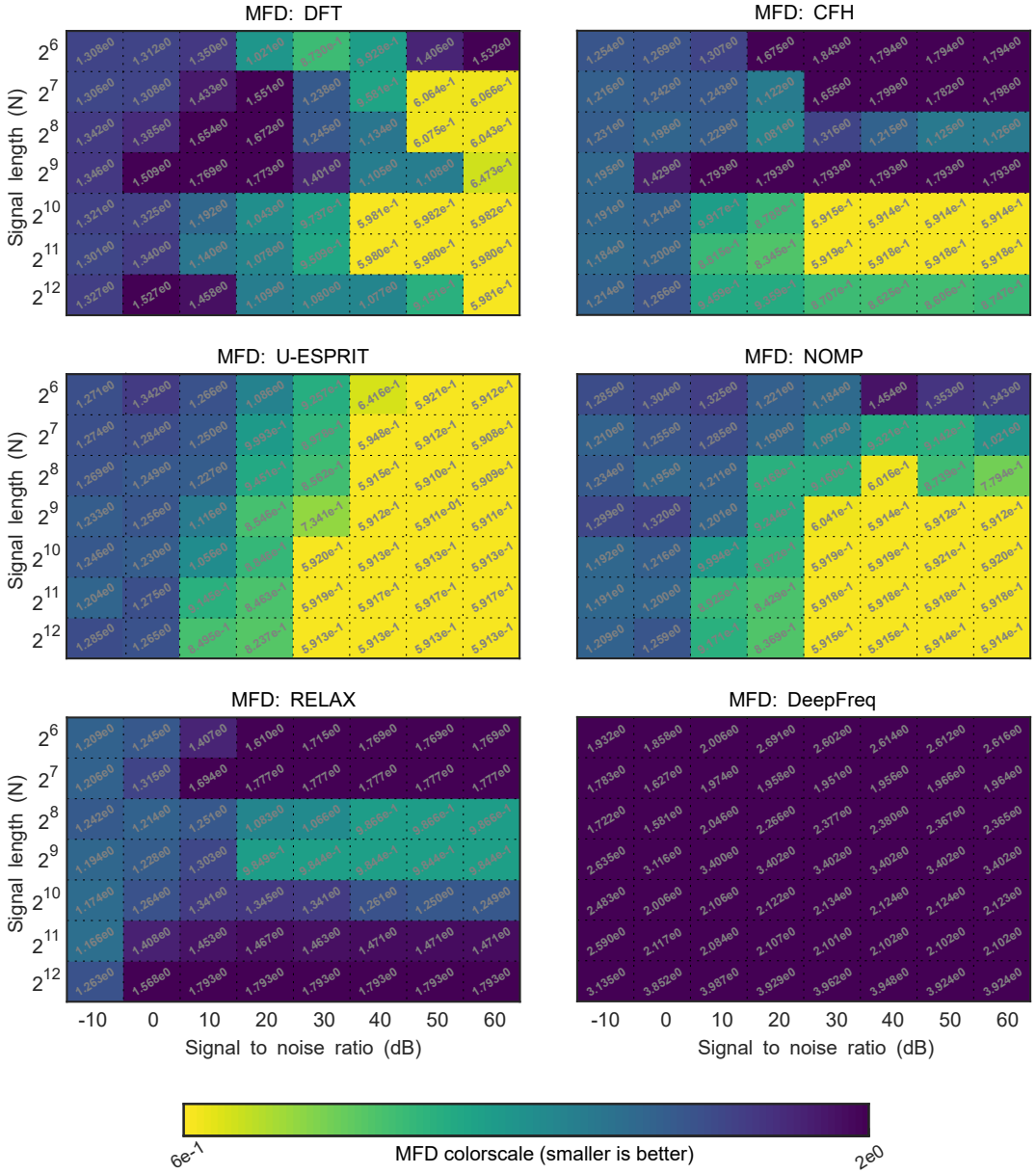

Figure 3.9: Simulation results as heatmaps of the MFD metric for each LSE, whose colorscales are plotted logarithmically.

with four virtual Intel Xeon CPUs clocked at 2.00 GHz, 32 Gb of memory, and an NVIDIA Tesla P100 GPU. It should be noted that Python (versions 3.8 and prior) is known to have poor just-in-time compilation, meaning that LSEs that utilize for-loops, namely CFH, RELAX, and NOMP, suffer with respect to their theoretical computational complexities. One can expect the LSEs to perform closer to their asymptotic complexities when programmed in a statically compiled language. A few options

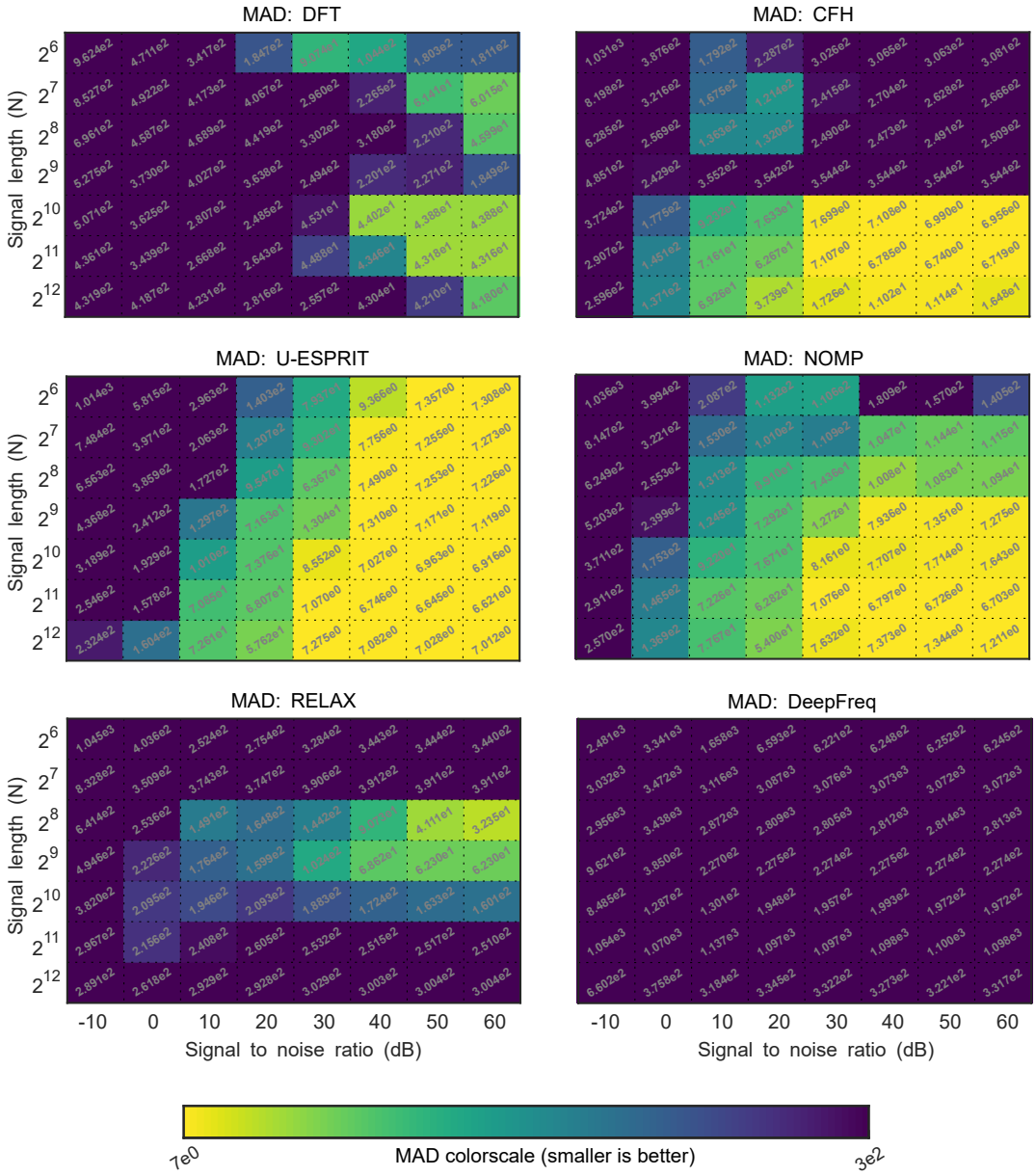

Figure 3.10: Simulation results as heatmaps of the MAD metric for each LSE, whose colorscales are plotted logarithmically.

exist to leverage static typing of existing Python code, e.g., using Pythran [Gue+15].

Discussion Ultrasonic fatigue vibration signals feature mostly quasi-stationary sinusoidal parameters, which slowly evolve with respect to many periods of the signal. When real-time usage is sought, the dichotomy between signal length, i.e., the Rayleigh limit $1/N$, and the quasi-stationarity of sinusoidal

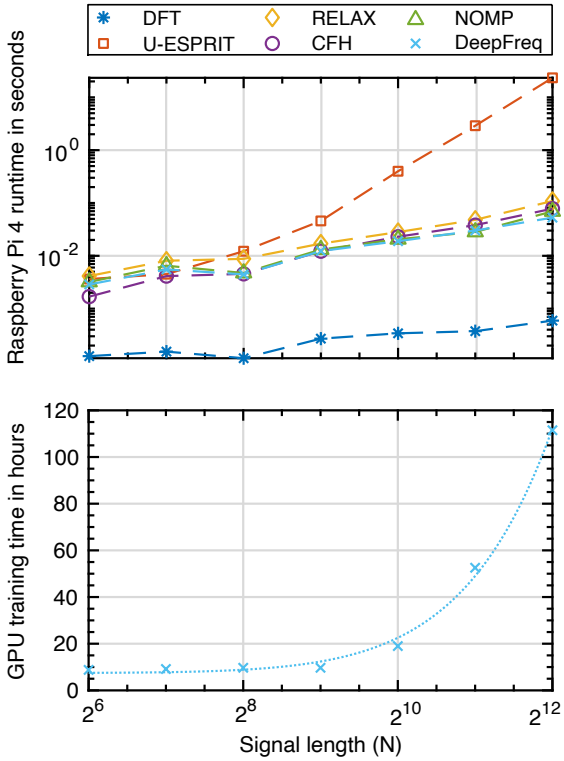

Figure 3.11: Averaged runtimes of LSEs on a Raspberry Pi 4 (top) and offline Tesla P100 GPU training time required for frequency representation module of DeepFreq (bottom) with respect to signal length N. The legend shown above applies to all plots.

components can pose difficulties for estimators whose original formulation relies on the assumption of stationary signals. This motivates an experimental benchmark comparing alternatives to the DFT. Notably, many LSEs are considered to have state-of-the-art results for purely stationary signals with unit amplitudes, which cannot be said for quasi-stationary signals with slowly time-varying non-unit amplitudes and frequencies (basis mismatch).

The benchmarks on a synthetic UFT signal and randomly generated signals with unique estimation challenges seen in ultrasonic vibration, show the capabilities of the various estimators in terms of their adaptability to quasi-stationary and the computational efficiencies. In general[1], ESPRIT and NOMP can be seen to offer the best performance with respect to the quasi-stationarity of a synthetic UFT

[1]In the full publication [Kis+23c], the algorithms are also benchmarked on their statistical performance against the Cramér-Rao lower bound on stationary signals. Specifically on amplitude variability (strong and weak signals), small interharmonic distance (super-resolution), and robustness to model order mismatch (number of sinusoidal components), which further validates the general usage of ESPRIT and NOMP for sinusoidal parameter estimation. A drawback of this study and current literature, however, is the lack of theory that precisely dictates when a signal is too nonstationary, thus prohibiting the use of LSEs. A small remark: DeepFreq should be understood to not be able to generalize to quasi-stationary data when trained on stationary data.

LSE	**Asymptotic complexity**
DFT	$\mathcal{O}(\, N \log N \,)$
Unitary ESPRIT	$\mathcal{O}(\, N^3 \,)$
RELAX	$\mathcal{O}(\, P Z_\mathrm{p} \log(Z_\mathrm{p}) \,)$
CFH	$\mathcal{O}(\, PN \log N \,)$
NOMP	$\mathcal{O}(\, P R_\mathrm{c} N \log N \,)$
DeepFreq*	$\mathcal{O}(\, \mathcal{L}\mathcal{K}\mathcal{N}\mathcal{R}^2 + N \,)$

Table 3.3: Comparison of asymptotic computational complexities of implemented line spectra estimators in big-$\mathcal{O}$ notation. *: The notation is defined where $\mathcal{L}$ is the layer depth, $\mathcal{N}$ is the sequence length, $\mathcal{R}$ is the representation dimension, $\mathcal{K}$ is the kernel size of convolutions.

signal. This motivates exploration into adapting ESPRIT into a more computationally efficient form for *in-situ* ultrasonic fatigue vibration signals.

3.3 Superfast signal subspace frequency estimation

In many practical applications, such as ultrasonic fatigue vibration signals, it is common to estimate LSEs to quasi-stationary signals despite the basis mismatch. It has been shown by benchmarks in the literature, e.g. vibration analysis [Kis+23c] and power system synchrophasors [Lac+20], that ESPRIT exceeded other state-of-the-art alternatives in performance metrics. However, this comes at much higher computational cost due to the full subspace estimation step by SVD $\mathcal{O}(N^3)$. Thus, for problems requiring real-time usage, subspace methods would benefit from fast estimations of the signal subspace. Multiple approaches in the literature leverage the fact that the span of the signal subspace is much smaller than its orthogonal subspace. In [TM85], they use the Lanczos algorithm to iteratively converge to the signal subspace. The work by [KS88] assumed that the signal subspace is an autoregressive process whose polynomials and rational functions form the sample covariance. Alternatively, the signal subspace is approximated in [KJ92] by using the DFT and the discrete cosine transforms for use in the MUSIC algorithm. Lastly, in [DAS18] the periodicity of an ideally long signal is estimated for, such that the estimated covariance matrix is approximately circulant, and thus the eigenvectors can be computed through an FFT, i.e. the signal subspace.

In this section, the problem formulation of kernel-based subspace estimates for LSE is introduced.

This naturally leads to two FFT-based ESPRIT algorithm for the line spectral problem, which achieve super-resolution without an (optionally truncated) SVD on the $M \times L$-sized data matrix. Specifically, only one Hankel matrix-Kernel matrix product is involved. This is in contrast to ESPRIT with partial SVDs and fast Hankel matrix-vector products presented in [PT15] which achieves time complexity $\mathcal{O}(MN \log N + M^3)$; or Nyström-based ESPRIT [QHS14] which achieves time complexity $\mathcal{O}(MNK + MK^2)$ for $K \leq \min(M, N)$, but requires tuning of their sub-vector length K and does not approach the asymptotic behavior ESPRIT. The main novelty of FFT-ESPRIT resides in the signal subspace estimation strategy by efficient use of the kernel of the DFT matrix. We build off the work of [KJ92], where a DFT-based signal subspace approximation is described, but its performance suffers from searching the pseudo-spectrum of MUSIC and lacks a theoretical analysis. We go one step further by using ESPRIT for *off-grid* frequency estimates, present errors due to basis mismatch between the Vandermonde signal model and the DFT kernels, utilize an iterative interpolated DFT algorithm (IIp-DFT) [YA15] to remediate the basis mismatch, and generalize the signal subspace estimate through performance analysis on the eigenspace perturbation. Lastly, we give a computationally efficient version which achieves a quasi-linear time complexity with respect to its signal length.

The notations are specified: It's denoted $\boldsymbol{y}$ and $\boldsymbol{Y}$ as vectors and matrices respectively. The ith entry of the vector $\boldsymbol{y}$ is denoted as $y[i]$. The ith column and row vector of $\boldsymbol{Y}$ is $\boldsymbol{y}_i$ and $\vec{\boldsymbol{y}}_i$ respectively. The complex conjugate, Hermitian transpose, and Moore-Penrose pseudo-inverse of complex matrix $\boldsymbol{Y}$ is denoted as $\boldsymbol{Y}^*$, $\boldsymbol{Y}^{\mathrm{H}}$, and $\boldsymbol{Y}^{\ddagger}$ respectively. The inner product for complex vectors $\boldsymbol{y}, \boldsymbol{z}$ is defined as $\boldsymbol{y}^{\mathrm{H}}\boldsymbol{z}$. A noise perturbed y is denoted $\check{y}$. The expected value of y is denoted $\mathbb{E}\{y\}$. The variance of the white noise is denoted η. The ℓ_2 and Frobenius norms are denoted $\|\boldsymbol{Y}\|$ and $\|\boldsymbol{Y}\|_{\mathrm{F}}$ respectively. The Hadamard product between $\boldsymbol{y}, \boldsymbol{z}$ is denoted $\boldsymbol{y} \circ \boldsymbol{z}$. The signal-to-noise ratio (SNR) defined as $\mathrm{SNR} \coloneqq \|\boldsymbol{A}_N\boldsymbol{\beta}\|^2/\eta$. The indexing of vectors and matrices start from zero.

Original ESPRIT algorithm Let the data matrix of the signal model of Eq. (3.1) be written:

$$\check{\boldsymbol{X}} \coloneqq \begin{bmatrix} \check{x}[0] & \check{x}[1] & \cdots & \check{x}[L-1] \\ \check{x}[1] & \check{x}[2] & \cdots & \check{x}[L] \\ \vdots & \vdots & \ddots & \vdots \\ \check{x}[M-1] & \check{x}[M] & \cdots & \check{x}[N-1] \end{bmatrix} \tag{3.49}$$

where $\check{\boldsymbol{X}} \in \mathbb{C}^{M \times L}$ is a Hankel matrix and M is a chosen sub-vector size such that:

$$P \leq M < N + 1 - P \tag{3.50}$$

Thus the remaining length is $L = N - M$. The ML form of the sample covariance $\widehat{\boldsymbol{R}} \in \mathbb{C}^{M\times M}$ is the statistically efficient approximation of the true covariance $\boldsymbol{R}$:

$$\widehat{\boldsymbol{R}} \coloneqq \frac{1}{L}\check{\boldsymbol{X}}\check{\boldsymbol{X}}^{\mathrm{H}} = \frac{1}{L}\sum_{n=0}^{L-1}\check{\boldsymbol{x}}_n\check{\boldsymbol{x}}_n^{\mathrm{H}} \tag{3.51}$$

The EVD on the true covariance $\boldsymbol{R}(\check{\boldsymbol{X}}) = \mathbb{E}\{\check{\boldsymbol{X}}\check{\boldsymbol{X}}^{\mathrm{H}}\}$ yields:

$$\begin{aligned}\boldsymbol{R} &\coloneqq \boldsymbol{U}\boldsymbol{\Sigma}^2\boldsymbol{U}^{\mathrm{H}} \\ &\coloneqq \boldsymbol{U}_{\mathrm{s}}\boldsymbol{\Sigma}_s^2\boldsymbol{U}_{\mathrm{s}}^{\mathrm{H}} + \ \boldsymbol{U}_{\perp}\boldsymbol{\Sigma}_{\perp}^2\boldsymbol{U}_{\perp}^{\mathrm{H}}\end{aligned} \tag{3.52}$$

where $\boldsymbol{\Sigma}$ corresponds to a diagonal matrix that contains the eigenvalues on the main diagonal sorted in descending order, $\boldsymbol{U}$ the left singular subspace, and the subscripts $\square_{\mathrm{s}}$, $\square_{\perp}$ denote the signal and orthogonal subspaces. For two sample-shifted overlapping signal subspaces:

$$\begin{aligned}\boldsymbol{U}_{\mathrm{s}}^{\uparrow} &\coloneqq \begin{bmatrix}\boldsymbol{I}_{M-1} & \boldsymbol{0}\end{bmatrix}\boldsymbol{U}_{\mathrm{s}} \coloneqq \boldsymbol{\Gamma}^{\uparrow}\boldsymbol{U}_{\mathrm{s}} \\ \boldsymbol{U}_{\mathrm{s}}^{\downarrow} &= \begin{bmatrix}\boldsymbol{0} & \boldsymbol{I}_{M-1}\end{bmatrix}\boldsymbol{U}_{\mathrm{s}} = \boldsymbol{\Gamma}^{\downarrow}\boldsymbol{U}_{\mathrm{s}}\end{aligned} \tag{3.53}$$

one can show the rotational invariance property [RK89]:

$$\boldsymbol{U}_{\mathrm{s}}^{\downarrow} = \boldsymbol{U}_{\mathrm{s}}^{\uparrow}\boldsymbol{T}^{-1}\boldsymbol{\Phi}\boldsymbol{T} \tag{3.54}$$

where $\boldsymbol{I}_{M-1}$ is an identity matrix of size $M-1$, $\boldsymbol{\Phi} \coloneqq \mathrm{diag}\{e^{\mathrm{j}2\pi\omega_0}, \ \ldots, \ e^{\mathrm{j}2\pi\omega_{P-1}}\}$, and $\boldsymbol{T} \in \mathbb{C}^{P\times P}$ is a nonsingular matrix. Since $\boldsymbol{T}$ is generally unknown, the ESPRIT algorithm [RK89] solves in the least-squares sense for $\boldsymbol{\Psi}$ where its eigenvalues are projected onto the complex unit circle to give the frequencies of $\boldsymbol{x}$:

$$\boldsymbol{\Psi} = \left(\boldsymbol{U}_{\mathrm{s}}^{\uparrow}\right)^{\dagger}\boldsymbol{U}_{\mathrm{s}}^{\downarrow} \tag{3.55}$$

3.3.1 Signal subspace estimation via kernels

The performance of certain subspace methods, like ESPRIT, depends on the estimated signal subspace obtained through a truncated EVD. This can be shown as the ith eigenvalue problem corresponding to the M descending eigenvalues $\{\sigma_0^2 \geq \ldots \geq \sigma_{M-1}^2\}$:

$$\boldsymbol{R}\boldsymbol{u}_i = \boldsymbol{u}_i\sigma_i^2 \tag{3.56}$$

Substitution of the sample covariance $\hat{\boldsymbol{R}}$ of Eq. (3.51) into Eq. (3.56) yields:

$$\frac{1}{L}\sum_{n=0}^{L-1}\left(\boldsymbol{x}_n(\boldsymbol{x}_n^{\mathrm{H}}\boldsymbol{u}_i)\right) \approx \boldsymbol{u}_i\sigma_i^2 \tag{3.57}$$

Eq. (3.57) shows that the ith unit eigenvector $\boldsymbol{u}_i$ is approximately a linear combination of $\boldsymbol{x}_n$. Thus it follows, that the estimate of ESPRIT does not need an estimate of each individual signal eigenvector by SVD or EVD (ℓ_2 optimality). Instead, it is sufficient that a combination of sparse basis vectors which have linear combinations span the same subspace of signal eigenvectors via the matrix $\boldsymbol{T}$ in Eq. (3.54). To demonstrate this idea, consider the following:

Proposition 1. *Let $\boldsymbol{X}$ be rank-deficient such that its Vandermonde decomposition is:*

$$\boldsymbol{X} = \boldsymbol{A}_M \boldsymbol{B} \boldsymbol{A}_L^{\mathrm{T}} \tag{3.58}$$

where $\boldsymbol{A}_M \in \mathbb{C}^{M\times P}$ and $\boldsymbol{A}_L^{\mathrm{T}} \in \mathbb{C}^{P\times L}$ are Vandermonde matrices of the undamped form:

$$\boldsymbol{A}_M \coloneqq \begin{bmatrix} 1 & 1 & \cdots & 1 \\ e^{\mathrm{j}2\pi\omega_0} & e^{\mathrm{j}2\pi\omega_1} & \cdots & e^{\mathrm{j}2\pi\omega_{P-1}} \\ e^{\mathrm{j}4\pi\omega_0} & e^{\mathrm{j}4\pi\omega_1} & \cdots & e^{\mathrm{j}4\pi\omega_{P-1}} \\ \vdots & \vdots & \ddots & \vdots \\ e^{\mathrm{j}2\pi\omega_0(M-1)} & e^{\mathrm{j}1\pi\omega_2(M-1)} & \cdots & e^{\mathrm{j}2\pi\omega_{P-1}(M-1)} \end{bmatrix}$$

where $\boldsymbol{B} = \operatorname{diag}\{\boldsymbol{\beta}\}$. Let the SVD of $\boldsymbol{X}$ be:

$$\boldsymbol{X} = \begin{bmatrix} \boldsymbol{U}_{\mathrm{s}} & \boldsymbol{U}_{\perp} \end{bmatrix} \begin{bmatrix} \boldsymbol{\Sigma}_{\mathrm{s}} & \\ & \boldsymbol{\Sigma}_{\perp} \end{bmatrix} \begin{bmatrix} \boldsymbol{V}_{\mathrm{s}}^{\mathrm{H}} \\ \boldsymbol{V}_{\perp}^{\mathrm{H}} \end{bmatrix} \tag{3.59}$$

where $\boldsymbol{U}_{\mathrm{s}} \in \mathbb{C}^{M\times P}$. Comparing Eqs. (3.58) *and* (3.59)*, the nonsingular matrix $\boldsymbol{T} \in \mathbb{C}^{P\times P}$ relates the two matrices:*

$$\boldsymbol{A}_M = \boldsymbol{U}_{\mathrm{s}} \boldsymbol{T} \tag{3.60}$$

and therefore it can be seen:

$$\operatorname{range}\{\boldsymbol{U}_{\mathrm{s}}\} = \operatorname{range}\{\boldsymbol{A}_M\} \tag{3.61}$$

This (continuous) Vandermonde representation is commonly referred to in the compressed sensing literature, in which the signal model of Eq. (3.2) is formulated as a nonlinear optimization problem. This is usually done using the DFT as a discretized initial estimate [Chi+11]:

$$\min_{\boldsymbol{\xi}} \big\{ \|\boldsymbol{\xi}\|_1 \big\} \quad \text{s.t.} \quad \|\boldsymbol{W}_N \boldsymbol{\xi} - \boldsymbol{x}\|_2 = 0 \tag{3.62}$$

where $\boldsymbol{W}_N \in \mathbb{C}^{N\times N}$ is the unitary DFT basis of the form:

$$\boldsymbol{W}_N \coloneqq \frac{1}{\sqrt{N}} \begin{bmatrix} 1 & 1 & \cdots & 1 \\ 1 & e^{\mathrm{j}\frac{2\pi}{N}} & \cdots & e^{\mathrm{j}\frac{2\pi(N-1)}{N}} \\ \vdots & \vdots & \ddots & \vdots \\ 1 & e^{\mathrm{j}\frac{2\pi}{N}(N-1)} & \cdots & e^{\mathrm{j}\frac{2\pi(N-1)^2}{N}} \end{bmatrix} \tag{3.63}$$

whose resolution is bounded by $1/N$ and $\boldsymbol{\xi}$ are Fourier coefficients. With the noiseless signal model of Eq. (3.2), the basis discrepancy can be understood from the expression:

$$\boldsymbol{x} = \boldsymbol{A}_N \boldsymbol{\beta} = \boldsymbol{W}_N \boldsymbol{\xi} \tag{3.64}$$

In the ideal *on-grid* setting, i.e. $\{\omega_i\}_{i=0}^{P-1} \subseteq \{j/N, j = 0, \cdots, N-1\}$, the matrix product $\boldsymbol{W}_N^{-1}\boldsymbol{A}_N$ yields a sub-matrix $\boldsymbol{I}$. The difficulty in the *off-grid* problem lies in the fact that the signal is sparse in the basis of $\boldsymbol{A}_N$, but not in the *on-grid* basis of $\boldsymbol{W}_N$, i.e. $\boldsymbol{\beta}$ is sparse in the $\boldsymbol{I}$ basis. This idea is easily demonstrated by the spectrum of the Fourier transformed signal compared to the true signal model of Eq. (3.2), see Fig. 3.12.

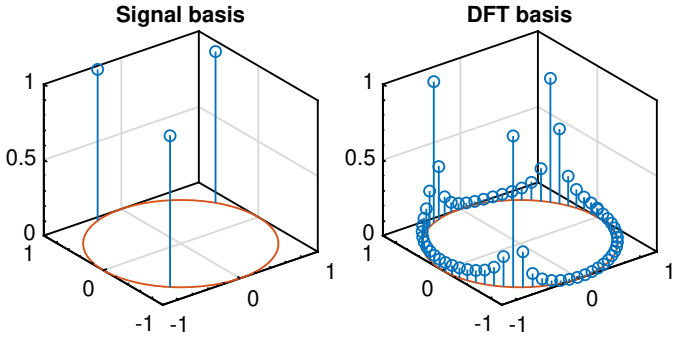

Figure 3.12: A true signal whose sparse basis lies in $\boldsymbol{A}$ represented by the signal model of Eq. (3.2) about a unit circle (left). The signal represented through the Fourier basis (right), whose mismatch is formed through a bandlimited sinc function, i.e. the Dirichlet kernel.

Given the signal subspace equivalence of Eq. (3.61) and its potential basis mismatch between $\boldsymbol{A}_N$ and $\boldsymbol{W}_N$ of Eq. (3.64), we wish to show that an approximate solution for subspace methods exist using the Vandermonde description of Eq. (3.58). Specifically, we will show that the DFT matrix, specifically as a kernel, can be used to achieve fast approximations of the signal subspace at the cost of creating basis mismatch.

Signal subspace estimation via "full" DFT kernel To avoid explicitly computing Eq. (3.56), we introduce the kernel-based subspace estimate problem:

Proposition 2. *Let the SVD of* $\boldsymbol{X} = \boldsymbol{U}\boldsymbol{\Sigma}\boldsymbol{V}^{\mathrm{H}}$. *The left singular subspace* $\boldsymbol{U}$ *has an approximation:*

$$\begin{aligned} \text{find} \quad & \boldsymbol{\mathcal{K}} \in \mathbb{C}^{L\times L} \quad \text{or} \quad \boldsymbol{\mathcal{K}} \in \mathbb{R}^{L\times L} \\ \text{such that} \quad & \text{range}\{\boldsymbol{U}\} \approx \text{range}\{\boldsymbol{X}\boldsymbol{\mathcal{K}}\} \\ & \boldsymbol{\mathcal{K}}\boldsymbol{\mathcal{K}}^{\text{H}} = c\boldsymbol{I} \\ & \boldsymbol{X}\boldsymbol{\mathcal{K}} \text{ is fast to compute} \end{aligned} \tag{3.65}$$

where c is an arbitrary constant and $\{\boldsymbol{\kappa}_i\}_{i=0}^{L-1}$ is the set of M vectorized kernels that span $\boldsymbol{\mathcal{K}}$.

The goal of Proposition 2 is to avoid the computation of an SVD/EVD by using a fast matrix product $\boldsymbol{X}\boldsymbol{\mathcal{K}}$. More notably, $\boldsymbol{X}\boldsymbol{\mathcal{K}}$ is not guaranteed to be orthogonal. This, however, is not a problem for subspace methods such as ESPRIT since $\boldsymbol{\Psi}$ is solved in the LS-sense, see Eq. (3.55). In vector notation of Eq. (3.57), the subspace of the problem can be written as:

$$\text{span}\{\boldsymbol{u}_0\sigma_0^2, \ldots, \boldsymbol{u}_{M-1}\sigma_{M-1}^2\} \approx \text{span}\left\{\sum_{n=0}^{L-1}\big(\boldsymbol{x}_n\boldsymbol{\kappa}_0[n]\big), \ldots, \sum_{n=0}^{L-1}\big(\boldsymbol{x}_n\boldsymbol{\kappa}_{M-1}[n]\big)\right\} \tag{3.66}$$

One may realize that the problem of finding the appropriate set of kernels $\{\boldsymbol{\kappa}_i\}$ in Eq. (3.66) leads to a computationally intractable M dimensional optimization. Similarly shown by [KJ92] for the signal subspace, the DFT kernel can approximate the kernel of Eq. (3.66). We demonstrate this approximation to Proposition 2 by explicitly rewriting Eq. (3.66):

$$\text{span}\{\boldsymbol{u}_0\sigma_0^2, \ldots, \boldsymbol{u}_{M-1}\sigma_{M-1}^2\} \approx \text{span}\left\{\sum_{n=0}^{L-1}\Big(\boldsymbol{x}_n e^{-\text{j}2\pi(0)(n)/L}\Big), \ldots, \sum_{n=0}^{L-1}\Big(\boldsymbol{x}_n e^{-\text{j}2\pi(M-1)(n)/L}\Big)\right\}$$

where an approximate in matrix form can be written as:

$$\text{range}\,\{\boldsymbol{U}\} \approx \text{range}\left\{\boldsymbol{Y}^{\text{alg1}}\right\} \tag{3.67}$$

where $\boldsymbol{Y}^{\text{alg1}} \coloneqq \widehat{\boldsymbol{X}}\boldsymbol{W}_L^*$ and $\boldsymbol{W}_L^*$ is the $L \times L$ DFT matrix. Therefore, the full subspace $\boldsymbol{U}$ can be approximated by the kernel of the Fourier transform on the row-space of the Hankel matrix $\boldsymbol{X}$. For application in the ESPRIT algorithm, the columns that span the signal subspace can be found in the optimal ℓ_2 norm sense:

$$\text{range}\,\{\boldsymbol{U}_{\text{s}}\} \approx \text{span}\left\{\underset{0<i<P-1}{\arg\max}\{\|\boldsymbol{y}_i \in \boldsymbol{Y}^{\text{alg1}}\|\}\right\} \coloneqq \text{range}\left\{\boldsymbol{Y}_{\text{s}}^{\text{alg1}}\right\} \tag{3.68}$$

We show this kernel-based signal subspace estimator implemented in Algorithm 1 using MATLAB functions. One may note that the performance of Algorithm 1 is tied to the constraint on $\boldsymbol{X}$ being

square $M = L$, which has been shown for SVD-based methods by [Van93] and proven for ESPRIT by [LLF20] where better performance is achieved. Note that, Algorithm 1 has an asymptotic complexity of $\mathcal{O}(N^2 \log N)$ due to line 2. Finally, since ESPRIT is invariant to the specific choice of orthonormal basis for range$\{\boldsymbol{U}_\mathrm{s}\}$ (see Eq. (3.60)), the QR decomposition is used to generate its orthogonal matrix for calculation of Eq. (3.55). We will show later that solving for $\boldsymbol{\Psi}$ using the orthogonalized form $\boldsymbol{Q}$ has a slight advantage in computational flops as opposed to using $\boldsymbol{Y}_\mathrm{s}$ directly.

Algorithm 1 ESPRIT with signal subspace approximation by DFT kernel

Input: $\boldsymbol{x} \in \mathbb{C}^{N\times 1}$, M, P
Output: $\boldsymbol{\omega}$
1: $\boldsymbol{X} \leftarrow (\boldsymbol{x}_0, \ldots, \boldsymbol{x}_{L-1})$
2: $\boldsymbol{Y} \leftarrow \texttt{fft}(X, [\,], 2)$
3: $\boldsymbol{Y}^{\mathrm{alg1}} \leftarrow \texttt{sortMax}(\|\boldsymbol{y}_0\|, \ldots, \|\boldsymbol{y}_{L-1}\|)$
4: $\boldsymbol{Y}_\mathrm{s}^{\mathrm{alg1}} \leftarrow (\boldsymbol{y}_0, \ldots, \boldsymbol{y}_{P-1})$
5: $\boldsymbol{Q} \leftarrow \texttt{qr}(\boldsymbol{Y}_\mathrm{s}^{\mathrm{alg1}}, \texttt{'econ'})$
6: $\boldsymbol{Q}^{\uparrow} \leftarrow (\vec{\boldsymbol{q}}_0; \ldots; \vec{\boldsymbol{q}}_{M-2})$
7: $\boldsymbol{Q}_{\downarrow} \leftarrow (\vec{\boldsymbol{q}}_1; \ldots; \vec{\boldsymbol{q}}_{M-1})$
8: $\boldsymbol{\Psi} \leftarrow \left(\boldsymbol{Q}^{\uparrow}\right)^{\ddagger}\boldsymbol{Q}_{\downarrow}$
9: $\boldsymbol{\omega} \leftarrow \texttt{mod}(\texttt{angle}(\texttt{eig}(\boldsymbol{\Psi})/2\pi,\, 1))$
10: **return** $\boldsymbol{\omega}$

From Eq. (3.58) and Algorithm 1, it can be seen that the calculation of $\boldsymbol{\Psi}$ from the signal subspace spanned by $\boldsymbol{X}\boldsymbol{W}_L^*$ contains the linear combinations of $\boldsymbol{A}\boldsymbol{\beta}$. However, the DFT kernel offers an approximation of *on-grid* elements, as mentioned previously. In Algorithm 1, there is a discrepancy between the grid by matrix product $\boldsymbol{A}_L^{\mathrm{T}}\boldsymbol{W}_L^*$ in:

$$\widehat{\boldsymbol{X}}\boldsymbol{W}_L^* = \boldsymbol{A}_M\boldsymbol{B}\boldsymbol{A}_L^{\mathrm{T}}\boldsymbol{W}_L^* + \boldsymbol{\mathcal{E}}\boldsymbol{W}_L^* \tag{3.69}$$

in which we wish to recover range$\{\boldsymbol{A}_M\}$ by assuming $\boldsymbol{\mathcal{E}}\boldsymbol{W}_L^*$ negligible in the ℓ_2 norm. The matrix product forms a defined frequency difference between the Vandermonde decomposed Hankel matrix $\boldsymbol{X}$ with the DFT grid of $\boldsymbol{W}_L^*$, $\{0,\, 1/L, \ldots, L - 1/L\}$. Without loss of generality, let $\boldsymbol{B} = \boldsymbol{I}$, and we first expand the product $\boldsymbol{A}_L^{\mathrm{T}}\boldsymbol{W}_L^*$ in Eq. (3.70):

$$\boldsymbol{A}_L^{\mathrm{T}}\boldsymbol{W}_L^* \coloneqq \sqrt{L}\begin{bmatrix} D_L\left(\omega_0\right) & D_L\left(\omega_0 - \frac{1}{L}\right) & \cdots & D_L\left(\omega_0 - \frac{L-1}{L}\right) \\ D_L\left(\omega_1\right) & D_L\left(\omega_1 - \frac{1}{L}\right) & \cdots & D_L\left(\omega_1 - \frac{L-1}{L}\right) \\ \vdots & \vdots & \ddots & \vdots \\ D_L\left(\omega_{P-1}\right) & D_L\left(\omega_{P-1} - \frac{1}{L}\right) & \cdots & D_L\left(\omega_{P-1} - \frac{L-1}{L}\right) \end{bmatrix} \tag{3.70}$$

where D_L represents the matrix elements:

$$D_L(f) \coloneqq \frac{1}{L}\sum_{i=0}^{L-1} e^{\mathrm{j}2\pi(i)f} = \frac{1}{L} e^{\mathrm{j}\pi f(L-1)} \frac{\sin(\pi f L)}{\sin(\pi f)} \tag{3.24}$$

which are the Dirichlet kernel such that $D_L(0) = 1$.

The product $[\boldsymbol{A}_L^{\mathrm{T}} \boldsymbol{W}_L^*]_{i,k}$ is a sample of the Dirichlet kernel at $f = \omega_i - k/L$ for $i = 0, \ldots, P-1$ and $k = 0, \ldots, L-1$. If $\boldsymbol{A}_M$ is to be obtained exactly, the product should yield a sub-matrix $\boldsymbol{I}_P$ such that $\boldsymbol{A}_L^{\mathrm{T}} \boldsymbol{W}_L^* = \boldsymbol{I}_P + \boldsymbol{E}_L$: one such case is when the frequencies are *on-grid*. In these cases, the columns of the elements in the sub-matrix $\boldsymbol{I}_P$ form the span of $\boldsymbol{U}_{\mathrm{s}}$. In all other cases, the difference between ω_i and k/L produces a mismatched row in the product $[\boldsymbol{A}_L^{\mathrm{T}} \boldsymbol{W}_L^*]_{i,k}$. Each frequencies' entries decay across each row with a closed form expression, first similarly noted by [Chi+11]. This decay is due to the Dirichlet kernel which has the relationship: $|D_L(f)| \leq 1/Lf : \forall |f| \leq 0.5$. The denominator of Eq. (3.24) has the property $|\sin(\pi f)| \geq 2|f| : \forall |f| \leq 0.5$, and thus $|1/Lf|$ is the envelope which captures the decay of $|D_L(f)|$, see Fig. 3.13.

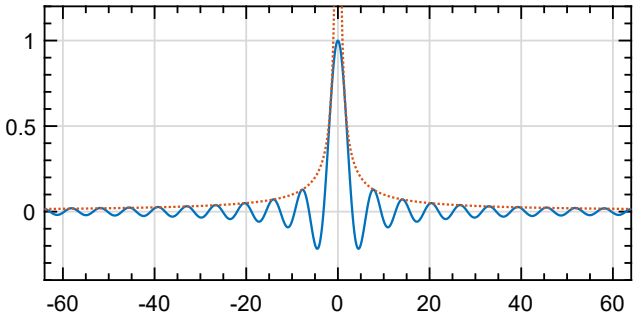

Figure 3.13: The function $(1/L)\sin(\pi f L)/\sin(\pi f)$ versus Lf (blue), and $|1/Lf|$ versus Lf (orange), for $L = 2^6$ and $f \in [-1, 1]$; adapted from [Chi+11].

This raises three observations for the *off-grid* setting: 1) a perfect identity sub-matrix is not obtainable; 2) it can be easily seen that increasing the grid resolution N does not help make the approximation closer; 3) even with a single frequency that is *off-grid* leads to an effect on the columns of $\boldsymbol{A}_L^{\mathrm{T}} \boldsymbol{W}_L^*$. This problem becomes more difficult to characterize when the signal is of damped complex sinusoids, which we expand upon in Appendix B.2. Finally, the selection criteria of maximum ℓ_2 norm can be seen to be sound: even with basis mismatch between a frequency and a sufficiently resolved DFT grid, the Dirichlet kernel is centered and maximum about 0, and the largest column norms will contain the entry of the sub-matrix $\boldsymbol{I}_P$.

Signal subspace estimation via truncated DFT kernel To improve the efficiency and performance of Algorithm 1, we propose a kernel of a truncated DFT matrix, in which the columns are chosen by their spectral energy prior to the matrix product. To demonstrate this idea, consider the following:

Proposition 3. *Let the SVD of* $\boldsymbol{X}$ *be:*

$$\boldsymbol{X} = \begin{bmatrix}\boldsymbol{U}_\mathrm{s} & \boldsymbol{U}_\perp\end{bmatrix} \begin{bmatrix}\boldsymbol{\Sigma}_\mathrm{s} & \\ & \boldsymbol{\Sigma}_\perp\end{bmatrix} \begin{bmatrix}\boldsymbol{V}_\mathrm{s}^\mathrm{H} \\ \boldsymbol{V}_\perp^\mathrm{H}\end{bmatrix}$$

where $\boldsymbol{U}_\mathrm{s} \in \mathbb{C}^{M\times P}$*. The signal subspace* $\boldsymbol{U}_\mathrm{s}$ *has an approximation when the sparsity* P *is known:*

$$\begin{aligned} \text{find} \quad & \boldsymbol{\mathcal{K}}_\mathbf{s} \in \mathbb{C}^{L\times P} \quad \text{or} \quad \boldsymbol{\mathcal{K}}_\mathbf{s} \in \mathbb{R}^{L\times P} \\ \text{such that} \quad & \operatorname{range}\{\boldsymbol{U}_\mathrm{s}\} \approx \operatorname{range}\{\boldsymbol{X}\boldsymbol{\mathcal{K}}_\mathbf{s}\} \\ & \boldsymbol{X}\boldsymbol{\mathcal{K}}_\mathrm{s} \text{ is fast to compute} \end{aligned} \tag{3.25}$$

where $\{\boldsymbol{\kappa}_i\}_{i=0}^{P-1}$ *is the set of* M *vectorized kernels that span* $\boldsymbol{\mathcal{K}}$*.*

By similar arguments as before, a solution to Proposition 3 is the product of $\widehat{\boldsymbol{X}}$ with the kernel $\boldsymbol{\mathcal{K}}_\mathrm{s} = \boldsymbol{W}^*_{L\times P}$. This corresponds to the kernel of the truncated DFT matrix of P columns, i.e. a rectangular matrix of size $L \times P$:

$$\begin{aligned} \widehat{\boldsymbol{X}}\boldsymbol{W}^*_{L\times P} &= \boldsymbol{A}_M \boldsymbol{B} \boldsymbol{A}_L^\mathrm{T} \boldsymbol{W}^*_{L\times P} + \boldsymbol{\mathcal{E}}\boldsymbol{W}^*_{L\times P} \\ &= \boldsymbol{X}\boldsymbol{W}^*_{L\times P} + \boldsymbol{\mathcal{E}}\boldsymbol{W}^*_{L\times P} \end{aligned} \tag{3.26}$$

which corresponds to an "eigenfilter" on the subspace by rejecting the least spectrally prominent orthogonal columns. Directly, we can estimate the signal subspace by the expression:

$$\operatorname{range}\{\boldsymbol{U}_\mathrm{s}\} \approx \operatorname{range}\left\{\boldsymbol{Y}_\mathrm{s}^{\mathrm{alg2}}\right\} \tag{3.27}$$

where $\boldsymbol{Y}_\mathrm{s}^{\mathrm{alg2}} \coloneqq \widehat{\boldsymbol{X}}\boldsymbol{W}^*_{L\times P}$. We present this truncated kernel-based signal subspace estimator implemented as FFT-ESPRIT in Algorithm 2. For use in an algorithm, the columns $\boldsymbol{W}^*_{L\times P}$ should correspond only to the true frequencies. To visualize this, let the truncated DFT kernel be made of P frequency differences $\{\delta_i \in [0,1)\}_{i=0}^{P-1}$:

$$\boldsymbol{W}^*_{L\times P} \coloneqq \begin{bmatrix} 1 & 1 & \cdots & 1 \\ e^{-\mathrm{j}\frac{2\pi}{L}\delta_0} & e^{-\mathrm{j}\frac{2\pi}{L}\delta_1} & \cdots & e^{-\mathrm{j}\frac{2\pi}{L}\delta_{P-1}} \\ \vdots & \vdots & \ddots & \vdots \\ e^{\mathrm{j}\frac{2\pi}{L}(L-1)\delta_0} & e^{\mathrm{j}\frac{2\pi}{L}(L-1)\delta_1} & \cdots & e^{\mathrm{j}\frac{2\pi}{L}(L-1)\delta_{P-1}} \end{bmatrix}$$

Thus the product $\boldsymbol{A}_L^{\mathrm{T}}\boldsymbol{W}_{L\times P}^*$ generates a similar matrix of size $P\times P$ whose entries are Dirichlet kernels are:

$$\boldsymbol{A}_L^{\mathrm{T}}\boldsymbol{W}_{L\times P}^* \coloneqq L\begin{bmatrix} D_L\left(\omega_0-\delta_0\right) & D_L\left(\omega_0-\delta_1\right) & \cdots & D_L\left(\omega_0-\delta_{P-1}\right) \\ D_L\left(\omega_1-\delta_0\right) & D_L\left(\omega_1-\delta_1\right) & \cdots & D_L\left(\omega_1-\delta_{P-1}\right) \\ \vdots & \vdots & \ddots & \vdots \\ D_L\left(\omega_{P-1}-\delta_0\right) & D_L\left(\omega_{P-1}-\delta_1\right) & \cdots & D_L\left(\omega_{P-1}-\delta_{P-1}\right) \end{bmatrix} \tag{3.28}$$

Given this form, is easy to see that $\boldsymbol{A}_M$ is to be obtained when the product yields the sub-matrix $\boldsymbol{I}_P$, such that $\boldsymbol{A}_L^{\mathrm{T}}\boldsymbol{W}_{L\times P}^* = \boldsymbol{I}_P + \boldsymbol{E}_{P\times P}$ when $\{\omega_i = \delta_i\}_{i=0}^{P-1}$. Therefore, we suggest that an FFT-based algorithm should be used which performs *off-grid* estimates for the columns of $\boldsymbol{W}_{L\times P}^*$: e.g. an IIp-DFT estimator [YA15], which is one of many DFT peak interpolation algorithms that can be used in Algorithm 2. Additionally, one may realize that $\boldsymbol{W}_{L\times P}^*$ must at minimum span P in order to lie in the signal subspace of $\boldsymbol{U}_{\mathrm{s}}$, which does not allow one to underestimate the model order. The IIp-DFT algorithm is programmed such that its frequency estimates are sorted descending by peak prominence.

Algorithm 2 FFT-ESPRIT

Input: $\boldsymbol{x}\in\mathbb{C}^{N\times 1}$, M, P
Output: $\boldsymbol{\omega}$

$\boldsymbol{X} \leftarrow (\boldsymbol{x}_0, \ldots, \boldsymbol{x}_{L-1})$
$\widehat{\boldsymbol{\omega}} \leftarrow \texttt{IIp-DFT}(\boldsymbol{x}, P)$
$\boldsymbol{W}_{L\times P}^* \leftarrow (\boldsymbol{a}_{-\widehat{\omega}_0}, \ldots, \boldsymbol{a}_{-\widehat{\omega}_{P-1}})$
$\boldsymbol{Y}_{\mathrm{s}}^{\mathrm{alg2}} \leftarrow \boldsymbol{X}\boldsymbol{W}_{L\times P}^*$
$\boldsymbol{Q} \leftarrow \texttt{qr}(\boldsymbol{Y}_{\mathrm{s}}^{\mathrm{alg2}}, \texttt{'econ'})$
$\boldsymbol{Q}^{\uparrow} \leftarrow (\vec{\boldsymbol{q}}_0; \ldots; \vec{\boldsymbol{q}}_{M-2})$
$\boldsymbol{Q}_{\downarrow} \leftarrow (\vec{\boldsymbol{q}}_1; \ldots; \vec{\boldsymbol{q}}_{M-1})$
$\boldsymbol{\Psi} \leftarrow \left(\boldsymbol{Q}^{\uparrow}\right)^{\ddagger}\boldsymbol{Q}_{\downarrow}$
$\boldsymbol{\omega} \leftarrow \texttt{mod}(\texttt{angle}(\texttt{eig}(\boldsymbol{\Psi})/2\pi,\, 1))$
return $\boldsymbol{\omega}$

Performance bounds of FFT-ESPRIT To understand the performance of these signal subspace estimates within the context of the ESPRIT algorithm, many performance bounds have been given in terms of statistical [SS91], first-order perturbation on the data matrix [BRD08], and more recently, as eigenspace perturbations [LLF20]. Herein, we work with the performance bounds presented in [LLF20], which work directly with perturbations to the signal subspace. The previous algorithms have signal subspace approximates $\boldsymbol{U}_{\mathrm{s}}$, i.e. $\boldsymbol{Y}_{\mathrm{s}}^{\mathrm{alg2}}$ not perfectly orthogonal due to the off-diagonal terms. Therefore, we opt for usage of the orthogonalized form found by QR decomposition such that $\boldsymbol{Q} \leftarrow \boldsymbol{Y}_{\mathrm{s}}^{\mathrm{alg2}}$.

First, we define the theorems of Davis-Kahan and Wedin [Wed72] from ℓ_2 eigenspace perturbation theory on the data matrix.

Theorem 1. *Let $\boldsymbol{X}, \widehat{\boldsymbol{X}} \in \mathbb{C}^{M\times L}$, where $\widehat{\boldsymbol{X}} = \boldsymbol{X} + \boldsymbol{\mathcal{E}}$ and has rank P. Let their SVDs be:*

$$\boldsymbol{X} = \sum_{i=0}^{\min\{M-1,L-1\}} \sigma_i \boldsymbol{u}_i \boldsymbol{v}_i^{\mathrm{H}} = \begin{bmatrix}\boldsymbol{U}_{\mathrm{s}} & \boldsymbol{U}_{\perp}\end{bmatrix} \begin{bmatrix}\boldsymbol{\Sigma}_{\mathrm{s}} & \\ & \boldsymbol{\Sigma}_{\perp}\end{bmatrix} \begin{bmatrix}\boldsymbol{V}_{\mathrm{s}}^{\mathrm{H}} \\ \boldsymbol{V}_{\perp}^{\mathrm{H}}\end{bmatrix}$$

$$\widehat{\boldsymbol{X}} = \sum_{i=0}^{\min\{M-1,L-1\}} \widehat{\sigma}_i \widehat{\boldsymbol{u}}_i \widehat{\boldsymbol{v}}_i^{\mathrm{H}} = \begin{bmatrix}\widehat{\boldsymbol{U}}_{\mathrm{s}} & \widehat{\boldsymbol{U}}_{\perp}\end{bmatrix} \begin{bmatrix}\widehat{\boldsymbol{\Sigma}}_{\mathrm{s}} & \\ & \widehat{\boldsymbol{\Sigma}}_{\perp}\end{bmatrix} \begin{bmatrix}\widehat{\boldsymbol{V}}_{\mathrm{s}}^{\mathrm{H}} \\ \widehat{\boldsymbol{V}}_{\perp}^{\mathrm{H}}\end{bmatrix}$$

whose ith descending singular values is $\{\sigma_i\}$.

Let the ith principle angle between two arbitrary subspace matrices $\boldsymbol{S}$, $\widehat{\boldsymbol{S}}$ with arbitrary dimension $M \times L$ be defined as:

$$\theta_i \coloneqq \arccos(|\widehat{\boldsymbol{s}}_i^{\mathrm{H}} \boldsymbol{s}_i|) = \arccos(\lambda_i) \tag{3.29}$$

where λ_i denotes the ith arbitrary descending singular value $\{\lambda_0 \geq \ldots \geq \lambda_i \geq \ldots \geq \lambda_{M-1}\}$ and let:

$$\boldsymbol{\Theta}\big(\widehat{\boldsymbol{S}}, \boldsymbol{S}\big) \coloneqq \mathrm{diag}\big\{\theta_0, \ldots, \theta_{M-1}\big\} \tag{3.30}$$

It follows from Wedin's $\sin\boldsymbol{\Theta}$ theorem that if $2\|\boldsymbol{\mathcal{E}}\| \leq \sigma_{P-1}(\widehat{\boldsymbol{X}})$, then it holds:

$$\sin\theta_0 \leq \frac{2\|\boldsymbol{\mathcal{E}}\|}{\sigma_{P-1}(\widehat{\boldsymbol{X}})} \tag{3.31}$$

Proof. See [Wed72]. □

Theorem 1 provides bounds that subspace methods must balance the perturbations $\boldsymbol{\mathcal{E}}$ caused to the signal subspace without affecting the smallest singular value of the signal subspace σ_{P-1}. To bridge the connection between classical singular values of the SVD for Davis-Kahan and Wedin's theorems with the singular values of the QR decomposition, one can refer to Proposition 4:

Proposition 4. *Let $\boldsymbol{U}_{\mathrm{s}} \in \mathbb{C}^{L\times P}$ of rank P where $L \geq P$. Let its thin QR decomposition give:*

$$\boldsymbol{U}_{\mathrm{s}} = \boldsymbol{Q}\boldsymbol{\mathfrak{R}}$$

where $\boldsymbol{Q} \in \mathbb{C}^{L\times P}$, $\boldsymbol{\mathfrak{R}} \in \mathbb{C}^{P\times P}$, and $\boldsymbol{Q}$ is a unitary matrix whose columns are sorted descending by eigenvalues. Then the singular values for the upper triangular matrix $\boldsymbol{\mathfrak{R}}$ are the same as the singular values of $\boldsymbol{U}_{\mathrm{s}}$, i.e. $\{\sigma_0(\boldsymbol{\mathfrak{R}}), \ldots, \sigma_{P-1}(\boldsymbol{\mathfrak{R}})\} = \{\sigma_0(\boldsymbol{U}_{\mathrm{s}}), \ldots, \sigma_{P-1}(\boldsymbol{U}_{\mathrm{s}})\}$.

For the original ESPRIT algorithm, perturbations to the signal subspace are usually caused by noise in practice, which can lead to subspace swap of the smallest signal singular value and the largest noise singular value [HNS01]. For Algorithms 1 and 2 in the noiseless and *on-grid* case, this perturbation is characterized by the off-diagonal terms of the products defined by Eq. (3.70) and Eq. (3.28) respectively.

Next, let us define the following matched distances of $\widehat{\boldsymbol{\Psi}} = \left(\widehat{\boldsymbol{U}}^{\uparrow}\right)^{\ddagger}\widehat{U}_{\downarrow}$ which is diagonalizable with eigenvalues $\{\widehat{\lambda}_i = e^{-\mathrm{j}2\pi\widehat{\omega}_i}\}_{i=0}^{P-1}$:

$$\mathrm{md}(\widehat{\boldsymbol{\Psi}}, \boldsymbol{\Psi}) \coloneqq \min_{\psi_i \in \boldsymbol{\Psi}} \max_i \left|\widehat{\lambda}_{\psi_i} - e^{-\mathrm{j}2\pi\omega_i}\right| \tag{3.32}$$

and subsequently the frequencies $\{\widehat{\omega}_i = -\angle\widehat{\lambda}_i/2\pi\}_{i=0}^{P-1}$:

$$\mathrm{md}(\widehat{\boldsymbol{\omega}}, \boldsymbol{\omega}) \coloneqq \min_{\psi_i \in \boldsymbol{\Psi}} \max_i |\widehat{\omega}_{\psi_i} - \omega_i| \tag{3.33}$$

These two matched distanced have the relationship, proven in [LLF20, Lemma 2]:

$$\mathrm{md}(\widehat{\boldsymbol{\omega}}, \boldsymbol{\omega}) \leq \frac{1}{2}\mathrm{md}(\widehat{\boldsymbol{\Psi}}, \boldsymbol{\Psi}) \leq \|\widehat{\boldsymbol{\Psi}} - \boldsymbol{\Psi}\| \tag{3.34}$$

The authors in [LLF20] provides performance bounds of ESPRIT with respect to its minimum singular value σ_{P-1} of the signal subspace:

Theorem 2. *Let the constraints of Eq.* (3.50) *be fixed. The original ESPRIT algorithm has the following bounds if the noise is moderate and bounded such that:*

$$\|\boldsymbol{\mathcal{E}}\| \leq \frac{\beta_{\min}\sigma_{P-1}(\boldsymbol{A}_M)\sigma_{P-1}(\boldsymbol{A}_L^{\mathrm{T}})\sigma_{P-1}(\boldsymbol{U}_{\mathrm{s}}^{\uparrow})}{4\sqrt{2P}} \tag{3.35}$$

then its eigenspace has the stability:

$$\|\widehat{\boldsymbol{\Psi}} - \boldsymbol{\Psi}\| \leq \frac{14\sqrt{2P}\|\boldsymbol{\mathcal{E}}\|}{\beta_{\min}\sigma_{P-1}(\boldsymbol{A}_M)\sigma_{P-1}(\boldsymbol{A}_L^{\mathrm{T}})\sigma_{P-1}^2(\boldsymbol{U}_{\mathrm{s}}^{\uparrow})} \tag{3.36}$$

and the performance on the frequency matched distance:

$$\mathrm{md}(\widehat{\boldsymbol{\omega}}, \boldsymbol{\omega}) = \frac{20P^2\sqrt{M+1}\|\boldsymbol{\mathcal{E}}\|}{\beta_{\min}\sigma_{P-1}^2(\boldsymbol{A}_M)\sigma_{P-1}(\boldsymbol{A}_L^{\mathrm{T}})\sigma_{P-1}^2(\boldsymbol{U}_{\mathrm{s}}^{\uparrow})} \tag{3.37}$$

Proof. See [LLF20]. □

The original ESPRIT algorithm is better understood through the stability of $\boldsymbol{\Psi}$, since it's computed from $\boldsymbol{U}_{\mathrm{s}}$. What is notable about Theorem 2 are the roles of the smallest singular value of the Vandermonde matrices $\boldsymbol{A}_M$, $\boldsymbol{A}_L^{\mathrm{T}}$ and the signal subspace matrix $\boldsymbol{U}_{\mathrm{s}}^{\uparrow}$ (with its last row removed) on the stability and performance bounds. In [LL21], an accurate lower bound is given for $\sigma_{P-1}(\boldsymbol{A}_{\square})$, and in [LLF20] for $\sigma_{P-1}(\boldsymbol{U}_{\mathrm{s}}^{\uparrow})$.

Given these bounds, and the fact we opt to use the QR decomposition as opposed to an SVD, the kernel-based signal subspace estimate of Eq. (3.26) has the bounds:

Theorem 3. *Let the constraints of Eq.* (3.50) *be fixed and the estimated matrix* $\boldsymbol{W}_{L\times P}^{*} \in \mathbb{C}^{L\times P}$*. Algorithm 2 has the following bounds if the noise is moderate and bounded such that:*

$$\|\boldsymbol{\mathcal{E}}\| \leq \frac{\beta_{\min}\sigma_{P-1}(\boldsymbol{A}_M)\sigma_{P-1}(\boldsymbol{A}_L^{\mathrm{T}})\sigma_{P-1}(\boldsymbol{W}_{L\times P}^{*})\sigma_{P-1}(\boldsymbol{Q}^{\uparrow})}{4\sqrt{2P}\|\boldsymbol{W}_{L\times P}^{*}\|} \tag{3.38}$$

then its eigenspace has the stability:

$$\|\widehat{\boldsymbol{\Psi}} - \boldsymbol{\Psi}\| \leq \frac{14\sqrt{2P}\|\boldsymbol{\mathcal{E}}\|\|\boldsymbol{W}_{L\times P}^{*}\|}{\beta_{\min}\sigma_{P-1}(\boldsymbol{A}_M)\sigma_{P-1}(\boldsymbol{A}_L^{\mathrm{T}})\sigma_{P-1}(\boldsymbol{W}_{L\times P}^{*})\sigma_{P-1}^{2}(\boldsymbol{Q}^{\uparrow})} \tag{3.39}$$

and the performance on the frequency matched distance:

$$\mathrm{md}(\widehat{\boldsymbol{\omega}}, \boldsymbol{\omega}) = \frac{20P^{2}\sqrt{M+1}\|\boldsymbol{\mathcal{E}}\|\|\boldsymbol{W}_{L\times P}^{*}\|}{\beta_{\min}\sigma_{P-1}^{2}(\boldsymbol{A}_M)\sigma_{P-1}(\boldsymbol{A}_L^{\mathrm{T}})\sigma_{P-1}(\boldsymbol{W}_{L\times P}^{*})\sigma_{P-1}^{2}(\boldsymbol{Q}^{\uparrow})} \tag{3.40}$$

Proof. See Appendix B.3 combined with [LLF20, Lemma 2]. □

One can see that in the moderate to high SNR regime, FFT-ESPRIT will offer a lower quality estimate, since $\|\boldsymbol{W}_{L\times P}^{*}\| \geq \sigma_{P-1}(\boldsymbol{W}_{L\times P}^{*})$. Between the no-information to low SNR regime, i.e. $2\|\boldsymbol{\mathcal{E}}\| \geq \sigma_{P-1}(\widehat{\boldsymbol{X}})$, one can show that the Wedin's bounds of Eq. (3.31) give $\sin\theta_0 \leq \frac{\sigma_{P-1}(\widehat{\boldsymbol{X}})}{2\|\boldsymbol{\mathcal{E}}\|}$. It is rudimentary to see that the moderate SNR regime performance bounds of Theorems 2 and 3 are inversed in this low SNR regime. We propose that there is a regime between the no-information and low SNR where FFT-ESPRIT can have better performance than the original ESPRIT algorithm, which we demonstrate numerically in the following section. The criticality of basis mismatch between $\boldsymbol{W}_{L\times P}^{*}$ and $\boldsymbol{A}_L^{\mathrm{T}}$ can be understood in two senses: 1) by invoking Theorem 3, its performance in the low SNR regime is proportional to:

$$\mathrm{md}(\widehat{\boldsymbol{\omega}}, \boldsymbol{\omega}) \propto \frac{\sigma_{P-1}^{2}(\boldsymbol{A}_M)\sigma_{P-1}(\boldsymbol{W}_{L\times P}^{*})}{\|\boldsymbol{\mathcal{E}}\|\|\boldsymbol{W}_{L\times P}^{*}\|} \tag{3.41}$$

FFT-ESPRIT will offer a better estimate since the subspace of the DFT matrix obeys $\|\boldsymbol{W}^*_{L\times P}\| \geq \sigma_{P-1}(\boldsymbol{W}^*_{L\times P})$; 2) the SNR is improved in Frobenius-sense such that: $\|\boldsymbol{X}\boldsymbol{W}^*_{L\times P}\|_{\mathrm{F}}/\|\boldsymbol{\mathcal{E}}\boldsymbol{W}^*_{L\times P}\|_{\mathrm{F}} \geq \|\boldsymbol{X}\|_{\mathrm{F}}/\|\boldsymbol{\mathcal{E}}\|_{\mathrm{F}}$. When $\boldsymbol{W}^*_{L\times P}$ deviates, i.e. the frequencies are no longer aligned with the main lobe of the Dirichlet kernel of Fig. 3.13, the inequality may no longer hold.

Fast version of FFT-ESPRIT In this section, we aim to accelerate the computations of Algorithm 2, namely to reduce the quadratic complexity dependency on M imposed by the matrix product of line 4 and to prevent inefficient computations of the pseudo-inverse of line 8. Due to the reduction of this time complexity, it enables one to create a fast version which obtains $\mathcal{O}(N \log N)$.

First, we will approach line 4 of Algorithm 2 and aim to leverage the properties of the Hankel matrix $\boldsymbol{X}$ to achieve a faster matrix product. In Algorithm 3 we show that the complexity can be reduced to $\approx 2PN \log N$, assuming the appropriate mixed radix FFT algorithms are available. Additionally, the Hankel matrix does not have to be explicitly formed. We take advantage of the circulant nature of the DFT, where the Hankel matrix can be Fourier transformed into a Toeplitz matrix, and the Vandermonde matrix can be Fourier transformed by taking its FFT. The product of these transformed matrices can then be obtained by element-wise multiplications, followed by an inverse FFT and a row-wise truncation.

Algorithm 3 Fast Hankel Matrix-Matrix product

Input: $\boldsymbol{x} \in \mathbb{C}^{N\times 1}$, $\boldsymbol{W}^*_{L\times P} = (\boldsymbol{a}_{-\widehat{\omega}_0}, \ldots, \boldsymbol{a}_{-\widehat{\omega}_{P-1}})$, M, P
Output: $\boldsymbol{Y}_{\mathrm{s}}$

1: $\boldsymbol{c} \leftarrow (x[M-1], \ldots, x[0])$
2: $\boldsymbol{r} \leftarrow (x[N-2], \ldots, x[M])$
3: $\boldsymbol{t} \leftarrow (\boldsymbol{c}, 0, \boldsymbol{r})$
4: $\boldsymbol{t}_{\mathrm{f}} \leftarrow \texttt{fft}(\boldsymbol{t})$
5: $\boldsymbol{G} \leftarrow \texttt{fft}(\boldsymbol{W}^*_{L\times P}, [\,], 1)$
6: **for** $i = 0$ to $P-1$ **do**
7: $\quad \boldsymbol{y}_i \leftarrow \texttt{ifft}(\boldsymbol{g}_i \circ \boldsymbol{t}_{\mathrm{f}})$
8: **end for**
9: $\boldsymbol{Y}_{\mathrm{s}} \leftarrow (\vec{\boldsymbol{y}}_0; \ldots; \vec{\boldsymbol{y}}_{M-1})$
10: $\boldsymbol{Y}_{\mathrm{s}} \leftarrow \texttt{flipud}(\boldsymbol{Y}_{\mathrm{s}})$
11: **return** $\boldsymbol{Y}_{\mathrm{s}}$

Next for line 8 of Algorithm 2, we will briefly reiterate that once the estimate of the signal subspace estimate is obtained due to the property in Eq. (3.61), $\boldsymbol{\Psi}$ is calculated by the rotation invariance prop-

erty by ESPRIT. One can use the estimate $\boldsymbol{Y}_{\mathrm{s}}$ directly using a Gaussian elimination-type solver since $\boldsymbol{\Psi} = \left(\boldsymbol{Y}_{\mathrm{s}}^{\uparrow}\right)^{\ddagger}\boldsymbol{Y}_{\mathrm{s}}^{\downarrow}$. An alternative choice is to naively use MATLAB's `pinv`, which relies on calculating a thin SVD on $\boldsymbol{Y}_{\mathrm{s}}^{\uparrow}$. However, the minimal norm least-squares solution is not useful since $\boldsymbol{Y}_{\mathrm{s}}^{\uparrow}$ is never rank-deficient. A preferred alternative relies on a QR solver for the least-squares solution, which is used by MATLAB's `mldivide` (\). Both these methods avoid the usage of the normal equations, which means their condition number is linear: $\kappa(\boldsymbol{Y}_{\mathrm{s}}^{\uparrow})$. However, we propose to first calculate its QR decomposition to obtain $\boldsymbol{Q} \leftarrow \boldsymbol{Y}_{\mathrm{s}}$ since the flops are nearly identical and become more efficient when $P > 4$.

Using the normal equation:

$$\boldsymbol{\Psi} = \left(\boldsymbol{Q}^{\uparrow}\right)^{\ddagger}\boldsymbol{Q}_{\downarrow} = \left(\left(\boldsymbol{Q}^{\uparrow}\right)^{\mathrm{H}}\boldsymbol{Q}^{\uparrow}\right)^{-1}\left(\boldsymbol{Q}^{\uparrow}\right)^{\mathrm{H}}\boldsymbol{Q}_{\downarrow}$$

when $\boldsymbol{Q}^{\uparrow}$ is full-column rank, and that $\left(\boldsymbol{Q}^{\uparrow}\right)^{\mathrm{H}}\boldsymbol{Q}^{\uparrow}$ is non-singular. By invoking the Woodbury matrix identity [HJ12] and storing the product $\left(\boldsymbol{Q}^{\uparrow}\right)^{\mathrm{H}}\boldsymbol{Q}_{\downarrow}$ in memory, one obtains a rank-one modification:

$$\boldsymbol{\Psi} = \left(\boldsymbol{Q}^{\uparrow}\right)^{\mathrm{H}}\boldsymbol{Q}_{\downarrow} + \left(\vec{\boldsymbol{q}}^{\mathrm{H}}\left(\vec{\boldsymbol{q}}\left(\left(\boldsymbol{Q}^{\uparrow}\right)^{\mathrm{H}}\boldsymbol{Q}_{\downarrow}\right)\right)\right)\left(\frac{1}{\vec{\boldsymbol{q}}^{\mathrm{H}}\vec{\boldsymbol{q}}}\right) \tag{3.42}$$

where $\vec{\boldsymbol{q}}$ corresponds to the last row of $\boldsymbol{Q}$. While Eq. (3.42) is a faster method since it has a lower flops requirement, its performance relies on the orthogonality of the matrix, i.e. $\left(\boldsymbol{Q}^{\uparrow}\right)^{\mathrm{H}}\boldsymbol{Q}^{\uparrow} = \boldsymbol{I}_P$, and therefore its condition number is quadratic: $\kappa(\left(\boldsymbol{Q}^{\uparrow}\right)^{\mathrm{H}}\boldsymbol{Q}^{\uparrow})$. The numerical error that is propagated due to corrupted data and/or poor orthogonality will lose twice as many digits of accuracy compared to the QR- or SVD-based methods. Therefore, the QR decomposition of $\boldsymbol{Y}_{\mathrm{s}}$ is recommended to use a Householder pseudo-reflection variant (for complex numbers) described by [HJ12, Theorem 2.1.13] as opposed to a Gram-Schmidt variant.

We compare all these options in Table 3.4 with respect to their flops and opt to use Eq. (3.42). Thus, when using Algorithm 3 and Eq. (3.42) for FFT-ESPRIT of Algorithm 2, one achieves the fast variant of FFT-ESPRIT with an asymptotic complexity of $\mathcal{O}(N \log N)$ since $P \ll M \propto N$.

3.3.2 Results and discussion

In this subsection, we compare the previous FFT-based ESPRIT algorithms with respect to two performance measures on the undamped signal model of Eq. (3.1) with length $N = 2^7$. Specifically, only the fast variant of FFT-ESPRIT (Algorithm 4) and Algorithm 1 are included. For all simulations,

Algorithm 4 Fast FFT-ESPRIT

Input: $\boldsymbol{x} \in \mathbb{C}^{N\times 1}$, P, M
Output: $\boldsymbol{\omega}$

1: $\widehat{\boldsymbol{\omega}} \leftarrow \texttt{IIp-DFT}(\boldsymbol{x}, P)$
2: $\boldsymbol{A}_L^* \leftarrow (\boldsymbol{a}_{-\widehat{\omega}_0}, \ldots, \boldsymbol{a}_{-\widehat{\omega}_{P-1}})$
3: $\boldsymbol{Y}_{\mathrm{s}} \leftarrow \texttt{Algorithm-3}(\boldsymbol{x}, \boldsymbol{A}_L^*, M, P)$
4: $\boldsymbol{Q} \leftarrow \texttt{qr}(\boldsymbol{Y}_{\mathrm{s}}, \texttt{'econ'})$
5: $\boldsymbol{Q}^{\uparrow} \leftarrow (\vec{\boldsymbol{q}}_0; \ldots; \vec{\boldsymbol{q}}_{M-2})$
6: $\boldsymbol{Q}_{\downarrow} \leftarrow (\vec{\boldsymbol{q}}_1; \ldots; \vec{\boldsymbol{q}}_{M-1})$
7: $\boldsymbol{E} \leftarrow \left(\boldsymbol{Q}^{\uparrow}\right)^{\mathrm{H}} \boldsymbol{Q}_{\downarrow}$
8: $\boldsymbol{\Psi} \leftarrow \boldsymbol{E} + \left(\vec{\boldsymbol{q}}^{\mathrm{H}} \left(\vec{\boldsymbol{q}}\boldsymbol{E}\right)\right) \left(\frac{1}{\vec{\boldsymbol{q}}^{\mathrm{H}}\vec{\boldsymbol{q}}}\right)$
9: $\boldsymbol{\omega} \leftarrow \texttt{mod}(\texttt{angle}(\texttt{eig}(\boldsymbol{\Psi})/2\pi,\, 1))$
10: **return** $\boldsymbol{\omega}$

Table 3.4: Comparison of LS solution of $\boldsymbol{\Psi}$ with respect to flops

Algorithm	**MATLAB Computation**	**Flops (mult. and adds.)**
SVD-based [GV13]	$\texttt{pinv}(\boldsymbol{Y}_{\mathrm{s}}^{\uparrow})\boldsymbol{Y}_{\mathrm{s}\downarrow}$	$2M^2P + M^2 + 6MP^2$ $+P - \frac{4}{3}P^3 - MP$
QR-based	$\boldsymbol{Y}_{\mathrm{s}}^{\uparrow} \backslash \boldsymbol{Y}_{\mathrm{s}\downarrow}$	$4MP^2 + \frac{1}{3}P^3 - P^2$
QR decomp. & Woodbury-based	$\boldsymbol{Q} \leftarrow \texttt{qr}(\boldsymbol{Y}_{\mathrm{s}}, \texttt{'econ'})$ & Eq. (3.42)	$4MP^2 + 3P^2 + P - \frac{2}{3}P^3 - 1$

the complex amplitudes β_i are generated independent and identically distributed whose magnitudes are then normalized to unity.

We define the following metrics: the mean square error (MSE) is used as a statistical measure of error:

$$\mathrm{MSE} \coloneqq \frac{1}{P}\sum_{j=1}^{P}\left(\min_{\widehat{\omega}_i \in \widehat{\boldsymbol{\omega}}} |\widehat{\omega}_i - \omega_j|\right)^2 \tag{3.43}$$

An approximate CRB is used alongside the MSE since it characterizes the asymptotic behavior at large N and/or high SNR [SM05] for a single sinusoid. This is given as:

$$\mathrm{CRB} \coloneqq \frac{6\eta}{N(N^2-1)} \tag{3.44}$$

The MSE can be misleading since it does not give an indication of the probability of failures and can be skewed by such outliers. Therefore, the frequency success rate (FSR) is defined as follows:

$$\mathrm{FSR} \coloneqq \frac{\sum_{\widehat{\omega}_i \in \widehat{\boldsymbol{\omega}}} \mathcal{S}\left(\widehat{\omega}_i, \boldsymbol{\omega}\right) + \sum_{\omega_j \in \boldsymbol{\omega}} \mathcal{S}\left(\omega_j, \widehat{\boldsymbol{\omega}}\right)}{2P} \tag{3.45}$$

with the success function defined as:

$$\mathcal{S}(i, \boldsymbol{j}) \coloneqq \mathbb{1}\left[\min_{j_k \in \boldsymbol{j}} |i - j_k| < \frac{1}{2N}\right] \tag{3.46}$$

where $\mathbb{1}[\square]$ denotes the indicator function. An FSR of 1 is obtained if all estimated frequencies are near one or more simulated frequencies and all simulated frequencies are near one or more estimated frequencies. All metrics are averaged over all independent runs.

To benchmark our algorithms, we use the original ESPRIT algorithm [RK89] which is given the same parameters as FFT-ESPRIT and Algorithm 1, i.e. $M = N/2$. The original ESPRIT algorithm and Algorithm 1 use a QR-based solver for $\boldsymbol{\Psi}$, whereas FFT-ESPRIT uses the Woodbury-based solution of Eq. (3.42). We also include the admission of the IIp-DFT algorithm to contrast the effect of its estimation performance on FFT-ESPRIT's performance.

Single sinusoid In the first simulation, we perform 10^4 Monte Carlo simulations of $P = 1$ complex sinusoid with zero-mean and is corrupted by AWGN with a varying SNR. In Fig. 3.14, the MSE is normalized by the CRB of Eq. (3.44). It can be seen that in the no-information to low SNR regimes, FFT-ESPRIT has better performance over the original ESPRIT algorithm in both MSE and FSR. As the SNR increases, this advantage slowly inverts, and ESPRIT has better asymptotic performance. Algorithm 1 can be seen to have the worst MSE in the single sinusoidal case. When contrasted with its FSR, one can conclude its performance is limited by the subspace swap introduced by using the full DFT matrix for a subspace estimate. IIp-DFT can be seen have worst MSE relative to FFT-ESPRIT throughout the SNR regimes. However, its estimate provides FFT-ESPRIT an advantage with an "eigenfilter" property which allows it to outperform ESPRIT from the no-information regime up to ≈ -3 dB.

Super-resolution of two closely-spaced sinusoids Here, the performance of the estimators with respect to their super-resolution is analyzed, i.e. ability to resolve closely-spaced frequencies beyond the Rayleigh limit $1/N$. We perform 10^4 Monte Carlo simulations of $P = 2$ complex sinusoids with one of the frequencies to be closely situated within a multiple of the Rayleigh limit $1/N$. The signals have zero mean and are chosen to have an SNR of 10 dB. In Fig. 3.15, one can observe that Algorithm 1 outperforms other estimators until $\approx 0.5/N$. After this threshold, all estimators but ESPRIT have a sharp transition in MSE. At this regime, FFT-ESPRIT, as well as Algorithm 1, has a performance advantage over the original ESPRIT algorithm up until $\approx 0.7/N$. Afterward, FFT-ESPRIT,

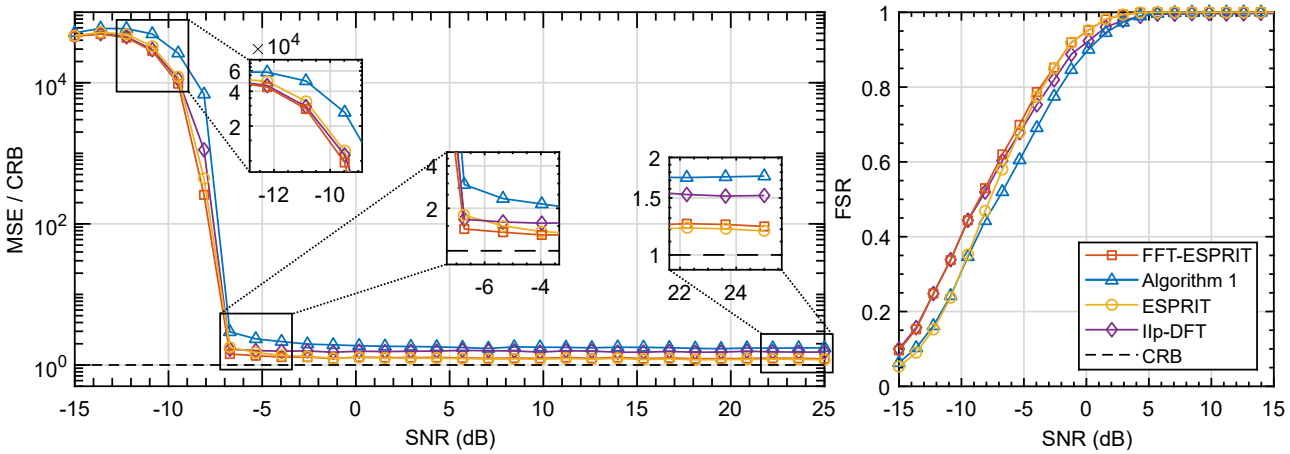

Figure 3.14: Simulation results of varying SNR for a single sinusoid ($P = 1$) with a fixed signal length of $N = 2^7$.

Algorithm 1, and ESPRIT all closely follow similar MSEs demonstrating the superiority of subspace methods and their ability of super-resolution. At first, one may be surprised by the MSE performance of IIp-DFT below $\approx 0.5/N$. However, its lower MSE can be ascribed to a precise, yet inaccurate frequency estimate, indicated by its very low FSR. The DFT can also be shown to suffer a similar limitation due to using the maximum peaks of *on-grid* frequency bins. IIp-DFT, however, is prone to bias introduced by interpolation [YA15], resulting in plateaus in its MSE and FSR. In terms of the FSR, all three subspace methods follow similar performance trajectories, with Algorithm 1 lagging behind after $\approx 0.7/N$.

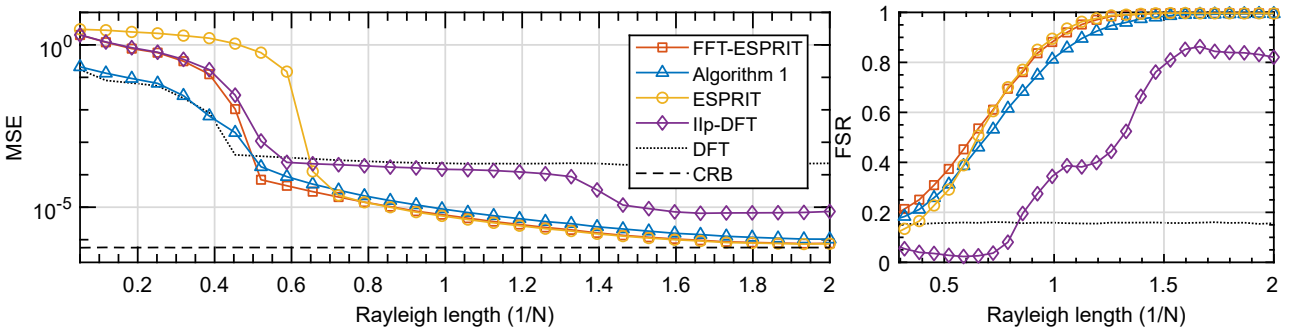

Figure 3.15: Simulation results for a pair of closely-spaced sinusoids ($P = 2$). The signal length is $N = 2^7$ and SNR is 10 dB, both fixed. The abscissa represents where one complex sinusoid is closely situated to another at a multiple of the Rayleigh limit. The DFT is included as a dotted line for reference.

Bias of two, well-separated sinusoids To contrast with the previous section, the bias of other well-separated sinusoids with respect to performance is investigated. The covariance between two sinusoids starts to become negligible when $|\omega_i - \omega_j| > 2/N$ [SM05]. Therefore, one can expect a compounding effect if an estimator is sensitive to the number of sinusoids. We perform 10^4 Monte Carlo simulations of $P = 2$ complex sinusoids which are ensured to be well-separated of at least $2/N$: the set of well-separated frequencies are drawn from a uniform distribution $\{\omega_i \in [0, 1) : \min\{|\omega_i - \omega_j|, |1 - |\omega_i - \omega_j||\} \geq 2/N : \forall i \neq j\}$. The signals have zero mean and are corrupted by AWGN with varying SNRs.

In Fig. 3.16, the MSE is normalized by the CRB of Eq. (3.44). Similarly to the single sinusoidal case, FFT-ESPRIT can be seen to have an advantage over the other estimators in the no-information to the low-SNR regime, until ≈ 2 dB. This behavior was conjectured after Theorem 3, where the truncated DFT matrix enhanced the SNR at a bounded noise perturbation, yielding the performance increase shown by Eq. (3.41). ESPRIT has a better MSE than FFT-ESPRIT after this inflection point. FFT-ESPRIT, being an approximation of the subspace, obtains nearly identical performance as ESPRIT in the medium SNR regime and above. Differently from the single sinusoidal case, Algorithm 1 begins to suffer greatly in its threshold transition from ≈ -10 dB to 2 dB: the approximation of the eigenvalues provided by the kernel of the full DFT matrix includes a small amount of subspace swap per sinusoid, in addition to the subspace swap of noise, thus compounding the effect. When looking at the FSR of Algorithm 1, one can see a relatively normal trajectory, indicating that the poor performance in its MSE is due to a spurious outlier.

Lastly, IIp-DFT suffers in MSE for multiple sinusoids, as opposed to the single sinusoidal case in both the SNR transitionary regime and the medium SNR regime and beyond. Interpolation methods are known to achieve ML performance in the single sinusoidal asymptotic case [SM05], but the iterative steps to detect and subtract multiple sinusoids cannot completely remove this bias effect for IIp-DFT.

Computation times In Fig. 3.17 we show algorithm runtimes for varying signal lengths, for single and multiple sinusoidal cases. The results are obtained from MATLAB's `timeit`, using an Intel Core i7-12800H processor. As discussed in Section 3.3.1, FFT-ESPRIT has an asymptotic time complexity of $\mathcal{O}(N \log N)$, which is juxtaposed onto the plot at larger N. For larger signals, the time complexity of ESPRIT ($\mathcal{O}(N^3)$) and Algorithm 1 ($\mathcal{O}(N^2 \log N)$) are evident. For the case of $P = 1$ sinusoid, ESPRIT and Algorithm 1 require ≈ 70 seconds at signal lengths $N = 2^{13}$ and $N = 2^{16}$ respectively.

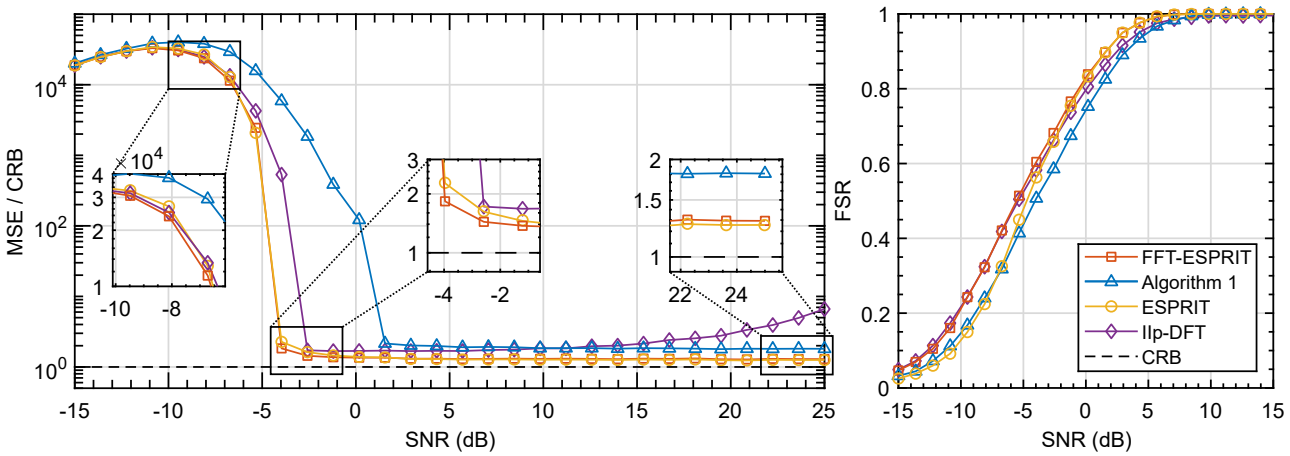

Figure 3.16: Simulation results of varying SNR for a pair of well-separated sinusoids ($P = 2$) with a fixed signal length of $N = 2^7$.

FFT-ESPRIT has a clear advantage due to the fast-multiplication of Algorithm 3, only taking ≈ 0.07 seconds at signal length $N = 2^{16}$.

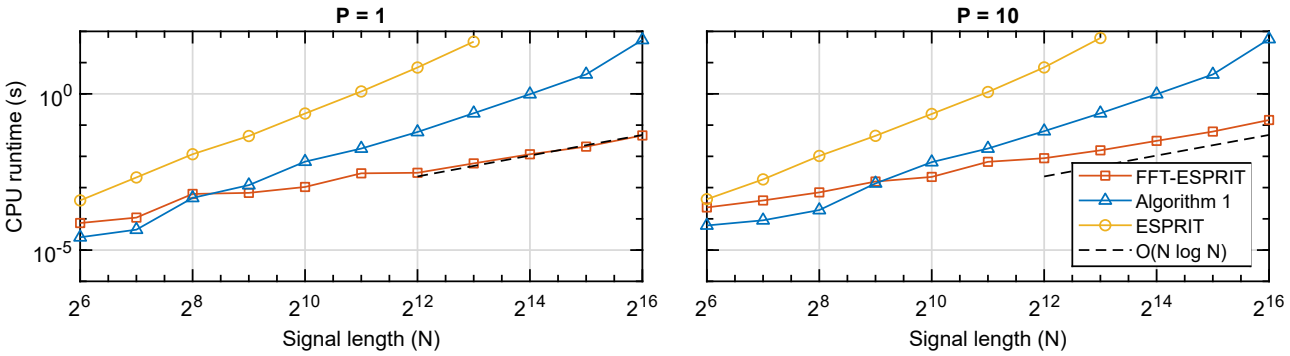

Figure 3.17: Simulation results of CPU runtimes versus signal length for the number of sinusoids $P = 1$ (left) and $P = 10$ (right). The timing in seconds is measured with MATLAB's `timeit`. The same asymptotic complexity line of $\mathcal{O}(N \log N)$ is shown on each plot.

Discussion Two FFT-based ESPRIT algorithms leveraging the kernels of the DFT matrix and truncated DFT matrix have been introduced. By employing a DFT kernel to estimate the signal subspace, both algorithms manage computational complexity below $\mathcal{O}(N^3)$. In the full DFT context of Algorithm 1, the discrepancy between the Vandermonde matrix and DFT kernel $\boldsymbol{A}_L^{\mathrm{T}}\boldsymbol{W}_L^*$ results in a matrix populated with the Dirichlet kernel evaluated at the variance between actual frequencies and the DFT grid. This discrepancy is speculated to prompt a subspace swap at a diminished threshold relative to the traditional ESPRIT, evident from its altered SNR transitional threshold in MSE.

FFT-ESPRIT (Algorithm 4) offers a partial solution, incorporating the IIp-DFT estimator in its off-grid kernel formulation of a truncated DFT matrix. Performance bounds suggest its superiority over the conventional ESPRIT in lower SNR regimes, a fact validated by numerical simulations. With its quasi-linear time complexity of $\mathcal{O}(N \log N)$ and close asymptotic performance to ESPRIT at high SNRs, FFT-ESPRIT emerges as a viable alternative for real-time applications with extensive signal lengths, exhibiting super-resolution prowess without the biases seen in interpolated DFT algorithms. In a broader context, FFT-ESPRIT can be viewed as a matrix pencil update of the signal model offered by the IIp-DFT algorithm with super-resolution.

3.4 Exact identification of nonlinear dynamical systems

Ideas from inverse modeling and data-driven system identification techniques are well situated for nonlinear dynamical systems in engineering domains. Classically, these techniques develop a nonparametric or parametric model of a physical system from coordinates, e.g. measurements. Parametric models require full state and latent variables of the system, which can be unknown in experiments. To deal with this, nonparametric identification methods can be leveraged since they only require input-output measurements, e.g. block-oriented Volterra [Réb+11], NARMAX [Bil13], and neural network models [Mas+00], since they are able to regress to functional mapping between inputs and outputs with high accuracies. However, they suffer from interpretability and the mappings can have no physical significance with respect to the dynamics of the underlying system. For that reason, identification of nonparametric models are often coined as a black-box method.

An alternative semi-parametric method named the Sparse Identification of Nonlinear Dynamics (SINDy), is a data-driven model discovery framework introduced to identify the ordinary differential equations (ODEs) of dynamical systems in the form $\dot{z}(t) = f(z(t))$; with known measurable state variables $z(t) \in \mathbb{R}^M, \forall t \in [0, T]$, from candidate state-dependent functions $f(z(t)) : \mathbb{R}^M \to \mathbb{R}^M$ [BPK16]. In discrete matrix vector-form the dynamics can be written for the jth state measurements of time-length M as:

$$\dot{\boldsymbol{z}}_j = \boldsymbol{\Theta}(\boldsymbol{z})\boldsymbol{\xi}_j, \quad j = 1, \cdots, N \tag{3.47}$$

for a predetermined library matrix of P candidate functions $\boldsymbol{\Theta} \in \{\mathbb{R}^{M \times P} : M \geq P\}$. This type of problem has equivalents in other domains, such as dictionary learning in signal processing or feature

selection in machine learning. For ease of notation we drop the $(\boldsymbol{z})$ from the library matrix henceforth. The goal is to extract the true governing dynamics with K sparsity:

$$\hat{\boldsymbol{\xi}}_j = \arg\min_{\boldsymbol{\xi}_j} \{ \ \|\boldsymbol{\Theta}\boldsymbol{\xi}_j - \dot{\boldsymbol{z}}_j\|_2^2 \ \} \quad \text{s.t.} \quad \|\boldsymbol{\xi}_j\|_0 = K, \quad j = 1, \ldots, N \tag{3.48}$$

where the ℓ_0 pseudo-norm is the card$(\boldsymbol{\xi}_j)$. However, Eq. (3.48), known as the best subset problem [Mil84a], is NP-hard and requires $\binom{P}{k}$ combinatorial search for unknown k. Thus, a computationally feasible form of the ℓ_0 pseudo-norm is highly sought for which selects the true sparse model, i.e. $\mathbb{P}(\hat{\boldsymbol{\mathcal{S}}}_j = \boldsymbol{\mathcal{S}}_j^*) \to 1$, for an estimated support $\hat{\boldsymbol{\mathcal{S}}}_j \coloneqq \{1; \ \hat{\xi}_j[k] \neq 0, k = 1, \ldots, P\}$ and true support $\boldsymbol{\mathcal{S}}_j^* \coloneqq \{1; \ \xi_j^*[k] \neq 0, k = 1, \ldots, P\}$. This framework combines elements of both black-box and white-box modeling approaches, and is considered a grey-box method.

SINDy has been applied to a large variety of dynamical systems, including nonlinear [LC22] and hysteretic [LN19] mechanical oscillators, the boundary volume problem of elastic beams [SBK21], reduced-order models of fluid flows [LB18], and multiple timescale dynamics [BK20]. Application of SINDy leads to parsimonious and interpretable solutions but suffers from many practical aspects when applied experimentally:

1. SINDy requires the inclusion of potential functions to be provided to form the library's basis. Too large of a basis leads to a violation of correlation conditions, i.e. multicollinearity for regression [FG67] and sparse regression [ZY06]. A large basis of many functions might be provided by practitioners in the case of completely unknown dynamics, which limits the applicability and reliability of sparse regression algorithms. Additionally, systems with unobservable latent variables, such as hysteresis, cannot be measured and their existence must be inferred.

2. The effect of noise on SINDy occurs from two aspects: noise intrinsic to the measurement data and noise introduced when making numerical approximations of derivatives or integrals. For the former, a variety of methods such as local and global denoising techniques [CPD22], by using a more robust optimization procedure [CPD21], or by enforcing simultaneously denoising and system recovery in optimization [HID22] can be used.

   For the latter, integral (weak) formulations of SINDy have been devised to mitigate noise propagated by numerical derivatives. The most obvious method [SM17] replaces the problem formulation by numerically estimating the integral formulation of SINDy. The method devised

by Messenger and Bortz [MB21] utilizes test functions for integration by parts to estimate the derivative, while the occupation kernel technique by Rosenfeld et al. [Ros+19] uses test functions for estimating the derivative via the fundamental theorem of calculus.

3. The hyperparameters used in the SINDy framework are intrinsically tied to the problem formulation and estimator. Thus, they are tuned by model selection algorithms: usually the minimization of an information criterion, through Bayesian or frequentist methods, or heuristically, see [DTY18] for a good overview. However, these selection criteria are prone to interpretability: the work by [Man+17] shown that minimization of information criteria is not always likely to select the exact model; the work by [CPD21] shown that corner selection for L-curve techniques can fail when the L-curve has multiple corners.

4. In the SINDy framework, the initial values are neglected from identification: this may be appropriate when dynamic systems are weakly nonlinear, are not chaotic, and tend to a steady-state. In practice, the initial condition is not estimated and is provided, which equates to assuming that noise does not affect this initial condition. It is critical to acknowledge that estimating the initial values have practical benefits when SINDy is used for model predictive control or forecasts.

Problematic identification can arise from dynamics corrupted by noise, finite data lengths, and a highly correlated library matrix. Furthermore, the estimator and the model selection algorithm should allow for an interpretable way for tuning hyperparameters. Specifically, we are interested in the property of exactly recovering the subset of candidate functions which make up the dynamics of the nonlinear model, i.e. the oracle variable selection $\mathbb{P}(\hat{\boldsymbol{\mathcal{S}}}_j = \boldsymbol{\mathcal{S}}_j^*) \to 1$.

The original SINDy algorithm employs the sequentially thresholded least squares (STLS) to solve Eq. (3.48). However, the STLS method introduces bias against coefficients with low magnitudes due to an increasing threshold parameter. It can be likened to a backward selection greedy algorithm, where coefficients of candidate functions are hard thresholded during sequential least squares on smaller supports until convergence. If a true coefficient is prematurely thresholded during optimization, the corresponding governing equation cannot be recovered, e.g. see [BNC18]. To overcome these limitations, an extension of SINDy incorporates bootstrap ensembling techniques (E-SINDy). E-SINDy utilizes statistics from the bootstrapped models, leading to enhanced robustness in variable selection

for finite and noisy data. In this study, we specifically refer to E-SINDy using the STLS estimator with a median bagging inclusion probability of ≈ 0.6. E-SINDy was recently shown that its approximations converge to a Bayesian inference via Markov chain Monte Carlo solution with a horseshoe prior [Gao+23a].

An alternative to the STLS stems from the Lasso formulation[2] which involves convex minimization of the squared ℓ_2 norm of the residual along with a penalized ℓ_1 norm. Literature in the statistical domain [Tib96] and signal processing domain [CD98] have characterized the theoretical performance of this convex penalty. One estimator with oracle properties is the Adaptive Lasso [Zou06] or iterative reweighted ℓ_1 minimization (IRL1) [CRT06], which uses a re-weighted ℓ_1 penalty. The reweighting scheme adjusts the ℓ_1 penalty by incorporating the individual coefficients from the previous iteration. The reweighted ℓ_1 penalty is stage-wise convex allowing for efficient computation through homotopy continuation methods [Efr+04; AR13]. However, similar to STLS, increasing the penalty parameter in the Lasso variant leads to the shrinkage of smaller coefficients of candidate functions.

Greedy and convex ℓ_1 penalty methods, including STLS and IRL1, occasionally achieve suboptimal sparse solutions since they approximate Eq. (3.48). This includes results such as $\hat{\boldsymbol{\mathcal{S}}}_j \supseteq \boldsymbol{\mathcal{S}}_j^*$, i.e. a sparse solution that includes the true support but is over complete, and/or $\boldsymbol{\Theta}\boldsymbol{\xi}_j^* \approx \boldsymbol{\Theta}\hat{\boldsymbol{\xi}}_j : \|\hat{\boldsymbol{\xi}}_j\|_0 \neq K$, i.e. a sparse solution that approximates the solution but does not satisfy the sparsity K. Several other non-convex penalties have been proposed in the literature to close the gap between Eq. (3.48) and its approximations. These include separable penalties such as the smoothly clipped absolute deviation [FL01], the Dantzig selector [CT07], and the minimax concave penalty [Zha10]. To maintain several desirable properties relevant to Eq. (3.48) and to promote further sparsity, non-separable non-convex penalties have been proposed such as sparse Bayesian learning [WN10], the moderately clipped Lasso [KLK15], or the Mnet [Hua+16].

In this study, we wish to introduce the Trimmed Lasso for robust identification of models (TRIM) for nonlinear dynamical initial value problems. Specifically, the Trimmed Lasso's non-convex penalty offers exact control over the desired level of sparsity for regression. Thus, its formulation is closer to Eq. (3.48) than previously mentioned convex methods for sparse estimation. While originally introduced over a decade ago in [CDD09] and its name coined recently by [BCM17], developments

[2]It is worth noting that the Lasso formulation can incorporate physics-based constraints such as structural symmetry or energy-based constraints, as explored in [LB18], but these must be known *a priori* and are not focused on for this general study.

in optimization have made convex approximations of the Trimmed Lasso. TRIM has a very intuitive hyperparameter tuning process, which directly probes the Pareto front. While E-SINDy has recently been shown to have oracle properties in [Gao+23b], and the IRL1/Adaptive Lasso by [Zou06], we will demonstrate across different dynamical systems that TRIM is postulated to have lenient conditions to satisfy its oracle properties, and thus better performance.

Our contributions can be described as follows: We provide the methodology of TRIM for identification for uncertainty quantification for sparse nonlinear dynamic initial value problems under high noise, multicollinearity, and finite data length. We affirm more recent studies of sparse regression that Lasso-based formulations with non-convex penalties can achieve better performance than the STLS used in SINDy and E-SINDy. Additionally, uncertainty quantification comes after model section for TRIM, meaning that resampling techniques are performed for only one set of hyperparameters. This is a computational advantage over E-SINDy, which requires multiple bootstrapping models per hyperparameter, from which model selection criteria identifies the dynamics. In this disseratation, TRIM is demonstrated on the the Bouc Wen oscillator from the nonlinear dynamics benchmark of Noël and Schoukens, 2016.

The notations are specified: We denote $\boldsymbol{x}$ and $\boldsymbol{X}$ as vectors and matrices respectively. The ith column vector of a matrix is denoted $\boldsymbol{X}_i$. A noise perturbed value x is denoted $\tilde{x}$ while an estimate is denoted $\hat{x}$. The variance of the white Gaussian noise is denoted σ^2. The ℓ_p norm is denoted $\|\boldsymbol{X}\|_p$. The Hadamard (element-wise) product and inner product between $\boldsymbol{x}, \boldsymbol{y}$ is denoted $\boldsymbol{x} \circ \boldsymbol{y}$ and $\langle \boldsymbol{x}, \boldsymbol{y} \rangle$ respectively.

3.4.1 Preliminaries

In this section, we introduce preliminaries within the SINDy framework of nonlinear dynamical model identification. Specifically we mention two sparsity promoting regressions in the literature. Finally, data-preprocessing and sparsity promoting regressions require tuning of hyperparameters, which we elucidate via automatic methods.

SINDy SINDy is a data-driven model discovery framework which was originally introduced to identify the governing equations in the form of Eq. (3.48). The underlying assumption is that the underlying

dynamics $f(z(t))$ are linearizable by $P \geq 2$ sparse candidate functions, such that:

$$\dot{z}(t) = f(z(t)) \approx \sum_{i=1}^{P} \xi_i \theta_i(z(t)) \tag{3.49}$$

where $\Theta = \{\theta_i(z(t))\}$ is an over complete set of candidate functions. Thus, the goal is to determine the weights ξ_i such that the balance between error and parsimony of the approximation is optimal, and ideally retrieving the true governing equations. The vector-matrix form of Eq. (3.48) can be expanded as:

$$\begin{gathered}
\dot{\boldsymbol{z}}_j = \begin{bmatrix} \dot{x}_j(t_1), & \dot{x}_j(t_2), & \cdots, & \dot{x}_j(t_M) \end{bmatrix}^{\mathrm{T}} \in \mathbb{R}^M; \\
\boldsymbol{\Theta}(\boldsymbol{z}) = \begin{bmatrix} \theta_1(z(t_1)) & \theta_2(z(t_1)) & \cdots & \theta_P(z(t_1)) \\ \theta_1(z(t_2)) & \theta_2(z(t_2)) & \cdots & \theta_P(z(t_2)) \\ \vdots & \vdots & \ddots & \vdots \\ \theta_1(z(t_M)) & \theta_2(z(t_M)) & \cdots & \theta_P(z(t_M)) \end{bmatrix} \in \mathbb{R}^{M \times P}; \\
\boldsymbol{\xi}_j = \begin{bmatrix} \xi_{j,1}, & \xi_{j,2}, & \cdots, & \xi_{j,P} \end{bmatrix}^{\mathrm{T}} \in \mathbb{R}^P
\end{gathered}$$

where the columns of the library matrix $\boldsymbol{\Theta}(\boldsymbol{z})$ are prescribed candidate functions (e.g. $\boldsymbol{z}$, $\boldsymbol{z}^2$, $\sin(\boldsymbol{z})$). SINDy is deemed a semi-parametric method since its intended to accommodate a parametric candidate library with a non-parametric data-driven regression. In this study, we restrict ourselves to the case $M \geq P$, i.e. a problem where the data lengths are larger than the potential candidate functions.

Sparsity promoting regression In order to approximate Eq. (3.48), [BPK16] proposes the sequentially thresholded least squares (STLS) estimator. In summary, it applies a hard thresholding to the coefficients $|\boldsymbol{\Xi}| < \varphi$ and sequentially performs least squares on new subsets of the support:

$$\begin{aligned}
\mathcal{S}(\hat{\boldsymbol{\Xi}}^{(i)}) &= \{ |\hat{\boldsymbol{\Xi}}^{(i)}| \geq \varphi \}; \quad \forall \varphi > 0, \\
\hat{\boldsymbol{\Xi}}^{(i+1)}_{\mathrm{STLS}} &= \underset{\boldsymbol{\Xi} \in \mathcal{S}^{(i)}}{\arg\min} \{ \ \| \boldsymbol{\Theta}\boldsymbol{\Xi} - \dot{\boldsymbol{Z}} \|_2^2 \ \} \quad \text{s. t.} \quad \mathcal{S}^{(i)} = \mathcal{S}(\hat{\boldsymbol{\Xi}}^{(i)})
\end{aligned} \tag{3.50}$$

for arbitrary i iterations, where $\boldsymbol{\Xi} = \begin{bmatrix} \boldsymbol{\xi}_1 & \cdots & \boldsymbol{\xi}_P \end{bmatrix}$, $\dot{\boldsymbol{Z}} = \begin{bmatrix} \dot{\boldsymbol{z}}_1 & \cdots & \dot{\boldsymbol{z}}_N \end{bmatrix}$, and $\mathcal{S}^{(i)}$ is the ith support of $\hat{\boldsymbol{\Xi}}$ which satisfies the constraint. However, STLS exhibits similarities to a backward selection greedy regressions where if a true coefficient is thresholded at an early stage during the iterative optimization, the true underlying equation cannot be recovered. Yet, STLS has been successfully applied to a large variety of dynamic systems, and only requires a single thresholding parameter ζ. Additionally, Eq. (3.50) has a computational complexity of $\mathcal{O}(MP^2)$ per thresholding parameter, making it efficient and easy to implement.

Alternatively, the Lasso estimator introduced by [Tib96], is well suited to sparse identification because of its property that it sets some coefficients exactly equal to zero:

$$\hat{\boldsymbol{\xi}}_{\text{Lasso},j} = \arg\min_{\boldsymbol{\xi}_j} \{ \ \|\boldsymbol{\Theta}\boldsymbol{\xi}_j - \dot{\boldsymbol{z}}_j\|_2^2 + \lambda\|\boldsymbol{\xi}_j\|_1 \ \}; \quad \forall\lambda > 0 \tag{3.51}$$

where the ℓ_1 term promotes the sparsity of the regression, the ℓ_2 term keeps the solution close to the measurement data, and λ is the regularization term which balances between the two. For the regularization path $0 < \lambda_1 < \ldots < \lambda_{\max}$ the solution path is piecewise linear, and thus solved efficiently by least angle regression [Efr+04] or homotopy methods [AR13]. Thus, the Lasso is typically stated with a per iteration complexity of $\mathcal{O}(MP)$ per regularization parameter.

Recent works in statistical and compressed sensing domains has provided theoretical performance for the Lasso, assuming that $\boldsymbol{\xi}^*$ is sparse and abides by the *beta-min* conditions [Zou06]: to ensure that a sparse model is obtained where the true sparse model is in the subset ($\mathbb{P}(\hat{\boldsymbol{\mathcal{S}}}_j \supseteq \boldsymbol{\mathcal{S}}_j^*) \to 1$ as $(M \to \infty)$) the library matrix $\tilde{\boldsymbol{\Theta}}$ must abide by the restricted eigenvalue condition [BV11]; to ensure that the exact sparse model is obtained ($\mathbb{P}(\hat{\boldsymbol{\mathcal{S}}}_j = \boldsymbol{\mathcal{S}}_j^*) \to 1$ as $(M \to \infty)$), the library matrix must abide by the irrepresentable condition [BV11]. When these conditions are not met, the Lasso produces large bias for the non-zero coefficients as it continuously shrinks all coefficients toward zero.

To correct for this behavior, the Adaptive Lasso [Zou06] or IRL1 [CRT06] replaces the ℓ_1 with a penalized weight vector:

$$\hat{\boldsymbol{\xi}}_{\text{IRL1},j}^{(i+1)} = \arg\min_{\boldsymbol{\xi}_j} \{ \ \|\boldsymbol{\Theta}\boldsymbol{\xi}_j - \dot{\boldsymbol{z}}_j\|_2^2 + \lambda\|\hat{\boldsymbol{w}}_j^{(i)} \circ \boldsymbol{\xi}_j\|_1 \ \}; \quad \forall\lambda > 0 \tag{3.52}$$

where the weight vector is defined as a function of previous selection's coefficients:

$$\hat{\boldsymbol{w}}_j^{(i)} \coloneqq \frac{1}{|\hat{\boldsymbol{\xi}}_{\text{IRL1},j}^{(i)}|^\gamma}; \quad \forall\gamma > 0 \tag{3.53}$$

for additional hyperparameters of i iterations and γ. The IRL1 was recently featured for nonlinear dynamical model identification by [CPD21]. This extension of the Lasso has oracle variable selection under less strict properties than the Lasso. Note that, if $|\hat{\boldsymbol{\xi}}_{\text{Lasso}}|$ is large, the Adaptive Lasso employs a smaller penalty (less shrinkage) which yields a smaller bias in the ℓ_2 sense. Since the irrepresentable condition for the Lasso is hard to meet in practice, the Lasso's estimates in the first stage effectively reduces the number of false positives for the Adaptive Lasso in the subsequent stage. This is due to the fact that the Lasso has high probability of the screening property [BV11] and that for $\hat{\boldsymbol{\xi}}_{\text{Lasso}} = 0 \to \hat{\boldsymbol{\xi}}_{\text{ALasso}} = 0$.

Automatic hyperparameter tuning For all regularized problems in this study, hyperparameter terms must be chosen in some optimal sense. These problems with a single hyperparameter λ have the form:

$$\arg\min_{\boldsymbol{\beta}} \left\{ \ \|\boldsymbol{X}\boldsymbol{\beta} - \boldsymbol{y}\|_2^2 + \mathcal{R}(\boldsymbol{\beta}, \lambda) \ \right\} \tag{3.54}$$

where $\mathcal{R}(\square)$ is an operator which applies a penalty on the solution for arbitrary $\boldsymbol{X}$, $\boldsymbol{\beta}$, $\boldsymbol{y}$. For model-based regressions, some proxy of the sparsity is weighed against the likelihood of the model. These parametric information criterion are general to the model and are well known, such as the Akaike information criterion (AIC) and its corrected variant (AICc), The Bayesian information criterion (BIC), to name a few. The AIC has been shown to be an *efficient* selector, since it uses the Kullback-Leibler divergence to balance model complexity and goodness of fit. The BIC instead tries to maximize the posterior model probability and thus is a *consistent* selector. The general form for information criterion is evaluated for all possible models $\mathcal{M}$:

$$\arg\min_{\hat{\boldsymbol{\beta}} \in \mathcal{M}} \left\{ \ \|\boldsymbol{X}\hat{\boldsymbol{\beta}} - \boldsymbol{y}\|_2^2 + \Pi\sigma^2 \|\hat{\boldsymbol{\beta}}\|_0 \ \right\} \tag{3.55}$$

where the left-hand side is the residual sum of squares and Π is a stochastic penalty. Since the true σ^2 is unknown, the least squares estimate of $\hat{\sigma}^2_{\mathrm{LS}} \coloneqq \|\boldsymbol{X}\hat{\boldsymbol{\beta}}_{\mathrm{LS}} - \boldsymbol{y}\|_2^2/(M-P)$ for normally distributed errors is commonly used instead. Eq. (3.55) can be shown to have the form of the AIC, BIC, and others with a linear penalty Π in Section 3.4.1. Since the intent is to identify the true models, i.e. *consistency*, we opt for usage of the corrected risk inflation criterion (RICc), which has shown superior performance in literature [ZS10; KKC12]. In short, the *risk* refers to the expected prediction error of a model; RIC adjusts the maximum increase in risk due to selecting predictors rather than knowing the *correct* predictors, and is proven to be a *consistent* selector [FG94].

Criterion	**Stochastic penalty** (Π)
AIC	$\Pi_{\mathrm{AIC}} = 2$
AICc	$\Pi_{\mathrm{AICc}} = 2 + \frac{2(\mathrm{card}(\boldsymbol{\beta})+1)}{M-\mathrm{card}(\boldsymbol{\beta})-1}$
BIC	$\Pi_{\mathrm{BIC}} = \log M$
HQC	$\Pi_{\mathrm{HQC}} = c \log\log M, \quad \text{for } c > 2$
RIC	$\Pi_{\mathrm{RIC}} = 2 \log P$
RICc	$\Pi_{\mathrm{RICc}} = 2(\log P + \log\log P)$

Table 3.5: Common penalty factors in parametric information criterions. Note that, the Hannan and Quinn criterion (HQC) requires a coefficient c to be chosen, see [HQ79].

When no model is known *a priori*, e.g. for denoising and derivatives estimations, nonparametric model selection techniques must be used. Commonly known are the leave-one-out and generalized cross-validation (GCV) methods. In this study, we propose an L-curve [Han92] be used for tuning λ. The L-curve represents a Pareto front on a log-log scale, with the penalty on the ordinate and the error on the abscissa:

$$\mathcal{L}_{\mathrm{c}}(\lambda) \coloneqq (a,\, o) \to \begin{cases} a \coloneqq \log \|\boldsymbol{X}\boldsymbol{\beta} - \boldsymbol{y}\|_2^2 \\ o \coloneqq \log \mathcal{R}(\boldsymbol{\beta}, \lambda) \end{cases} \tag{3.56}$$

The L-curve has the name due to the fact an L shape is formed, occasionally with a well-defined corner point which would have a large curvature. Certain methods exist to find the maximum curvature, some notable being [Han92; CC20]. We opt for our own method which determines the maximum curvature through arc length approximations along the L-curve.

While the L-curve is originally a heuristic tool in choosing the regularization parameter, a theoretical basis on why regularization parameters corner point works well has been studied in [Han92; Reg96]. A recent Bayesian formulation of the regularization problem [AIB23], demonstrates that the L-curve is a graphical way of searching for the maximum *a posteriori* solution after marginalization over the priors. Additionally, the L-curve corner criterion has an advantage over the cross validation which presumes noise that is additive white Gaussian (AWGN) [KBS19].

To see this, consider the leave-one-out cross-validation set which has the expectation:

$$\mathbb{E}\big((\boldsymbol{X}\hat{\boldsymbol{\beta}})^{\mathrm{out}} - \tilde{\boldsymbol{y}}\big)^2 = \mathbb{E}\big(((\boldsymbol{X}\hat{\boldsymbol{\beta}})^{\mathrm{out}} - \tilde{\boldsymbol{y}})^2\big) + \sigma^2 + 2\,\mathrm{cov}\left((\boldsymbol{X}\hat{\boldsymbol{\beta}})^{\mathrm{out}},\, \tilde{\boldsymbol{y}}\right)$$

where $\mathbb{E}(\square)$ is the expectation operator, $\square^{\mathrm{out}}$ is an estimate on a portion of data, and $\tilde{\boldsymbol{y}} = \boldsymbol{y}^* + \boldsymbol{\varepsilon}$ is the true data with AWGN of variance $\mathbb{E}(\boldsymbol{\varepsilon}) = \sigma^2$. Cross-validation explicitly assume that $\mathrm{cov}\left((\boldsymbol{X}\hat{\boldsymbol{\beta}})^{\mathrm{out}},\, \tilde{\boldsymbol{y}}\right) \asymp \mathbf{0}$. Thus, if the regularized expression of Eq. (3.55) describes the denoising scenario, a smooth signal plus correlated noise will regress towards a solution of a less smooth signal plus white Gaussian noise. A denoising demonstration of this phenomena can be found in Fig. 3.18, where it's shown that the L-curve is the most robust when this assumption is violated. In this sense, the L-curve has an advantage that it does not rely on an *a priori* statistical measure; corner points are where the solution norm and penalty have a Pareto front. However, the L-curve fails when the discrete picard condition is not met [Han90], i.e. the Fourier coefficients of the data $\tilde{\boldsymbol{y}}$ decay to zero faster than their singular values.

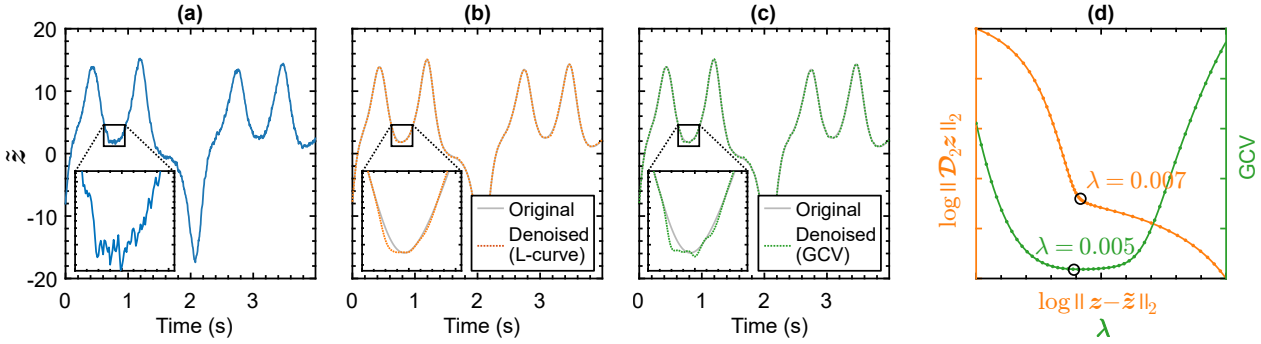

Figure 3.18: Demonstration of the effect of autocorrelation on model selection criterion for the non-parametric problem of the form of Eq. (B.4). In **(a)**, we simulate the popular Lorenz 63 system and corrupt the second degree of freedom (DOF) with correlated noise and plot its path. Tikhonov regularized denoising defined in Eq. (B.4) is used to denoise the data, where the L-curve and GCV in **(d)** is used to determine the regularization parameter. Tikhonov denoising in **(b)** using the corner point of the L-curve (RMSE= $1.3 \cdot 10^{-3}$) can denoise correlated noise better than the minimum of the GCV (RMSE= $1.9 \cdot 10^{-3}$) in **(c)**. The full systematic parameters used for the simulation are given in Appendix B.4.3.

3.4.2 TRIM overview

In this section, we introduce the methodology of TRIM, first by introducing the non-convex penalty of the Trimmed Lasso, followed by an intuitive hyperparameter tuning method which directly probes the Pareto front and allows for a forward selection if higher accuracy is needed. Finally, TRIM extends upon the usual derivative form of SINDy to estimate the initial values of nonlinear dynamical models.

The Trimmed Lasso For the problem of Eq. (3.48), a solution that respects the ℓ_0 pseudo-norm becomes computationally infeasible as P grows. However, an attractive property of Eq. (3.48) is the ability to enforce the sparsity. An ideal penalty would be able to be penalized by λ and enforce sparsity K simultaneously, which would take the form of:

$$\hat{\boldsymbol{\xi}}_j = \arg\min_{\boldsymbol{\xi}_j} \left\{ \|\boldsymbol{\Theta}\boldsymbol{\xi}_j - \dot{\boldsymbol{z}}_j\|_2^2 + \mathcal{R}(\boldsymbol{\xi}_j, \lambda) \right\} \quad \text{s. t.} \quad \|\boldsymbol{\xi}_j\|_0 = K$$

One such penalty, the Trimmed Lasso, has a non-convex penalty that satisfies both control of the sparsity and can be penalized. It is defined as [CDD09]:

$$\mathcal{T}(\boldsymbol{\xi}_j, k) = \sum_{i=k+1}^{P} |\xi_{j,i}| \tag{3.57}$$

where $|\xi_{j,1}| \geq |\xi_{j,2}| \geq \ldots \geq |\xi_{j,P}|$ are the sorted descending entries of the coefficient vector. Intuitively, Eq. (3.57) penalizes the $k+1$ entries by the ℓ_1 distance between $\boldsymbol{\xi}_j$ and the closest k sparse vector. This forms a proxy for Eq. (3.48):

$$\hat{\boldsymbol{\xi}}_{\text{TRIM},j} = \arg\min_{\boldsymbol{\xi}_j} \left\{ \|\boldsymbol{\Theta}\boldsymbol{\xi}_j - \dot{\boldsymbol{z}}_j\|_2^2 + \lambda \mathcal{T}(\boldsymbol{\xi}_j, k) \right\}; \quad \forall \lambda > 0 \tag{3.58}$$

The Trimmed Lasso is a generalization of the standard Lasso, which recovers the Lasso when $k = 0$. For $k > 0$ and an increasing value of λ, the shrinkage effect on the smallest $P - k$ entries increases. When λ reaches or exceeds a threshold $\acute{\lambda}$, the smallest $P - k$ entries are forced to zero [ABN21]. This exactness property uniquely characterizes the Trimmed Lasso through the existence of $\acute{\lambda}$, and for λ sufficiently large, Eq. (3.58) becomes a solution to the constrained best subset selection problem as defined in Eq. (3.48) [ABN21; GTT18].

However, if one sets λ arbitrarily large, so does the non-convexity of the problem. The optimization of Eq. (3.58) then is carried out by incrementally solving for λ, where $\lambda_1 < \lambda_2 < \ldots < \lambda_i < \ldots$. For each λ_i greater than or equal to $\acute{\lambda}$, the estimate $\hat{\boldsymbol{\xi}}_j(\lambda_i \geq \acute{\lambda})$ is projected onto the closest k sparse vector. While the Trimmed Lasso has an intuitive but non-convex form, its "convexification" allows for efficient computation. An example of this can be formulated using an alternating minimization formulation [BCM17] of Eq. (3.58):

$$\begin{aligned} f(\boldsymbol{\xi}_j) &= \|\boldsymbol{\Theta}\boldsymbol{\xi}_j - \dot{\boldsymbol{z}}_j\|_2^2/2 + \lambda \mathcal{T}(\boldsymbol{\xi}_j, k) + \eta \|\boldsymbol{\xi}_j\|_1 \\ f_1(\boldsymbol{\xi}_j) &= \|\boldsymbol{\Theta}\boldsymbol{\xi}_j - \dot{\boldsymbol{z}}_j\|_2^2/2 + (\eta + \lambda)\|\boldsymbol{\xi}_j\|_1 \\ f_2(\boldsymbol{\xi}_j) &= \langle \boldsymbol{\gamma}, \boldsymbol{\xi}_j \rangle \end{aligned} \tag{3.59}$$

such that $f(\boldsymbol{\xi}_j) \approx f_1(\boldsymbol{\xi}_j) - f_2(\boldsymbol{\xi}_j)$ and:

$$\boldsymbol{\chi}_j = \arg\operatorname{sort}(|\boldsymbol{\xi}_j|); \quad \text{and} \quad \boldsymbol{\gamma}[\chi_{j,i}] = \begin{cases} \lambda \operatorname{sign}(\boldsymbol{\xi}_j[\chi_{j,i}]) & \text{if } i \leq k \\ 0 & \text{if } i > k \end{cases}; \quad \text{for } i = 1, \ldots, P \tag{3.60}$$

where $\arg\operatorname{sort}(\cdot)$ returns a vector of descending index values and the square brackets indicate the vector entry with 1-indexing. Given the convexity of $f_1(\boldsymbol{\xi}_j)$ and $f_2(\boldsymbol{\xi}_j)$, the alternating minimization scheme of Algorithm 5 can be utilized. More efficient implementations have been algorithmically pursued via alternating direction method of multipliers (ADMM) [BCM17], block coordinate descent [Yun+19], and a surrogate penalty called the generalized soft-min coupled with the fast iterative shrinkage-thresholding algorithm (FISTA) [ABN21]. These implementations make Eq. (3.58) computationally feasible, with each bringing its own unique theoretical convergences and guarantees.

Algorithm 5 Alternating minimization of Trimmed Lasso

Input: ℓ_2 norm scaled $\breve{\boldsymbol{\Theta}}$ (see Appendix B.4.2), $\dot{\boldsymbol{z}}$, sparsity k, $\nu \geq 5$, $\eta = 10^{-3}$, tolerance ε
Output: $\breve{\boldsymbol{\xi}}_{\text{TRIM}}$

$j \leftarrow 1$
$\boldsymbol{\lambda} \leftarrow \exp(\texttt{logspace}(\|\dot{\boldsymbol{z}}\|_2 \cdot 10^{-3},\, \|\dot{\boldsymbol{z}}\|_2,\, \nu))$ ▷ See [ABN21, Theorem 2.1].
for $i = 1$ to ν **do**
  $\lambda \leftarrow \boldsymbol{\lambda}_i$; $\breve{\boldsymbol{\xi}}^{(1)} \leftarrow \mathcal{N}(\mathbf{0}, \mathbf{1})$; $s \leftarrow 1$
  while $\|\boldsymbol{\Theta}\breve{\boldsymbol{\xi}}^{(s)} - \dot{\boldsymbol{z}}\|_2^2/2 + \lambda\mathcal{T}(\breve{\boldsymbol{\xi}}^{(s)}, k) + \eta\|\breve{\boldsymbol{\xi}}^{(s)}\|_1 > \varepsilon$ **do**
    $\boldsymbol{\gamma}^{(s)} \leftarrow$ Eq. (3.60)
    $\breve{\boldsymbol{\xi}}^{(s+1)} = \arg\min_{\boldsymbol{\xi}}\{\ \|\boldsymbol{\Theta}\boldsymbol{\xi} - \dot{\boldsymbol{z}}\|_2^2/2 + (\eta + \lambda)\|\boldsymbol{\xi}\|_1 - \langle\boldsymbol{\gamma}^{(s)}, \boldsymbol{\xi}\rangle\}$ ▷ Resolved using any Lasso solver.
    $s \leftarrow s + 1$
  end while
  if $\text{card}(\breve{\boldsymbol{\xi}}^{(s)}) = k$ **then**
    $\mathcal{M}(j) \leftarrow \breve{\boldsymbol{\xi}}^{(s)}$
    $\mathcal{L}(j) \leftarrow \|\boldsymbol{\Theta}\breve{\boldsymbol{\xi}}^{(s)} - \dot{\boldsymbol{z}}\|_2^2/2 + \lambda\mathcal{T}(\breve{\boldsymbol{\xi}}^{(s)}, k) + \eta\|\breve{\boldsymbol{\xi}}^{(s)}\|_1$
    $j \leftarrow j + 1$
  end if
end for
$\breve{\boldsymbol{\xi}}_{\text{TRIM}} \leftarrow \mathcal{M}(j) \leftarrow \arg\min_j\{\mathcal{L}(j)\}$ ▷ Take the support that gives the smallest residual.
return $\breve{\boldsymbol{\xi}}_{\text{TRIM}}$

This leads to the Trimmed Lasso having its sparsity k as its single tunable hyperparameter. The easiest implementation is to simply utilize the information criterion approaches in Eq. (3.55), namely RICc. Alternatively, we can utilize an augmented L-curve hyperparameter for tuning the Trimmed Lasso within the SINDy framework, i.e TRIM. This approach allows us to directly probe the Pareto frontier between the residual and the sparsity k:

$$\mathcal{L}_{\text{TRIM},j}(k) \coloneqq (a,\, o) \rightarrow \begin{cases} a \coloneqq \log\|\boldsymbol{\Theta}\hat{\boldsymbol{\xi}}_j - \dot{\boldsymbol{z}}_j\|_2 \\ o \coloneqq k \end{cases} \tag{3.61}$$

If one does not want to rely on minimization of information criterion, Eq. (3.61) facilitates an intuitive process for hyperparameter tuning. As the desired level of sparsity k increases, the solution residual generally decreases. The occurrence of a sudden drop in the residual is considered indicative of the parsimonious model, representing a corner point on the L-curve. Following the identification of this corner point, practitioners can further employ a forward step selection method, allowing for a trade-off between increased sparsity and a tolerated decrease in the residual distance between consecutive models (e.g., $\text{dist}(k_i, k_{i+1}) > \text{tol}$). Conversely, the hyperparameter tuning procedure of the STLS and IRL1 estimators of Section 3.4.1 increase the magnitude of their hyperparameter(s) to promote sparsity. It

is important to note that their on-grid hyperparameters do not guarantee a k sparse solution, whereas TRIM provides this guarantee. This automatic model selection process is demonstrated for the Lorenz system in Fig. 3.19.

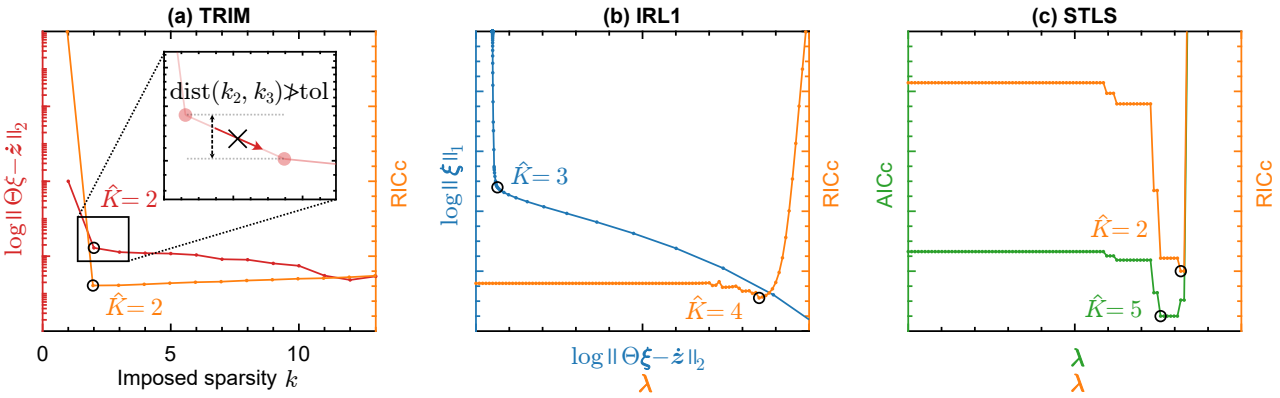

Figure 3.19: A demonstration of automatic model selection criteria paired with their respective sparse regression estimators for the noisy third DOF of the Lorenz 63 where the true sparsity is $K^* = 2$. In **(a)**, TRIM's corner point in the L-curve defined by Eq. (3.61) as well as RICc achieves the true sparsity ($\hat{K} = 2$). A forward step selection criteria is shown where an additional coefficient is permitted if the distance between the residuals satisfies a tolerance. In **(b)**, IRL1 obtains differing results: the L-curve method ($\hat{K} = 3$) and the RICc ($\hat{K} = 4$). In **(c)**, STLS obtains more consistent results with RICc ($\hat{K} = 2$) and more efficient results with AICc ($\hat{K} = 5$), confirming with theory. The full systematic parameters used for the simulation are given in Appendix B.4.3.

Initial value problem formulation Here we detail the initial value problem formulation for the SINDy framework. While the initial conditions for SINDy in the literature are often presented as known with exact certainty, this issue is frequently overlooked, whether intentionally or unintentionally. Specifically for TRIM, the classical derivative formulation of Eq. (3.47) is changed by adding the initial values z_0 to the problem formulation:

$$\begin{cases} \dot{z}(t) = f(z(t)) \approx \sum_{i=1}^{P} \xi_i \theta_i(z(t)) \\ z(t_0) = z_0 \end{cases} \quad ; \quad \forall t \geq t_0 \tag{3.62}$$

In matrix-vector notation, the integral formulation of the problem can be formulated as:

$$\boldsymbol{z}_j = \boldsymbol{T}_1 \boldsymbol{\Theta} \boldsymbol{\xi}_j + z_0 \mathbf{1}_M + \boldsymbol{\varepsilon}_q \tag{3.63}$$

where $\mathbf{1}_M \in \mathbb{R}^M$ a vector of ones and $\boldsymbol{T}_1$ is a matrix integral operator defined in Eq. (B.3). The integral formulation of [SM17], however, discards the initial values by regression on the augmented

data $\boldsymbol{z}'_j = \boldsymbol{z}_j - z_0\mathbf{1}_M$. Instead, we will treat the initial values as an additional coefficient. Using the Trimmed Lasso penalty and defining $\boldsymbol{\Gamma} \coloneqq \begin{bmatrix}\mathbf{1}_M & \boldsymbol{T}_1\boldsymbol{\Theta}\end{bmatrix}$, the corresponding minimization problem which minimizes the quadrature error is and allows initial value estimates is:

$$\hat{\boldsymbol{\psi}}_{\text{TRIM},j} = \underset{\boldsymbol{\psi}_j}{\arg\min}\{\ \|\boldsymbol{\Gamma}\boldsymbol{\psi}_j - \boldsymbol{z}_j\|_2^2 + \mathcal{T}(\boldsymbol{\psi}_j, k)\ \}; \quad \forall\lambda > 0 \tag{3.64}$$

where $\hat{\boldsymbol{\psi}}_j = \begin{bmatrix}-\hat{z}_{0,j} & \hat{\boldsymbol{\xi}}_j\end{bmatrix}^{\mathrm{T}}$ is the recovered initial values and the coefficients of the problem. The formulation for first-order ODEs benefits from estimating numerical quadrature instead numerical derivatives.

3.4.3 Results and discussion

In this subsection, we evaluate the performance of three sparsity-promoting estimators, paired with model selection criteria, in identifying a hysteretic oscillator. This oscillator is useful due to the fact that dynamical systems with dissipation and history can be modeled. Specifically, this includes the STLS estimator from the original SINDy[3] [BPK16], its ensembled counterpart E-SINDy[4] [Fas+22], the IRL1 estimator[5] by [AR13], and TRIM which implements the FISTA[6] implementation of the Trimmed Lasso. For IRL1, we fix the number of reweighting iterations to two, while keeping γ and λ tunable parameters. We will use SINDy and E-SINDy to denote the original and ensembled (median bagging) implementation of STLS. E-SINDy conducts 100 bootstrap resamples across all examples, requiring bootstrapping and ensembling for each thresholding parameter before performing model selection on the resultant ensembled models.

The default model selection criterion for each methods are: SINDy and E-SINDy with the model selection criterion RICc of Eq. (3.55), IRL1 with the L-curve corner criterion of Eq. (3.56), and TRIM with the L-curve criterion of Eq. (3.61). Unless otherwise mentioned, the TRIM with the L-curve criterion includes a forward step selection tolerance of tol = 5% with a distance measurement:

$$\text{dist}(k_i, k_{i+1}) = \frac{\|\boldsymbol{\Theta}\hat{\boldsymbol{\xi}}_j(k_i) - \dot{\boldsymbol{z}}_j\|_2^2}{\|\boldsymbol{\Theta}\hat{\boldsymbol{\xi}}_j(k_{i+1}) - \dot{\boldsymbol{z}}_j\|_2^2}$$

These model selection criteria are chosen due to their optimal performance observed by the authors in this study as well as the theoretical justifications in Section 3.4.1. If not indicated differently,

[3] `https://faculty.washington.edu/sbrunton/sparsedynamics.zip`
[4] `https://github.com/urban-fasel/EnsembleSINDy`
[5] `https://intra.ece.ucr.edu/~sasif/homotopy/`
[6] `https://github.com/tal-amir/sparse-approximation-gsm`

the hyperparameters for SINDy and E-SINDy are defined for a log-spaced grid of size 100, $\boldsymbol{\varphi} = \{10^{-3}, \dots, 10^{3}\}$, for IRL1 a log-spaced grid of size 75, $\boldsymbol{\lambda} = \{10^{-10}, \dots, 10^{6}\}$ and $\boldsymbol{q} = \{2, 2.5, \dots 5\}$, and for TRIM $\boldsymbol{k} = \{1, 2, \dots, 8\}$ and $\nu = 10$.

For all simulations, we recommend conditioning the library matrix to lower the condition number of the matrix, see Appendix B.4.2. To characterize the data and library matrix, we include the definition of noisy data:

$$\tilde{\boldsymbol{z}} \coloneqq \boldsymbol{z}^* + \boldsymbol{\varepsilon}; \quad \boldsymbol{\varepsilon} \sim \mathcal{N}(\mathbf{0}, \sigma^2 \mathbf{1}_M)$$

where the noise of variance $\mathbb{E}(\boldsymbol{\varepsilon}) = \sigma^2$. To assemble the library matrix, we use the notation for an n combinatorial polynomial, for example:

$$\mathcal{P}(\tilde{\boldsymbol{z}}_1, \tilde{\boldsymbol{z}}_2, n = 2) = \begin{bmatrix} \tilde{\boldsymbol{z}}_1 & \tilde{\boldsymbol{z}}_2 & \tilde{\boldsymbol{z}}_1^2 & \tilde{\boldsymbol{z}}_2^2 & \tilde{\boldsymbol{z}}_1 \circ \tilde{\boldsymbol{z}}_2 \end{bmatrix} \tag{3.65}$$

to represent the generation of the library matrix through combinatorial candidates. For evaluation metrics, a root-mean-square error (RMSE) is utilized:

$$\text{RMSE} \coloneqq \sqrt{\frac{1}{MP} \sum_{j=1}^{N} \sum_{i=1}^{P} (\boldsymbol{\Theta}\hat{\boldsymbol{\Xi}} - \boldsymbol{\Theta}\boldsymbol{\Xi}^*)_{ji}^2} \tag{3.66}$$

where $\boldsymbol{\Xi} = \begin{bmatrix} \boldsymbol{\xi}_1 & \cdots & \boldsymbol{\xi}_P \end{bmatrix}$ is the column concatenation of all state measurements.

Bouc Wen hysteretic oscillator The Bouc-Wen hysteresis oscillator is a widely studied model in the field of nonlinear dynamics and materials. The behavior of the Bouc-Wen hysteresis nonlinearity is characterized by its ability to model complex, nonlinear phenomena such as rate-dependent effects, memory, and asymmetric responses. These phenomena manifest as hysteresis loops, which are a result of the system's input-output being dependent on both the current state and the history of the input. This system consists of a set of nonlinear differential equations:

$$\begin{cases} m\ddot{x} + c\dot{x} + kx + z = u_{\text{in}} \\ \dot{z} = \alpha\dot{x} - \beta|\dot{x}||z|^{\nu-1}z - \delta\dot{x}|z|^{\nu} \end{cases} \tag{3.67}$$

where $m = 2$, $c = 10$, $k = 5 \cdot 10^4$ denote the linear mass, damping, and stiffness coefficients of a linear oscillator respectively, $u(t)$ the input, and $\alpha = 5 \cdot 10^4$, $\beta = 8 \cdot 10^2$, $\nu = 1$, and $\delta = 1.1 \cdot 10^3$, which are the given parameters of the Bouc Wen nonlinearity to be identified from the benchmark [NS16]. Additionally, the benchmark uses noiseless data and the initial conditions of the benchmark

set $\dot{x}(0) = 0$, $x(0) = 0$, and $z(0) = 0$. It is to be noted that the form given by Eq. (3.67) has redundant coefficients [Ma+04], i.e. the same behavior can be generated for multiple sets of coefficients.

In this example, we aim to demonstrate that TRIM is well situated to recovering the exact support of hysteretic nonlinearities, especially of the Bouc Wen oscillator. This is validated using the two test datasets are presented in [NS16] of purely input and output data[7] and identified models' RMSE is to be given as a figure of merit. We present two Bouc Wen input-output phase plot and the benchmark output data in Fig. 3.20.

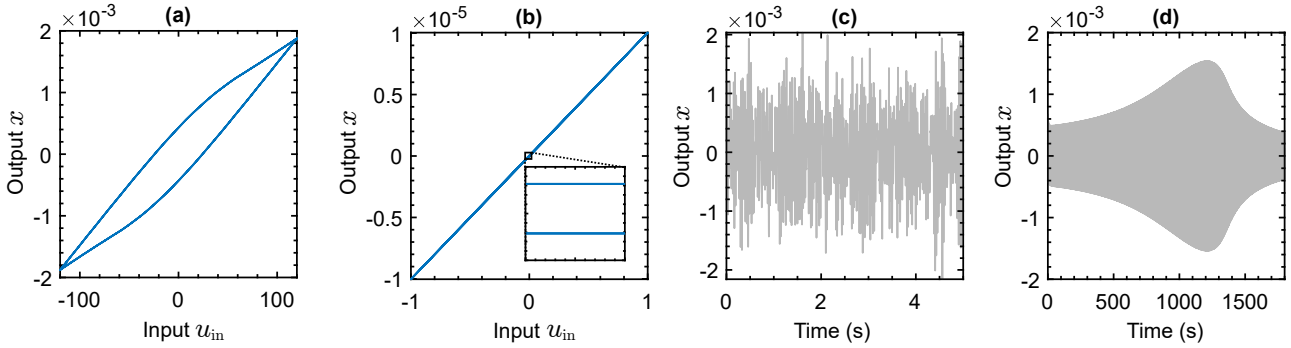

Figure 3.20: The Bouc Wen oscillator is simulated with a single sinusoidal input with amplitude 120 Newton in **(a)** and 1 Newton in **(b)**. The two datasets used for RMSE validation are provided by [NS16], where the outputs are shown: **(c)** is a multi-sine excitation and **(d)** a sine sweep. Their respective inputs are included by the benchmark but not shown.

This nonlinear system is challenging for identification since the internal variable z is not a measurable quantity, and the absolute values to the power of ν do not allow Taylor or binomial expansions. Expanding on [LN19], we show that hysteresis can easily be handled by TRIM with some algebraic manipulation. Consider Eq. (3.67) in which a mass-normalized linear oscillator is estimated *a priori* to yield a discrepancy model:

$$\begin{cases} f_{\text{lin}} + z = u_{\text{in}} \\ \dot{z} = \alpha\dot{x} - \beta|\dot{x}||z|^{\nu-1}z - \delta\dot{x}|z|^{\nu} \end{cases} \tag{3.68}$$

where f_{lin} is a linear approximation. To capture the latent history variable between input-outputs, we introduce the calculable state:

$$y \coloneqq u_{\text{in}} - f_{\text{lin}} = z \tag{3.69}$$

[7]It should be reminded that the test datasets are not to be utilized during the process of training.

This yields the form to be identified:

$$\dot{y} = \alpha\dot{x} - \beta|\dot{x}||y|^{\nu-1}y - \delta\dot{x}|y|^{\nu} \tag{3.70}$$

It can be seen that the memory and latent variables are captured by the difference between the input and the linear oscillator. Note, to identify system of Eq. (3.70) via TRIM, the library matrix must have within the library of candidate functions $\{\boldsymbol{y},\ \dot{\boldsymbol{x}},\ |\dot{\boldsymbol{x}}| \circ |\boldsymbol{y}|^{\nu-1},\ \dot{\boldsymbol{x}} \circ |\boldsymbol{y}|^{\nu}\}$.

To address this Bouc Wen benchmark, we propose a three-step method by separating the estimation of linear and nonlinear components. First, $\hat{f}_{\text{lin}}$ is estimated from the free decay of training data. Second, TRIM is used to identify the remaining Bouc Wen nonlinearity and initial conditions. Lastly, the linear oscillator's coefficients are estimated. The training data used is simulated via MATLAB's `ode45` with a single sinusoidal input with an amplitude of 50 Newtons, ending with a free decay, for a total length of 12 seconds, $\Delta t = 0.01$. We outline the steps taken as follows:

1. Approximate $\hat{f}_{\text{lin}} = \hat{\ddot{x}} + 2\hat{\zeta}\hat{\omega}_n\hat{\dot{x}} + \hat{\omega}_n^2 x$, where the numerical derivatives are estimated using Tikhonov regularization defined in Appendix B.4.2, the damping ratio $\hat{\zeta}$ is estimated from the averaged log decrement of the free decay, and the damped natural frequency $\hat{\omega}_d$ from the maximum frequency peak using an appropriate super-resolution method [Kis+23c].

2. Use initial value problem formulation of TRIM (Eq. (3.64)) on $\dot{y}$ with the library $\boldsymbol{\Theta} = \begin{bmatrix}\mathcal{P}(\boldsymbol{x}, |\boldsymbol{x}|, \dot{\boldsymbol{x}}, |\dot{\boldsymbol{x}}|, \boldsymbol{y}, |\boldsymbol{y}|, n) & \boldsymbol{u}\end{bmatrix}$, to identify the initial values and the coefficients and structure of the Bouc Wen model of $\hat{\dot{y}}$. For exact recovery, this yields $\{\hat{\dot{y}}(0), \hat{\alpha}, \hat{\beta}, \hat{\delta}, \hat{\nu}\}$.

3. Estimate the linear oscillator's coefficients using a nonlinear regression, e.g. a quasi-Newton method, on $m\hat{\ddot{x}} + c\hat{\dot{x}} + k\hat{x} = u_{\text{in}} - \int \hat{\dot{y}}$, where the numerical integration of the estimated nonlinear model uses the discovered initial values $\hat{\dot{y}}(0)$. This yields $\{\hat{m}, \hat{c}, \hat{k}\}$.

The role of the first step is to estimate the linear energy which is required for latent (memory) variables in a hysteretic nonlinearity. For the second step, the library for sparse regression is assembled with candidate functions that one would expect when there is hysteretic behavior: $\boldsymbol{\Theta} = \begin{bmatrix}\mathcal{P}(\boldsymbol{x}, |\boldsymbol{x}|, \dot{\boldsymbol{x}}, |\dot{\boldsymbol{x}}|, \boldsymbol{y}, |\boldsymbol{y}|, n) & \boldsymbol{u}\end{bmatrix}$. This is made with $n = 2$ such that the library column space is $P = 28$. The last step uses a nonlinear regression to refit the true coefficients of the problem. Note, that steps 1-3 can form an iterative method that refines linear and nonlinear coefficient estimates.

We apply these steps to all three estimators and show their results of step 2 in Table 3.6. When it comes to identifying the hysteretic nonlinearity in step 2, SINDy, E-SINDy, and IRL1 are unable to recover the exact model with sparsity $K^* = 6$ despite the training data being noiseless and providing a densely defined grid of hyperparameters. As a result, we omit the presentation of their results for the benchmark. We remark the that identified initial values corresponds to the error accumulated by the approximation of $\hat{f}_{\text{lin}}$. The initial conditions identified in step 3 do not align with the actual initial conditions; instead, they ensure the accuracy of the linear oscillator's coefficients. Finally, the estimated linear coefficients of TRIM's model are $\hat{m} = 2.037$, $\hat{c} = 12.700$, and $\hat{k} = 5.108 \cdot 10^4$.

Estimator	**Recovered model**	**Recovered I.C.**
TRIM	$\dot{y} = (4.93 \cdot 10^4)\dot{x} - (8.16 \cdot 10^2)\|\dot{x}\|\|y\|^{\nu-1}y - (1.16 \cdot 10^3)\dot{x}\|y\|^{\nu}$	$\dot{y}(0) = -19.061$
SINDy	$\dot{y} = (5.14 \cdot 10^4)\dot{x} - (1.04 \cdot 10^3)\|\dot{x}\|\|y\|^{\nu-1}y - (1.17 \cdot 10^3)\dot{x}\|y\|^{\nu} - (1.32 \cdot 10^6)x$ $- (2.57 \cdot 10^1)y - (4.69 \cdot 10^7)x\|x\| + (5.49 \cdot 10^6)x\|\dot{x}\| - (1.85 \cdot 10^3)x\|y\|$ $- (2.78 \cdot 10^6)\|x\|\dot{x} + (1.91 \cdot 10^3)\|x\|y - (3.32 \cdot 10^5)\dot{x}\|\dot{x}\| + (1.57 \cdot 10^{-2})y\|y\|$ $+ (2.60 \cdot 10^1)u_{\text{in}}$	$\dot{y}(0) = -19.061$
E-SINDy	$\dot{y} = (4.89 \cdot 10^4)\dot{x} - (8.47 \cdot 10^2)\|\dot{x}\|\|y\|^{\nu-1}y - (1.14 \cdot 10^3)\dot{x}\|y\|^{\nu} - (7.21 \cdot 10^5)$ $x - (1.39 \cdot 10^1)y - (1.23 \cdot 10^3)x\|y\| + (8.68 \cdot 10^2)\|x\|y + (1.41 \cdot 10^1)u_{\text{in}}$	$\dot{y}(0) = -19.064$
IRL1	$\dot{y} = (4.92 \cdot 10^4)\dot{x} - (7.88 \cdot 10^2)\|\dot{x}\|\|y\|^{\nu-1}y - (1.14 \cdot 10^3)\dot{x}\|y\|^{\nu} + (8.92 \cdot 10^3)x$ $- (7.20 \cdot 10^6)x\|x\| - (2.08 \cdot 10^6)x\|\dot{x}\| - (1.60 \cdot 10^3)x\|y\| + (1.39 \cdot 10^3)\|x\|y$ $- (1.73 \cdot 10^4)\dot{x}\|\dot{x}\|$	$\dot{y}(0) = -19.064$

Table 3.6: The identification results of TRIM, SINDy, E-SINDy, and IRL1 for the Bouc Wen hysteretic nonlinearity outlined in Step 2. The correct functions are colored in green and misidentified functions are colored in black. While all estimators obtain a sparse solution that includes the true support $\hat{\boldsymbol{\mathcal{S}}}_j \supseteq \boldsymbol{\mathcal{S}}_j^*$, only TRIM obtains the exact model with other estimators only obtaining a sparse approximation of the true Bouc Wen nonlinearity.

In Fig. 3.21 we show the TRIM identified model's hysteretic force's phase plot on the training data and the simulation of the two benchmark test datasets. Since TRIM recovers the exact support, the residual errors are simply due to coefficient and quadrature errors. Additionally, we show other benchmark results with respect to their RMSE and number of parameters in Table 3.7; a majority of the other methods in the literature are black-box methods. TRIM can be shown to yield competitive results since it recovers the exact model, and its accuracy is only limited by its method of numerical integration. This is shown by the result notated "Oracle", where the true results are integrated using the provided MATLAB `.p` file from the benchmark [NS16] with the provided test external forcing data.

TRIM has the advantage of accurately identifying the precise governing equation and coefficients while being applicable to systems with general nonlinearities. However, its effectiveness is dependent on the availability of data capturing the free-decay behavior of the system.

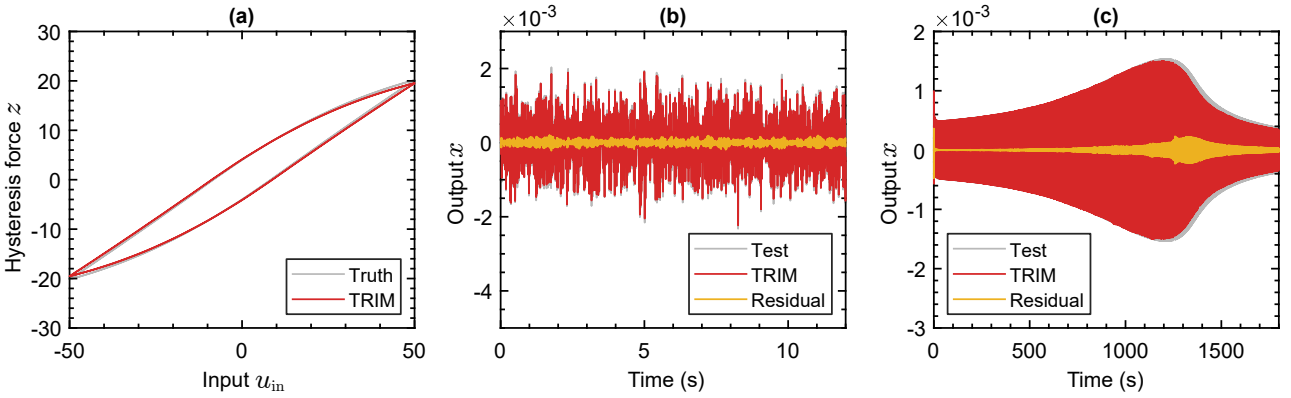

Figure 3.21: In **(a)**, the Bouc Wen training data is is simulated with a single sinusoidal input with amplitude 50 Newton, where the true and TRIM estimated model's hysteretic force z overlayed. The two datasets used for RMSE validation provided by [NS16] are shown: **(c)** is a multi-sine excitation and **(d)** a sine sweep. The residuals between TRIM estimated model's and the test data output are shown in yellow.

Estimator	**RMSE Multi-sine** $(\cdot 10^{-5})$	**RMSE Sine Sweep** $(\cdot 10^{-5})$	**Parameters** (sparsity $\hat{K}$)	**Exact recovery**
TRIM	**6.569**	**4.949**	**6**	✓
Volterra feedback [SS16]	8.409	5.601	14	×
Decoupled NARX [Wes+18]	5.360	1.670	206	×
EHH NN [Xu+20]	4.949	2.402	436	×
LSTM [SMN19]	5.980	2.800	21730	×
MIMO PNLSS [Fak+18]	1.871	1.202	217	×
Decoupled PNLSS [Fak+18]	1.338	1.117	51	×
Oracle	5.098	4.182	6	-

Table 3.7: Results from TRIM and the literature for the Bouc Wen benchmark of [NS16]. The "Oracle" entry refers to the RMSE found when using the true Bouc Wen parameters and the provided input data for simulation using the MATLAB p-file provided by the benchmark. Some acronyms are given: NARX refers to NARMAX without the moving average models; EHH NN stands for efficient hinging hyperplanes neural network, which is a wide but single hidden layer neural network; LSTM stands for a specific deep recurrent neural network (RNN) which uses long short-term memory layers; MIMO stands for multiple-in-multiple-out; PNLSS stands for polynomial nonlinear state space model.

Discussion The Sparse Identification of Nonlinear Dynamical Systems (SINDy) integrates expert knowledge with data-driven sparse regression to identify nonlinear dynamical systems. While initially proposed estimators for SINDy, like STLS or the newer IRL1, propose efficient computational means for sparse model identification, their performance can suffer with finite, noisy data or high multicollinearity in the library matrix. E-SINDy, an extension to SINDy, was designed for robustness against finite and noisy data via bootstrapping and ensembling, has been demonstrated to have limitations. Its effectiveness hinges on the premise that variance reduction through ensembling outweighs bias introduced by bootstrapped models resampled from data – a balance not consistently achieved when the model is misidentified. On the other hand, TRIM, employing the non-convex penalty of the Trimmed Lasso and a Pareto-based L-curve model selection criteria, achieves exact model recovery across a broad spectrum of dynamical systems. Its penalty mechanism aligns more naturally with the ℓ_0 pseudo-norm than the ℓ_1 norm. Moreover, the "convexification" of the Trimmed Lasso accentuates TRIM's computational efficacy. Despite TRIM's successful identifications for the Bouc Wen hysteretic benchmark, the exploration of additional model selection criteria with respect to Trimmed Lasso is warranted. This rationale stems from TRIM's tendency to obtain monotonically decreasing residuals versus sparsity, and high likelihood of the true model residing near the L-corner. This suggests future studies into suitable criteria for adversarial scenarios lacking an L-shaped curve.

3.5 Summary

For vibration analysis of ultrasonic fatigue signals, motivated by approach of [Kum+09], the traditional approach of estimating sinusoidal parameters is by using the DFT, or its fast algorithmic counterpart the FFT. However, the signals exhibited in ultrasonic fatigue, especially for long fatigue tests have slowly varying sinusoidal components. Line spectral algorithms are explored in terms of smaller time window lengths, because of the enhanced local stationarity in the fatigue vibration signals, and against their real-time computational complexity. Specifically, estimators face a frequency and time uncertainty dictated by the Rayleigh limit, and estimators assume a stationary signal model face basis-mismatch problem when used on quasi-stationary signal. ESPRIT was found to be the best performing for synthetic and experimental quasi-stationary signals in ultrasonic fatigue. However, (Unitary-)ESPRIT is an algorithm that is computationally prohibited with an asymptotic complexity at $\mathcal{O}(N^3)$ due to using the SVD/EVD.

Therefore in the second section, efforts were made towards the reduction of the time-complexity of ESPRIT by avoiding the computation of the SVD/EVD. This is done by realizing that the data's Hankel matrix has a Vandermonde matrix decomposition, and that right most Vandermonde matrix of the decomposition can be "removed" by multiplication, i.e. results in an identity matrix plus an error. In the on-grid case, when multiplied with a complex conjugate DFT matrix, it can be shown that the error has an analytical form by the Dirichlet kernel. In the off-grid case, further steps must be taken, and thus a refinment of the DFT matrix with interpolation is utilized. Due to the fast ability to multiply with the DFT matrix, the complexity of estimating the signal subspace drops to $\mathcal{O}(N \log N)$. Numerical results demonstrate that it's performance is nearly identical to ESPRIT, and numerical proofs are provided on eigenspace perturbation and super-resolution abilities.

Finally, the last section deals with nonlinear dynamical system identification. The sparse identification of nonlinear dynamics (SINDy) using the sequentially thresholded least squares (STLS) algorithm has gained traction for identifying nonlinear dynamical systems. While various SINDy extensions cater to finite, noisy experimental data, many only achieve sparse approximations, struggling with multicollinearity issues like the irrepresentable condition for the Lasso. However, the Trimmed Lasso for robust model identification (TRIM) has demonstrated superior performance, achieving exact system recovery even under significant noise, data limitations, and multicollinearity. Notably, TRIM's computational efficiency is on par with STLS due to its sparsity parameter's compatibility with convex solvers. The future goal here is to encourage a data-driven framework that can be applied to an oscillator model of the fatigue specimen, when input and output measurement data are avalible for identification.

Chapter 4

Ultrasonic fatigue experimental results

Contents

In this chapter, a multifaceted approach is taken to exploit the vibration data from a two laser vibrometer setup. The source of the nonlinear harmonic generation is to be simulated with the multiscale ultrasonic fatigue specimen model proposed in Chapter 2. The multi-harmonic vibration forms the fatigue specimen's base motion, and the resulting harmonics at the specimen's tip are then extracted. Thus the fatigue specimen model is treated as an inverse problem: i.e. correlating the nonlinear harmonic generation by identifying model parameters. The results of this identification process is applied to copper and steel ultrasonic fatigue test data, and the results are analyzed.

4.1 Introduction

In this chapter, the approach of the multiscale model from Chapter 2 is utilized with experimental vibration data. To derive the model parameters that describe standing wave dynamics and harmonic generation at the tip vibration, a regression problem is formulated to minimize the discrepancy between model predictions and experimental results. These model parameters correspond to the nonlinear mesoscopic response due to microcracks and microplastic inclusions and the contribution of the multi-harmonics at the base vibration.

For the first section, the bulk of the experimental procedure is detailed, including the ultrasonic fatigue test machine configuration, the fatigue specimen material and fatigue loading, and the selection of model parameters. Polycrystalline copper and C70 steel are tested in the VHCF regime, whose vibration signals are recorded. To supplement this vibration data, thermographic signals as well as basic fractographs are used to categorize the onset of microcrack and its failure mode. For the second section, the multiscale model has its micromechanical parameters identified to predict the harmonic generation seen in experimental vibration data of ultrasonic fatigue tests. The identification procedure relies on a regression of the fundamental, second, and third harmonics between the experiment and model by varying the micromechanical parameters. The results of the multiscale model with respect to the micromechanical parameters are discussed and juxtaposed.

4.2 Ultrasonic fatigue experiments

Material and geometry of ultrasonic fatigue specimen As mentioned previously in Chapter 1, the fatigue specimens used are a pure polycrystalline copper with a cylindrical fatigue specimen and a high-strength C70 steel with a rectangular cross section. These are designed in accordance to the method described in Section 1.3.1: The geometrical design ensures a Gaussian-like stress distribution along the longitudinal axis, with the peak stress concentrated at the centroid. Then the shaft length is modified with respect to the centroid length in order to coincide the ultrasonic fatigue specimen's eigenfrequency with the anti-resonance frequency of the ultrasonic fatigue machine ($f_{\mathrm{a}} \approx 20231$ Hz as found in Fig. 2.35). The rectangular centroid shape of the C70 specimens are non-conventional, as they were produced for X-ray diffraction campaigns, see [Jac22].

According to the VHCF material categorization of Mughrabi (Section 1.2.3), polycrystalline copper

and C70 steel are Type I and Type II materials respectively. The composition of the C70 steel is detailed in Table 4.1, and SEM of both copper and C70 steel materials have been taken in Fig. 4.1, where the microstructure particularities and grain size are shown. Note that, the particular heat treatments on all fatigue specimens are unknown. The manufactured fatigue specimens along with their macroscopic properties are adopted from [Mar+20] for pure polycrystalline copper and [Jac22] for C70 steel, and shown in Figs. 4.2 and 4.3 and Tables 4.2 and 4.3 respectively.

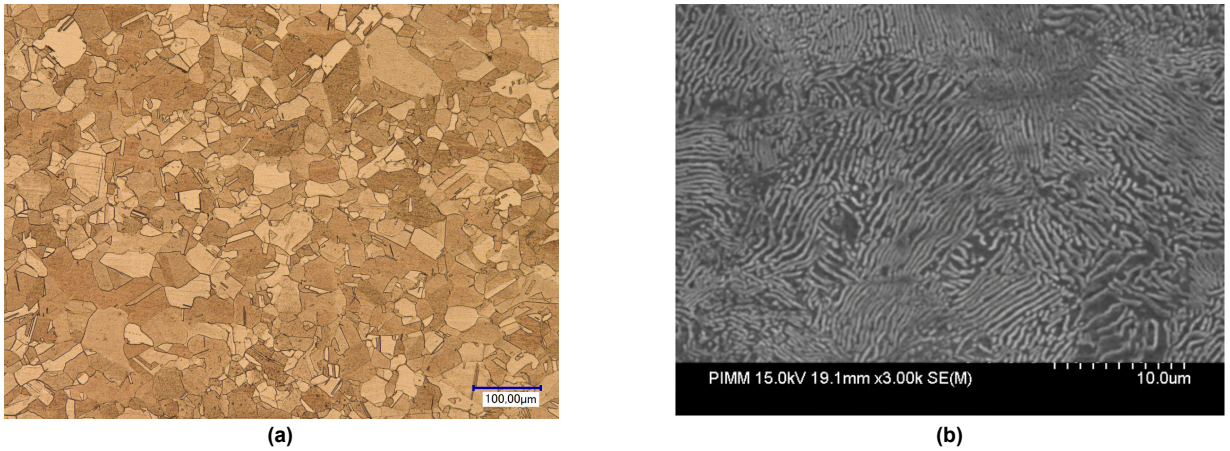

Figure 4.1: In **(a)**, an optical microscope image of the copper's grain size, with the average $\approx 30\mu$m, taken from [Mar+20]. In **(b)**, a SEM image of the C70 steel featuring pearlite microstructure, with lamellar mixture of ferrite and cementite, taken from [Yah13].

C	Si	Mn	S	P	Ni	Cr	Mo	Cu	Al	Sn	Fe
0.68	0.192	0.846	0.01	0.01	0.114	0.16	0.027	0.205	0.042	0.016	balance

Table 4.1: C70 composition by percent weight.

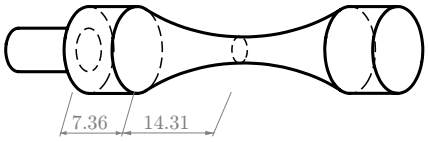

Figure 4.2: Copper fatigue specimen geometry, in mm.

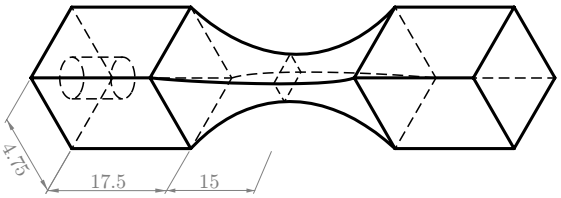

Figure 4.3: C70 fatigue specimen geometry, in mm.

Ultrasonic fatigue machine, instrumentation setup Here the experimental setup and measurements are briefly mentioned. The particular mechanical load train utilized is the one mentioned in Section 2.2:

Parameter	Value
Young's modulus E	130 GPa
Density ρ	8920 kg·m^{-3}
Poisson's ratio ν	0.34
Specimen volume V	$1.819 \cdot 10^{-6}$ m^3

Table 4.2: Copper specimen macroscopic material and geometry parameters.

Parameter	Value
Young's modulus E	211 GPa
Density ρ	7839 kg·m^{-3}
Poisson's ratio ν	0.29
Specimen volume V	$6.492 \cdot 10^{-6}$ m^3

Table 4.3: C70 specimen material macroscopic and geometry parameters.

a titanium booster (Branson 800-series, 1:1 amplification) followed by a titanium horn (1:2.65 amplification). The ultrasonic transducer (Branson CR-20), which drives the mechanical load train, is driven by a signal and power generator (Branson DC480b). The particular ultrasonic fatigue test machine setup is horizontal, which is a configuration normally used for X-ray diffraction, see [Jac22, Fig. 2.27].

Three measurements are utilized *in-situ*, one laser vibrometer (Polytec HSV 700) focused to the horn, i.e. base of the fatigue specimen, and the other (Polytec Vibroflex Xtra) at the tip of the fatigue specimen using a $\approx 45°$ angled mirror. These measurement signals were recorded using a high-speed data acquisition (HBM genesis) at a sampling frequency of $F_s = 10^6$ Hz. To capture the moment of microcrack initiation, the infrared camera (FLIR X6900sc) is focused according to the surface of the fatigue specimen with a blackbody reference (HGH DCN 1000). Copper and C70 specimens were polished with SiC paper up to 1000 grit. To increase temperature fidelity, the surface of the ultrasonic fatigue specimens' centroid sections were coated in a matte black emissive paint (Nextel 811-21). Finally, continuous air cooling was provided to the ultrasonic transducer, as well as to the ultrasonic fatigue specimens (VORTEC). A balance is struck between refreshing the fatigue specimen and maintaining temperature accuracy, ensuring a comparable stress loading and lifespan as reported in literature.

Presented ultrasonic fatigue tests A planned campaign of ultrasonic fatigue tests are performed to test specimens at the VHCF regimes. This is done by referring to to the S-N plots for polycrystalline copper provided by Fig. 4.5 and C70 steel (cylindrical specimen geometry) provided by Jacquemain [Jac22, Fig. 2.3]. The specimen used by Jacquemain [Jac22] are cylindrical as opposed to the rectangular used in this study, which has a centroid cross-sectional area of approximately 7 mm^2, compared to the 15 mm^2 in this study. Therefore, the discrepancy in fatigue life can be attributed to the size effect [Fur08]. The tests presented in this dissertation were specifically chosen based on their fatigue

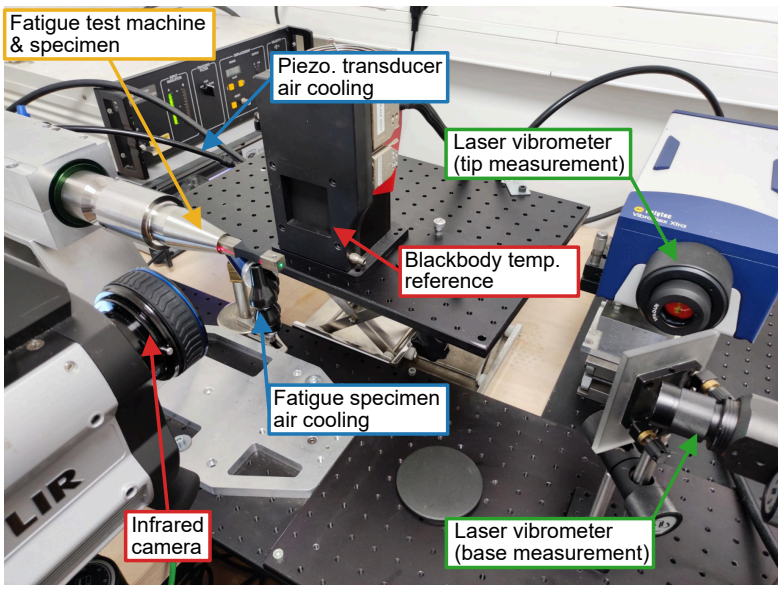

Figure 4.4: A photo of the two laster experimental setup used in the thesis.

failure mode, standardized instrumentation setup (keeping consistent angles for the laser vibrometer), and the clarity of post-fracture imagery.

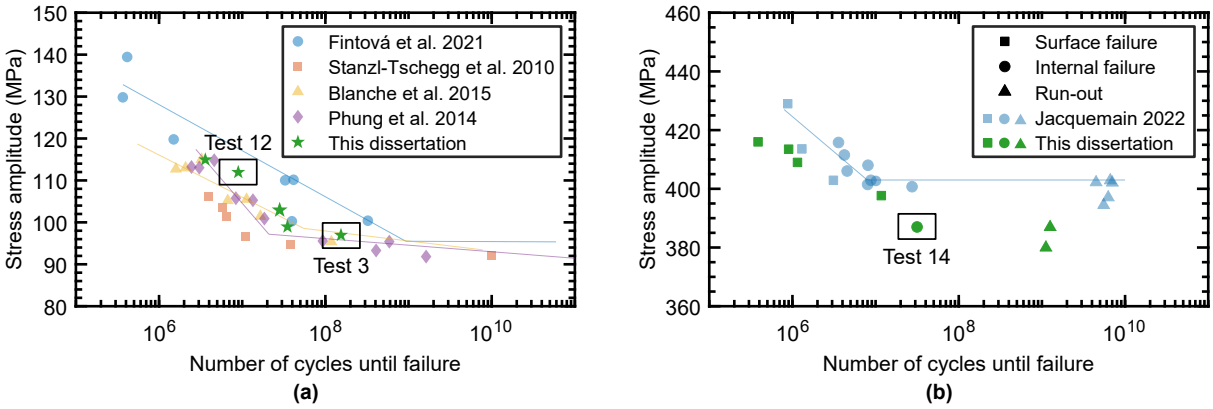

Figure 4.5: In **(a)**, a combined S-N curve for polycrystalline copper, with the green markers indicating testing done in this dissertation. Compiled from the studies (in order) of [Fin+21; SS10b; Bla+15; Phu+14; WFJ17]. In **(b)**, a combined S-N curve from [Jac22, Fig. 2.3] for C70 steel, with the green markers indicating tested done in this dissertation.

Modal analysis of the ultrasonic fatigue specimen A few relevant quantities are taken from a finite element modal/dynamic analysis:

- The vibration modal properties which are typically available when designing the ultrasonic fa-

Material / test number	Longitudinal stress amplitude	Cycles till failure
Copper / 3	97 MPa	$1.545 \cdot 10^8$
Copper / 12	112 MPa	$8.961 \cdot 10^6$
C70 steel / 14	386 MPa	$1.798 \cdot 10^7$

Table 4.4: Selected ultrasonic fatigue test, whose vibration data are analyzed for Chapter 4. The test number is an internal reference.

tigue specimen via finite element analysis. For the reduced order model, the static and first mass-normalized longitudinal mode shapes and their respective eigenfrequency can be extracted.

- An estimated longitudinal stress-amplitude (at the centroid), which is required for plotting a S-N curve with respect to numbers of cycles.

The modal properties of each ultrasonic fatigue specimen, copper (Table 4.2) and C70 steel (Table 4.3), are determined via linear finite element modal analysis in ABAQUS. The geometry used in the modal analysis differs from Figs. 4.2 and 4.3 where the fixation screw or hole is not included. These relevant quantities are shared in Table 4.5 and Table 4.6. The longitudinal stress-amplitude (at the centroid) is determined alongside with the determination of the nonlinear volume. Both the copper and C70 specimens have their elongation determined from vibration data from the ultrasonic fatigue test. This is done by taking the two velocity signals and using the relationship of Eq. (2.115) with knowledge of the fundamental harmonic's frequency to find their displacement, see Eq. (1.1). Thus the maximum longitudinal stress-amplitude at the centroid is estimated using a fixed-free periodic simulation in ABAQUS under the assumptions of a linear elastic material. This particular estimate is almost identical to the method used by Jacquemain et al. [Jac+21], except that Eq. (2.115) corrects for the case when the base vibration is slightly out of phase. This maximum stress-amplitude estimate is used for plotting the S-N curve in Fig. 4.5 and is what is shown in Table 4.4.

Finite element model parameters	Value
Rigid longitudinal eigenmode at tip $\boldsymbol{\phi}_0(\boldsymbol{X}_{\text{tip}})$	$\begin{bmatrix}0 & 7.537 & 0\end{bmatrix}^{\text{T}}$ m/$\sqrt{\text{kg}}$
First longitudinal eigenmode at tip $\boldsymbol{\phi}_1(\boldsymbol{X}_{\text{tip}})$	$\begin{bmatrix}0 & 8.039 & 0\end{bmatrix}^{\text{T}}$ m/$\sqrt{\text{kg}}$
Rigid longitudinal eigenmode at base $\boldsymbol{\phi}_0(\boldsymbol{X}_{\text{base}})$	$\begin{bmatrix}0 & 7.537 & 0\end{bmatrix}^{\text{T}}$ m/$\sqrt{\text{kg}}$
First longitudinal eigenmode at base $\boldsymbol{\phi}_1(\boldsymbol{X}_{\text{base}})$	$\begin{bmatrix}0 & -8.039 & 0\end{bmatrix}^{\text{T}}$ m/$\sqrt{\text{kg}}$

Table 4.5: Mass-normalized modal coefficients determined from FEA for the copper fatigue specimen.

Finite element model parameters	**Value**
Rigid longitudinal eigenmode at tip $\boldsymbol{\phi}_0(\boldsymbol{X}_{\text{tip}})$	$\begin{bmatrix}0 & 4.433 & 0\end{bmatrix}^{\text{T}}$ m/$\sqrt{\text{kg}}$
First longitudinal eigenmode at tip $\boldsymbol{\phi}_1(\boldsymbol{X}_{\text{tip}})$	$\begin{bmatrix}0 & 4.771 & 0\end{bmatrix}^{\text{T}}$ m/$\sqrt{\text{kg}}$
Rigid longitudinal eigenmode at base $\boldsymbol{\phi}_0(\boldsymbol{X}_{\text{base}})$	$\begin{bmatrix}0 & 4.433 & 0\end{bmatrix}^{\text{T}}$ m/$\sqrt{\text{kg}}$
First longitudinal eigenmode at base $\boldsymbol{\phi}_1(\boldsymbol{X}_{\text{base}})$	$\begin{bmatrix}0 & -4.771 & 0\end{bmatrix}^{\text{T}}$ m/$\sqrt{\text{kg}}$

Table 4.6: Mass-normalized modal coefficients determined from FEA for the C70 fatigue specimen.

Post-processing of ultrasonic fatigue test measurements Here we detail the post-processing of vibration data and the temperature data: the vibration data is used directly by the models, whereas the temperature data is used only as a reference. For vibration data, the extraction of harmonics in the base and tip vibration measurements uses a sliding window approach. Specifically, both signals are downsampled to $F_{\text{s}} = 2.5 \cdot 10^5$ and each window has a sample size $N = 2^{12}$. These velocity signals are laser vibrometer measurements and are taken to be a sum of three harmonics:

$$\dot{u}_{\square}^{(i)}(t) = \text{real}\big(\tilde{A}_1^{(i)} e^{\text{j}\omega_1 t} + \tilde{A}_2^{(i)} e^{\text{j}\omega_2 t} + \tilde{A}_3^{(i)} e^{\text{j}\omega_3 t}\big)_{\square} \tag{4.1}$$

where $\tilde{A}$ is the complex amplitude and $\omega \coloneqq 2\pi f$ is the angular frequency. Extracting these first three harmonics corresponds to denoising the signal (the remaining spectra is ignored). The algorithm used to extract the frequencies is the algorithm FFT-ESPRIT (Chapter 3,Algorithm 4, algorithm parameters of $P \leq 20$, $M = N/2$). Using the found frequencies, the complex amplitudes $\{\tilde{A}_1, \tilde{A}_2, \tilde{A}_3\}$ are estimated using least squares.

An example of this harmonic extraction process using the copper specimen (test number 3) is demonstrated in Fig. 4.6. The first sliding window of the measured base $\dot{u}_{\text{base}}^{(i=1)}$ and tip $\dot{u}_{\text{tip}}^{(i=1)}$ vibrations are depicted in Fig. 4.6 **(a)** and **(b)**, respectively. The frequency spectra of the FFT is shown in the background as reference. The harmonic frequencies extracted using FFT-ESPRIT correspond to the straight vertical lines whose magnitudes are estimated using least-squares. This process is repeated for all ith sliding windows across the entire vibration signal. The normalized amplitudes $A^{(i>1)}/A^{(i=1)}$ of the fundamental, second, and third harmonics are extracted and presented relative to the number of cycles of the fatigue test in Fig. 4.6 **(c)** and **(d)**. Notably, the base fundamental harmonic's amplitude shows a gradual increase compared to a gradual decrease of the tip's fundamental harmonic amplitude. The higher harmonics at the base, are not perfectly constant but are notably more stable than those at the tip. The nonlinearities of the ultrasonic test machine and the material nonlinearities at the

specimen's center manifests as evolution of the second and third harmonics's amplitudes of the tip vibration. As highlighted in Section 2.3, the ultrasonic fatigue machine provides a multi-harmonic excitation to the fatigue specimen.

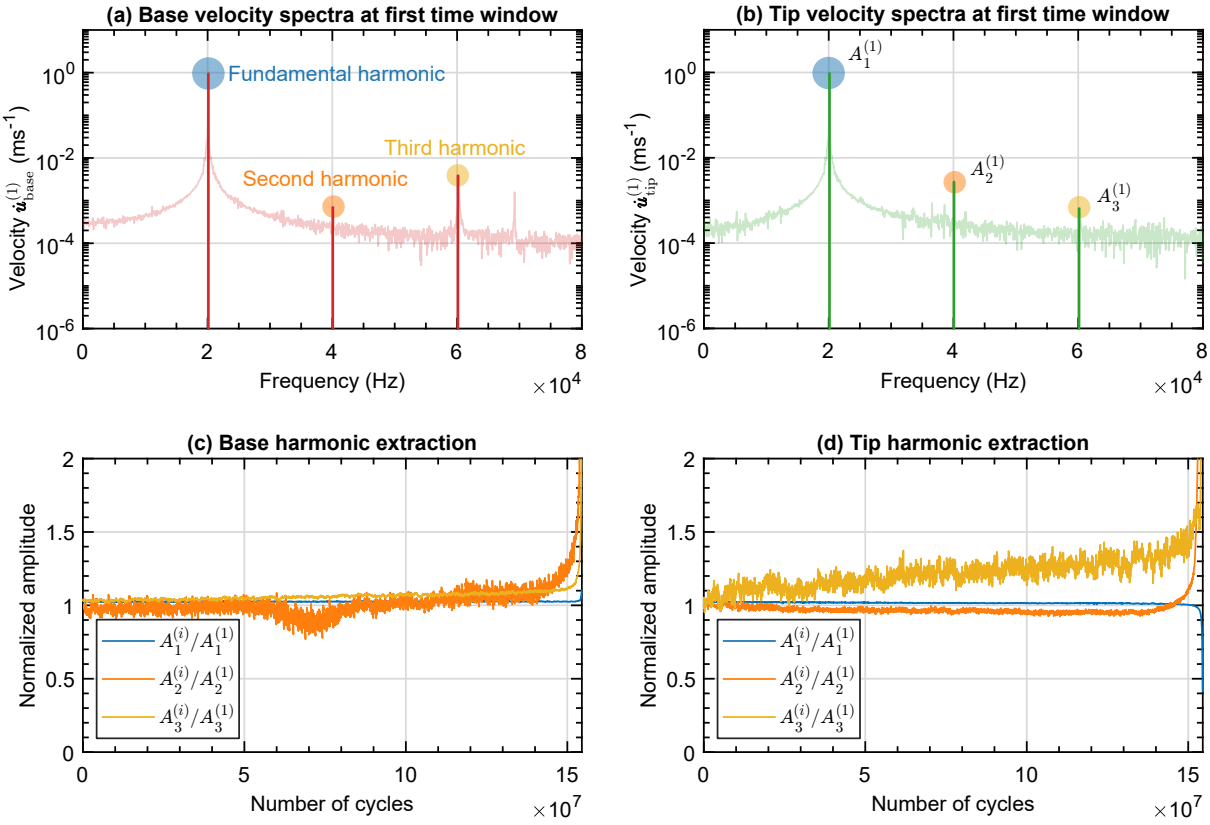

Figure 4.6: Processed velocity signals of the base and tip vibration for the copper specimen (test 3). In **(a)** and **(b)**, the frequency spectra of the first time window ($N = 2^{12}$ or ≈ 327 cycles) of the base and tip vibration, respectively. In **(c)** and **(d)**, the normalized fundamental, second, and third harmonics' amplitude of the base and tip vibration, respectively.

Infrared thermography measurements are not used for the model, but to capture macrocrack propagation, according to the method shown by Ranc et al. [RWP08]. A thermographic image is shown in Fig. 4.7, where a reference blackbody temperature appears in the background. Fig. 4.7 **(a)** corresponds to before the start of a ultrasonic fatigue test with ambient air cooling in an upward direction. At loading, the corresponding thermography Fig. 4.7 **(b)** can be seen with a rectangular box which is utilized to obtain a pixel area average of the temperature.

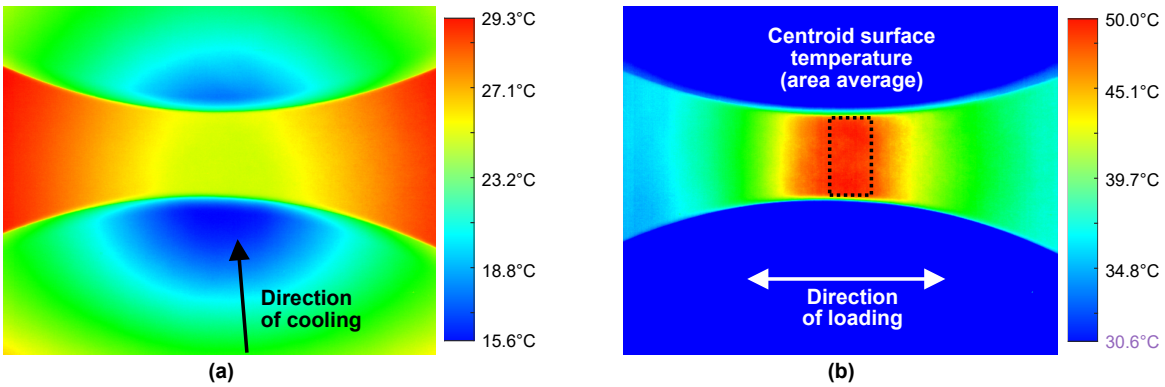

Figure 4.7: In **(a)**, a thermography of an air-cooled ultrasonic fatigue specimen before testing. In **(b)**, a thermography of the surface temperature distribution for a vibrating ultrasonic fatigue specimen. The purple temperature in **(b)** indicates a value outside calibrated settings of the infrared camera.

4.3 Parameter identification of the multiscale ultrasonic fatigue specimen model

This section presents a model of the tip vibration in the ultrasonic fatigue specimen, aimed at understanding the cumulative effect of a multi-harmonic input combined with nonlinear micromechanical models within the specimen's structure. This is done by the analysis on the generation and evolution the second and third harmonics. These higher harmonics have the largest amplitudes, corresponding to the first-order nonlinear effects. To accurately identify the model parameters that replicate the nonlinear harmonic generation, the process involves two key steps: simulating the model for varying micromechanical parameters and subsequently conducting a regression to align the model's predictions with the experimental data. The successful identification of the micromechanical parameters allows for the interpretation of the degree of diffuse microplastic and/or microcrack volume fractions. This is correlated with a post-fracture fractographs using optical and scanning electron microscopy (SEM), to further validate the mode of fatigue failure.

4.3.1 Simulation methodology

The simulation of the multiscale model involves three steps, which is schematized in Fig. 4.8. First, the ith base velocity window has its harmonics' frequencies and amplitudes extracted, as shown in **(a)**. Using Eq. (4.3), the estimated acceleration amplitudes are used as the base motion quantity $\ddot{u}_{\text{base}}$ for

the model's global equation of motion (Chapter 2, Eqs. (2.111) and (2.114)):

$$\ddot{u}_{\text{tip}} = 2\phi_{1,\text{tip}}(\overline{G}\ddot{u}_{\text{base}} - \overline{F}_{\text{int},1}) + \ddot{u}_{\text{base}}; \quad \text{and} \quad \ddot{q}_1 + \underbrace{2\overline{\zeta}_1\overline{\omega}_1\dot{q}_1 + \overline{\omega}_1^2 q_1 + \overline{F}_{\text{nl},1}}_{\overline{F}_{\text{int},1}} = \overline{G}\ddot{u}_{\text{base}}$$

This corresponds to Fig. 4.8 **(b)**. For a set of micromechanical parameters $\{\xi_{\text{cr}}, \xi_{\text{pl}}, \sigma_{\text{pl}}^{\text{Y}}\}$, the simulation of the model's tip vibration is obtained and the fundamental, second, and third harmonics' amplitudes can be extracted, as shown in Fig. 4.8 **(c)**.

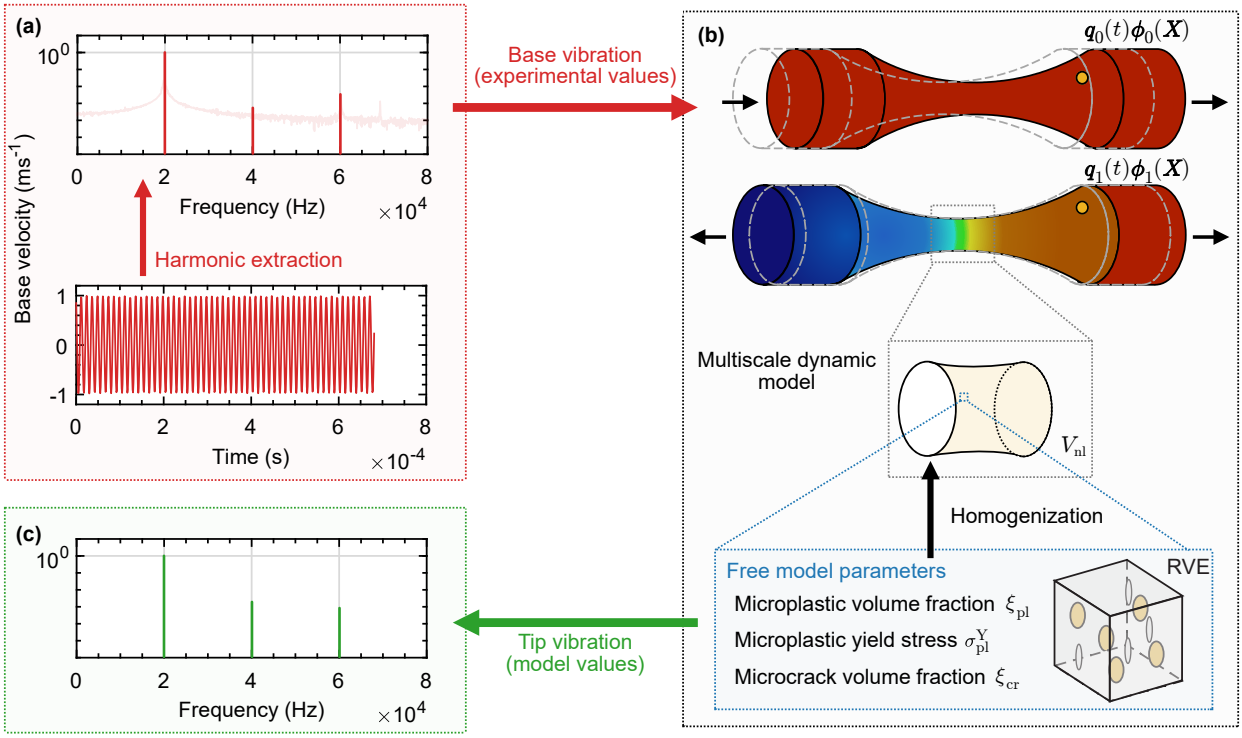

Figure 4.8: A schematic of the simulation procedure of the multiscale ultrasonic fatigue specimen.

The numerical solution to the equation of the modal coordinate q_1 is obtained using the harmonic balance method (HBM) [Gus07], which approximates a periodic solution $q(t) = q(t+T)$ for the time window with a truncated Fourier series:

$$q(t) \approx a_0 + \sum_{h=1}^{H} a_h \cos(h\omega t) + b_h \sin(h\omega t) \tag{4.2}$$

where a, b represent Fourier coefficients and $H \geq 3$ is the number of harmonics. The amplitudes of each harmonic are simply $A_h = \sqrt{a_h^2 + b_h^2}$. This computational method is detailed extensively in

Appendix C.1 and is programmed using an in-house MATLAB code[1].

There are a few parameters yet to be defined: the value of the damping ratio ζ_1 for the first longitudinal mode, the estimation of the base acceleration $\ddot{u}_{\text{base}}$, and the set of free micromechanical parameters which represent the microcracks and microplastic inclusions. Once these are defined, the equation of motions can be solved for.

Estimation of the damping ratio An experimental estimate of the damping ratio ζ_1 of an undamaged specimen from the same material batch is chosen and loaded with increasing displacements. This is shown in Fig. 4.9 **(a)**, where for each pulse, the free vibration decay of the copper fatigue specimen's tip is measured. Using the logarithmic decrement method [GR15] the damping ratio ζ_1 per loading amplitude is estimated (Fig. 4.9 **(b)**). The decay envelope can be represented as an exponential decay $\mathrm{e}^{-\zeta_1 t}$. The frequency of successive oscillations is always the same ω_1, and the ratio of successive peak amplitudes is given by $\mathrm{e}^{2\pi\zeta_1}$. An amplitude-dependency of the damping ratio is seen in Fig. 4.9 **(c)** by a second-order polynomial fit, but the changes due to loading are negligible.

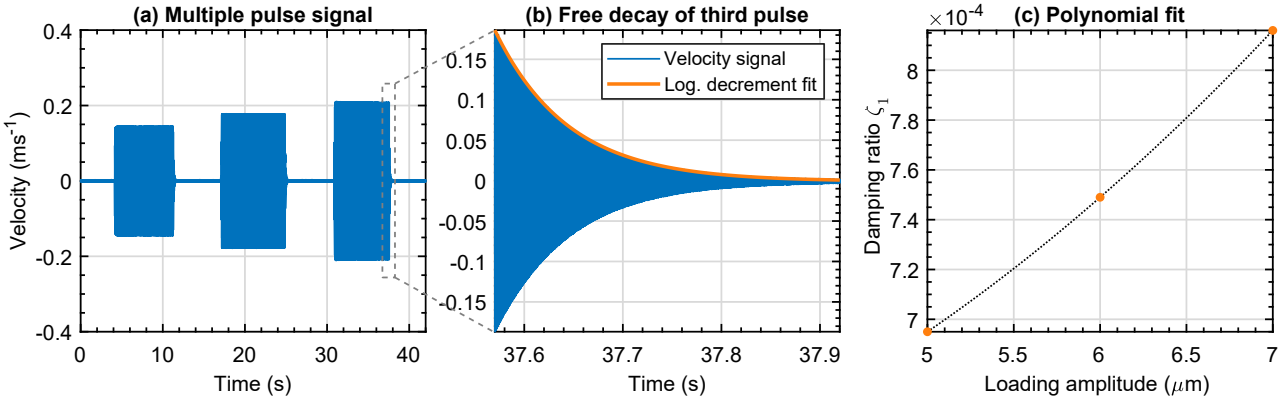

Figure 4.9: Estimation of the damping ratio ζ_1 for a dummy copper fatigue specimen. In **(a)**, three pulses corresponding to an increase in amplitude, and in **(b)**, the logarithmic decrement fit gives an estimate. In **(c)**, a second order-polynomial is shown to fit the damping ratio's amplitude-dependency.

[1]The algorithmic parameters used for the HBM simulations are the following: the truncated number of harmonics is four (including the zeroth harmonic); the number of time samples per period and number of periods used for alternating frequency-time scheme used is 2^{10} and one respectively; the step size used for arc-length continuation is approximately 5 rad.s^{-1} with adaptive step control; the jacobian is estimated using central finite difference; the regression problem is solved using MATLAB's `fsolve` which utilizes a variant of a quasi-Newton method. See Appendix C.1 for further explanation.

Estimation of the base acceleration The base acceleration $\ddot{u}^{(i)}_{\text{base}}(t)$ is estimated from the laser vibrometer velocity measurement $\dot{u}^{(i)}_{\text{base}}$, per ith time window. The acceleration using a denoised velocity signal is found through a spectral derivative:

$$\begin{aligned}\ddot{u}^{(i)}_{\text{base}}(t) &= \text{real}\left(\frac{1}{2\pi}\int_{-\infty}^{\infty}\left(\text{j}\omega\int_{-\infty}^{\infty}\dot{u}^{(i)}_{\text{base}}(\tau)e^{-\text{j}\omega\tau}d\tau\right)e^{\text{j}\omega\tau}d\omega\right)\\ &= \text{real}\left(\mathcal{F}^{-1}\left(\text{j}\omega\cdot\mathcal{F}\left(\dot{u}^{(i)}_{\text{base}}\right)\right)\right)\\ &= \text{real}\left(\mathcal{F}^{-1}\left(\text{j}\omega\cdot\left(\tilde{A}^{(i)}_1 e^{\text{j}\omega_1 t}+\tilde{A}^{(i)}_2 e^{\text{j}\omega_2 t}+\tilde{A}^{(i)}_3 e^{\text{j}\omega_3 t}\right)_{\text{base}}\right)\right)\end{aligned} \tag{4.3}$$

where $\mathcal{F}$ and $\mathcal{F}^{-1}$ are operators that represent the Fourier transform and inverse Fourier transform.

Choice of micromechanical parameters The choice of micromechanical parameters represent a scenario of diffuse microcracks and microplastic Eshelby's inclusions. Thus a three-phase material is defined according the two stage Mori-Tanaka model of Chapter 2, with two separate inclusion phases exhibiting nonlinear material behavior (crack closure and elasto-plastic behaviors) and a linear elastic matrix. The random distribution of microcracks are aligned to the direction of loading (mode I), and here it is imposed that the microcracks have aspect ratio $\alpha_{\text{cr}} = 0.05$ based off micrographs shown in Fig. 2.4. The matrix and the microplastic inclusions have the same elastic stiffness and Poisson ratio $\mathbb{C}_{\text{mat}} = \mathbb{C}_{\text{pl}}$ and $\nu_{\text{mat}} = \nu_{\text{pl}}$ for use in calculating its Eshelby's tensor $\mathbb{E}_{\text{pl}}$. The microcrack inclusions also shares the Poisson ratio of the matrix when calculating the opened and closed crack strain concentration tensors $\mathbb{T}_{\text{cr}}$ and $\tilde{\mathbb{T}}_{\text{cr}}$ respectively. The microplastic inclusions are represented by a sphere $\alpha_{\text{pl}} = 1$ with perfect plasticity law whose fictitious yield stress can be related to the macroscopic yield stress $\sigma^{\text{Y}}_{\text{pl}}/\sigma^{\text{Y}}$. Finally, it can be seen that the three remaining parameters are the volume fraction of the microcracks ξ_{cr} and microplastic inclusions ξ_{pl}, and the fictitious yield stress of the microplastic inclusions $\sigma^{\text{Y}}_{\text{pl}}$. These are calibrated in order to fit the ultrasonic fatigue specimen's vibration response and higher harmonic generation.

The parameter space is represented by tuples $\{\xi_{\text{cr}}, \xi_{\text{pl}}, \sigma^{\text{Y}}_{\text{pl}}\}^{(i)}$ for each ith time window. To understand their behavior and sensitivity, a simulation of the model is performed for the first time window of test 3 for varying values of $\{\xi_{\text{cr}}, \xi_{\text{pl}}, \sigma^{\text{Y}}_{\text{pl}}\}^{(1)}$. The parameter space's four-dimensional aspect arises from the relationship between the three parameters against the harmonics' amplitudes, as depicted in Fig. 4.10. Here, the isosurface is plotted with the values on the x-,y-,and z-axis respectively and the color corresponding to the harmonic's amplitude. The goal is search for the value of these model pa-

rameters which gives the red isosurface. The global solution corresponds to when all three isosurfaces intersect in the parameter space.

In Fig. 4.10 **(a)**, a red isosurface at $A_1^{(1)} \approx 1$ ms^{-1} is shown, which corresponds to all possible values of the three parameters which can give this value. The blue isosurfaces are to visualize the global behavior, and correspond to a 10% offset from the red isosurface. Likewise, the second and third harmonics have isosurfaces drawn at $A_2^{(1)} \approx 3 \cdot 10^{-3}$ ms^{-1} and $A_3^{(1)} \approx 7 \cdot 10^{-4}$ ms^{-1} in Fig. 4.10 **(b)** and **(c)** respectively.

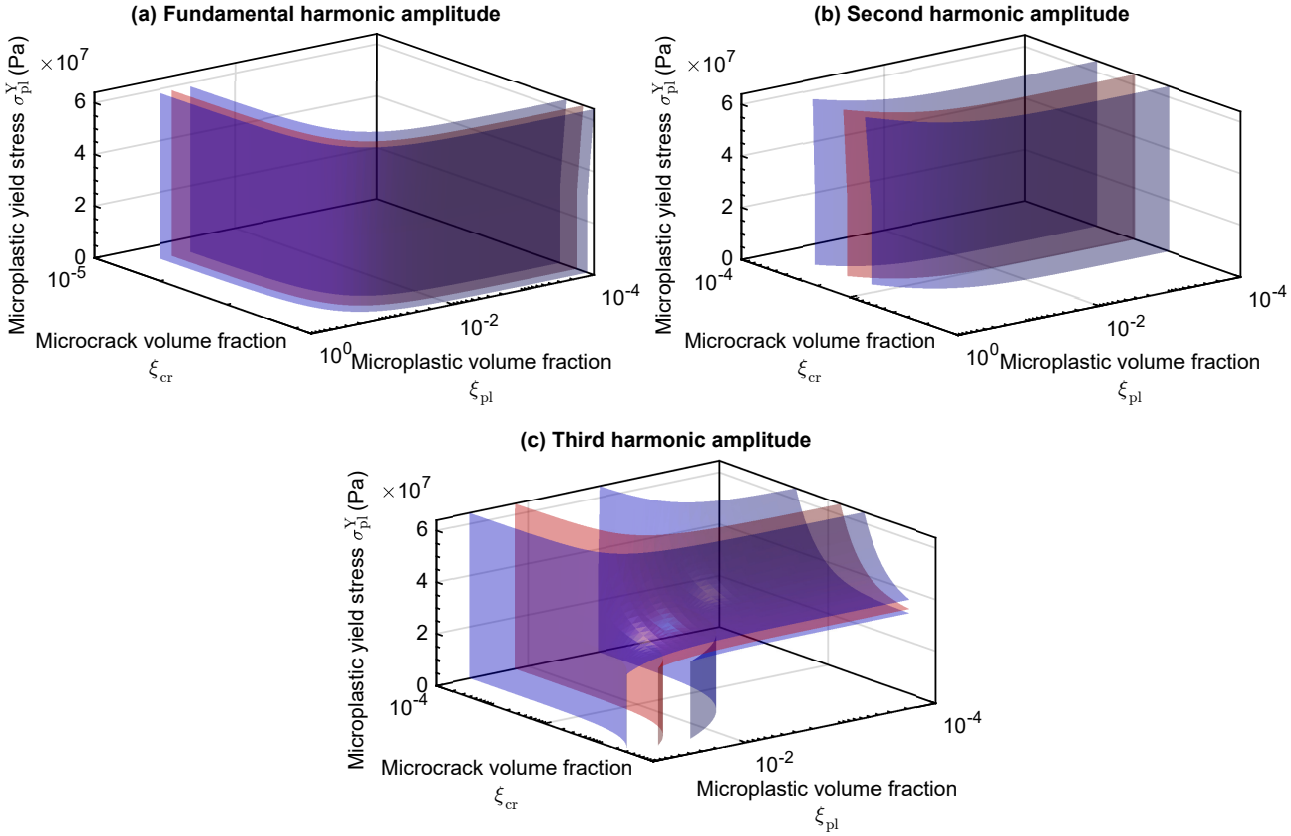

Figure 4.10: A four-dimensional representation of the parameter space of the copper fatigue specimen model at the first time window of the vibration signal (test 3). The isosurface represents all micromechanical parameters that provide a solution to the fundamental **(a)** ($A_1^{(1)} \approx 1$ ms^{-1}), second **(b)** ($A_2^{(1)} \approx 3 \cdot 10^{-3}$), and third harmonic amplitudes **(c)** ($A_3^{(1)} \approx 7 \cdot 10^{-4}$ ms^{-1}).

The z-axis in Fig. 4.10 corresponds to the fictitious yield stress, $\sigma_{\mathrm{pl}}^{\mathrm{Y}}$, of the microplastic inclusions. Both fundamental and second harmonic amplitudes (**(a)** and **(b)** respectively) show a low sensitivity to the value of $\sigma_{\mathrm{pl}}^{\mathrm{Y}}$, which can be visualized as an invariance in the z direction. The third harmonic

amplitude has a diverging behavior at $\sigma_{\text{pl}}^{\text{Y}} \approx 30$ MPa, shown by the diverging surface of the third harmonic in Fig. 4.10 **(c)**. Above this value, the plastic response in the microplastic inclusions and microcracks can reproduce the third harmonic amplitude. This sweet spot indicates a low sensitivity to the value fictitious yield stress. Fixing this parameter away from this divergence point is essential to avoid spurious oscillations in the minimization of Eq. (4.4). Furthermore, setting a fixed microplastic yield stress aligns more with classical plasticity models, serving as a comparable material parameter. When a fixed value of the microplastic yield stress is chosen, the red isosurfaces become a line in the parameter space. The global solution then becomes the intersection of these three lines (a point) which identifies the values of ξ_{cr} and ξ_{pl}.

4.3.2 Results and discussion

Calibration of the model parameters by regression

The model parameters that describe standing wave dynamics and harmonic generation at the tip vibration can be found via a regression problem. Here, it is formulated to minimize the discrepancy between model harmonic amplitudes and experimental harmonic amplitudes. To avoid the dominance of the fundamental harmonic over others in a regression problem, the amplitude of each harmonic can be weighted such that:

$$\begin{aligned} \{\hat{\xi}_{\text{pl}}, \hat{\xi}_{cr}, \hat{\sigma}_{\text{pl}}^{\text{Y}}\}^{(i)} = & \underset{\{\xi_{\text{cr}}, \xi_{\text{pl}}, \sigma_{\text{pl}}^{\text{Y}}\}^{(i)}}{\arg\min} \mathcal{C}(\xi_{\text{cr}}, \xi_{\text{pl}}, \sigma_{\text{pl}}^{\text{Y}}); \\ & \text{with} \quad \mathcal{C}(\{\xi_{\text{cr}}, \xi_{\text{pl}}, \sigma_{\text{pl}}^{\text{Y}}\}^{(i)}) = \sum_{h=1}^{3} \left(\frac{A_h(\{\xi_{\text{cr}}, \xi_{\text{pl}}, \sigma_{\text{pl}}^{\text{Y}}\}^{(i)}) - \hat{A}_h}{\hat{A}_h} \right)^2 \end{aligned} \tag{4.4}$$

where i corresponds to the ith time window, and $h = 1, 2, 3$ correspond to the fundamental, second, and third harmonic amplitudes. Eq. (4.4) is a regression on the harmonic amplitudes (standing wave assumption) performed per time window. This is justified since there are significant differences in harmonic amplitudes in the tip vibration: in Fig. 4.6, $\hat{A}_1^{(1)} \approx 1$ ms^{-1}, $\hat{A}_2^{(1)} \approx 3 \cdot 10^{-3}$ ms^{-1}, and $\hat{A}_3^{(1)} \approx 7 \cdot 10^{-4}$ ms^{-1}.

Copper at the onset and at the very high cycle fatigue regime

First, the results by fitting the parameters for the copper specimen of test number 3 are presented, which corresponds to the VHCF regime. First the fictitious yield stress is fixed to 10 MPa, giving

a ratio of $\sigma_{\mathrm{pl}}^{\mathrm{Y}}/\sigma^{\mathrm{Y}} \approx 0.1$ if the macroscopic yield stress of polycrystalline copper is $\sigma^{\mathrm{Y}} = 87$ MPa [Mar+20]. This provides a more interpretable parameter space in three dimensions: using the same data at the first time window, this parameter space is shown in Fig. 4.11. It can be seen here that the harmonic amplitudes' characteristics are more explicit: for the fundamental harmonic amplitude, an asymmetric decrease can be seen as the microcrack and microplastic volumes vary; the second harmonic amplitude is insensitive to the microplastic volume fraction; the third harmonic amplitude is influenced by both the microcrack and microplastic volumes.

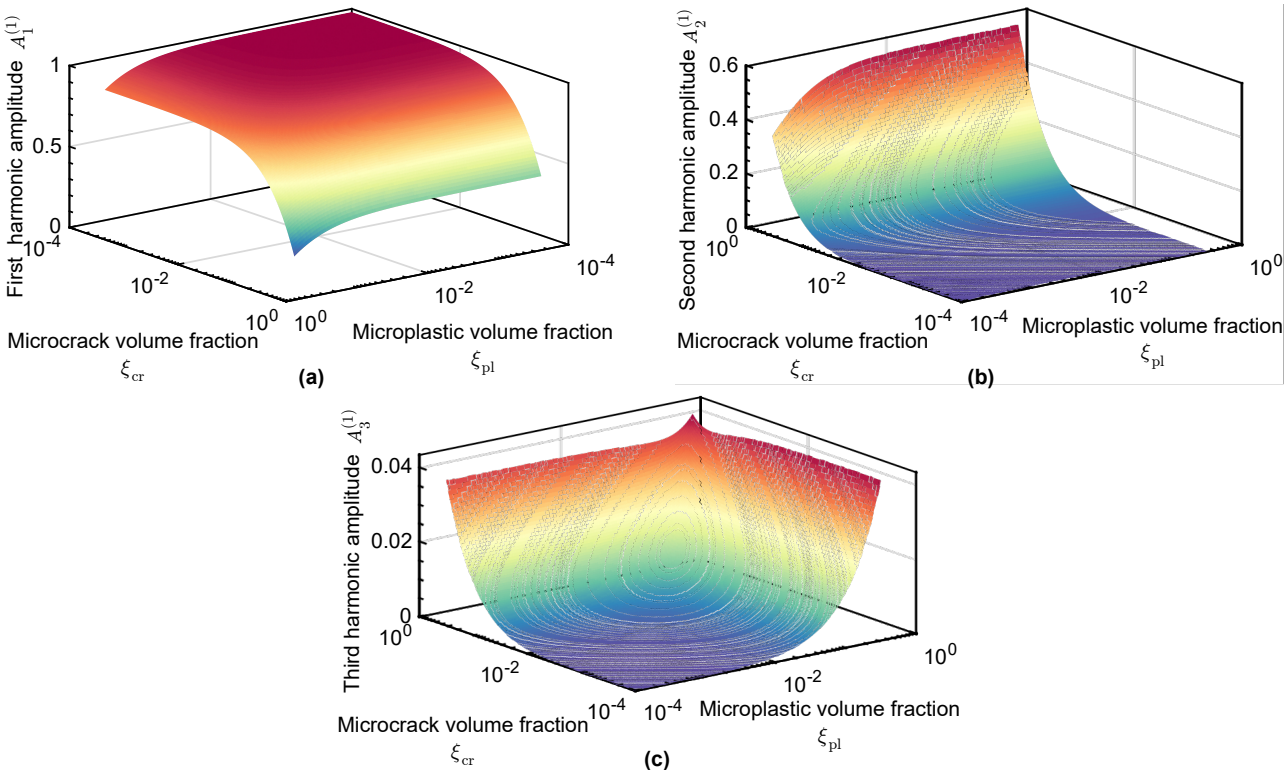

Figure 4.11: A three-dimensional parameter space of the copper fatigue specimen model (test 3) where the fundamental **(a)**, second **(b)**, and third harmonic amplitudes **(c)** are shown. This is using the base vibration signal at the first time window and fixing $\sigma^{\mathrm{Y}} = 10$ MPa.

Using the regression of Eq. (4.4) in a sliding window manner, the cost function is minimized (results shown in Fig. 4.12) to obtain the micromechanical parameters. The model can identify the corresponding micromechanical parameters up until the macrocrack formation, making it suitable to characterize harmonic generation of a copper fatigue at the VHCF regime. This can be seen in regression's cost function who has an acceptable error which decreases (as the higher harmonics

amplitudes vary according to Fig. 4.6) until the reaching $\approx 15 \cdot 10^7$ cycles where the error increase rapidly. The large error in the cost function at the end of the fatigue test is due to the fact that a macrocrack nonlinearity cannot be accurately represented by a diffuse microcracks in this model.

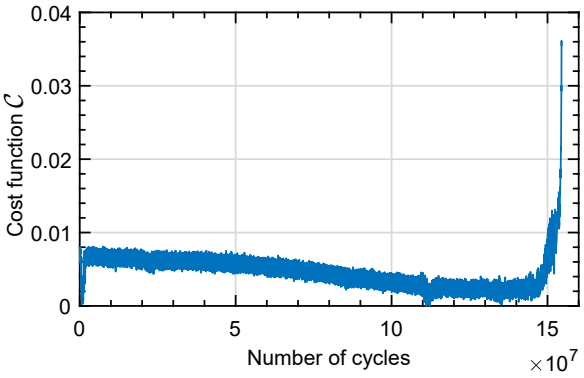

Figure 4.12: The evolution of the cost function of Eq. (4.4) versus the number of cycles (test 3).

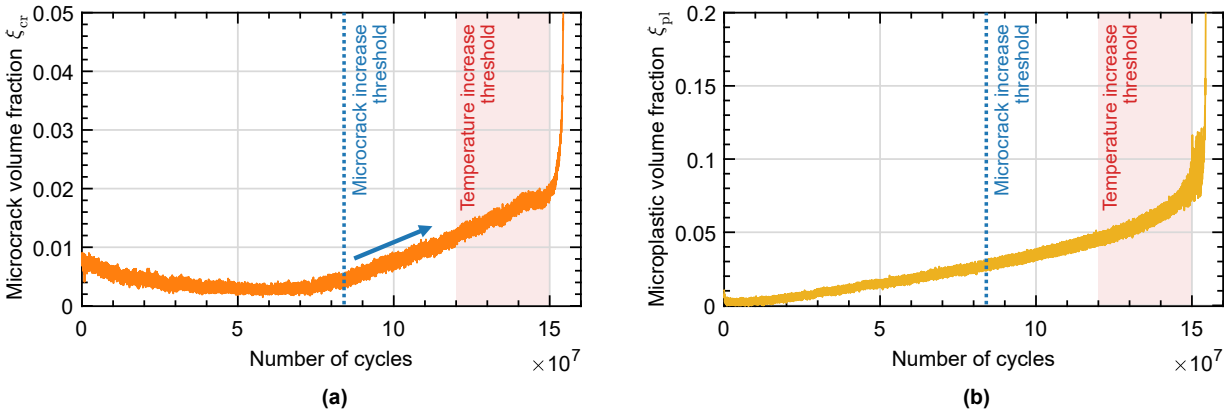

Figure 4.13: The calibrated micromechanical parameters, the microcrack **(a)** and microplastic inclusion **(b)** volume fractions, which replicate the higher harmonic generation between the copper fatigue specimen and model (test 3).

The relationship between the calibrated micromechanical parameters and the number of cycles for the copper fatigue specimen of test 3 is depicted in Fig. 4.13. In **(a)**, the variation of the microcrack volume fraction ξ_{cr} is shown: characteristically it shows a value above zero at the first time window. Subsequently, there is a slight decline in ξ_{cr}, followed by a stable phase, until it reaches the marked "microcrack increase threshold" at approximately 8.4×10^7 cycles. Beyond this point, there is a linear rise until about 15×10^7 cycles, after which an exponential increase is observed, culminating in large crack fracture. A red rectangle labeled "temperature increase threshold" marks the juncture

where there's a notable rise in the average surface temperature, as captured by the in-situ infrared thermography. The value of this threshold is defined in Fig. 4.14 as a small increase in the change of temperature can be seen near the latter half of the fatigue test. Note that the clarity and reliability of using this temperature increase is limited since the fatigue specimens are continuously refreshed. In Fig. 4.13 **(b)**, the microplastic volume fraction ξ_{pl} is shown to have a linear then exponential-like increase.

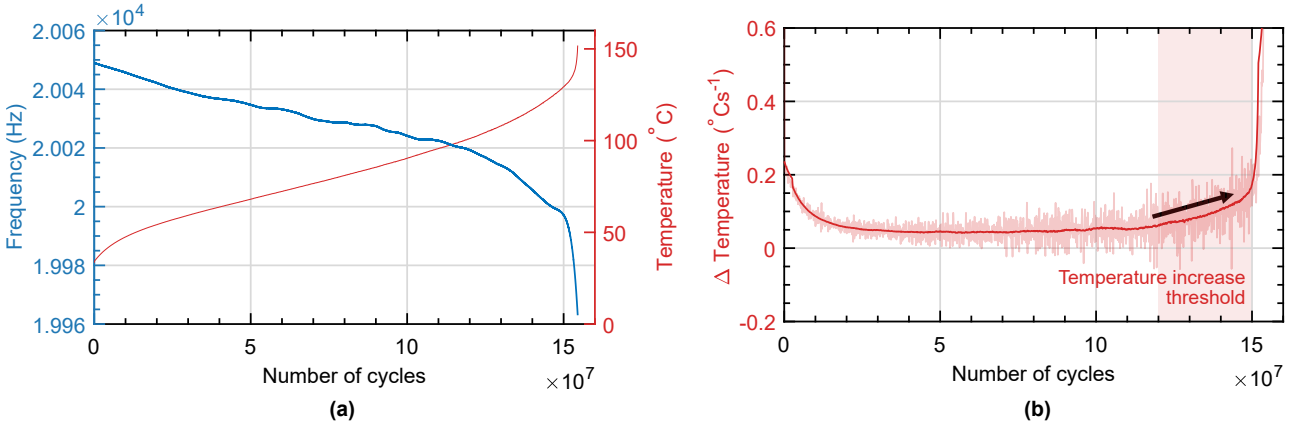

Figure 4.14: In **(a)**, the working frequency of the ultrasonic fatigue machine and average surface temperature of the fatigue specimen (test 3). In **(b)**, the change in temperature is plotted, where at $12 \cdot 10^7$ cycles a threshold of temperature increase before fatigue failure is marked.

Turning the attention to the copper fatigue test 12, this test corresponds to the onset of the VHCF regime, refer to the SN curve Fig. 4.5 (a). The model parameters ξ_{cr} and ξ_{pl} are varied, whereas $\sigma_{\text{pl}}^{\text{Y}} = 40$ MPa is fixed. What differs in this case is the experimental signal base and tip vibration. By using by Eq. (4.4), the subsequent calibrated micromechanical parameters and number of cycles for copper fatigue specimen of test 12 is shown in Fig. 4.15. Notable here is a similar trend is found for the microcrack volume fraction ξ_{cr}: an initial value which transitions to a minima, followed by an increase. In this case, the shape is reminiscent of the microcrack model's decrease (results seen in Chapter 2 Fig. 2.14 **(b)**) for the second harmonic evolution. In regards to the microplastic volume fraction, a steady increase can be seen, where the inflection point of the "microcrack increase threshold" is marked. For copper in the VHCF regime, the percent of life before on onset of microcrack volume fraction growth occurs at about 50% of its fatigue life for the fatigue specimen model, as shown in Fig. 4.13 **(a)**; whereas in Fig. 4.15 **(a)** this occurs at about 77% and a much steeper increase in the volume fraction following. Notably, the first time instant of microplastic volume fraction between test

3 and test 12 are not the same, whereas their final values seem to converge.

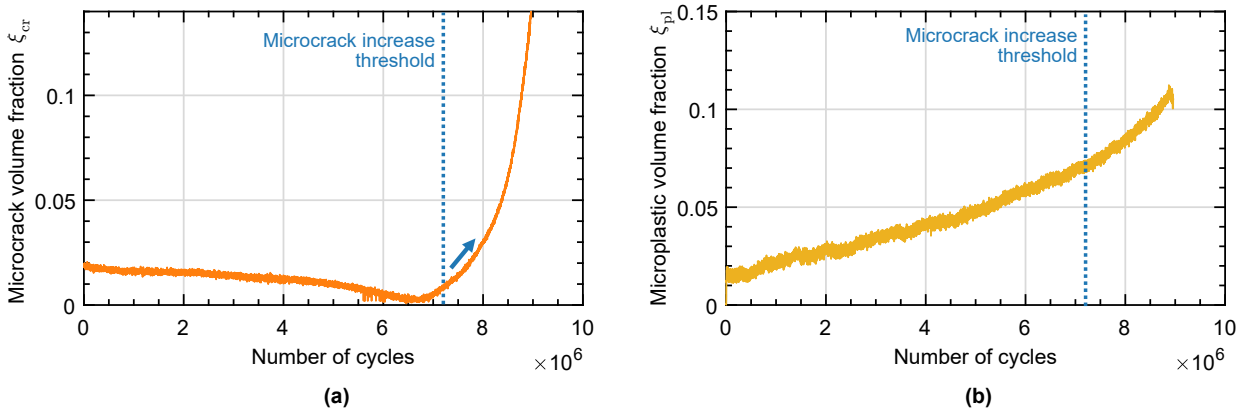

Figure 4.15: The calibrated micromechanical parameters, the microcrack **(a)** and microplastic inclusion **(b)** volume fractions, which replicate the higher harmonic generation between the copper fatigue specimen and model (test 12).

Discussion A notable characteristic of the evolution of micromechanical parameters of both models can be seen in the behavior of the microcrack volume fraction ξ_{cr}. For example, in Fig. 4.13 **(a)**, ξ_{cr} has a much higher sensitivity compared to other *in-situ* measurements in the VHCF regime: the second harmonic amplitude ratio's evolution of Fig. 4.6 is a steady decrease until a sudden increase due to microcrack initiation; the use of tracking the working frequency of the ultrasonic fatigue test machine or the monitoring of the average surface temperature (Fig. 4.14 **(a)**). The "microcrack increase threshold" has an associated microplastic volume fraction at 3.5%, which suggests that a threshold amount of microplasticity is required before the microcrack volume fraction parameter increases. If ξ_{cr} and ξ_{pl} are taken as physically consistent values, this would support the idea that microplasticity is the precursor for microcrack initiation.

High-speed infrared thermography shown in Fig. 4.16 was able to capture the nucleation of a macrocrack propagation for test 3, following the method of Ranc [RWP08]. This supports the fact that the increase of the microcrack volume fraction is not due to only a surface macrocrack, but more likely due to subsurface mechanisms. This is due to the fact that an increase of the microcrack volume fraction preludes the observation of a significant change in the average surface temperature. Post-failure fractography in Fig. 4.17 substantiates a macrocrack propagation inwards from the surface, showing classical oxidation due to large heat dissipation from crack propagation.

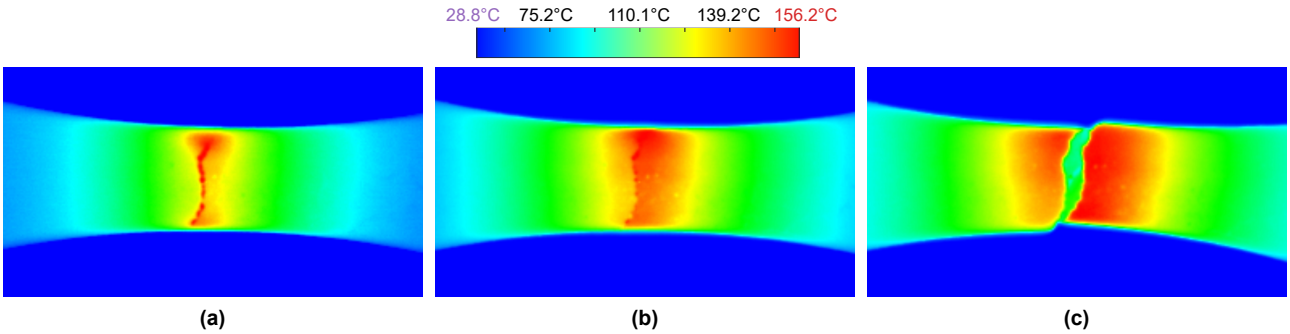

Figure 4.16: High-speed infrared thermography with of surface macrocrack propagation recording at 480 Hz for 2 sequential frames, where **(a)** the crack propagation before total fracture is shown, and **(c)** corresponds to the last time instance of the vibration signal (test 3).

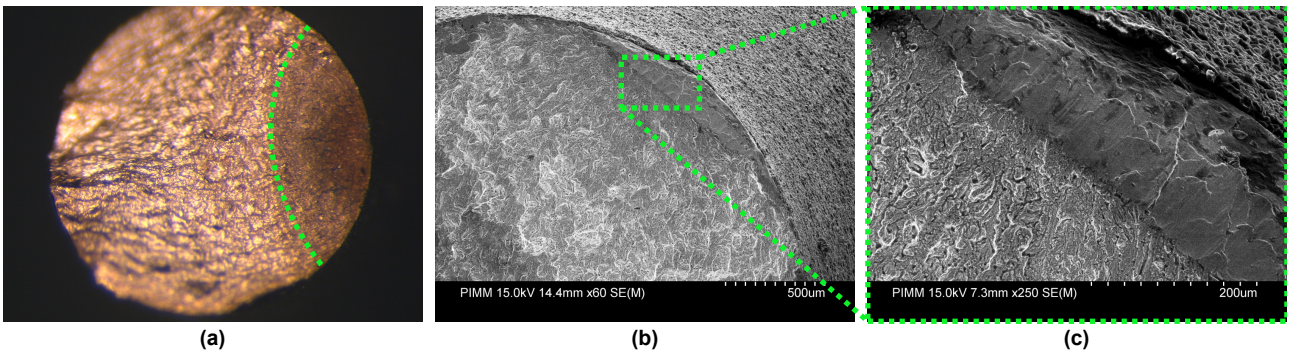

Figure 4.17: Post-fracture microscopy of the copper fatigue specimen of test 3.

However, there are issues about the physicality ξ_{cr}. First, the volume fraction above zero at the first time window implies the existence of microcracks at the onset. This value of ξ_{cr} is required as it contributes the majority of the second harmonic generation of the model. The subsequent decrease in the volume fraction ξ_{cr} implies a reduction of the microcracks, which is a non-recoverable phenomena. However, as demonstrated in the microcrack model of Fig. 2.14, a multi-harmonic input can elicit a decrease the second harmonic as the microcrack volume fraction increases. Second, the value of the microcrack volume fraction is larger than expected in reality: this is especially true for Fig. 4.15 where at $\approx 8.3 \cdot 10^6$ cycles indicates a 5% volume fraction. Finally, the microcrack parameter directly models diffuse microcracks orientated in mode-I: as discussed in Chapter 2, the overlap in the micro- and macrocrack models in harmonic generation do not allow a distinguished between the two phenomena by harmonic generation by itself.

While it is tempting to interpret the microplasticity further, for example a analysis of the cumu-

lative plastic strains, or dissipation, we remind the readers that the modeling efforts here have made strong assumptions. Microcracks likely have plastic fronts during the opening of their aperture, and this plastic front is neglected since the microcracks are modeled as purely elastic and non-propagating. The yield stress, as well as the plasticity law (classic perfect plasticity), are chosen to elicit an opening of the aperture of the hysteresis loop, and is done so by a single fixed parameter. It's not known if the zones of microplasticity (e.g. inelastic dislocations glide) exhibit a response similar to that macroscopic continuum theories. This suggests an further study into crystal plasticity and dislocation dynamics, and adopting a more pertinent plasticity law.

C70 steel at the very high cycle fatigue regime

Following the similar procedure as shown previously for the copper specimen model, the analysis for the first time window in the C70 steel fatigue test utilizes regression, setting the microplastic fictitious yield stress at 1% of C70's macroscopic yield stress, i.e. $\sigma_{\text{pl}}^{\text{Y}} = 49$ MPa. A comparison between the parameter spaces of copper (Fig. 4.11) and C70 steel (Fig. 4.18) models reveals notable distinctions. For the C70 steel, the third harmonic amplitude is lower, a phenomenon attributable to the different structural dynamics of the problem. Experimentally, this reduced amplitude in the third harmonic is also observed in the tip vibration of C70 steel, contrasting with the results from both copper tests. Furthermore, in the parameter space for the first harmonic of the C70 steel model in Fig. 4.18 **(a)**, there is a discernible trend: as $\xi_{\text{pl}} \to 1$, there is an increase in the first harmonic amplitude, in contrast to the decrease observed in the copper fatigue specimen model of Fig. 4.11 **(a)**. Additionally, the parameter space for the third harmonic in the C70 steel fatigue specimen model exhibits a notable asymmetry about the zero-origin on the x-y axes.

By implementing a sliding window approach with the regression of Eq. (4.4) on the C70 fatigue specimen model, the micromechanical parameters are obtained and evolution of the error is given in Fig. 4.19. Here the error evolution remains more steady compared to Fig. 4.12, which can be attributed to the relatively less harmonic generation measured by the laser vibrators for the C70 fatigue specimen model. The error jumps at just before the point of fracture during the ultrasonic fatigue test. The calibration of micromechanical parameters reveals nuanced differences when compared to the copper fatigue specimen models. The evolution of these parameters, as represented in Fig. 4.20, demonstrates a non-existent evolution of microcrack ξ_{cr} and microplastic ξ_{pl} volume fractions. The microcrack

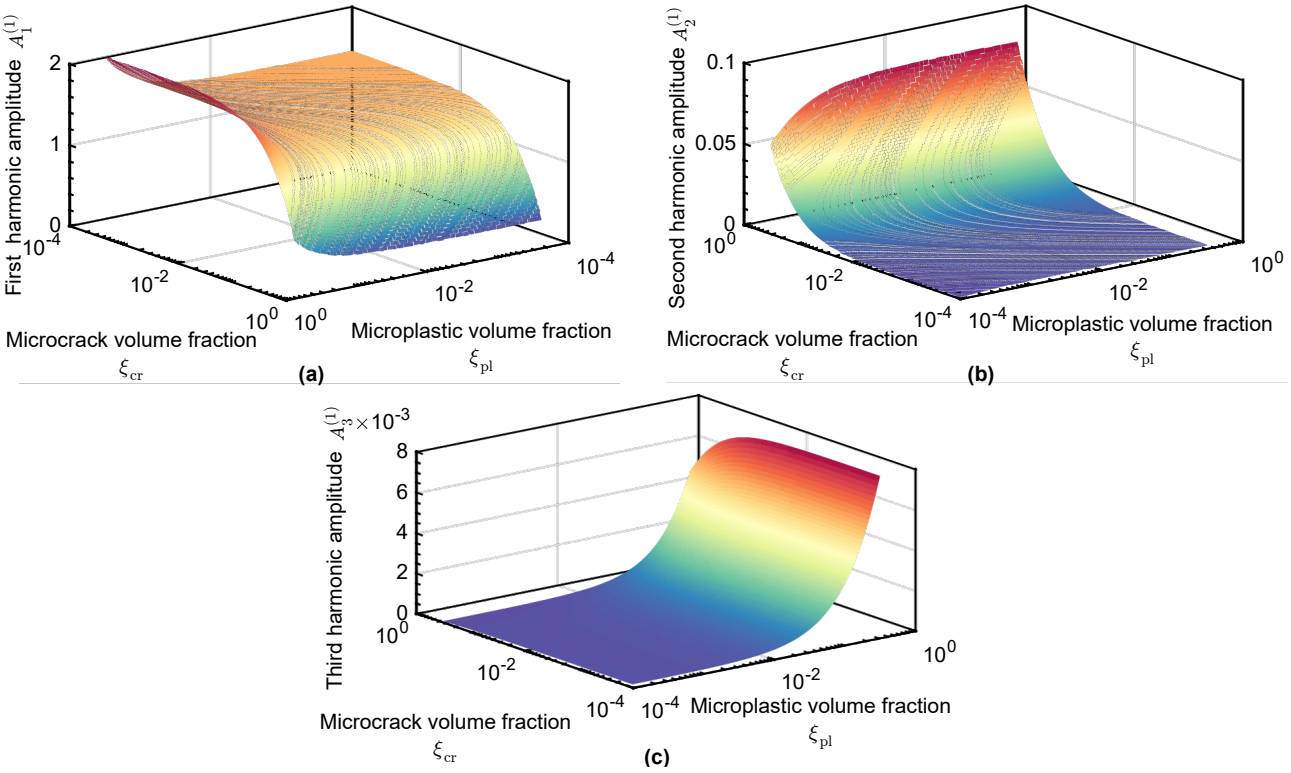

Figure 4.18: A three-dimensional parameter space of the C70 fatigue specimen model (test 14) where the fundamental **(a)**, second **(b)**, and third harmonic amplitudes **(c)** are shown. This is using the base vibration signal at the first time window and fixing $\sigma^{\mathrm{Y}} = 45$ MPa.

volume fraction ξ_{cr} in **(a)** initially exhibits a minimal value, and only begins increasing at around $1.5 \cdot 10^7$ cycles due to the initiation of suspected micro- to macrocrack. More notably, no trench-like shape is observed leading to an increase of the volume fraction, as seen in for the copper specimen models of Fig. 4.13 **(a)** and Fig. 4.15 **(a)**. The red rectangle labeled "temperature increase threshold" in Fig. 4.20 marks the moment a measurable rise in the average surface temperature change in Fig. 4.21. Notably, the microcrack volume fraction parameter in the C70 fatigue specimen model does not precede this moment as seen in the copper specimen models.

Fig. 4.20 **(b)** illustrates the behavior of the microplastic volume fraction ξ_{pl} in C70 fatigue specimen mode, which shows an oscillatory behavior, suggesting a problem with the parameter space not able to recreate the third harmonic generation seen in the experimental data. This slope and sudden rate of increase in the C70 steel model is similar to the microcrack volume fraction ξ_{cr}, indicating a non-observable microplastic accumulation under similar fatigue conditions: the modeling efforts here clearly diverge from the trends observed in copper specimen models.

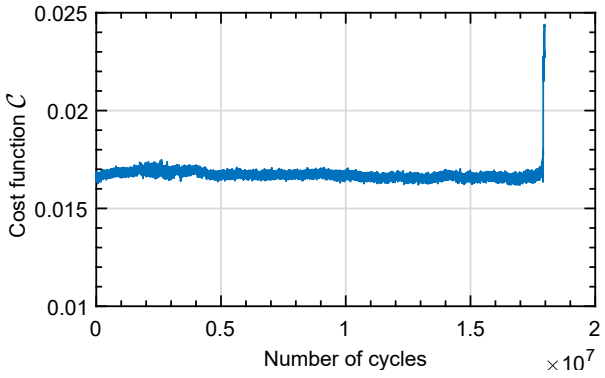

Figure 4.19: The evolution of the cost function of Eq. (4.4) versus the number of cycles (test 14).

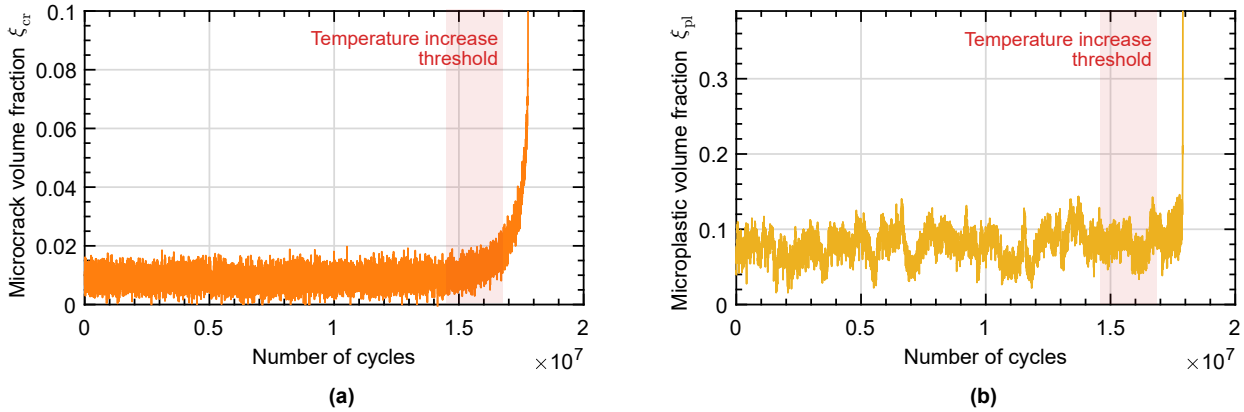

Figure 4.20: The calibrated micromechanical parameters, the microcrack **(a)** and microplastic inclusion **(b)** volume fractions, which replicate the higher harmonic generation between the C70 fatigue specimen and model (test 14).

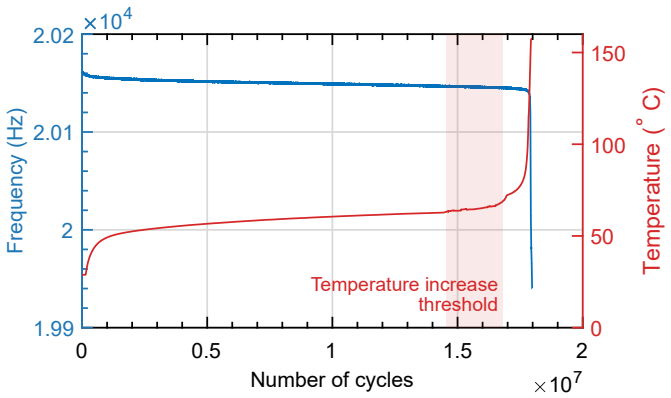

Figure 4.21: The working frequency of the ultrasonic fatigue machine and average surface temperature of the fatigue specimen (test 14).

Discussion Contrary to the copper fatigue specimen models' results, the C70 fatigue specimen model does not exhibit an early threshold or increase with the micromechanical parameters. It is uncertain if this observation underscores any unique fatigue characteristics of C70 steel when compared to copper. This is mostly likely due to the small increase of higher harmonics in the experimental data. The results after model parameter identification shows a plateau follow by a rapid increase of microcrack and microplastic volume fractions, point to fundamental differences in fundamental assumptions between the models and experimental data.

One notable difference is the fish-eye failure seen by the C70 steel fatigue specimen in the fractographs of Fig. 4.23. An examination of the optical micrograph in **(a)** reveals the bright area, where at its center a void-like profile can be seen. A closer examination using SEM in Fig. 4.22 **(b)** and **(c)** reveals an initiation source from a Pearlite super grain, similarly found by Bathias et al. in [Bat+13]. However, these experimental observations do not necessarily give an explanation on why the presented C70 steel specimen (test 14), as well as other C70 steel fatigue specimen in the same test campaign, has little to no evolution of micromechanical model parameters. If these model parameters are to be interpreted, they suggest that the harmonic generation due to any possible microcrack and/or microplastic phenomena are not strong enough relative to the effect of a multi-harmonic base vibration. Thus, any early indication by the micromechanical parameters are suppressed. This can be understood from the micromechanical simulations shown in Chapter 2, where the evolution of the higher harmonics were insensitive due to the presence of a multi-harmonic input.

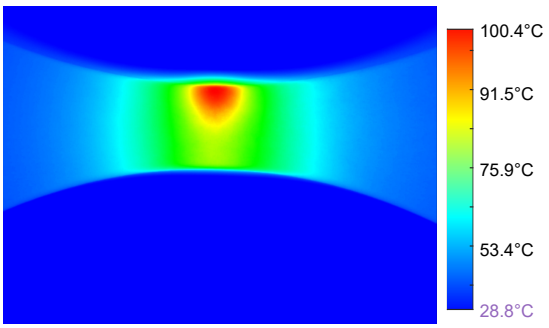

Figure 4.22: High-speed infrared thermography showing a heat source located near the corner and planar face about the centroid of the C70 steel fatigue specimen (test 14).

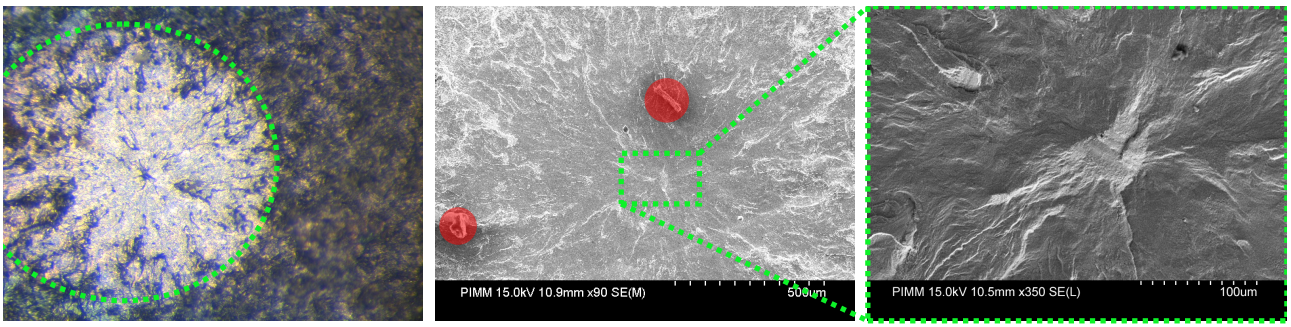

Figure 4.23: Post-fracture microscopy of the C70 steel fatigue specimen of test 14. The red zones in **(b)** correspond to foreign particles and not of the fracture surface.

4.4 Summary

This chapter discusses the calibration of model parameters to describe standing wave dynamics and harmonic generation at the tip vibration through regression. The regression problem is formulated to minimize the discrepancies between model and experimental fundamental, second, and third harmonic amplitudes. For the both fatigue specimen:

- The multiscale model was successfully able to describe the second and third harmonic generation in experimental data for both fatigue specimen.
- The parameter space of the models show that the model is insensitive to the choice of the microplastic yield stress parameter, as long as it is between the two points where hysteresis is present in the microplastic inclusions.
- A large error in the cost function towards the end of the fatigue test indicates a limitation in representing the strong nonlinearity due to macrocrack propagation for both copper and steel specimen models.
- For the copper specimen, the evolution of the parameters reveals a linear growth to exponential growth in the microcrack volume fraction in the VHCF regime, whereas before the HCF regime the linear growth is not present. The life spent before these changes in correspond to 50% for the VHCF regime ($N_f = 1.5 \cdot 10^8$) and 77% for the HCF regime ($N_f = 8.9 \cdot 10^6$). Both regimes see a steady increase in microplastic inclusion volume fraction at the onset.

- For the C70 steel specimen, there is little evolution in both the microcrack and microplastic volume fraction parameters, until the onset of a macrocrack propagation. The posited reasons of this discrepancy are due are the combination of different in material behavior with multi-harmonic nature of the base vibration. pronounced in the case of the steel

- However, the initial non-zero values for both copper and steel, and the decreasing then increasing behavior of the microcrack volume fraction for copper raise questions about its the model parameter's physical interpretation.

Conclusions and perspectives

This dissertation aimed to develop a *in-situ* methodology for estimating and interpreting the nonlinearities present during ultrasonic fatigue tests in the VHCF domain. It's shown that the high-frequency loading of the ultrasonic fatigue test machine manifests higher harmonics in the vibration signal. The source of the this harmonic generation is studied from both experimental and modeling perspectives. The goal is aimed at isolating the material nonlinearities due to the micromechanical changes from other nonlinearities in the system. This is complicated by the fact that ultrasonic fatigue test machines have a multi-harmonic input wave which solicits an ultrasonic fatigue specimen. A summary of the major conclusions are provided below:

Nonlinear material models

- The analysis of the nonlinear acoustic parameter is shown to be flawed for ultrasonic fatigue tests: the material nonlinearity has a small contribution to second harmonic generation. A difference of magnitude is approximately ten for polycrystalline copper at the VHCF.
- The models of Eshelby-based homogenization of diffuse microcracks with closure and microplastic inclusions are demonstrated to be a candidate for mesoscopic source of nonlinear harmonic generation. When subject to a multi-harmonic input, the behavior of the nonlinear harmonic generation becomes increasingly complex and insensitive compared to a single-harmonic input, as the volume fraction of the heterogeneities increase.
- A mode-I macroscrack model with closure is shown to have a similar nonlinear harmonic generation with the microcrack model, except it is parameterized by the crack surface. The analytical form of the model also demonstrates that under different load ratios, the nonlinear harmonic generation becomes increasing complex due to a sinc modulation.

Signal processing for ultrasonic fatigue signals

- The estimation of sinusoidal parameters is influenced by the tradeoffs of finite window lengths and accuracy when dealing with quasi-stationarity and the Rayleigh limit. A small time window is more locally stationary compared to larger windows, lowers the computational time for sinusoidal estimation algorithms, and provides more discrete parameter estimates.

- The benchmark performed on quasi-stationary signals found in VHCF vibration revealed that ESPRIT and NOMP algorithms have the best trade-off between signal length and accuracy. However, ESPRIT is a cubic-complex algorithm. This motivates exploration into adapting ESPRIT into a more computationally efficient form for *in-situ* ultrasonic fatigue vibration signals.

- An ESPRIT-based algorithm is developed, namely FFT-ESPRIT, which approximates the signal subspace from the FFT. The algorithm achieves similar accuracy with the original ESPRIT algorithm. The computational complexity is reduced from cubic to quasi-linear complexity through heavily implementation of the FFT and the Hankel matrix properties of the signal.

Ultrasonic fatigue specimen model

- The steady-state nature of the ultrasonic fatigue system's dynamics allows for a reduce order model of the ultrasonic fatigue specimen. This enables rapid computation using modal shape functions. The localized nature of fatigue is accounted for by the modal contribution of nonlinearities at a centroid volume. A solution of the global equations of motion is computed by the harmonic balance method. This avoids costly finite element-based dynamic solutions.

- The boundary conditions of the model demonstrate the base vibration substantiate the use of a second laser vibrometer to account for the multi-harmonic input.

- For polycrystalline copper and C70 steel specimens experimental data, the simulated multiscale model was successfully able to describe the second and third harmonic generation in experimental data for both fatigue specimen with low error before macrocrack propagation.

- For polycrystalline copper, the evolution of the microcrack volume fraction transitions from linear growth to exponential growth in the in the VHCF regime, whereas before the HCF regime the linear growth is not present pronounced. The life spent before these changes in correspond to 50% for the VHCF regime ($N_f = 1.5 \cdot 10^8$) and 77% for the HCF regime ($N_f = 8.9 \cdot 10^6$). Both regimes see a steady increase in microplastic inclusion volume fraction at the onset.

- The physical interpretation of these parameters suggest that ultrasonic fatigue tests of copper sees monotonically increasing microplasticity, and is precursor for damage.

- For C70 steel, the evolution of the microcrack and microplastic inclusion volume fractions reflect the negligible harmonic generation seen in the ultrasonic fatigue experiments. The parameters' evolution are consistent when the macrocrack forms.
- The physical interpretation of these parameters suggest that the harmonic generation due to any possible microcrack and/or microplastic phenomena are not strong enough relative to the effect of a multi-harmonic base vibration.

Here, it's remarked that some key aspects can be explored in order to improve the understand or results shown in this dissertation:

- The multiple harmonics present in the input to the fatigue specimen is suspected to decrease the sensitivity of higher harmonic generation of the material nonlinearities. Therefore, one effort to improve the fidelity of the harmonic amplitudes can come from an improvement of the ultrasonic fatigue test machine's linearity. A successful predistortion technique applied the input voltage signal, e.g. the work of [NSL18], can linearize the nonlinearity due to the ultrasonic transducer, ideally providing less prominent higher harmonics.
- Further exploration into the discrepancy between the physical sources of harmonic generation, and the nonlinear material models is warranted. This is suggested for both polycrystalline copper (or ductile single phase metals) as well as C70 steel (or type II materials). The physical interpretation of the micromechanical parameters suggest both promising and impossible phenomena (the decrease of microcrack volume fraction in copper).
- The nonlinear material models can be improved to account for increasingly complex behavior which better match the physics. For example, a crack with perfect contact (no friction) is not a dissipative source. However in reality, the microcracks and microplasticity are intrinsically tied, due to the plasticity of the crack front, and the energy used to propagate the crack.
- A significant focus was placed on introducing a data-driven approach to the analysis of vibration measurement data. As part of this endeavor, contributions were made to enhance the algorithm used in the SINDy framework. However, the practical application of TRIM on the ultrasonic fatigue experiments could not be realized within the time constraints of this dissertation. This remains an area for future exploration, which encourages interpretable machine learning.

Bibliography

[21] *https://github.com/slkiser/lineSpectraVibration*. Nov. 25, 2021.

[3R] 3R. *Fully Reversed Fatigue Tests – MEG20*. URL: https://3r-labo.com/en/produit/fully-reversed-fatigue-tests/ (visited on 09/13/2023).

[Aba+19] S. G. Abaimov et al. "Multi-Step Homogenization in the Mori-Tanaka-Benveniste Theory". In: *Composite Structures* 223 (Sept. 2019), p. 110801. DOI: 10.1016/j.compstruct.2019.03.073.

[ABN21] T. Amir, R. Basri, and B. Nadler. "The Trimmed Lasso: Sparse Recovery Guarantees and Practical Optimization by the Generalized Soft-Min Penalty". In: *SIAM Journal on Mathematics of Data Science* 3.3 (Jan. 2021), pp. 900–929. DOI: 10.1137/20M1330634.

[AG] T. AG. *Linear Ultrasound Converters*. URL: https://www.telsonic.com/en/products/linear-ultrasound-converters-se-series/.

[AIB23] J. Antoni, J. Idier, and S. Bourguignon. "A Bayesian Interpretation of the L-curve". In: *Inverse Problems. An International Journal on the Theory and Practice of Inverse Problems, Inverse Methods and Computerized Inversion of Data* 39.6 (May 2023), p. 065016. DOI: 10.1088/1361-6420/accdfc.

[AM05] E. Aboutanios and B. Mulgrew. "Iterative Frequency Estimation by Interpolation on Fourier Coefficients". In: *IEEE Transactions on Signal Processing* 53.4 (Apr. 2005), pp. 1237–1242. DOI: 10.1109/tsp.2005.843719.

[AR13] M. S. Asif and J. Romberg. "Fast and Accurate Algorithms for Re-Weighted L1-Norm Minimization". In: *IEEE Transactions on Signal Processing* 61.23 (Dec. 2013), pp. 5905–5916. DOI: 10.1109/TSP.2013.2279362.

[ASM96] ASM Handbook Committee. *Fatigue and Fracture*. ASM International, Jan. 1, 1996. DOI: 10.31399/asm.hb.v19.9781627081931.

[Ava+22] M. Avateffazeli et al. "Very High Cycle Fatigue at Elevated Temperatures: A Review on High Temperature Ultrasonic Fatigue". In: *Journal of Space Safety Engineering* 9.4 (Dec. 1, 2022), pp. 488–512. DOI: 10.1016/j.jsse.2022.07.006.

[Ban+18] M. V. Bannikov et al. "Investigation of Damage Accumulation in a Prestrained Aluminum-Magnesium Alloy under Gigacycle Fatigue". In: *AIP Conference Proceedings* 2053.1 (Dec. 19, 2018), p. 030003. DOI: 10.1063/1.5084364.

[Bar+08] A. R. Barron et al. "Approximation and Learning by Greedy Algorithms". In: *The Annals of Statistics* 36.1 (Feb. 2008), pp. 64–94. DOI: 10.1214/009053607000000631.

[Bas85] M. Bastiaans. "On the Sliding-Window Representation in Digital Signal Processing". In: *IEEE Transactions on Acoustics, Speech, and Signal Processing* 33.4 (Aug. 1985), pp. 868–873. DOI: 10.1109/tassp.1985.1164653.

[Bat+13] C. Bathias et al. "Microplasticity , Microdamage, Microcracking in Ultrasonic Fatigue". In: *13th International Conference on Fracture 2013, ICF 2013* 6 (Jan. 1, 2013), pp. 5048–5057.

[Bat06] C. Bathias. "Piezoelectric Fatigue Testing Machines and Devices". In: *International Journal of Fatigue*. Third International Conference on Very High Cycle Fatigue (VHCF-3) 28.11 (Nov. 1, 2006), pp. 1438–1445. DOI: 10.1016/j.ijfatigue.2005.09.020.

[Bat99] C. Bathias. "There Is No Infinite Fatigue Life in Metallic Materials". In: *Fatigue & Fracture of Engineering Materials & Structures* 22.7 (1999), pp. 559–565. DOI: 10.1046/j.1460-2695.1999.00183.x.

[BBG01] M. Bornert, T. Bretheau, and P. Gilormini. *Homogénéisation en mécanique des matériaux: Matériaux aléatoires élastiques et milieux périodiques*. Hermès Science Publications, 2001. 255 pp. Google Books: PMNwOwAACAAJ.

[BBL20] J. Bluthé, B. Bary, and E. Lemarchand. "Closure of Parallel Cracks: Micromechanical Estimates versus Finite Element Computations". In: *European Journal of Mechanics - A/Solids* 81 (May 1, 2020), p. 103952. DOI: 10.1016/j.euromechsol.2020.103952.

[BCM17] D. Bertsimas, M. S. Copenhaver, and R. Mazumder. *The Trimmed Lasso: Sparsity and Robustness*. Aug. 15, 2017. DOI: 10.48550/arXiv.1708.04527. arXiv: 1708.04527 [math, stat]. URL: http://arxiv.org/abs/1708.04527 (visited on 06/28/2023). preprint.

[BDC91] Y. Benveniste, G. J. Dvorak, and T. Chen. "On Diagonal and Elastic Symmetry of the Approximate Effective Stiffness Tensor of Heterogeneous Media". In: *Journal of the Mechanics and Physics of Solids* 39.7 (Jan. 1, 1991), pp. 927–946. DOI: 10.1016/0022-5096(91)90012-D.

[BE79] J. Bonneville and B. Escaig. "Cross-Slipping Process and the Stress-Orientation Dependence in Pure Copper". In: *Acta Metallurgica* 27.9 (Sept. 1, 1979), pp. 1477–1486. DOI: 10.1016/0001-6160(79)90170-6.

[Ben87] Y. Benveniste. "A New Approach to the Application of Mori-Tanaka's Theory in Composite Materials". In: *Mechanics of Materials* 6.2 (June 1, 1987), pp. 147–157. DOI: 10.1016/0167-6636(87)90005-6.

[BF65] M. A. Breazeale and J. Ford. "Ultrasonic Studies of the Nonlinear Behavior of Solids". In: *Journal of Applied Physics* 36.11 (1965), pp. 3486–3490. DOI: 10.1063/1.1703023.

[Bil13] S. A. Billings. *Nonlinear System Identification: NARMAX Methods in the Time, Frequency, and Spatio-Temporal Domains*. Chichester, West Sussex, United Kingdom: John Wiley & Sons, Inc, 2013. 1 p.

[BK20] J. J. Bramburger and J. N. Kutz. "Poincaré Maps for Multiscale Physics Discovery and Nonlinear Floquet Theory". In: *Physica D: Nonlinear Phenomena* 408 (July 1, 2020), p. 132479. DOI: 10.1016/j.physd.2020.132479.

[Bla+15] A. Blanche et al. "Dissipation Assessments during Dynamic Very High Cycle Fatigue Tests". In: *Experimental Mechanics* 55.4 (Apr. 2015), pp. 699–709. DOI: 10.1007/s11340-014-9857-3.

[BLR11] B. Bourdin, C. J. Larsen, and C. L. Richardson. "A Time-Discrete Model for Dynamic Fracture Based on Crack Regularization". In: *International Journal of Fracture* 168.2 (Apr. 1, 2011), pp. 133–143. DOI: 10.1007/s10704-010-9562-x.

[BM86] Y. Bresler and A. Macovski. "Exact Maximum Likelihood Parameter Estimation of Superimposed Exponential Signals in Noise". In: *IEEE Transactions on Acoustics, Speech, and Signal Processing* 34.5 (Oct. 1986), pp. 1081–1089. DOI: 10.1109/tassp.1986.1164949.

[BNC18] L. Boninsegna, F. Nüske, and C. Clementi. "Sparse Learning of Stochastic Dynamical Equations". In: *The Journal of Chemical Physics* 148.24 (June 28, 2018), p. 241723. DOI: 10.1063/1.5018409.

[Boa18] N. T. S. Board. *Left Engine Failure and Subsequent Depressurization, Southwest Airlines Flight 1380, Boeing 737-7H4, N772SW*. Nov. 5, 2018. URL: https://www.ntsb.gov/investigations/Pages/DCA18MA142.aspx (visited on 09/21/2023).

[BP05] C. Bathias and P. C. Paris. *Gigacycle Fatigue in Mechanical Practice*. New York: Marcel Dekker, 2005. 304 pp.

[BP07] C. Bathias and P. C. Paris. "Initiation in the Gigacycle Fatigue Regime". In: *4th Int. Conference on Very High Cycle Fatigue*. 2007.

[BPK16] S. L. Brunton, J. L. Proctor, and J. N. Kutz. "Discovering Governing Equations from Data by Sparse Identification of Nonlinear Dynamical Systems". In: *Proceedings of the National Academy of Sciences* 113.15 (Apr. 12, 2016), pp. 3932–3937. DOI: 10.1073/pnas.1517384113.

[Bra] Branson. *Branson Converters Brochure*. URL: https://www.emerson.com/documents/automation/brochure-converters-branson-en-us-164730.pdf.

[BRD08] R. Badeau, G. Richard, and B. David. "Performance of ESPRIT for Estimating Mixtures of Complex Exponentials Modulated by Polynomials". In: *IEEE Transactions on Signal Processing* 56.2 (Feb. 2008), pp. 492–504. DOI: 10.1109/TSP.2007.906744.

[Bro+14] D. Broda et al. "Modelling of Nonlinear Crack–Wave Interactions for Damage Detection Based on Ultrasound—A Review". In: *Journal of Sound and Vibration* 333.4 (Feb. 14, 2014), pp. 1097–1118. DOI: 10.1016/j.jsv.2013.09.033.

[Bru64] K. Brugger. "Thermodynamic Definition of Higher Order Elastic Coefficients". In: *Physical Review* 133 (6A Mar. 16, 1964), A1611–A1612. DOI: 10.1103/PhysRev.133.A1611.

[BT63] M. A. Breazeale and D. O. Thompson. "Finite-Amplitude Ultrasonic Waves in Aluminum". In: *Applied Physics Letters* 3.5 (Sept. 1, 1963), pp. 77–78. DOI: 10.1063/1.1753876.

[BTR13] B. N. Bhaskar, G. Tang, and B. Recht. "Atomic Norm Denoising With Applications to Line Spectral Estimation". In: *IEEE Transactions on Signal Processing* 61.23 (Dec. 2013), pp. 5987–5999. DOI: 10.1109/tsp.2013.2273443.

[BV11] P. Bühlmann and S. Van de Geer. *Statistics for High-Dimensional Data: Methods, Theory and Applications*. Springer Series in Statistics. Berlin, Heidelberg: Springer-Verlag Berlin Heidelberg Springer e-books, 2011.

[BWM22] S. Barton, M. K.-B. Weiss, and H. J. Maier. "In-Situ Characterization of Microstructural Changes in Alloy 718 during High-Temperature Low-Cycle Fatigue". In: *Metals* 12.11 (11 Nov. 2022), p. 1871. DOI: 10.3390/met12111871.

[Can11] C. Candan. "A Method For Fine Resolution Frequency Estimation From Three DFT Samples". In: *IEEE Signal Processing Letters* 18.6 (June 2011), pp. 351–354. DOI: 10.1109/lsp.2011.2136378.

[Can84] J. H. Cantrell. "Acoustic-Radiation Stress in Solids. I. Theory". In: *Physical Review B* 30.6 (Sept. 15, 1984), pp. 3214–3220. DOI: 10.1103/PhysRevB.30.3214.

[Can94] J. H. Cantrell. "Crystalline Structure and Symmetry Dependence of Acoustic Nonlinearity Parameters". In: *Journal of Applied Physics* 76.6 (Sept. 15, 1994), pp. 3372–3380. DOI: 10.1063/1.357463.

[Cap69] J. Capon. "High-Resolution Frequency-Wavenumber Spectrum Analysis". In: *Proceedings of the IEEE* 57.8 (Aug. 1969), pp. 1408–1418. DOI: 10.1109/proc.1969.7278.

[CC20] A. Cultrera and L. Callegaro. "A Simple Algorithm to Find the L-curve Corner in the Regularisation of Ill-Posed Inverse Problems". In: *IOP SciNotes* 1.2 (Aug. 2020), p. 025004. DOI: 10.1088/2633-1357/abad0d.

[CD98] S. Chen and D. Donoho. "Application of Basis Pursuit in Spectrum Estimation". In: *Proceedings of the 1998 IEEE International Conference on Acoustics, Speech and Signal Processing, ICASSP '98 (Cat. No.98CH36181)*. 1998 IEEE International Conference on Acoustics, Speech, and Signal Processing. Vol. 3. Seattle, WA, USA: IEEE, 1998, pp. 1865–1868. DOI: 10.1109/icassp.1998.681827.

[CDD09] A. Cohen, W. Dahmen, and R. Devore. "Compressed Sensing and Best k -Term Approximation". In: *Journal of the American Mathematical Society* 22 (Jan. 1, 2009), pp. 211–231. DOI: 10.1090/S0894-0347-08-00610-3.

[CDY01] T. Chondros, A. Dimarogonas, and J. Yao. "Vibration of a Beam with a Breathing Crack". In: *Journal of Sound and Vibration* 239.1 (Jan. 2001), pp. 57–67. DOI: 10.1006/jsvi.2000.3156.

[CF14] E. J. Candès and C. Fernandez-Granda. "Towards a Mathematical Theory of Super-resolution". In: *Communications on Pure and Applied Mathematics* 67.6 (June 2014), pp. 906–956. DOI: 10.1002/cpa.21455.

[CG89] T. M. Cameron and J. H. Griffin. "An Alternating Frequency/Time Domain Method for Calculating the Steady-State Response of Nonlinear Dynamic Systems". In: *Journal of Applied Mechanics* 56.1 (Mar. 1, 1989), pp. 149–154. DOI: 10.1115/1.3176036.

[Cha+18] M. Chai et al. "Assessment of Fatigue Crack Growth in 316LN Stainless Steel Based on Acoustic Emission Entropy". In: *International Journal of Fatigue* 109 (Apr. 1, 2018), pp. 145–156. DOI: 10.1016/j.ijfatigue.2017.12.017.

[Cha10] K. S. Chan. "Roles of Microstructure in Fatigue Crack Initiation". In: *International Journal of Fatigue*. Emerging Frontiers in Fatigue 32.9 (Sept. 1, 2010), pp. 1428–1447. DOI: 10.1016/j.ijfatigue.2009.10.005.

[Che+21] Y. Chen et al. *Spectral Methods for Data Science: A Statistical Perspective*. Vol. 14. 2021. arXiv: 2012.08496 [cs, eess, math, stat].

[Chi+11] Y. Chi et al. “Sensitivity to Basis Mismatch in Compressed Sensing”. In: *IEEE Transactions on Signal Processing* 59.5 (May 2011), pp. 2182–2195. DOI: 10.1109/TSP.2011.2112650.

[Chr90] R. M. Christensen. “A Critical Evaluation for a Class of Micro-Mechanics Models”. In: *Journal of the Mechanics and Physics of Solids* 38.3 (Jan. 1990), pp. 379–404. DOI: 10.1016/0022-5096(90)90005-O.

[CKM11] O. Couteau, T. Kruml, and J.-L. Martin. “About the Activation Volume for Cross-Slip in Cu at High Stresses”. In: *Acta Materialia* 59.10 (June 1, 2011), pp. 4207–4215. DOI: 10.1016/j.actamat.2011.03.045.

[CL87] K. S. Chan and G. R. Leverant. “Elevated-Temperature Fatigue Crack Growth Behavior of MAR-M200 Single Crystals”. In: *Metallurgical Transactions A* 18.4 (Apr. 1, 1987), pp. 593–602. DOI: 10.1007/BF02649475.

[Coc94] B. Cochelin. “A Path-Following Technique via an Asymptotic-Numerical Method”. In: *Computers & Structures* 53.5 (Dec. 1994), pp. 1181–1192. DOI: 10.1016/0045-7949(94)90165-1.

[CPD21] A. Cortiella, K.-C. Park, and A. Doostan. “Sparse Identification of Nonlinear Dynamical Systems via Reweighted L1-regularized Least Squares”. In: *Computer Methods in Applied Mechanics and Engineering* 376 (Apr. 1, 2021), p. 113620. DOI: 10.1016/j.cma.2020.113620.

[CPD22] A. Cortiella, K.-C. Park, and A. Doostan. “A Priori Denoising Strategies for Sparse Identification of Nonlinear Dynamical Systems: A Comparative Study”. In: *Journal of Computing and Information Science in Engineering* 23.1 (July 18, 2022). DOI: 10.1115/1.4054573.

[CRT06] E. J. Candès, J. K. Romberg, and T. Tao. “Stable Signal Recovery from Incomplete and Inaccurate Measurements”. In: *Communications on Pure and Applied Mathematics* 59.8 (Aug. 2006), pp. 1207–1223. DOI: 10.1002/cpa.20124.

[CSK10] D. H. Chae, P. Sadeghi, and R. A. Kennedy. “Effects of Basis-Mismatch in Compressive Sampling of Continuous Sinusoidal Signals”. In: *2010 2nd International Conference on Future Computer and Communication*. 2010 2nd International Conference on Future Computer and Communication. Wuhan, China: IEEE, 2010, pp. V2-739-V2–743. DOI: 10.1109/icfcc.2010.5497605.

[CT07] E. Candes and T. Tao. “The Dantzig Selector: Statistical Estimation When p Is Much Larger than n”. In: *The Annals of Statistics* 35.6 (Dec. 1, 2007). DOI: 10.1214/009053606000001523.

[DAS18] O. Das, J. S. Abel, and J. O. Smith III. “Fast MUSIC–an Efficient Implementation of the MUSIC Algorithm for Frequency Estimation of Approximately Periodic Signals”. In: *Proceedings of the 21st International Conference on Digital Audio Effects*. 2018, pp. 1–7.

[DB13] M. F. Duarte and R. G. Baraniuk. “Spectral Compressive Sensing”. In: *Applied and Computational Harmonic Analysis* 35.1 (July 2013), pp. 111–129. DOI: 10.1016/j.acha.2012.08.003.

[Deu+02] V. Deudé et al. "Micromechanical Approach to Nonlinear Poroelasticity: Application to Cracked Rocks". In: *Journal of Engineering Mechanics* 128.8 (Aug. 2002), pp. 848–855. DOI: 10.1061/(ASCE)0733-9399(2002)128:8(848).

[DF05] I. Doghri and C. Friebel. "Effective Elasto-Plastic Properties of Inclusion-Reinforced Composites. Study of Shape, Orientation and Cyclic Response". In: *Mechanics of Materials* 37.1 (Jan. 2005), pp. 45–68. DOI: 10.1016/j.mechmat.2003.12.007.

[DGK03] A. Dhooge, W. Govaerts, and Yu. A. Kuznetsov. "MATCONT: A MATLAB Package for Numerical Bifurcation Analysis of ODEs". In: *ACM Transactions on Mathematical Software* 29.2 (June 2003), pp. 141–164. DOI: 10.1145/779359.779362.

[DK16] L. Dormieux and D. Kondo. *Micromechanics of Fracture and Damage*. Mechanical Engineering and Solid Mechanics Series: Micromechanics Set Volume 1. London: ISTE, 2016. 310 pp.

[DKS19] M. Dodaran, M. M. Khonsari, and S. Shao. "Critical Operating Stress of Persistent Slip Bands in Cu". In: *Computational Materials Science* 165 (July 1, 2019), pp. 114–120. DOI: 10.1016/j.commatsci.2019.04.036.

[DO03] I. Doghri and A. Ouaar. "Homogenization of Two-Phase Elasto-Plastic Composite Materials and Structures: Study of Tangent Operators, Cyclic Plasticity and Numerical Algorithms". In: *International Journal of Solids and Structures* 40.7 (Apr. 1, 2003), pp. 1681–1712. DOI: 10.1016/s0020-7683(03)00013-1.

[Dod+20] M. S. Dodaran et al. "Investigating the Interaction between Persistent Slip Bands and Surface Hard Coatings via Crystal Plasticity Simulations". In: *Crystals* 10.11 (11 Nov. 2020), p. 1012. DOI: 10.3390/cryst10111012.

[Doe+07] E. J. Doedel et al. *AUTO-07P: Continuation and Bifurcation Software for Ordinary Differential Equations*. 2007.

[Dog00] I. Doghri. *Mechanics of Deformable Solids*. Berlin, Heidelberg: Springer Berlin Heidelberg, 2000. DOI: 10.1007/978-3-662-04168-0.

[Don06] D. Donoho. "Compressed Sensing". In: *IEEE Transactions on Information Theory* 52.4 (Apr. 2006), pp. 1289–1306. DOI: 10.1109/tit.2006.871582.

[dPro95] G. R. de Prony. "Essai Expérimental et Analytique: Sur Les Lois de La Dilatabilité de Fluides Elastiques et Sur Celles de La Force Expansive de La Vapeur de l'eau et de La Vapeur de l'alkool, à Différentes Temperatures". In: *Jour. de L'Ecole Polytechnique* 1 (1795), pp. 24–76.

[DTY18] J. Ding, V. Tarokh, and Y. Yang. "Model Selection Techniques: An Overview". In: *IEEE Signal Processing Magazine* 35.6 (Nov. 2018), pp. 16–34. DOI: 10.1109/MSP.2018.2867638.

[EE78] I. of Electrical and E. Engineers. *IEEE Standard on Piezoelectricity*. American National Standards Institute New York, NY: ANSI/IEEE Std. 1978.

[Efr+04] B. Efron et al. "Least Angle Regression". In: *The Annals of Statistics* 32.2 (Apr. 1, 2004). DOI: 10.1214/009053604000000067.

[ES10] B. Everitt and A. Skrondal. *The Cambridge Dictionary of Statistics*. 4th ed. Cambridge, UK ; New York: Cambridge University Press, 2010. 468 pp.

[Esh57] J. D. Eshelby. "The Determination of the Elastic Field of an Ellipsoidal Inclusion, and Related Problems". In: *Proceedings of the Royal Society of London. Series A. Mathematical and Physical Sciences* 241.1226 (Aug. 20, 1957), pp. 376–396. DOI: 10.1098/rspa.1957.0133.

[Fak+18] A. Fakhrizadeh Esfahani et al. "Parameter Reduction in Nonlinear State-Space Identification of Hysteresis". In: *Mechanical Systems and Signal Processing* 104 (May 1, 2018), pp. 884–895. DOI: 10.1016/j.ymssp.2017.10.017.

[Fas+22] U. Fasel et al. "Ensemble-SINDy: Robust Sparse Model Discovery in the Low-Data, High-Noise Limit, with Active Learning and Control". In: *Proceedings of the Royal Society A: Mathematical, Physical and Engineering Sciences* 478.2260 (Apr. 2022), p. 20210904. DOI: 10.1098/rspa.2021.0904.

[FB95] D. Fang and A. Berkovits. "Fatigue Design Model Based on Damage Mechanisms Revealed by Acoustic Emission Measurements". In: *Journal of Engineering Materials and Technology* 117.2 (Apr. 1, 1995), pp. 200–208. DOI: 10.1115/1.2804530.

[FG67] D. E. Farrar and R. R. Glauber. "Multicollinearity in Regression Analysis: The Problem Revisited". In: *The Review of Economics and Statistics* 49.1 (Feb. 1967), p. 92. DOI: 10.2307/1937887. JSTOR: 1937887.

[FG94] D. P. Foster and E. I. George. "The Risk Inflation Criterion for Multiple Regression". In: *The Annals of Statistics* 22.4 (Dec. 1, 1994). DOI: 10.1214/aos/1176325766.

[FGS08] J. Feenstra, J. Granstrom, and H. Sodano. "Energy Harvesting through a Backpack Employing a Mechanically Amplified Piezoelectric Stack". In: *Mechanical Systems and Signal Processing* 22.3 (Apr. 2008), pp. 721–734. DOI: 10.1016/j.ymssp.2007.09.015.

[Fin+21] S. Fintová et al. "Frequency-Dependent Fatigue Damage in Polycrystalline Copper Analyzed by FIB Tomography". In: *Acta Materialia* 211 (June 2021), p. 116859. DOI: 10.1016/j.actamat.2021.116859.

[Fit+14] M. Fitzka et al. "Variable Amplitude Loading of Spray-Formed Hypereutectic Aluminium Silicon Alloy DISPAL® S232 in the VHCF Regime". In: *Fatigue & Fracture of Engineering Materials & Structures* 37.9 (2014), pp. 945–957. DOI: 10.1111/ffe.12178.

[Fit+20] M. Fitzka et al. "High Speed In Situ Synchrotron Observation of Cyclic Deformation and Phase Transformation of Superelastic Nitinol at Ultrasonic Frequency". In: *Experimental Mechanics* 60.3 (Mar. 1, 2020), pp. 317–328. DOI: 10.1007/s11340-019-00562-8.

[Fit+21] M. Fitzka et al. "Ultrasonic Fatigue Testing of Concrete". In: *Ultrasonics* 116 (Sept. 1, 2021), p. 106521. DOI: 10.1016/j.ultras.2021.106521.

[FL01] J. Fan and R. Li. "Variable Selection via Nonconcave Penalized Likelihood and Its Oracle Properties". In: *Journal of the American Statistical Association* 96.456 (Dec. 1, 2001), pp. 1348–1360. DOI: 10.1198/016214501753382273.

[FS84] M. W. Finnis and J. E. Sinclair. "A Simple Empirical N-body Potential for Transition Metals". In: *Philosophical Magazine A* 50.1 (July 1, 1984), pp. 45–55. DOI: 10.1080/01418618408244210.

[Fur+22] Y. Furuya et al. "Standardization of an Ultrasonic Fatigue Testing Method in Japan". In: *Fatigue & Fracture of Engineering Materials & Structures* 45.8 (Aug. 2022), pp. 2415–2420. DOI: 10.1111/ffe.13727.

[Fur08] Y. Furuya. "Specimen Size Effects on Gigacycle Fatigue Properties of High-Strength Steel under Ultrasonic Fatigue Testing". In: *Scripta Materialia* 58.11 (June 2008), pp. 1014–1017. DOI: 10.1016/j.scriptamat.2008.01.039.

[FW88] M. Feder and E. Weinstein. "Parameter Estimation of Superimposed Signals Using the EM Algorithm". In: *IEEE Transactions on Acoustics, Speech, and Signal Processing* 36.4 (Apr. 1988), pp. 477–489. DOI: 10.1109/29.1552.

[GA20] S. Glodez and B. Abersek. *The Life of Cracks: Theory and Application*. Newcastle upon Tyne: Cambridge Scholars Publishing, 2020. 165 pp.

[GAE97] D. Guyomar, N. Aurelle, and L. Eyraud. "Piezoelectric Ceramics Nonlinear Behavior. Application to Langevin Transducer". In: *Journal de Physique III* 7.6 (June 1997), pp. 1197–1208. DOI: 10.1051/jp3:1997183.

[Gao+23a] L. M. Gao et al. *Convergence of Uncertainty Estimates in Ensemble and Bayesian Sparse Model Discovery*. Apr. 26, 2023. DOI: 10.48550/arXiv.2301.12649. arXiv: 2301.12649 [cs, math, stat]. URL: http://arxiv.org/abs/2301.12649 (visited on 07/09/2023). preprint.

[Gao+23b] L. M. Gao et al. *Convergence of Uncertainty Estimates in Ensemble and Bayesian Sparse Model Discovery*. Apr. 26, 2023. DOI: 10.48550/arXiv.2301.12649. arXiv: 2301.12649 [cs, math, stat]. URL: http://arxiv.org/abs/2301.12649 (visited on 06/18/2023). preprint.

[GDS11] D. Guyomar, B. Ducharne, and G. Sebald. "High Nonlinearities in Langevin Transducer: A Comprehensive Model". In: *Ultrasonics* 51.8 (Dec. 1, 2011), pp. 1006–1013. DOI: 10.1016/j.ultras.2011.05.017.

[GH13] A. Gholami and S. M. Hosseini. "A Balanced Combination of Tikhonov and Total Variation Regularizations for Reconstruction of Piecewise-Smooth Signals". In: *Signal Processing* 93.7 (July 2013), pp. 1945–1960. DOI: 10.1016/j.sigpro.2012.12.008.

[GJ99] R. A. Guyer and P. A. Johnson. "Nonlinear Mesoscopic Elasticity: Evidence for a New Class of Materials". In: *Physics Today* 52.4 (Apr. 1, 1999), pp. 30–36. DOI: 10.1063/1.882648.

[GL90] A. C. Gavazzi and D. C. Lagoudas. "On the Numerical Evaluation of Eshelby's Tensor and Its Application to Elastoplastic Fibrous Composites". In: *Computational Mechanics* 7.1 (Jan. 1, 1990), pp. 13–19. DOI: 10.1007/bf00370053.

[GN01] L. Gaul and R. Nitsche. "The Role of Friction in Mechanical Joints". In: *Applied Mechanics Reviews* 54.2 (Mar. 1, 2001), pp. 93–106. DOI: 10.1115/1.3097294.

[Gol11] N. Golyandina. "On the Choice of Parameters in Singular Spectrum Analysis and Related Subspace-Based Methods". July 20, 2011. arXiv: 1005.4374 [stat].

[Gor+23] Y. Gorash et al. "Ultrasonic Fatigue Testing of Structural Steel S275JR+AR with Insights into Corrosion, Mean Stress and Frequency Effects". In: *Materials* 16.5 (5 Jan. 2023), p. 1799. DOI: 10.3390/ma16051799.

[GR15] M. Géradin and D. Rixen. *Mechanical Vibrations: Theory and Application to Structural Dynamics*. Third edition. Chichester, West Sussex, United Kingdom: Wiley, 2015. 598 pp.

[GTT18] J.-y. Gotoh, A. Takeda, and K. Tono. "DC Formulations and Algorithms for Sparse Optimization Problems". In: *Mathematical Programming* 169.1 (May 1, 2018), pp. 141–176. DOI: 10.1007/s10107-017-1181-0.

[Gue+15] S. Guelton et al. "Pythran: Enabling Static Optimization of Scientific Python Programs". In: *Computational Science & Discovery* 8.1 (Mar. 16, 2015), p. 014001. DOI: 10.1088/1749-4680/8/1/014001.

[Gus07] M. Guskov. "Dynamique Non-Linéaire Des Systèmes Multirotors. Etudes Numérique et Expérimentale". 2007.

[GV13] G. H. Golub and C. F. Van Loan. *Matrix Computations*. Fourth edition. Johns Hopkins Studies in the Mathematical Sciences. Baltimore: The Johns Hopkins University Press, 2013. 756 pp.

[Hac+21] S. Hachisuka et al. "Dynamic Resonant Frequency Control System of Ultrasonic Transducer for Non-Sinusoidal Waveform Excitation". In: *Sensors and Actuators A: Physical* 332 (Dec. 1, 2021), p. 113124. DOI: 10.1016/j.sna.2021.113124.

[Han+11] Z. Han et al. "Acoustic Emission during Fatigue Crack Propagation in a Micro-Alloyed Steel and Welds". In: *Materials Science and Engineering: A* 528.25 (Sept. 25, 2011), pp. 7751–7756. DOI: 10.1016/j.msea.2011.06.065.

[Han+14] T. L. Hansen et al. "A Sparse Bayesian Learning Algorithm with Dictionary Parameter Estimation". In: *2014 IEEE 8th Sensor Array and Multichannel Signal Processing Workshop (SAM)*. 2014 IEEE 8th Sensor Array and Multichannel Signal Processing Workshop (SAM). A Coruna, Spain: IEEE, June 2014, pp. 385–388. DOI: 10.1109/sam.2014.6882422.

[Han71] E. J. Hannan. "Non-Linear Time Series Regression". In: *Journal of Applied Probability* 8.4 (Dec. 1971), pp. 767–780. DOI: 10.2307/3212240.

[Han87] P. C. Hansen. "The Truncated SVD as a Method for Regularization". In: *BIT* 27.4 (Dec. 1987), pp. 534–553. DOI: 10.1007/BF01937276.

[Han90] P. C. Hansen. "The Discrete Picard Condition for Discrete Ill-Posed Problems". In: *BIT Numerical Mathematics* 30.4 (Dec. 1, 1990), pp. 658–672. DOI: 10.1007/BF01933214.

[Han92] P. C. Hansen. "Analysis of Discrete Ill-Posed Problems by Means of the L-Curve". In: *SIAM Review* 34.4 (Dec. 1992), pp. 561–580. DOI: 10.1137/1034115.

[Har15] F. E. Harrell. *Regression Modeling Strategies: With Applications to Linear Models, Logistic and Ordinal Regression, and Survival Analysis*. Springer Series in Statistics. Cham: Springer International Publishing, 2015. DOI: 10.1007/978-3-319-19425-7.

[Hay84] G. Hayward. "A Systems Feedback Representation of Piezoelectric Transducer Operational Impedance". In: *Ultrasonics* 22.4 (July 1, 1984), pp. 153–162. DOI: 10.1016/0041-624X(84)90030-1.

[HB97] L. Han and S. K. Biswas. "Neural Networks for Sinusoidal Frequency Estimation". In: *Journal of the Franklin Institute* 334.1 (Jan. 1997), pp. 1–18. DOI: 10.1016/s0016-0032(96)00079-8.

[Heb+23] L. Hebrard et al. "Environment Effect on Internal Fatigue Crack Propagation Studied with In-Situ X-ray Microtomography". In: *Materials Science and Engineering: A* 882 (Aug. 2023), p. 145462. DOI: 10.1016/j.msea.2023.145462.

[Hei+13] S. Heinz et al. "Analysis of Fatigue Properties and Failure Mechanisms of Ti6Al4V in the Very High Cycle Fatigue Regime Using Ultrasonic Technology and 3D Laser Scanning Vibrometry". In: *Ultrasonics*. Ultrasonic Fatigue of Advanced Materials 53.8 (Dec. 1, 2013), pp. 1433–1440. DOI: 10.1016/j.ultras.2013.03.002.

[Hes83] W. Hess. *Pitch Determination of Speech Signals*. Red. by K.-s. Fu, T. S. Huang, and M. R. Schroeder. Vol. 3. Springer Series in Information Sciences. Berlin, Heidelberg: Springer Berlin Heidelberg, 1983. DOI: 10.1007/978-3-642-81926-1.

[HFR18] T. L. Hansen, B. H. Fleury, and B. D. Rao. "Superfast Line Spectral Estimation". In: *IEEE Transactions on Signal Processing* 66.10 (May 15, 2018), pp. 2511–2526. DOI: 10.1109/tsp.2018.2807417.

[HID22] J. M. Hokanson, G. Iaccarino, and A. Doostan. *Simultaneous Identification and Denoising of Dynamical Systems*. 2022. DOI: 10.48550/ARXIV.2203.13837. URL: https://arxiv.org/abs/2203.13837. preprint.

[Hil65] R. Hill. "A Self-Consistent Mechanics of Composite Materials". In: *Journal of the Mechanics and Physics of Solids* 13.4 (Aug. 1965), pp. 213–222. DOI: 10.1016/0022-5096(65)90010-4.

[HJ12] R. A. Horn and C. R. Johnson. *Matrix Analysis*. 2nd ed. Cambridge ; New York: Cambridge University Press, 2012. 643 pp.

[HN95] M. Haardt and J. Nossek. "Unitary ESPRIT: How to Obtain Increased Estimation Accuracy with a Reduced Computational Burden". In: *IEEE Transactions on Signal Processing* 43.5 (May 1995), pp. 1232–1242. DOI: 10.1109/78.382406.

[HNS01] M. Hawkes, A. Nehorai, and P. Stoica. "Performance Breakdown of Subspace-Based Methods: Prediction and Cure". In: *2001 IEEE International Conference on Acoustics, Speech, and Signal Processing. Proceedings (Cat. No.01CH37221)*. 2001 IEEE International Conference on Acoustics, Speech, and Signal Processing. Proceedings. Vol. 6. Salt Lake City, UT, USA: IEEE, 2001, pp. 4005–4008. DOI: 10.1109/ICASSP.2001.940722.

[HQ79] E. J. Hannan and B. G. Quinn. "The Determination of the Order of an Autoregression". In: *Journal of the Royal Statistical Society. Series B (Methodological)* 41.2 (1979), pp. 190–195. DOI: 10.1111/j.2517-6161.1979.tb01072.x. JSTOR: 2985032.

[Hua+16] J. Huang et al. "The Mnet Method for Variable Selection". In: *Statistica Sinica* (2016). DOI: 10.5705/ss.202014.0011.

[IBF19] G. Izacard, B. Bernstein, and C. Fernandez-Granda. "A Learning-based Framework for Line-spectra Super-resolution". In: *ICASSP 2019 - 2019 IEEE International Conference on Acoustics, Speech and Signal Processing (ICASSP)*. ICASSP 2019 - 2019 IEEE International Conference on Acoustics, Speech and Signal Processing (ICASSP). Brighton, United Kingdom: IEEE, May 2019, pp. 3632–3636. DOI: 10.1109/icassp.2019.8682882.

[ILI20] P. Ilie, X. Lesperance, and A. Ince. "Development of an Ultrasonic Fatigue Testing System for Gigacycle Fatigue". In: *Material Design & Processing Communications* 2.6 (2020), e120. DOI: 10.1002/mdp2.120.

[IMC21] S. Invernizzi, F. Montagnoli, and A. Carpinteri. "Experimental Evidence of Specimen-Size Effects on EN-AW6082 Aluminum Alloy in VHCF Regime". In: *Applied Sciences* 11.9 (9 Jan. 2021), p. 4272. DOI: 10.3390/app11094272.

[IMF21] G. Izacard, S. Mohan, and C. Fernandez-Granda. "Data-Driven Estimation of Sinusoid Frequencies". Feb. 3, 2021. arXiv: 1906.00823 [cs, eess, stat].

[Inm14] D. J. Inman. "Base Excitation". In: *Engineering Vibration*. Fourth edition. Boston: Pearson, 2014, pp. 151–160.

[Jac+21] V. Jacquemain et al. "Estimation of Stress in Specimens Loaded with Ultrasonic Fatigue Machines". In: *International Journal of Fatigue* 153 (Dec. 1, 2021), p. 106474. DOI: 10.1016/j.ijfatigue.2021.106474.

[Jac22] V. Jacquemain. "Fast Determination of Fatigue Properties of Metals during Fatigue Tests at 20kHz by Using in Situ Time-Resolved X-ray Diffraction." PhD thesis. HESAM Université, Oct. 7, 2022.

[JR18] W. D. C. Jr and D. G. Rethwisch. *Materials Science and Engineering: An Introduction, 10th Edition*. 10th edition. Wiley, Feb. 23, 2018. 992 pp.

[JS96] Jian Li and P. Stoica. "Efficient Mixed-Spectrum Estimation with Applications to Target Feature Extraction". In: *IEEE Transactions on Signal Processing* 44.2 (Feb./1996), pp. 281–295. DOI: 10.1109/78.485924.

[JS99] M. Jansson and P. Stoica. "Forward-Only and Forward-Backward Sample Covariances – A Comparative Study". In: *Signal Processing* 77.3 (Sept. 1999), pp. 235–245. DOI: 10.1016/s0165-1684(99)00037-7.

[Kap+22] A. Kaptanoglu et al. "PySINDy: A Comprehensive Python Package for Robust Sparse System Identification". In: *Journal of Open Source Software* 7.69 (Jan. 29, 2022), p. 3994. DOI: 10.21105/joss.03994.

[Kar+17] U. Karr et al. "Very High Cycle Fatigue Testing of Concrete Using Ultrasonic Cycling". In: *Materials Testing* 59.5 (May 2, 2017), pp. 438–444. DOI: 10.3139/120.111021.

[Kar12] S. Karkar. "Méthodes Numériques Pour Les Systèmes Dynamiques Non Linéaires. Application Aux Instruments de Musique Auto-Oscillants". Theses. Aix-Marseille Université, Jan. 2012.

[KBS19] P. S. Karlsson, L. Behrenz, and G. Shukur. "Performances of Model Selection Criteria When Variables Are Ill Conditioned". In: *Computational Economics* 54.1 (June 2019), pp. 77–98. DOI: 10.1007/s10614-017-9682-8.

[KG22] U. Krupp and A. Giertler. "Surface or Internal Fatigue Crack Initiation during VHCF of Tempered Martensitic and Bainitic Steels: Microstructure and Frequency/Strain Rate Dependency". In: *Metals* 12.11 (11 Nov. 2022), p. 1815. DOI: 10.3390/met12111815.

[Kis+21] S. L. Kiser et al. "Harmonic Balance Framework for Ultrasonic Fatigue Vibration". In: *Proceedings of the 2021 Eighth International Conference on Very High Cycle Fatigue*. Eighth International Conference on Very High Cycle Fatigue. Sapporo, Hokkaido, Japan: Hokkaido University, July 2021, pp. 215–220.

[Kis+23a] S. L. Kiser et al. "Exact Identification of Nonlinear Dynamical Systems by Trimmed Lasso". In: 10.48550/arXiv.2308.01891 [cs, eess, math], Aug. 3, 2023. DOI: 10.48550/arXiv.2308.01891. arXiv: 2308.01891 [cs, eess, math].

[Kis+23b] S. L. Kiser et al. "Fast Kernel-based Signal Subspace Estimates for Line Spectral Estimation". In: 10.36227/techrxiv.22294222, June 2, 2023. DOI: 10.36227/techrxiv.22294222.

[Kis+23c] S. L. Kiser et al. “Real-Time Sinusoidal Parameter Estimation for Damage Growth Monitoring during Ultrasonic Very High Cycle Fatigue Tests”. In: *Mechanical Systems and Signal Processing* 182 (Jan. 1, 2023), p. 109544. DOI: 10.1016/j.ymssp.2022.109544.

[KJ92] J. Karhunen and J. Joutsensalo. “Sinusoidal Frequency Estimation by Signal Subspace Approximation”. In: *IEEE Transactions on Signal Processing* 40.12 (Dec. 1992), pp. 2961–2972. DOI: 10.1109/78.175740.

[KK00] D. Khireddine and M.-H. Khireddine. “Low Cycle Fatigue Behaviour of an Aluminium Alloy with Small Shearable Precipitates: Effect of Surface Coating”. In: *International Journal of Fatigue* 22.7 (Aug. 2000), pp. 585–591. DOI: 10.1016/S0142-1123(00)00028-1.

[KKC12] Y. Kim, S. Kwon, and H. Choi. “Consistent Model Selection Criteria on High Dimensions”. In: *Journal of Machine Learning Research* 13.36 (2012), pp. 1037–1057.

[Kle+17] A. Klepka et al. “Experimental Investigations of Contact-Type Damage Nonlinearity”. In: *Journal of Physics: Conference Series* 842.1 (May 2017), p. 012054. DOI: 10.1088/1742-6596/842/1/012054.

[Kle65] M. Klesnil. “The Degree of Damage at the French Curve and at the Fatigue Limit during Oscillating Bend Loading”. In: *Metal Treat. Drop Forging* 55 (1965), pp. 55–63.

[KLK15] S. Kwon, S. Lee, and Y. Kim. “Moderately Clipped LASSO”. In: *Computational Statistics & Data Analysis* 92 (Dec. 2015), pp. 53–67. DOI: 10.1016/j.csda.2015.07.001.

[KM07] H. Kuhn and D. Medlin. “Ultrasonic Fatigue Testing”. In: *ASM Handbook. 8: Mechanical Testing and Evaluation.* 2. print. Materials Park, Ohio: ASM International, 2007, pp. 717–729.

[KR14] I. Knowles and R. J. Renka. “Methods for Numerical Differentiation of Noisy Data”. In: *Electron. J. Differ. Equ* 21 (2014), pp. 235–246.

[KS88] S. Kay and A. Shaw. “Frequency Estimation by Principal Component AR Spectral Estimation Method without Eigendecomposition”. In: *IEEE Transactions on Acoustics, Speech, and Signal Processing* 36.1 (Jan. 1988), pp. 95–101. DOI: 10.1109/29.1492.

[KSJ17] J. Kim, D.-G. Song, and K.-Y. Jhang. “Absolute Measurement and Relative Measurement of Ultrasonic Nonlinear Parameters”. In: *Research in Nondestructive Evaluation* 28.4 (Oct. 2, 2017), pp. 211–225. DOI: 10.1080/09349847.2016.1174322.

[Kum+09] A. Kumar et al. “Nonlinear Ultrasonics for in Situ Damage Detection during High Frequency Fatigue”. In: *Journal of Applied Physics* 106.2 (July 15, 2009), p. 024904. DOI: 10.1063/1.3169520.

[Kum+10] A. Kumar et al. “In Situ Characterization of Fatigue Damage Evolution in a Cast Al Alloy via Nonlinear Ultrasonic Measurements”. In: *Acta Materialia* 58.6 (Apr. 1, 2010), pp. 2143–2154. DOI: 10.1016/j.actamat.2009.11.055.

[Kum+11] A. Kumar et al. “In Situ Damage Assessment in a Cast Magnesium Alloy during Very High Cycle Fatigue”. In: *Scripta Materialia* 64.1 (Jan. 1, 2011), pp. 65–68. DOI: 10.1016/j.scriptamat.2010.09.008.

[Lac+20] V. A. Lacerda et al. “Signal Processing Techniques for Synchrophasors Considering Short-Circuit Signals: A Comparative Study”. In: *IET Generation, Transmission & Distribution* 14.19 (2020), pp. 3962–3971. DOI: 10.1049/iet-gtd.2020.0208.

[Lag+12] Y. Lage et al. “Instumentation of Ultrasonic High-Frequency Machine to Estimate Applied Stress in Middle Section of Specimen”. In: *Procs of 15th International Conference on Experimental Mechanics: ICEM15*. 15th International Conference on Experimental Mechanics. July 2012.

[LB18] J.-C. Loiseau and S. L. Brunton. “Constrained Sparse Galerkin Regression”. In: *Journal of Fluid Mechanics* 838 (Mar. 2018), pp. 42–67. DOI: 10.1017/jfm.2017.823.

[LC22] D. M. S. Lopes and A. Cunha Jr. “On the Physical Consistency of Evolution Laws Obtained with Sparse Regression”. In: *Advances in Nonlinear Dynamics*. Ed. by W. Lacarbonara et al. NODYCON Conference Proceedings Series. Cham: Springer International Publishing, 2022, pp. 463–473. DOI: 10.1007/978-3-030-81166-2_41.

[LCS02] J. Lemaitre, J.-L. Chaboche, and B. Shrivastava. *Mechanics of Solid Materials*. 1. paperback ed., repr., transferred to digital print. Cambridge: Cambridge Univ. Press, 2002. 556 pp.

[Li+11] P. Li et al. “Fundamental Factors on Formation Mechanism of Dislocation Arrangements in Cyclically Deformed Fcc Single Crystals”. In: *Progress in Materials Science* 56.3 (Mar. 2011), pp. 328–377. DOI: 10.1016/j.pmatsci.2010.12.001.

[Li+15] W. Li et al. “In Situ Nonlinear Ultrasonic for Very High Cycle Fatigue Damage Characterization of a Cast Aluminum Alloy”. In: *Materials Science and Engineering: A* 645 (Oct. 2015), pp. 248–254. DOI: 10.1016/j.msea.2015.08.029.

[Li+16] W. Li et al. “In Situ Characterization of Humidity Effect on the Fatigue Damage Evolution of a Cast Aluminium Alloy”. In: *Fatigue & Fracture of Engineering Materials & Structures* 39.10 (2016), pp. 1263–1271. DOI: 10.1111/ffe.12441.

[Li+19] W. Li et al. “Characterization of Microstructural Evolution by Ultrasonic Nonlinear Parameters Adjusted by Attenuation Factor”. In: *Metals* 9.3 (3 Mar. 2019), p. 271. DOI: 10.3390/met9030271.

[Li+85] P. Li et al. “Dependence of Acoustic Nonlinearity Parameter on Second Phase Precipitates of Aluminum Alloys”. In: *IEEE 1985 Ultrasonics Symposium*. IEEE 1985 Ultrasonics Symposium. San Francisco, CA, USA: IEEE, 1985, pp. 1113–1115. DOI: 10.1109/ULTSYM.1985.198690.

[LK73] P. Lukáš and M. Klesnil. “Cyclic Stress-Strain Response and Fatigue Life of Metals in Low Amplitude Region”. In: *Materials Science and Engineering* 11.6 (June 1973), pp. 345–356. DOI: 10.1016/0025-5416(73)90125-0.

[LKS09] G. Leonov, N. Kuznetsov, and S. Seledzhi. “Nonlinear Analysis and Design of Phase-Locked Loops”. In: Dec. 1, 2009.

[LL21] W. Li and W. Liao. “Stable Super-Resolution Limit and Smallest Singular Value of Restricted Fourier Matrices”. In: *Applied and Computational Harmonic Analysis* 51 (Mar. 2021), pp. 118–156. DOI: 10.1016/j.acha.2020.10.004.

[LLF20] W. Li, W. Liao, and A. Fannjiang. “Super-Resolution Limit of the ESPRIT Algorithm”. In: *IEEE Transactions on Information Theory* 66.7 (July 2020), pp. 4593–4608. DOI: 10.1109/TIT.2020.2974174.

[LN19] Z. Lai and S. Nagarajaiah. "Sparse Structural System Identification Method for Nonlinear Dynamic Systems with Hysteresis/Inelastic Behavior". In: *Mechanical Systems and Signal Processing* 117 (Feb. 2019), pp. 813–842. DOI: 10.1016/j.ymssp.2018.08.033.

[Ma+04] F. Ma et al. "Parameter Analysis of the Differential Model of Hysteresis". In: *Journal of Applied Mechanics* 71.3 (May 1, 2004), pp. 342–349. DOI: 10.1115/1.1668082.

[Mac76] D. E. MacDonald. "Ultrasonic Frequency Metal Fatigue: A Review of the Investigations of the Institute for the Study of Fatigue (Fracture) and (Structural) Reliability". In: *Engineering Fracture Mechanics* 8.1 (Jan. 1, 1976), pp. 17–29. DOI: 10.1016/0013-7944(76)90074-6.

[MAH79] H. Mughbrabi, F. Ackermann, and K. Herz. "Persistent Slipbands in Fatigued Face-Centered and Body-Centered Cubic Metals". In: *Fatigue Mechanisms*. Ed. by J. Fong. 100 Barr Harbor Drive, PO Box C700, West Conshohocken, PA 19428-2959: ASTM International, Jan. 1, 1979, pp. 69-69–37. DOI: 10.1520/STP35885S.

[Man+17] N. M. Mangan et al. "Model Selection for Dynamical Systems via Sparse Regression and Information Criteria". In: *Proceedings of the Royal Society A: Mathematical, Physical and Engineering Sciences* 473.2204 (Aug. 2017), p. 20170009. DOI: 10.1098/rspa.2017.0009.

[Man65] J. Mandel. "Generalisation de la theorie de plasticite de W. T. Koiter". In: *International Journal of Solids and Structures* 1.3 (July 1965), pp. 273–295. DOI: 10.1016/0020-7683(65)90034-X.

[Mar+07] I. Marinesgarcia et al. "Fatigue Crack Growth from Small to Long Cracks in VHCF with Surface Initiations". In: *International Journal of Fatigue* 29.9-11 (Sept. 2007), pp. 2072–2078. DOI: 10.1016/j.ijfatigue.2007.03.015.

[Mar+20] N. Marti et al. "Correlation of the Low and High Frequency Fatigue Responses of Pure Polycrystalline Copper with Mechanisms of Slip Band Formation". In: *Materials Science and Engineering: A* 772 (Jan. 2020), p. 138619. DOI: 10.1016/j.msea.2019.138619.

[Mas+00] S. F. Masri et al. "Application of Neural Networks for Detection of Changes in Nonlinear Systems". In: *Journal of Engineering Mechanics* 126.7 (July 2000), pp. 666–676. DOI: 10.1061/(ASCE)0733-9399(2000)126:7(666).

[Mát+12] K. Máthis et al. "Exploring Plastic Deformation of Metallic Materials by the Acoustic Emission Technique". In: *Acoustic Emission*. IntechOpen, Mar. 2, 2012. DOI: 10.5772/31660.

[Mat+15] K. H. Matlack et al. "Review of Second Harmonic Generation Measurement Techniques for Material State Determination in Metals". In: *Journal of Nondestructive Evaluation* 34.1 (Mar. 2015), p. 273. DOI: 10.1007/s10921-014-0273-5.

[May06] H. Mayer. "Ultrasonic Torsion and Tension–Compression Fatigue Testing: Measuring Principles and Investigations on 2024-T351 Aluminium Alloy". In: *International Journal of Fatigue*. Third International Conference on Very High Cycle Fatigue (VHCF-3) 28.11 (Nov. 1, 2006), pp. 1446–1455. DOI: 10.1016/j.ijfatigue.2005.05.020.

[MB21] D. A. Messenger and D. M. Bortz. "Weak SINDy: Galerkin-Based Data-Driven Model Selection". In: *Multiscale Modeling & Simulation* 19.3 (Jan. 2021), pp. 1474–1497. DOI: 10.1137/20M1343166.

[MB51] W. P. Mason and H. Baerwald. "*Piezoelectric Crystals and Their Applications to Ultrasonics*". In: *Physics Today* 4.5 (May 1, 1951), pp. 23–24. DOI: 10.1063/1.3067231.

[Mbr] Mbrozia. *Specialized in Ultrasonic Fatigue Testing and Evaluation Equipment.* URL: http://www.mbrosia.co.kr/product/product0103.php (visited on 09/13/2023).

[MDK11] R. Madec, B. Devincre, and L. P. Kubin. "New Line Model for Optimized Dislocation Dynamics Simulations". In: *MRS Online Proceedings Library* 653.1 (Mar. 21, 2011), p. 181. DOI: 10.1557/PROC-653-Z1.8.

[Mes+20] A. Messager et al. "In Situ Synchrotron Ultrasonic Fatigue Testing Device for 3D Characterisation of Internal Crack Initiation and Growth". In: *Fatigue & Fracture of Engineering Materials & Structures* 43.3 (2020), pp. 558–567. DOI: 10.1111/ffe.13140.

[MFS13] H. Mayer, M. Fitzka, and R. Schuller. "Constant and Variable Amplitude Ultrasonic Fatigue of 2024-T351 Aluminium Alloy at Different Load Ratios". In: *Ultrasonics*. Ultrasonic Fatigue of Advanced Materials 53.8 (Dec. 1, 2013), pp. 1425–1432. DOI: 10.1016/j.ultras.2013.02.012.

[MHW10] C. Miehe, M. Hofacker, and F. Welschinger. "A Phase Field Model for Rate-Independent Crack Propagation: Robust Algorithmic Implementation Based on Operator Splits". In: *Computer Methods in Applied Mechanics and Engineering* 199.45 (Nov. 15, 2010), pp. 2765–2778. DOI: 10.1016/j.cma.2010.04.011.

[Mil84a] A. J. Miller. "Selection of Subsets of Regression Variables". In: *Journal of the Royal Statistical Society. Series A (General)* 147.3 (1984), pp. 389–425. DOI: 10.2307/2981576. JSTOR: 2981576.

[Mil84b] K. J. Miller. "Initiation and Growth Rates of Short Fatigue Cracks". In: *Fundamentals of deformation and fracture* (1984), pp. 477–500.

[Miy+19] S. Miyake et al. "High-Power Piezoelectric Vibration Model Considering the Interaction between Nonlinear Vibration and Temperature Increase". In: *Ultrasonics* 93 (Mar. 1, 2019), pp. 93–101. DOI: 10.1016/j.ultras.2018.10.014.

[MRM16] B. Mamandipoor, D. Ramasamy, and U. Madhow. "Newtonized Orthogonal Matching Pursuit: Frequency Estimation Over the Continuum". In: *IEEE Transactions on Signal Processing* 64.19 (Oct. 1, 2016), pp. 5066–5081. DOI: 10.1109/tsp.2016.2580523.

[MT73] T. Mori and K. Tanaka. "Average Stress in Matrix and Average Elastic Energy of Materials with Misfitting Inclusions". In: *Acta Metallurgica* 21.5 (May 1, 1973), pp. 571–574. DOI: 10.1016/0001-6160(73)90064-3.

[Mug+83] H. Mughrabi et al. "Fatigue Crack Initiation by Cyclic Slip Irreversibilities in High-Cycle Fatigue". In: *Fatigue Mechanisms: Advances in Quantitative Measurement of Physical Damage*. Ed. by J. Lankford et al. 100 Barr Harbor Drive, PO Box C700, West Conshohocken, PA 19428-2959: ASTM International, Jan. 1, 1983, pp. 5-5–41. DOI: 10.1520/STP30551S.

[Mug02] H. Mughrabi. "On 'multi-Stage' Fatigue Life Diagrams and the Relevant Life-Controlling Mechanisms in Ultrahigh-Cycle Fatigue". In: *Fatigue & Fracture of Engineering Materials and Structures* 25.8-9 (Sept. 2002), pp. 755–764. DOI: 10.1046/j.1460-2695.2002.00550.x.

[Mug06] H. Mughrabi. “Specific Features and Mechanisms of Fatigue in the Ultrahigh-Cycle Regime”. In: *International Journal of Fatigue* 28.11 (Nov. 2006), pp. 1501–1508. DOI: 10.1016/j.ijfatigue.2005.05.018.

[Mug09] H. Mughrabi. “Cyclic Slip Irreversibilities and the Evolution of Fatigue Damage”. In: *Metallurgical and Materials Transactions A* 40.6 (June 2009), pp. 1257–1279. DOI: 10.1007/s11661-009-9839-8.

[Mug13] H. Mughrabi. “Cyclic Slip Irreversibility and Fatigue Life: A Microstructure-Based Analysis”. In: *Acta Materialia* 61.4 (Feb. 1, 2013), pp. 1197–1203. DOI: 10.1016/j.actamat.2012.10.029.

[Mug15] H. Mughrabi. “Microstructural Mechanisms of Cyclic Deformation, Fatigue Crack Initiation and Early Crack Growth”. In: *Philosophical Transactions of the Royal Society A: Mathematical, Physical and Engineering Sciences* 373.2038 (Mar. 28, 2015), p. 20140132. DOI: 10.1098/rsta.2014.0132.

[Mug84] H. Mughrabi. “Dislocations in Fatigue”. In: *Dislocations and Properties of Real Materials*. 1984.

[Mug99] Mughrabi. “On the Life-Controlling Microstructural Fatigue Mechanisms in Ductile Metals and Alloys in the Gigacycle Regime: Fatigue Mechanisms in Ductile Metals and Alloys”. In: *Fatigue & Fracture of Engineering Materials & Structures* 22.7 (July 1999), pp. 633–641. DOI: 10.1046/j.1460-2695.1999.00186.x.

[Mur51] F. D. Murnaghan. *Finite Deformation of an Elastic Solid*. Wiley, 1951. 160 pp. Google Books: 4rq7AAAAIAAJ.

[MVK15] P. Mazal, F. Vlasic, and V. Koula. “Use of Acoustic Emission Method for Identification of Fatigue Micro-cracks Creation”. In: *Procedia Engineering*. Fatigue Design 2015, International Conference Proceedings, 6th Edition 133 (Jan. 1, 2015), pp. 379–388. DOI: 10.1016/j.proeng.2015.12.667.

[MZW22] M. Madia, U. Zerbst, and T. Werner. “Estimation of the Kitagawa-Takahashi Diagram by Cyclic R Curve Analysis”. In: *Procedia Structural Integrity* 38 (2022), pp. 309–316. DOI: 10.1016/j.prostr.2022.03.032.

[Nab97] F. R. N. Nabarro. “Fifty-Year Study of the Peierls-Nabarro Stress”. In: *Materials Science and Engineering: A* 234–236 (Aug. 30, 1997), pp. 67–76. DOI: 10.1016/S0921-5093(97)00184-6.

[NH99] S. Nemat-Nasser and M. Hori. *Micromechanics: Overall Properties of Heterogeneous Materials*. 2nd rev. ed. Amsterdam ; New York: Elsevier, 1999. 786 pp.

[NK99] Nishijima and Kanazawa. “Stepwise S-N Curve and Fish-Eye Failure in Gigacycle Fatigue: Gigacycle Failure”. In: *Fatigue & Fracture of Engineering Materials & Structures* 22.7 (July 1999), pp. 601–607. DOI: 10.1046/j.1460-2695.1999.00206.x.

[NP00] J. Newman and R. Piascik, eds. *Fatigue Crack Growth Thresholds, Endurance Limits, and Design*. 100 Barr Harbor Drive, PO Box C700, West Conshohocken, PA 19428-2959: ASTM International, Jan. 1, 2000. DOI: 10.1520/STP1372-EB.

[NS16] J.-P. Noel and M. Schoukens. “Hysteretic Benchmark with a Dynamic Nonlinearity”. In: *Workshop on Nonlinear System Identification Benchmarks*. 2016, pp. 7–14.

[NSL18] A. Novak, L. Simon, and P. Lotton. "A Simple Predistortion Technique for Suppression of Nonlinear Effects in Periodic Signals Generated by Nonlinear Transducers". In: *Journal of Sound and Vibration* 420 (Apr. 2018), pp. 104–113. DOI: 10.1016/j.jsv.2018.01.038.

[OVK92] B. Ottersten, M. Viberg, and T. Kailath. "Analysis of Subspace Fitting and ML Techniques for Parameter Estimation from Sensor Array Data". In: *IEEE Transactions on Signal Processing* 40.3 (Mar. 1992), pp. 590–600. DOI: 10.1109/78.120802.

[Pap+02] M. Papakyriacou et al. "Cyclic Plastic Deformation of Tantalum and Niobium at Very High Numbers of Cycles". In: *Materials Science and Engineering: A* 325.1-2 (Feb. 2002), pp. 520–524. DOI: 10.1016/S0921-5093(01)01446-0.

[Par+21] S.-H. Park et al. "Measurement of Absolute Acoustic Nonlinearity Parameter Using Laser-Ultrasonic Detection". In: *Applied Sciences* 11.9 (May 3, 2021), p. 4175. DOI: 10.3390/app11094175.

[Par60] K. R. Parthasarathy. "On the Estimation of the Spectrum of a Stationary Stochastic Process". In: *The Annals of Mathematical Statistics* 31.3 (Sept. 1960), pp. 568–573. DOI: 10.1214/aoms/1177705784.

[PE63] P. Paris and F. Erdogan. "A Critical Analysis of Crack Propagation Laws". In: *Journal of Basic Engineering* 85.4 (Dec. 1, 1963), pp. 528–533. DOI: 10.1115/1.3656900.

[Pea99] R. K. Pearson. "Linear Dynamic Models". In: *Discrete-Time Dynamic Models*. Topics in Chemical Engineering. New York: Oxford University Press, 1999, pp. 57–91.

[Phu+14] N. Phung et al. "Very High Cycle Fatigue of Copper: Evolution, Morphology and Locations of Surface Slip Markings". In: *International Journal of Fatigue* 63 (June 2014), pp. 68–77. DOI: 10.1016/j.ijfatigue.2014.01.007.

[Pol+17] J. Polák et al. "Profiles of Persistent Slip Markings and Internal Structure of Underlying Persistent Slip Bands". In: *Fatigue & Fracture of Engineering Materials & Structures* 40 (Jan. 12, 2017). DOI: 10.1111/ffe.12567.

[Ppr] Pprime. *Machine Ultrasonore*. URL: https://pprime.fr/wp-content/uploads/2020/02/2016-10-22_ess-machine_us.pdf (visited on 09/13/2023).

[PT15] D. Potts and M. Tasche. "Fast ESPRIT Algorithms Based on Partial Singular Value Decompositions". In: *Applied Numerical Mathematics* 88 (Feb. 1, 2015), pp. 31–45. DOI: 10.1016/j.apnum.2014.10.003.

[Pus93] A. Puskar. "Ultrasonic Fatigue Testing Equipment and New Procedures for Complex Material Evaluation". In: *Ultrasonics* 31.1 (Jan. 1, 1993), pp. 61–67. DOI: 10.1016/0041-624X(93)90034-W.

[QHS14] C. Qian, L. Huang, and H. So. "Computationally Efficient ESPRIT Algorithm for Direction-of-Arrival Estimation Based on Nyström Method". In: *Signal Processing* 94 (Jan. 2014), pp. 74–80. DOI: 10.1016/j.sigpro.2013.05.007.

[Ran04] N. Ranc. "Etude Des Champs de Température et de Déformation Dans Les Matériaux Métalliques Sollicités à Grande Vitesse de Déformation". Universit\'e de Nanterre - Paris X, 2004, X–153 f.

[Ran14] N. Ranc. "Contribution a l'etude Du Comportement Thermomecanique Des Solides et Des Structures". Université Pierre et Marie Curie, 2014.

[RB74] D. Rife and R. Boorstyn. “Single Tone Parameter Estimation from Discrete-Time Observations”. In: *IEEE Transactions on Information Theory* 20.5 (Sept. 1974), pp. 591–598. DOI: 10.1109/tit.1974.1055282.

[Réb+11] M. Rébillat et al. “Identification of Cascade of Hammerstein Models for the Description of Nonlinearities in Vibrating Devices”. In: *Journal of Sound and Vibration* 330.5 (Feb. 2011), pp. 1018–1038. DOI: 10.1016/j.jsv.2010.09.012.

[Reg96] T. Regińska. “A Regularization Parameter in Discrete Ill-Posed Problems”. In: *SIAM Journal on Scientific Computing* 17.3 (May 1996), pp. 740–749. DOI: 10.1137/S1064827593252672.

[RFB94] A. Reilly, G. Frazer, and B. Boashash. “Analytic Signal Generation-Tips and Traps”. In: *IEEE Transactions on Signal Processing* 42.11 (Nov./1994), pp. 3241–3245. DOI: 10.1109/78.330385.

[RK89] R. Roy and T. Kailath. “ESPRIT-estimation of Signal Parameters via Rotational Invariance Techniques”. In: *IEEE Transactions on Acoustics, Speech, and Signal Processing* 37.7 (July 1989), pp. 984–995. DOI: 10.1109/29.32276.

[Ros+19] J. A. Rosenfeld et al. “Occupation Kernels and Densely Defined Liouville Operators for System Identification”. In: *2019 IEEE 58th Conference on Decision and Control (CDC)*. 2019 IEEE 58th Conference on Decision and Control (CDC). Dec. 2019, pp. 6455–6460. DOI: 10.1109/CDC40024.2019.9029337.

[RP99] P. Ribeiro and M. Petyt. “Geometrical Non-Linear, Steady State, Forced, Periodic Vibration of Plates, Part I: Model and Convergence Studies”. In: *Journal of Sound and Vibration* 226.5 (Oct. 1999), pp. 955–983. DOI: 10.1006/jsvi.1999.2306.

[Ruo+96] R. Ruotolo et al. “Harmonic Analysis of the Vibrations of a Cantilevered Beam with a Closing Crack”. In: *Computers & Structures* 61.6 (Dec. 1996), pp. 1057–1074. DOI: 10.1016/0045-7949(96)00184-8.

[RWP08] N. Ranc, D. Wagner, and P. Paris. “Study of Thermal Effects Associated with Crack Propagation during Very High Cycle Fatigue Tests”. In: *Acta Materialia* 56.15 (Sept. 2008), pp. 4012–4021. DOI: 10.1016/j.actamat.2008.04.023.

[Sal+09] L. Salles et al. “Dynamic Analysis of a Bladed Disk With Friction and Fretting-Wear in Blade Attachments”. In: *Volume 6: Structures and Dynamics, Parts A and B*. ASME Turbo Expo 2009: Power for Land, Sea, and Air. Orlando, Florida, USA: ASMEDC, Jan. 1, 2009, pp. 465–476. DOI: 10.1115/gt2009-60151.

[Sar+18] J. M. Sargado et al. “High-Accuracy Phase-Field Models for Brittle Fracture Based on a New Family of Degradation Functions”. In: *Journal of the Mechanics and Physics of Solids* 111 (Feb. 1, 2018), pp. 458–489. DOI: 10.1016/j.jmps.2017.10.015.

[SBK21] D. E. Shea, S. L. Brunton, and J. N. Kutz. “SINDy-BVP: Sparse Identification of Nonlinear Dynamics for Boundary Value Problems”. In: *Physical Review Research* 3.2 (June 29, 2021), p. 023255. DOI: 10.1103/PhysRevResearch.3.023255.

[Sch+20] A. Schmiedel et al. “Ultrasonic Fatigue Testing of Cast Steel G42CrMo4 at Elevated Temperatures”. In: *Fatigue & Fracture of Engineering Materials & Structures* 43.10 (Oct. 2020), pp. 2455–2475. DOI: 10.1111/ffe.13316.

[Sch12] W. E. Schiesser. *The Numerical Method of Lines: Integration of Partial Differential Equations*. Elsevier, July 27, 2012. 341 pp.

[Sch86] R. Schmidt. "Multiple Emitter Location and Signal Parameter Estimation". In: *IEEE Transactions on Antennas and Propagation* 34.3 (Mar. 1986), pp. 276–280. DOI: 10.1109/tap.1986.1143830.

[Sel+21] M. Seleznev et al. "Novel Method for in Situ Damage Monitoring during Ultrasonic Fatigue Testing by the Advanced Acoustic Emission Technique". In: *International Journal of Fatigue* 142 (Jan. 2021), p. 105918. DOI: 10.1016/j.ijfatigue.2020.105918.

[Sel17] J. Selva. "ML Estimation and Detection of Multiple Frequencies Through Periodogram Estimate Refinement". In: *IEEE Signal Processing Letters* 24.3 (Mar. 2017), pp. 249–253. DOI: 10.1109/lsp.2016.2645283.

[Ser19] A. Serbes. "Fast and Efficient Sinusoidal Frequency Estimation by Using the DFT Coefficients". In: *IEEE Transactions on Communications* 67.3 (Mar. 2019), pp. 2333–2342. DOI: 10.1109/tcomm.2018.2886355.

[Sey10] R. Seydel. *Practical Bifurcation and Stability Analysis*. 3rd ed. Interdisciplinary Applied Mathematics 5. New York: Springer, 2010. 483 pp.

[She+97] S. Sherrit et al. "An Accurate Equivalent Circuit for the Unloaded Piezoelectric Vibrator in the Thickness Mode". In: *Journal of Physics D: Applied Physics* 30.16 (Aug. 1997), p. 2354. DOI: 10.1088/0022-3727/30/16/014.

[Shi+10] M. Shiwa et al. "Fatigue Process Evaluation of Ultrasonic Fatigue Testing in High Strength Steel Analyzed by Acoustic Emission and Non-Linear Ultrasonic". In: *Materials Transactions* 51.8 (2010), pp. 1404–1408. DOI: 10.2320/matertrans.M2010074.

[Shi+21] T. Shinko et al. "Controlling Factors and Mechanisms of Fatigue Crack Growth Influenced by High Pressure of Gaseous Hydrogen in a Commercially Pure Iron". In: *Theoretical and Applied Fracture Mechanics* 112 (Apr. 1, 2021), p. 102885. DOI: 10.1016/j.tafmec.2020.102885.

[SHJ00] P. Stoica, Hongbin Li, and Jian Li. "Amplitude Estimation of Sinusoidal Signals: Survey, New Results, and an Application". In: *IEEE Transactions on Signal Processing* 48.2 (Feb. 2000), pp. 338–352. DOI: 10.1109/78.823962.

[SHJ99] P. Stoica, Hongbin Li, and Jian Li. "A New Derivation of the APES Filter". In: *IEEE Signal Processing Letters* 6.8 (Aug. 1999), pp. 205–206. DOI: 10.1109/97.774866.

[Shr+21] S. Shrestha et al. "In-Situ Fatigue Life Analysis by Modal Acoustic Emission, Direct Current Potential Drop and Digital Image Correlation for Steel". In: *International Journal of Fatigue* 142 (Jan. 1, 2021), p. 105924. DOI: 10.1016/j.ijfatigue.2020.105924.

[Shy+04] A. Shyam et al. "Development of Ultrasonic Fatigue for Rapid, High Temperature Fatigue Studies in Turbine Engine Materials". In: *Superalloys 2004 (Tenth International Symposium)*. Superalloys. TMS, 2004, pp. 259–268. DOI: 10.7449/2004/Superalloys_2004_259_268.

[SKB02] I. Yu. Solodov, N. Krohn, and G. Busse. "CAN: An Example of Nonclassical Acoustic Nonlinearity in Solids". In: *Ultrasonics* 40.1 (May 1, 2002), pp. 621–625. DOI: 10.1016/S0041-624X(02)00186-5.

[SM05] P. Stoica and R. L. Moses. *Spectral Analysis of Signals*. Upper Saddle River, N.J: Pearson/Prentice Hall, 2005. 452 pp.

[SM17] H. Schaeffer and S. G. McCalla. "Sparse Model Selection via Integral Terms". In: *Physical Review E* 96.2 (Aug. 2, 2017), p. 023302. DOI: 10.1103/PhysRevE.96.023302.

[SMN19] M. Schüssler, T. Münker, and O. Nelles. "Deep Recurrent Neural Networks for Nonlinear System Identification". In: *2019 IEEE Symposium Series on Computational Intelligence (SSCI)*. 2019 IEEE Symposium Series on Computational Intelligence (SSCI). Dec. 2019, pp. 448–454. DOI: 10.1109/SSCI44817.2019.9003133.

[SQ20] A. Serbes and K. Qaraqe. "A Fast Method for Estimating Frequencies of Multiple Sinusoidals". In: *IEEE Signal Processing Letters* 27 (2020), pp. 386–390. DOI: 10.1109/LSP.2020.2970837.

[SS10a] S. Stanzl-Tschegg and B. Schönbauer. "Near-Threshold Fatigue Crack Propagation and Internal Cracks in Steel". In: *Procedia Engineering*. Fatigue 2010 2.1 (Apr. 1, 2010), pp. 1547–1555. DOI: 10.1016/j.proeng.2010.03.167.

[SS10b] S. E. Stanzl-Tschegg and B. Schönbauer. "Mechanisms of Strain Localization, Crack Initiation and Fracture of Polycrystalline Copper in the VHCF Regime". In: *International Journal of Fatigue*. Selected Papers of the 17th European Conference of Fracture (ECF 17) 32.6 (June 1, 2010), pp. 886–893. DOI: 10.1016/j.ijfatigue.2009.03.016.

[SS11] E. Sarrouy and J.-J. Sinou. "Non-Linear Periodic and Quasi-Periodic Vibrations in Mechanical Systems - On the Use of the Harmonic Balance Methods". In: *Advances in Vibration Analysis Research* (Apr. 4, 2011). DOI: 10.5772/15638.

[SS16] M. Schoukens and F. G. Scheiwe. "Modeling Nonlinear Systems Using a Volterra Feedback Model". In: *Workshop on Nonlinear System Identification Benchmarks*. 2016.

[SS91] P. Stoica and T. Soderstrom. "Statistical Analysis of MUSIC and ESPRIT Estimates of Sinusoidal Frequencies". In: *[Proceedings] ICASSP 91: 1991 International Conference on Acoustics, Speech, and Signal Processing*. [Proceedings] ICASSP 91: 1991 International Conference on Acoustics, Speech, and Signal Processing. Toronto, Ont., Canada: IEEE, 1991, 3273–3276 vol.5. DOI: 10.1109/icassp.1991.150152.

[SSC11] J. O. Smith, Stanford University, and Center for Computer Research in Music and Acoustics. *Spectral Audio Signal Processing*. Stanford, Calif.: W3K, 2011.

[SSP16] B. Sahoo, R. K. Satpathy, and S. K. Panigrahi. "Analysis of a Turbine Blade Failure in a Military Turbojet Engine". In: *International Journal of Turbo & Jet-Engines* 33.2 (Jan. 1, 2016). DOI: 10.1515/tjj-2015-0018.

[Sta99] Stanzl-Tschegg. "Fracture Mechanisms and Fracture Mechanics at Ultrasonic Frequencies: Fatigue Tests at Ultrasonic Frequencies". In: *Fatigue & Fracture of Engineering Materials & Structures* 22.7 (July 1999), pp. 567–579. DOI: 10.1046/j.1460-2695.1999.00180.x.

[Sur98] S. Suresh. *Fatigue of Materials*. 2nd ed. Cambridge ; New York: Cambridge University Press, 1998. 679 pp.

[Tah+23] K. Tahmasbi et al. "Dynamic Frequency-Dependent Fatigue Damage in Metals: A State-of-the-Art Review". In: *Forces in Mechanics* 10 (Feb. 1, 2023), p. 100167. DOI: 10.1016/j.finmec.2023.100167.

[Tib96] R. Tibshirani. "Regression Shrinkage and Selection Via the Lasso". In: *Journal of the Royal Statistical Society: Series B (Methodological)* 58.1 (Jan. 1996), pp. 267–288. DOI: 10.1111/j.2517-6161.1996.tb02080.x.

[TM82] K. Tanaka and T. Mura. "A Theory of Fatigue Crack Initiation at Inclusions". In: *Metallurgical Transactions A* 13.1 (Jan. 1982), pp. 117–123. DOI: 10.1007/BF02642422.

[TM85] D. Tufts and C. Melissinos. "Simple, Effective Computation of Principal Eigenvectors and Their Eigenvalues and Application to High-Resolution Estimation of Frequencies". In: *ICASSP '85. IEEE International Conference on Acoustics, Speech, and Signal Processing.* ICASSP '85. IEEE International Conference on Acoustics, Speech, and Signal Processing. Vol. 10. Apr. 1985, pp. 320–323. DOI: 10.1109/ICASSP.1985.1168496.

[Tor+17] N. Torabian et al. "Correlation of the High and Very High Cycle Fatigue Response of Ferrite Based Steels with Strain Rate-Temperature Conditions". In: *Acta Materialia* 134 (Aug. 1, 2017), pp. 40–52. DOI: 10.1016/j.actamat.2017.05.064.

[TT77] R. B. Thompson and H. F. Tiersten. "Harmonic Generation of Longitudinal Elastic Waves". In: *The Journal of the Acoustical Society of America* 62.1 (July 1, 1977), pp. 33–37. DOI: 10.1121/1.381501.

[Van93] S. Van Huffel. "Enhanced Resolution Based on Minimum Variance Estimation and Exponential Data Modeling". In: *Signal Processing* 33.3 (Sept. 1993), pp. 333–355. DOI: 10.1016/0165-1684(93)90130-3.

[Voi66] W. Voigt. *Lehrbuch der Kristallphysik*. Wiesbaden: Vieweg+Teubner Verlag, 1966. DOI: 10.1007/978-3-663-15884-4.

[Wag+09] D. Wagner et al. "Fatigue Crack Initiation Detection by an Infrared Thermography Method". In: *Fatigue & Fracture of Engineering Materials & Structures* (Nov. 2009). DOI: 10.1111/j.1460-2695.2009.01410.x.

[Wan+99] Q. Y. Wang et al. "Technical Note High-cycle Fatigue Crack Initiation and Propagation Behaviour of High-Strength Sprin Steel Wires". In: *Fatigue and Fracture of Engineering Materials and Structures* 22.8 (Aug. 1999), pp. 673–677. DOI: 10.1046/j.1460-2695.1999.t01-1-00184.x.

[Wed72] P.-Å. Wedin. "Perturbation Bounds in Connection with Singular Value Decomposition". In: *BIT* 12.1 (Mar. 1972), pp. 99–111. DOI: 10.1007/BF01932678.

[Wei+10] A. Weidner et al. "Fatigue Damage in Copper Polycrystals Subjected to Ultrahigh-Cycle Fatigue below the PSB Threshold". In: *International Journal of Fatigue* 32.6 (June 2010), pp. 872–878. DOI: 10.1016/j.ijfatigue.2009.04.004.

[Wei+22] H. Wei Lee et al. "Modeling Fatigue of Pre-Corroded Body-Centered Cubic Metals with Unified Mechanics Theory". In: *Materials & Design* 224 (Dec. 1, 2022), p. 111383. DOI: 10.1016/j.matdes.2022.111383.

[Wes+18] D. T. Westwick et al. "Using Decoupling Methods to Reduce Polynomial NARX Models". In: *IFAC-PapersOnLine* 51.15 (2018), pp. 796–801. DOI: 10.1016/j.ifacol.2018.09.133.

[WFJ17] X. Wang, E. Feng, and C. Jiang. "A Microplasticity Evaluation Method in Very High Cycle Fatigue". In: *International Journal of Fatigue* 94 (Jan. 2017), pp. 6–15. DOI: 10.1016/j.ijfatigue.2016.09.004.

[Wil80] L. E. Willertz. "Ultrasonic Fatigue". In: *International Metals Reviews* 25.1 (Jan. 1, 1980), pp. 65–78. DOI: 10.1179/imtr.1980.25.1.65.

[WN10] D. Wipf and S. Nagarajan. "Iterative Reweighted \ell_1 and \ell_2 Methods for Finding Sparse Solutions". In: *IEEE Journal of Selected Topics in Signal Processing* 4.2 (Apr. 2010), pp. 317–329. DOI: 10.1109/JSTSP.2010.2042413.

[WNF09] S. Wright, R. Nowak, and M. Figueiredo. "Sparse Reconstruction by Separable Approximation". In: *IEEE Transactions on Signal Processing* 57.7 (July 2009), pp. 2479–2493. DOI: 10.1109/tsp.2009.2016892.

[Wöh58] A. Wöhler. "Bericht Über Die Versuche, Welche Auf Der Königl. Niederschlesisch-märkischen Eisenbahn Mit Apparaten Zum Messen Der Biegung Und Verdrehung von Eisenbahnwagen-Achsen Während Der Fahrt Angestellt Wurden". In: *Zeitschrift für Bauwesen* 8.1858 (1858), pp. 641–652.

[Woi+20] L. Woiwode et al. "Comparison of Two Algorithms for Harmonic Balance and Path Continuation". In: *Mechanical Systems and Signal Processing* 136 (Feb. 2020), p. 106503. DOI: 10.1016/j.ymssp.2019.106503.

[Xu+20] J. Xu et al. "Efficient Hinging Hyperplanes Neural Network and Its Application in Nonlinear System Identification". In: *Automatica* 116 (June 1, 2020), p. 108906. DOI: 10.1016/j.automatica.2020.108906.

[YA15] S. Ye and E. Aboutanios. "An Algorithm for the Parameter Estimation of Multiple Superimposed Exponentials in Noise". In: *2015 IEEE International Conference on Acoustics, Speech and Signal Processing (ICASSP)*. ICASSP 2015 - 2015 IEEE International Conference on Acoustics, Speech and Signal Processing (ICASSP). South Brisbane, Queensland, Australia: IEEE, Apr. 2015, pp. 3457–3461. DOI: 10.1109/ICASSP.2015.7178613.

[Yah13] H. Yahiaoui. "Effet de l'espacement interlamellaire sur le comportement sous chargements monotone et cyclique de l'acier perlitique C70." PhD thesis. Ecole nationale supérieure d'arts et métiers - ENSAM ; ecole supérieure des sciences et technique de tunis, July 2, 2013.

[YCB81] W. T. Yost, J. H. Cantrell, and M. A. Breazeale. "Ultrasonic Nonlinearity Parameters and Third-Order Elastic Constants of Copper between 300 and 3 °K". In: *Journal of Applied Physics* 52.1 (Jan. 1, 1981), pp. 126–128. DOI: 10.1063/1.328443.

[Yun+19] J. Yun et al. "Trimming the 1 Regularizer: Statistical Analysis, Optimization, and Applications to Deep Learning". In: International Conference on Machine Learning. International Machine Learning Society (IMLS), June 9, 2019.

[YX15] Z. Yang and L. Xie. "On Gridless Sparse Methods for Line Spectral Estimation From Complete and Incomplete Data". In: *IEEE Transactions on Signal Processing* 63.12 (June 2015), pp. 3139–3153. DOI: 10.1109/tsp.2015.2420541.

[Zha+18] Y. Zhang et al. "On the Microstructures and Fatigue Behaviors of 316L Stainless Steel Metal Injection Molded with Gas- and Water-Atomized Powders". In: *Metals* 8.11 (Nov. 1, 2018), p. 893. DOI: 10.3390/met8110893.

[Zha+19] J.-G. Zhang et al. "Electromechanical Dynamics Model of Ultrasonic Transducer in Ultrasonic Machining Based on Equivalent Circuit Approach". In: *Sensors* 19.6 (6 Jan. 2019), p. 1405. DOI: 10.3390/s19061405.

[Zha+23] K. Zhang et al. “Review of the Design of Power Ultrasonic Generator for Piezoelectric Transducer”. In: *Ultrasonics Sonochemistry* 96 (June 1, 2023), p. 106438. DOI: 10.1016/j.ultsonch.2023.106438.

[Zha10] C.-H. Zhang. “Nearly Unbiased Variable Selection under Minimax Concave Penalty”. In: *The Annals of Statistics* 38.2 (Apr. 1, 2010). DOI: 10.1214/09-AOS729.

[Zou06] H. Zou. “The Adaptive Lasso and Its Oracle Properties”. In: *Journal of the American Statistical Association* 101.476 (Dec. 1, 2006), pp. 1418–1429. DOI: 10.1198/016214506000000735.

[ZS10] Y. Zhang and X. Shen. “Model Selection Procedure for High-Dimensional Data”. In: *Statistical analysis and data mining* 3.5 (Oct. 1, 2010), pp. 350–358. DOI: 10.1002/sam.10088. pmid: 21116443.

[ZY06] P. Zhao and B. Yu. “On Model Selection Consistency of Lasso”. In: *Journal of Machine Learning Research* 7 (2006), pp. 2541–2563.

Appendix A

Supplement to Chapter 2

Contents

A.1 Eshelby tensors for ellipsoidal inclusions

In this appendix, the closed-form expressions of Eshelby's tensor [Esh57] is given for aligned spheroidal inclusions embedded in an isotropic matrix. A spheroid is simply an ellipsoid with the principle axes a, b, c with two axes equal, e.g. $a = b$. In all other cases (non-aligned inclusions or an anisotropic matrix), Eshelby's tensor must be numerically evaluated using the method of Gavazzi et al. [GL90]. The non-zero components of the Eshelby's tensor $\mathbb{E}$ are given, which is a function of the Poisson's ratio ν_{m} of the matrix/bulk phase, and the aspect ratio α for spheroidal inclusions embedded in an isotropic matrix aligned along the direction 1:

$$\begin{aligned}
\mathbb{E}_{1111} &= \frac{1}{2(1-\nu_{\mathrm{m}})}\left(2(1-\nu_{\mathrm{m}})(1-g)+g-\alpha^2\frac{3g-2}{\alpha^2-1}\right)\\
\mathbb{E}_{2222} = \mathbb{E}_{3333} &= \frac{1}{4(1-\nu_{\mathrm{m}})}\left(2(2-\nu_{\mathrm{m}})g-\frac{1}{2}-(\alpha^2-\frac{1}{4})\frac{3g-2}{\alpha^2-1}\right)\\
\mathbb{E}_{1122} = \mathbb{E}_{1133} &= \frac{1}{4(1-\nu_{\mathrm{m}})}\left(4\nu_{\mathrm{m}}(1-g)-g+\alpha^2\frac{3g-2}{\alpha^2-1}\right)\\
\mathbb{E}_{2233} = \mathbb{E}_{3322} &= \frac{1}{4(1-\nu_{\mathrm{m}})}\left((2\nu_{\mathrm{m}}-1)g+\frac{1}{2}-\frac{1}{4}\frac{3g-2}{\alpha^2-1}\right)\\
\mathbb{E}_{2211} = \mathbb{E}_{3311} &= \frac{1}{4(1-\nu_{\mathrm{m}})}\left((2\nu_{\mathrm{m}}-1)g+\alpha^2\frac{3g-2}{\alpha^2-1}\right)\\
\mathbb{E}_{1212} = \mathbb{E}_{1313} &= \frac{1}{4(1-\nu_{\mathrm{m}})}\left((1-\nu_{\mathrm{m}})(2-g)-g+\alpha^2\frac{3g-2}{\alpha^2-1}\right)\\
\mathbb{E}_{2323} &= \frac{\mathbb{E}_{2222}-\mathbb{E}_{1122}}{2}
\end{aligned} \tag{A.1}$$

where:

$$\begin{aligned}
g &= \frac{\alpha}{(\alpha^2-1)^{3/2}}\left(\alpha(\alpha^2-1)^{1/2}-\cos^{-1}(\alpha)\right) \qquad \text{for} \quad 0<\alpha<1\\
g &= \frac{\alpha}{(1-\alpha^2)^{3/2}}\left(\cosh^{-1}(\alpha)-\alpha(1-\alpha^2)^{1/2}\right) \qquad \text{for} \quad 1<\alpha<\infty
\end{aligned} \tag{A.2}$$

For the particular case of spherical inclusions, previous equations become invalid and require a study of these functions around $\alpha = 1$. These are given as:

$$\begin{aligned}
\mathbb{E}_{1111} = \mathbb{E}_{2222} = \mathbb{E}_{3333} &= \frac{7-5\nu_{\mathrm{m}}}{15(1-\nu_{\mathrm{m}})}\\
\mathbb{E}_{1122} = \mathbb{E}_{1133} = \mathbb{E}_{2233} &= \frac{5\nu_{\mathrm{m}}-1}{15(1-\nu_{\mathrm{m}})}\\
\mathbb{E}_{1212} = \mathbb{E}_{1313} = \mathbb{E}_{2323} &= \frac{4-5\nu_{\mathrm{m}}}{15(1-\nu_{\mathrm{m}})}
\end{aligned} \tag{A.3}$$

A.2 Principle of virtual work derivation

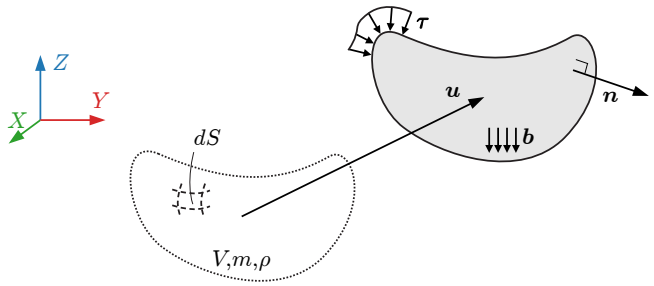

Figure A.1: An arbitrary volume V in motion $\boldsymbol{u}$ with surface boundary S and outer unit vector $\boldsymbol{n}$: with traction $\boldsymbol{\tau}$ and body $\boldsymbol{b}$ forces shown.

Consider an arbitrary body of an isotropic three-dimensional solid, the equations of motion for a given volumetric region V can be described using Newton's second law on Fig. A.1:

$$\int_S \boldsymbol{\tau}\, dS + \int_V \boldsymbol{b}\, dV = \int_V \rho \ddot{\boldsymbol{u}}\, dV \tag{A.4}$$

where $\boldsymbol{\tau}$ are traction forces applied to V on S, $\boldsymbol{b}$ are body forces on V, ρ is the mass density, and $\ddot{\boldsymbol{u}}$ is the acceleration vector. For small displacements, the compatibility equation for the strain tensor is $\boldsymbol{\varepsilon} = \frac{1}{2}\left(\mathrm{grad}(\boldsymbol{u}) + \mathrm{grad}(\boldsymbol{u})^{\mathrm{T}}\right)$. Recall the Gauss divergence theorem, for an arbitrary second-order tensor $\boldsymbol{A}$ and outward normal vector $\boldsymbol{n}$ from the surface S:

$$\int_S \boldsymbol{A}\boldsymbol{n}\, dS = \int_V \mathrm{div}(\boldsymbol{A})\, dV \tag{A.5}$$

Since the traction forces by definition $\boldsymbol{\tau} = \boldsymbol{\sigma}\boldsymbol{n}$, where $\boldsymbol{\sigma} = \boldsymbol{\sigma}^{\mathrm{T}}$ is the stress tensor, and combining Eqs. (A.4) and (A.5), one arrives at:

$$\int_V \left(\mathrm{div}(\boldsymbol{\sigma}) + \boldsymbol{b} - \rho\ddot{\boldsymbol{u}}\right)\, dV = \boldsymbol{0}$$

This equation holds for arbitrary regions of volume, and yields the Cauchy's equation (the strong form of the equations of motion) [LCS02]:

$$\mathrm{div}(\boldsymbol{\sigma}) + \boldsymbol{b} = \rho\ddot{\boldsymbol{u}} \tag{A.6}$$

In many real-world problems, the solution to Eq. (A.6) to might have discontinuities or singularities posing a problem to derivatives: the variational form is more accommodating by turning the differential equation into an integral equation. The principle of virtual work (the weak form) is used instead, which requires assumptions on virtual displacement and virtual strain $\delta\boldsymbol{u}$, $\delta\boldsymbol{\varepsilon}$ to be compatible:

- $\delta\boldsymbol{u}$ is an infinitesimal, regular, time independent field of displacement.
- $\delta\boldsymbol{u}$ satisfies the boundary conditions on S such that $\delta\boldsymbol{u}|_S = \mathbf{0}$.
- $\delta\boldsymbol{u}$ satisfies the compatibility equation for infinitesimal deformations such that $\delta\boldsymbol{\varepsilon} = \frac{1}{2}\left(\mathrm{grad}(\delta\boldsymbol{u}) + \mathrm{grad}(\delta\boldsymbol{u})^{\mathrm{T}}\right)$.

The virtual work done by the traction forces $\boldsymbol{\tau}$ applied to V on S by a virtual displacement is:

$$\int_S \boldsymbol{\tau}\cdot\delta\boldsymbol{u}\,dS - \int_S \boldsymbol{\sigma}\boldsymbol{n}\cdot\delta\boldsymbol{u}\,dS = \int_V \rho\ddot{\boldsymbol{u}}\cdot\delta\boldsymbol{u}\,dV \tag{A.7}$$

Given the identity involving divergence and gradients for arbitrary second-order tensors $\boldsymbol{A}$ and $\boldsymbol{z}$:

$$\mathrm{div}(\boldsymbol{A}^{\mathrm{T}}\boldsymbol{z}) = \boldsymbol{A} : \mathrm{grad}(\boldsymbol{z}) + \boldsymbol{v}\cdot\mathrm{grad}(\boldsymbol{A}) \tag{A.8}$$

The second term of Eq. (A.7)expanded as:

$$\begin{aligned}
\int_S \boldsymbol{\sigma}\boldsymbol{n}\cdot\delta\boldsymbol{u}\,dS &= \int_S \boldsymbol{\sigma}^{\mathrm{T}}\delta\boldsymbol{u}\cdot\boldsymbol{n}\,dS \\
&= \int_V \mathrm{div}\left(\boldsymbol{\sigma}^{\mathrm{T}}\delta\boldsymbol{u}\right)\,dV = \int_V \left(\boldsymbol{\sigma} : \mathrm{grad}\left(\delta\boldsymbol{u}\right) + \delta\boldsymbol{u}\cdot\mathrm{div}\,\boldsymbol{\sigma}\right)\,dV \\
&= \int_V \boldsymbol{\sigma} : \mathrm{grad}\left(\delta\boldsymbol{u}\right)\,dV - \int_V \boldsymbol{b}\cdot\delta\boldsymbol{u}\,dV \\
&= \int_V \boldsymbol{\sigma} : \delta\boldsymbol{\varepsilon}\,dV - \int_V \boldsymbol{b}\cdot\delta\boldsymbol{u}\,dV
\end{aligned}$$

where:

$$\begin{aligned}
\boldsymbol{\sigma} : \mathrm{grad}\left(\delta\boldsymbol{u}\right) &= \frac{1}{2}\left(\boldsymbol{\sigma} : \mathrm{grad}\left(\delta\boldsymbol{u}\right) + \boldsymbol{\sigma} : \mathrm{grad}\left(\delta\boldsymbol{u}\right)^{\mathrm{T}}\right) \\
&= \boldsymbol{\sigma} : \frac{1}{2}\left(\mathrm{grad}\left(\delta\boldsymbol{u}\right) + \mathrm{grad}\left(\delta\boldsymbol{u}\right)^{\mathrm{T}}\right) \\
&= \boldsymbol{\sigma} : \delta\boldsymbol{\varepsilon}
\end{aligned}$$

Eq. (A.7) becomes the weak form, properly known as the principle of virtual work:

$$\underbrace{-\int_V \boldsymbol{\sigma} : \delta\boldsymbol{\varepsilon}\,dV}_{\delta\mathcal{W}_{\mathrm{int}}} + \underbrace{\int_V \boldsymbol{b}\cdot\delta\boldsymbol{u}\,dV + \int_S \boldsymbol{\tau}\cdot\delta\boldsymbol{u}\,dS}_{\delta\mathcal{W}_{\mathrm{ext}}} = \underbrace{\int_V \rho\ddot{\boldsymbol{u}}\cdot\delta\boldsymbol{u}\,dV}_{\delta\mathcal{W}_{\mathrm{acc}}} \tag{A.9}$$

where $\delta\mathcal{W}_{\mathrm{int}}$, $\delta\mathcal{W}_{\mathrm{ext}}$, and $\delta\mathcal{W}_{\mathrm{acc}}$ denote the virtual work due to internal forces, external forces, and inertial forces respectively. Note that, Eq. (A.9) is valid for any deformable body because no constitutive law is used, and thus is extendable to any non-elastic deformations.

A.3 Expansion of principle of virtual work internal forces

Here, the derivation of equation Eq. (2.102) is shown. First the modal approximation of $\boldsymbol{u}(\boldsymbol{X},t)$ of Eq. (2.96) is substituted into $\delta\mathcal{W}_{\text{int}}$ of Eq. (2.102):

$$
\begin{aligned}
-\delta\mathcal{W}_{\text{int}} &= \int_V (\delta\boldsymbol{\varepsilon})^{\mathrm{T}}\boldsymbol{\sigma}\, dV \\
&= \int_V (\delta\boldsymbol{\varepsilon})^{\mathrm{T}} \left(\mathbb{C}\boldsymbol{\varepsilon} + \mathbb{V}\dot{\boldsymbol{\varepsilon}}\right) dV + \int_{V_{\text{nl}}} (\delta\boldsymbol{\varepsilon})^{\mathrm{T}} \left(\langle\boldsymbol{\sigma}_{\text{nl}}\rangle - \mathbb{C}\boldsymbol{\varepsilon}\right) dV_{\text{nl}} \\
&= \int_V (\mathbb{D}\delta\boldsymbol{u})^{\mathrm{T}}\mathbb{C}\mathbb{D}\boldsymbol{u}\, dV + \int_V (\mathbb{D}\delta\boldsymbol{u})^{\mathrm{T}}\mathbb{V}\mathbb{D}\dot{\boldsymbol{u}}\, dV + \int_{V_{\text{nl}}} (\mathbb{D}\delta\boldsymbol{u})^{\mathrm{T}} \left(\mathbb{C}^* - \mathbb{C}\right) d\mathbb{D}\boldsymbol{u}\, V_{\text{nl}} \\
&= \begin{bmatrix}\delta q_0 \\ \delta q_1\end{bmatrix}^{\mathrm{T}} \int_V (\mathbb{D}\left[\begin{array}{c|c}\boldsymbol{\phi}_0 & \boldsymbol{\phi}_1\end{array}\right])^{\mathrm{T}}\mathbb{C}\mathbb{D}\left[\begin{array}{c|c}\boldsymbol{\phi}_0 & \boldsymbol{\phi}_1\end{array}\right] dV \begin{bmatrix}q_0 \\ q_1\end{bmatrix} \\
&\quad + \begin{bmatrix}\delta q_0 \\ \delta q_1\end{bmatrix}^{\mathrm{T}} \int_V (\mathbb{D}\left[\begin{array}{c|c}\boldsymbol{\phi}_0 & \boldsymbol{\phi}_1\end{array}\right])^{\mathrm{T}}\mathbb{V}\mathbb{D}\left[\begin{array}{c|c}\boldsymbol{\phi}_0 & \boldsymbol{\phi}_1\end{array}\right] dV \begin{bmatrix}\dot{q}_0 \\ \dot{q}_1\end{bmatrix} \\
&\quad + \begin{bmatrix}\delta q_0 \\ \delta q_1\end{bmatrix}^{\mathrm{T}} \int_{V_{\text{nl}}} (\mathbb{D}\left[\begin{array}{c|c}\boldsymbol{\phi}_0 & \boldsymbol{\phi}_1\end{array}\right])^{\mathrm{T}}\mathbb{C}^*\mathbb{D}\left[\begin{array}{c|c}\boldsymbol{\phi}_0 & \boldsymbol{\phi}_1\end{array}\right] dV_{\text{nl}} \begin{bmatrix}q_0 \\ q_1\end{bmatrix} \\
&\quad - \begin{bmatrix}\delta q_0 \\ \delta q_1\end{bmatrix}^{\mathrm{T}} \int_{V_{\text{nl}}} (\mathbb{D}\left[\begin{array}{c|c}\boldsymbol{\phi}_0 & \boldsymbol{\phi}_1\end{array}\right])^{\mathrm{T}}\mathbb{C}\mathbb{D}\left[\begin{array}{c|c}\boldsymbol{\phi}_0 & \boldsymbol{\phi}_1\end{array}\right] dV_{\text{nl}} \begin{bmatrix}q_0 \\ q_1\end{bmatrix}
\end{aligned}
\tag{A.10}
$$

First, the gradient operator is shown to be distributive over column space:

$$
\begin{aligned}
(\mathbb{D}\left[\begin{array}{c|c}\boldsymbol{\phi}_0 & \boldsymbol{\phi}_1\end{array}\right])^{\mathrm{T}} &= \left(\begin{bmatrix}
\frac{\partial}{\partial x} & 0 & 0 \\
0 & \frac{\partial}{\partial y} & 0 \\
0 & 0 & \frac{\partial}{\partial z} \\
0 & \frac{\sqrt{2}}{2}\frac{\partial}{\partial z} & \frac{\sqrt{2}}{2}\frac{\partial}{\partial y} \\
\frac{\sqrt{2}}{2}\frac{\partial}{\partial z} & 0 & \frac{\sqrt{2}}{2}\frac{\partial}{\partial x} \\
\frac{\sqrt{2}}{2}\frac{\partial}{\partial y} & \frac{\sqrt{2}}{2}\frac{\partial}{\partial x} & 0
\end{bmatrix}\left[\begin{array}{c|c}
\phi_{0,1} & \phi_{1,1} \\
\phi_{0,2} & \phi_{1,2} \\
\phi_{0,3} & \phi_{1,3}
\end{array}\right]\right)^{\mathrm{T}} \\
&= \left(\begin{bmatrix}
\frac{\partial\phi_{0,1}}{\partial x} & \frac{\partial\phi_{1,1}}{\partial x} \\
\frac{\partial\phi_{0,2}}{\partial x} & \frac{\partial\phi_{1,2}}{\partial x} \\
\frac{\partial\phi_{0,3}}{\partial x} & \frac{\partial\phi_{1,3}}{\partial x} \\
\frac{\sqrt{2}}{2}\left(\frac{\partial\phi_{0,2}}{\partial z} + \frac{\partial\phi_{0,3}}{\partial y}\right) & \frac{\sqrt{2}}{2}\left(\frac{\partial\phi_{1,2}}{\partial z} + \frac{\partial\phi_{1,3}}{\partial y}\right) \\
\frac{\sqrt{2}}{2}\left(\frac{\partial\phi_{0,1}}{\partial z} + \frac{\partial\phi_{0,3}}{\partial x}\right) & \frac{\sqrt{2}}{2}\left(\frac{\partial\phi_{1,1}}{\partial z} + \frac{\partial\phi_{1,3}}{\partial x}\right) \\
\frac{\sqrt{2}}{2}\left(\frac{\partial\phi_{0,1}}{\partial y} + \frac{\partial\phi_{0,2}}{\partial x}\right) & \frac{\sqrt{2}}{2}\left(\frac{\partial\phi_{1,1}}{\partial y} + \frac{\partial\phi_{1,2}}{\partial x}\right)
\end{bmatrix}\right)^{\mathrm{T}} = (\left[\begin{array}{c|c}\mathbb{D}\boldsymbol{\phi}_0 & \mathbb{D}\boldsymbol{\phi}_1\end{array}\right])^{\mathrm{T}}
\end{aligned}
\tag{A.11}
$$

Since $\boldsymbol{\phi}_0$ is a rigid longitudinal eigenmode, it's spatial derivatives are zero, which means that the expression is equivalent to:

$$(\mathbb{D}\left[\begin{array}{c|c} \boldsymbol{\phi}_0 & \boldsymbol{\phi}_1 \end{array}\right])^{\mathrm{T}} = (\left[\begin{array}{c|c} \mathbf{0} & \mathbb{D}\boldsymbol{\phi}_1 \end{array}\right])^{\mathrm{T}} \tag{A.12}$$

Thus, the overall expansion can be shown to be:

$$\begin{aligned}
(\mathbb{D}\left[\begin{array}{c|c} \boldsymbol{\phi}_0 & \boldsymbol{\phi}_1 \end{array}\right])^{\mathrm{T}}\mathbb{C} &= \left(\begin{bmatrix} 0 & \frac{\partial \phi_{1,1}}{\partial x} \\ 0 & \frac{\partial \phi_{1,2}}{\partial x} \\ 0 & \frac{\partial \phi_{1,3}}{\partial x} \\ 0 & \frac{\sqrt{2}}{2}\left(\frac{\partial \phi_{1,2}}{\partial z} + \frac{\partial \phi_{1,3}}{\partial y}\right) \\ 0 & \frac{\sqrt{2}}{2}\left(\frac{\partial \phi_{1,1}}{\partial z} + \frac{\partial \phi_{1,3}}{\partial x}\right) \\ 0 & \frac{\sqrt{2}}{2}\left(\frac{\partial \phi_{1,1}}{\partial y} + \frac{\partial \phi_{1,2}}{\partial x}\right) \end{bmatrix}\right)^{\mathrm{T}} \begin{bmatrix} | & | & | & | & | & | \\ \mathbb{C}_{11} & \mathbb{C}_{22} & \mathbb{C}_{33} & \mathbb{C}_{23} & \mathbb{C}_{13} & \mathbb{C}_{12} \\ | & | & | & | & | & | \end{bmatrix} \\
&= \left(\begin{bmatrix} 0 & \mathbb{D}\boldsymbol{\phi}_1\mathbb{C}_{11} \\ 0 & \mathbb{D}\boldsymbol{\phi}_1\mathbb{C}_{22} \\ 0 & \mathbb{D}\boldsymbol{\phi}_1\mathbb{C}_{33} \\ 0 & \mathbb{D}\boldsymbol{\phi}_1\mathbb{C}_{23} \\ 0 & \mathbb{D}\boldsymbol{\phi}_1\mathbb{C}_{13} \\ 0 & \mathbb{D}\boldsymbol{\phi}_1\mathbb{C}_{12} \end{bmatrix}\right)^{\mathrm{T}}
\end{aligned} \tag{A.13}$$

$$\begin{aligned}
&(\mathbb{D}\left[\begin{array}{c|c} \boldsymbol{\phi}_0 & \boldsymbol{\phi}_1 \end{array}\right])^{\mathrm{T}}\mathbb{C}\mathbb{D}\left[\begin{array}{c|c} \boldsymbol{\phi}_0 & \boldsymbol{\phi}_1 \end{array}\right] = \\
&= \begin{bmatrix} 0 & 0 & 0 & 0 & 0 & 0 \\ \mathbb{D}\boldsymbol{\phi}_1\mathbb{C}_{11} & \mathbb{D}\boldsymbol{\phi}_1\mathbb{C}_{22} & \mathbb{D}\boldsymbol{\phi}_1\mathbb{C}_{33} & \mathbb{D}\boldsymbol{\phi}_1\mathbb{C}_{23} & \mathbb{D}\boldsymbol{\phi}_1\mathbb{C}_{13} & \mathbb{D}\boldsymbol{\phi}_1\mathbb{C}_{12} \end{bmatrix} \begin{bmatrix} 0 & \mathbb{D}\boldsymbol{\phi}_1\mathbb{C}_{11} \\ 0 & \mathbb{D}\boldsymbol{\phi}_1\mathbb{C}_{22} \\ 0 & \mathbb{D}\boldsymbol{\phi}_1\mathbb{C}_{33} \\ 0 & \mathbb{D}\boldsymbol{\phi}_1\mathbb{C}_{23} \\ 0 & \mathbb{D}\boldsymbol{\phi}_1\mathbb{C}_{13} \\ 0 & \mathbb{D}\boldsymbol{\phi}_1\mathbb{C}_{12} \end{bmatrix} \\
&= \left[\begin{array}{c} \mathbb{D}\boldsymbol{\phi}_0\mathbb{C} \\ \hline \mathbb{D}\boldsymbol{\phi}_1\mathbb{C} \end{array}\right] \left[\begin{array}{c|c} \mathbb{D}\boldsymbol{\phi}_0 & \mathbb{D}\boldsymbol{\phi}_1 \end{array}\right] \\
&= \left[\begin{array}{c|c} \mathbb{D}\boldsymbol{\phi}_0\mathbb{C}\mathbb{D}\boldsymbol{\phi}_0 & \mathbb{D}\boldsymbol{\phi}_0\mathbb{C}\mathbb{D}\boldsymbol{\phi}_1 \\ \hline \mathbb{D}\boldsymbol{\phi}_1\mathbb{C}\mathbb{D}\boldsymbol{\phi}_0 & \mathbb{D}\boldsymbol{\phi}_1\mathbb{C}\mathbb{D}\boldsymbol{\phi}_1 \end{array}\right] \\
&= \left[\begin{array}{c|c} 0 & 0 \\ \hline 0 & \mathbb{D}\boldsymbol{\phi}_1\mathbb{C}\mathbb{D}\boldsymbol{\phi}_1 \end{array}\right]
\end{aligned} \tag{A.14}$$

Therefore Eq. (A.10) can be shown to be:

$$-\delta\mathcal{W}_{\mathrm{int}} = \begin{bmatrix} \delta q_0 \\ \delta q_1 \end{bmatrix}^{\mathrm{T}} \left(\boldsymbol{K}\begin{bmatrix} q_0 \\ q_1 \end{bmatrix} + \boldsymbol{C}\begin{bmatrix} \dot{q}_0 \\ \dot{q}_1 \end{bmatrix} + \boldsymbol{K}_{\mathrm{nl}}\begin{bmatrix} q_0 \\ q_1 \end{bmatrix}\right) \tag{A.15}$$

with:

$$\boldsymbol{K} = \begin{bmatrix} 0 & 0 \\ 0 & K_1 \end{bmatrix}; \quad K_1 \coloneqq \int_V (\mathbb{D}\boldsymbol{\phi}_1)^{\mathrm{T}} \mathbb{C} \mathbb{D}\boldsymbol{\phi}_1 dV \tag{A.16}$$

$$\boldsymbol{C} = \begin{bmatrix} 0 & 0 \\ 0 & C_1 \end{bmatrix}; \quad C_1 \coloneqq \int_V (\mathbb{D}\boldsymbol{\phi}_1)^{\mathrm{T}} \mathbb{V} \mathbb{D}\boldsymbol{\phi}_1 dV \tag{A.17}$$

$$\boldsymbol{K}_{\mathrm{nl}} = \begin{bmatrix} 0 & 0 \\ 0 & K_{\mathrm{nl},1} \end{bmatrix}; \quad K_{\mathrm{nl},1} \coloneqq \int_{V_{\mathrm{nl}}} (\mathbb{D}\boldsymbol{\phi}_1)^{\mathrm{T}} \mathbb{C}^* \mathbb{D}\boldsymbol{\phi}_1 \, dV_{\mathrm{nl}} - \int_{V_{\mathrm{nl}}} (\mathbb{D}\boldsymbol{\phi}_1)^{\mathrm{T}} \mathbb{C} \mathbb{D}\boldsymbol{\phi}_1 dV_{\mathrm{nl}} \tag{A.18}$$

A.4 Tensor notation for isotropic elasticity and piezoelectricity

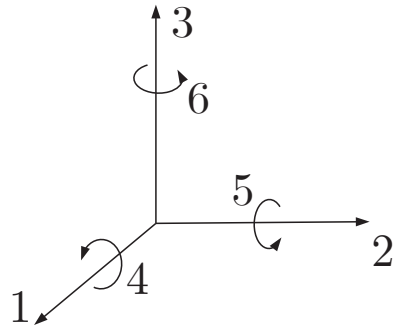

Figure A.2: Notation of axes for 3D cartesian system.

ij or kl	p or q
11	1
22	2
33	3
23 or 32	4
13 or 31	5
12 or 21	6

Table A.1: Conversion from tensor to Voigt matrix notations.

Voigt notation is obtained by replacing indices ij or kl by p or q according to Table A.1. The left one of the two subscripts always denotes the direction of the resulting field, where the right one says in which direction the field operates. For example, c_{13}^E indicates that at constant electrical field the mechanical stress is direction in 1 and the mechanical strain is in direction 3. Numbers 4, 5, 6 denote shear around the axes 1, 2 and 3, see Figure A.2. Here, Voigt notation is given for mechanical stress tensor $\boldsymbol{T}$, strain tensor $\boldsymbol{S}$ and stiffness tensor $\boldsymbol{c}$:

$$T_p = T_{ij}, \quad S_p = \begin{cases} S_{ij}, & \text{for } p = 1,2,3 \\ 2S_{ij}, & \text{for } p = 4,5,6 \end{cases} \tag{A.19}$$

$$c_{pq} = c_{(ij)(kl)}, \quad s_{pq} = \begin{cases} s_{(ij)(kl)}, & \text{for } p = 1,2,3 \text{ and } q = 1,2,3 \\ 2s_{(ij)(kl)}, & \text{for } p = 4,5,6 \text{ and } q = 1,2,3 \\ 2s_{(ij)(kl)}, & \text{for } p = 1,2,3 \text{ and } q = 4,5,6 \\ 4s_{(ij)(kl)}, & \text{for } p = 4,5,6 \text{ and } q = 4,5,6 \end{cases} \tag{A.20}$$

If the z-axis (corresponding to direction 3 in Figure A.2) is taken as the symmetry axis, the structure is defined by five independent elastic moduli ($c_{11}^E = c_{22}^E$, c_{33}^E, c_{12}^E, $c_{13}^E = c_{23}^E$, $c_{44}^E = c_{55}^E$, $c_{66}^E = \frac{1}{2}\left(c_{11}^E + c_{12}^E\right)$). The linear constitutive equation is expanded in matrix notation:

$$\begin{bmatrix} T_1 \\ T_2 \\ T_3 \\ T_4 \\ T_5 \\ T_6 \end{bmatrix} = \begin{bmatrix} c_{11}^E & c_{12}^E & c_{13}^E & \cdot & \cdot & \cdot \\ c_{12}^E & c_{11}^E & c_{13}^E & \cdot & \cdot & \cdot \\ c_{13}^E & c_{13}^E & c_{33}^E & \cdot & \cdot & \cdot \\ \cdot & \cdot & \cdot & c_{44}^E & \cdot & \cdot \\ \cdot & \cdot & \cdot & \cdot & c_{44}^E & \cdot \\ \cdot & \cdot & \cdot & \cdot & \cdot & c_{66}^E \end{bmatrix} \begin{bmatrix} S_1 \\ S_2 \\ S_3 \\ S_4 \\ S_5 \\ S_6 \end{bmatrix} \tag{A.21}$$

Similarly, for an electromechanical coupling with piezoelectricity with the three piezoelectric moduli ($e_{15} = e_{24}$, $e_{31} = e_{32}$, e_{33}), and two permittivities ($\eta_{11}^S = \eta_{22}^S$, η_{33}^S), the linear constitutive equation is

given in matrix notation, for dielectric displacement tensor $\boldsymbol{\mathcal{D}}$ and electric field $\boldsymbol{E}$:

$$\begin{bmatrix} T_1 \\ T_2 \\ T_3 \\ T_4 \\ T_5 \\ T_6 \\ \mathcal{D}_1 \\ \mathcal{D}_2 \\ \mathcal{D}_3 \end{bmatrix} = \begin{bmatrix} c_{11}^E & c_{12}^E & c_{13}^E & \cdot & \cdot & \cdot & \cdot & \cdot & -e_{13} \\ c_{12}^E & c_{11}^E & c_{13}^E & \cdot & \cdot & \cdot & \cdot & \cdot & -e_{13} \\ c_{13}^E & c_{13}^E & c_{33}^E & \cdot & \cdot & \cdot & \cdot & \cdot & -e_{33} \\ \cdot & \cdot & \cdot & c_{44}^E & \cdot & \cdot & \cdot & -e_{15} & \cdot \\ \cdot & \cdot & \cdot & \cdot & c_{44}^E & \cdot & -e_{15} & \cdot & \cdot \\ \cdot & \cdot & \cdot & \cdot & \cdot & c_{66}^E & \cdot & \cdot & \cdot \\ \cdot & \cdot & \cdot & \cdot & e_{15} & \cdot & \eta_{11}^S & \cdot & \cdot \\ \cdot & \cdot & \cdot & e_{15} & \cdot & \cdot & \cdot & \eta_{11}^S & \cdot \\ e_{13} & e_{13} & e_{33} & \cdot & \cdot & \cdot & \cdot & \cdot & \eta_{33}^S \end{bmatrix} \begin{bmatrix} S_1 \\ S_2 \\ S_3 \\ S_4 \\ S_5 \\ S_6 \\ E_1 \\ E_2 \\ E_3 \end{bmatrix} \tag{A.22}$$

This can be more compactly written as an augmented matrix system:

$$\begin{array}{rcrcl} \boldsymbol{T} & = & \boldsymbol{c}^E\boldsymbol{S} & - & \boldsymbol{e}^{\mathrm{T}}\boldsymbol{E} \\ \boldsymbol{\mathcal{D}} & = & \boldsymbol{e}\boldsymbol{S} & + & \boldsymbol{\varepsilon}^S\boldsymbol{E} \end{array} \tag{A.23}$$

It's inverse, where $s_{66}^{\mathcal{D}} = \frac{1}{2}\left(s_{11}^{\mathcal{D}} - S_{12}^{\mathcal{D}}\right)$:

$$\begin{array}{rcrcl} \boldsymbol{S} & = & \boldsymbol{s}^{\mathcal{D}}\boldsymbol{T} & + & \boldsymbol{g}^{\mathrm{T}}\boldsymbol{\mathcal{D}} \\ \boldsymbol{E} & = & -\boldsymbol{g}\boldsymbol{T} & + & \boldsymbol{\beta}^T\boldsymbol{\mathcal{D}} \end{array} \tag{A.24}$$

The set of state equations in terms of intensive variables where $c_{66}^{\mathcal{D}} = \frac{1}{2}\left(c_{11}^{\mathcal{D}} - c_{12}^{\mathcal{D}}\right)$:

$$\begin{array}{rcrcl} \boldsymbol{T} & = & \boldsymbol{c}^{\mathcal{D}}\boldsymbol{S} & - & \boldsymbol{h}^{\mathrm{T}}\boldsymbol{\mathcal{D}} \\ \boldsymbol{E} & = & -\boldsymbol{h}\boldsymbol{S} & + & \boldsymbol{\beta}^S\boldsymbol{\mathcal{D}} \end{array} \tag{A.25}$$

The set of state equations in terms of extensive variables where $s_{66}^E = \frac{1}{2}\left(s_{11}^E + s_{12}^E\right)$:

$$\begin{array}{rcrcl} \boldsymbol{S} & = & \boldsymbol{s}^E\boldsymbol{T} & + & \boldsymbol{d}^{\mathrm{T}}\boldsymbol{E} \\ \boldsymbol{\mathcal{D}} & = & \boldsymbol{d}\boldsymbol{T} & + & \boldsymbol{\varepsilon}^T\boldsymbol{E} \end{array} \tag{A.26}$$

Depending on the coupling coefficient occurring in the piezoelectric (Eqs. (A.23) and (A.26)) are of the e, h, h or d-form, according to IEEE standards [EE78].

Appendix B

Supplement to Chapter 3

Contents

B.1 Synthetic ultrasonic fatigue vibration signal parameters

In this section, we detail the cubic fits of the time varying sinusoidal parameters seen in right of Fig. 3.5, specifically $a_1(t)$, $a_2(t)$, $a_3(t)$ and $f_1(t)$. The original signal comes from a pure copper fatigue specimen subject to an ultrasonic fatigue test. It is reminded that $f_2(t)$ and $f_3(t)$ are integer multiples of f_1(t), since they correspond to higher harmonics used for the first test in Section 3.2.2. The cubic fits for the amplitudes in meters per second are:

$$a_1(t) = -(7.564 \times 10^{-10})t^3 + (1.038 \times 10^{-6})t^2 - (4.818 \times 10^{-4})t + 7.378 \times 10^{-1}$$

$$a_2(t) = (6.094 \times 10^{-12})t^3 - (7.455 \times 10^{-9})t^2 + (5.791 \times 10^{-6})t + 2.751 \times 10^{-3}$$

$$a_3(t) = (2.346 \times 10^{-11})t^3 - (2.904 \times 10^{-8})t^2 + (1.09 \times 10^{-5})t + 1.823 \times 10^{-2}$$

The cubic fits for the frequencies in cycles per second are:

$$f_1(t) = -(2.859 \times 10^{-7})t^3 + (4.286 \times 10^{-4})t^2 - (2.628 \times 10^{-1})t + 2.013 \times 10^{4}$$

B.2 Mismatch for damped signal model

For a damped signal model represented as a data matrix:

$$\boldsymbol{X} = \bar{\boldsymbol{A}}_M \boldsymbol{B} \bar{\boldsymbol{A}}_L^{\mathrm{T}}$$

where $\bar{\boldsymbol{A}}_M \in \mathbb{C}^{M\times P}$ and $\bar{\boldsymbol{A}}_L^{\mathrm{T}} \in \mathbb{C}^{P\times L}$ are Vandermonde matrices of the damped form:

$$\bar{\boldsymbol{A}}_M \coloneqq \begin{bmatrix} 1 & \cdots & 1 \\ e^{d_0+\mathrm{j}2\pi\omega_0} & \cdots & e^{d_{P-1}+\mathrm{j}2\pi\omega_{P-1}} \\ e^{d_0+\mathrm{j}4\pi\omega_0} & \cdots & e^{d_{P-1}+\mathrm{j}4\pi\omega_{P-1}} \\ \vdots & \ddots & \vdots \\ e^{d_0+\mathrm{j}2\pi\omega_0(M-1)} & \cdots & e^{d_{P-1}+\mathrm{j}2\pi\omega_{P-1}(M-1)} \end{bmatrix}$$

where $\{d_i \leq 0\}_{i=0}^{P-1}$ are the damping factors. The full DFT kernel has a basis mismatch with the frequencies as well as the damping factors, represented by the product $\bar{\boldsymbol{A}}_L^{\mathrm{T}} \boldsymbol{W}_L^* \in \mathbb{C}^{P\times L}$:

$$[\bar{\boldsymbol{A}}_L^{\mathrm{T}} \boldsymbol{W}_L^*]_{m,l} = \frac{1}{L} \sum_{i=0}^{L-1} \left(e^{d_m+\mathrm{j}2\pi(i)(\omega_m - \frac{l}{L})} \right)$$

for $m = 0,\, 1,\, \ldots,\, P-1$ and $l = 0,\, 1,\, \ldots,\, L-1$. The product with a truncated DFT kernel $\bar{\boldsymbol{A}}_L^{\mathrm{T}} \boldsymbol{W}_{L\times P}^* \in \mathbb{C}^{P\times P}$:

$$[\bar{\boldsymbol{A}}_L^{\mathrm{T}} \boldsymbol{W}_{L\times P}^*]_{m,l} = \frac{1}{L} \sum_{i=0}^{L-1} \left(e^{d_m+\mathrm{j}2\pi(i)(\omega_m - \delta_l)} \right)$$

where P frequency differences $\{\delta_i \in [0,1)\}_{i=0}^{P-1}$ define $\boldsymbol{W}_{L\times P}^*$ and for $m = 0,\, 1,\, \ldots,\, P-1$ and $l = 0,\, 1,\, \ldots,\, P-1$..

B.3 Proof of Theorem 5

Here we will follow almost identically to the derivation of [LLF20] for certain perturbation bounds for FFT-ESPRIT of Algorithm 2, which has the form:

$$\begin{aligned}\widehat{\boldsymbol{X}}\boldsymbol{W}_{L\times P}^{*} &= \boldsymbol{A}_{P}\boldsymbol{B}\boldsymbol{A}_{L}^{\mathrm{T}}\boldsymbol{W}_{L\times P}^{*} + \boldsymbol{\mathcal{E}}\boldsymbol{W}_{L\times P}^{*} \\ &= \boldsymbol{X}\boldsymbol{W}_{L\times P}^{*} + \boldsymbol{\mathcal{E}}\boldsymbol{W}_{L\times P}^{*}\end{aligned}$$

First Eq. (3.31) is rewritten from Theorem 1 with respect to the estimated matrix, which states that if $2\|\boldsymbol{\mathcal{E}}\boldsymbol{W}_{L\times P}^{*}\| \leq 2\|\boldsymbol{\mathcal{E}}\|\|\boldsymbol{W}_{L\times P}^{*}\| \leq \sigma_{P-1}(\widehat{\boldsymbol{X}}\boldsymbol{W}_{L\times P}^{*})$:

$$\sin\theta_0 \leq \frac{2\|\boldsymbol{\mathcal{E}}\boldsymbol{W}_{L\times P}^{*}\|}{\sigma_{P-1}(\widehat{\boldsymbol{X}}\boldsymbol{W}_{L\times P}^{*})} \leq \frac{2\|\boldsymbol{\mathcal{E}}\|\|\boldsymbol{W}_{L\times P}^{*}\|}{\sigma_{P-1}(\widehat{\boldsymbol{X}}\boldsymbol{W}_{L\times P}^{*})} \tag{B.1}$$

Given that ESPRIT is invariant to the choice of orthonormal basis by Proposition 4, we work with $\boldsymbol{Q} \leftarrow \boldsymbol{X}\boldsymbol{W}_{L\times P}^{*}$. Eq. (B.1) shows that when the rotation between $\boldsymbol{Q}, \widehat{\boldsymbol{Q}}$ are small, the column spaces are close when the noise is negligible.

Lemma 1. *Let the size constraints of the data matrix Eq.* (3.50) *be fixed. If* $2\|\boldsymbol{\mathcal{E}}\boldsymbol{W}_{L\times P}^{*}\| \leq \beta_{\min}\sigma_{P-1}(\boldsymbol{A}_{M})\sigma_{P-1}(\boldsymbol{A}_{L}^{\mathrm{T}})\sigma_{P-1}(\boldsymbol{W}_{L\times P}^{*})$*, then:*

$$\|\widehat{\boldsymbol{Q}} - \boldsymbol{Q}\| \leq \frac{2\sqrt{2P}\|\boldsymbol{\mathcal{E}}\boldsymbol{W}_{L\times P}^{*}\|}{\beta_{\min}\sigma_{P-1}(\boldsymbol{A}_{M})\sigma_{P-1}(\boldsymbol{A}_{L}^{\mathrm{T}})\sigma_{P-1}(\boldsymbol{W}_{L\times P}^{*})} \leq \frac{2\sqrt{2P}\|\boldsymbol{\mathcal{E}}\|\|\boldsymbol{W}_{L\times P}^{*}\|}{\beta_{\min}\sigma_{P-1}(\boldsymbol{A}_{M})\sigma_{P-1}(\boldsymbol{A}_{L}^{\mathrm{T}})\sigma_{P-1}(\boldsymbol{W}_{L\times P}^{*})}$$

Proof. For $k = 0, \ldots, P-1$:

$$\begin{aligned}\|\widehat{\boldsymbol{q}}_k - \boldsymbol{q}_k\|^2 &= 4\sin^2\left(\frac{\theta_k}{2}\right) \\ &= 2\left(1-\cos\theta_k\right) \leq 2\left(1-\cos^2\theta_k\right) \leq 2\sin^2\theta_k\end{aligned}$$

By the properties of matrix norms, and the above inequality, one gets:

$$\begin{aligned}\|\widehat{\boldsymbol{Q}} - \boldsymbol{Q}\| \leq \|\widehat{\boldsymbol{Q}} - \boldsymbol{Q}\|_{\mathrm{F}} &= \left(\sum_{k=0}^{P-1}\|\widehat{\boldsymbol{q}}_k - \boldsymbol{q}_k\|^2\right)^{1/2} \\ &\leq \left(2P\sin^2\theta_0\right)^{1/2} = \sqrt{2P}\sin\theta_0\end{aligned}$$

Given the definition of the ℓ_2 norm on $\boldsymbol{X}\boldsymbol{W}_{L\times P}^{*}$:

$$\|\boldsymbol{X}\boldsymbol{W}_{L\times P}^{*}\| = \|\boldsymbol{A}_{M}\boldsymbol{B}\boldsymbol{A}_{L}^{\mathrm{T}}\boldsymbol{W}_{L\times P}^{*}\| \geq \beta_{\min}\sigma_{P-1}(\boldsymbol{A}_{M})\sigma_{P-1}(\boldsymbol{A}_{L}^{\mathrm{T}})\sigma_{P-1}(\boldsymbol{W}_{L\times P}^{*})$$

This combined with Eq. (B.1) completes the proof. □

Thus, the next step is to relate $\|\widehat{\boldsymbol{Q}} - \boldsymbol{Q}\|$ with $\|\widehat{\boldsymbol{\Psi}} - \boldsymbol{\Psi}\|$ since $\boldsymbol{\Psi} \leftarrow \boldsymbol{Q}$.

Lemma 2. *Let the size constraints of the data matrix Eq.* (3.50) *be fixed. Since* $\|\widehat{\boldsymbol{Q}} - \boldsymbol{Q}\| \leq \sigma_{P-1}(\boldsymbol{Q}^{\uparrow})/2$, *then:*

$$\|\widehat{\boldsymbol{\Psi}} - \boldsymbol{\Psi}\| \leq \frac{7\|\widehat{\boldsymbol{Q}} - \boldsymbol{Q}\|}{\sigma^2_{P-1}(\boldsymbol{Q}^{\uparrow})}$$

Proof. The perturbation of $\|\widehat{\boldsymbol{\Psi}} - \boldsymbol{\Psi}\|$ can be decomposed via triangle inequalities in ℓ_2 space [Che+21]:

$$\begin{aligned}
\|\widehat{\boldsymbol{\Psi}} - \boldsymbol{\Psi}\| &= \big\|\big((\widehat{\boldsymbol{Q}}^{\uparrow})^{\ddagger} - (\boldsymbol{Q}^{\uparrow})^{\ddagger}\big)\widehat{\boldsymbol{Q}}_{\downarrow} + (\boldsymbol{Q}^{\uparrow})^{\ddagger}(\widehat{\boldsymbol{Q}}_{\downarrow} - \boldsymbol{Q}_{\downarrow})\big\| \\
&\leq \big\|(\widehat{\boldsymbol{Q}}^{\uparrow})^{\ddagger} - (\boldsymbol{Q}^{\uparrow})^{\ddagger}\big\|\big\|\widehat{\boldsymbol{Q}}_{\downarrow}\big\| + \big\|(\boldsymbol{Q}^{\uparrow})^{\ddagger}\big\|\big\|\widehat{\boldsymbol{Q}}_{\downarrow} - \boldsymbol{Q}_{\downarrow}\big\| \\
&\leq \big\|(\widehat{\boldsymbol{Q}}^{\uparrow})^{\ddagger} - (\boldsymbol{Q}^{\uparrow})^{\ddagger}\big\| + \big\|(\boldsymbol{Q}^{\uparrow})^{\ddagger}\big\|\big\|\widehat{\boldsymbol{Q}} - \boldsymbol{Q}\big\|
\end{aligned}$$

since $\|\widehat{\boldsymbol{Q}}^{\uparrow}\| \leq \|\widehat{\boldsymbol{Q}}\| = 1$ and $\|\widehat{\boldsymbol{Q}} - \boldsymbol{Q}\| \leq \|\widehat{\boldsymbol{Q}} - \boldsymbol{Q}\|$. When assuming (well-conditioned) signal subspaces:

$$\|\widehat{\boldsymbol{Q}}^{\uparrow} - \boldsymbol{Q}^{\uparrow}\| \leq \|\widehat{\boldsymbol{Q}} - \boldsymbol{Q}\| \leq \frac{1}{2\sigma_{P-1}(\boldsymbol{Q}^{\uparrow})}$$

This allows application of the truncated SVD theorem [Han87]:

$$\begin{aligned}
\big\|(\widehat{\boldsymbol{Q}}^{\uparrow})^{\ddagger} - (\boldsymbol{Q}^{\uparrow})^{\ddagger}\big\| &\leq \frac{3\|\widehat{\boldsymbol{Q}}^{\uparrow} - \boldsymbol{Q}^{\uparrow}\|}{\sigma_{P-1}(\boldsymbol{Q}^{\uparrow})\big(\sigma_{P-1}(\boldsymbol{Q}^{\uparrow}) - \|\widehat{\boldsymbol{Q}}^{\uparrow} - \boldsymbol{Q}^{\uparrow}\|\big)} \\
&\leq \frac{6\|\widehat{\boldsymbol{Q}} - \boldsymbol{Q}\|}{2\sigma^2_{P-1}(\boldsymbol{Q}^{\uparrow})}
\end{aligned}$$

Therefore, one can relate the eigenspace with the signal subspace:

$$\begin{aligned}
\|\widehat{\boldsymbol{\Psi}} - \boldsymbol{\Psi}\| &\leq \left(\frac{6}{\sigma^2_{P-1}(\boldsymbol{Q}^{\uparrow})} + \frac{1}{\sigma_{P-1}(\boldsymbol{Q}^{\uparrow})}\right)\|\widehat{\boldsymbol{Q}} - \boldsymbol{Q}\| \\
&\leq \frac{7\|\widehat{\boldsymbol{Q}} - \boldsymbol{Q}\|}{\sigma^2_{P-1}(\boldsymbol{Q}^{\uparrow})}
\end{aligned}$$

This combined with triangle inequality completes the proof. □

B.4 Supplement to TRIM

B.4.1 Integration and differentiation matrix operators

The matrix form of the forward first and $i+1$th discrete differential operators, $\boldsymbol{D}_1 \in \mathbb{R}^{M-1\times M}$ and $\boldsymbol{D}_{i+1} \in \mathbb{R}^{M-i\times M}$ respectively, are given by:

$$\boldsymbol{D}_1 \coloneqq \frac{1}{\Delta t}\begin{bmatrix} -1 & 1 & & & \\ & -1 & 1 & & \\ & & \ddots & \ddots & \\ & & & -1 & 1 \end{bmatrix}; \quad \boldsymbol{D}_{i+1} \coloneqq \boldsymbol{D}_1\boldsymbol{D}_i \tag{B.2}$$

where $\Delta t = T/(M-1) : t \in [0, T]$. For numerical integrals, we use a matrix form of the first and $i+1$th cumulative integral operators, $\boldsymbol{T}_1$, $\boldsymbol{T}_i \in \mathbb{R}^{M\times M}$:

$$\boldsymbol{T}_1 \coloneqq \boldsymbol{L}\boldsymbol{B}^{(\text{order})}; \quad \boldsymbol{T}_{i+1} \coloneqq \boldsymbol{T}_1\boldsymbol{T}_i \tag{B.3}$$

where $\boldsymbol{L} \in \mathbb{R}^{M\times M}$ is a zero-padded lower triangular matrix and $\boldsymbol{B}^{(\text{order})} \in \mathbb{R}^{M\times M}$ are the Newton polynomial matrices, e.g. $\boldsymbol{B}^{(1)}$ corresponding to trapezoidal rule. The lower triangular matrix is given as:

$$\boldsymbol{L} = \begin{bmatrix} 0 & 0 & 0 & 0 & \cdots & 0 & 0 \\ 0 & 1 & 0 & 0 & \cdots & 0 & 0 \\ 0 & 1 & 1 & 0 & \cdots & 0 & 0 \\ 0 & 1 & 1 & 1 & \cdots & 0 & 0 \\ \vdots & \vdots & \vdots & \vdots & \ddots & \vdots & \vdots \\ 0 & 1 & 1 & 1 & \cdots & 1 & 0 \\ 0 & 1 & 1 & 1 & \cdots & 1 & 1 \end{bmatrix}$$

The first-order Newton polynomial with forward difference gives the classic trapezoidal rule, whereas the third-order Newton polynomial gives Simpson's rule. We give the explicit matrices for the first three orders of polynomials:

$$\boldsymbol{B}^{(1)} = \frac{\Delta t}{2}\begin{bmatrix} 0 & 0 & 0 & & \\ 1 & 1 & 0 & & \\ 0 & 1 & 1 & & \\ & \ddots & \ddots & \ddots & \\ & & 0 & 1 & 1 \end{bmatrix}; \quad \boldsymbol{B}^{(2)} = \frac{\Delta t}{12}\begin{bmatrix} 0 & 0 & 0 & 0 & & \\ 5 & 8 & -1 & 0 & & \\ 0 & 5 & 8 & -1 & & \\ & \ddots & \ddots & \ddots & \ddots & \\ & & 0 & 5 & 8 & -1 \\ & & 0 & -1 & 8 & 5 \end{bmatrix};$$

$$\boldsymbol{B}^{(3)} = \frac{\Delta t}{24}\begin{bmatrix} 0 & 0 & 0 & 0 & & \\ 9 & 19 & -5 & 1 & & \\ -1 & 13 & 13 & -1 & & \\ & \ddots & \ddots & \ddots & \ddots & \\ & & -1 & 13 & 13 & -1 \\ & & 1 & -5 & 19 & 9 \end{bmatrix}$$

B.4.2 Data-preprocessing

Nonparametric denoising When there is noise in the measurement, a unique solution to Eq. (3.48) is no longer guaranteed. The library of candidate functions are built from the noisy measurements, $\tilde{\boldsymbol{z}} = \boldsymbol{z} + \boldsymbol{\varepsilon}$, which are assumed to be corrupted by AWGN. With nonlinearities, noise can be nonlinear transformed when formed as a candidate function: e.g. $\theta(\tilde{\boldsymbol{z}}_1 \circ \tilde{\boldsymbol{z}}_2) = (\boldsymbol{z}_1^* + \boldsymbol{\varepsilon}_1) \circ (\boldsymbol{z}_2^* + \boldsymbol{\varepsilon}_2)$ which contains higher order noise corrupted terms. Data that is noise-free lets numerical derivatives, which are known to be unstable, have a lower error accumulation. This inspires *a priori* denoising techniques for data-preprocessing before applying SINDy, e.g. knowing the trajectory should be smooth. In this study, we opt for a global denoising techniques by regularization, which can be expressed as convex optimization. The most prominent in literature is by Tikhonov regularization, the right-hand side is penalized by an ℓ_2 norm:

$$\begin{aligned} \hat{\boldsymbol{z}} &= \arg\min_{\boldsymbol{z}} \left\{ \ \|\boldsymbol{z} - \tilde{\boldsymbol{z}}\|_2^2 + \lambda \|\boldsymbol{D}_2 \boldsymbol{z}\|_2^2 \ \right\}; \\ &= \left(\boldsymbol{I} + \lambda \boldsymbol{D}_2^{\mathrm{T}} \boldsymbol{D}_2\right)^{-1} \tilde{\boldsymbol{z}}; \end{aligned} \qquad \forall \lambda > 0 \tag{B.4}$$

Note that denoising data with the penalization $\boldsymbol{D}_2$ corresponds to projecting its trajectory onto a smooth Poincaré map. If this is not suitable for the dynamics, e.g. trajectories that are piece-wise smooth, one can use a combined Tikhonov and total-variation method [GH13]. It's been shown that this global smoothing technique, requiring one hyperparameter, outperforms various local smoothing techniques requiring multiple hyperparameters [CPD22].

Regularized derivatives The regression data $\dot{\boldsymbol{z}}$ is typically numerically estimated by finite difference approximations on the measurements $\boldsymbol{z}$. We opt for global methods by regularization, since it has been shown to outperform local methods [KR14], e.g. finite differentiation on local windows which are smoothed by a Savitsky-Golay filter or LOWESS (moving average and/or polynomial fits). For a jth

order derivative, this can be written as the integration:

$$\boldsymbol{T}_j \partial_j(\boldsymbol{z}) + z_0 \mathbf{1}_M = \boldsymbol{z} + \boldsymbol{\varepsilon}_q$$

where $\boldsymbol{\varepsilon}_q$, $z_0\mathbf{1}_M$ is the error due to quadrature and initial values respectively and $\partial_j(\boldsymbol{z}) \coloneqq d^j/dt^j(\boldsymbol{z})$ notates the jth order derivative. This formulation has resulted into methods of differentiation to reduce the quadrature error and instabilities. Like previously in Eq. (3.56), the expression can be ℓ_2 regularized to approximate for the jth order derivatives $\partial_j(\boldsymbol{z}) \in \mathbb{R}^{M-j\times 1}$:

$$\begin{aligned} \hat{\partial_j(\boldsymbol{z})} &= \underset{\partial_j(\boldsymbol{z})}{\arg\min}\{\ \|\boldsymbol{T}_j\partial_j(\boldsymbol{z}) - \boldsymbol{z}\|_2^2 + \lambda\|\boldsymbol{D}_2\partial_j(\boldsymbol{z})\|_2^2\ \}; \qquad \forall\lambda > 0 \\ &= \left(\boldsymbol{T}_j^{\mathrm{T}}\boldsymbol{T}_j + \lambda\boldsymbol{D}_2^{\mathrm{T}}\boldsymbol{D}_2\right)^{-1}\boldsymbol{T}_j^{\mathrm{T}}\boldsymbol{z}; \end{aligned} \tag{B.5}$$

where $\boldsymbol{z}' = \boldsymbol{z} - z_0\mathbf{1}_M$. Here the finite difference matrix operators are used in the penalty, e.g. $\boldsymbol{I}$, $\boldsymbol{D}_1$, $\boldsymbol{D}_2$ which penalize the amplitudes, the gradient, and the curvature of the solution respectively. Heuristically, $\boldsymbol{D}_2$ regularization balances the closeness to the data and the smoothness of the derivative. More importantly, the instability of finite difference is bypassed by reducing the numerical differentiation problem to a family of well-posed convex problems. These global method also allows for a Pareto front selection of the regularization parameter, where a standard-finite difference quadrature does not. The operator of $\boldsymbol{T}_1$ can be shown that it has an approximation error $\mathcal{O}((\Delta t)^2)$ (bias) and a noise amplification (variance) that scales $\mathcal{O}(\sigma^2/(\Delta t)^2)$. Finally, global methods tend to produce aliasing at the ends of the estimate, where the ends of the vector are trimmed.

Scaling Due to coefficient magnitude bias, some sparse regression estimators can be challenged to recover the true underlying dynamics if in two regards: one, if the estimator is LS-based, large condition numbers[1] will grossly degrade performance, i.e. ill-conditioned; two, the regularization parameter effectively thresholds/shrinks the coefficients based on magnitude. Therefore, an ℓ_2 norm scaling matrix $\boldsymbol{H} \in \mathbb{R}^{P\times P}$ is defined:

$$\boldsymbol{H}_{ii} \coloneqq \sqrt{(\boldsymbol{\theta}_i^{\mathrm{T}}\boldsymbol{\theta}_i)}, \quad \text{for } i = 1, \ldots, P \tag{B.6}$$

and when applied to SINDy framework of Eq. (3.49):

$$\dot{\boldsymbol{z}} = \breve{\boldsymbol{\Theta}}\breve{\boldsymbol{\xi}}; \quad \text{where} \quad \breve{\boldsymbol{\Theta}} \coloneqq \boldsymbol{\Theta}\boldsymbol{H}^{-1}; \quad \breve{\boldsymbol{\xi}} \coloneqq \boldsymbol{H}\boldsymbol{\xi} \tag{B.7}$$

[1]The library basis has a condition number that is linear $\kappa(\boldsymbol{\Theta})$ or quadratic $\kappa(\boldsymbol{\Theta}^{\mathrm{T}}\boldsymbol{\Theta})$ depending on if the normal equations are used for an LS-based estimator.

Thus it's easy to see that there is a dual benefit: one, that $\kappa(\breve{\boldsymbol{\Theta}}) < \kappa(\boldsymbol{\Theta})$ and two, that the penalization of the scaled coefficients $\breve{\boldsymbol{\xi}}$ are equal weighted. Notably, scaling has been commonly practiced in statistical domains for Lasso-based regression [Har15] and in the PySINDy Python library [Kap+22], and is adopted in this study.

B.4.3 Simulation parameters for figures

Both Fig. 3.18 and Fig. 3.19 were generated using the Bouc Wen system:

$$\begin{cases} \dot{x} = \sigma(y - x); & \dot{x}(0) = -8 \\ \dot{y} = \rho x - y - xz; & \dot{y}(0) = 7 \\ \dot{z} = xy - \beta z; & \dot{z}(0) = 27 \end{cases}$$

with the coefficients $\sigma = 10$, $\rho = 28$, $\beta = 8/3 = 2.6\bar{6}$.

For Fig. 3.18, a four-second simulation of the Lorenz system using `ode45` with enforced time stepping of $\Delta t = 0.005$ yielded a signal of length $M = 800$. The autocorrelative noise with a level of 3% was added to the path data using the function $R[n] = \sigma^2 * \exp(-|n|/2)$. Tikhonov denoising was performed on the second DOF using Eq. (B.4), with L-curve and GCV criterions with the log-spaced hyperparameter grid $\boldsymbol{\lambda} = \{10^{-}11, \ldots, 10^{0}\}$.

For Fig. 3.19, a three-second simulation of the Lorenz system using `ode45` with enforced time stepping of $\Delta t = 0.01$ yielded a signal of length $M = 300$. AWGN noise with a level of 2% s was added to both the path and trajectory data. Specifically, the third DOF was used for TRIM, IRL1 and STLS estimators: whose hyperparameters are summarized: STLS uses log-spaced grid of size 100, $\boldsymbol{\varphi} = \{10^{-3}, \ldots, 10^{3}\}$, for IRL1 a log-spaced grid of size 50 $\boldsymbol{\lambda} = \{10^{-20}, \ldots, 10^{2}\}$ and $q = \{1\}$, and for TRIM $\boldsymbol{k} = \{1, 2, \ldots, 13\}$ and $\nu = 10$.

Appendix C

Supplement to Chapter 4

Contents

C.1 Nonlinear periodic solutions via harmonic balance method

The second-order nonlinear ordinary differential equations (ODEs) can be expressed in the form of two nonlinear first-order equations for time-domain numerical integration, (e.g. by using `ode45` in MATLAB). However, numerical approximation in the time domain are undesirable since they are computationally lengthy and numerical errors may build up (instability). The harmonic balance method (HBM) [SS11] avoids these issues by assuming a periodic solution in the form of a truncated Fourier series. These unknown Fourier coefficients are cast into a nonlinear algebraic system of equations whose rank is the truncated harmonic order. HBM can achieve good accuracy with a low truncation order with less computational effort by several orders of magnitude compared to time-domain numerical integration [Woi+20]. HBM can also solve for many types of nonlinearities including contact and hysteresis [Sal+09] and geometric nonlinearities [RP99].

To visualize the HBM for a scalar vibration equation of motion, one can represent this as a residual to minimize:

$$r(q, \dot{q}, \ddot{q}, t) = m\ddot{q}(t) + c\dot{q}(t) + kq(t) + f_{\text{nl}} - g(t) = 0 \tag{C.1}$$

where m, k, and c, represent scalar coefficients for $\ddot{q}$, $\dot{q}$, and q respectively. The periodic solution of $q(t) = q(t+T)$ when subjected to a periodic displacement $g(t) = g(t+T)$ is approximated via a truncated Fourier series where:

$$q(t) \approx a_0 + \sum_{h=1}^{H} a_h \cos(h\omega t) + b_h \sin(h\omega t) \qquad \{a_0, a_h, b_h\} \in \mathbb{R} \tag{C.2}$$

$$\approx \sum_{h=-H}^{H} Q_h e^{\mathrm{j}h\omega t} \qquad \{Q_h\} \in \mathbb{C} \tag{C.3}$$

$$\approx \text{real}\left(\sum_{h=0}^{H} Q_h e^{\mathrm{j}h\omega t}\right) \qquad \{Q_h\} \in \mathbb{C} \tag{C.4}$$

where a, b, Q represent Fourier coefficients for q and H is the harmonic order. While Eqs. (C.2) to (C.4) are mathematically equivalent, each has benefits and drawbacks for specific purposes (ease of notation, mathematical developments, programmability, etc.). Eq. (C.3) is chosen since it allows for easy notation and avoids special treatment of the zeroth harmonic. Substituting Eq. (C.3) into

Eq. (C.1) yields:

$$\begin{aligned} r &= \sum_{h=-H}^{H} \left(-h^2\omega^2 m + \mathrm{j}h\omega c + k\right) Q_h e^{\mathrm{j}h\omega t} + f_{\mathrm{nl}} - g(t) \\ &= \sum_{h=-H}^{H} \Big(\underbrace{\left(-h^2\omega^2 m + \mathrm{j}h\omega c + k\right)}_{L_h(\omega)} Q_h + F_{\mathrm{nl},\,h} - G_h \Big) e^{\mathrm{j}h\omega t} \qquad \{L_h, F_{\mathrm{nl},\,h}, G_h\} \in \mathbb{C} \end{aligned} \tag{C.5}$$

where L_h represents a scalar form of the dynamic stiffness and $F_{\mathrm{nl},\,h}$, G_h are the hth Fourier coefficients of f_{nl} and $g(t)$ respectively. The time variable in Eq. (C.5) is then removed by projecting the resulting system onto the Fourier basis $e^{\mathrm{j}h\omega t}$ using the scalar product corresponding to the Galerkin method:

$$\frac{1}{T}\int_0^T r(t) e^{\mathrm{j}h\omega t} dt = 0 \quad \text{for} \quad h = -H, \ldots, H \tag{C.6}$$

Eq. (C.5) becomes a residual of the nonlinear equation of motion in the frequency domain. This can be visualized as set of $(2H+1)\times 1$ nonlinear equations of Fourier coefficients of which can be represented as column vectors, notated with $\tilde{\square}$:

$$\tilde{\boldsymbol{r}}(\tilde{\boldsymbol{Q}}, \omega) = \tilde{\boldsymbol{L}}(\omega)\tilde{\boldsymbol{Q}} + \tilde{\boldsymbol{F}}_{\mathrm{nl}} - \tilde{\boldsymbol{G}} = \boldsymbol{0} \tag{C.7}$$

where the dynamic stiffness matrix $\tilde{\boldsymbol{L}}$ can be shown to be:

$$\tilde{\boldsymbol{L}} = \omega^2 m \boldsymbol{\nabla}^2 + \omega c \boldsymbol{\nabla}^1 + k\boldsymbol{\nabla}^0 \tag{C.8}$$

with $\boldsymbol{\nabla}$ serving as a time differential operator:

$$\boldsymbol{\nabla} = \mathrm{diag}\begin{bmatrix} -\mathrm{j}H & \cdots & 0 & \cdots & \mathrm{j}H \end{bmatrix} \tag{C.9}$$

Consequently the vector representation of Fourier coefficients of Eq. (C.3) can be expressed as:

$$q(t) \approx \begin{bmatrix} e^{-\mathrm{j}H\omega t} & \cdots & 1 & \cdots & e^{\mathrm{j}H\omega t} \end{bmatrix} \underbrace{\begin{bmatrix} Q_{-H} \\ \vdots \\ Q_0 \\ \vdots \\ Q_H \end{bmatrix}}_{\tilde{\boldsymbol{Q}}} \tag{C.10}$$

Eq. (C.7) represents a set of nonlinear equations of Fourier coefficients in which an iterative algorithm, e.g. the Newton-Raphson method, can compute solutions. However, the complex Fourier coefficients

for analytical nonlinearities in Eq. (C.5) are not complex differentiable, so they must be converted into the real-valued sine-cosine notation of Eq. (C.2). This can be shown as followed:

$$\tilde{\boldsymbol{r}}(\tilde{\boldsymbol{a}},\omega)=\mathbf{0};\quad \text{where}\quad \tilde{\boldsymbol{a}}=\begin{bmatrix} a_0 \\ a_1 \\ b_1 \\ \vdots \\ a_H \\ b_H \end{bmatrix} \tag{C.11}$$

The Newton-Raphson solution to Eq. (C.11) for the $(i+1)^{\text{th}}$ iteration for a chosen $\omega_{(j)}$ can be found by linearization via Taylor expansion:

$$\tilde{\boldsymbol{r}}\left(\tilde{\boldsymbol{a}}_{(j)}^{(i+1)}\right)=\tilde{\boldsymbol{r}}\left(\tilde{\boldsymbol{a}}_{(j)}^{(i)}\right)+\frac{\partial\tilde{\boldsymbol{r}}\left(\tilde{\boldsymbol{a}}_{(j)}^{(i)}\right)}{\partial\tilde{\boldsymbol{a}}}\left(\tilde{\boldsymbol{a}}_{(j)}^{(i+1)}-\tilde{\boldsymbol{a}}_{(j)}^{(i)}\right)+\mathcal{O}\left(\left(\tilde{\boldsymbol{a}}_{(j)}^{(i+1)}-\tilde{\boldsymbol{a}}_{(j)}^{(i)}\right)^2\right)+\cdots=\mathbf{0}$$

where the solution $\tilde{\boldsymbol{a}}_{(j)}^{(i+1)}$ can be approximated to the first order to yield:

$$\begin{aligned}\tilde{\boldsymbol{a}}_{(j)}^{(i+1)} &\approx \tilde{\boldsymbol{a}}_{(j)}^{(i)}-\underbrace{\left[\frac{\partial\tilde{\boldsymbol{r}}\left(\tilde{\boldsymbol{a}}_{(j)}^{(i)}\right)}{\partial\tilde{\boldsymbol{a}}}\right]^{-1}}_{\mathbf{J}\left(\tilde{\boldsymbol{a}}_{(j)}^{(i)}\right)}\tilde{\boldsymbol{r}}\left(\tilde{\boldsymbol{a}}_{(j)}^{(i)}\right)\\ &\approx \tilde{\boldsymbol{a}}_{(j)}^{(i)}+\Delta\tilde{\boldsymbol{a}}_{(j)}^{(i)}\end{aligned} \tag{C.12}$$

where $\mathbf{J}\left(\tilde{\boldsymbol{a}}^{(i)}\right)$ represents the Jacobian matrix of the residual $\tilde{\boldsymbol{r}}$ for the $(i)^{\text{th}}$ iteration. It should be noted that the inverse Jacobian of Eq. (C.12) does not need to be computed since the definition of $\Delta\tilde{\boldsymbol{a}}^{(i)}$ allows for a linear solution:

$$\mathbf{J}\left(\tilde{\boldsymbol{a}}_{(j)}^{(i)}\right)\Delta\tilde{\boldsymbol{a}}_{(j)}^{(i)}=-\tilde{\boldsymbol{r}}\left(\tilde{\boldsymbol{a}}_{(j)}^{(i)}\right) \tag{C.13}$$

Once $\tilde{\boldsymbol{a}}_{(j)}^{(i)}$ is known, $\tilde{\boldsymbol{r}}\left(\tilde{\boldsymbol{a}}_{(j)}^{(i)}\right)$ can be evaluated and thus $\mathbf{J}\left(\tilde{\boldsymbol{a}}_{(j)}^{(i)}\right)$ can be directly calculated. Thus Eq. (C.13) is a linear matrix system for $\Delta\tilde{\boldsymbol{a}}_{(j)}^{(i)}$ which can be solved using Gaussian elimination. After $\Delta\tilde{\boldsymbol{a}}_{(j)}^{(i)}$ has been determined, Eq. (C.12) is repeated until the ℓ_2 norm of the residual is sufficiently small for some tolerance ϵ, e.g. $\|\tilde{\boldsymbol{r}}\left(\tilde{\boldsymbol{a}}_{(j)}^{(i+1)}\right)\|_2<\epsilon$. The required derivatives of the Jacobian $\mathbf{J}\left(\tilde{\boldsymbol{a}}_{(j)}^{(i)}\right)$ can be calculated analytically or approximated via finite-differences at a higher computational cost. Thus, the HBM has the advantage to transform a nonlinear time-domain differential equation into an easily solvable nonlinear algebraic equation in the frequency domain.

C.1.1 Numerical solutions to the Harmonic Balance equations

The solution to Eq. (C.11) with respect to a free parameter ω are typically solved via continuation methods. Prediction-correction continuation methods are carried out in two successive steps, the prediction, which is tangent to the solution curve, and the correction, and iterative solution to the prediction. Often, Eq. (C.11) can exhibit complex dynamic behaviors such as multiple solutions, so parameterization is often combined with continuation methods. The arc-length parameterization is one of them. The frequency is added to the variables and a tangent equation is added to the equation of motion as a supplementary constraint equation.

These methods can then be combined with an adaptive step scheme [Sey10] to enhance the robustness of a prediction-correction continuation algorithm. This technique is interesting for nonlinear dynamics analysis because continuation methods can reverse about the continuation parameter in order to obtain complete solution curves, including the multiple solutions. Continuation algorithms have been implemented in several softwares such as MATCONT [DGK03], AUTO [Doe+07], MANLAB [Kar12]. Note, MANLAB uses continuation techniques combined with asymptotical numerical method [Coc94], not AFT.

Zero- and first-order continuation methods The periodic solution of the Eq. (C.11) can evolve under variation of continuation parameter(s). Most commonly, the frequency response the dynamic system is of interest in which a continuation parameter ω is sought. A subclass of continuation methods, specifically predictor-corrector methods are detailed. The continuation parameter's $(j)^{\text{th}}$ step of steady state solutions $\omega_{(\text{start})} \leq \omega_{(j)} \leq \omega_{(\text{end})}$ each require Newton-Raphson iterations solving Eq. (C.11). Thus in zero-order continuation, the (converged) steady state solution for $\tilde{\boldsymbol{a}}^{(i)}$ at the $\omega_{(j)}$ step is used as a predictor, or initial guess, for the next Newton-Raphson iteration of $\omega_{(j+1)}$ step, such that:

$$\tilde{\boldsymbol{a}}_{(j+1)}^{(\kappa)} = \tilde{\boldsymbol{a}}_{(j)}^{(i=\text{converged})} \tag{C.14}$$

in which the Newton-Raphson iterations serve as a corrector to the prediction at trial κ, seen in Fig. C.1. In first-order continuation, the sensitivity of Eq. (C.11) to the continuation parameter, whose geometrical interpretation is the tangent to the solution curve, is found by taking the differential:

$$d\tilde{\boldsymbol{r}}(\tilde{\boldsymbol{a}}, \omega) = \frac{\partial \tilde{\boldsymbol{r}}}{\partial \tilde{\boldsymbol{a}}} d\tilde{\boldsymbol{a}} + \frac{\partial \tilde{\boldsymbol{r}}}{\partial \omega} d\omega = \boldsymbol{0} \tag{C.15}$$

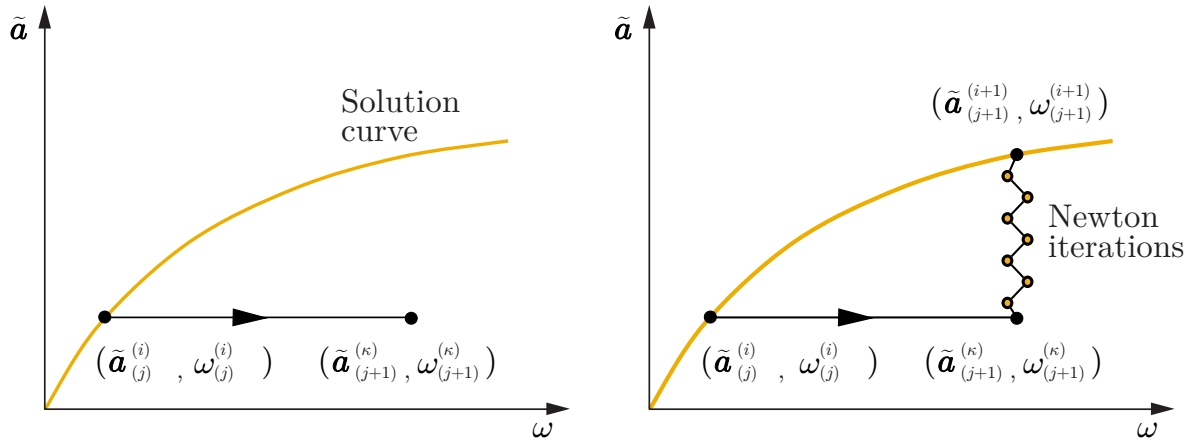

Figure C.1: Zero-order continuation method, with a zero-order prediction (left) and a Newton-Raphson iteration correction (right).

which can be simplified to:

$$\frac{d\tilde{\boldsymbol{a}}}{d\omega} = -\underbrace{\left[\frac{\partial \tilde{\boldsymbol{r}}}{\partial \tilde{\boldsymbol{a}}}\right]^{-1}}_{\mathbf{J}\left(\tilde{\boldsymbol{a}}\right)} \frac{\partial \tilde{\boldsymbol{r}}}{\partial \omega}$$

Hence an additional linear solve of the system is required per Newton-Raphson iteration:

$$\mathbf{J}\left(\tilde{\boldsymbol{a}}^{(i)}_{(j)}\right) \frac{\partial \tilde{\boldsymbol{a}}^{(i)}_{(j)}}{\partial \omega} = -\frac{\partial \boldsymbol{r}^{(i)}_{(j)}}{\partial \omega} \tag{C.16}$$

where $\mathbf{J}\left(\tilde{\boldsymbol{a}}^{(i)}_{(j)}\right)$ is the Jacobian matrix at step $\omega_{(j)}$ for a converged Newton iteration (previously defined in Eq. (C.12)) and $\partial \boldsymbol{r}^{(i)}_{(j)}/\partial\omega$ is a forward-difference approximation obtained by perturbing $\omega_{(j)}$ a small amount δ and reassembling the residual:

$$\frac{\partial \boldsymbol{r}^{(i)}_{(j)}}{\partial \omega} = \frac{\boldsymbol{r}\left(\omega_{(j)} + \delta\right) - \boldsymbol{r}\left(\omega_{(j)}\right)}{\delta} \tag{C.17}$$

The first-order prediction of $\tilde{\boldsymbol{a}}^{(i)}_{(j+1)}$ at the next continuation step is then:

$$\tilde{\boldsymbol{a}}^{(\kappa)}_{(j+1)} = \tilde{\boldsymbol{a}}^{(i)}_{(j)} + \frac{d\tilde{\boldsymbol{a}}^{(i)}_{(j)}}{d\omega}\Delta\omega \tag{C.18}$$

where $\Delta\omega$ represents the step size such that $\omega_{(j+1)} = \omega_{(j)} + \Delta\omega$. Thus, first-order continuation entails one additional linear solve per $(j)^{\text{th}}$ continuation step, but can reduce the number of Newton iterations required compared to zero-order continuation, seen in Fig. C.2. Step size can be controlled, which refers to the methods used to determine the change in the continuation parameter for each continuation step in Eq. (C.18). Step size control will be detailed in the next section, but many implemented algorithms utilize heuristic rules and/or step size equations [Sey10].

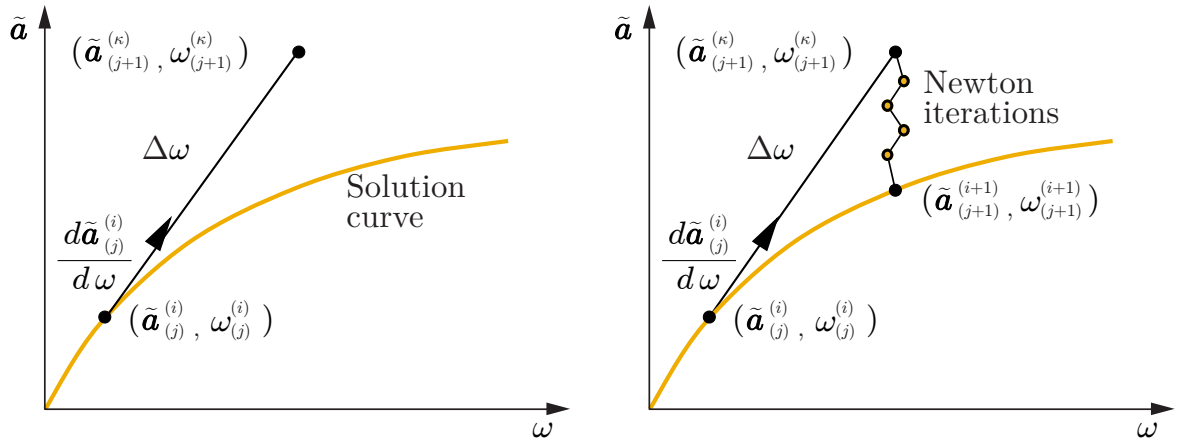

Figure C.2: First-order continuation method, with a first-order prediction via tangent $d\tilde{\boldsymbol{a}}^{(i)}_{(j)}/d\omega$ with step length $\Delta\omega$ (left) and a Newton-Raphson iteration correction (right).

Arc-length continuation method First-order continuation can have problem at continuation parameter in the vicinity of a stability limit (i.e. near a turning point or bifurcation point), which manifests as the Jacobian matrix $\mathbf{J}(\tilde{\boldsymbol{a}})$ becoming singular. The arc-length continuation scheme aims to improve first-order continuation by constraining the prediction step in order to reduce Newton-Raphson iterations per $(j)^{\text{th}}$ continuation step [Gus07; Sey10]. An equation of constraint, typically called parameterization, along with an arc-length parameter s is introduced as an additional unknown which augments Eq. (C.11) as a system of equations:

$$\tilde{\boldsymbol{r}}(\tilde{\boldsymbol{a}}(s), \omega(s)) = \mathbf{0} \tag{C.19}$$

$$p(\tilde{\boldsymbol{a}}(s), \omega(s), s) = 0 \tag{C.20}$$

where p is the equation of constraint. Both $\tilde{\boldsymbol{a}}$ and ω are parameterized as functions of s, which changes Eq. (C.15) into:

$$d\tilde{\boldsymbol{r}}(\tilde{\boldsymbol{a}}(s), \omega(s)) = \frac{\partial \tilde{\boldsymbol{r}}}{\partial \tilde{\boldsymbol{a}}}\frac{\partial \tilde{\boldsymbol{a}}}{\partial s} + \frac{\partial \tilde{\boldsymbol{r}}}{\partial \omega}\frac{\partial \omega}{\partial s} = \mathbf{0} \tag{C.21}$$

and the equation of constraint p is bounded by the arc-length s of a hypersphere:

$$\left\| \frac{\partial \tilde{\boldsymbol{a}}}{\partial s} \right\|_2^2 + \left(\frac{\partial \omega}{\partial s} \right)^2 = 1$$

which is equivalent in the Δ notation:

$$p(\tilde{\boldsymbol{a}}(s), \omega(s), s) = \|\Delta\tilde{\boldsymbol{a}}\|_2^2 + (\Delta\omega)^2 - (\Delta s)^2 = 0 \tag{C.22}$$

The augmented system of equations seen in Eqs. (C.19) and (C.20) resembles the form of Eq. (C.12) with a new solution step:

$$\begin{aligned}\begin{bmatrix}\tilde{\boldsymbol{a}}\\ \omega\end{bmatrix}_{(j)}^{(i+1)} &\approx \begin{bmatrix}\tilde{\boldsymbol{a}}\\ \omega\end{bmatrix}_{(j)}^{(i)} - \left[\mathbb{J}_{(j)}^{(i)}\right]^{-1}\begin{bmatrix}\tilde{\boldsymbol{r}}\left(\tilde{\boldsymbol{a}},\omega\right)\\ p\left(\tilde{\boldsymbol{a}},\omega,s\right)\end{bmatrix}_{(j)}^{(i)}\\ &\approx \begin{bmatrix}\tilde{\boldsymbol{a}}\\ \omega\end{bmatrix}_{(j)}^{(i)} + \begin{bmatrix}\Delta\tilde{\boldsymbol{a}}\\ \Delta\omega\end{bmatrix}_{(j)}^{(i)}\end{aligned} \tag{C.23}$$

and Eq. (C.13) augmented as a linear system:

$$\underbrace{\begin{bmatrix}\dfrac{\partial\tilde{\boldsymbol{r}}}{\partial\tilde{\boldsymbol{a}}} & \dfrac{\partial\tilde{\boldsymbol{r}}}{\partial\omega}\\ 2\left(\dfrac{\partial\tilde{\boldsymbol{a}}}{\partial s}\right)^{\mathrm{T}} & 2\dfrac{\partial\omega}{\partial s}\end{bmatrix}_{(j)}^{(i)}}_{\left[\mathbb{J}_{(j)}^{(i)}\right]}\begin{bmatrix}\Delta\tilde{\boldsymbol{a}}\\ \Delta\omega\end{bmatrix}_{(j)}^{(i)} = -\begin{bmatrix}\tilde{\boldsymbol{r}}\left(\tilde{\boldsymbol{a}},\omega\right)\\ p\left(\tilde{\boldsymbol{a}},\omega,s\right)\end{bmatrix}_{(j)}^{(i)} \tag{C.24}$$

where $\partial\tilde{\boldsymbol{r}}/\partial\tilde{\boldsymbol{a}} = \mathbf{J}(\tilde{\boldsymbol{a}})$, $\boldsymbol{r}$, and $\Delta\tilde{\boldsymbol{a}}$ are computed during each Newton iteration using a guessed value of ω. To solve the augmented system of Eq. (C.24), it is necessary to update both ω and the solution update $\tilde{\boldsymbol{a}}$ at each Newton-Raphson iteration. Arc-length continuation constraints steady state solutions at pre-determined intervals of step size Δs rather than of the parameter $\Delta\omega$ as seen in Eq. (C.18). The procedure is outlined next.

Initialization of the arc-length predictor step The prediction step consists in finding the local tangent of the solution curve. Then the current periodic solution is perturbed along this tangent to obtain an approximated periodic solution following the curve. First, an initial guess $\begin{bmatrix}\tilde{\boldsymbol{a}} & \omega\end{bmatrix}_{(j)}^{(i)}$ is solved for via Newton-Raphson in Eqs. (C.12) and (C.13). Then the standard continuation method is then initialized. For any predictor step, the tangent vector $\begin{bmatrix}\Delta\tilde{\boldsymbol{a}} & \Delta\omega\end{bmatrix}_{(j)}^{(i)}$ must solve the first line of Eq. (C.24):

$$\tilde{\boldsymbol{r}}\left(\tilde{\boldsymbol{a}},\omega\right)_{(j)}^{(i)} = \frac{\partial\tilde{\boldsymbol{r}}_{(j)}^{(i)}}{\partial\tilde{\boldsymbol{a}}}\Delta\tilde{\boldsymbol{a}}_{(j)}^{(i)} + \frac{\partial\tilde{\boldsymbol{r}}_{(j)}^{(i)}}{\partial\omega}\Delta\omega_{(j)}^{(i)} = \mathbf{0} \tag{C.25}$$

The initialization of the continuation method cannot use the arc-length constraint because no previous tangent vector has been computed. Therefore, to compute the first tangent vector, the value of $\Delta\omega_{(j)}^{(i)}$ is chosen as 1 or -1 depending on the targeted direction of continuation, which simplifies Eq. (C.25):

$$\frac{\partial\tilde{\boldsymbol{r}}_{(j)}^{(i)}}{\partial\tilde{\boldsymbol{a}}}\Delta\tilde{\boldsymbol{a}}_{(j)}^{(i)} = \pm\frac{\partial\tilde{\boldsymbol{r}}_{(j)}^{(i)}}{\partial\omega} \tag{C.26}$$

Then the tangent $\begin{bmatrix}\tilde{\boldsymbol{a}} & \omega\end{bmatrix}_{(j)}^{(i)}$ is normalized and multiplied to have the a magnitude of Δs, and added to the point:

$$\begin{bmatrix}\tilde{\boldsymbol{a}}\\ \omega\end{bmatrix}_{(j+1)}^{(\kappa)} \approx \begin{bmatrix}\tilde{\boldsymbol{a}}\\ \omega\end{bmatrix}_{(j)}^{(i)} + \Delta s \frac{\begin{bmatrix}\Delta\tilde{\boldsymbol{a}}\\ \Delta\omega\end{bmatrix}_{(j)}^{(i)}}{\left\| \begin{bmatrix}\Delta\tilde{\boldsymbol{a}}\\ \Delta\omega\end{bmatrix}_{(j)}^{(i)} \right\|_2} \tag{C.27}$$

Standard arc-length predictor step Once the first step has been performed, a tangent vector can be calculated with Eq. (C.25). Since a previous tangent vector has already been computed, the next tangent vector $\begin{bmatrix}\Delta\tilde{\boldsymbol{a}} & \Delta\omega\end{bmatrix}_{(j)}^{(i)}$ can be normalized as:

$$\left(\Delta\tilde{\boldsymbol{a}}_{(j-1)}^{(i)}\right)^{\mathrm{T}} \Delta\tilde{\boldsymbol{a}}_{(j)}^{(i)} + \Delta\omega_{(j-1)}^{(i)}\Delta\omega_{(j)}^{(i)} = 1 \tag{C.28}$$

To compute the tangent, the Eqs. (C.25) and (C.28) are combined to form the following augmented system:

$$\begin{bmatrix} \dfrac{\partial\tilde{\boldsymbol{r}}_{(j)}^{(i)}}{\partial\tilde{\boldsymbol{a}}} & \dfrac{\partial\tilde{\boldsymbol{r}}_{(j)}^{(i)}}{\partial\omega} \\ \left(\Delta\tilde{\boldsymbol{a}}_{(j-1)}^{(i)}\right)^{\mathrm{T}} & \Delta\omega_{(j-1)}^{(i)} \end{bmatrix} \begin{bmatrix}\Delta\tilde{\boldsymbol{a}}\\ \Delta\omega\end{bmatrix}_{(j)}^{(i)} = -\begin{bmatrix}\boldsymbol{0}\\ 1\end{bmatrix}_{(j)}^{(i)} \tag{C.29}$$

Then, the normalized tangent is multiplied by a step length Δs and the sign of the scalar product between the current tangent and the previous one:

$$\begin{aligned} \begin{bmatrix}\tilde{\boldsymbol{a}}\\ \omega\end{bmatrix}_{(j+1)}^{(\kappa)} &\approx \begin{bmatrix}\tilde{\boldsymbol{a}}\\ \omega\end{bmatrix}_{(j)}^{(i)} + \Delta s \begin{bmatrix}\Delta\tilde{\boldsymbol{a}}\\ \Delta\omega\end{bmatrix}_{(j)}^{(i)} \quad \text{if} \quad \Delta\tilde{\boldsymbol{a}}_{(j-1)}^{(i)} \cdot \Delta\tilde{\boldsymbol{a}}_{(j)}^{(i)} > 0 \\ \begin{bmatrix}\tilde{\boldsymbol{a}}\\ \omega\end{bmatrix}_{(j+1)}^{(\kappa)} &\approx \begin{bmatrix}\tilde{\boldsymbol{a}}\\ \omega\end{bmatrix}_{(j)}^{(i)} - \Delta s \begin{bmatrix}\Delta\tilde{\boldsymbol{a}}\\ \Delta\omega\end{bmatrix}_{(j)}^{(i)} \quad \text{if} \quad \Delta\tilde{\boldsymbol{a}}_{(j-1)}^{(i)} \cdot \Delta\tilde{\boldsymbol{a}}_{(j)}^{(i)} < 0 \end{aligned} \tag{C.30}$$

This condition permits an enhanced robustness by preventing any direction leading to a previously calculated periodic solution to be taken [Sey10].

Arc-length corrector step When an error criteria defined for Eq. (C.23) is not met, e.g. $\|\tilde{\boldsymbol{r}}\left(\tilde{\boldsymbol{a}}_{(j+1)}^{(\kappa)}\right)\|_2 < \epsilon$, a correction step $\begin{bmatrix}\delta\tilde{\boldsymbol{a}} & \delta\omega\end{bmatrix}_{(j+1)}^{(\kappa)}$ is added to the continuation algorithm to make corrections to Eq. (C.24):

$$\frac{\partial\tilde{\boldsymbol{r}}_{(j+1)}^{(\kappa)}}{\partial\tilde{\boldsymbol{a}}}\delta\tilde{\boldsymbol{a}}_{(j+1)}^{(\kappa)} + \frac{\partial\tilde{\boldsymbol{r}}_{(j+1)}^{(\kappa)}}{\partial\omega}\delta\omega_{(j+1)}^{(\kappa)} = -\tilde{\boldsymbol{r}}\left(\tilde{\boldsymbol{a}},\omega\right)_{(j+1)}^{(\kappa)} \tag{C.31}$$

with κ corresponding to the current iteration of Newton-Raphson algorithm. The corrections are made with respect to the radius Δs in the arc-length constraint Eq. (C.22):

$$\left(\Delta\tilde{\boldsymbol{a}}^{(i)}_{(j+1)}\right)^{\mathrm{T}} \delta\tilde{\boldsymbol{a}}^{(\kappa)}_{(j+1)} + \Delta\omega^{(i)}_{(j+1)}\delta\omega^{(\kappa)}_{(j+1)} = \Delta s \tag{C.32}$$

To calculate the correction, the following augmented system of equations composed of Eqs. (C.31) and (C.32) is solved:

$$\begin{bmatrix} \dfrac{\partial\tilde{\boldsymbol{r}}^{(\kappa)}_{(j+1)}}{\partial\tilde{\boldsymbol{a}}} & \dfrac{\partial\tilde{\boldsymbol{r}}^{(\kappa)}_{(j+1)}}{\partial\omega} \\ \left(\Delta\tilde{\boldsymbol{a}}^{(i)}_{(j+1)}\right)^{\mathrm{T}} & \Delta\omega^{(i)}_{(j+1)} \end{bmatrix} \begin{bmatrix}\delta\tilde{\boldsymbol{a}} \\ \delta\omega\end{bmatrix}^{(\kappa)}_{(j+1)} = -\begin{bmatrix}\tilde{\boldsymbol{r}}\left(\tilde{\boldsymbol{a}},\omega\right)^{(\kappa)}_{(j+1)} \\ \Delta s\end{bmatrix} \tag{C.33}$$

Once the correction $\begin{bmatrix}\delta\tilde{\boldsymbol{a}} & \delta\omega\end{bmatrix}^{(\kappa)}_{(j+1)}$ are calculated, they are added to $\begin{bmatrix}\tilde{\boldsymbol{a}} & \omega\end{bmatrix}^{(\kappa)}_{(j+1)}$ to obtain the new corrected variables:

$$\begin{bmatrix}\tilde{\boldsymbol{a}} \\ \omega\end{bmatrix}^{(\kappa+1)}_{(j+1)} \approx \begin{bmatrix}\tilde{\boldsymbol{a}} \\ \omega\end{bmatrix}^{(\kappa)}_{(j+1)} + \begin{bmatrix}\delta\tilde{\boldsymbol{a}} \\ \delta\omega\end{bmatrix}^{(\kappa)}_{(j+1)} \tag{C.34}$$

The corrections to $\begin{bmatrix}\tilde{\boldsymbol{a}} & \omega\end{bmatrix}^{(\kappa+1)}_{(j+1)}$ are made until the error criteria is satisfied:

$$\begin{bmatrix}\tilde{\boldsymbol{a}} \\ \omega\end{bmatrix}^{(i+1)}_{(j+1)} = \begin{bmatrix}\tilde{\boldsymbol{a}} \\ \omega\end{bmatrix}^{(\kappa+1)}_{(j+1)} \quad \text{if} \quad \|\tilde{\boldsymbol{r}}\left(\tilde{\boldsymbol{a}}^{(\kappa+1)}_{(j+1)}\right)\|_2 < \epsilon \tag{C.35}$$

The obtained solution corresponds to the new periodic solution along the solution curve. To compute the complete response curve, the continuation algorithm is repeated with solution being the new point of reference for the next continuation step $(j+1)$, as seen in Fig. C.3.

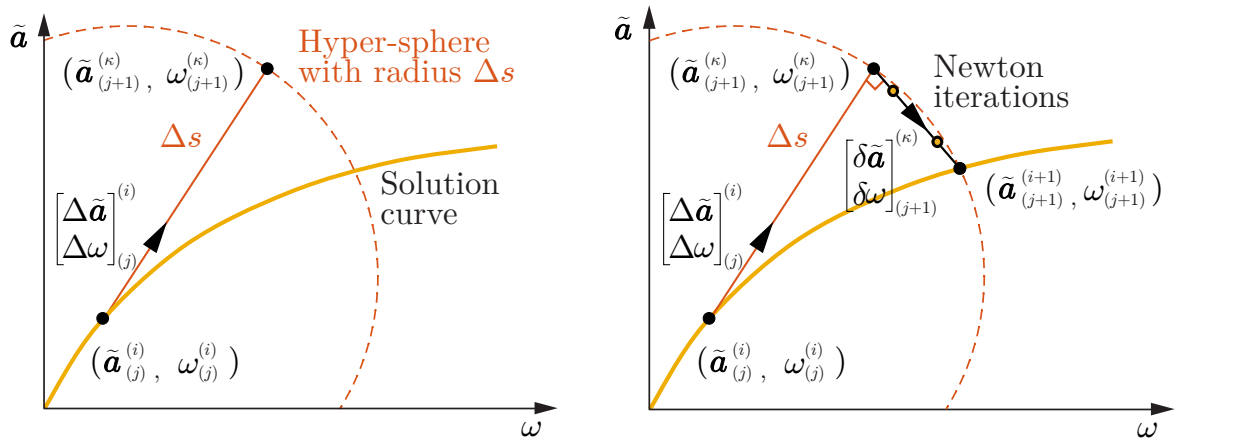

Figure C.3: Arc-length continuation method, with a first-order prediction via tangent $[\Delta\tilde{\boldsymbol{a}}\ \Delta\omega]^{(i)}_{(j)}$ constrained by step length Δs (left) and a Newton-Raphson iteration correction (right).

Step size control The step size Δs is chosen to be as small as necessary to ensure fast convergence and not overlook important characteristics of the solution, but not too large to lose resolution. Therefore, Δs is adapted using heuristic rules:

- When corrector steps fail to converge, the predictor step is rejected, the step size is reduced by an integer factor, and a new prediction step is generated. This is limited to prevent an infinite trial of smaller prediction steps.
- When the number of Newton-Raphson iterations for consecutive continuation steps exceed an upper-bound, the step length is halved, and it is doubled if this number falls below a lower-bound.
- The step size is reduced by an integer factor when the Fourier coefficients' second derivative with respect to the free parameter is negative. This is to improve the bandwidth resolution about the resonance frequency.
- The maximum step size is a global constraint which supersedes the previous rules.

C.1.2 Computation of nonlinear terms with AFT scheme

When analytical expressions cannot be derived for f_{nl}, it cannot be projected onto the Fourier basis $e^{\mathrm{j}h\omega t}$ as shown in the following:

$$f_{\mathrm{nl}} = \frac{1}{T}\int_0^T F_{\mathrm{nl},\,h}\, e^{-\mathrm{j}h\frac{2\pi}{T}t}\, dt \quad \text{for} \quad h = -H, \dots, H \tag{C.36}$$

to yield a system of its corresponding Fourier coefficients $\tilde{\boldsymbol{F}}_{\mathrm{nl}}$, where $\omega = 2\pi/T$ is defined for a period. To remedy this fact, $\tilde{\boldsymbol{F}}_{\mathrm{nl}}$ is computed through the use of an alternate frequency-time scheme (AFT) in conjunction with the HBM [CG89].

In this demonstration, the AFT scheme will be shown for nonlinear terms whose dependence is on both displacements and velocities $f_{\mathrm{nl}}(q, \dot{q})$, and in terms of complex-exponential form shown in Eq. (C.3). The AFT scheme consists of evaluating $\tilde{\boldsymbol{F}}_{\mathrm{nl}}$ via the discrete Fourier transform (DFT) before evaluating the residual in Eq. (C.7):

$$\tilde{\boldsymbol{Q}} \xrightarrow{\mathrm{DFT}^{-1}} \hat{\boldsymbol{q}}, \hat{\dot{\boldsymbol{q}}} \longrightarrow \hat{\boldsymbol{f}}_{\mathrm{nl}}(\hat{\boldsymbol{q}}, \hat{\dot{\boldsymbol{q}}}) \xrightarrow{\mathrm{DFT}} \tilde{\boldsymbol{F}}_{\mathrm{nl}}(\tilde{\boldsymbol{Q}})$$

where the time-discretized coordinates are expressed in column vectors for coordinates $\hat{\boldsymbol{q}}$ and velocities $\hat{\dot{\boldsymbol{q}}}$, notated by $\hat{\square}$. Each of the vector components $q(t_n)$ are first determined for an equidistant

discretization of the interval $[0,\, T)$ into N time instants $t_0, t_1, ..., t_{N-1}$:

$$t_n = n\Delta t; \quad \Delta t = \frac{T}{N}; \quad n = 0, 1, ..., N-1 \tag{C.37}$$

where N must be sufficiently large enough to resolve the highest harmonic H in accordance with the Nyquist-Shannon theorem. Then nonlinear forces $\hat{\boldsymbol{F}}_{\mathrm{nl}}$ are then evaluated in the (time-discretized) time domain. This lets one express Eq. (C.36) as:

$$\begin{aligned}\tilde{F}_{\mathrm{nl},\,h} &\approx \frac{1}{T}\sum_{n=0}^{N-1} f_{\mathrm{nl}}\left(q(t_n),\, \dot{q}(t_n)\right) e^{-\mathrm{j}h\frac{2\pi}{T}t_n}\Delta t \\ &\approx \frac{1}{N}\sum_{n=0}^{N-1} f_{\mathrm{nl}}\left(q(t_n),\, \dot{q}(t_n)\right) e^{-\mathrm{j}h\frac{2\pi}{N}n}\end{aligned} \tag{C.38}$$

Finally, the Fourier coefficients $\hat{\boldsymbol{F}}_{\mathrm{nl}}$ are approximated using the DFT:

$$\begin{aligned}\tilde{\boldsymbol{F}}_{\mathrm{nl}}\left(\tilde{\boldsymbol{q}}, \tilde{\dot{\boldsymbol{q}}}, \omega\right) &\overset{\mathrm{AFT}}{\approx} \boldsymbol{T}\hat{\boldsymbol{F}}_{\mathrm{nl}}(\boldsymbol{T}^{-1}\hat{\boldsymbol{q}},\, \boldsymbol{T}^{-1}\underbrace{\boldsymbol{\nabla}\omega\hat{\boldsymbol{q}}}_{\hat{\dot{\boldsymbol{q}}}}) \quad \{\hat{\boldsymbol{F}}_{\mathrm{nl}} \in \mathbb{C}\} \\ &\overset{\mathrm{AFT}}{\approx} \underbrace{\frac{1}{N}\begin{bmatrix} e^{-\mathrm{j}(-H)\frac{2\pi}{N}t_0} & \dots & e^{-\mathrm{j}(-H)\frac{2\pi}{N}t_{N-1}} \\ \vdots & & \vdots \\ e^{-\mathrm{j}(H)\frac{2\pi}{N}t_0} & \dots & e^{-\mathrm{j}(H)\frac{2\pi}{N}t_{N-1}} \end{bmatrix}}_{\boldsymbol{T}} \underbrace{\begin{bmatrix} \hat{F}_{\mathrm{nl},\,0} \\ \vdots \\ \hat{F}_{\mathrm{nl},\,N-1} \end{bmatrix}}_{\hat{\boldsymbol{F}}_{\mathrm{nl}}}\end{aligned} \tag{C.39}$$

where $\boldsymbol{T}$ represents a DFT operation matrix and $\hat{\boldsymbol{F}}_{\mathrm{nl}}$ are the time-discretized nonlinear forces.
Eq. (C.39) can then be reinserted into the residual of Eq. (C.7).

Derivatives of the nonlinear terms During the continuation steps presented in Appendix C.1.1, the following derivatives are defined in sine-cosine notation Fourier coefficients:

$$\frac{\partial\tilde{\boldsymbol{r}}}{\partial\tilde{\boldsymbol{a}}} = \tilde{\boldsymbol{L}}(\omega) + \frac{\partial\tilde{\boldsymbol{F}}_{\mathrm{nl}}}{\partial\tilde{\boldsymbol{a}}}; \quad \frac{\partial\tilde{\boldsymbol{r}}}{\partial\omega} = \frac{\partial\tilde{\boldsymbol{L}}}{\partial\omega}\tilde{\boldsymbol{a}} + \frac{\partial\tilde{\boldsymbol{F}}_{\mathrm{nl}}}{\partial\omega} \tag{C.40}$$

with:

$$\frac{\partial\tilde{\boldsymbol{L}}}{\partial\omega} = 2\omega\boldsymbol{\Lambda}^2 m + \boldsymbol{\Lambda} c \tag{C.41}$$

The derivatives of nonlinear terms are computed as follows:

$$\frac{\partial\tilde{\boldsymbol{F}}_{\mathrm{nl}}}{\partial\tilde{\boldsymbol{a}}} = \boldsymbol{\Gamma}^{-1}\frac{\partial\hat{\boldsymbol{F}}_{\mathrm{nl}}}{\partial\hat{\boldsymbol{q}}}\boldsymbol{\Gamma} + \boldsymbol{\Gamma}^{-1}\frac{\partial\hat{\boldsymbol{F}}_{\mathrm{nl}}}{\partial\hat{\dot{\boldsymbol{q}}}}\omega\boldsymbol{\Lambda}\boldsymbol{\Gamma} \tag{C.42}$$

$$\frac{\partial \tilde{\boldsymbol{F}}_{\mathrm{nl}}}{\partial \omega} = \boldsymbol{\Gamma}^{-1} \frac{\partial \hat{\boldsymbol{F}}_{\mathrm{nl}}}{\partial \hat{\dot{\boldsymbol{q}}}} \boldsymbol{\Gamma} \boldsymbol{\Lambda} \tilde{\boldsymbol{a}} \tag{C.43}$$

with the diagonal matrices:

$$\frac{\partial \hat{\boldsymbol{F}}_{\mathrm{nl}}}{\partial \hat{\boldsymbol{q}}} = \mathrm{diag} \left[\left. \frac{\partial f_{\mathrm{nl}}}{\partial q} \right|_{t_0}, \cdots, \left. \frac{\partial f_{\mathrm{nl}}}{\partial q} \right|_{t_{N-1}} \right] \tag{C.44}$$

$$\frac{\partial \hat{\boldsymbol{F}}_{\mathrm{nl}}}{\partial \hat{\dot{\boldsymbol{q}}}} = \mathrm{diag} \left[\left. \frac{\partial f_{\mathrm{nl}}}{\partial \dot{q}} \right|_{t_0}, \cdots, \left. \frac{\partial f_{\mathrm{nl}}}{\partial \dot{q}} \right|_{t_{N-1}} \right] \tag{C.45}$$

The time differential operator $\boldsymbol{\Lambda}$ for sine-cosine notation Fourier coefficients:

$$\boldsymbol{\Lambda} = \mathrm{diag}\left[\boldsymbol{0}, \Lambda_1, \ldots, \Lambda_h, \ldots, \Lambda_H\right] \quad \text{with} \quad \Lambda_h = h \begin{bmatrix} 0 & 1 \\ -1 & 0 \end{bmatrix} \tag{C.46}$$

The DFT operation matrices, which do not depend on ω and do not need to be updated during the continuation, are given as:

$$\boldsymbol{\Gamma} = \begin{bmatrix} 1 & \cos(\omega t_0) & \sin(\omega t_0) & \ldots & \cos(H\omega t_0) & \sin(H\omega t_0) \\ \vdots & \vdots & \vdots & & \vdots & \vdots \\ 1 & \cos(\omega t_N) & \sin(\omega t_N) & \ldots & \cos(H\omega t_N) & \sin(H\omega t_N) \end{bmatrix} \tag{C.47}$$

$$\boldsymbol{\Gamma}^{-1} = \frac{1}{N} \begin{bmatrix} 2 & \ldots & 2 \\ \cos(\omega t_0) & \ldots & \cos(\omega t_N) \\ \sin(\omega t_0) & \ldots & \sin(\omega t_N) \\ \vdots & & \vdots \\ \cos(H\omega t_0) & \ldots & \cos(H\omega t_N) \\ \sin(H\omega t_0) & \ldots & \sin(H\omega t_N) \end{bmatrix} \tag{C.48}$$

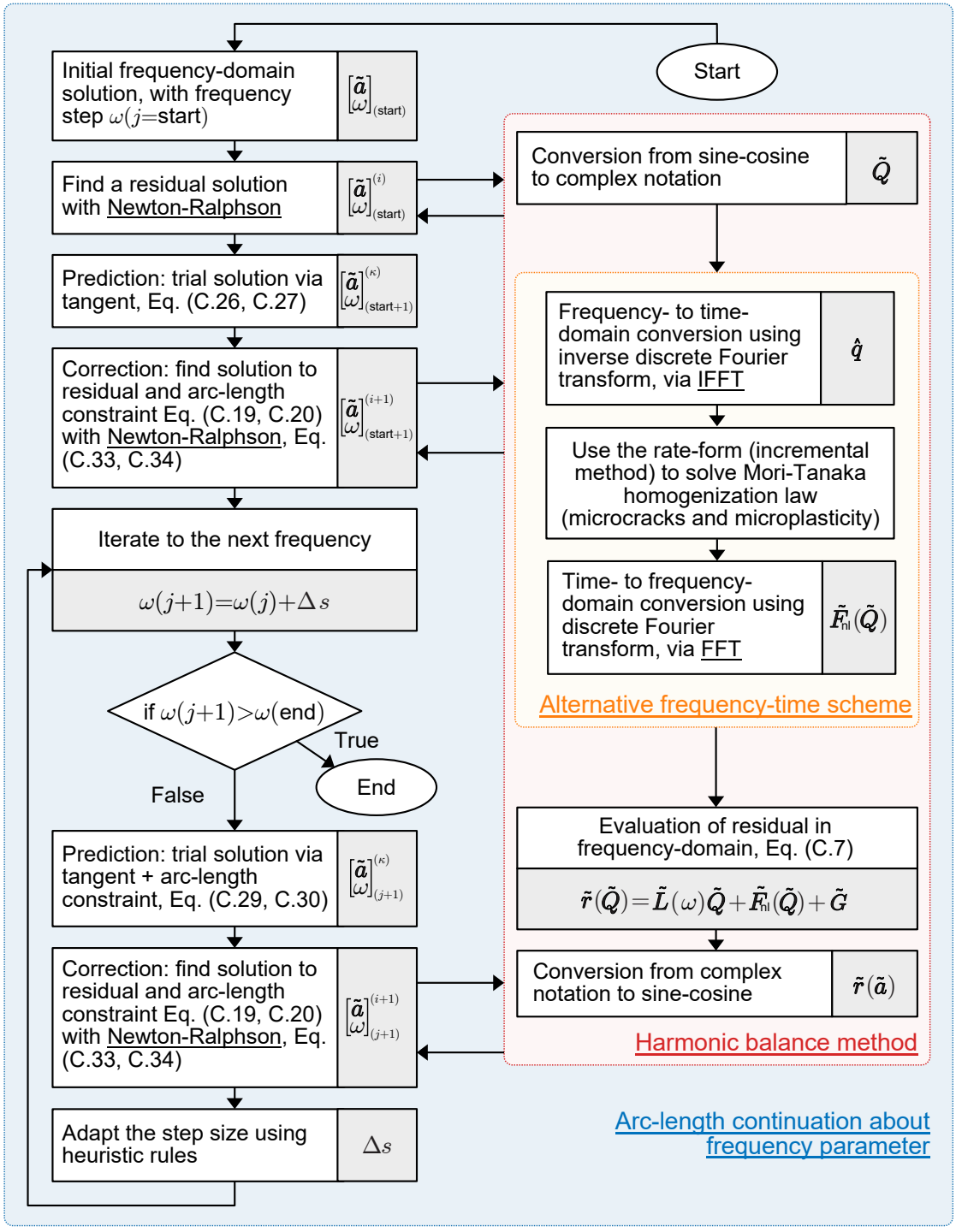

Figure C.4: Flowchart of arc-length continuation with respect to frequency ω coupled with HBM-AFT. The subscripts $_{(j)}$ indicate a frequency step ω along the continuation path. The superscripts indicate a point on the solution path for $\tilde{\boldsymbol{a}}$, where $^{(\kappa)}$ indicates a trial solution and $^{(i+1)}$ is an accepted solution, refer to Fig. C.3. Underlined names indicate algorithms not expanded within the flowchart.

Appendix D

Résumé étendu

Contents

D.1 Introduction

Le contexte L'étude de la fatigue des métaux, qui remonte au 19e siècle, se concentre sur l'initiation et la propagation des fissures dans les métaux soumis à des charges répétées, conduisant à la rupture à des niveaux de contrainte inférieurs à leur résistance à la traction. L'outil essentiel de cette recherche est la courbe de durée de vie en fatigue (S-N), qui établit une correspondance entre l'amplitude de la contrainte et les cycles de défaillance. Récemment, l'attention s'est portée sur le régime de fatigue à très haut cycle (VHCF), au-delà de 10^7 cycles, et l'on s'est rendu compte que la rupture par fatigue dépendait du régime. Cela a stimulé l'utilisation des essais de fatigue par ultrasons, fonctionnant autour de 20 kHz, pour des essais rapides dans des secteurs tels que l'automobile et l'aérospatiale, où les composants doivent supporter une fatigue à cycle très élevé sans se rompre. Cependant, les défis actuels résident dans la caractérisation *in-situ* au cours de ces essais, la plupart des études se concentrant sur l'analyse après défaillance plutôt que sur les processus de fatigue en cours, résumant souvent le comportement de fatigue simplement comme un point sur la courbe S-N.

Problèmes et difficultés dans la littérature La caractérisation de la fatigue dans la littérature couvre la défaillance post-fatigue et les mesures *in-situ*, la première s'appuyant sur les courbes S-N et les méthodes d'observation telles que la microscopie, et la seconde sur les données en temps réel pendant les essais de fatigue. La recherche sur la fatigue à très haut cycle (VHCF) pose des problèmes, notamment en ce qui concerne la détection des fissures internes et l'estimation de leur taille, car les méthodes de mesure traditionnelles ne sont pas adaptées aux phénomènes de microplasticité et d'endommagement dans le cadre de la VHCF. Les faibles amplitudes de contrainte dans la VHCF conduisent à des taux de croissance des fissures plus lents, qui ne sont pas bien décrits par la mécanique des fractures conventionnelle. Par conséquent, une évolution vers des mesures à haute fréquence *in-situ*, chevauchant l'évaluation non destructive et l'acoustique, est en train d'émerger. Ces méthodes, sensibles aux non-linéarités des matériaux et capables de surveiller la cinétique des dommages et la croissance interne des fissures, impliquent l'analyse des harmoniques dans les signaux de vibration, comme l'ont démontré Kumar et al. [Kum+09], Fig. D.1 qui ont corrélé la deuxième harmonique relative à la première dans les essais de fatigue par ultrasons, en la reliant à la fractographie post-fatigue. Cependant, la relation entre ces harmoniques et les mécanismes de fatigue sous-jacents reste un domaine d'étude ouvert.

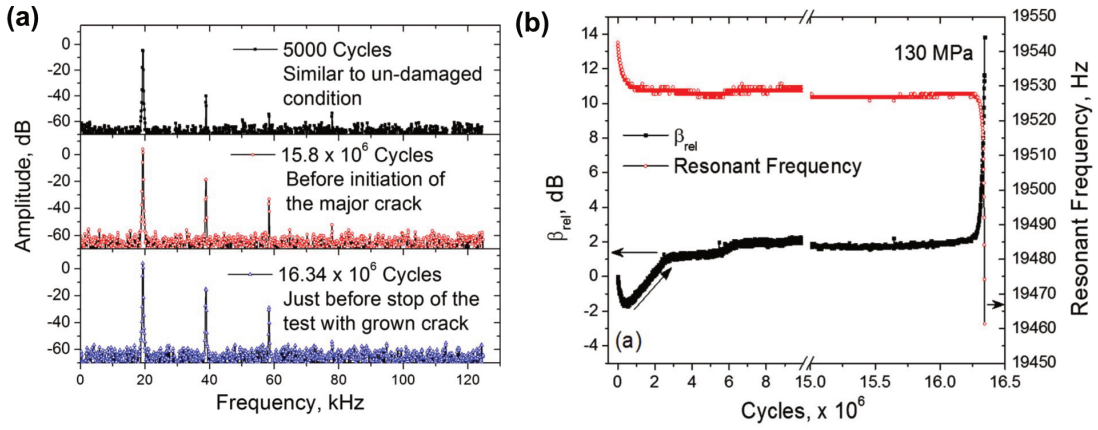

Figure D.1: Dans **(a)**, l'apparition d'harmoniques dans les spectres de fréquence des signaux de vibration recueillis à différents cycles au cours d'un essai de fatigue ultrasonore de l'alliage 6061-T6511 Al à 130 MPa. Dans **(b)**, les changements de β_{rel} et de la fréquence de résonance au cours du même essai de fatigue ultrasonore, extraits de [Kum+09].

Objectif de la thèse Cette thèse vise à développer une nouvelle méthodologie *in-situ* pour estimer et interpréter les non-linéarités des matériaux pendant les essais de fatigue par ultrasons, en se concentrant sur la détection de la microplasticité, des microfissures et des comportements de fissures macroscopiques. Ces mécanismes, considérés comme des sources de non-linéarités générant des harmoniques supérieures, sont essentiels pour comprendre le comportement des matériaux soumis à des charges de fatigue à haute fréquence. L'approche proposée vise à discerner les non-linéarités lentes et rapides correspondant à différents états du matériau pendant l'essai de fatigue. La méthodologie comprend deux composantes principales :

- Développement d'un modèle dynamique non linéaire qui intègre la fermeture des microfissures, le comportement microplastique et le développement des fissures macroscopiques, simulant le comportement de l'échantillon sous des charges de tension-compression à haute fréquence. Ce modèle vise à représenter avec précision les effets à méso-échelle des zones microplastiques et de la fermeture des microfissures, en utilisant des données de vibration à haute fréquence *in-situ* pour paramétrer un modèle dynamique reflétant les comportements de fatigue tout au long de la durée de vie de l'essai.

- Proposer des algorithmes avancés de traitement des signaux pour analyser les signaux de vibration de fatigue ultrasonore, en se concentrant sur la précision et l'efficacité de calcul pour une application en temps réel.

La méthodologie utilisera la vibrométrie laser Doppler sans contact pour l'acquisition des données vibratoires. La définition et l'optimisation du dispositif expérimental sont cruciales pour une acquisition fiable des données, y compris la sélection des points de mesure, la fréquence d'échantillonnage et la configuration générale du dispositif. Cette approche vise à améliorer la compréhension et la prédiction des mécanismes de fatigue des matériaux basés sur les ultrasons.

Approche scientifique Cette thèse adopte une approche scientifique méthodique, principalement axée sur le développement et la mise en œuvre d'un dispositif expérimental et de techniques de modélisation non linéaire correspondantes pour étudier les mécanismes de fatigue. La méthodologie comprend trois éléments clés :

1. Développement d'un dispositif expérimental pour mesurer la vitesse en différents points de l'échantillon. Les emplacements de mesure sont choisis stratégiquement pour tenir compte des effets non linéaires introduits par la machine d'essai.

2. Formulation de modèles non linéaires classiques des mécanismes de fatigue, intégrés dans un modèle macroscopique dynamique pour simuler avec précision la génération d'harmoniques dans des conditions d'essai de fatigue par ultrasons.

3. Établissement d'une méthodologie de traitement des signaux pour estimer avec précision l'amplitude des harmoniques générées, essentielle pour l'analyse des données vibratoires des essais de fatigue.

L'approche expérimentale consiste à utiliser un vibromètre laser pour mesurer les vibrations à la base et à la pointe libre de l'échantillon de fatigue, ce qui permet de mesurer les harmoniques. Un modèle dynamique non linéaire à plusieurs échelles est utilisé, dont les microfissures et les inclusions microplastiques sont modélisées à l'aide de l'homogénéisation du champ moyen de Mori-Tanaka [MT73] et des inclusions d'Eshelby [Esh57]. Cette approche de modélisation est représentée dans Fig. D.2 où le comportement non linéaire des microfissures et des inclusions microplastiques est défini au niveau du centroïde.

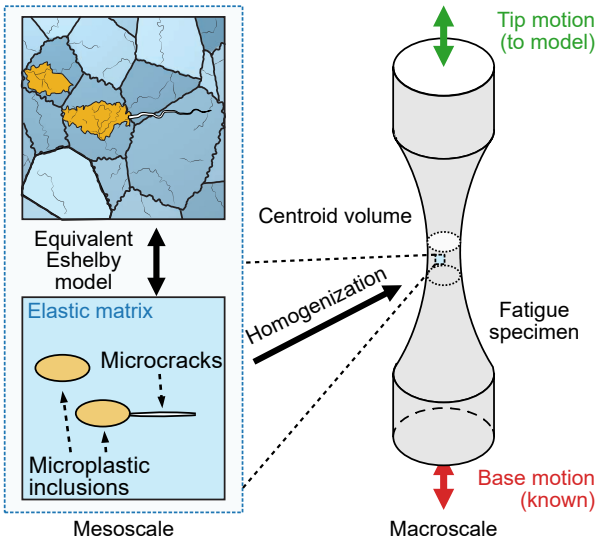

Figure D.2: L'approche de modélisation proposée dans cette thèse.

D.2 Chapitre 1 – Bibliographie et préliminaires

Caractérisation des régimes LCF à HCF La courbe S-N de Wöhler, qui met en corrélation l'amplitude de la contrainte avec le nombre logarithmique de cycles jusqu'à la rupture, délimite la durée de vie en fatigue (N_f) dans trois domaines : la fatigue à faible nombre de cycles à (LCF) 10^4 impliquant une déformation plastique significative, la fatigue à grand nombre de cycles (HCF) de 10^4 à 10^7, et la fatigue oligocyclique (VHCF) au-delà de 10^7 cycles, étudiée à l'aide de machines de fatigue à ultrasons pour des essais accélérés. La limite de fatigue conventionnelle, ou limite d'endurance, indique la résistance d'un matériau à la rupture par fatigue au-delà de 10^6 à 10^7 cycles, suggérant une durée de vie en fatigue infinie au-delà de cette plage.

Étapes de la rupture par fatigue La rupture par fatigue dans les métaux ductiles se déroule en quatre étapes : durcissement ou adoucissement cyclique, évolution des dommages dus à la fatigue en raison de phénomènes micromécaniques, amorçage et croissance des fissures menant à la rupture. En revanche, les métaux non ductiles contournent souvent les deux premières étapes en raison des défauts existants qui servent de concentrateurs de contraintes. Ces étapes, essentielles pour comprendre la fatigue, ont été étayées par diverses études et soulignent l'importance des mécanismes initiaux conduisant à la rupture par fatigue.

Influence des mécanismes de déformation plastique à micro-échelle L'adoucissement ou le durcissement cyclique des matériaux conduit à une boucle d'hystérésis stabilisée dans le diagramme contrainte-déformation, dont la surface diminue à mesure que la durée de vie en fatigue augmente. Dans le régime LCF, la plasticité macroscopique est mesurable, passant à des mécanismes de déformation plastique à micro-échelle dans les cycles plus élevés. Le régime VHCF se caractérise par une localisation cyclique de la déformation dans le cuivre sous forme de bandes de glissement persistantes (PSB), contribuant à l'apparition de dommages dus à la fatigue. L'irréversibilité du glissement, quantifiée par le rapport entre la déformation de cisaillement plastique irrécupérable et la déformation de cisaillement plastique totale, joue un rôle essentiel dans l'apparition des dommages dus à la fatigue. Les PSB, qui se forment dans une gamme spécifique d'amplitude de déformation plastique de cisaillement, contribuent à des comportements complexes tels que les bandes de glissement et la fissuration intergranulaire, leur densité et leur structure variant avec l'amplitude de la charge. Ces observations à micro- ou méso-échelle dans les régimes LCF à HCF soulignent la nécessité d'explorer les mécanismes fondamentaux de la fatigue dans le régime VHCF.

Caractérisation des régimes VHCF L'adoption de machines d'essai de fatigue par ultrasons a mis en évidence la nature spécifique des matériaux des mécanismes de fatigue dans le régime VHCF. Dans les matériaux présentant des hétérogénéités microstructurales telles que des inclusions, l'origine de la rupture dans le régime VHCF passe de la surface à des fractures internes en "œil de poisson". Pour les matériaux ductiles monophasés, la VHCF coïncide avec des amplitudes de contrainte inférieures au seuil PSB, ce qui se traduit par l'absence de structures PSB claires. La classification de Mughrabi des matériaux métalliques dans la VHCF, basée sur la microstructure et les mécanismes d'initiation des fissures, fournit un cadre pour la compréhension de ces variations.

Matériaux de type I et de type II Les matériaux de type I, généralement des métaux et alliages ductiles monophasés sans précipités ni inclusions, présentent une nucléation de la rupture à la surface. Cette catégorie comprend les aciers à faible teneur en carbone, certains aciers inoxydables et la fonte à graphite sphéroïdal. En revanche, les matériaux de type II présentent une microstructure complexe avec des inclusions, des pores et des particules de seconde phase grossières, qui agissent comme des concentrateurs de contraintes pour l'initiation de fissures de fatigue internes. Les exemples incluent les aciers à haute résistance et les alliages multiphases comme Ti6Al4V, où les fissures VHCF

s'initient principalement dans le volume du matériau au niveau des défauts ou des hétérogénéités microstructurales.

Ambiguïtés dans l'identification de l'initiation des fissures L'identification du début de l'amorçage et de la croissance des fissures lors des essais de fatigue par ultrasons, en particulier dans le régime VHCF, présente des ambiguïtés, surtout à des amplitudes de chargement plus faibles. Les premières études, telles que celles portant sur les aciers à faible teneur en carbone, utilisaient la courbe française parallèlement à la courbe S-N pour différencier les phases d'amorçage et de propagation des fissures, révélant que l'amorçage des fissures peut constituer une part importante de la durée de vie en fatigue dans le régime HCF. Cependant, la littérature basée sur la LEFM soutient que la propagation des fissures est inhérente dès le début en raison des défauts préexistants du matériau, un point de vue étayé par les résultats obtenus sur les matériaux commerciaux de type II. Des recherches récentes, telles que des études sur l'acier DP600 soumis à des charge ultrasonore, indiquent que des microvides se forment et fusionnent le long des bandes de glissement, entraînant l'apparition de microfissures, ce qui suggère l'existence de mécanismes distincts à différentes fréquences de chargement. Pour les matériaux de type I, en particulier en dessous du seuil PSB, le concept de propagation immédiate des fissures n'est pas universellement applicable, comme le démontrent des études telles que l'observation par Weidner et al. de microfissures de stade I dans le cuivre polycristallin après de nombreux cycles en dessous du seuil PSB, remettant en question les catégorisations conventionnelles de l'initiation et de la propagation des fissures dans les différents types de matériaux.

Exploitation de la charge à haute fréquence dans les essais de fatigue par ultrasons La charge à haute fréquence dans les essais de fatigue par ultrasons offre des perspectives uniques sur les états des matériaux, comme l'ont démontré Kumar et al. [Kum+09] en analysant l'extrémité libre vibrante d'éprouvettes de fatigue. Dans ces essais, la distorsion non linéaire de l'onde élastique à haute fréquence qui traverse l'échantillon se manifeste par un transfert d'énergie de l'harmonique fondamentale vers les harmoniques supérieures. Ce phénomène, illustré dans Fig. D.3, a été utilisé par Kumar et al. pour introduire un indice d'endommagement non linéaire, défini comme le rapport de l'amplitude de la deuxième harmonique à l'harmonique fondamentale au carré. Cette approche donne des indications *in-situ* pendant les essais, comme le montre Fig. D.1, où l'évolution de β_{rel} et de la fréquence de résonance indique l'apparition et la progression de fissures importantes dans un alliage d'aluminium. Alors que

les premières diminutions de β_{rel} ont été attribuées à l'adoucissement cyclique ou à l'augmentation de la température, son augmentation rapide plus tard dans le test a été liée à la croissance des fissures, ce qui correspond bien à l'analyse fractographique. Cependant, cela met également en évidence des problèmes fondamentaux dans l'utilisation du paramètre non linéaire acoustique β dans les essais ultrasonores, qui seront examinés plus en détail dans le Chapter 2. L'approche montre un potentiel pour le chargement à haute fréquence dans les essais de fatigue par ultrasons afin de révéler les phénomènes non linéaires dans les matériaux soumis à des contraintes.

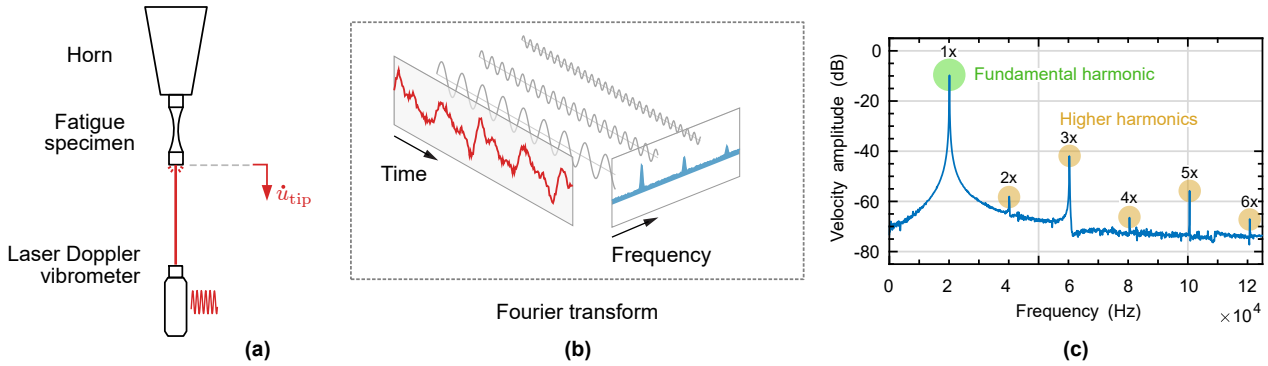

Figure D.3: Dans **(a)**, les signaux de vibration sont mesurés et dans **(b)** sont visualisés dans le domaine des fréquences par la transformée de Fourier du signal de vibration. Dans **(c)**, un spectre de fréquence d'un essai de fatigue par ultrasons montre une harmonique fondamentale à environ 20 kHz et ses harmoniques supérieures.

D.3 Chapitre 2 – Modèles pour les problèmes directs de fatigue par ultrasons

Le chapitre 2 est consacré à la modélisation complète d'une éprouvette de fatigue ultrasonore et d'une machine d'essai afin de comprendre la génération d'harmoniques observée dans la vibration de l'éprouvette de fatigue. L'accent est mis sur la distinction des sources de génération d'harmoniques et sur la compréhension des non-linéarités matérielles qui se manifestent à partir des mécanismes d'endommagement et de microplasticité dans l'éprouvette de fatigue. La structure de ce chapitre suit un ordre hiérarchique qui reflète les différentes échelles de longueur présentes dans l'éprouvette de fatigue. Cette organisation facilite l'examen systématique des réponses de l'éprouvette sous chargement de fatigue ultrasonore.

D.3.1 Acoustique non linéaire des réseaux atomiques

Tout d'abord, l'élasticité non linéaire (ou non-linéarité acoustique) est prise en compte car elle est fréquemment décrite par la communauté acoustique et récemment adoptée par la communauté de la fatigue ultrasonore. Le potentiel interatomique de deux atomes dans un réseau cristallin a une énergie potentielle non linéaire. L'élasticité non linéaire à la limite du continuum est approximée par une série de Taylor, qui donne le paramètre non linéaire classique β dans le mouvement des ondes longitudinales qui se propagent. Les mesures expérimentales de β n'existent que pour les éléments de base tels que le cuivre monocristallin ou polycristallin [Li+19], mais elles proviennent d'un échantillon et négligent la microstructure du matériau. Les mesures expérimentales sont basées sur la propagation de l'épaisseur à l'aide d'un transducteur et d'un récepteur ultrasonique avec la solution de Eq. (2.18).

Dans le contexte des essais de fatigue par ultrasons, une solution d'onde stationnaire longitudinale est recherchée puisque ce type de mouvement d'onde est formé pour une éprouvette de fatigue pendant les essais de fatigue par ultrasons. Un modèle de barre élancée et sa première longueur d'onde longitudinale sont simulés à l'aide de l'équation du mouvement Eq. (2.9), avec des coefficients de matériau dans le cuivre (β, ρ, E) et à sa longueur de résonance ultrasonore. Cette dernière présente une onde stationnaire si elle est chargée à sa fréquence de résonance et pour $t \to \infty$.

Trois points essentiels sont soulevés : tout d'abord, l'étude montre que le rapport entre l'amplitude de la seconde harmonique et celle de l'harmonique fondamentale diffère de plusieurs dizaines de degrés par rapport aux résultats expérimentaux obtenus pour un échantillon non endommagé dans le Chapter 4. Cet écart ne peut s'expliquer par la variation de β mesurée expérimentalement et indiquée dans Table 2.2 ; deuxièmement, l'onde d'entrée dans les essais de fatigue par ultrasons est en fait multi-harmonique selon les observations de l'auteur [Kis+21] et d'autres [Heb+23] ; enfin, le paramètre de non-linéarité acoustique est une propriété matérielle distribuée. Cela ne reflète pas le fait que les mécanismes actifs de fatigue sont localisés au volume du centroïde de cette éprouvette de fatigue ultrasonore. Cela justifie une approche de modélisation différente au-dessus de l'échelle atomique.

D.3.2 Modèles d'homogénéisation de la microplasticité et des microfissures

Au lieu de relier les harmoniques supérieures (dues à la génération d'harmoniques supérieures non linéaires) au paramètre de non-linéarité acoustique, la description à méso-échelle de la microplasticité et des microfissures sera prise en compte. Il est bien connu que la déformation plastique dans les matériaux métalliques est une conséquence de la dynamique des dislocations. Il est donc concevable qu'à des échelles de longueur plus grandes, il existe une corrélation entre les densités de microplasticité et de microfissures diffuses et la quantité de charge de fatigue dans chaque éprouvette de fatigue ultrasonique. Sous une charge dynamique à haute fréquence, on soupçonne qu'il y a une génération d'harmoniques non linéaires et une onde reçue (pointe de l'éprouvette de fatigue) lorsqu'elle traverse le volume du centroïde avec une microplasticité diffuse et/ou des microfissures qui se referment sous l'effet de la compression.

Pour modéliser ce phénomène mésoscopique, les objectifs de cette sous-section sont multiples : Tout d'abord, les théories d'homogénéisation du champ moyen sont introduites car elles offrent une alternative intéressante en termes de calcul à la modélisation directe des hétérogénéités microscopiques par l'analyse par éléments finis. L'approche Mori-Tanaka [MT73; Esh57] est adoptée pour la microplasticité et les microfissures : ici, les inclusions microplastiques (avec une géométrie ellipsoïdale) peuvent être décrites à l'aide de la théorie conventionnelle de plasticité J_2 [Dog00] ; les microfissures peuvent être représentées comme des fissures en forme de penny qui ont un critère de fermeture adopté de [Deu+02; BBL20] (avec une géométrie sphéroïdale), qui subissent une interface parfaite sans frottement.

Des inclusions à plasticité parfaite sont employées car le comportement de la microplasticité dans un matériau fatigué réel n'est pas bien quantifié. Deux paramètres sont libres selon le modèle (après avoir fixé la géométrie des inclusions, ses paramètres élastiques), la limite d'élasticité des inclusions microplastiques $\sigma_{\mathrm{pl}}^{\mathrm{Y}}$, la fraction de volume ξ_{pl}. La génération d'harmoniques supérieures est étudiée par rapport à la fraction de volume pour une onde d'entrée harmonique unique, qui représente une accumulation au cours d'une charge de fatigue. Dans le graphique du rapport harmonique, la troisième harmonique est la plus importante, suivie de la deuxième, qui augmentent toutes deux de façon monotone à mesure que ξ_{pl} augmente. Les modèles conventionnels d'hystérésis (macroscopique) ne génèrent pas d'harmoniques paires car ils négligent les complexités telles que les géométries et leurs effets de contrainte triaxiale. Dans le cas d'une onde d'entrée multi-harmonique, voir Fig. D.4, l'écart entre les

rapports des deuxième et troisième harmoniques diffère largement par rapport aux résultats obtenus pour une onde de déformation multi-harmonique unique (représentée par des lignes pointillées). Cela indique que la présence d'entrées multi-harmoniques peut entraîner des inexactitudes dans une analyse qui suppose une onde d'entrée harmonique unique.

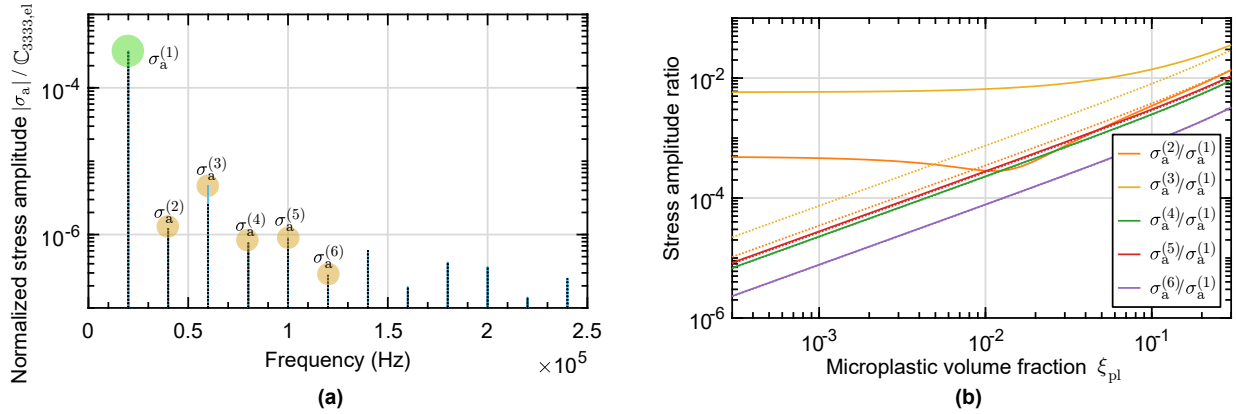

Figure D.4: Dans **(a)**, les spectres de fréquence normalisés d'une onde de contrainte uniaxiale dans la RVE pour une contrainte multi-harmonique Eq. (2.70) à $f_0 = 20$ kHz avec un rapport de charge $R = -1$ et $\xi_{cr} = 10^{-1}$. Dans **(b)**, le rapport entre les harmoniques supérieures et l'harmonique fondamentale ne suit plus la même trajectoire. Les lignes pointillées représentent les rapports harmoniques extraits précédemment de Fig. 2.8 pour une onde de déformation harmonique unique.

Pour la phase de microfissure, seule sa fraction de volume ξ_{cr} est libre (après avoir fixé la géométrie). Lorsque l'on étudie la génération d'harmoniques supérieures due à une onde d'entrée harmonique unique, les rapports harmoniques révèlent des harmoniques paires fortes croissantes avec de petites harmoniques impaires révélées. Comme dans le cas des inclusions microplastiques, ce phénomène n'est généralement pas observé dans la littérature sur l'acoustique et la dynamique non linéaires. La différence est due au fait qu'un état de contrainte anisotrope est généré en raison de la forme de disque des microfissures. Pour l'onde multi-harmonique, la rigidité asymétrique conduit à un changement abrupt (instabilité) pour la deuxième harmonique à $\xi_{cr} \approx 1.5 \cdot 10{-}3$ dans Fig. D.5.

Le modèle de rigidité de Mori-Tanaka peut être adapté aux matériaux multiphasés, où l'homogénéisation des hétérogénéités peut être effectuée en une seule étape ou en plusieurs étapes, chaque étape utilisant les propriétés effectives de l'étape précédente comme nouvelle phase de la matrice. Abaimov et al. [Aba+19] ont constaté qu'un processus d'homogénéisation en plusieurs étapes, commençant par les inhomogénéités les plus distinctes, permet d'obtenir des prévisions de rigidité plus précises, en particulier lorsque les inhomogénéités sont prédominantes dans les étapes initiales.

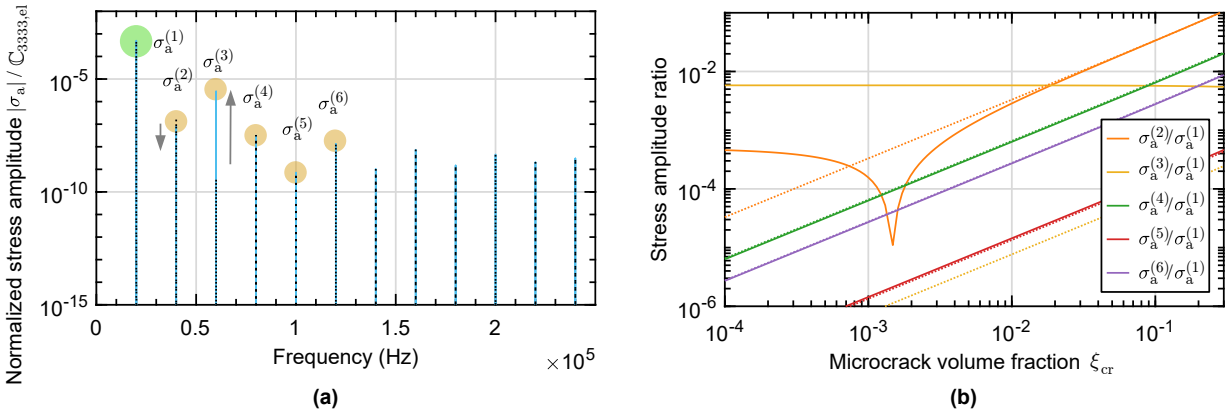

Figure D.5: Dans **(a)**, les spectres de fréquence normalisés d'une onde de contrainte uniaxiale dans la RVE pour la contrainte sinusoïdale multi-harmonique Eq. (2.70) à $f_0 = 20$ kHz avec un rapport de charge $R = -1$ et $\xi_{cr} = 10^{-1}$. Dans **(b)**, le rapport entre les harmoniques supérieures et l'harmonique fondamentale ne suit plus la même trajectoire que les variations de la fraction de volume des microfissures, qui sont indépendantes de l'amplitude et de la fréquence. Les lignes en pointillé représentent les rapports harmoniques précédemment extraits de Fig. 2.13 pour une onde de déformation harmonique unique.

Ainsi, un schéma d'homogénéisation en deux étapes est utilisé : homogénéiser d'abord la phase la plus conforme (microfissures) avec la matrice élastique, puis les inclusions microplastiques, simplifiant ainsi le problème de la tangente non linéaire en traitant les phases séparément. Lorsque les deux inclusions non linéaires sont intégrées dans le schéma d'homogénéisation Mori-Tanaka en deux étapes de Eq. (2.84), le comportement devient de plus en plus complexe.

D.3.3 Modèle de fissure uniaxiale

Un modèle de fissure rudimentaire est introduit dans les cas où la longueur de la fissure viole les hypothèses d'échelle de longueur faites par les théories d'homogénéisation. Cela correspond à l'effet d'une grande fissure près de la rupture de fatigue pendant les essais de fatigue par ultrasons. Des simplifications utilisant des hypothèses uniaxiales peuvent être appliquées pour capturer les effets dynamiques de premier ordre d'une fissure de mode I, mais cette approche ne tient pas compte d'autres complexités telles que les forces de contact par frottement, la modélisation de la croissance de la fissure ou la pointe plastique de la fissure. La rigidité bilinéaire d'une fissure rudimentaire de mode I dans les régimes de compression et de tension reflète une rigidité réduite due à un changement de la zone engagée.

En raison de l'expression de la forme proche, les harmoniques peuvent être résolues analytiquement. Dans le cas d'une entrée d'onde harmonique unique, le comportement de la fissure macroscopique et celui de la microfissure homogénéisée se chevauchent. Les deux montrent la génération d'harmoniques encore plus élevées. Un comportement similaire est attendu dans le cas multi-harmonique, c'est pourquoi l'effet du rapport de charge R est étudié à la place. Dans le cas d'une tension appliquée, les harmoniques révèlent une plus forte génération d'harmoniques impaires par rapport aux harmoniques paires. En faisant varier la charge de $-1 \leq R < 0$ utilisée pour les métaux dans les essais de fatigue par ultrasons, les effets non linéaires de l'asymétrie de la rigidité peuvent être vus comme affectant fortement les harmoniques supérieures. Lorsque $R \to 0$, la fermeture de la fissure ne peut pas se produire pendant la compression.

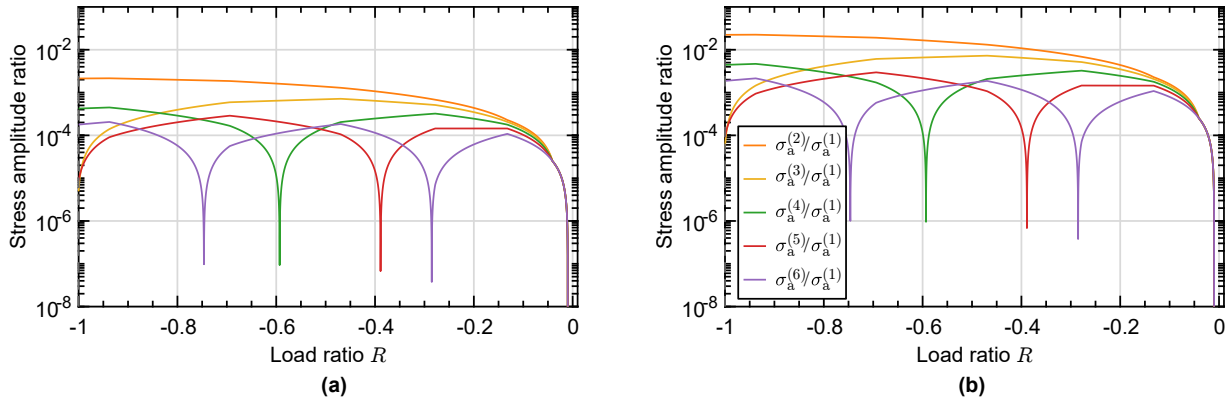

Figure D.6: Le rapport entre les harmoniques supérieures et les harmoniques fondamentales révèle que la génération d'harmoniques impaires dépend de la contrainte statique et de la modulation, c'est-à-dire du rapport de charge R. Les rapports harmoniques montrent une translation vers le haut de **(a)**, $\Lambda = 10^{-2}$ à **(b)** $\Lambda = 10^{-1}$, Λ est le paramètre de dégénérescence de la rigidité.

D.3.4 Modèle modal de l'éprouvette de fatigue ultrasonique

L'utilisation d'un modèle macroscopique de l'éprouvette de fatigue par AEF peut s'avérer fastidieuse lorsqu'il s'agit de générer diverses variations des densités de microplastiques et de microfissures. Cependant, le dispositif expérimental d'un essai de fatigue par ultrasons possède des propriétés dynamiques qui peuvent être exploitées, à savoir que l'éprouvette de fatigue par ultrasons est sollicitée à sa fréquence propre longitudinale et forme ainsi une onde stationnaire. Avant les essais de fatigue ultrasonique prévus, l'éprouvette de fatigue ultrasonique est conçue de manière à ce que les autres modes propres de vibration soient bien séparés de la fréquence propre longitudinale (20 $\pm$ 2 kHz),

ce qui permet d'éviter tout couplage de mode parasite. Un modèle d'ordre réduit dans cette gamme étroite de fréquences par les modes normaux de vibration peut être utilisé, à savoir l'approche classique de la troncature modale [GR15], voir le schéma Fig. D.7.

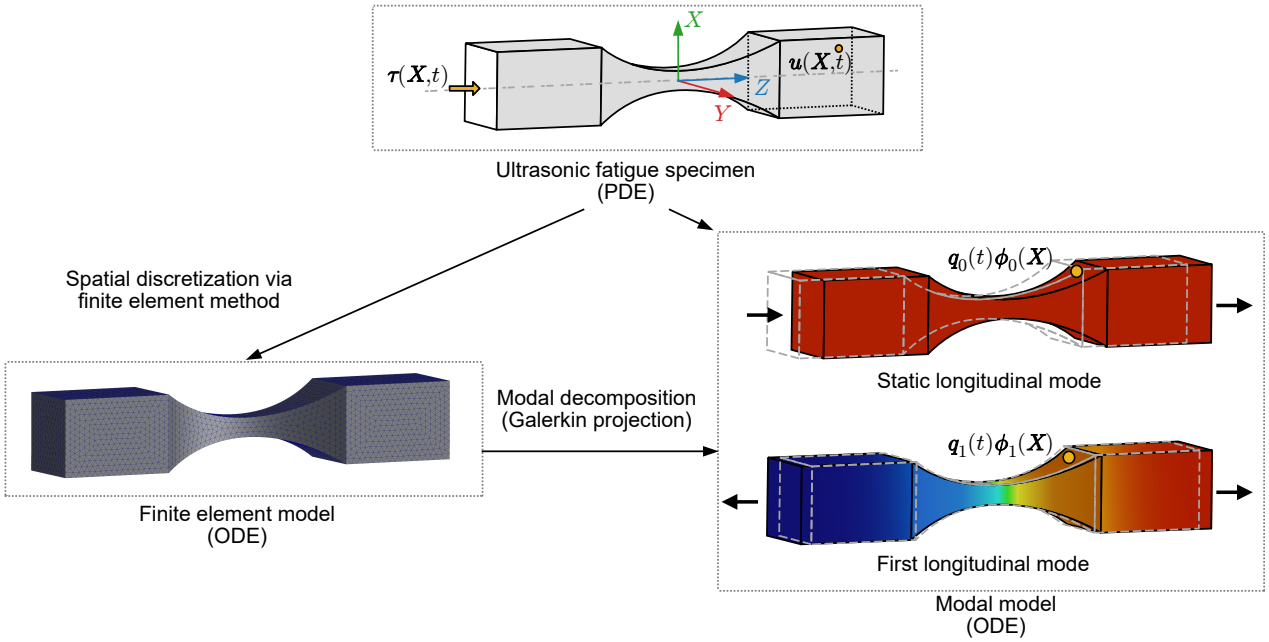

Figure D.7: Modèle modal d'une éprouvette de fatigue ultrasonique utilisant la réduction de l'ordre du modèle, montrant les fonctions de forme modale dérivées de la discrétisation spatiale du modèle d'éléments finis.

L'équation de mouvement résultante du modèle modal, qui englobe un volume centroïde de microplasticité diffuse et/ou de microfissures, peut être simulée avec des hypothèses périodiques. Cependant, en fonction de la force de la non-linéarité, l'équation de mouvement résultante peut être rigide pour les techniques classiques d'intégration numérique dans le domaine temporel, comme Runge-Kutta. Un bon candidat pour résoudre les équations de mouvement peut utiliser la méthode de balance harmonique (HBM) [SS11]. Cette méthode évite ces problèmes en supposant une solution périodique sous la forme d'une série de Fourier tronquée. Ces coefficients de Fourier inconnus sont ensuite intégrés dans un système d'équations algébriques non linéaires dont le rang est l'ordre harmonique tronqué. La méthode HBM permet d'obtenir une bonne précision avec un effort de calcul réduit de plusieurs ordres de grandeur par rapport à l'intégration numérique dans le domaine temporel [Woi+20]. La simulation rapide du modèle modal permet de générer l'espace des paramètres, qui représente la microplasticité diffuse et/ou les densités de microfissures en harmoniques supérieures.

D.3.5 Machine à fatigue ultrasonique et sollicitation piézoélectrique

Ici, un modèle électrodynamique de la machine d'essai de fatigue par ultrasons est décrit sans éprouvette de fatigue attachée, décrit par des fonctions de transfert et validé avec des données expérimentales. Cependant, une analyse de fréquence de la tension appliquée expérimentale, du courant au transducteur piézoélectrique et des données expérimentales de vitesse du pavillon acoustique révèle de petites non-linéarités du système qui se manifestent sous la forme d'harmoniques supérieures. Cela remet en question l'hypothèse conventionnelle de la littérature sur la fatigue ultrasonique selon laquelle le pavillon acoustique fournit une onde d'entrée harmonique pure à l'éprouvette de fatigue.

Les non-linéarités au niveau du pavillon acoustique de l'équipement d'essai de fatigue par ultrasons peuvent provenir de plusieurs sources : Premièrement, le générateur de signal et d'énergie peut introduire une non-linéarité en raison de la complexité de son circuit et de sa nature non linéaire, ce qui affecte l'excitation du transducteur piézoélectrique et la génération de la forme d'onde. Deuxièmement, la non-linéarité du matériau des céramiques piézoélectriques, telles que le PZT, contribue à la non-linéarité de leurs relations contrainte-déformation, au comportement hystérique de la polarisation ferroélectrique et à la non-linéarité de saturation sous de grands champs électriques, aggravée par la sensibilité thermique. Enfin, les interfaces mécaniques et les fixations au sein du système, y compris la friction et la non-linéarité liée au contact au niveau des interfaces et des articulations, contribuent également à la non-linéarité globale observée dans le système.

D.4 Chapitre 3 – Traitement des signaux pour l'estimation des harmoniques et l'identification des systèmes non linéaires

D.4.1 Traitement des signaux de vibrations ultrasoniques pour l'extraction d'harmoniques

L'estimation précise des harmoniques supérieures dans les signaux de vibration est cruciale pour les relier aux densités de microplastiques et de microfissures et pour contribuer aux approches de l'indice d'endommagement. L'équilibre entre la précision de l'estimation et la complexité du calcul est essentiel pour l'utilisation de *in-situ* pendant les essais de fatigue par ultrasons. Les défis comprennent les limitations de l'incertitude de fréquence et de temps par la limite de Rayleigh et l'utilisation d'estimateurs de modèles de signaux stationnaires sur des signaux quasi-stationnaires, où la minimisation de la longueur de la fenêtre améliore la résolution temporelle au détriment de la résolution de

fréquence. En outre, la performance statistique des estimateurs, largement étudiée à l'aide de signaux synthétiques purement stationnaires, peut ne pas refléter avec précision leur efficacité sur des signaux quasi-stationnaires dont les amplitudes et les fréquences varient dans le temps.

Cinq estimateurs spectraux de ligne (LSE), à savoir ESPRIT unitaire [HN95], RELAX [JS96], CFH [SQ20], NOMP [MRM16], et DeepFreq [IMF21] en ce qui concerne les problèmes susmentionnés. Ces cinq algorithmes ont été choisis car leurs fondements théoriques constituent une représentation diversifiée (basée sur le sous-espace, basée sur le maximum de vraisemblance, basée sur l'interpolation des pics DFT, basée sur l'algorithme gourmand pour le raffinement de la grille, et basée sur les réseaux neuronaux profonds, respectivement) des nombreux LSE qui existent dans la littérature. Notamment, de nombreux LSE sont considérés comme ayant des résultats de pointe pour les signaux purement stationnaires avec des amplitudes unitaires, ce qui n'est pas le cas pour les signaux quasi-stationnaires avec des amplitudes et des fréquences non unitaires variant lentement dans le temps (non-concordance des bases).

Les bancs d'essai sur un signal synthétique de vibration ultrasonique de fatigue et des signaux générés aléatoirement avec des défis d'estimation uniques vus dans la vibration ultrasonique, montrent les capacités des différents estimateurs en termes d'adaptabilité au quasi-stationnaire et d'efficacité de calcul. En général, ESPRIT et NOMP offrent les meilleures performances en ce qui concerne la quasi-stationnarité d'un signal synthétique de vibration ultrasonique de fatigue. Cela motive l'exploration de l'adaptation d'ESPRIT dans une forme plus efficace sur le plan du calcul pour les signaux de vibration de fatigue ultrasonique *in-situ*.

D.4.2 Estimation rapide de la fréquence du sous-espace du signal

L'objectif de ce chapitre est de réduire la complexité de calcul d'ESPRIT, qui correspond à l'estimation du sous-espace du signal. Ce problème n'est pas nouveau, car il existe de nombreuses approches dans la littérature qui s'appuient sur le fait que l'étendue du sous-espace du signal est beaucoup plus petite que son sous-espace orthogonal. Pour n'en citer que quelques-unes, dans [TM85], ils utilisent l'algorithme de Lanczos pour converger de manière itérative vers le sous-espace du signal ; une autre utilise des SVD partielles et des produits matrice-vecteur de Hankel rapides présentés dans [PT15] ; et un ESPRIT basé sur Nyström [QHS14]. La contribution apportée ici est d'éviter le calcul de la SVD/EVD, et d'exploiter le modèle de signal de Vandermonde et la matrice DFT.

Pour le premier algorithme, il est démontré que le sous-espace complet (sous-espace du signal et du bruit) peut être approximé par le noyau de la transformée de Fourier sur l'espace des lignes de la matrice de données de Hankel. Cette approximation du sous-espace présente une inadéquation de base caractérisée par le noyau de Dirichlet, ce qui indique qu'il existe une inadéquation de base lorsque les fréquences ne se situent pas sur la grille d'échantillons uniformément espacés (fréquences *off-grid*). Cela signifie que l'augmentation de la longueur du signal n'améliorera pas l'estimation. Une fois multiplié, le sous-espace du signal correspond aux vecteurs colonnes orthogonalisés ayant les normes l2 les plus élevées. Cet algorithme a une complexité de calcul de $\mathcal{O}(N^2 \log N)$. Pour améliorer la vitesse et atténuer le problème des fréquences *off-grid*, il est proposé de tronquer la matrice DFT en fonction de l'énergie spectrale et d'interpoler *off-grid*. Le résultat est l'algorithme appelé FFT-ESPRIT, qui a une complexité de calcul de $\mathcal{O}(N \log N)$: cette accélération peut être vue dans Fig. D.8. Les limites de performance de la perturbation de l'espace propre sont comparées à celles de l'ESPRIT original. Les limites de performance suggèrent la supériorité de la FFT-ESPRIT sur l'ESPRIT conventionnel dans les régimes SNR inférieurs, ce qui est validé par des simulations numériques. Ses performances sont proches de celles de l'ESPRIT à des RSN élevés, et la FFT-ESPRIT apparaît donc comme une alternative viable pour les applications en temps réel avec des signaux de grande longueur. Dans un contexte plus large, la FFT-ESPRIT peut être considérée comme une mise à jour par "matrix pencil" du modèle de signal offert par la FFT interpolée avec super-résolution.

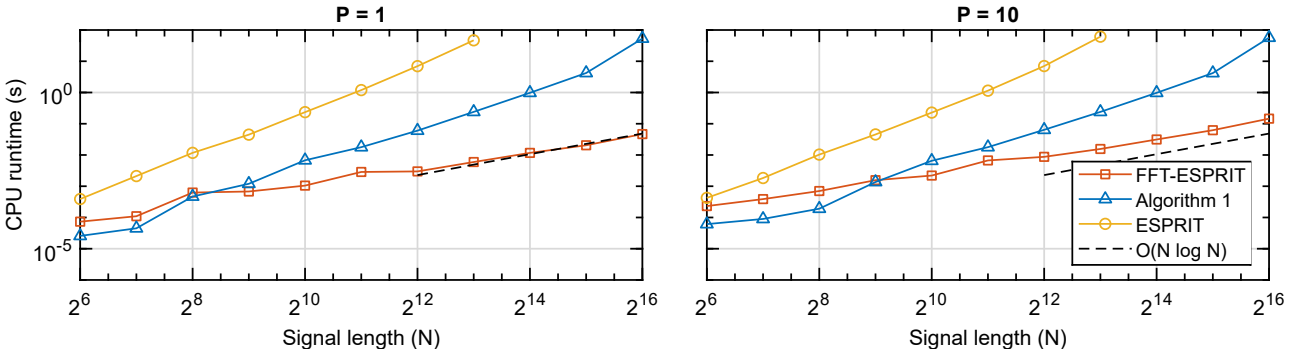

Figure D.8: Résultats de la simulation des durées d'exécution de l'unité centrale en fonction de la longueur du signal pour le nombre de sinusoïdes $P = 1$ (à gauche) et $P = 10$ (à droite). La durée en secondes est mesurée à l'aide de la fonction MATLAB `timeit`. La même ligne de complexité asymptotique de $\mathcal{O}(N \log N)$ est indiquée sur chaque graphique.

D.4.3 Identification exacte de systèmes dynamiques non linéaires

La méthode SINDy (sparse identification of nonlinear dynamics) [BPK16], qui utilise l'algorithme STLS (sequentially thresholded least squares), a gagné en popularité dans l'identification des systèmes dynamiques non linéaires. Les développements récents comprennent diverses extensions de la méthode SINDy, comme l'assemblage de modèles SINDy bootstrappés (E-SINDy) [Fas+22], conçus pour traiter des données expérimentales finies et très bruyantes. Cependant, bien que ces extensions favorisent l'éparpillement, elles ne produisent parfois que des approximations éparses plutôt qu'une récupération exacte de la dynamique sous-jacente. En outre, ces estimateurs souffrent de la multicollinéarité, par exemple la condition d'irreprésentabilité pour le Lasso [Tib96; FL01]. Dans cette section, le Trimmed Lasso (TRIM) [BCM17], une pénalité non convexe, peut fournir une récupération exacte dans des conditions plus sévères de bruit, de données finies et de multicollinéarité, contrairement à l'E-SINDy. En outre, le coût de calcul du TRIM est asymptotiquement égal à celui du STLS, car le paramètre de dispersion du TRIM peut être résolu efficacement par des solveurs convexes.

Les performances sont comparées sur l'oscillateur de Bouc Wen du benchmark de dynamique non linéaire de Noël et Schoukens [NS16]. TRIM surpasse d'autres régressions éparses dans le cadre de SINDy, ainsi que d'autres résultats de référence en ce qui concerne leur RMSE et le nombre de paramètres dans Table D.1. La majorité des autres méthodes de la littérature sont des méthodes de boîte noire. On peut montrer que TRIM donne des résultats compétitifs puisqu'il récupère le modèle exact et que sa précision n'est limitée que par sa méthode d'intégration numérique.

Estimator	**RMSE Multi-sine** ($\cdot 10^{-5}$)	**RMSE Sine Sweep** ($\cdot 10^{-5}$)	**Parameters** (sparsity $\hat{K}$)	**Exact recovery**
TRIM	**6.569**	**4.949**	**6**	✓
Volterra feedback [SS16]	8.409	5.601	14	×
Decoupled NARX [Wes+18]	5.360	1.670	206	×
EHH NN [Xu+20]	4.949	2.402	436	×
LSTM [SMN19]	5.980	2.800	21730	×
MIMO PNLSS [Fak+18]	1.871	1.202	217	×
Decoupled PNLSS [Fak+18]	1.338	1.117	51	×
Oracle	5.098	4.182	6	-

Table D.1: Résultats de TRIM et de la littérature pour le benchmark de Bouc Wen de [NS16]. L'entrée "Oracle" fait référence à la RMSE trouvée en utilisant les vrais paramètres de Bouc Wen et les données d'entrée fournies pour la simulation à l'aide du fichier p MATLAB fourni par le benchmark.

D.5 Chapitre 4 – Ultrasonic fatigue experimental results

Dans ce chapitre, l'approche du modèle multi-échelle de Chapter 2 est utilisée avec des données de vibration expérimentales. Pour dériver les paramètres du modèle qui décrivent la dynamique des ondes stationnaires et la génération d'harmoniques à la vibration de la pointe, un problème de régression est formulé pour minimiser l'écart entre les prédictions du modèle et les résultats expérimentaux. les prévisions du modèle et les résultats expérimentaux. Ces paramètres de modèle correspondent à la réponse mésoscopique non linéaire due aux microfissures et aux inclusions microplastiques et à la contribution des multi-harmoniques à la vibration de la base.

Dans la première section, l'essentiel de la procédure expérimentale est détaillé, y compris la configuration de la machine d'essai de fatigue par ultrasons, le matériau de l'éprouvette de fatigue et la charge de fatigue, ainsi que la sélection des paramètres du modèle. Le cuivre polycristallin et l'acier C70 sont testés dans le régime VHCF, dont les signaux de vibration sont enregistrés. Pour compléter ces données vibratoires, des signaux thermographiques ainsi que des fractographies de base sont utilisés pour catégoriser l'apparition de la microfissure et son mode de défaillance. Pour la deuxième section, les paramètres micromécaniques du modèle multi-échelle sont identifiés pour prédire la génération d'harmoniques observée dans les données vibratoires expérimentales des essais de fatigue par ultrasons, voir Fig. D.9.

La procédure d'identification repose sur une régression des harmoniques fondamentales, secondes et troisièmes entre l'expérience et le modèle en faisant varier les paramètres micromécaniques :

$$\{\hat{\xi}_{\mathrm{pl}}, \hat{\xi}_{cr}, \hat{\sigma}^{\mathrm{Y}}_{\mathrm{pl}}\}^{(i)} = \underset{\{\xi_{\mathrm{cr}}, \xi_{\mathrm{pl}}, \sigma^{\mathrm{Y}}_{\mathrm{pl}}\}^{(i)}}{\arg\min} \mathcal{C}(\xi_{\mathrm{cr}}, \xi_{\mathrm{pl}}, \sigma^{\mathrm{Y}}_{\mathrm{pl}});$$

$$\text{avec} \quad \mathcal{C}(\{\xi_{\mathrm{cr}}, \xi_{\mathrm{pl}}, \sigma^{\mathrm{Y}}_{\mathrm{pl}}\}^{(i)}) = \sum_{h=1}^{3} \left(\frac{A_h(\{\xi_{\mathrm{cr}}, \xi_{\mathrm{pl}}, \sigma^{\mathrm{Y}}_{\mathrm{pl}}\}^{(i)}) - \hat{A}_h}{\hat{A}_h} \right)^2$$

où i correspond à la $i$ème fenêtre temporelle, et $h = 1, 2, 3$ correspondent aux amplitudes de l'harmonique fondamentale, de la deuxième et de la troisième harmonique. Appendix D.5 est une régression sur les amplitudes harmoniques (hypothèse de l'onde stationnaire) effectuée par fenêtre temporelle. Les résultats du modèle multi-échelle en ce qui concerne les paramètres micromécaniques sont discutés et juxtaposés.

L'évolution des paramètres micromécaniques dans les modèles, en particulier la fraction volumique

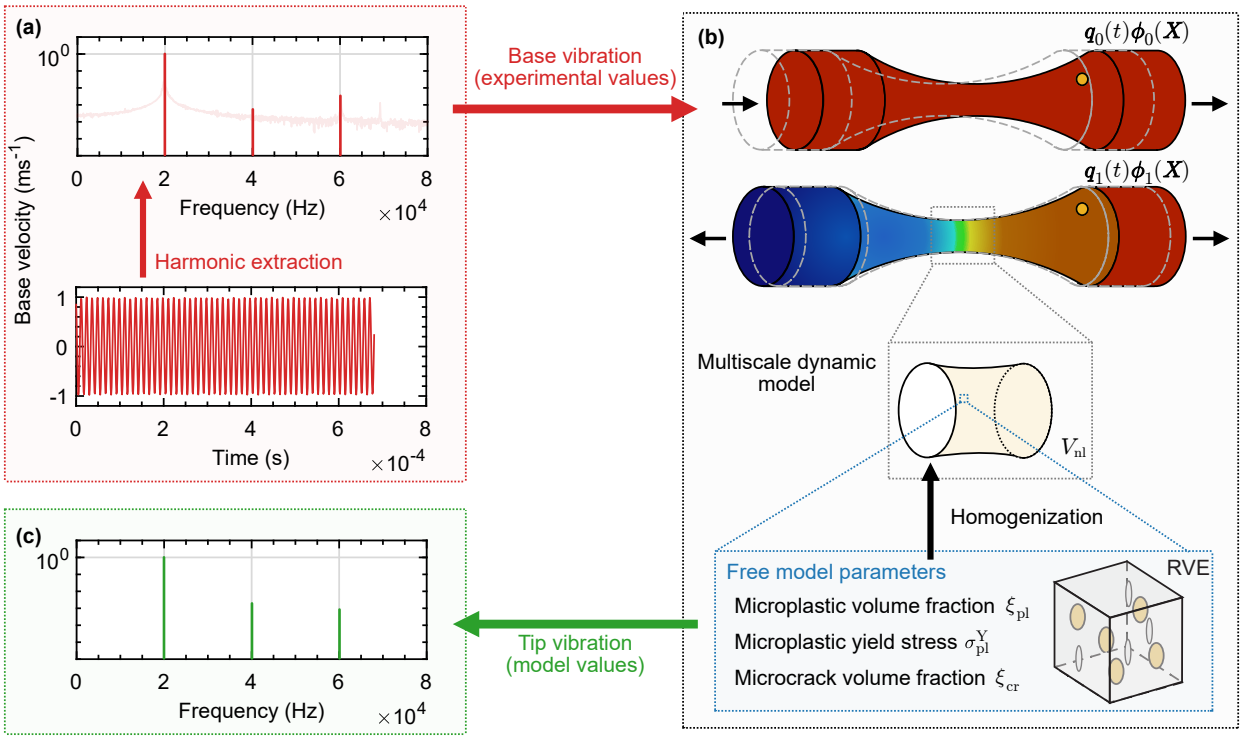

Figure D.9: Schéma de la procédure de simulation de l'éprouvette de fatigue ultrasonique multi-échelle.

des microfissures ξ_{cr}, présente des comportements distincts. Comme le montre Fig. D.10 **(a)**, ξ_{cr} est plus sensible que d'autres mesures *in-situ* dans le régime VHCF, présentant une forte augmentation après un seuil de fraction de volume microplastique, suggérant que la microplasticité est un précurseur de l'initiation des microfissures. La thermographie infrarouge à grande vitesse, suivant la méthode de Ranc [RWP08], a capturé la nucléation des macrofissures, indiquant que l'augmentation de la fraction de volume des microfissures est probablement due à des mécanismes souterrains plutôt qu'à des macrofissures superficielles. La fractographie après rupture confirme la propagation des macrofissures vers l'intérieur à partir de la surface.

Cependant, l'interprétation de ξ_{cr} soulève des questions quant à son caractère physique. La valeur initiale non nulle implique l'existence de microfissures préexistantes, contribuant à la génération de seconde harmonique, tandis qu'une diminution ultérieure contredit l'irréversibilité de la formation de microfissures. En outre, les valeurs de la fraction volumique sont plus importantes que ce qui est généralement attendu, ce qui remet en question la modélisation directe des microfissures diffuses en tant que mode I orienté. Bien qu'il soit tentant d'approfondir l'analyse de la microplasticité, les

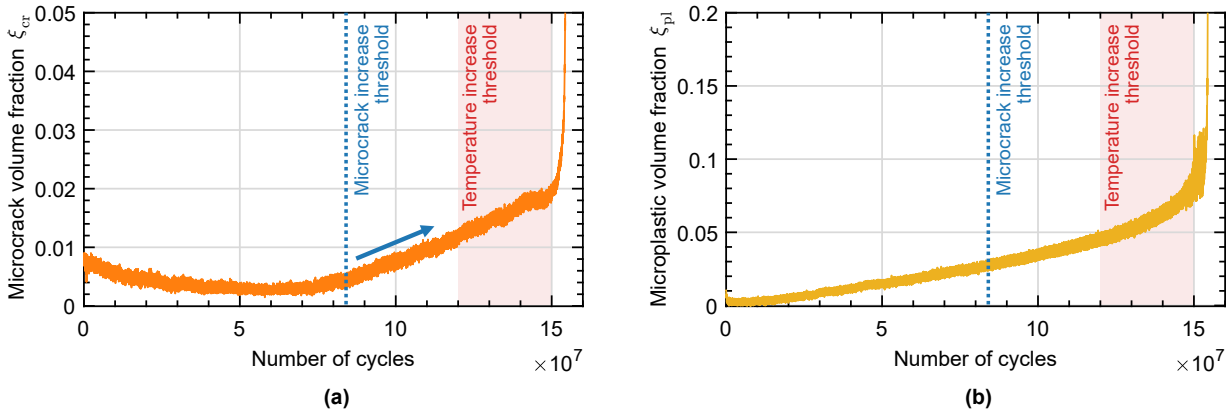

Figure D.10: Les paramètres micromécaniques calibrés, les fractions de volume de microfissure **(a)** et d'inclusion microplastique **(b)**, qui reproduisent la génération d'harmoniques supérieures entre l'éprouvette de fatigue en cuivre et le modèle (essai 3).

hypothèses fortes de la modélisation, telles que la négligence des fronts plastiques dans les microfissures et l'adoption de lois de plasticité simples, soulignent la nécessité de poursuivre les études sur la plasticité cristalline et la dynamique des dislocations à l'aide de lois de plasticité plus précises.

Contrairement aux modèles d'éprouvettes de fatigue en cuivre, le modèle d'éprouvettes en acier C70 ne montre pas d'augmentation précoce du seuil des paramètres micromécaniques, ce qui pourrait indiquer des caractéristiques de fatigue uniques de l'acier C70 par rapport au cuivre, bien que cela reste incertain en raison des changements harmoniques supérieurs minimes dans les données expérimentales. Le plateau observé et l'augmentation rapide des fractions de volume des microfissures et des microplastiques dans les résultats du modèle suggèrent une disparité entre les hypothèses du modèle et les résultats expérimentaux. Notamment, l'analyse fractographique de l'acier C70, comme le montrent, révèle une rupture en œil de poisson provenant d'un super grain de perlite, mais ces observations n'expliquent pas entièrement la faible, voire l'absence d'évolution des paramètres du modèle micromécanique dans les données expérimentales. Cela suggère que la génération d'harmoniques provenant de microfissures ou de phénomènes microplastiques n'est pas suffisamment importante par rapport à la vibration de base multi-harmonique, supprimant les indications précoces des paramètres micromécaniques, une conclusion soutenue par les simulations micromécaniques dans Chapter 2.

D.6 Conclusions et perspectives

Cette thèse visait à développer une méthodologie *in-situ* pour estimer et interpréter les non-linéarités présentes pendant les essais de fatigue par ultrasons dans le domaine VHCF. Il est démontré que la charge à haute fréquence de la machine d'essai de fatigue ultrasonique produit des harmoniques plus élevées dans le signal de vibration. La source de cette génération d'harmoniques est étudiée à la fois du point de vue expérimental et du point de vue de la modélisation. L'objectif est d'isoler les non-linéarités du matériau dues aux changements micromécaniques des autres non-linéarités du système. Ceci est compliqué par le fait que les machines d'essai de fatigue par ultrasons ont une onde d'entrée multi-harmonique qui sollicite une éprouvette de fatigue par ultrasons. Vous trouverez ci-dessous un résumé des principales conclusions :

Modèles de matériaux non linéaires

- L'analyse du paramètre acoustique non linéaire s'avère erronée pour les essais de fatigue ultrasonique : la non-linéarité du matériau ne contribue que faiblement à la génération de la deuxième harmonique. La différence de magnitude est d'environ dix pour le cuivre polycristallin au VHCF.
- Les modèles d'homogénéisation basés sur Eshelby des microfissures diffuses avec fermeture et inclusions microplastiques se révèlent être un candidat pour la source mésoscopique de génération d'harmoniques non linéaires. Lorsqu'il est soumis à une entrée multi-harmonique, le comportement de la génération d'harmoniques non linéaires devient de plus en plus complexe et insensible par rapport à une entrée mono-harmonique, à mesure que la fraction de volume des hétérogénéités augmente.
- Un modèle de macrofissure en mode I avec fermeture présente une génération d'harmoniques non linéaires similaire à celle du modèle de microfissure, sauf qu'il est paramétré par la surface de la fissure. La forme analytique du modèle démontre également que sous différents rapports de charge, la génération harmonique non linéaire devient de plus en plus complexe en raison d'une modulation sincère.

Traitement des signaux de fatigue ultrasonique

- L'estimation des paramètres sinusoïdaux est influencée par les compromis entre la longueur des fenêtres et la précision lorsqu'il s'agit de la quasi-stationnarité et de la limite de Rayleigh. Une petite fenêtre temporelle est plus localement stationnaire que des fenêtres plus grandes, réduit le temps de calcul des algorithmes d'estimation sinusoïdale et fournit des estimations de paramètres plus discrètes.
- Le benchmark réalisé sur les signaux quasi-stationnaires trouvés dans les vibrations VHCF a révélé que les algorithmes ESPRIT et NOMP présentent le meilleur compromis entre la longueur du signal et la précision. Cependant, ESPRIT est un algorithme cubique-complexe. Cela motive l'exploration de l'adaptation d'ESPRIT dans une forme plus efficace en termes de calcul pour les signaux de vibration de fatigue ultrasonique *in-situ*.
- Un algorithme basé sur ESPRIT est développé, à savoir FFT-ESPRIT, qui approxime le sous-espace du signal à partir de la FFT. L'algorithme atteint une précision similaire à celle de l'algorithme ESPRIT original. La complexité de calcul est réduite d'une complexité cubique à une complexité quasi-linéaire grâce à une implémentation lourde de la FFT et aux propriétés de la matrice de Hankel du signal.

Modèle d'éprouvette de fatigue ultrasonique

- La nature en régime permanent de la dynamique du système de fatigue ultrasonore permet d'obtenir un modèle d'ordre réduit de l'éprouvette de fatigue ultrasonore. Cela permet un calcul rapide à l'aide de fonctions de forme modales. La nature localisée de la fatigue est prise en compte par la contribution modale des non-linéarités à un volume centroïde. Une solution des équations globales du mouvement est calculée par la méthode de l'équilibre harmonique. Cela permet d'éviter les solutions dynamiques coûteuses basées sur les éléments finis.
- Les conditions limites du modèle démontrent que la vibration de base justifie l'utilisation d'un second vibromètre laser pour tenir compte de l'entrée multi-harmonique.
- Pour les données expérimentales des éprouvettes de cuivre polycristallin et d'acier C70, le modèle multiéchelle simulé a réussi à décrire la génération des deuxième et troisième harmoniques dans les données expérimentales pour les deux éprouvettes de fatigue avec une faible erreur avant la propagation de la macrofissure.

- Pour le cuivre polycristallin, l'évolution de la fraction volumique des microfissures passe d'une croissance linéaire à une croissance exponentielle dans le régime VHCF, alors qu'avant le régime HCF, la croissance linéaire n'est pas prononcée. La durée de vie avant ces changements correspond à 50% pour le régime VHCF ($N_f = 1.5 \cdot 10^8$) et 77% pour le régime HCF ($N_f = 8.9 \cdot 10^6$). Dans les deux régimes, on observe une augmentation régulière de la fraction volumique des inclusions microplastiques dès le début. Ł'interprétation physique de ces paramètres suggère que les essais de fatigue ultrasonique du cuivre montrent une augmentation monotone de la microplasticité, qui est un précurseur de dommages.

- Pour l'acier C70, l'évolution des fractions volumiques des microfissures et des inclusions microplastiques reflète la génération d'harmoniques négligeable observée dans les expériences de fatigue ultrasonique. L'évolution des paramètres est cohérente lorsque la macrofissure se forme. Ł'interprétation physique de ces paramètres suggère que la génération d'harmoniques due à d'éventuelles microfissures et/ou à des phénomènes microplastiques n'est pas assez forte par rapport à l'effet d'une vibration de base multi-harmonique.

Ici, on remarque que certains aspects clés peuvent être explorés afin d'améliorer la compréhension ou les résultats présentés dans cette thèse :

- Les harmoniques multiples présents dans l'entrée de l'éprouvette de fatigue est soupçonné de diminuer la sensibilité de la génération d'harmoniques supérieures des non-linéarités matérielles. Par conséquent, un effort pour améliorer la fidélité des amplitudes harmoniques peut provenir d'une amélioration de la linéarité de la machine d'essai de fatigue par ultrasons. Une technique de prédistorsion efficace appliquée au signal de tension d'entrée, par exemple les travaux de [NSL18], peut linéariser la non-linéarité due au transducteur ultrasonique, en fournissant idéalement des harmoniques supérieures moins proéminentes.

- Une exploration plus poussée des divergences entre les sources physiques de génération d'harmoniques et les modèles de matériaux non linéaires est justifiée. Cela est suggéré pour le cuivre polycristallin (ou les métaux ductiles à phase unique) ainsi que pour l'acier C70 (ou les matériaux de type II). L'interprétation physique des paramètres micromécaniques suggère des phénomènes à la fois prometteurs et impossibles (la diminution de la fraction volumique des microfissures dans le cuivre).

- Les modèles de matériaux non linéaires peuvent être améliorés pour prendre en compte des comportements de plus en plus complexes qui correspondent mieux à la physique. Par exemple, une fissure avec un contact parfait (pas de frottement) n'est pas une source dissipative. Cependant, dans la réalité, les microfissures et la microplasticité sont intrinsèquement liées, en raison de la plasticité du front de la fissure et de l'énergie utilisée pour propager la fissure. La prise en compte des effets de la température au niveau de ce centroïde peut permettre d'obtenir des résultats.

- Une attention particulière a été accordée à l'introduction d'une approche axée sur les données pour l'analyse des données de mesure des vibrations. Dans ce cadre, des contributions ont été faites pour améliorer l'algorithme utilisé dans le cadre de SINDy. Cependant, l'application pratique de TRIM sur les expériences de fatigue ultrasonique n'a pas pu être réalisée dans le temps imparti de cette thèse. Cela reste un domaine d'exploration future, qui encourage l'apprentissage automatique interprétable.

Shawn L. KISER

Ultrasonic gigacyclic fatigue, nonlinear dynamics, crack propagation, nonlinear signal processing

Résumé : La recherche sur le régime de fatigue à très haut cycle (VHCF) est rendue possible par l'utilisation d'essais de fatigue ultrasonore qui permettent d'atteindre en quelques jours des milliard de cycles. Les mesures et analyses classiques sont cependant limitées car peu sensibles à la microplasticité ou aux dommages (microfissures et microvides) qui conduisent finalement à la rupture par fatigue lors de ces essais. Ces mécanismes de fatigue sont donc en pratique difficiles à détecter expérimentalement à un stade précoce. Cependant, les dommages décrits précédemment peuvent présenter un comportement dynamique non linéaire qui peut être exploiter pour surveiller l'apparition d'endommagement par fatigue. Ainsi, les vibrations non-linéaires d'ondes stationnaires dans un l'échantillon de fatigue endommagé sont étudiées dans le contexte de la détection d'endommagement lors d'essais de fatigue ultrasonore. La modélisation de différents phénomènes non linéaires est étudiée à différentes échelles spatiales. Les modèles mésoscopiques d'inclusions microplastiques diffuses et de microfissures se situent à une échelle de longueur du même ordre que la longueur d'onde de la vibration, et sont considérés comme une source potentielle de génération d'harmoniques. L'entrée multi-harmonique fournie par la machine d'essai de fatigue ultrasonique influence de manière significative la sensibilité et le comportement de la génération d'harmoniques des non-linéarités du spécimen. Pour y remédier, un modèle de spécimen de fatigue multi-échelle qui accompagne cette condition limite est utilisé. Le dispositif expérimental est modifié pour inclure un vibromètre laser supplémentaire afin de tenir compte de cet effet. Des algorithmes de traitement du signal permettant l'extraction des paramètres harmoniques expérimentaux sont comparés, et un nouvel algorithme est développé et sélectionné pour sa rapidité et sa précision. Une pénalité non convexe est introduite pour l'identification de systèmes non linéaires guidée par les données, surpassant les algorithmes de pointe existants. Enfin, les signaux de vibration des essais de fatigue par ultrasons des éprouvettes de fatigue en cuivre et en acier dans le régime VHCF sont utilisés pour évaluer la capacité du modèle multi-échelle à modéliser la génération d'harmoniques observée.

Mots clés : Fatigue à très grand nombre de cycles, Génération d'harmoniques d'ordre élevé, Micromécanique, Homogénéisation, Traitement du signal, Dynamique non linéaire, Optimisation.

Abstract : Research into the very high cycle fatigue (VHCF) regime is made possible through the usage of ultrasonic fatigue tests, which can achieve billions of cycles in just a few days. However classical measurement and analysis are insensitive to microplasticity and/or damage (microcracks and microvoids), which eventually lead to fatigue failure. Consequently, these fatigue mechanisms are difficult to detect at early stages. However, the material nonlinearities maybe sensitive to high-frequency loading and exhibit nonlinear behavior such as higher harmonic generation at multiples of the applied frequency. Thus, the standing wave vibration of the fatigue specimen is explored in the context of nonlinear harmonic generation. The modeling of different nonlinear material phenomena is explored at their different length scales. Mesoscopic models of diffuse microplastic inclusions and microcracks are at a length scale of the same order as the vibration wavelength, and is attributed to be a potential source of harmonic generation. The multi-harmonic input given by the ultrasonic fatigue testing machine significantly influences the sensitivity and behavior of harmonic generation of the material nonlinearities. To address this, a multiscale fatigue specimen model which accompanies this boundary condition is employed. The experimental setup is modified to include an additional laser vibrometer to account for this effect. Accurate signal processing algorithms for the extraction of experimental harmonic parameters are benchmarked, and a new algorithm is developed for speed and accuracy. A non-convex penalty is introduced for data-driven sparse nonlinear system identification, surpassing existing state-of-the-art algorithms. Finally, the ultrasonic fatigue test vibration signals from copper and steel fatigue specimens in the VHCF regime are used to assess the multiscale model's ability to model the observed harmonic generation.

Keywords : Very high cycle fatigue, Higher harmonic generation, Micromechanics, Homogenization, Signal processing, Nonlinear dynamics, Optimization.